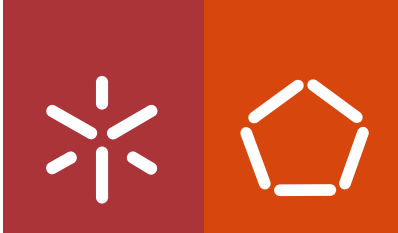**Universidade do Minho**

Escola de Engenharia

Esmaeel Esmaeeli

**Development of Hybrid Composite Plate (HCP) for Strengthening and Repair of RC Structures**

setembro de 2015

**Universidade do Minho**
Escola de Engenharia

Esmaeel Esmaeeli

**Development of Hybrid Composite Plate (HCP) for Strengthening and Repair of RC Structures**

Tese de Doutoramento em Engenharia Civil

Trabalho efetuado sob a orientação do
**Professor Joaquim António Oliveira de Barros**
e do
**Professor Said Jalali**

setembro de 2015

# STATEMENT OF INTEGRITY

I hereby declare having conducted my thesis with integrity. I confirm that I have not used plagiarism or any form of falsification of results in the process of the thesis elaboration.

I further declare that I have fully acknowledged the Code of Ethical Conduct of the University of Minho.

University of Minho, September 30, 2015

Esmaeel Esmaeeli

# ACKNOWLEDGEMENTS

My special thanks to:

Prof. Miguel Azenha, for his kind support when I was involved with a health issue in the second year of my PhD; Lucila for her unconditional support, kindness, suggestions and availability; Hamid, Mahsa, Mohammadreza, Arman, Farank, Rajendra, Konrad, Luisa, Mohammad, Prof. Farhangmehr and others, who I may have forgotten to mention, for their concern and care in the most difficult moments of my life; Nuno and Gianpaolo, who were more than just flat-mates, but friends who will ever remain deep in my heart; Security personnel of Campus de Azurem of Univ. Minho, who with their smiles gave me energy in all those holidays and weekends I was in the laboratory; master students Elizabeth, Luca and Fabio for their joyful collaboration.

I need to appreciate the collaboration of the material suppliers: SIKA, Dow Chemical Co., S&P and Hilti. Finally, the ENDESA Compostilla Power Station in Spain and specifically Mr. Pedro Gómez-Yagüe are greatly acknowledged for providing us generously with Fly Ash.

To My Family

# ABSTRACT

This research work deals with development of a novel retrofitting element for RC structures designated as "Hybrid Composite Plate (HCP)". This prefabricated element is composed of a thin strain hardening cementitious composite (SHCC) plate reinforced with either near surface mounted CFRP (NSM-CFRP) laminates, designated as HCP$^{(L)}$, or externally bonded CFRP (EB-CFRP) sheets, designated as HCP$^{(S)}$. From the material-structural point of view, this system benefits from the high ductility of SHCC and the high tensile strength of CFRP in retrofitting of RC structures. HCP is essentially tailored to be significantly free of the shortcomings identified in the most advanced available retrofitting techniques, such as textile reinforced mortar (TRM) and conventional FRP systems. Furthermore, it is possible to attach this proposed system to the RC members by means of either adhesive, chemical anchors or a combination thereof.

The investigation carried out is mainly dedicated to the development of HCP and assessment of its structural efficiency for upgrading/repairing RC members with a variety of retrofitting demands. In this framework, series of experimental tests are executed to assess HCP retrofitting efficiency for upgrading shear, flexural and energy dissipation capacity of RC members. Results of these experimental tests confirmed HCP's high potential for retrofitting RC structures. An analytical approach is presented to estimate the ultimate flexural capacity of the beams with an HCP attached to their soffit, which is further complemented with a numerical strategy to predict the load-deflection response of such retrofitted beams. The proposed analytical and numerical approaches accurately predict the flexural capacity and load-deflection response, of flexurally strengthened beams using HCP. Finally, adopting a combination of experimental tests and finite element modelling, recommendations for an optimized HCP$^{(L)}$ and its connection with concrete are provided. The local bond stress-slip models at the interface of CFRP-SHCC and interface of HCP$^{(L)}$-concrete are determined. Based on results obtained, equations correlating the pull force capacity of the HCP$^{(L)}$ to the CFRP-SHCC bond length for CFRP laminates with two different axial stiffness are derived.

# RESUMO

Esta tese apresenta a investigação realizada para o desenvolvimento de um novo elemento visando o reforço de estruturas de betão armado (BA) designado por *Hybrid Composite Plate* (HCP). Este elemento consiste num painel pré-fabricado composto por uma fina camada de material de matriz cimentícia apresentando comportamento de endurecimento em tração ( SHCC) reforçada laminados de matriz polimérica reforçada com fibras de carbono (CFRP) inseridos à superfície (*Near Surface Mounted*), designado por HCP$^{(L)}$, ou com manta de CFRP aplicada segundo a técnica de colagem exterior (externally bonded, EB-CFRP), designadas por HCP$^{(S)}$. Do ponto de vista estrutural, este sistema beneficia da alta ductilidade do SHCC e da elevada resistência à tração do CFRP no reforço de estruturas de BA. O HCP afigura-se como uma solução apropriada essencialmente por não apresentar as deficiências identificadas nas técnicas mais avançadas de reforço estrutural atualmente disponíveis, tais como TRM (*Textile Reinforced Mortar*) e sistemas FRP (*Fiber Reinforced Polymer*). O sistema proposto permite uma ligação aos elementos de BA através de resina epóxi, ancoragem química ou uma combinação entre estes. A investigação realizada foi dedicada ao desenvolvimento do HCP e avaliação da sua eficiência estrutural para melhorar ou reparar elementos de BA para uma variedade de exigências de reforço. Com este objetivo, uma série de ensaios foram realizados para avaliar a eficiência do reforço do HCP ao corte, flexão e capacidade de dissipação de energia de elementos de BA. Uma formulação analítica foi desenvolvida para estimar a resistência à flexão de vigas de BA reforçadas com HCP ligado à sua face inferior. Esta abordagem foi completada com um modelo numérico para prever a resposta carga-deformação destas vigas. A formulação analítica e o modelo numérica propostos previram com precisão, respetivamente, a capacidade de flexão e a resposta carga-deformação de vigas reforçadas com HCP. Finalmente, com base na combinação de resultados de ensaios experimentais e modelos de elementos finitos, são fornecidas recomendações para a otimização do HCP$^{(L)}$ e a sua ligação ao betão. Para a caracterização das interfaces CFRP-SHCC betão-HCP$^{(L)}$ foram determinadas leis tensão versus deslizamento. Com base nos resultados obtidos, apresentam-se as equações que relacionam a capacidade de carga à tração do HCP$^{(L)}$ com o comprimento de ligação do CFRP-SHCC composto por camadas de CFRP dotadas de rigidez distinta.

# Table of Contents

# Index of Tables

# Index of Figures

## Index of Symbols

**Uppercase English Letters**

| | |
|---|---|
| $A_f^b$ | Balanced section area of CFRP laminates |
| $A_{sc}$ | Section area of the compression steel reinforcement |
| $A_{st}$ | Section area of the tension steel reinforcement |
| $A_{sh}$ | Section area of SHCC |
| $COD_{cm}^{pc}$ | Composite crack opening displacement corresponding to $f_{cm}^{pc}$ |
| $D_b$ | Diameter of the anchor rods |
| $D_{cm}^{avg}$ | Average spread diameter of slump test on a fresh composite |
| $D_{max}$ | Maximum aggregate size in a concrete mixture |
| $D_m^{avg}$ | Average diameter of the spread of slump test on a mortar mixture |
| $D_{nt}^{II}$ | Shear stiffness for a crack opening and sliding along $n$ and $t$, respectively, in cracking model |
| $E_{4\%}$ | Cumulative dissipated energy at 4% drift |
| $E_b$ | Distance of the anchors from bottom edge of the HCP[(L)] |
| $E_c$ | Modulus of elasticity of concrete |
| $E_f$ | Modulus of elasticity of CFRP laminates |
| $(EI)_{Te}^q$ | Tangential flexural rigidity of each beam's element |
| $E_{sc}$ | Modulus of elasticity of compression steel reinforcement |
| $E_{sh}$ | Modulus of elasticity of SHCC |
| $F_{400}$ | Service load at $\delta_{400}$ |
| $F_{4\%}$ | The residual lateral load carrying capacity at 4% drift |
| $F_{cc}$ | Resultant force in compression concrete |
| $F_{cr}$ | Load at the onset of the first flexural crack in the beam |
| $F_f$ | Resultant force in CFRP laminates |
| $F_m$ | Maximum flexural load of a beam subjected to bending or maximum lateral load of a beam-column joint subjected to lateral cycling loading |

| | |
|---|---|
| $F_p$ | Peak pull force of an HCP[(L)]-RC connection |
| $F_{sc}$ | Resultant force in compression steel rebars |
| $F_{sh}$ | Resultant force in SHCC |
| $F_{st}$ | Resultant force in tension steel bars |
| $F_y$ | Flexural load corresponding to the yield of tension steel reinforcement |
| $F_u$ | Ultimate flexural load of the beam |
| $G$ | Material intact shear modulus in cracking model |
| $G_a$ | Shear modulus of interface adhesive |
| $G_c$ | Debonding fracture energy in traction-separation model |
| $G_d$ | Chemical debonding energy of fibers |
| $G_f^I$ | Material mode I fracture energy |
| $G_{sh}$ | SHCC shear modulus |
| $H_p$ | Height of the HCP[(L)] |
| $H_p^{ef}$ | Effective height of the HCP[(L)] |
| $J_{tip}$ | Matrix crack tip toughness |
| $J_b$ | Complementary energy of fibers-bridging |
| $\mathbf{K}$ | Interfacial elasticity stiffness matrix in traction-separation model |
| $K_s$ | Secant stiffness of beam-column joint at each drift level |
| $K_s^i$ | Initial secant stiffness of beam-column joint |
| $\underline{K}_{Te}^q$ | Tangential stiffness matrix of each beam's element |
| $\underline{K}_{TE}^q$ | Tangential stiffness of the beam |
| $L_u$ | CFRP-SHCC un-bonded length inside the groove |
| $L_b$ | Length of beam in beam-column joint in Chapter 5, or CFRP-SHCC bond length in Chapter 7 |
| $L_b^{ef}$ | Effective CFRP-SHCC bond length |
| $L_c$ | The total length of the top and bottom column between the lateral supports |
| $L_s$ | Beam's supporting span |

| | |
|---|---|
| $M$ | Bending moment at any given curvature ($\chi$) |
| $M_e^q$ | Bending moment at the centroid of each element after each $\Delta F^q$ |
| $M_R$ | Maximum resisting bending moment |
| $M^R$ and $M^L$ | The values of the internal bending moment developed at the beam-column interfaces of the right and the left beam, respectively |
| $N_b$ | Number of chemical anchors |
| $N_R$ | Number of repeated tests |
| $P$ | Flow function of CDP model |
| $S_g$ | Distance between adjacent anchor and groove |
| $T$ | Composite flow time out of V-funnel |
| U | fiber's loaded-end displacement during pulling out from the matrix |
| $V_c$ | Column shear force |
| $V_f$ | Volume fraction of fibers in a composite |
| $\left(V_f^{crit}\right)_{tension}$ | Critical volume fraction of fibers in a composite to achieve a tensile strain hardening response |
| $\left(V_f^{crit}\right)_{bending}$ | Critical volume fraction of fibers in a composite to achieve a deflection hardening response |
| $X_i$ | Distance of center of slice $i$ from the fixed end of the element |
| $\chi$ | Curvature of a beam's section |
| $W_p$ | Width of the HCP$^{(L)}$ |
| $W_p^{ef}$ | Effective width of the HCP$^{(L)}$ |

**Lowercase English Letters**

| | |
|---|---|
| $a$ | Distance of resultant compressive force from neutral axis |
| $b$ | Width of beam |
| $d$ | Damage parameter in CDP and traction-separation models |
| $d'$ | Distance between the centroid of compression steel and the extreme concrete compressive fiber |

| | |
|---|---|
| $d_c^{js}$ | Contribution of joint panel in lateral displacement at the loaded section of the superior column |
| $d_c^{flb}$ | Contribution of flexural deformations in lateral displacement of the loaded section of the superior column |
| $d^{fl,e}$ | The flexural deformation at the end of the element |
| $d_f$ | Fiber's diameter in Chapter 3 // Distance between centroid of CFRP laminates and the extreme compressive fiber in Chapter 6 |
| $d_i$ | The distance between DTs |
| $d_m$ | Drift value corresponding to $F_m$ |
| $d_y$ | Displacement corresponding to the yield load in equivalent elastoplastic response of lateral load versus displacement of beam-column joint |
| $d_u$ | Ultimate lateral displacement in equivalent elastoplastic response of lateral load versus displacement of beam-column joint |
| $d_{sh}$ | Distance between centroid of SHCC and the extreme compressive fiber |
| $d_{st}$ | Distance between centroid of tension steel rebars and the extreme compressive fiber |
| $f_c'$ | Composite compressive strength |
| $f_{cc}$ | Compressive stress in concrete |
| $f_{cd}$ | Concrete compressive design strength |
| $f_{cc}^m$ | Mean compressive strength of concrete cylinder |
| $f_{cc}^t$ | Strain in the extreme compressive fiber of the concrete |
| $f_{cm}^{cr}$ | Stress at composite first crack initiation |
| $f_{cm}^{pc}$ | Composite post-cracking tensile strength |
| $f_{ct}$ | Tensile stress in concrete |
| $f_{ct}^{cr}$ | Concrete uniaxial tensile strength (stress at tensile cracking) |
| $f_f$ | Stress in CFRP |
| $f_f^r$ | Rupture stress of CFRP |
| $f_{sc}^y$ | Yield strength of compression steel bars |

| | |
|---|---|
| $f_{sh}$ | Stress in SHCC |
| $f_{sh}^{cr}$ | Cracking strength of SHCC (tensile stress at the onset of first crack) |
| $f_{sh}^{u}$ | Ultimate tensile strength of SHCC |
| $f_{st}$ | Stress at tension steel rebars |
| $f_{st}^{y}$ | Yield strength of tensile steel bars |
| $f_{st}^{u}$ | Ultimate (maximum) tensile strength of tension steel bars |
| $h_b$ | Overall depth of beam's section |
| $h_c$ | Overall depth of column's section |
| $l_b$ | Length of beam between supporting-end and intersection with the column |
| $l_c$ | Length of column between supporting-end and intersection with the beam |
| $l_{cr}$ | Element's characteristic length (crack band width) |
| $l_d$ | Debonded length of fiber |
| $l_d$ | Initial distance between supporting points of DT |
| $l_e$ | Embedded length of a fiber in a matrix |
| $l_f$ | Fiber's length |
| $n$ | Depth of natural axis of a beam's section |
| $p(\emptyset)$ | Probability density function of fibers' orientation angle |
| $p(z)$ | Probability density function of fibers' centroidal distance from the crack plan |
| $\bar{p}$ | Mises equivalent effective stress |
| $\bar{q}$ | Mises equivalent effective hydrostatic pressure |
| $t_a$ | Adhesive thickness at interface zone |
| $t_n$ | Normal traction component (along $n$) in traction- separation model |
| $t_p$ | HCP$^{(L)}$ thickness |
| $t_s$ | Transverse traction component (along $s$) in traction-separation model |

| | |
|---|---|
| $t_{sh}$ | Thickness of SHCC remained bonded to the concrete after a cohesive failure |
| $t_t$ | Transverse traction component (along $t$) of traction-separation model |
| $u$ | Separation in traction-separation constitutive model |
| $\underline{u}^q$ | Matrix of nodal displacements |
| $w$ | Crack width |
| $w_0$ | Crack width at which the tensile stresses cannot be any further transferred |

**Uppercase Greek Letters**

| | |
|---|---|
| $\Delta_1$ and $\Delta_2$ | The shortening and elongation measured by pair of diagonal DTs installed in the joint region |
| $\Delta_d$ | The elongation of diagonal LVDT installed in shear span of short-span beam |
| $\Delta_i^t$ and $\Delta_i^b$ | The measures of each of two DTs installed on slice $i$ of beam-column joint |
| $\Delta F^q$ | Load increment |
| $\Delta \underline{u}^q$ | Increment in deflection of the beam at each $\Delta F^q$ |

**Lowercase Greek Letters**

| | |
|---|---|
| $\alpha_{4\%}$ | Average degradation in peak load at 4% drift |
| $\gamma_{nt}^{cr}$ | Total shear strain caused by a crack opening and sliding along $n$ and $t$, respectively, in cracking model |
| $\gamma_s$ | Tangential strain component (along $s$) in traction-separation model |
| $\gamma_t$ | Tangential strain component (along $t$) in traction- separation model |
| $\gamma_j$ | Shear distortion in the joint panel |
| $\delta$ | Mid-span deflection at each given load |

| | |
|---|---|
| $\delta_{cr}$ | mid-span deflections at the onset of the first crack |
| $\delta_m$ | Mid-span deflection corresponding to the beam's maximum flexural load |
| $\delta_y$ | Mid-span deflections corresponding to the yield of the beam's tension rebars |
| $\delta_u$ | Mid-span deflection corresponding to the beam's ultimate flexural load |
| $\varepsilon_{cc}$ | Compressive strain in concrete |
| $\varepsilon_{cc}^m$ | Strain corresponding to the concrete compressive strength |
| $\varepsilon_{cc}^t$ | Compressive strain in extreme fiber of concrete |
| $\varepsilon_{cc}^u$ | Ultimate concrete compressive strain |
| $\varepsilon_{cr}$ | Tensile strain at first cracking in composite |
| $\varepsilon^{cr}$ | Cracking strain in CDP model |
| $\varepsilon_{ct}$ | Concrete tensile strain |
| $\varepsilon_{ct}^{cr}$ | Strain corresponding to the onset of tensile cracking in concrete |
| $\varepsilon_f$ | Strain in CFRP laminates |
| $\varepsilon_f^r$ | Strain corresponding to the rupture of CFRP laminates |
| $\tilde{\varepsilon}_{cc}^{in}$ | Inelastic compression strain in CDP Model |
| $\tilde{\varepsilon}_{cc}^{pl}$ | Plastic strain in compression in CDP Model |
| $\tilde{\varepsilon}_{ct}^{cr}$ | Tensile cracking strain in CDP Model |
| $\tilde{\varepsilon}_{ct}^{pl}$ | Tension plastic strain in CDP Model |
| $\varepsilon_n^{cr}$ | Normal crack opening strain in cracking model |
| $\varepsilon_{n,max}^{cr}$ | Strain corresponding to a fully open crack in cracking model |
| $\varepsilon_{sc}$ | Strain at the compression steel reinforcement |
| $\varepsilon_{sc}^y$ | Strain corresponding to the yield of compression steel reinforcement |
| $\varepsilon_{sh}$ | Strain at the centroid of the SHCC |
| $\varepsilon_{sh}^{cr}$ | Strain at the first tensile crack in SHCC |
| $\varepsilon_{sh}^u$ | Strain at the ultimate tensile strength of SHCC (tensile strain capacity of SHCC) |

| $\varepsilon_{st}$ | Strain in tension steel reinforcement |
| $\varepsilon_{st}^{y}$ | Strain corresponding to the yield of tension steel reinforcement |
| $\varepsilon_{st}^{sh}$ | Strain at the onset of pseudo strain-hardening in the steel reinforcement |
| $\varepsilon_{st}^{u}$ | Strain corresponding to the tensile strength of the steel reinforcement |
| $\varepsilon_{u}$ | Strain corresponding to composite ultimate tensile strength ($\sigma_u$) |
| $\epsilon$ | Flow potential eccentricity used in CDP model |
| $\theta_i^R$ | Relative rotation between sections at the extremities of each slice |
| $\theta_j$ | Absolute value of rotation at extremities of the slices |
| $\mu$ | User-defined shear retention factor |
| $\mu_d$ | Lateral displacement ductility factor for a beam-column joint |
| $\mu_\delta$ | Deflection ductility factor of a beam subjected to bending |
| $\mu_\varphi$ | Curvature Ductility Index |
| $\tau_0$ | Fiber-matrix frictional bond |
| $\tau_{nt}$ | Total shear stress in plane $n$ and along $t$ in cracking model |
| $\varphi_y$ | Curvature at the yield of tension rebars of a beam's section |
| $\varphi_u$ | Ultimate curvature of a beam's section |
| $\psi$ | Dilation angle of concrete in CDP model |

# Chapter 1: Introduction

## 1.1 Background

The deterioration or deficient functioning of reinforced concrete (RC) structures can be caused by ageing effects on its intervening materials, design and/or construction inaccuracies, or loading conditions not considered in the design phase. To restore, or even to increase the aimed working performance for this type of structures, fiber reinforced polymer (FRP) systems have been used with appreciable success during the last 25 years, mainly due to the well-known advantages of these materials (e.g., lightness and high tensile strength) and the associated strengthening techniques (easy and fast application, small interference on the dimensions of the structure to be retrofitted) [1-3].

Externally Bonded FRP sheets (EB-FRP) and Near Surface Mounted strips/rods of FRP (NSM-FRP), are the most common FRP-based techniques used for the strengthening of existing RC structures. According to these techniques, in an EB-FRP system the fabric/laminate is bonded to the external face of the RC element to be strengthened, while, in the NSM system FRP laminates/rods are bonded into the pre-sawn grooves on the concrete cover of the element.

In FRP-based strengthening techniques, epoxy resin is often used as both the polymeric matrix of FRP composite and the adhesive to bond FRP system to the substrate. Although epoxy resin assures a relatively high bond strength at the interface of FRP and the concrete member, durability of resin epoxies and their performance at high temperatures (higher than glass transition temperature of epoxy, $T_g$) are the concerns that need to be properly addressed for a an even more extensive use of FRP-based retrofitting systems [4-6].

Moreover, premature failure of FRP systems, due to debonding from the substrate or detachment of concrete cover (rip-off), restricts the maximum tensile strain that these systems can sustain. These shortcomings cause a severe FRP material underutilization, since to assure a safe FRP-to-concrete interface performance, the design FRP strain is limited to a fraction of its ultimate tensile capacity. This fraction of FRP tensile capacity can be even less than 25% [7].

The other issue, mainly associated with exposed FRP systems, is their vulnerability against vandalism and impact loads.

It should be noted that although the abovementioned shortcomings are of less concern in the case of NSM-FRP, this technique has lower application versatility than EB-FRP. In fact, the number and shape of the FRPs in NSM technique are limited to the depth of the concrete cover, and in the case of flexural strengthening also to the width of the element to be retrofitted. Furthermore, cutting grooves in the NSM technique not only involves the risk of introducing damages to the internal reinforcements of an RC member, but also can result in weakening of the concrete cover.

In an effort to delay or overcome the debonding/detachment issue in EBR system, various configurations of mechanical anchors have been studied by different researchers [8, 9]. These mechanical anchors are often made of either metallic or FRP materials. Metallic based anchors not only involve the possibility of corrosion, they may also cause stress concentration at the anchored regions, and consequently promote the risk of premature rupture of the strengthening layer. If mechanical anchors are made of FRPs, they are susceptible to the aforementioned drawbacks of FRP systems, e.g. vulnerability against vandalism, and the risk of degradation in mechanical properties of the bonding epoxy resin due to the high temperature or attacking of harmful chemicals.

Mechanically Fastened FRP (MF-FRP) systems have been proposed as an alternative to adhesively bonded FRPs, mainly developed to be a rapid retrofitting technique for RC members [10-12]. According to this technique, pre-cured FRP laminates with an enhanced bearing capacity are attached to the concrete substrate by means of mechanical fasteners, without applying any adhesive at the FRP-Concrete interface. When compared to adhesively bonded FRP systems, the MF-FRP technique is a promising retrofitting approach, since it provides rapid installation, higher ductility, and potentially higher FRP-RC connection durability. However, some concerns can still be underlined, such as limitation in stress transfer between concrete and FRP (depends on the number and strength of the installed discrete fasteners and the quality of concrete cover), the potential of galvanic corrosion of the fasteners in contact with carbon FRP laminate, and the reliability of the FRP laminate yet exposed to the environmental conditions and vandalism.

Replacing epoxy resin of an FRP system with cementitious matrix is one of the most recent efforts to alleviate shortcomings associated with the bonding agents in FRP systems. In the case of using conventional fiber sheets, despite epoxy resin, the granular inherent of cementitious matrices is not appropriate for penetration and impregnation of fiber sheets, hence, achieving a strong interface bond between fibers and matrix remains a challenge. Therefore, in this recently developed system, textiles or fiber grids are used in place of fiber sheets to enhance the composite action between the cementitious matrix and the fabric through an interlocking mechanism.

Depending on the structure of the fabric, the type of the cementitious matrix and the application technique, these systems are designated in literature as Textile Reinforced Mortar or Textile Reinforced Concrete (TRM or TRC) [13-15], Fabric Reinforced Cementitious Matrix (FRCM) [16] and Mineral Based Composites (MBC) [17]. Hereafter, for the sake of convenience, the designation of TRM is used to refer to all different types of this cement based retrofitting composite.

Although, TRMs are free of FRP's deficiencies such as a poor performance of epoxy resin at high temperatures and the vulnerability of the exposed FRPs to vandalism or impact loads, premature debonding either at the interface between cementitious matrix and the retrofitted member, or between the matrix and the fibers restricts their retrofitting efficiency [14, 15]. Furthermore, TRMs are highly deformable, which is favorable to increase ductility and energy dissipation capacity of the upgraded/repaired elements subjected to extreme loading conditions, but their excessive deflection and wide crack openings adversely affect the efficiency of these systems in enhancing serviceability functions of the upgraded/repaired concrete structures.

The risk of drying shrinkage of the fresh cementitious matrix in contact with the concrete substrate is another concern regarding the use of TRMs in retrofitting designs. Finally, as compared to the installation process of FRP systems, applying several layers of fabrics in TRM increases the in-situ workmanship job, which in consequence causes higher retrofitting costs.

## 1.2 Motivations

While the need to repair and upgrade the existing structures is an ongoing demand, sustainability and reliability of the intervening elements play a significant role in long-term cost-efficiency of retrofitting proposals, prolonging the serviceability of the structure to be retrofitted.

Moreover, in general, the concrete cover of aged and deteriorated RC members has a poor condition, e.g. cracked and/or spalled concrete covers due to the long-term creep of RC elements and/or expansion of their corroded steel reinforcements. To achieve effective performance of the externally bonded strengthening elements, the deficient concrete covers should be firstly either repaired or replaced. However, even after repairing/replacing, the concrete cover often acts as the weakest link in the shear stress transference path between the concrete member and the retrofitting scheme. Hence, the connection of an external retrofitting system should be capable of safely mobilizing the strengthening potential of the retrofitting layer to the member subjected to the upgrade/repair. This aim can be attained if the bearing capacity of the strengthening element is sufficient to mobilize the developed forces, even if partially, through shearing and bending of the anchor rods to the core concrete of the retrofitted member. Therefore, if such strengthening elements are attached to members possessing poor concrete cover, a combination of anchor rods and adhesive is most likely suitable to avoid a very premature failure at the interlayers shear transference path.

Finally, to achieve a robust retrofitting solution, the feasibility of in-situ application of the intervening elements, including the required time and skill for their installation, should be combined with the above-mentioned features (durability and reliability). However, to date, none of the existing retrofitting techniques offers these features integrated, which indicates the need of developing new sustainable strengthening systems.

## 1.3 Thesis Objectives and Methodology

The present research work proposes to study a novel retrofitting element, author has designated as "Hybrid Composite Plate (HCP)", which combines the potential structural effectiveness of prefabricated plates made of Strain Hardening Cementitious Composite (SHCC) with Carbon FRP (CFRP) for the retrofitting practices.

HCP constituents are selected and tailored aiming to achieve an alternative solution to the conventional applications of FRP systems, offering a higher durability, enduring temperatures relatively higher than $T_g$ (with marginal degradation), providing the capability of being attached to the concrete substrate by means of anchor rods, adhesive or a combination thereof, and finally, assuring an in-situ installation feasibility.

Therefore, in alignment with the objectives outlined above, the present research work is dedicated to the development of HCP and assessing its constructability, applicability, and retrofitting efficiency for upgrading and repairing RC members. To this end, initially, two different configurations of HCP are developed and their retrofitting efficiency is assessed, within a preliminary study, by means of the three-point bending tests carried out on shear-critical short RC beams. The shear capacity of these beams is upgraded adopting different retrofitting schemes, including each of the proposed HCPs. The results of these experimental tests are analyzed and compared to each other and to those obtained by testing reference specimens in order to evaluate shear retrofitting potential of the proposed schemes. In this phase of study, the fabrication process of each HCPs (including developing SHCC), techniques to attach these elements to the RC members and their retrofitting efficiency are evaluated.

Furthermore, this research work is continued with the assessment of the HCP retrofitting efficiency in enhancing seismic performance of full-scale damaged RC beam-column joints, and also upgrading flexural capacity of relatively large-scale RC beams. Moreover, analytical and numerical approaches are proposed to predict the performance of flexurally retrofitted RC beams using HCP.

Finally, based on a combination of experimental and numerical approaches, optimizing HCP and its connection with RC elements are investigated.

## 1.4 Thesis Organization

Including the present chapter, this thesis is composed of eight chapters and an annex, described briefly below:

**Chapter 2** is a literature review on the applications of FRP as the most common to date retrofitting solution for the existing RC members. This chapter reviews different FRP strengthening techniques and highlights their known advantages and shortcomings.

**Chapter 3** is an introduction on SHCC, its micromechanical design concept, durability and applications.

**Chapter 4** discusses the methodology adopted to develop HCP and verifies its constructability and applicability as a prefabricated retrofitting solution. Two different types of HCPs- HCP$^{(S)}$ and HCP$^{(L)}$- are proposed and developed. Further in this chapter, the methodology used for SHCC processing and characterizing, for the purpose being used for development of HCP, is described. Finally, through a series of preliminary experimental tests on short-span shear-critical RC beams, the strengthening effectiveness of both types of HCPs is assessed and discussed.

**Chapter 5** addresses the assessment of effectiveness of HCP for upgrading the energy dissipation capacity of the RC elements, required for example in the case of structures deficient against seismic action. This aim is achieved with experimental investigations on the cyclic performance of damaged full-scale interior RC beam-column joints repaired by attaching HCPs at their critical regions. Moreover, counterpart's specimens repaired using a cast-in-place solution were tested. Results of these two test series are compared to verify the influence of interface bond between the strengthening scheme and the concrete substrate on global seismic performance of the repaired specimens.

**Chapter 6** is dedicated to the assessment of the effectiveness of the HCP$^{(L)}$ for the flexural strengthening of under-reinforced RC beams. Series of these beams strengthened with different configurations of HCP$^{(L)}$ and a variety of attaching techniques, are experimentally tested under four point bending. To verify the effectiveness of HCP$^{(L)}$ as a flexural strengthening scheme, the performances of these beams are compared with each other and with that of the as-built RC beam. Flexural performance of the retrofitted beams adopting different HCP$^{(L)}$ connection systems are also compared to assess the influence of the attaching technique. Moreover, within this chapter, an analytical and a numerical approach to predict the flexural performance of HCP$^{(L)}$ strengthened RC beams are presented.

**Chapter 7** is focused on optimizing the constituents of HCP$^{(L)}$ and its connection system for retrofitting of RC members. Initially, the behavior of connections between the FRP laminate and the SHCC plate, and also between the HCP and the RC block is studied through a combination of experimental tests and finite element analysis on the models of pull-out connection. Finally, finite element models are used to optimize both HCP$^{(L)}$ and its connection to the RC elements.

**Chapter 8** summarizes the most relevant conclusions regarding development and applications of HCP in this research work. It also identifies advantages and shortcomings of this proposed retrofitting technique, and recommends further researches needs to be carried out as the extension of present research work.

**Annex A** represents the VBA-code written to numerically predict moment-curvature of a composite beam-section

**Bibliography**

[1] Teng J, Chen J, Smith ST, Lam L. Behaviour and strength of FRP-strengthened RC structures: a state-of-the-art review. Proceedings of the ICE-Structures and Buildings. 2003;156(1):51-62.

[2] Kachlakev D, McCurry DD. Behavior of full-scale reinforced concrete beams retrofitted for shear and flexural with FRP laminates. Composites Part B: Engineering. 2000;31(6–7):445-52.

[3] De Lorenzis L, Teng JG. Near-surface mounted FRP reinforcement: An emerging technique for strengthening structures. Composites Part B: Engineering. 2007;38(2):119-43.

[4] Shrestha J, Ueda T, Zhang D. Durability of FRP Concrete Bonds and Its Constituent Properties under the Influence of Moisture Conditions. Journal of Materials in Civil Engineering. 2014 (Special Issue):A4014009.

[5] Burke PJ, Bisby LA, Green MF. Effects of elevated temperature on near surface mounted and externally bonded FRP strengthening systems for concrete. Cement and Concrete Composites. 2013;35(1):190-9.

[6] Benmokrane B, Mohamed HM. Durability Issues of FRP for Civil Infrastructure. In: 11th International Symposium on Fiber Reinforced Polymers for Reinforced Concrete Structures (FRPRCS11). Guimaraes; 2013:11-4.

[7] ACI 440.2R-08:2008. Guide for the Design and Construction of Externally Bonded FRP Systems for Strengthening Concrete Structures: American Concrete Institute.

[8] Brena SF, Bramblett RM, Wood SL, Kreger ME. Increasing Flexural Capacity of Reinforced Concrete Beams Using Carbon Fiber-Reinforced Polymer Composites. ACI Structural Journal. 2003;100(1).

[9] Grelle SV, Sneed LH. Review of anchorage systems for externally bonded FRP laminates. International Journal of Concrete Structures and Materials. 2013;7(1):17-33.

[10] Arora D. Rapid Strengthening of Reinforced Concrete Bridge with Mechanically Fastened - Fiber Reinforced Polymer Strips [MSc Thesis]: University of Wisconsin – Madison; 2003.

[11] Lamanna AJ, Bank LC, Borowicz DT. Mechanically fastened FRP strengthening of large scale RC bridge T beams. Advances in structural engineering. 2004;7(6):525-38.

[12] Bank LC, Borowicz DT, Lamanna AJ, Ray JC, Velazquez GI. Rapid strengthening of full-sized concrete beams with powder-actuated fastening systems and Fiber-Reinforced Polymer (FRP) composite materials. DTIC Document; 2002.

[13] Brückner A, Ortlepp R, Curbach M. Textile reinforced concrete for strengthening in bending and shear. Materials and Structures. 2006;39(8):741-8.

[14] Triantafillou TC, Papanicolaou CG. Textile Reinforced Mortars (TRM) versus Fiber Reinforced Polymers (FRP) as Strengthening Materials of Concrete Structures. ACI Special Publication. 2005;230:99-118.

[15] Tetta ZC, Koutas LN, Bournas DA. Textile-reinforced mortar (TRM) versus fiber-reinforced polymers (FRP) in shear strengthening of concrete beams. Composites Part B: Engineering. 2015;77:338-48.

[16] Azam R, Soudki K. FRCM Strengthening of Shear-Critical RC Beams. Journal of Composites for Construction. 2014;18(5).

[17] Täljsten B, Blanksvärd T. Mineral-Based Bonding of Carbon FRP to Strengthen Concrete Structures. Journal of Composites for Construction. 2007;11(2):120-8.

## Chapter 2: FRP for Retrofitting of RC Structures

## 2.1 Introduction

Fiber Reinforced Polymers (FRPs) are composed of a polymeric matrix that is reinforced with fibers, with a wide range of applicability from aerospace industry to constructional practices. The most commercially available FRPs for structural applications are comprised of continuous fibers of carbon, glass, or aramid. Thermosetting polymers such as epoxy and vinyl-ester are often used as the polymeric matrix for these systems. Depending on the type of structural application, FRP systems can be delivered as a dry-fabric or a pre-cured composite. A dry fabric is impregnated with epoxy resin in job-site, which provides feasibility to its wet layup application for different structural shapes. This FRP application procedure is designated "wet-layup". FRP laminates (strips) and bars are the examples of pre-cured FRP systems. FRP laminates are often supplied in a roll of thin strip with a variety of widths and thicknesses, upon the request of the designer, and they are generally used in retrofitting applications of structural members. FRP rods are utilized as both a constructional member, for example as a replacement of reinforcing steel rebars, and a retrofitting element.

Nowadays it is widely accepted that FRPs are an efficient retrofitting alternative for reinforced concrete (RC) elements, in place of externally bonded steel plates as a traditional retrofitting technique [1-4]. While corrosion deficiency of steel plates, their high weight, and their poor interfacial bond performance with concrete substrate are generally characterized as the major shortcomings of externally bonded steel plates, FRP materials offer a high tensile strength-to-weight ratio, corrosion resistance, and application versatility.

Depending on the technique employed to enhance the load carrying capacity of an RC structural member, FRP strengthening systems can be categorized in three groups: Externally Bonded FRP sheets/laminates (EB-FRP), Near Surface Mounted FRP laminate/rods (NSM-FRP) and Multi-Fastened FRP laminates (MF-FRP). A description of each of these techniques can be found in the following section.

As listed below, there are also concerns regarding the performance of FRP materials for the strengthening applications [5-8], however, depending on the adopted attaching technique the impact of these concerns for the strengthening of RC elements may be varied:

(i) Premature failure due to debonding/detachment from the retrofitted substrate that limits the effective utilization of FRP capacity. In most of the experiments on the strengthened RC elements, debonding of FRP at a strain much lower than its tensile capacity (rupture) is reported;

(ii) The bond performance of FRP systems subjected to elevated temperatures (higher than glass transition temperature of epoxy, $T_g$) deteriorates rapidly;

(iii) The bond strength is also susceptible to degradation by a long-time exposure to severe environmental conditions, hence arising durability concerns;

(iv) Finally, exposed FRPs are vulnerable against vandalism.

Another issue, which may not be categorized as a concern but as an unsatisfactory performance, is related to the linear-elastic behavior of FRP composites up to their tensile rupture. This linearity of the tensile response of FRP materials, adversely affects the ductility of the retrofitted elements, and restricts the effectiveness of this retrofitting solution if utilized for enhancing the energy dissipation capacity of the structural elements.

To achieve a secure FRP-to-concrete stress transfer through the contact bond, allowable FRP strain should be lowered as the degree of strengthening demand increases [9]. Therefore, low level of FRP strengthening efficiency is expected if higher modulus fibers and multiple composite layers are used.

Since issues related to both the premature debonding/detachment and the procedures resulting in weakening of FRP bonded systems are still under study, they are not yet well identified or formulated. Consequently, most of the design codes impose relatively large reduction parameters to limit the maximum strain development in FRP systems, aiming at providing a higher reliability for applications of this strengthening technique, e.g. ACI 440.2R-08 [10]. To maintain a reliable FRP-to-concrete bond stress, the strain restriction in the case of using high stiffness strengthening layer (e.g. multi-ply FRPs), can be even less than 25% of the FRP rupture strain that results in a too conservative utilization of the FRP

strengthening potential [9]. Obviously, this approach affects sustainability of FRP composites based retrofitting solutions by increasing the eventual cost of designed schemes.

Anchorage of the FRP (mechanical anchoring or other means) is a technique to significantly improve the efficiency of FRP systems, hence, providing a solution to premature debonding/detachment. Nonetheless, taking into account brittleness and anisotropic nature of FRPs, anchoring these composites is a challenge. Moreover, the data available regarding the performance of these systems is still too limited to propose design strategies. Hence, according to most of the FRP strengthening design codes (for example [10]) an extensive examination on the anchorage performance before field implementation is compulsory.

In this chapter, a literature review on FRP applications for flexural strengthening of RC beams and also enhancing seismic characteristics of RC beam-column joints are presented. Common FRP strengthening techniques and their general failure modes are introduced. Moreover, a review on most to-date researched anchorage systems for externally bonded FRPs together with a description of their advantages and shortcomings are available.

## 2.2 FRP for Flexural Strengthening of RC Beams

For the purpose of flexural strengthening, apart from the strengthening technique, the FRP material will be attached to the tension face (or into the grooves pre-sawn in this face) of the RC beam to have its maximum efficiency in enhancing load carrying capacity of the retrofitted member. Rarely, FRP is also attached to the lower parts of the lateral faces of the beam, especially when its bottom face is not readily accessible and achieving a high increase in ultimate flexural capacity is not a design objective.

Following, a description on each of these FRP strengthening techniques combined with a literature review on their applications and practical challenges for enhancing flexural performance of RC beams can be found.

### 2.2.1 Externally Bonded FRP Systems (EB-FRP)

One of the concerns in the application of FRP adhesively bonded to the external faces of RC members is the restriction in developing the full capacity of the strengthening composite

due to a premature debonding/detachment (see Figure 2.1) [11-14]. Debonding occurs either at the interface of the adhesive and the FRP, at the interface of the adhesive and the concrete, or by the cohesive failure of the adhesive material itself. On the other hand, detachment is identified when a horizontal crack progresses in concrete cover, often below the longitudinal tension steel bars, causing the separation of the FRP together with a layer of concrete cover bonded to it. Although a number of experimental and theoretical investigations have been conducted, the fully understanding of the mechanism of debonding/detachment is not yet a reality.

FRP inter-layers delamination, which is associated with employing multi layers of bonded fabrics in the strengthening layout, can also be mentioned as another recognized premature failure mode of this strengthening system.

As presented in Figure 2.1, the occurrence of any of these three failure modes (debonding, detachment or delamination) and their progress path follows the least resistant link in a FRP-RC joint. As a consequence of a sudden energy release, all of these failure modes are quite brittle; hence, there is a lack of warning at the failure of the retrofitted element. FRP debonding is the most brittle failure and it can be avoided/delayed up to a great extent by the choice of an appropriate FRP-to-concrete bond adhesive, the proper surface preparation of concrete substrate, by extending the FRP reinforcement as close as possible to the supports of the beam, or using appropriate anchorages [15, 16].

Teng et al. [17] classified the observed failure modes of EB-FRP flexurally strengthened RC beams in two main categories: (i) flexural failure at critical section that includes either FRP rupture or crushing of concrete in a compression block (Figure 2.2), and (ii) FRP plate separation (Figures 2.3 and 2.4). The flexural failure preserves composite action between the FRP layer and the RC beam almost up to the ultimate failure load, while in the FRP plate separation failure the loss of composite action restricts the ultimate load carrying capacity of the strengthened beam. Considering that nowadays structural adhesives are available, and proper preparation of concrete substrate is a mandatory job-site, Teng et al. [17] stated that FRP plate separation often occurs in the form of concrete cover detachment.
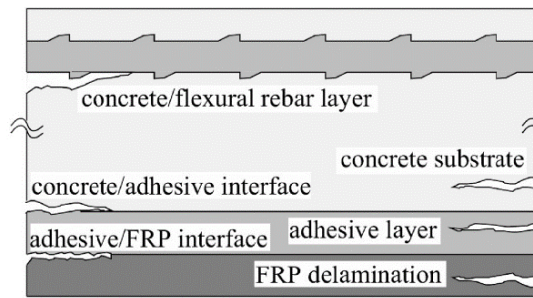
Figure 2.1: Possible types of premature failure in an FRP strengthened RC element [15]
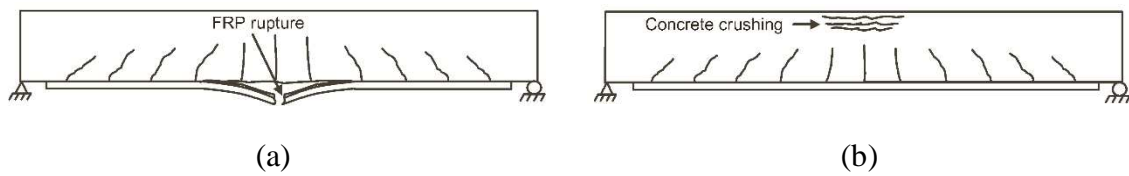


Figure 2.2: Flexural failure of FRP strengthened beams at critical sections (a) FRP rupture, and (b) concrete crushing, [17].
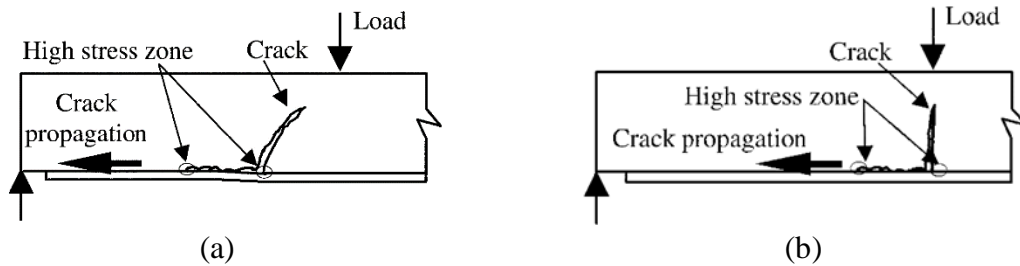


Figure 2.3: Intermediate crack (IC) induced debonding/detachment initiated at location of (a) flexural-shear crack, and (b) flexural crack, [7].

Locations of high stress concentration, such as flexural or flexural-shear cracks, are potentials for the onset of debonding/detachment. As presented in Figure 2.4, the debonding/detachment, originated at the location of these cracks, progresses towards the beam's support. This type of concrete failure is often called "intermediate crack (IC) induced debonding/detachment" in the literature.

Typically in RC beams with a short and thick layer of FRP bonded to their soffit, debonding/detachment may initiate at the termination of the FRP plate and will progress

towards the mid-span in each of the different modes illustrated in Figure 2.4a to Figure 2.4e and listed below as well [18, 19]:

(a) FRP debonding initiated at a critical diagonal crack (CDC) (Figure 2.4a);

(b) CDC debonding together with concrete cover detachment (Figure 2.4b);

(c) Detachment of concrete cover initiated at the termination sections of FRP (concrete cover rip-off) (Figure 2.4c and Figure 2.4d);

(e) Interfacial debonding at the end of the FRP plate (end-peeling) (Figure 2.4e).



(a)

(b)

(c)

(d)

(e)
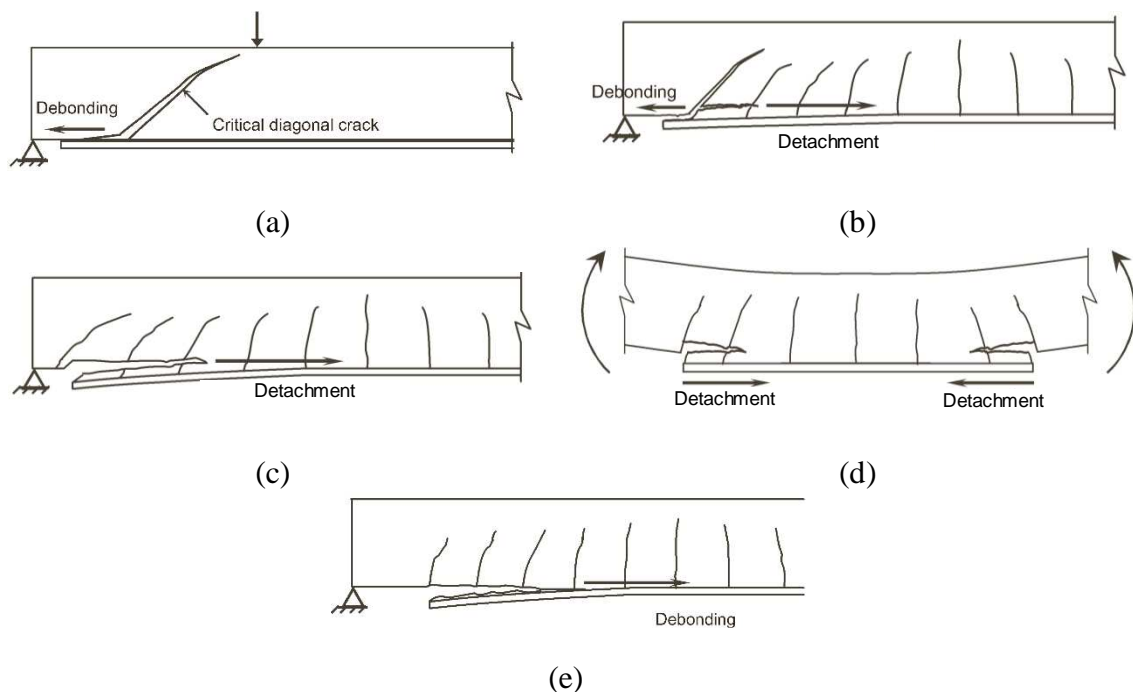
Figure 2.4: Premature failure modes associated with FRP debonding/detachment: (a) FRP debonding initiated at a critical diagonal crack (CDC), (b) CDC debonding together with concrete cover detachment, (c) and (d) detachment of concrete cover initiated at the ends of FRP plate (concrete cover rip-off) , (e) interfacial debonding at the end of the plate (end-peeling) (represented with modification from [17]).

Aiming to delay/prevent the premature debonding/detachment of the strengthening layer and, therefore, achieving a material cost efficiency by exploiting a higher level of

strengthening potential of bonded FRP composite, several researchers have proposed and investigated the applications of mechanical anchors [16, 20-23]. Metallic anchors, U-jackets or wrap configuration of FRPs, and FRP spikes (FRP anchors) can be exemplified as the most studied anchorage systems.

Depending on the expected debonding/detachment mechanism, each of these anchorage systems may be installed either close to the terminated ends of the strengthening FRP, or distributed along the strengthened span of the beam to prevent/delay the debonding/detachment failure modes indicated in Figure 2.3 and Figure 2.4. Continuous U-jacket or wrap of FRP bonded along the retrofitted span can be also adopted if its performance efficiency justifies the increased retrofitting cost [24]. As compared to the behavior of flexurally retrofitted beams based on FRP bonding without any anchorage system, in general, the benefit of adding continuous FRP anchor is more notable in preserving a higher ductility than enhancing the load carrying capacity [25]. Following, a review on each of these anchorage systems, their performance, and their advantages or shortcomings, where applicable, is presented.

### 2.2.1.1 Metallic anchorage systems

Steel anchors were found to be the most effective solution to suppress premature debonding/detachment associated with EB-FRP strengthening technique, since they have high stiffness, and if secured with fasteners, effectively contribute in both tensile and shear resisting mechanisms [22]. However, this solution is labor intensive, costly, and its durability issues (such as galvanic corrosion between steel and CFRP, and the possible electrochemical oxidation) remains of concern.

Based on the results of four point bending tests on both flexurally strengthened beams and the as-built one (reference beam), Spadea et al. [26] indicated that bonding U-Shaped steel anchorages at the ends and along the CFRP retrofitted span of the flexurally strengthened beam results in a notable enhancement in composite action between FRP and beam up to very close the ultimate load. According to their investigation, the low utilization of the tensile capacity of the bonded FRP without any anchorage system, only 50%, shifted to 86% when an appropriate layout of the U-Shaped steel anchorages was implemented. This improvement in material usage efficiency provided a 32% increase over the flexural load

carrying capacity of the counterpart FRP strengthened beam without any anchorage system. Moreover, by shifting the explosive end-peeling failure observed in the latter specimen to a gradual slipping of the CFRP below the anchorage system, a noticeable success in preserving a high ductility was assured. Equations (2-1) and (2-2) present the relationships for the deflection ($\mu_\delta$) and the curvature ($\mu_\varphi$) ductility indices, respectively. According to authors calculations, the normalized $\mu_\varphi$ and $\mu_\delta$ (the ratio of ductility of the strengthened beam to the as-built one) of 0.2 and 0.3, respectively, for the FRP bonded beam without any anchorage, reached up to 0.3 and 0.65, for the retrofitted beams with U-Shaped steel anchorage system.

Deflection ductility: $\quad \mu_\delta = \frac{\delta_u}{\delta_y}$ $\hfill$ (2-1)

Curvature ductility: $\quad \mu_\varphi = \frac{\varphi_u}{\varphi_y}$ $\hfill$ (2-2)

where, $\delta_u$ and $\varphi_u$ are the beam's mid-span deflection and curvature at the ultimate load, respectively, while $\delta_y$ and $\varphi_y$ are the mid-span deflection and curvature at the yield of tension longitudinal steel bars, respectively.

Spaced steel capping plates placed on the EB-FRP and secured to the concrete beam using fasteners (hammer pins or chemical anchors) are another type of mechanical anchors, known as Hybrid Bonded FRP plate (HB-FRP) [27]. In addition to the fasteners, adhesive may be used to bond the capping plate to the EB-FRP. According to this technique, the normal pressure exerted by the capping plates enhances the interfacial bond resistance between FRP and concrete, which consequently prevents a premature debonding. Although a hammered pin fastening system was found effective in exploiting the full strengthening potential of a few number of FRP plies, increasing the number of FRP layers adversely affected the anchorage effectiveness. According to the experimental observations of these researchers, in the latter case a sudden global detachment of FRP with the failure of a large number of anchorage capping plates at their pins-to-concrete connection is expected. Moreover, by using a hammer pinning process, not only the normal pressure cannot be controlled, but also it may introduce detrimental effects to the concrete cover. These shortcomings were overcome by replacing the pins with chemical anchors [28, 29]. This improved technique is then called Frictional Hybrid Bonded FRP plate (FHB-FRP).

Chemical anchors are composed of a threaded rod, washer and nut. The rod is fixed into a drilled hole filled with adhesive. Tightening of the nut causes a pre-tension into the fixed rod. The amount of this tensile load can be controlled if a torque measure wrench is used for the tightening of the nut. This controlled normal pressure enhances the FRP-concrete interfacial bond significantly.

Zhou et al. [29] examined the effectiveness of capping plates fastened with chemical anchors versus pinned connection by performing four points bending tests on flexurally FRP retrofitted RC T-beams containing either of these mechanical fasteners (see Figure 2.5). These results were also compared with those obtained from testing another counterpart's retrofitted beam but with spaced bonded U-Shaped FRPs as the anchorage system.

The geometry and steel reinforcement detailing of the tested RC beams along with configuration of four point bending test setup are represented in Figure 2.6. The flexural strengthening scheme of the abovementioned beams was composed of four plies of a CFRP with a length of 5500 mm and a width of 200 mm, longitudinally bonded to the beams' soffit. Each ply had a nominal thickness of 0.111 mm with an ultimate tensile strength of 3623 MPa at a rupture strain of 0.0157.

According to the tests observations and the measured FRP strain at the beam's mid-span, it was reported that the U-Shaped CFRP jacketing failed with a very premature breaking as shown in Figure 2.7a. For this anchorage method, the maximum developed strain in longitudinal CFRP, before its debonding, was 0.0013. This level of strain was as low as 8.2% of CFRP tensile capacity. For the beams with metallic anchorages, while slipping of the FRP adjacent to the supports and the shear-off of the fasteners in a pinned connection system caused a premature debonding of FRP in a maximum strain of 0.0035, employing chemical anchors resulted in partial rupture of CFRP in an average strain of 0.0067 (see Figure 2.7b).

(a)                                                    (b)
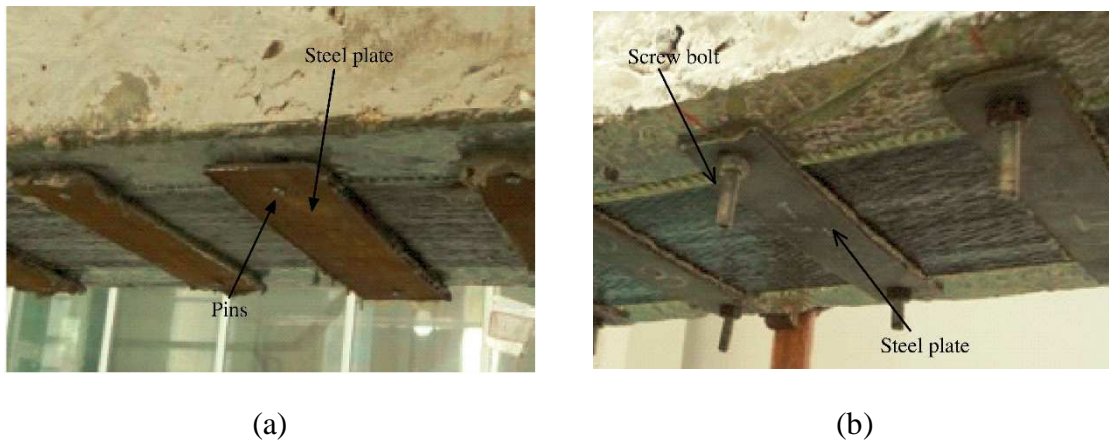
Figure 2.5: Friction Hybrid Bonded FRP (FHB-FRP) systems: steel caps placed over FRP plate and then connected to the beam's soffit using (a) pins, and (b) screw bolts, to prevent composite layer debonding by imposing plate normal pressure, [29].
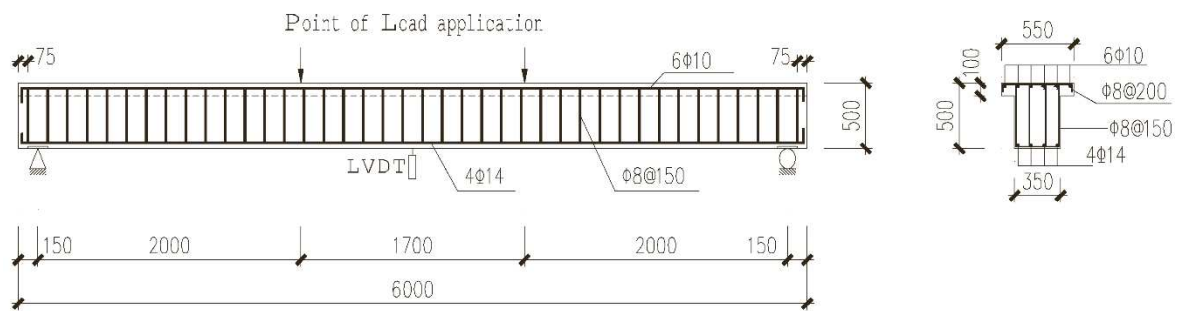


Figure 2.6: Load configuration and the detail of as-built beams tested by Zhou et al. [29]

Moreover, comparison of the results obtained from testing beams with two different layouts of similar FRP anchorage systems revealed a remarkable beneficial effect in increasing interfacial bond by decreasing the spacing between mechanical anchorages in the shear span. This closer spacing of mechanical anchorages led to a 46% increase in exploiting CFRP tensile capacity.

Although authors did not mention, it can be noted that only a partial rupture of CFRP layers (in some of the layers and at a portion of CFRP cross-section) occurred in all the retrofitted beams containing mechanical anchorages fastened by chemical anchors. This can be possibly attributed to the delamination progress between the FRP plies and also a non-

uniform distribution of the normal pressure exerted by the capping plates to the strengthening layers, which eventually results in the underutilization of the strengthening material.



<div align="center">(a)          (b)</div>
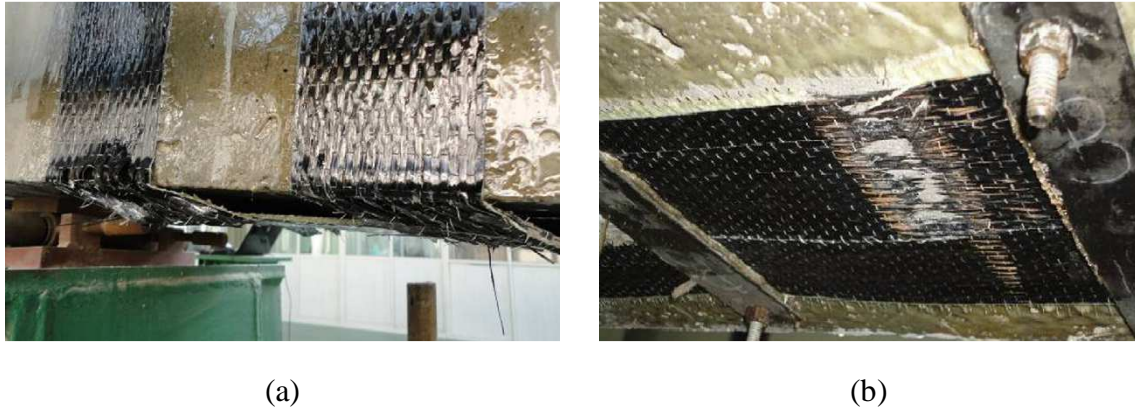
Figure 2.7: Observed failure modes of the strengthened beams: (a) rupture of the U-shaped CFRP anchor, and (b) CFRP rupture of in the beam containing capping plates with chemical anchors, [29].

### *2.2.1.2 U-Shaped FRP systems*

The results of experimental tests on FRP retrofitted beams showed that the premature end-peeling observed in the beams without any anchorage system can be shifted to an IC debonding if end U-Shaped FRPs are used [30, 31]. This is the effect of FRP jackets confinement that improves the FRP-to-concrete interfacial bond strength and results in a higher resistance to tensile stresses developed in the concrete cover, hence, delaying the initiation of the horizontal cracks and preventing their progress. However, it was found that the restraining effect of U-Shaped FRP jacket decreases when moving from the edges of the beam's section to the center [32], see Figure 2.8. Therefore, by increasing the width of the beam, FRP U-jacket is less effective in preventing FRP debonding and sliding.

Yalim et al. [25] tested T-beams flexurally strengthened with CFRP layers with or without anchorages. The utilized anchorage system was 4, 7, 11 or a continuous configuration of bonded strips of U-shaped unidirectional CFRP. Authors reported that the configurations with 4 and 7 strips of CFRP jacket bonded to the plate ends altered the end-peeling failure mode, observed in the specimen without any anchorages, to the IC debonding. CFRP debonding in these beams only took place after the U-shape strips were ruptured. The

failure of both specimens with eleven U-Shaped CFRP strips and continuous jacketing was the rupture of longitudinal CFRP.

Test results also confirmed the finding of the other researchers indicating that although enhancement in both ductility and ultimate flexural capacity can be achieved adopting a continuous FRP U-shaped jacket, the benefit from enhancement in ductility is much more substantial than in ultimate flexural capacity. However, material inefficiency in the cases where a large number of U-Shaped CFRPs or a continuous CFRP scheme is used in order to only prevent the debonding of the retrofitting composite, was still remained as a challenge [33].

Several researchers have investigated the application of hybrid FRP systems as a cost competitive anchorage solution to prevent/delay premature debonding and to achieve sufficient ductility together with enhanced load carrying capacity for the strengthened RC members [24, 34-37]. For example, Xiong et al [34] proposed a cost competitive solution aiming to prevent peeling failure (concrete cover detachment) and to achieve a satisfactory deformation capacity in the RC beams flexurally strengthened with CFRP sheets. According to their proposal, a bi-directional Glass FRP (GFRP) sheet was introduced as a continuous U-Shaped wrap anchorage for the CFRP strengthened beams. Their proposal relied on the lower cost and much larger rupture strain of GFRP comparing to CFRP composites. However, they mentioned that the effectiveness of this technique is limited to those beams free of shear or flexural-shear failures in their end-block, since the tensile strength of GFRP is relatively low. To assess the effectiveness of their proposal, authors tested a total of 8 FRP flexurally strengthened beams and compared their behavior with the results of testing two reference beams (beams without external reinforcements). The strengthened beams and one of the reference specimens had identical geometry and steel configuration, as represented in Figure 2.9. The other reference beam, with the same geometry, included a higher amount of tensile steel reinforcement, 2Ø12 mm steel bars, to provide a capacity almost equivalent to the expected flexural resistance of the CFRP strengthened beams.
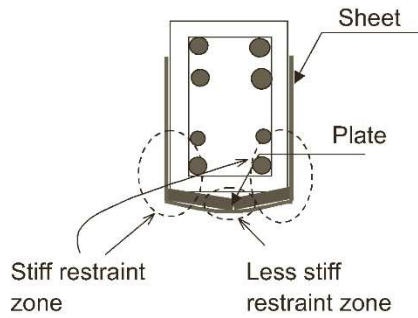
Figure 2.8: Non-uniform restraining condition along the width of the beam [32]
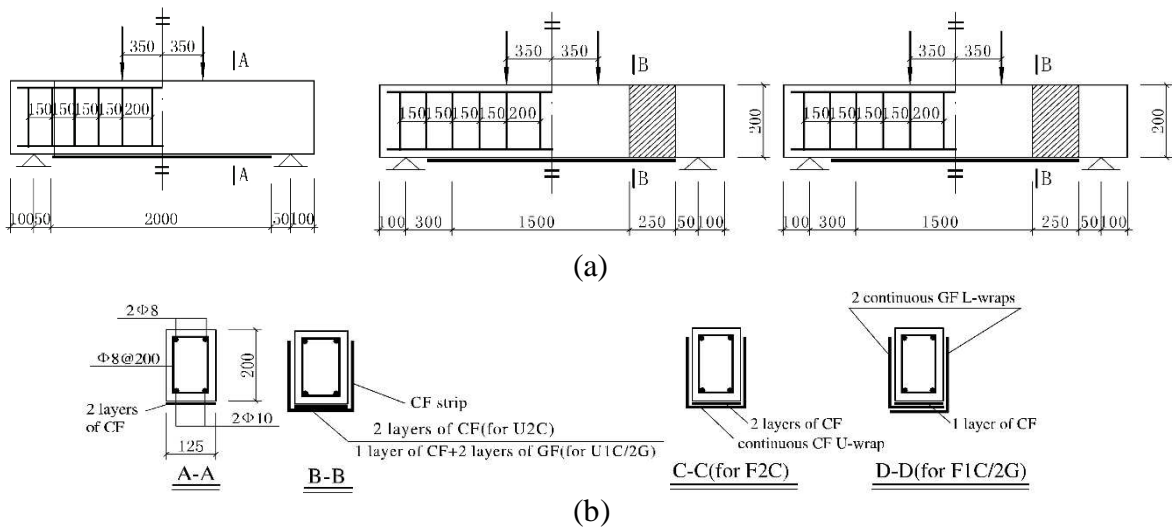


Figure 2.9: Configurations, test setup and strengthening layouts of the beams tested by Xiong et al [34], (a) lateral views, and (b) cross-sections

The strengthened specimens comprised: a beam with two layers of adhesively bonded CFRP laminates to its soffit (beam 2C); a beam similar to beam 2C but with CFRP U-shaped strips bonded at the strengthened end (beam U2C); two identical beams similar to 2C but with continuous CFRP U-shaped jacket along the length of the longitudinal CFRP laminates (beams F2C(1) and F2C(2)); two beams identically strengthened with one layer of CFRP laminate and two layers of GFRP sheets together with CFRP U-shaped jacket bonded at plate ends (beams U1C/2G(1); and U1C/2G(2)) two beams similarly strengthened with one layer of CFRP laminate and two layers of L-shaped GFRP sheets (beams F1C/2G(1) and F1C/2G(2)). As illustrated in Figure 2.10, three distinct failure modes were recognized: end

cover detachment (end-peeling) corresponding to the failure of beam 2C; mid-span cover detachment for beams with end U-shaped FRP anchorages (beams U1C/2G and U2C); and FRP fracture for beams with a continuous anchorage along the strengthened span of the beam (beams F2C and F1C/2G). Based on the results of the flexural tests and the evaluation of the strengthening costs, authors concluded that strengthening with a hybrid system composed of CFRP and GFRP, compared to the CFRP strengthening techniques, prevents concrete cover detachment, thus achieving a higher fracture load (30%) and ultimate deflection capacity (52%), while a 66% reduction in strengthening cost is obtained.

As a remark to the authors' research, it should be mentioned that for an overall assessment of the hybrid system, the influence of different thermal responses of GFRP and CFRP, and also the vulnerability of GFRP against alkalinity in aggressive environments, both affecting the efficacy of this system, still need to be taken into account.
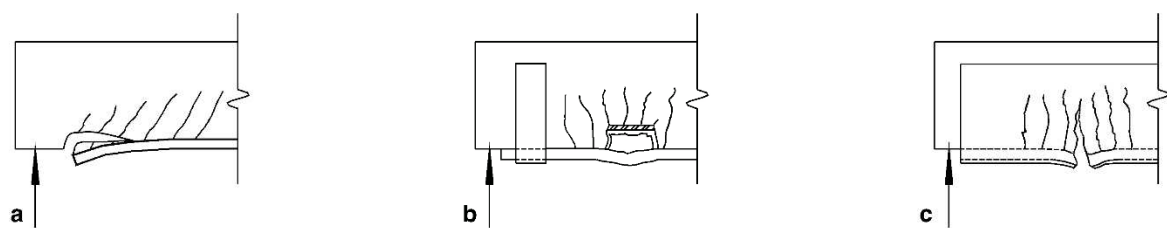
Figure 2.10: Failure modes observed with different types of strengthening schemes: (a) beam 2C, (b) Beams U2C or U1C/2G, and (c) Beams F2C or F1C/2G , [34]

### 2.2.1.3 FRP spikes (FRP anchors)

These kind of anchors are made either from rolled FRP sheets or bundled loose fibers, with one of their ends bonded into a predrilled hole filled with epoxy in the concrete cover (generally called anchor dowel) and the other end (generally known as anchor fan) bonded onto the surface of the strengthening FRP plate (for example, see Figure 2.11). In order to prevent stress concentration, the anchor fan is splayed and epoxy bonded. FRP anchors are interesting mainly because of their application feasibility on different shapes of elements, such as slabs [38, 39], walls [40, 41] and curved surfaces [42].

24

(a)            (b)
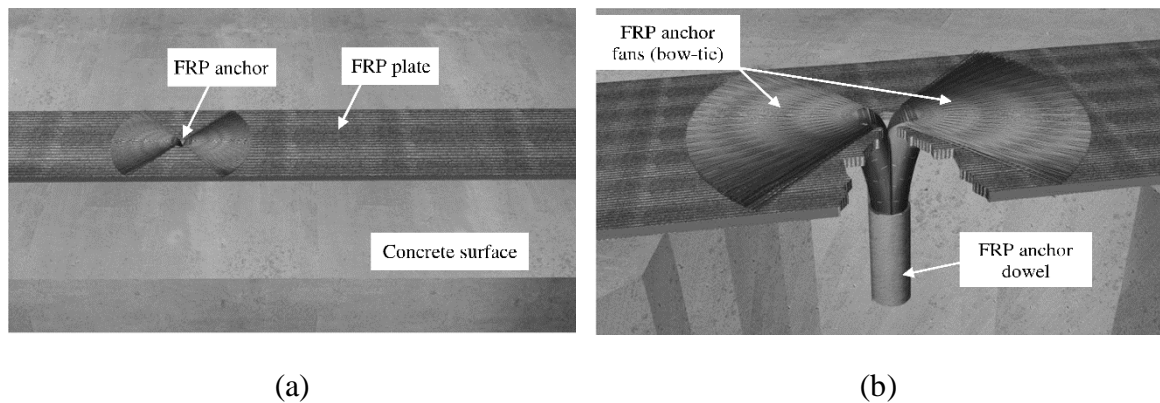
Figure 2.11: FRP anchor (spike) configuration (a) overall view, and (b) cut-away close up view, [43]

An interesting study on the performance of FRP anchors, among others [44-46], is probably the experimental investigation of Smith et al. [43], where different layouts and types of FRP anchors were applied to the flexurally strengthened one-way RC slabs with FRP bonded tension face. Both types of FRP anchors adopted in their research were handmade from the same carbon sheet used for the flexural strengthening of RC slabs, but Type 1 anchors had twice the amount of fibers than Type 2. A configuration of four point bending test setup was selected to study the behavior of RC slabs. The researchers categorized in two groups the observed flexural performance of the anchored strengthened slabs (compared to the obtained result of the unanchored strengthened slab and taking into account the adopted layout of anchors): (i) those layouts improved the deflection capacity, but resulted only in marginal increase in ultimate flexural load (S4 and S6 slabs, see Figure 2.12 and Figure 2.13a), and (ii) the layouts enhanced both flexural strength and deflection capacity (S3, S5 and S7 slabs, see Figure 2.12 and Figure 2.13b). Following the analysis of the performance of these specimens, the authors proposed an optimized configuration of FRP anchors and tested an extra anchored FRP strengthened RC slab to examine its effectiveness. This optimized layout was composed of a combination of both types of anchors applied only onto the shear-spans of the FRP strengthened slab (slab S8 in Figure 2.12). The proposed optimized scheme resulted in largest enhancement in flexural strength (30%) along with a notable improvement in deflection capacity (91%), compared to the results of the unanchored strengthened slab (see Figure 2.13b).
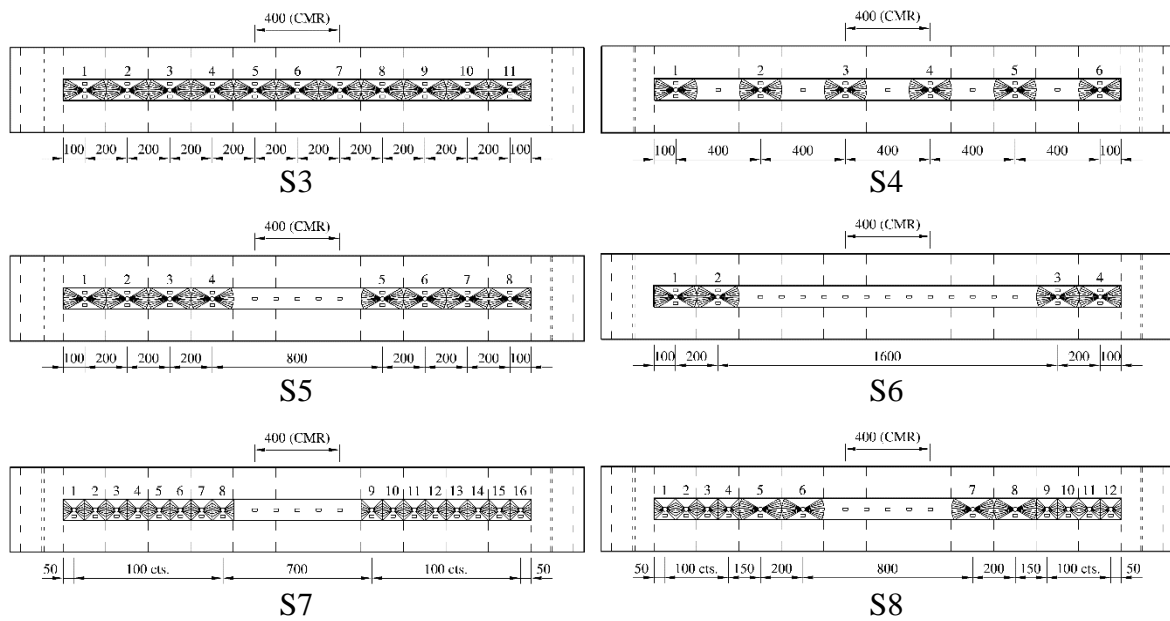
Type 1 FRP anchor; Type 2 FRP anchor; ····· Support lines; CMR: constant moment region; ---
Cross bars (longitudinal tension bars are not shown)

Figure 2.12: layouts of FRP anchors applied to CFRP strengthened slabs in the investigation of Smith et al. [43]



(a)

(b)
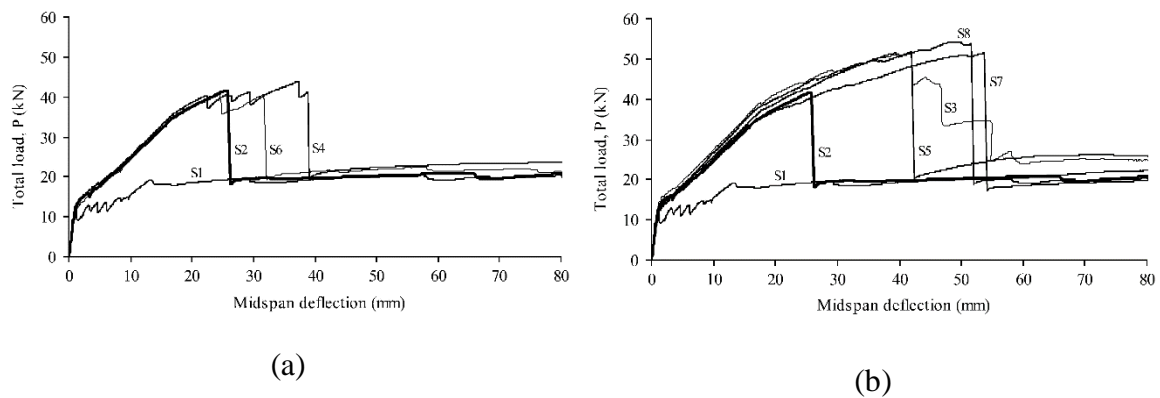
Figure 2.13: Load-deflection response of the tested slabs investigated by Smith et al. [43] (S1 is the control un-strengthened slab and S2 is the unanchored strengthened one), (a) anchors layouts resulted in a notable improvement in deflection capacity rather than strength, (b) anchors layouts enhanced both strength and deflection capacities

### *2.2.2 Near Surface Mounted FRP (NSM-FRP)*

According to this technique the FRP bar/strip is inserted into a pre-sawn groove on concrete cover that is already filled by a fresh groove-filler. Two components epoxies are the most used groove-fillers, since their appropriate mechanical and bond characteristics makes them capable of transferring a high shear stress between FRP and its surrounding concrete. Although cementitious materials have been studied as groove-fillers as well, compared to the epoxies they are not only more susceptible to durability issues but also they have much lower tensile strength, causing a premature bond failure at a very low strain level in FRP [47].

FRP bars either with a round, rectangular, square cross section, or in the form of thin strips, are the most common composites whose efficacy for the strengthening of RC structures according to the NSM technique has been investigated in the last decades. Depending on practical feasibilities, FRP can be fully or only three-sided covered by the groove-filler (see Figure 2.14). For an identical tensile strain in FRP, a fully covered FRP outperforms the three sided covered configuration, since a lower bond stresses due to a larger interface bond area is expected. FRP-strips (laminates) are identified as the most efficient shape in the applications of NSM-FRP technique, since there is a low possibility of their debonding from the surrounding adhesive [48-50]. This enhanced interfacial bond characteristic relies on the (i) minimized bond stresses as a result of a large ratio of bonded surface to the cross-sectional area of the strips, and (ii) the reduced risk of splitting failure along the epoxy cover and the concrete groove, which often occurs in NSM-round and rectangular bars.

NSM-FRP offers a relatively enhanced protection against elevated temperatures, vandalism and impact loads compared to EB-FRP [51]. However, its practical application is restricted to the depth of concrete cover and its soundness. The possibility of cutting or introducing damages to the existing reinforcing elements of the RC member can be perhaps mentioned as the main practical challenge in using the NSM-FRP system. Moreover, the provisions aiming to prevent overlapping of the tensile stresses of the FRP rods/laminates impose a minimum spacing between the adjacent grooves and also from the edge of the concrete element. Thus, these spacing provisions and the width of the RC member are the

other constraints restricting the application of higher amounts of strengthening material. For example, following the finding of other researchers [52, 53], ACI 440.2R-08 [10] recommended a clear grooves spacing of at least twice the grooves depth, and a clear element edge distance of four times of the groove depth if the groove is an exterior one.

While the mechanisms of flexural failure discussed for EB-FRP can be generalized to the NSM-FRP strengthened beams as well, the premature failure of the latter is also noted considering the debonding/detachment paths observed in the NSM-FRP direct bond tests. The premature failure of NSM-FRP system subjected to a pull load may take place with any of three possible scenarios mentioned herein [54]: (i) the interface bond failure between FRP and epoxy (BE), (ii) the interface bond failure between epoxy and concrete (EC), and (iii) failure associated to the splitting of the epoxy cover and/or fracture of its surrounding concrete in the inclined planes (SP). As illustrated in Figure 2.15, each of these failure modes includes subcategories taking into account their different patterns.
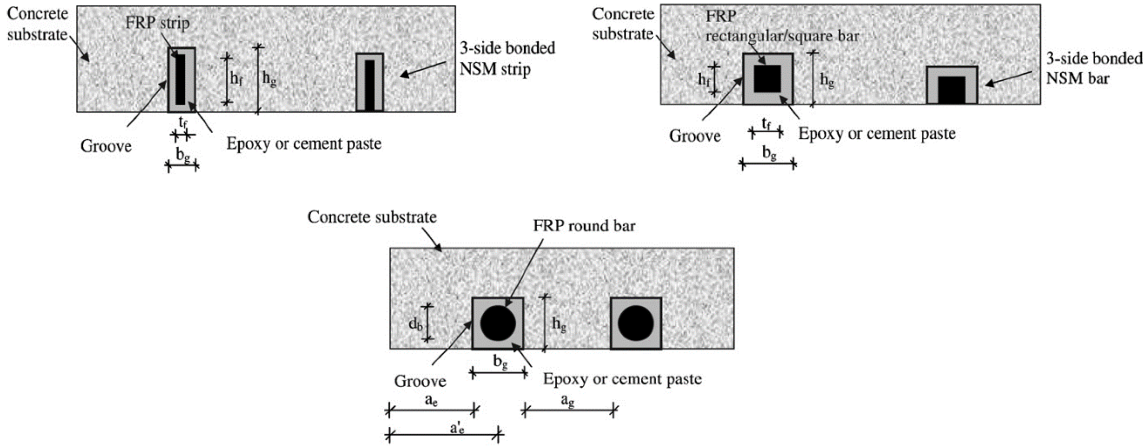


Figure 2.14: Different FRP shapes and adopted bonding configurations into the pre-sawn grooves on the concrete cover [54]

| | | | |
|---|---|---|---|
| **BE** | | Bar-epoxy interfacial failure | Cohesive shear failure in epoxy |
| **EC** | | Interfacial failure | Cohesive shear failure in the concrete |
| **SP** | Splitting of epoxy cover without concrete cover cracking | Cracking of epoxy cover, and fracture of concrete along inclined planes | No visible cracking of epoxy cover, and fracture of concrete along inclined planes |
| | | Fracture of the concrete edge | |

Figure 2.15: Failure modes observed in bond tests on NSM-FRP systems (BE: bar-epoxy interface failure, EC: epoxy-concrete interface failure, SP: failure associated to the splitting of the epoxy cover and/or fracture of its surrounding concrete in the inclined planes) [54]

Following there is a review of some of the experimental investigations and their most relevant results, available in the literature, on the application of NSM-FRP system for the flexural strengthening of RC beams.

El-Hacha and Rizkalla [49], reported the methodology and the results of an experimental investigation aiming to compare the performances of NSM-FRP and EB-FRP techniques for flexural strengthening of RC beams, assuming a progressed corrosion in their longitudinal

rebars. Application of different shapes and types of FRP materials (CFRP and GFRP-thermoplastic) were taken as the other study parameter.

Details of test setup, beam's geometry and steel configuration are depicted in Figure 2.16. To simulate the influence of corrosion, bars #16 (15.9 mm in diameter) were terminated with a 90 degrees bend at a distance of 100 mm from mid-span of the beams at the left and right sides, while bars #13 (12.7 mm in diameter) were continued along the beam span.
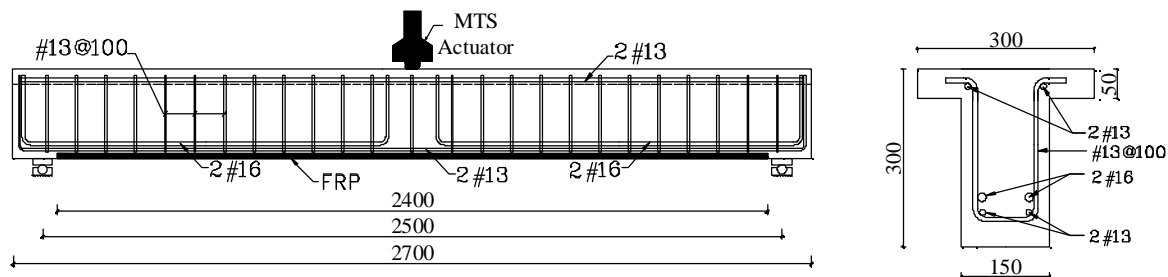


Figure 2.16: Details of test setup, beam's geometry and steel configuration adopted in the experimental research conducted by El Hacha and Rizkalla [49].

As schematically presented in Figure 2.17, seven beams were strengthened either with CFRP bar, CFRP strips type 1 or type 2, or GFRP-thermoplastic, following NSM or EB techniques. The only remained beam was tested as the control specimen in its as-built condition. All the strengthening layers were designed with an identical axial stiffness ($E_f A_f$, where $E_f$ is the elasticity modulus and $A_f$ is the total section area of the bonded FRP composites). To prevent/delay end-peeling of EB-FRP strips, U-shaped jacket of CFRP sheets were bonded to the plate ends (see Figure 2.17b). Details of FRP materials in terms of dimension and mechanical properties can be found in Table 2.1.

Results of this experimental study showed that NSM-FRP yields to a much higher enhancement in load carrying capacity of the reference beams as compared to the EB-FRP. While for all beams strengthened with NSM-CFRP strips full composite action with a CFRP rupture were observed, the EB-CFRP reinforced beams failed by a progressive debonding of CFRP strips and not more than 44% of tensile capacity of the composite layer was exploited. Higher efficiency of NSM-FRP versus EB-FRP was also confirmed according to

the test results of the beams strengthened with GFRP, since the increase in ultimate load carrying capacity of the former beam compared to the latter was at least three times larger.

For the case of the beam reinforced with NSM-CFRP bar, a high tensile stress at the interface of the CFRP and the epoxy caused splitting failure in adhesive together with cracking in surrounding concrete (failure mode SP-C1 in Figure 2.15) and thereby a premature debonding of CFRP occurred. In the case of EB-GFRP, as a consequence of progressive debonding at the interface of concrete/epoxy and then sliding of this strengthening layer below one of the U-shaped FRP jackets, the maximum measured GFRP strips strain in the mid-span was as low as 28% of its rupture strain. In contrast, NSM-GFRP strips achieved 61% of their strain capacity. Thus, an increase of 85% in flexural load carrying capacity of the beam strengthened with NSM-GFRP compared to the reference beam was obtained, whereas the corresponding value for the EB-GFRP strengthened beam was only 28%.

The overall ductility of NSM-FRP strengthened beams was superior to the EB-FRP strengthened ones. Among the strengthened beams, retrofitting by NSM-CFRP strips type 2 (see Table 2.1 and Figure 2.17a) showed the highest flexural capacity with a strength gain of 99% over the flexural capacity of the reference beam.

Table 2.1: Geometry and mechanical properties of FRP materials used for the strengthening of the beams tested by El Hacha and Rizkalla  [49]

| FRP products | Dimensions (mm) | Section Area (mm$^2$) | Elastic modulus (GPa) | Ultimate tensile strength (MPa) | Ultimate tensile strain (%) |
|---|---|---|---|---|---|
| CFRP bars | 9.5 | 71.3 | 122.5 | 1408 | 1.14 |
| CFRP strips (Type 1) | $2 \times 16$ | 32 | 140 | 1525 | 1.08 |
| CFRP strips (Type 2) | $1.2 \times 25$ | 30 | 150 | 2000 | 1.33 |
| GFRP strips | $2 \times 20$ | 40 | 45 | 1000 | 2.22 |

18X30     75     6.4X19     75     6.4X25     75     6.4X25     38

1 NSM CFRP rebar     2 NSM CFRP strips (type 1)     2 NSM CFRP strips (type 2)     5 NSM GFRP strips

(a)

2 externally bonded CFRP strips (type 1)     5 externally bonded GFRP strips

(b)
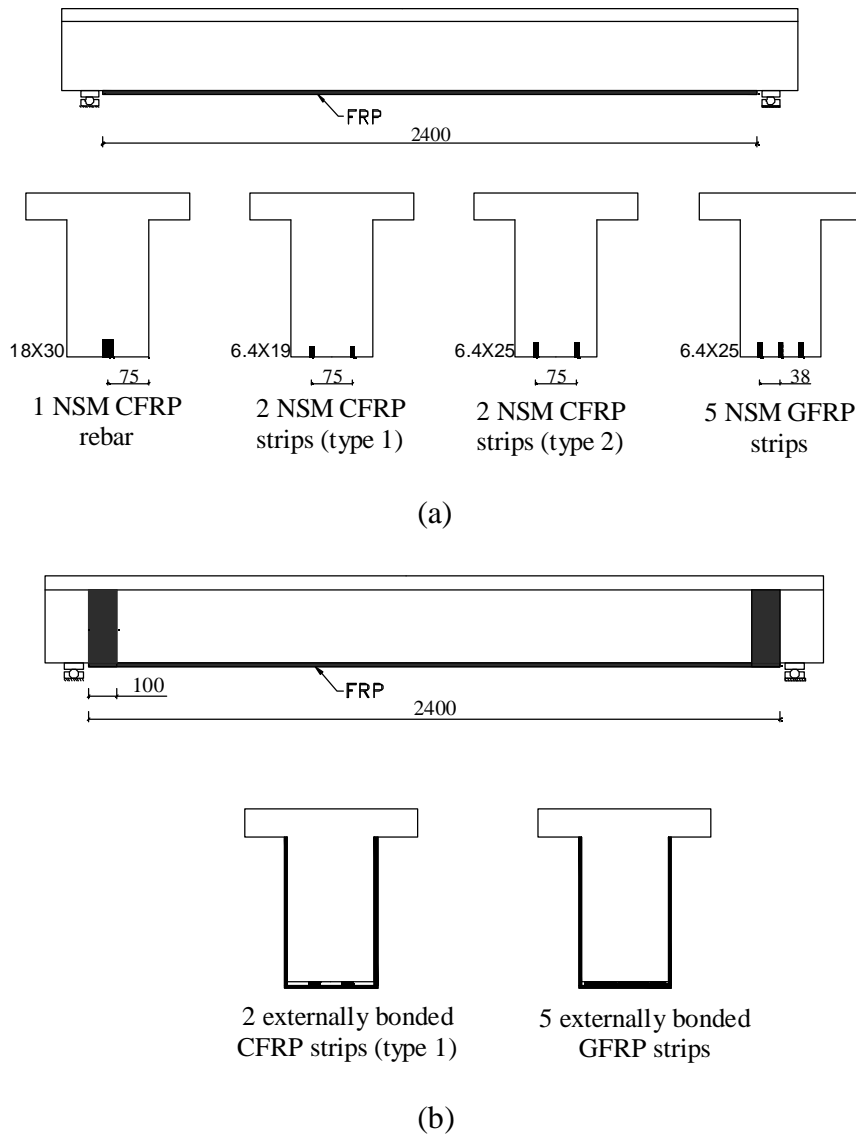
Figure 2.17: Details of adopted flexural strengthening layout (a) NSM-FRP strips configurations, and (b) Externally bonded FRP strips (experimental program of El-Hacha and Rizkalla [49])

Barros and Fortes [50] tested four series of beams under a four point bending configuration. Each series of specimens was composed of two beams identical in their as-built conditions. However, each series was different from the other one at the as-built condition only by the amount of longitudinal tensile steel reinforcement. One of the beams in each series was tested as the reference specimen without any strengthening layout, while the other one was tested after strengthening with NSM-CFRP strips. The strengthened beams

in each series had either one, two or three CFRP strips (laminates). Details of these beams, test configuration and nominations are represented in Figure 2.18.

Except for the beam V1R1, which test was interrupted at 20 mm of its deflection, the failure of the other strengthened beams was identified as the detachment of a relatively thick concrete cover with CFRP laminates bonded to it (see Figure 2.19). With an average increase of 91%, all of the strengthened beams showed a higher flexural load carrying capacity compared to their corresponding reference specimen. The increase at the load corresponding to the yield of tensile steel bars was 39% in average. Moreover, achieving a maximum increase of 45%, in comparison with the reference beams, all the strengthened beams had a higher load carrying capacity at the deflection corresponding to serviceability limit. At the failure of the strengthened beams, between 62 to 91% of the strain capacity of the CFRP laminates was utilized.

According to test results, except for B500, the strengthened beams had a noticeable increase in both flexural capacity and post cracking strength compared to those of the reference specimen (the one without any external strengthening). The beam B500 failed by concrete cover detachment initiated at the termination of CFRP strips and promoted by flexural strength limitation of the un-strengthened portion in the pure bending zone. Therefore, no increase in the flexural strength of this beam was achieved. For both B1200 and B1800, a detachment that started at the termination of CFRP strips was the governing failure mode. In the case of these beams, similarly to beam B500, a limited flexural capacity of the un-strengthened sections was the trigger for the onset of concrete cover detachment. Beam B2900 failed by concrete crushing followed by concrete cover separation close to the maximum moment region. This beam exhibited the maximum flexural load carrying capacity, with an increase of 106% compared with the control specimen. Although the bond stresses attained in beams B1800 and B2900 were comparable with (even in some cases higher than) the local bond strength obtained by the bond tests, no direct correlation was found between the failure modes observed in flexural and bond tests. Therefore, authors concluded that the results of bond tests cannot be simply generalized for theoretical prediction of the behavior of flexural beams and there is a need for extensive research to overcome this challenge.

Ceroni [55] performed monotonic and cyclic tests on beams flexurally strengthened either by EB-CFRP sheets or NSM-CFRP round bars, adopting a four point bending configuration. Investigated parameters were: (i) the performance of EB *vs.* NSM, (ii) the influence of different amounts of longitudinal tensile steel bars on efficiency of adopted strengthening scheme, (iii) the termination lengths of CFRPs, (iv) the number of CFRP sheet layers, and (v) the efficiency of U-shaped CFRP end-anchorages or spaced-ones to delay/prevent EB-CFRP debonding.
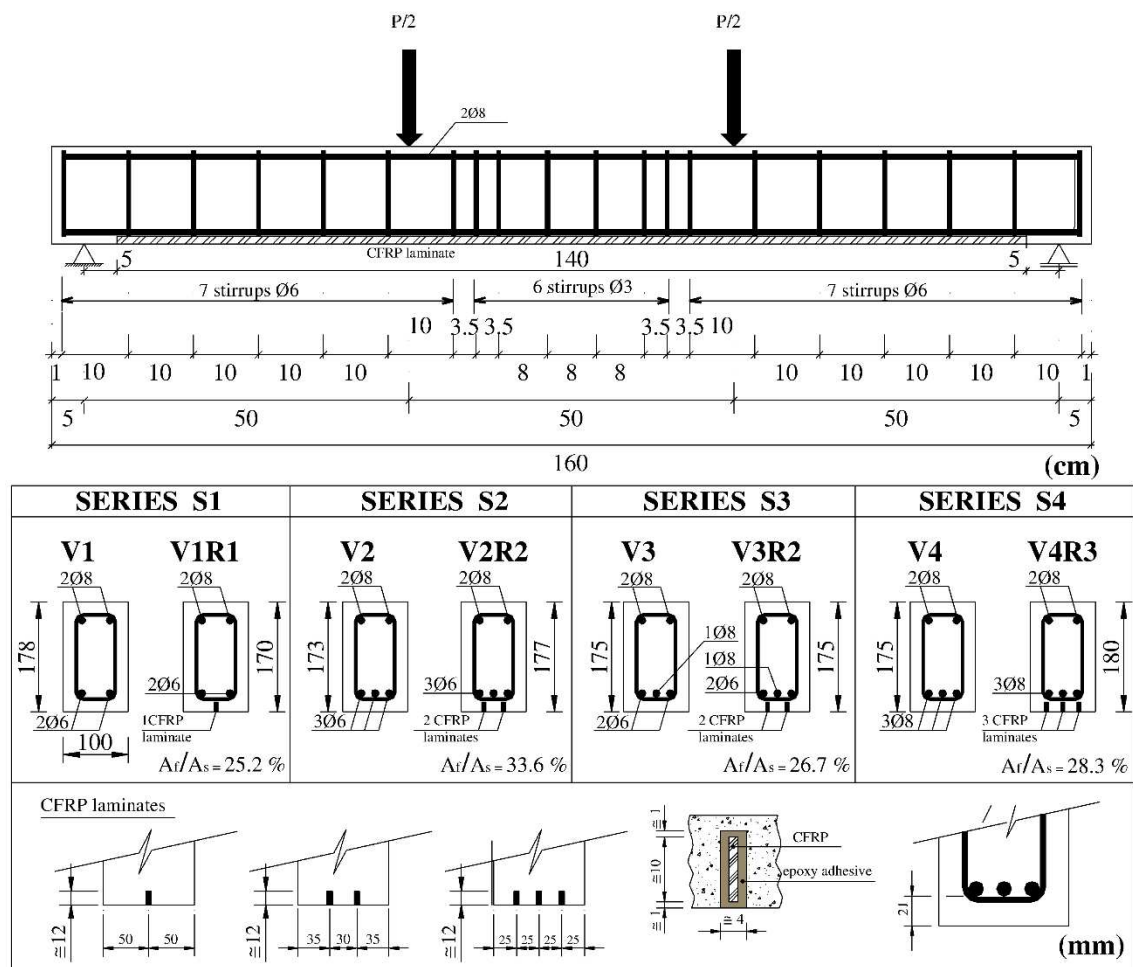


Figure 2.18: Details of test setup, beams geometry and steel configuration, and the adopted strengthening layouts for the RC beams tested by Barros and Fortes [50]

V1R1

V3R2

V2R2

V4R3
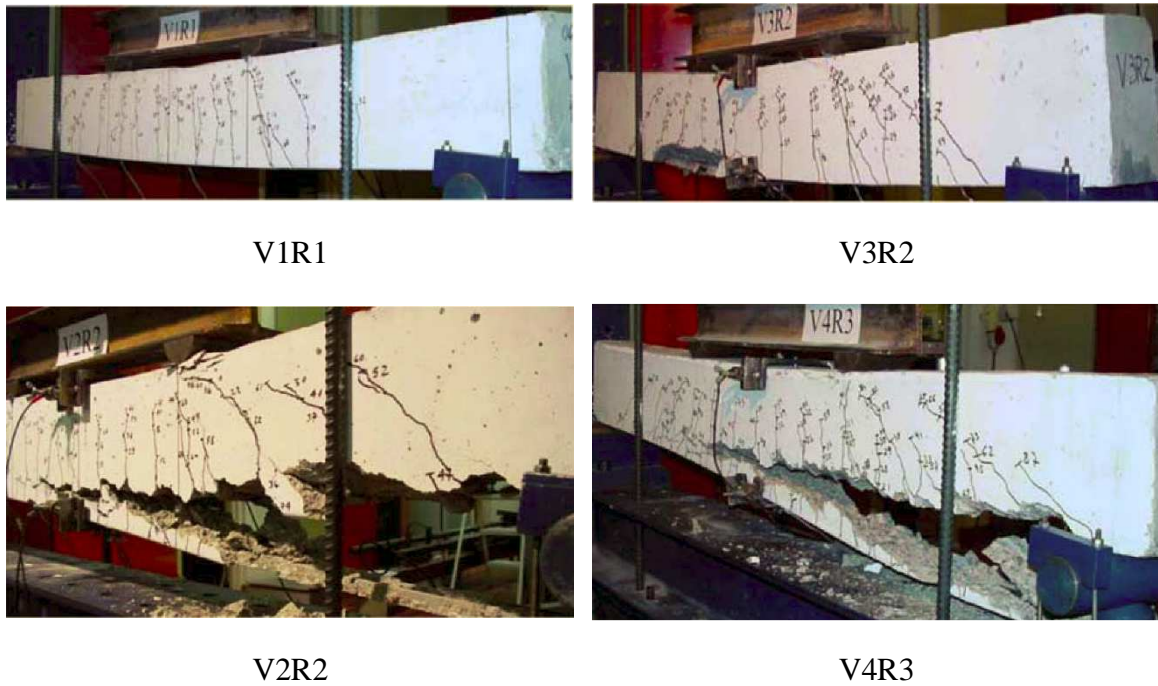
Figure 2.19: Failure modes and damages observed after testing the NSM-FRP strengthened RC beams, experimental program of Barros and Fortes [50]

The author also compared the obtained ultimate load from experimental tests with the estimated ones adopting different theoretical formulations proposed in literature. She reported that (i) an increase in the amount of tension steel bars caused a decrease in the rate of enhancement in the ultimate load of EB-CFRP strengthened beams, (ii) NSM-CFRP, in comparison with equivalent EB-CFRP, showed a much better performance in both ductility and the ultimate flexural load, (iii) U-shaped CFRP anchorages improved the ductility of beams strengthened by EB-CFRP with a superior performance for the spaced U-shaped anchorages compared with the end anchorages, (iv) cyclic loading imposed to EB-CFRP beams contributed to a reduction of at least 10% in the load carrying capacity obtained under monotonic loading of identical beams, (v) despite the embedded length of NSM-CFRP, the failure modes of NSM strengthened beams containing a low percentage of tensile steel was a sudden detachment of the concrete cover surrounding the NSM bars (Figure 2.21a), while the beams with higher amount of tension steel bars exhibited a more ductile failure which was crushing of concrete in compressive block together with peeling-off of the concrete

cover (Figure 2.21b), and (vi) the maximum tensile strain developed at NSM-CFRP round bars was only 60% of their tensile capacity.
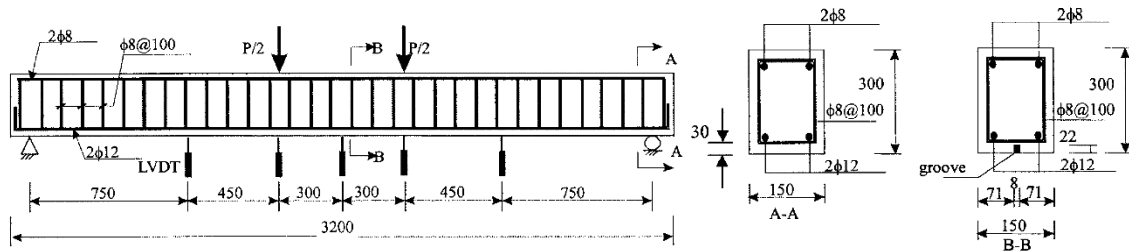


Figure 2.20: Details of geometry, steel configuration and the four point bending test setup of the beams tested in the experimental research of Teng et al. [6].



(a)                                                                (b)

Figure 2.21: Observed failure modes for beams with different tensile steel percentage ratio [55]: (a) a sudden detachment of the concrete cover surrounding the NSM bars in the beam with low percentage, and (b) a relatively ductile failure mode with concrete crushing in compressive block together with peeling-off of the concrete cover for the beam with higher amount of steel bars

### 2.2.3 Mechanically Fastened FRP (MF-FRP)

Recently Mechanically-Fastened FRP systems (MF-FRP) have emerged as a rapid retrofitting technique for RC members [56-60]. Pre-cured laminates used in this technique are generally composed of a glass and carbon hybrid pultruded strip embedded in a vinylester resin with enhanced bearing capacity due to adding fiberglass mats. Mechanical fasteners are used to attach these laminates (Figure 2.22) to the retrofitted element without applying any adhesive at FRP-RC interface; therefore, a higher durability for this system compared

to the EB-FRP or NSM-FRP is expected. The origin of the study of MF-FRP goes back to the late 1990s when US Army was seeking a rapid strengthening technique for concrete bridges that can be installed independent of environmental condition such as temperature and humidity, with minimal concrete surface preparation and workers training [61]. Notable shortcomings for this technique are reported, such as: scale effects, limitation in shear stress transfer between concrete and FRP depending on the number of discrete attached points and the fasteners strength, the requisite for initial slip to engage laminate and fasteners, and also galvanic corrosion of fasteners in contact with CFRP.



Figure 2.22: Installing MF-FRP strips on the Edgerton Bridge [62]

Nails, wedge bolts and wedge anchors (see Figure 2.23) are the most commonly used fasteners in this technique. Nails are applied using the explosive energy of a power actuated gun, and thus this fastening technique is known as PAF method. This fastening technique is more suitable for concrete with compression stress lower than 27 MPa, since at concretes with higher compressive strength, the presence of hard aggregates can prevent the full penetration of fasteners into the element substrate. Although the process of PAF installation is considerably fast, concrete spalling and surface cracking are the main drawbacks. Nails rotation and pulling-out, and poor performance of PAF connections subjected to fatigues loadings [63, 64] were the other shortcomings that motivated researchers to study wedge expanding anchors and concrete bolts as the alternative fasteners in place of PAF for MF-FRP connections [65-68].

Connection of a fastened laminate can fail due to the yield or even rupture of fastener, spalling of concrete (prayout), or failure of FRP laminate. Yield/rupture of fasteners may occur if the strength of anchors is low or the embedded depth is large. Prayout is characterized by concrete crushing ahead of the anchor together with fracture of a wedge of concrete behind it resulting in anchor rotation and then pullout (see Figure 2.24). This failure mode depends on the quality of concrete nearby the substrate (concrete cover), the embedded depth of the anchor, and the distance from the edge of retrofitted element (e.g., shorter embedded depth promotes the initiation of concrete prayout failure).

Power actuated nail          Wedge bolt          Wedge anchor
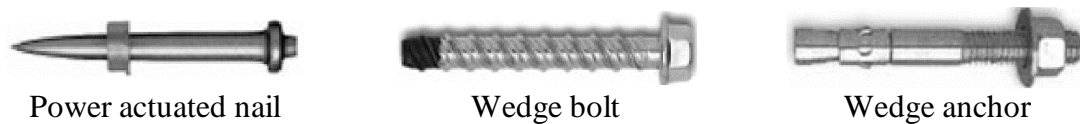
Figure 2.23: Different types of mechanical fasteners studied in MF-FRP system [67]
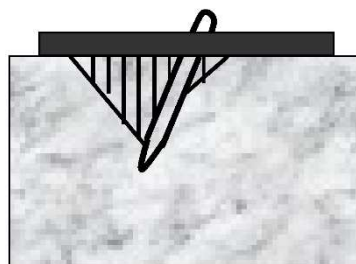
Figure 2.24: Nail rotation as a consequence of concrete paryout failure [67]

As it is shown in Figure 2.25, in general there are four recognized failure mechanisms associated with laminate performance: Net tension, Cleavage-tension, Shear out and Bearing failures [69-71]. According to the results of connection tests [72, 73], a bearing failure, despite other failure modes, is highly ductile and is recognized with a pseudo-plastic load-displacement response (Figure 2.26). Thus, a bearing failure design oriented MF-FRP system, as a desirable failure mode, can significantly enhance the ductility of beams flexurally strengthened with this technique.

Following a review on application and performance of MF-FRP system for flexural strengthening of RC beams, found in literature, is presented.

| Net tension | Leavage tension | Shear out | Bearing |
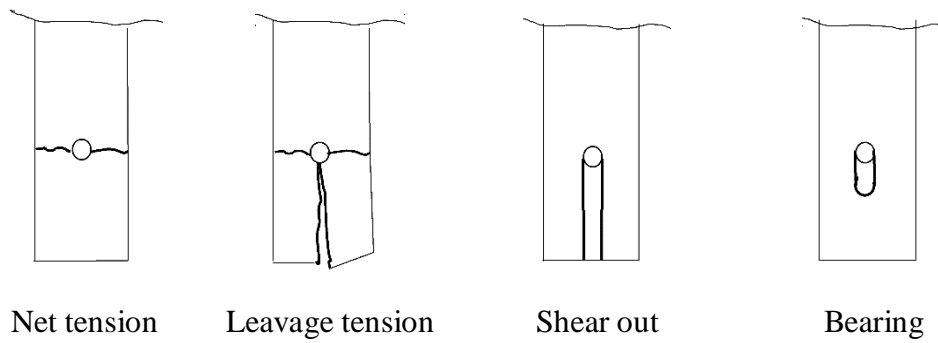
Figure 2.25: Different failure modes associated with laminate performance in a MF-FRP connection [67]
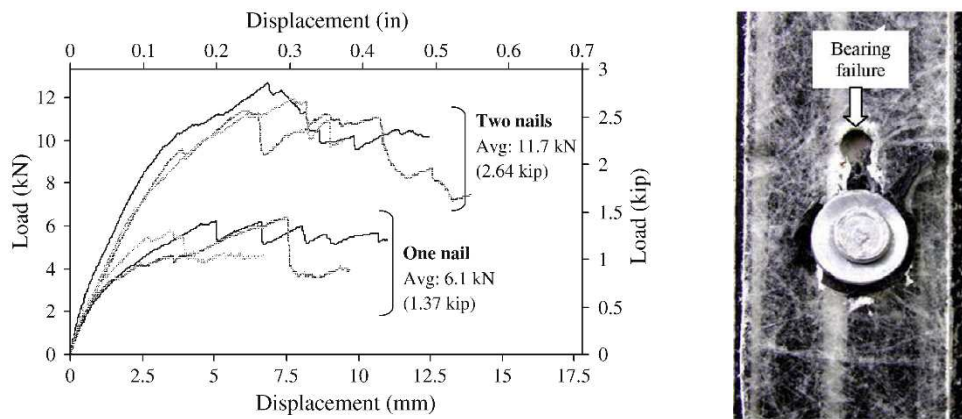


Figure 2.26: Typical load *vs.* displacement from bearing tests of MF-FRP systems [72]

In the experimental study conducted by Lamanna et al. [74], flexural testing of large scale beams (304.8mm×304.8mm×3657.6mm) strengthened with MF-FRP technique, a maximum increase of 21.6% and 20.1% in the yield and ultimate moments, respectively, was obtained as compared to the as-built beams. For an identical amount of FRP strips, the MF-FRP method was found comparable with EB-FRP in terms of ultimate moment capacity, however, the enhancement in the yield moment was lower. In comparison with EB-FRP technique, an increased ductility for MF-FRP strengthened beams with long predrilled fasteners was obtained. Authors also stated that a predrilling fastened method can result in a gradual failure of the beam by concrete crushing in compression zone, while without predrilling a strip detachment most likely occurs.

Quattlebaum et al. [63] examined and compared the performance of EB-FRP, NSM-FRP and MF-FRP (with PAF connections) techniques for flexural strengthening of medium-scale beams. The beams had dimensions of 4750 mm, 254 mm, and 152 mm in the length, the depth, and the width, respectively. Tensile steel yielding and then premature CFRP debonding originated at the beam's mid-span and propagated towards one end of the beam, was the failure mode of EB-FRP strengthened specimen. Both beams strengthened with NSM-FRP and MF-FRP failed by crushing of concrete in compression block following the yield of tensile steel bars. In terms of yield load of tension steel bars, compared to the un-retrofitted specimen, an increase of 26, 25, and 21% was obtained for EB-FRP, NSM-FRP, and MF-FRP, respectively. The same trend of load increase at the ultimate state but the amounts of 33, 32, and 28% was reported for these techniques. Results of these experiments also confirmed that displacement ductility of MF-FRP system is substantially high, in the range of corresponding value of the reference beam [75].

Napoli [67] studied the effects of laminate length and fasteners arrangement (layout) on strength enhancement and failure modes of one-way slabs flexurally strengthened with MF-FRP. The experimental program consisted of six slabs, four of them strengthened with MF-FRP, one strengthened with EB-FRP and the only remained one was taken as the reference specimen. All slabs had identical geometry and steel configuration, a total length of 3658 mm and a width and depth of 305 and 154 mm, with a longitudinal tensile steel ratio of 0.98%. Monotonic loading under a four point bending test setup, in a clear span of 3048 mm and a shear span of 1219 mm, was employed to characterize performance of each of these slabs. To attach laminates to the concrete substrate, power wedge bolts were used. Two different staggered configurations for the fasteners, as shown in Figure 2.27, and different laminate lengths for each configuration, were the investigated parameters. Staggered configurations were adopted to better exploit the tensile strength of the laminate by lowering shear lag effects associated with a single row configuration of fasteners [65] and also to distribute the tensile forces across the width of laminate in a greater extent [76]. Following the observations and recommendations of the previous researchers [56, 57, 60, 65, 76] fasteners spacing and layout were designed to prevent: (i) the premature shear-out failure between adjacent fasteners and also at the last fastener, (ii) the prayout failure of concrete substrate, and (iii) cleavage failure at the end of the laminate. According to the results of the

experimental tests, all MF-FRP strengthened beams failed by concrete crushing after the tension steel was yielded. Since failure of none of the MF-FRP strengthened slabs was due to deficient performance of the FRP-RC connection, the effectiveness of the adopted fasteners schemes, fasteners type and laminate characteristics for a successful strengthening solution was approved. The strength increase obtained with MF-FRP strengthening technique was comparable with the corresponding strength gain in EB-FRP strengthened slab, noting that the latter failed by premature debonding of the composite layer. As compared to the reference specimen, the MF-FRP strengthened specimens exhibited an increase in the range of 15.4 to 23.1% at the yield and 30.9 to 58.6% at the ultimate moments. The author concluded that both the length of the laminate and the spacing of the fasteners play a significant role in achieving higher strength and ductility together. She also indicated that when laminate is attached with a lower number of fasteners to the substrate, the amount of obtained ductility is greater.
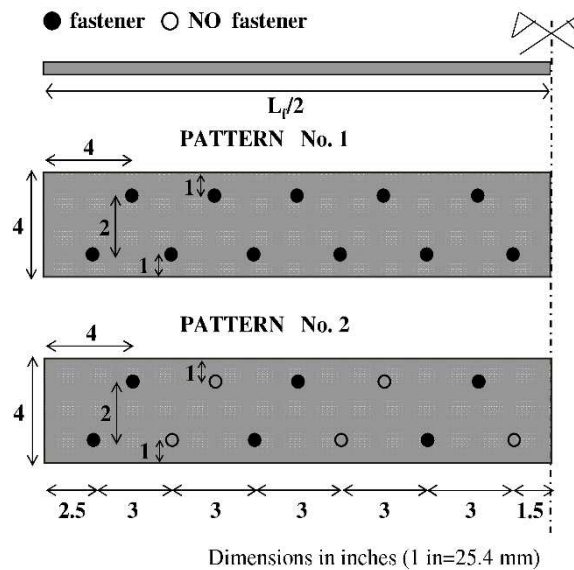


Figure 2.27: Adopted MF-FRP fasteners layout for the beams tested by Napoli [67]

## 2.3 FRP for Strengthening of Beam-Column Joints

The local performance of the elements composing framed systems in RC structures has direct impact on the potential of these structures to withstand lateral seismic loads. The high inelastic rotation capacity of the beams at the vicinity of the framing region into the column,

the sufficient shear strength and stiffness of the beam-column joint panel, and a predominant elastic response of the column can dissipate a high amount of seismic energy, while the stability of the structure to transfer the gravity load to its supports is assured. According to the provisions of the modern codes oriented to seismic design, the strength hierarchy design, along with a proper detailing of the internal steel arrangement should be taken into account to achieve such a ductile and safe response of the designed RC structures for locations with moderate and high seismic risks. However, there is a considerable number of RC structures with only Gravity Load Design (GLD) considerations, especially those designed according to pre-1970th codes provisions. These structures have, in general, inadequate detailing to resist the lateral loads induced by earthquake actions.

The most relevant vulnerabilities of these RC structures as recognized by Moehle et al. [77] and Sezan et al. [78], and reported by ACI Committee 440 [79], are: (i) insufficient transverse reinforcement and their improper detailing, causing the lack of ductility in plastic hinge regions, low shear resistance and deficient lap-splices, (ii) improper end anchorage of longitudinal reinforcement inside the panel of the joint, (iii) low moment resistance of framed elements due to inadequate longitudinal reinforcement, (iv) inadequate configurations of lap-splices at the vicinity of potential plastic hinge regions and the location of lap-splices immediately above the floor level, (v) possible soft-story failure due to adopted beams with higher moment capacity than columns reaching a joint.

Material deficiencies, such as low concrete compressive strength and plain steel bars used as the reinforcement, are the other causes for poor seismic performance of the old RC buildings. For example, following an experimental investigation on characterization of cyclic behavior of GLD structures, Fernandes et al. [80] tested and compared the response of series of similar full-scale interior beam-column joint specimens. Two of these specimens were detailed to study the influence of bond stress-slip on the seismic performance of the beam-column joints, one with plain steel bars and the other with deformed steel bars, used as the longitudinal and transverse reinforcement of their elements. In the specimen with plain steel bars a poor bond stress-slip performance resulted in significant sliding of longitudinal reinforcements with concentrated damages at the beam-joint and column-joint interfaces. Contrary to this response, spread damages along the elements' lengths and in the joint region

were observed in the other specimen. Consequently, a larger energy dissipation capacity for the specimen with deformed bars due to a distributed damage was assured.

Beam-column joints are probably the most crucial regions of a moment resisting frame, whose failures during the seismic actions, either in the joint panel or in the columns, may result in catastrophic collapse, since the structure may lose its gravity load carrying capacity (see Figure 2.28). On the other hand, formation of plastic hinges on the beams, at the vicinity of beam-column connection, is a desired failure mode assuring a beam sideway mechanism that provides a significant earthquake energy dissipation capacity.

There are two main mechanisms contributing in the shear transfer of an RC joint panel, a main concrete diagonal strut and a truss mechanism. Figure 2.29, as an example, illustrates the idealized configuration of acting forces and resisting mechanisms in an interior beam-column joint, subjected to a lateral force simultaneous with a column axial load. Concrete diagonal compressive strut equilibrates with the compressive forces developed in the beams and columns at the joint interfaces, and with that part of bond forces of longitudinal bars located in compression zones. The contribution of truss mechanism depends on the bond quality between longitudinal rebars passing through the joint and concrete, and the existing vertical and transverse reinforcement in the joint core. Truss mechanism is activated only after diagonal tension cracks form in the joint region. Hence, the bond forces should be equilibrated with the elements of truss mechanism, transverse reinforcements and secondary diagonal struts. Once the bond between the longitudinal rebars and the concrete at the joint panel is deteriorated, due to a poor bond condition and cyclic effects, concrete diagonal compressive strut becomes the main mechanism for withstanding the joint shear forces. Under this circumstance, the main contribution of the existing joint's reinforcement is limited to the confining of the concrete in the joint core. In consequence of diagonal tension strains and excessive opening and closing of the inclined cracks, the compressive strength of the diagonal strut degrades, which results in failure caused by the crushing of concrete of the strut.

(b)

(a)                                                                  (c)

Figure 2.28: Failure of beam-column joints observed in the 1999 İzmit, Turkey earthquake (photo credits: (a) Courtesy of National Information Service for Earthquake Engineering, University of California, Berkeley, (b) Prof. Güney Özcebe, personal communication (1999), (c) Said and Nehdi [81])



forces from beams an columns acting on the joint

crack pattern and bond forces after diagonal tension cracking initiates in the joint core

concrete diagonal strut mechanism, equilibrating concrete compression forces in beams and columns and some bond forces in the compression zones

truss mechanism of concrete diagonal compression field and horizontal and vertical reinforcement needed for equilibrium after diagonal tension cracking

Figure 2.29: Idealized representation of the forces acting on an interior beam-column joint subjected to seismic loading, and the joint shear resisting mechanisms [82]

The most common identified vulnerabilities of interior beam-column joints in seismic actions are caused by the lack of joint reinforcement, existence of columns with lower moment capacities than beams, inadequate bond length of longitudinal rebars passing through the joint region or a poor bond performance, insufficient reinforcements at the bottom of the beam and/or shortness of their termination (development) length, lap-spliced longitudinal bars of column right above the floor level, and low concrete compressive strength.

Once deficiencies of the existing RC beam-column joints were recognized, the scientific community on seismic design and structural rehabilitation started proposing several strategies for their seismic rehabilitation and retrofitting [83, 84]. According to the literature [85-94], application of FRPs is the most common proposed solution. The adopted FRP configuration depends on the geometry of beam-column joint and the retrofitting objective, e.g. enhancing the joint shear capacity through joint concrete confining, increasing columns' capacity, and altering the brittle shear failure in the joint region to a ductile failure mode by the formation of plastic hinges at the ends of beams.

However, as reported by several researchers [95-98], premature FRP de-bonding often occurs in retrofitted RC beam-column joints. Hence, further researches on seismic rehabilitation of these deficient beam-column joints using FRP composites were mainly oriented toward using mechanical anchorages, such as those discussed in section 2.2.1, to prevent/delay debonding failure [81, 85, 86, 94, 96, 97, 99-101]. Following, some of these studies are reviewed.

The importance of using appropriate anchorages for FRP retrofitted beam-column joints is well highlighted in the experimental investigation conducted by Ghobarah and Said [96], examining different strengthening techniques based on GFRP wrapping of exterior beam-column joints. Since there were no transverse reinforcements in the joint panel of these specimens, the proposed strengthening aimed at altering the expected joint brittle failure mode to a more ductile and secure one by forming plastic hinge at the beam end. The adopted strengthening configurations are represented in Figure 2.30. Two damaged RC beam-column joints, already tested as control specimens in their as-built conditions, were repaired and then retrofitted following the configurations designated T1R and T2R in Figure 2.30. For both of

these specimens, steel plates fastened with through bolts were used to mechanically anchor free edges of the GFRP wraps in the joint region, at the vicinity of beam-joint interface. One of the remaining specimens, T4, had a similar strengthening configuration of T1R but without any anchorage system. For the last specimen, designated as T9, diagonal configuration of GFRP wraps was adopted. To facilitate GFRP diagonal wrapping, at each corner of beam-column connection an angle shape profile was used with an inclined plate welded to its free edges. A reversed cyclic displacement pattern, imposed to the beam tip, in the presence of a constant column axial load was applied to test these specimens.
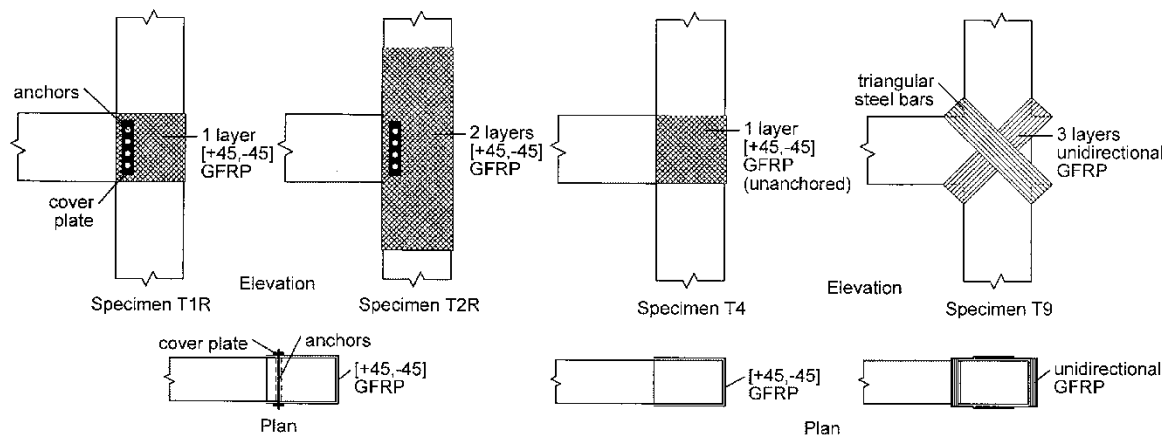


Figure 2.30: Different configurations of GFRP wraps investigated by Ghobarah and Said [96] for the strengthening of shear deficient exterior RC beam-column joints (represented from [83])

A premature debonding of GFRP in specimen T4 led to a response very similar to that obtained from testing the control specimen. Both of these specimens, T4 and control one, failed due to the lack of joint shear capacity, with severe X-shape cracking in the joint panel. In the case of T1R, even though debonding of GFRP from column sides was observed, the applied anchorage system prevented end-debonding of the composite layer. Consequently, the confining exerted from GFRP wrap to the joint concrete increased its shear capacity sufficiently for a flexural plastic hinge to be formed at the beam's end. The diagonal configuration of unidirectional GFRP wraps, applied to the specimen T9, successfully delayed the joint shear failure. However, together with the plastic hinge formation at the beam's end, the joint shear failure also occurred. This mode of failure indicated a poor

confinement in the joint panel, which was also evident by the bulging of concrete in the joint panel. The strengthening configuration used for T2R was the most efficient scheme, since GFRP debonding was prevented and a full beam plastic hinge was formed without any failure in the joint region. This superior performance resulted in the highest capacities in terms of drift (displacement ductility), lateral load and dissipated energy, when compared to the other specimens (see Figure 2.31).



(a)                                                                (b)
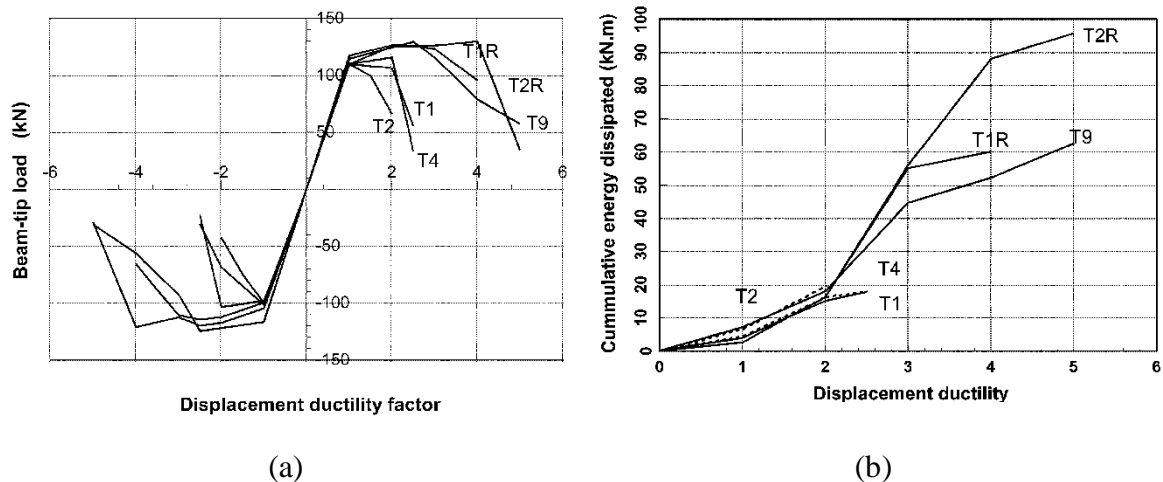
Figure 2.31: Results of cyclic tests on the strengthened and as-built exterior beam-column joints (investigated by Ghobarah and Said [96]), (a) envelope of the hysteretic loops, and (b) cumulative energy dissipation.

Al-Salloum and Almusallam [85] also reported the important role of mechanical anchors to prevent debonding of CFRP layers applied for strengthening or repairing interior RC beam-column joints. These one-way beam-column subassemblies were half-scale models of a prototype with a part of slab (T-beam), without any transverse reinforcement in the joint panel. Authors examined the effectiveness of two different CFRP configurations, schemes 1 and 2 in Figure 2.32, for enhancing joint shear capacity and directing the failure mode from the joint panel to the beams' end. Two control specimens, after being tested in their as-built conditions, were repaired with each of these techniques. There was a counterpart's specimen for each of these repaired beam-column joints, but strengthened in their virgin conditions (no initial damage).

Testing these specimens, under simultaneous lateral cyclic displacements and constant column axial load, revealed that bulging of CFRP in the joint region and its debonding along the beam occurred in the scheme 1, while the mechanical anchorages used in scheme 2 successfully prevented the debonding of the composite layer. Although both schemes were effective in delaying joint shear-failure, only in the case of scheme 2 the failure was fully directed to the beams without any damage in the joint panel. In general the performance of these schemes, reflected as the failure mode of the specimens, was similar for both strengthening and repair applications. As compared to the results of the control specimens, both repaired and strengthened beam-column joints presented higher displacement ductility. However, improvement in ductility of the strengthened specimens was much higher than in the repaired one. Strengthening with schemes 1 and 2 led to an increase of 72% and 61%, respectively, in displacement ductility factors (the displacement corresponding to 10% drop in the peak load was adopted as the ultimate displacement).



(a)                                    (b)
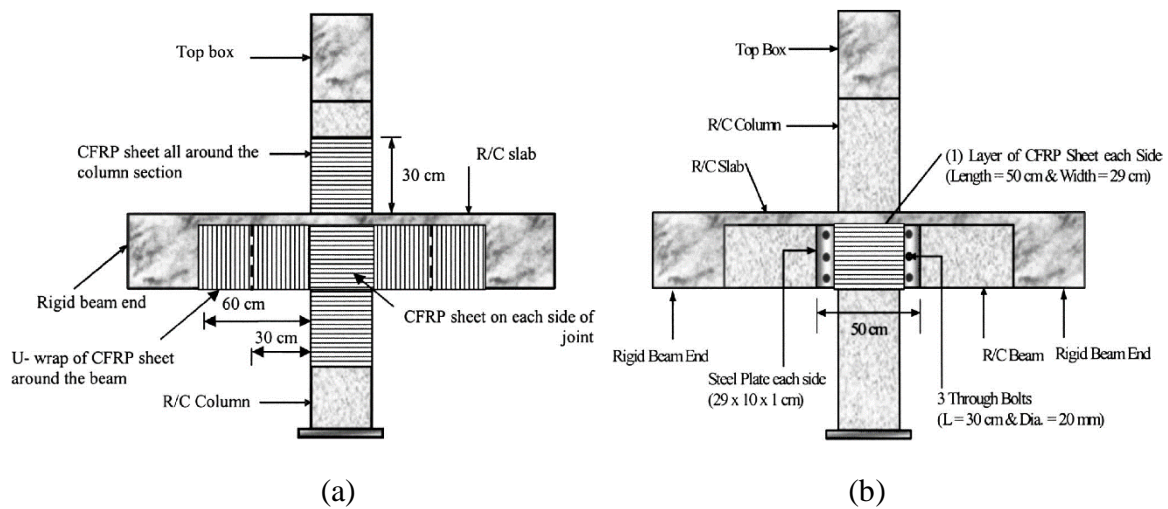
Figure 2.32: Schematic representation of FRP configurations used for the strengthening of interior beam-column joints in the investigation of Al-Salloum and Almusallam [85], (a) Scheme 1, and (b) Scheme 2.

Esmaeeli and Danesh [94] proposed a combination of bidirectional GFRP layers and angle-shaped steel profiles for the strengthening of three-dimensional exterior beam-column joints suffering from insufficient joint shear capacity. Their proposed scheme eliminates the need for perforation of concrete to secure fasteners of the mechanical anchorages. As

represented in Figure 2.33a, according to this scheme the free edges of GFRP layers in the joint region were secured to a cage, made of four angle-shaped steel profiles connected to each other using series of threaded rods, around the joint region. This strengthened specimen and the as-built one were tested adopting a simultaneous bidirectional cyclic loading imposed to the beams' free ends and a constant axial load applied to the column's end.

The strengthening scheme efficiently confined the concrete in the joint panel and altered the joint shear failure mode of the control specimen to the beam's flexural failure at the beam-column interface (Figure 2.33b). Consequently, as presented in Figure 2.33c and calculated based on the examination of the results in the plane of one of the beams, an average increase of 50% in lateral load carrying capacity together with 60% increase in displacement ductility, for the strengthened specimen, as compared to the control one, was obtained. Moreover, the contribution of the joint panel deformation in the story drift, measured at a drift angle of 3%, was reduced to 20% in the case of the strengthened specimen, while it was measured as 54% for the control beam-column joint (see Figure 2.33d).

Li and Kai [101] examined the effectiveness of a proposed EB-FRP configuration for the repair of interior beam-wide column joints already tested as the control specimens. These control specimens were vulnerable against seismic loading because of their inadequate seismic detailing such as the 90° bend of transverse reinforcements of beams and columns, lack of transverse reinforcements in the joint region, and the absence of additional transverse reinforcement at the potential length of plastic hinging in the beams.

The adopted FRP strengthening configuration used for the repair of all four tested specimens is shown in Figure 2.34a. As depicted in this figure, depending on the type of the utilized FRP material, two different schemes based on this proposed rehabilitation configuration were investigated, scheme 1 with only GFRP layers and scheme 2 with a combination of GFRP and CFRP layers. FRP spikes of 110 mm in total length were used to anchor U-shaped and L-shaped FRP layers to the lateral faces of beams, according to the configuration depicted in Figure 2.34a.

(a)                                                                      (b)



(c)                                                                      (d)
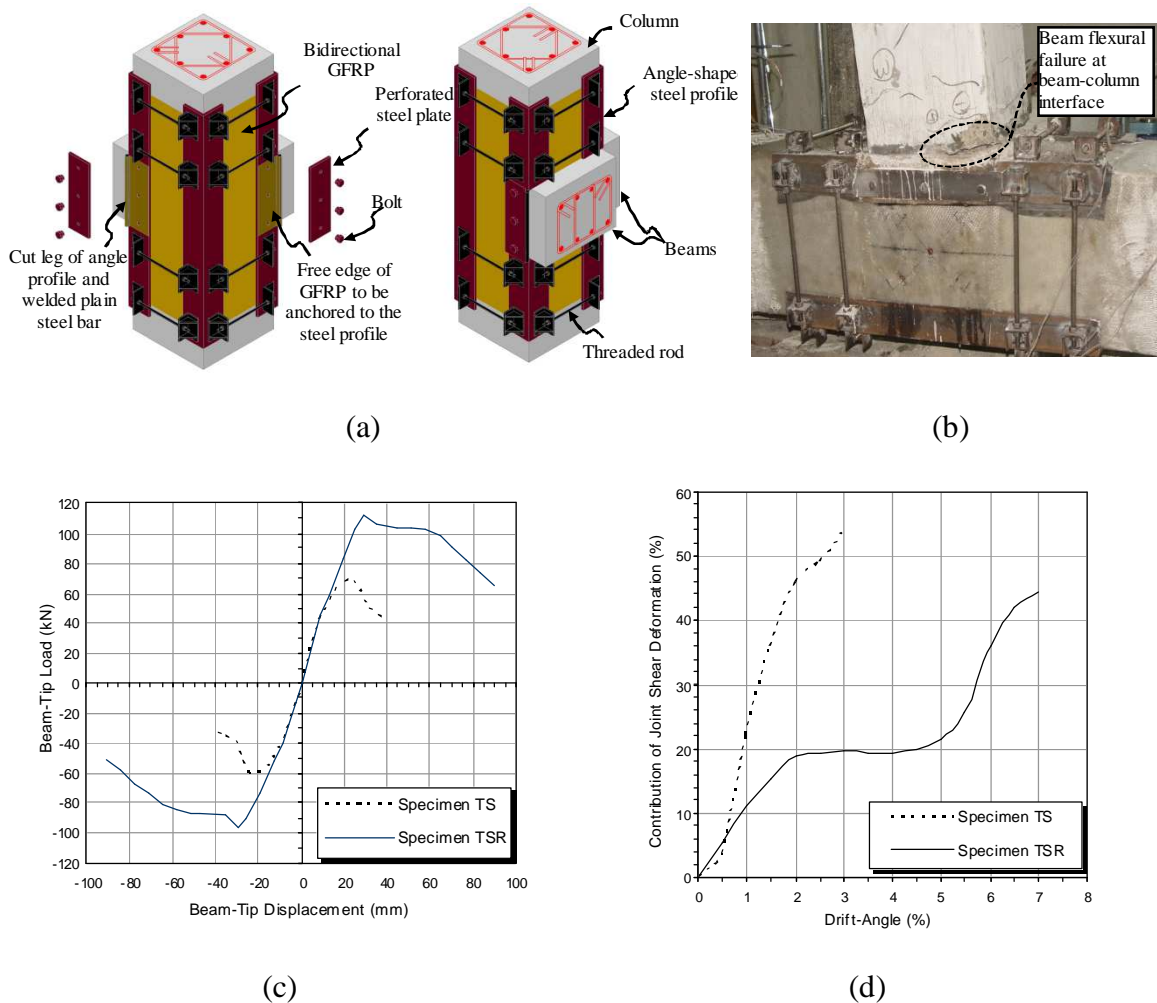
Figure 2.33: Investigation on strengthening of 3D corner RC beam-column joint by Esmaeeli and Danesh [94], (a) the proposed strengthening scheme, (b) failure mode of the strengthened specimen (TSR), (c) envelop of the hysteresis response of beam-tip displacement versus beam–tip load, (d) contribution of joint shear deformation in total drift.

Following the cyclic tests of the specimens, the authors reported that although FRP spikes effectively delayed debonding of FRP layers, in all the repaired specimens, debonding of FRP L-wrap close to the beam-column interface was observed (see Figure 2.34b). Hence, to prevent FRP debonding, the use of additional anchors, and one of them as close as possible to the beam-column interface, was suggested. The superior performance of the specimens with scheme 2, as compared with those repaired with scheme 1, suggests that CFRP is not only more efficient in confining the joint region but also contributes in a higher stiffness

recovery. Specimens repaired with scheme 2 fairly recovered the energy dissipation capacity registered in testing of their as-built conditions (in average 96%), while the repair with scheme 1 resulted in recovery in average of only 68%.



(a)                                              (b)
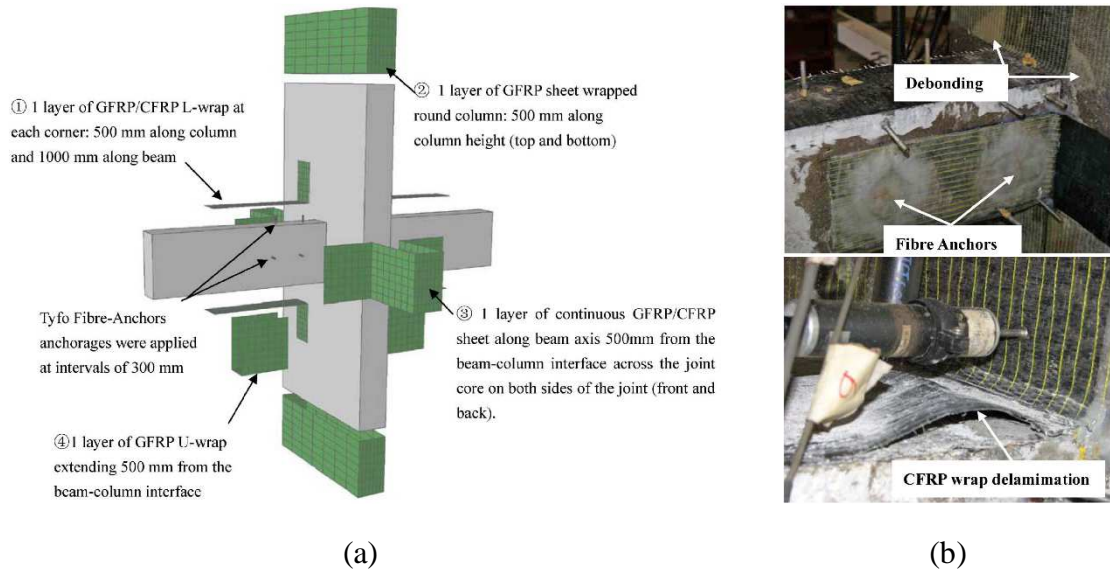
Figure 2.34: Rehabilitation of interior RC beam-wide column joints by Li and Kai [101], (a) proposed FRP strengthening schemes with FRP spikes as anchorage system, and (b) examples of debonding observed in the rehabilitated specimens.

Parvin et al. [100] proposed and tested two seismic strengthening techniques for exterior beam-column joints based on adhesively bonded CFRP sheets and wraps together with CFRP strips anchored into the perforated holes on the beam. Details of as-built specimens are shown in Figure 2.35a. These specimens were vulnerable against cyclic actions due to the lack of the ties in the joint panel, shortness of the embedded length of beam's bottom longitudinal steel bars into the joint panel, lap-spliced column's longitudinal steel bars just above story level, and insufficient column's confining ties at the vicinity of the joint region. The proposed FRP configurations were aimed at enhancing the joint shear capacity, preventing or delaying debonding of the beam's bottom bars, and assuring a higher flexural capacity for columns than beam. These two strengthening schemes with the main difference in the number of layers of the straight and U-shaped FRP sheets bonded to the column-joint and beam-joint regions, respectively, are represented in Figure 2.35b and Figure 2.35c.

These schemes were also different according to the configurations adopted for the CFRP strips which were passed through the perforated holes on the beams and bonded to the lateral faces of the specimen. As it is shown in Figure 2.35b and Figure 2.35c, while strip 1 was applied to prevent the sliding of the beam's bottom bars and the debonding of the U-shaped joint-beam CFRP sheets, strips 2 to 4 were only designed as the local anchorages for the U-shaped joint-beam CFRP sheets. For the scheme with higher numbers of CFRP sheets (scheme RC3U3), the U-shaped layer bonded to the joint-beam region was tailored in the way that a thin extension of that can be passed through the hole of the beam, perforated close to the level of the beam's bottom bars, and bonded to its opposite face. Three as-built beam-column joints and their counterparts' specimens strengthened with either of the aforementioned schemes were tested under simultaneous effects of axial load and cyclic reversal displacements imposed to the top of the column. Two different levels of column axial load (12% and 24% of column capacity) were examined as one of the parameters of this experimental investigation.

According to the test results all of the strengthened specimens significantly outperformed the control ones in terms of lateral load and deformation capacities, stiffness degradation, and the dissipated energy at their failure. However, up to the failure of the control specimens, no improvement in energy dissipation capacity of the strengthened specimens was observed. As depicted in Figure 2.36 all strengthened specimens, independent of the adopted CFRP configuration, failed by debonding of U-shaped CFRP layers at the top of the beam during the pull loading direction (top face of the beam in tension), and the rupture of these layers together with FRP strip 1 during the push loading direction (bottom face of the beam in tension). However, as it was expected, the increase in the joint shear strength for the strengthened specimens was sufficient enough to prevent the joint shear failure observed in control specimens. Both strengthening schemes resulted in a notable increase in the joint shear stiffness and deformation capacities (for example see Figure 2.37). Finally, while a higher axial load resulted in a higher lateral load capacity in the case of control specimens, a slight increase (12%) was attained in the lateral load carrying capacity of the CFRP strengthened specimen, only for the push direction of loading.

(a)                (b)                (c)
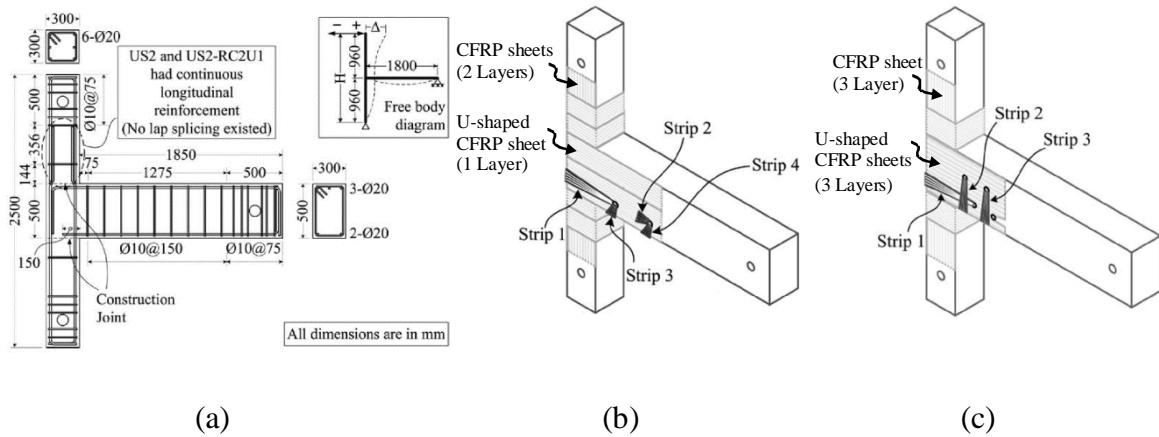
Figure 2.35: Experimental investigation on retrofitting of exterior beam-column joints by Parvin et al. [100], (a) specimen details and test configuration, (b) proposed CFRP scheme RC2U1, and (c) CFRP scheme RC3U3
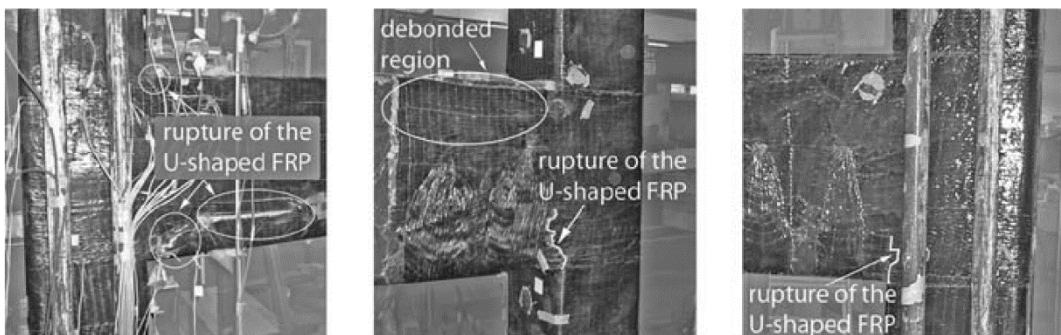


Figure 2.36: Failure of the retrofitted specimens investigated by Parvin et al. [100]
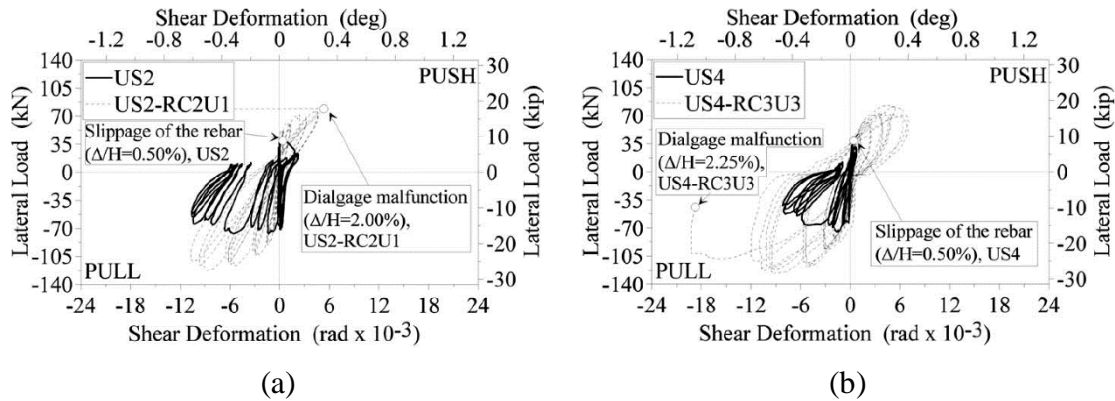
Figure 2.37: Comparison of joint shear deformation capacity before and after strengthening based on each of two CFRP schemes proposed by Parvin et al. [100]

As represented in Figure 2.38a, Eslami and Ronagh [102] proposed an alternative solution to transfer tensile stresses of the beam's longitudinal FRPs beyond beam-column interface, the beam moment critical section. According to their proposal, FRP laminates bonded to the top and bottom faces of the beam were anchored into a groove, executed at the concrete cover of the column. Small width FRP wraps were applied to the ends of longitudinal FRP sheets to enhance FRP-to-RC interfacial bond properties. Initially, series of specimens were tested adopting monotonic loading. After analyzing these tests results the most appropriate retrofitting configurations were designed and applied to the second series of specimens and their behavior was studied under cyclic load test. The results of monotonic loading revealed that concrete cone failure at the anchored region of FRP into the column is the governing failure mode, and it can be prevented if there are columns' FRP wraps at the vicinity of the joint region (see Figures 2.38b and 2.38c).

However, this technique is limited to the depth of concrete cover and might involve the risk of damaging column's longitudinal bars while carving the groove. Moreover, the joint region should resist higher demands associated to the shear stresses introduced by FRP anchorage, while the joint panel itself is prone to shear deficiency in RC structures with seismic retrofitting requirements. The solution studied by Mukherjee and Joshi [86] based on using the "L" shape FRP strengthening technique in combination with FRP wraps on both beam and column elements might be an alternative to partially treat the aforementioned concerns.

(a)                                (b)                (c)
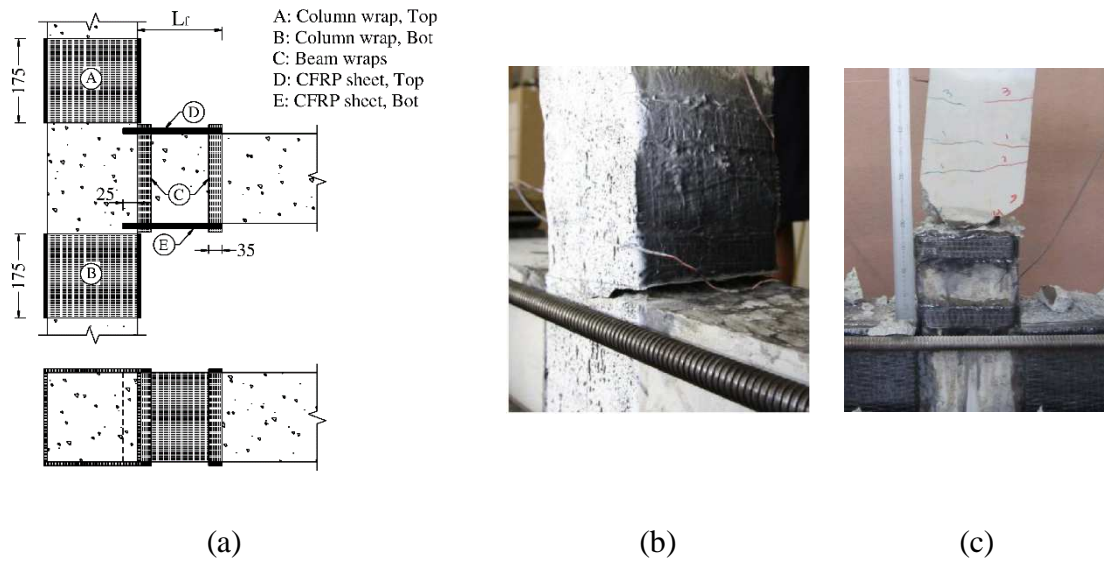
Figure 2.38: Retrofitting of exterior beam-column joints investigated by Eslami and Ronagh [102], (a) proposed retrofitting technique with beams longitudinal FRP anchored into a grooved carved in the concrete cover of the column, (b) concrete failure at the carved location in the absence of column FRP wraps (monotonic loading), (c) columns wraps prevented failure at the carved concrete location, and the flexural plastic hinge that formed on the beam (cyclic loading)

## 2.4 Durability of FRP Systems

Properties of FRP materials, specially their polymeric matrix, and their bonding adhesive to the concrete substrate are susceptible to degradation under exposure to a variety of environmental conditions such as high temperatures, temperature variations, wet-dry cycles related to moisture (including tap water, seawater and other chemical aqueous), alkalinity, and freeze-thaw cycles. A summary of the literature review on the influence of each of the aforementioned environmental conditions on performance of FRP as a retrofitting system for RC members is presented. A relatively comprehensive review on the topic of durability of FRP composites either as a constructional element or a retrofitting system is reported by Benmokrane and Mohamed [5].

### *2.4.1.1 Effects of High Temperature and Temperature Variations*

FRP and its bond to the concrete substrate can be affected by both high temperatures and temperature variations. There are two mechanisms contributing to the changes in characteristics of bonded FRP composites as a result of temperature variations: (i) different thermal expansion of resin matrix, fibers and concrete substrate that results in residual stresses due to thermal variations, and (ii) deterioration in mechanical properties of resin polymers in temperatures higher than their glass transition temperature $T_g$.

Woods [103] investigated the behavior of 364 carbon coupons bonded to concrete blocks, which were subjected to different environmental conditions. Four FRP coupons were externally bonded by means of epoxy adhesive to the opposite faces of each concrete block and they were tested sequentially at different exposure times. Six different environmental conditions were simulated and their effects on each series of specimens were studied according to the changes in mode II fracture toughness obtained by pull test. The decrease level of the fracture toughness over the time was dependent of the moisture content, chemical solution, and temperature. The highest degradation in bond strength was attributed to seawater conditioning, and the calcium hydroxide environment was reported to have the least effect. Results of the specimens subjected to 140°F to 160°F (60°C to 71°C) also showed a decreasing trend in mode II fracture toughness as the temperature was increased. According to these studies, a combined effect of high temperature, 140°F (60°C), and high humidity showed a large decrease in fracture mode II at crack initiation load, as compared to the corresponding value obtained by testing the control specimens. While for temperatures lower than 50°C the failure mode consisted of concrete fracture in combination with failure in epoxy adhesive, at temperatures higher than 60°C, a rapid reduction in bond strength of CFRP sheets bonded to concrete blocks by means of epoxy resin, with CFRP dobonding being the failure mode, was reported by Gamage at el. [104].

Burke at el. [8] preformed experimental tests on FRP flexurally strengthened RC beams subjected to sustained load at temperatures higher than glass transition temperature, $T_g$, of matrix/adhesive polymers. In this way, they investigated and compared performance of near surface mounted (NSM) and externally bonded FRP systems at the elevated temperatures under a service load. According to their results, both NSM and externally bonded FRP

strengthening systems are susceptible to the strength degradation at the elevated temperature. Although it was believed that the NSM systems might have a better thermal stability due to being embedded within the concrete cover, they reported that based on their limited data the epoxy bonded NSM-CFRP system has only an endurance time of 40 minutes at 100°C. This endurance time was decreased significantly and reached to 10 min at 200°C. Authors also reported that thermal stability performance was greatly enhanced when epoxy was replaced with a cementitious grout adhesive. However, with this alternative the strain development in FRP system is limited to lower values, as compared to epoxy bonded FRP laminates, which conversely affects the eventual cost of the strengthening system.

Yu and Kodur [105] reported that the bond strength of NSM-CFRP decreases up to 80% at 200° C compared to the bond strength of pull-out specimens tested at 20°C.

Silva et al. [106] examined the effects of thermal cycles on concrete specimens strengthened with NSM-CFRP strips (laminates). CFRP-NSM strengthened RC slabs, pull-out specimens composed of concrete cubes with CFRP laminates bonded to it and each of the individual materials (plain concrete, cured epoxy and CFRP laminates) were the studied specimens. These specimens were exposed to four or eight months of thermal cycles that ranged between -15°C and 60°C. After each of these conditioning periods, series of these specimens were tested to examine their performance. Strength gain after imposing thermal cycles to the epoxy samples was observed. Only negligible changes in the strength of concrete and CFRP samples subjected to these thermal cycles were reported. The bond strength, measured by testing pull-out specimens, indicated a slight increase while the failure mode was not affected by thermal cycles. Flexural load carrying capacity of strengthened slabs also found to be not sensitive to this range of exposed thermal cycles.

### 2.4.1.2 Effects of Freeze and Thaw Cycles

Concrete blocks with two CFRP strips bonded to their opposite faces, were exposed to cycles of freeze and thaw, in temperatures ranging between -18°C and +4°C in a dry environment. These specimens were subjected to pull-pull tests in an experimental research conducted by Colombi et al. [107]. CFRP strips bonded to opposite faces of each block differed only in their bonded length. In agreement with finding of Green et al.[108], Colombi et al. [107] indicated that the effect on bond deterioration due to freeze and thaw exposure

is marginal. In contrary to these results, Ghosh and Karbhari [109] stated that freezing exposure condition at 0°F (-17.8°C) was the most deteriorative among all environmental conditions studied in their experimental program, since the epoxy resin/adhesive matrix becomes brittle when exposed to low temperature. The deteriorative effects of freeze and thaw cycles on FRP bond strength is also supported by results of the experiments conducted by shearing the single lab specimens (SLBs) made of epoxy bonded GFRP-GFRP or CFRP-CFRP strips [110]. In both cases Homam and Sheikh [110] concluded that the bond strength was adversely affected by cycles of freeze and thaw, but with a lesser extent for CFRP SLB specimens.

### 2.4.1.3 Effects of Marine Environment

Results of pull-off tests on epoxy bonded CFRP strips to concrete block which were exposed to saltwater, to simulate marine environment, showed a significant bond strength degradation of 69% after 12 months and 100% at the end of 18 months of exposure [109]. The deteriorative effect of seawater was also reported by Woods [103], which was attributed to the accumulation of chloride ions at the interface of epoxy-concrete causing deterioration of the concrete right below the bonded FRP.

Qiao et al. [111] performed three-point bending tests on beams strengthened with CFRP and obtained mode-I fracture energy to measure the influence of each of the wet-dry and freeze-thaw cycles conditioning on FRP-concrete bonded interface immersed in calcium chloride (CaCl) solution. For both exposure conditions, reduction in mode-I fracture energy by increasing the number of cycles was reported. Authors concluded that, deterioration of CFRP-concrete bond interface under both of these examined conditions was relatively substantial.

### 2.4.1.4 Effects of Alkalinity

Homam and Sheikh [110] reported that alkaline environment (NaOH with pH10 and pH 12 at 38°C) had an adverse effect on bond of SLB specimens made of epoxy bonded GFRP-GFRP or CFRP-CFRP. Bond strength reduction up to 15% for exposure to pH10 was observed.

In the experimental program conducted by Pan et al. [112], the effect of immersion time in different concentrations of sodium chloride solution was studied. Direct shear tests as the strategy to measure the strength of CFRP strengthened concrete members was performed. CFRP plates were bonded to concrete blocks by means of epoxy adhesive. Specimens were fully immersed in solutions of sodium chloride with different concentrations and were tested in different aging after exposure. FRP debonding was the governing failure mode for all of the specimens. As a consequence of degradation in properties of epoxy adhesive in the specimens conditioned up to 30 days, and the degradation in properties of both concrete and epoxy adhesive of specimens with an exposure time longer than 90 days, reduction in ultimate pull load capacity was occurred. Specimens between 30 and 60 days of conditioning exhibited a load increase which was explained by the further hydration process of cement and therefore some strength gain of concrete.

## Bibliography

[1] Oehlers D, Moran J. Premature Failure of Externally Plated Reinforced Concrete Beams. Journal of Structural Engineering. 1990;116(4):978-95.

[2] Roberts TM, Haji-Kazemi H. Strengthening of under-reinforced concrete beams with mechanically attached steel plates. International Journal of Cement Composites and Lightweight Concrete. 1989;11(1):21-7.

[3] Jones R, Swamy R, Charif A. Plate separation and anchorage of reinforced concrete beams strengthened by epoxy-bonded steel plates. Structural Engineer. 1988;66(5).

[4] Hussain M, Sharif A, Baluch IBM, Al-Sulaimani G. Flexural behavior of precracked reinforced concrete beams strengthened externally by steel plates. ACI Structural Journal. 1995;92(1).

[5] Benmokrane B, Mohamed HM. Durability Issues of FRP for Civil Infrastructure. In: 11th International Symposium on Fiber Reinforced Polymers for Reinforced Concrete Structures (FRPRCS11). Guimaraes; 2013:11-4.

[6] Teng J, De Lorenzis L, Wang B, Li R, Wong T, Lam L. Debonding Failures of RC Beams Strengthened with Near Surface Mounted CFRP Strips. Journal of Composites for Construction. 2006;10(2):92-105.

[7] Teng JG, Smith ST, Yao J, Chen JF. Intermediate crack-induced debonding in RC beams and slabs. Construction and Building Materials. 2003;17(6–7):447-62.

[8] Burke PJ, Bisby LA, Green MF. Effects of elevated temperature on near surface mounted and externally bonded FRP strengthening systems for concrete. Cement and Concrete Composites. 2013;35(1):190-9.

[9] Kalfat R, Al-Mahaidi R. Investigation into bond behaviour of a new CFRP anchorage system for concrete utilising a mechanically strengthened substrate. Composite Structures. 2010;92(11):2738-46.

[10] ACI 440.2R-08:2008. Guide for the Design and Construction of Externally Bonded FRP Systems for Strengthening Concrete Structures: American Concrete Institute.

[11] Ritchie PA, Thomas DA, Lu L-W, Conelly GM. External reinforcement of concrete beams using fiber reinforced plastics. ACI Structural Journal. 1991;88(4).

[12] Shahawy M, Beitelman T. Static and Fatigue Performance of RC Beams Strengthened with CFRP Laminates. Journal of Structural Engineering. 1999;125(6):613-21.

[13] Fanning P, Kelly O. Ultimate Response of RC Beams Strengthened with CFRP Plates. Journal of Composites for Construction. 2001;5(2):122-7.

[14] Shin Y-S, Lee C. Flexural behavior of reinforced concrete beams strengthened with carbon fiber-reinforced polymer laminates at different levels of sustaining load. ACI Structural Journal. 2003;100(2).

[15] Buyukozturk O, Gunes O, Karaca E. Progress on understanding debonding problems in reinforced concrete and steel members strengthened using FRP composites. Construction and Building Materials. 2004;18(1):9-19.

[16] Grelle SV, Sneed LH. Review of anchorage systems for externally bonded FRP laminates. International Journal of Concrete Structures and Materials. 2013;7(1):17-33.

[17] Teng JG, Chen JF. Mechanics of debonding in FRP-plated RC beams. In: Proceedings of the ICE - Structures and Buildings. 2009;162:335-45.

[18] Tumialan G, Serra P, Nanni A, Belarbi A. Concrete cover delamination in reinforced concrete beams strengthened with carbon fiber reinforced polymer sheets. ACI Special Publication. 1999;188.

[19] Seim W, Hörman M, Karbhari V, Seible F. External FRP Poststrengthening of Scaled Concrete Slabs. Journal of Composites for Construction. 2001;5(2):67-75.

[20] Garden HN, Hollaway LC. An experimental study of the influence of plate end anchorage of carbon fibre composite plates used to strengthen reinforced concrete beams. Composite Structures. 1998;42(2):175-88.

[21] Ceroni F, Pecce M, Matthys S, Taerwe L. Debonding strength and anchorage devices for reinforced concrete elements strengthened with FRP sheets. Composites Part B: Engineering. 2008;39(3):429-41.

[22] Kalfat R, Al-Mahaidi R, Smith S. Anchorage Devices Used to Improve the Performance of Reinforced Concrete Beams Retrofitted with FRP Composites: State-of-the-Art Review. Journal of Composites for Construction. 2011;17(1):14-33.

[23] Breña S, McGuirk G. Advances on the Behavior Characterization of FRP-Anchored Carbon Fiber-Reinforced Polymer (CFRP) Sheets Used to Strengthen Concrete Elements. International Journal of Concrete Structures and Materials. 2013;7(1):3-16.

[24] Attari N, Amziane S, Chemrouk M. Flexural strengthening of concrete beams using CFRP, GFRP and hybrid FRP sheets. Construction and Building Materials. 2012;37(0):746-57.

[25] Yalim B, Kalayci A, Mirmiran A. Performance of FRP-Strengthened RC Beams with Different Concrete Surface Profiles. Journal of Composites for Construction. 2008;12(6):626-34.

[26] Spadea G, Bencardino F, Swamy R. Structural Behavior of Composite RC Beams with Externally Bonded CFRP. Journal of Composites for Construction. 1998;2(3):132-7.

[27] Wu Y, Huang Y. Hybrid Bonding of FRP to Reinforced Concrete Structures. Journal of Composites for Construction. 2008;12(3):266-73.

[28] Wu Z-M, Hu C-H, Wu Y-F, Zheng J-J. Application of improved hybrid bonded FRP technique to FRP debonding prevention. Construction and Building Materials. 2011;25(6):2898-905.

[29] Zhou Y, Gou M, Zhang F, Zhang S, Wang D. Reinforced concrete beams strengthened with carbon fiber reinforced polymer by friction hybrid bond technique: Experimental investigation. Materials & Design. 2013;50(0):130-9.

[30] Pham H, Al-Mahaidi R. Prediction Models for Debonding Failure Loads of Carbon Fiber Reinforced Polymer Retrofitted Reinforced Concrete Beams. Journal of Composites for Construction. 2006;10(1):48-59.

[31] Smith ST, Teng JG. Shear-Bending Interaction in Debonding Failures of FRP-Plated RC Beams. Advances in structural engineering. 2003;6(3):183-99.

[32] Pimanmas A, Pornpongsaroj P. Peeling behaviour of reinforced concrete beams strengthened with CFRP plates under various end restraint conditions. Magazine of Concrete Research. 2004;56(2):73-81.

[33] Orton S, Jirsa J, Bayrak O. Design Considerations of Carbon Fiber Anchors. Journal of Composites for Construction. 2008;12(6):608-16.

[34] Xiong GJ, Jiang X, Liu JW, Chen L. A way for preventing tension delamination of concrete cover in midspan of FRP strengthened beams. Construction and Building Materials. 2007;21(2):402-8.

[35] Hosny A, Shaheen H, Abdelrahman A, Elafandy T. Performance of reinforced concrete beams strengthened by hybrid FRP laminates. Cement and Concrete Composites. 2006;28(10):906-13.

[36] Grace NF, Ragheb WF, Abdel-Sayed G. Flexural and shear strengthening of concrete beams using new triaxially braided ductile fabric. ACI Structural Journal. 2003;100(6).

[37] Wu Z, Li W, Sakuma N. Innovative externally bonded FRP/concrete hybrid flexural members. Composite Structures. 2006;72(3):289-300.

[38] Teng J, Lam L, Chan W, Wang J. Retrofitting of Deficient RC Cantilever Slabs Using GFRP Strips. Journal of Composites for Construction. 2000;4(2):75-84.

[39] Lam L, Teng J. Strength of RC Cantilever Slabs Bonded with GFRP Strips. Journal of Composites for Construction. 2001;5(4):221-7.

[40] Tan K, Patoary M. Strengthening of Masonry Walls against Out-of-Plane Loads Using Fiber-Reinforced Polymer Reinforcement. Journal of Composites for Construction. 2004;8(1):79-87.

[41] Antoniades KK, Salonikios TN, Kappos AJ. Evaluation of hysteretic response and strength of repaired R/C walls strengthened with FRPs. Engineering Structures. 2007;29(9):2158-71.

[42] Eshwar N, Ibell TJ, Nanni A. Effectiveness of CFRP Strengthening on Curved Soffit RC Beams. Advances in structural engineering. 2005;8(1):55-68.

[43] Smith ST, Hu S, Kim SJ, Seracino R. FRP-strengthened RC slabs anchored with FRP anchors. Engineering Structures. 2011;33(4):1075-87.

[44] Oh HS, Sim J. Interface debonding failure in beams strengthened with externally bonded GFRP. Composite Interfaces. 2004;11(1):25-42.

[45] Micelli F, Rizzo A, Galati D. Anchorage of composite laminates in RC flexural beams. Structural Concrete. 2010;11(3):117-26.

[46] Seliem H, Seracino R, Sumner E, Smith S. Case Study on the Restoration of Flexural Capacity of Continuous One-Way RC Slabs with Cutouts. Journal of Composites for Construction. 2011;15(6):992-8.

[47] Täljsten B, Carolin A, Nordin H. Concrete structures strengthened with near surface mounted reinforcement of CFRP. Advances in structural engineering. 2003;6(3):201-13.

[48] Hassan T, Rizkalla S. Flexural strengthening of prestressed bridge slabs with FRP systems. PCI journal. 2002;47(1):76-93.

[49] El-Hacha R, Rizkalla SH. Near-surface-mounted fiber-reinforced polymer reinforcements for flexural strengthening of concrete structures. ACI Structural Journal. 2004;101(5).

[50] Barros JAO, Fortes AS. Flexural strengthening of concrete beams with CFRP laminates bonded into slits. Cement and Concrete Composites. 2005;27(4):471-80.

[51] Täljsten B. CFRP-strengthened-concrete structures strengthened with near surface mounted CFRP laminates. In: Proc, 3rd Int Conf on Composites in Infrastructure. San Francisco, Calif.; 2002.

[52] De Lorenzis L, Nanni A. Characterization of FRP Rods as Near-Surface Mounted Reinforcement. Journal of Composites for Construction. 2001;5(2):114-21.

[53] Hassan T, Rizkalla S. Investigation of Bond in Concrete Structures Strengthened with Near Surface Mounted Carbon Fiber Reinforced Polymer Strips. Journal of Composites for Construction. 2003;7(3):248-57.

[54] De Lorenzis L, Teng JG. Near-surface mounted FRP reinforcement: An emerging technique for strengthening structures. Composites Part B: Engineering. 2007;38(2):119-43.

[55] Ceroni F. Experimental performances of RC beams strengthened with FRP materials. Construction and Building Materials. 2010;24(9):1547-59.

[56] Lamanna AJ. Flexural strengthening of reinforced concrete beams with mechanically fastened fiber reinforced polymer strips [PhD Thesis]: University of Wisconsin – Madison; 2002.

[57] Arora D. Rapid Strengthening of Reinforced Concrete Bridge with Mechanically Fastened - Fiber Reinforced Polymer Strips [MSc Thesis]: University of Wisconsin – Madison; 2003.

[58] Lamanna AJ, Bank LC, Borowicz DT. Mechanically fastened FRP strengthening of large scale RC bridge T beams. Advances in structural engineering. 2004;7(6):525-38.

[59] Martinelli E, Napoli A, Nunziata B, Realfonzo R. RC Beams Strengthened with Mechanically Fastened Composites: Experimental Results and Numerical Modeling. Polymers. 2014;6(3):613-33.

[60] Bank LC, Borowicz DT, Lamanna AJ, Ray JC, Velazquez GI. Rapid strengthening of full-sized concrete beams with powder-actuated fastening systems and Fiber-Reinforced Polymer (FRP) composite materials. DTIC Document; 2002.

[61] Bank LC, Lamanna AJ, Ray JC, Velazquez GI. Rapid Strengthening of RC Beams with MF-FRP Composite Materials. 2002.

[62] Bank L. Mechanically-fastened FRP (MF-FRP)–a viable alternative for strengthening RC members. FRP Composites in Civil Engineering-CICE 2004: Proceedings of the 2nd International Conference on FRP Composites in Civil Engineering-CICE 2004, 8-10 December 2004, Adelaide, Australia: Taylor & Francis; 2006. p. 3.

[63] Quattlebaum J, Harries K, Petrou M. Comparison of Three Flexural Retrofit Systems under Monotonic and Fatigue Loads. Journal of Bridge Engineering. 2005;10(6):731-40.

[64] Tan KH, Saha MK. Mechanically Fastened FRP-Strengthened RC Beams under Cyclic Loading. In: Proc of FRPRCS8. Patras, Greece; 2007.

[65] Rizzo A. Application of Mechanically Fastened FRP (MF-FRP) Pre-cured Laminates in Off- System Bridges [M.Sc.]: University of Missuri-Rolla; 2005.

[66] Ekenel M, Rizzo A, Myers J, Nanni A. Flexural Fatigue Behavior of Reinforced Concrete Beams Strengthened with FRP Fabric and Precured Laminate Systems. Journal of Composites for Construction. 2006;10(5):433-42.

[67] Napoli A. RC Structures Strengthened with Mechanically Fastened FRP Systems [MSc Thesis]: University of Miami; 2008.

[68] Elsayed W, Ebead U, Neale K. Mechanically Fastened FRP-Strengthened Two-Way Concrete Slabs with and without Cutouts. Journal of Composites for Construction. 2009;13(3):198-207.

[69] Camanho PP, Matthews FL. Stress analysis and strength prediction of mechanically fastened joints in FRP: a review. Composites Part A: Applied Science and Manufacturing. 1997;28(6):529-47.

[70] Hassan N, Mohamedien M, Rizkalla S. Multibolted Joints for GFRP Structural Members. Journal of Composites for Construction. 1997;1(1):3-9.

[71] Hassan N, Mohamedien M, Rizkalla S. Rational Model for Multibolted Connections for GFRP Members. Journal of Composites for Construction. 1997;1(2):71-8.

[72] Lee JH, Lopez MM, Bakis CE. Slip effects in reinforced concrete beams with mechanically fastened FRP strip. Cement and Concrete Composites. 2009;31(7):496-504.

[73] Hart-Smith LJ. Mechanically-Fastened Joints for Advanced Composites — Phenomenological Considerations and Simple Analyses. In: Lenoe E, Oplinger D, Burke J, editors. Fibrous Composites in Structural Design: Springer US; 1980. p. 543-74.

[74] Lamanna AJ, Bank LC, Scott DW. Flexural strengthening of reinforced concrete beams by mechanically attaching fiber-reinforced polymer strips. Journal of Composites for Construction. 2004;8(3):203-10.

[75] Borowicz DT. Rapid strengthening of concrete beams with powder-actuated fastening systems and fiber reinforced polymer (FRP) composite materials [MSc Thesis]: University of Wisconsin – Madison; 2002.

[76] Martin J, Lamanna A. Performance of Mechanically Fastened FRP Strengthened Concrete Beams in Flexure. Journal of Composites for Construction. 2008;12(3):257-65.

[77] Moehle J, Elwood K, Sezen H. Gravity Load Collapse of Building Frame During Earthquakes. ACI Special Publication. 2002;197.

[78] Sezen H, Whittaker AS, Elwood KJ, Mosalam KM. Performance of reinforced concrete buildings during the August 17, 1999 Kocaeli, Turkey earthquake, and seismic design and construction practise in Turkey. Engineering Structures. 2003;25(1):103-14.

[79] Alkhrdaji T, Silva P. Seismic Strengthening of Concrete Buildings Using FRP Composites. American Concrete Institute; 2008.

[80] Fernandes C, Melo J, Varum H, Costa A. Cyclic Behavior of Substandard Reinforced Concrete Beam-Column Joints with Plain Bars. ACI Structural Journal. 2013;110(1):11.

[81] Said AM, Nehdi ML. Use of FRP for RC frames in seismic zones: Part I. Evaluation of FRP beam-column joint rehabilitation techniques. Applied Composite Materials. 2004;11(4):205-26.

[82] Hakuto S, Park R, Tanaka H. Seismic Load Tests on Interior and Exterior Beam-Column Joints with Substandard Reinforcing Details. ACI Structural Journal. 2000;97(1):15.

[83] Engindeniz M, Kahn LF, Zureick A-H. Repair and Strengthening of Reinforced Concrete Beam-Column Joints: State of the Art. ACI Structural Journal. 2005;102(2):14.

[84] Bousselham A. State of Research on Seismic Retrofit of RC Beam-Column Joints with Externally Bonded FRP. Journal of Composites for Construction. 2010;14(1):49-61.

[85] Al-Salloum Y, Almusallam T. Seismic Response of Interior RC Beam-Column Joints Upgraded with FRP Sheets. I: Experimental Study. Journal of Composites for Construction. 2007;11(6):575-89.

[86] Mukherjee A, Joshi M. FRPC reinforced concrete beam-column joints under cyclic excitation. Composite Structures. 2005;70(2):185-99.

[87] Pantelides CP, Okahashi Y, Reaveley LD. Seismic Rehabilitation of RC Frame Interior Beam-Column Joints with FRP Composites. In: The 14th World Conference on Earthquake Engineering. Beijing; 2008.

[88] Karayannis CG, Sirkelis GM. Strengthening and rehabilitation of RC beam–column joints using carbon-FRP jacketing and epoxy resin injection. Earthquake Engineering & Structural Dynamics. 2008;37(5):769-90.

[89] Tsonos AG. Effectiveness of CFRP-jackets and RC-jackets in post-earthquake and pre-earthquake retrofitting of beam–column subassemblages. Engineering Structures. 2008;30(3):777-93.

[90] Danesh F, Esmaeeli E, Alam MF. Shear Strengthening of 3D RC Beam-Column Connection Using GFRP: FEM Study. Asian Journal of Applied Sciences. 2008;1(3):217-27.

[91] Ha G-J, Cho C-G, Kang H-W, Feo L. Seismic improvement of RC beam–column joints using hexagonal CFRP bars combined with CFRP sheets. Composite Structures. 2013;95(0):464-70.

[92] Lee WT, Chiou YJ, Shih MH. Reinforced concrete beam–column joint strengthened with carbon fiber reinforced polymer. Composite Structures. 2010;92(1):48-60.

[93] Mahini SS, Ronagh HR. Strength and ductility of FRP web-bonded RC beams for the assessment of retrofitted beam–column joints. Composite Structures. 2010;92(6):1325-32.

[94] Esmaeeli E, Danesh F. Shear Strengthening of 3D corner beam–column connection using bidirectional GFRP layers. Proceeding of fourth international conference on FRP composites in civil engineering (CICE2008) Zurich. 2008.

[95] Antonopoulos C, Triantafillou T. Experimental Investigation of FRP-Strengthened RC Beam-Column Joints. Journal of Composites for Construction. 2003;7(1):39-49.

[96] Ghobarah A, Said A. Shear strengthening of beam-column joints. Engineering Structures. 2002;24(7):881-8.

[97] Al-Salloum Y, Almusallam T, Alsayed S, Siddiqui N. Seismic Behavior of As-Built, ACI-Complying, and CFRP-Repaired Exterior RC Beam-Column Joints. Journal of Composites for Construction. 2011;15(4):522-34.

[98] Engindeniz M, Kahn LF, Zureick A-H. Pre-1970 RC Corner Beam-Column-Slab Joints: Seismic Adequacy and Upgradability with CFRP Composites. In: The 14th World Conference on Earthquake Engineering. Beijing; 2008.

[99] El-Amoury T, Ghobarah A. Seismic rehabilitation of beam–column joint using GFRP sheets. Engineering Structures. 2002;24(11):1397-407.

[100] Parvin A, Altay S, Yalcin C, Kaya O. CFRP Rehabilitation of Concrete Frame Joints with Inadequate Shear and Anchorage Details. Journal of Composites for Construction. 2009;14(1):72-82.

[101] Li B, Kai Q. Seismic Behavior of Reinforced Concrete Interior Beam-Wide Column Joints Repaired Using FRP. Journal of Composites for Construction. 2011;15(3):327-38.

[102] Eslami A, Ronagh H. Experimental Investigation of an Appropriate Anchorage System for Flange-Bonded Carbon Fiber–Reinforced Polymers in Retrofitted RC Beam–Column Joints. Journal of Composites for Construction. 2014;18(4):04013056.

[103] Woods JM. Accelerated testing for bond reliability of fiber-reinforced polymers (FRP) to concrete and steel in aggressive environments [Doctoral]: The University of Arizona; 2003.

[104] Gamage J, Wong M-B, Al-Mahaidi R. Performance of CFRP strengthened concrete members under elevated temperatures. Proceedings of the International Symposium on Bond Behaviour of FRP in Structures (BBFS 2005), International Institute for FRP in Construction, Hong Kong2005. p. 119-8.

[105] Yu B, Kodur VKR. Effect of high temperature on bond strength of near-surface mounted FRP reinforcement. Composite Structures. 2014;110(0):88-97.

[106] Silva P, Fernandes P, Sena-Cruz J, Azenha M, BARROS J. Behaviour of Concrete Elements Strengthened with Near Surface Mounted CFRP Strips under Thermal Cycles. Proceeding of 7th International Conference on FRP Composites in Civil Engineering (CICE2008). Vancouver, British Columbia, Canada: International Institute for FRP in construction (IIFC); 2014.

[107] Colombi P, Fava G, Poggi C. Bond strength of CFRP–concrete elements under freeze–thaw cycles. Composite Structures. 2010;92(4):973-83.

[108] Green MF, Bisby LA, Beaudoin Y, Labossière P. Effect of freeze-thaw cycles on the bond durability between fibre reinforced polymer plate reinforcement and concrete. Canadian Journal of Civil Engineering. 2000;27(5):949-59.

[109] Ghosh KK, Karbhari VM. A critical review of infrared thermography as a method for non-destructive evaluation of FRP rehabilitated structures. International Journal of Materials & Product Technology. 2006;25(4):24-266.

[110] Homam SM, Sheikh SA. Durability of Fibre Reinforced Polymers Used in Concrete Structures. In: Proceedings of the 3rd International Conference on Advanced Composite Materials in Bridges and Structures. Ottawa, Canada; 2000:751-8.

[111] Qiao P, Xu Y. Effects of Freeze-Thaw and Dry-Wet Conditionings on the Mode-I Fracture of FRP-Concrete Interface Bonds. Engineering, Construction, and Operations in Challenging Environments 2004. p. 601-8.

[112] Pan J, Huang Y, Xing F. Effect of chloride content on bond behavior between FRP and concrete. Trans Tianjin Univ. 2010;16(6):405-10.

# Chapter 3: Strain Hardening Cementitious Composites (SHCC)

## 3.1 Introduction

Adding short discrete fibers into a cement based matrix (mortar or concrete) may turn its brittle post-cracking response into a ductile one. The shape of the tensile post-cracking response of this composite depends on the mechanical properties of the matrix, geometrical and mechanical properties of the fibers and their volume fraction in composite mixture, and fiber-matrix interface characteristics. Depending on how these parameters are tailored, as shown in Figure 3.1, a fiber reinforced cementitious composite (FRCC) can present a tensile post-cracking either with a smooth tensile load decay (strain softening behavior), or with a load increasing branch (strain hardening behavior) followed by a load decreasing regime just beyond composite ultimate tensile strength. Cementitious composites with strain softening response are often called conventional/ordinary fiber reinforced concretes (FRCs) in literature, while the other one refers to an advanced composite designated as tensile strain hardening cementitious composite (SHCC).

As shown in Figure 3.1, under tensile loading, contrary to FRC, whose elongation beyond the formation of the first crack $(\varepsilon_{cr}$ , $\sigma_{cr})$ is dominated by the opening of this individual crack, the SHCC exhibits multiple diffused fine cracks in a strain hardening regime. When SHCC reaches its ultimate tensile capacity, $\sigma_u$ , similarly to FRC, a crack opening localization dominates its further elongation, and its residual strength is characterized with a strain softening response. As depicted in Figure 3.1, $\varepsilon_u$ represents the strain corresponding to the tensile strength $(\sigma_u)$ of SHCC, which quantifies the composite's tensile ductility. $\varepsilon_u$ is literally designated as "strain capacity" of the composite, which is associated to the potential of SHCC to develop multiple cracks along its stretched length, and to the maximum opening of these cracks at the composite's tensile strength.

SHCCs were often known as High Performance Fiber Reinforced Cementitious Composites (HPFRCC) up to 2003, when Naaman and Reinhardt [1] suggested a classification for the FRCCs. In fact, the term "high performance" was in use long before to distinguish concretes possessing a high compressive strength or a high durability from the

ordinary ones. Hence, Naaman and Reinhardt [1] established a classification for FRCCs taking into account the composite post-cracking response. According to their proposed classification, a critical volume fraction of fibers, $\left(V_f^{crit}\right)_{tension}$, defines a border between two distinct tensile behaviors of FRCCs. If the fibers volume fraction in the composite mixture, $V_f$, exceeds this critical volume fraction, $\left(V_f^{crit}\right)_{tension}$, this FRCC is characterized as tensile Strain Hardening Cementitious Composite (SHCC). On the other hand, if $V_f$ is lower than $\left(V_f^{crit}\right)_{tension}$, the resulting FRCC exhibits a tensile Strain Softening in its post-cracking regime, known as ordinary Fiber Reinforced Concrete (FRC).
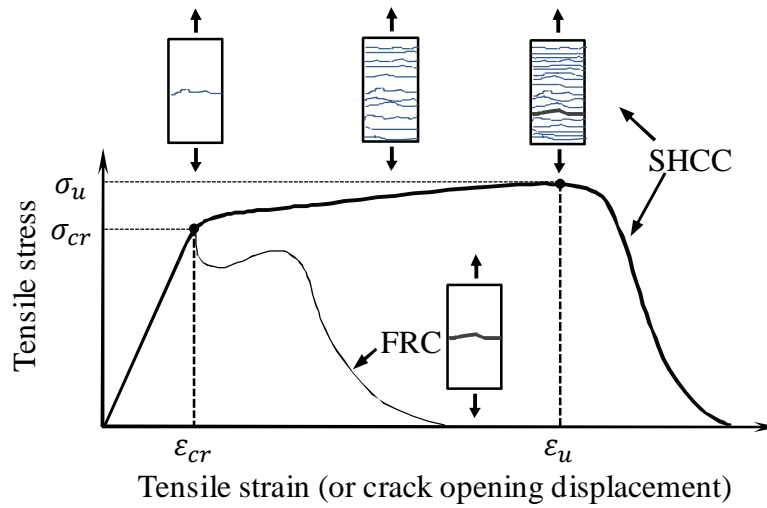


Figure 3.1: Typical tensile stress *versus* strain (displacement) response of SHCC and ordinary FRC (Note: in softening regime the horizontal axis is scaled with the crack opening displacement instead of strain)

Furthermore, FRCCs were also categorized considering their post-cracking behavior in pure bending. In this case, the definition of a critical volume of fibers $\left(V_f^{crit}\right)_{bending}$ to achieve a deflection hardening response beyond the composite first cracking in bending is used. According to this criterion the deflection hardening in an FRC occurs only if $V_f \geq \left(V_f^{crit}\right)_{bending}$. Note that $V_f$ of an SHCC is always larger than $\left(V_f^{crit}\right)_{bending}$, hence SHCC essentially presents a deflection hardening under bending.

The aforementioned classification is schematically presented in Figure 3.2. Following this classification, the terminology of the SHCC may be then customized to take into account a specific performance, such as high strength (HS-SHCC) or ultra-ductility (UD-SHCC).

The trend line of SHCCs evolution was oriented by the generation of different types of fibers, the technological advances in fiber's surface treatment, the progress in designing cementitious matrix, and the emerging of micromechanical models for optimizing SHCC design.

The earliest development of SHCC, when the occurrence of multiple cracking under tensile loading was reported, possibly goes back to the 1980's, with the emerge of SIFCON, an infiltrated low-viscosity cement slurry into a bed of high percentage of steel fibers pre-packed into a mold [2]. SIFCON with 12% of hooked ends steel fibers (length, $l_f$, and diameter, $d_f$, of 30 and 0.5 mm, respectively) presented a tensile strength, $\sigma_u$, of 15.6 MPa at a corresponding strain capacity, $\varepsilon_u$, of 1.25%. This composite possessed a high compressive strength, $f_c'$, of 120 MPa.

The early 1990's can be probably referred as a milestone towards the development of high strain capacity SHCCs by employing a relatively low volume of fibers. At those years, Li et al [3, 4] developed an ultra-ductile composite mixing only 2% short discrete plasma treated ultra-high molecular weight Polyethylene fibers (PE) into a finely graded cementitious matrix. The resulting composite, designated Engineered Cementitious Composite (PE-ECC), presented a tensile strain capacity, $\varepsilon_u$, of 7% with a tensile strength, $\sigma_u$, reaching to 6 MPa and an average compressive strength, $f_c'$, around 45 MPa.

Further efforts aimed at producing a cost efficient SHCC with a high ductility characteristic. This goal was achieved by replacing PE fibers with Polyvinyl Alcohol (PVA) ones, as a cheaper alternative [5-8]. The resulting composite, designated as "PVA-ECC", contained 2% of short PVA fibers and achieved a tensile strain capacity, $\varepsilon_u$, of 4% at the presence of a tensile strength of, $\sigma_u$, 6.5 MPa.

| |
|---|
| $V_f \geq \left(V_f^{crit}\right)_{tension}$ |
| **SHCC (Strain Hardening Cementitious Composite)** |
| $\left(V_f^{crit}\right)_{bending} < V_f < \left(V_f^{crit}\right)_{tension}$ |
| **DHCC (Deflection Hardening Cementitious Composite)** |
| $V_f < \left(V_f^{crit}\right)_{bending}$ |
| **FRC (Conventional/Ordinary Fiber Reinforced Composite)** |
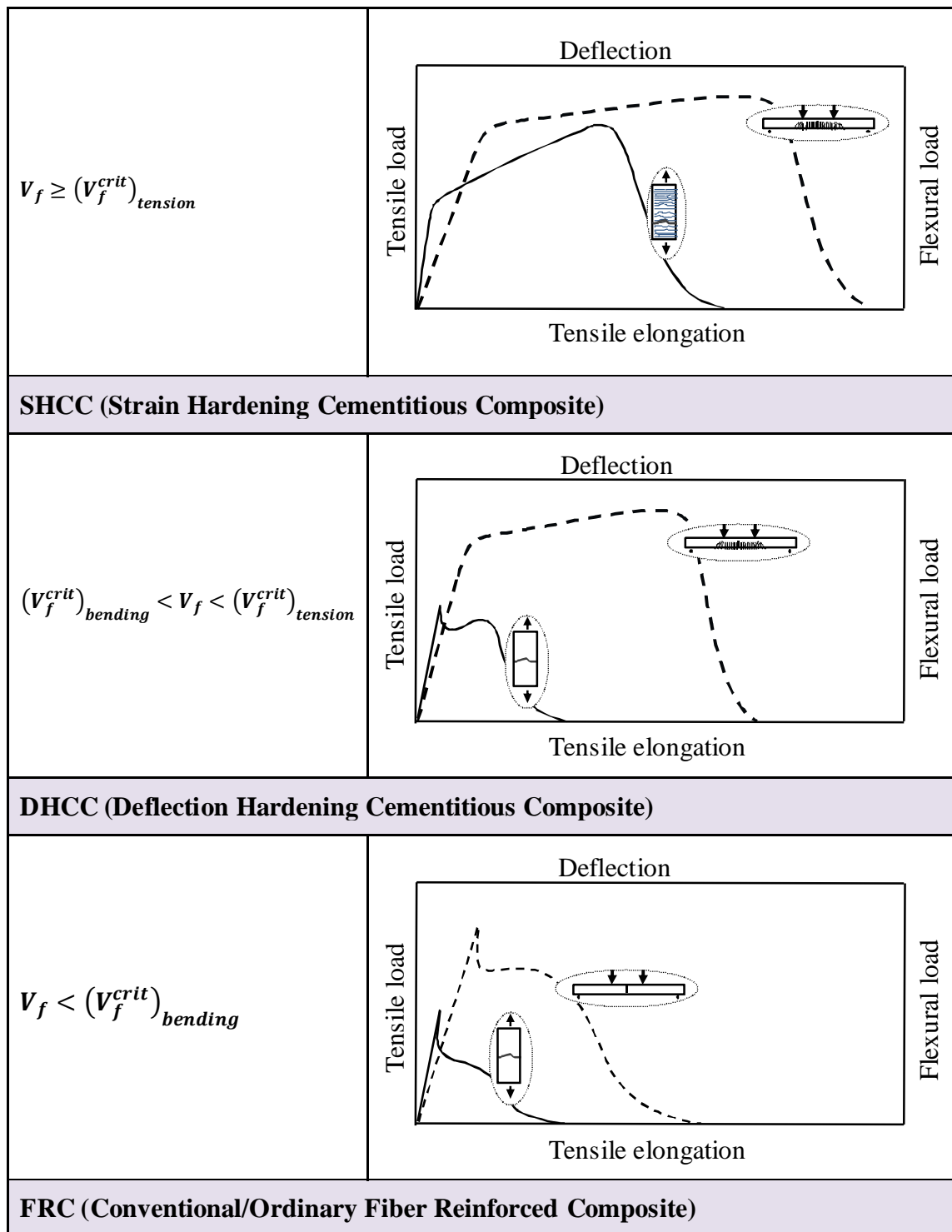
Figure 3.2: Classification of FRCCs based on their post-cracking response

Fiber reinforced concretes with very high compressive strength, known also as ultra-high performance fiber reinforced cementitious composites (UHPFRCCs), are the other generation of SHCCs. However, despite their very high compressive strength ($f_c' > 150\ MPa$) and relatively high tensile strength ($\sigma_u = 10\sim15\ MPa$), their tensile strain capacity, $\varepsilon_u$, is much lower than 1%. Ductal [9] and CARDIFRC [10-14] are two examples of these composites, both commercially available off-the-shelf materials. The former one, Ductal, contains 2% of steel fibers ($l_f =$13-15 mm and $d_f = 0.2$ mm) in composite volume fraction. This composite is characterized with a compressive strength, $f_c'$, ranging from 160 to 240 MPa, a tensile strength, $\sigma_u$, of 12 MPa and a tensile strain capacity of 0.3%. CARDIFRC offers an average compressive strength of 207 MPa with a tensile strength in the range of 10-15 MPa, however, despite a high steel fiber content (up to 8%), its tensile strain capacity is restricted to a maximum of 0.6%.

The most recent advances in SHCCs aimed at developing a composite with both high strength (tensile and compressive) and high ductility to assure the resiliency demand of critical structural elements under extraordinary actions, where a high ductility, a high energy dissipation capacity or a high toughness of the material is the crucial performance criteria. Such structural demands can be exampled as the requisite for combined axial and flexural resistance together with a high rotational capacity at the lower portion of the columns of tall buildings subjected to an earthquake event, or the elements designed to withstand actions of blast and impact loadings. UHP-FRC [15] and HSHDC [16] are two utmost examples of recent developments of SHCCs offering high strength and high ductility.

UHP-FRC (ultra-high performance fiber reinforced concrete) [15] is a SIFCON processing composite that incorporates 5.5% twisted steel fibers of 24 mm in length and 0.3 mm in diameter. The ultimate tensile strength of this composite, with a compressive strength of 270 MPa, reaches to 37.2 MPa with a corresponding tensile strain capacity of 1.1%.

HSHDC (high strength high ductility concrete) [16], however, is a micromechanical-based design composite (see section 3.2) that adopts conventional casting to disperse 2% of ultra-high molecular weight short discrete PE fibers ($l_f =$12.7 mm and $d_f = 0.038$ mm) into a finely graded cementitious matrix. The resulting composite exhibits an average tensile strength of 11.8 MPa at a strain capacity of 3.5%, while a high compressive strength of

around 160 MPa is assured. Figure 3.3 illustrates the typical tensile stress-strain response of three distinct classes of SHCCs, namely PVA-ECC, UHP-FRC and HSHDC.
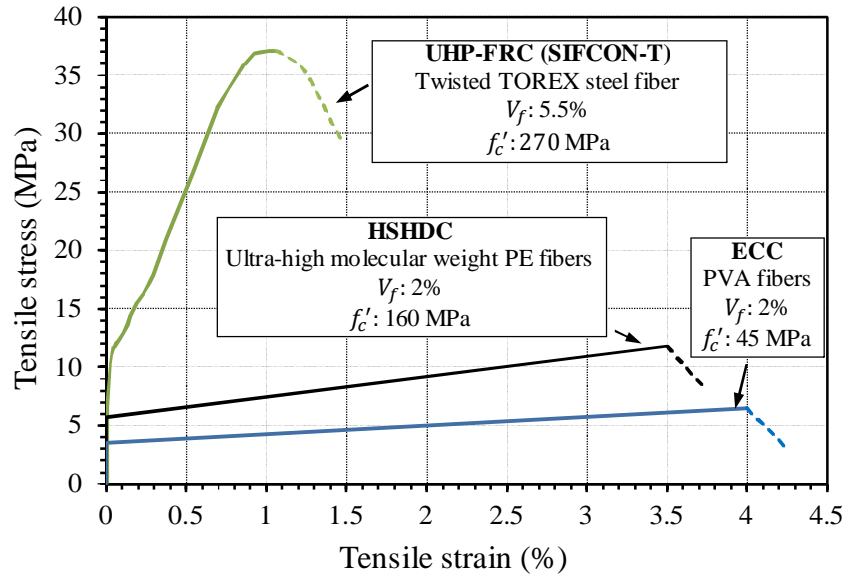


Figure 3.3: Typical tensile stress-strain response of three distinct classes of SHCCs

## 3.2 Micromechanics of Strain Hardening Response

Theory of strain hardening and multiple cracking in a brittle matrix composite is fundamentally defined based on the concept of steady-state crack propagation. A steady-state cracking takes place if a crack propagates in length while its maximum opening width remains constant. For such circumstance, further crack progress is independent of the total crack length and occurs under a constant ambient stress.

Figure 3.4a illustrates crack propagation mechanics for a composite approximated to a continuum with average composite elastic properties and a uniform ambient stress of $\sigma_a$. In this figure, bridging of fibers are represented as a crack surface traction that is a function of crack local opening, $\sigma(w)$. Fibers-bridging stress increases monotonically, along the crack, from zero at the crack tip, and provided that the crack length is sufficiently long, approaches to an asymptotic limit of $\sigma_a$ corresponding to a constant average crack opening of $w_a$. For such crack configuration Marshal and Cox [17] used a J-integral method [18] to evaluate the state of the stresses and the strains close to the crack tip. By subtracting the crack surface

traction, $\sigma(w)$, from the remotely applied uniform stress, $\sigma_a$, the opening pressure acting over the crack surface, $\sigma_0$, can be defined as follows:

$$\sigma_0 = \sigma_a - \sigma(w) \tag{3-1}$$

This opening pressure is maximum at the crack tip and approaches to zero where the crack wakes are merged into a flatten shape (see Figure 3.4b). Evaluation of the J-integral for this crack configuration leads to the following expression:

$$\sigma_a w_a - \int_0^{w_a} \sigma(w)dw = J_{tip} \tag{3-2}$$

According to the Equation (3-2), the net energy available to drive the crack tip propagation, $\sigma_a w_a - \int_0^{w_a} \sigma(w)dw$, must be equal or greater than the matrix crack tip toughness, $J_{tip}$.



(a)                             (b)
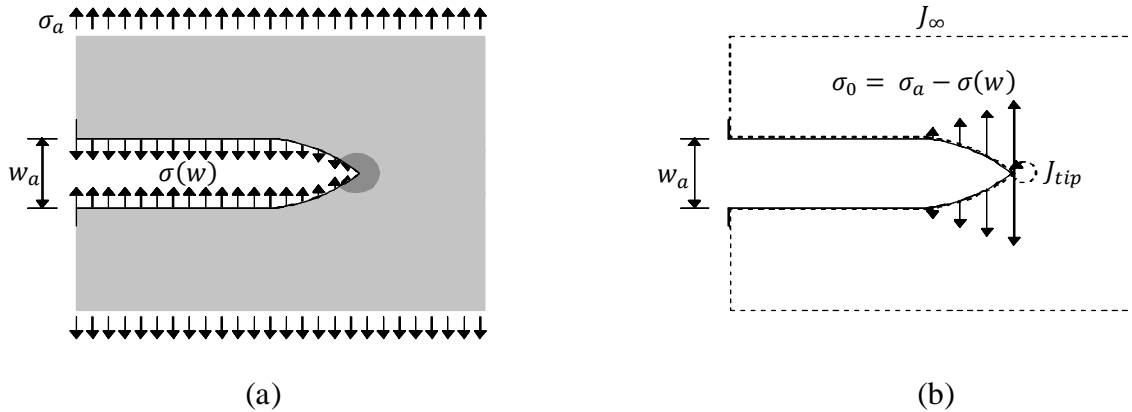
Figure 3.4: Crack propagation mechanics, (a) crack configuration based on uniform remote stress distribution and crack surface traction equivalent to fibers bridiging stress, and (b) crack configuration convenient to be solved using J-integral approach [19]

As depicted in Figure 3.5, this net energy is equivalent with fibers-bridging complementary energy, $J_b$, which is the difference between the external work input energy, $\sigma_a w_a$, and the energy consumed by fibers during crack opening from zero to $w_a$, $\int_0^{w_a} \sigma(w)dw$. Hence, to assure a steady-state crack propagation at $(w_{ss}, \sigma_{ss})$, the critical

amount of the complementary energy, $\sigma_{ss}w_{ss} - \int_0^{w_{ss}} \sigma(w)dw$, must reaches the crack tip toughness, $J_{tip}$. This is the fundamental "energy based criterion" for a strain hardening response to occur.

However, still a "strength based criterion" must be satisfied to achieve a strain hardening response. According to this strength criterion, the peak of fibers-bridging stress, $\sigma_a$, must exceed the matrix cracking strength, $\sigma_{cr}$.

The, abovementioned criteria to assure multiple cracking in a composite can be then rewritten in the following form:

- $J_b = \sigma_a w_a - \int_0^{w_a} \sigma(w)dw \geq J_{tip}$      (energy criterion)      (3-3)

- $\sigma_a \geq \sigma_{cr}$      (strength criterion)      (3-4)



$$J_b \equiv \sigma_a w_a - \int_0^{w_a} \sigma(w)dw$$

$$J_{tip} = \sigma_{ss}w_{ss} - \int_0^{w_{ss}} \sigma(w)dw$$
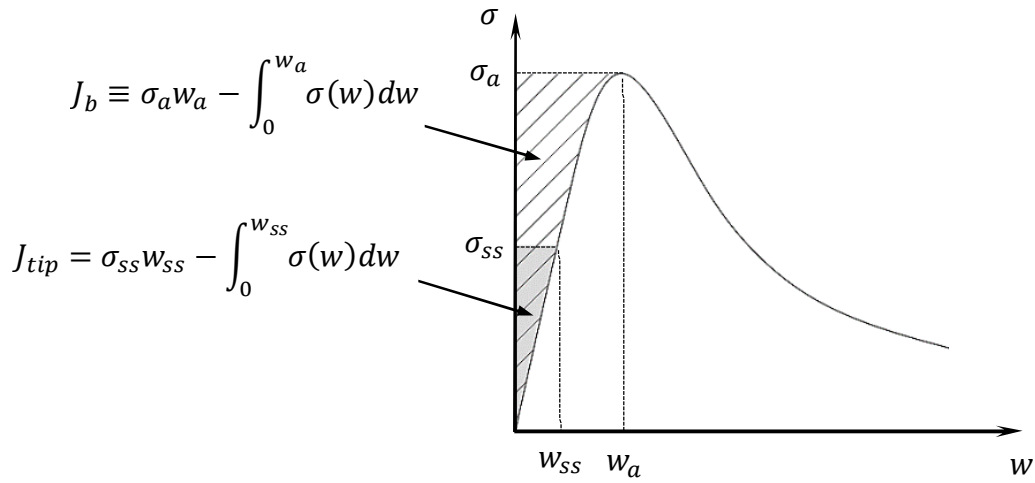
Figure 3.5: Typical fibers-bridging stress *versus* individual crack opening response

### 3.2.1 Micromechanical Model of SHCCs

A micromechanical model of an SHCC correlates a micro-scale single fiber pullout response to the crack-bridging behavior of fibers in mesoscale. This mesoscale response further determines multiple cracking potential of the SHCC at a macroscale. The correlation between these three distinct scale levels is schematically demonstrated in Figure 3.6.

Following the experimental measurements, at a micro-scale level the pullout response of a single fiber embedded in a brittle matrix can be formulated based on pullout force *versus* fiber's loaded-end displacement, $P(U)$. This single fiber pullout response can be then utilized to analytically predict fibers-bridging stress *versus* individual crack opening, $\sigma_B(w)$, that defines fibers contribution in a meso-scale composite response.

This meso-scale composite response can be then translated into the composite macro-scale, by predicting its multiple cracking potential. To this end, the statistical distribution of flaws, flaw sizes, fibers, and variation in fiber-matrix interface properties for a given composite needs to be estimated.
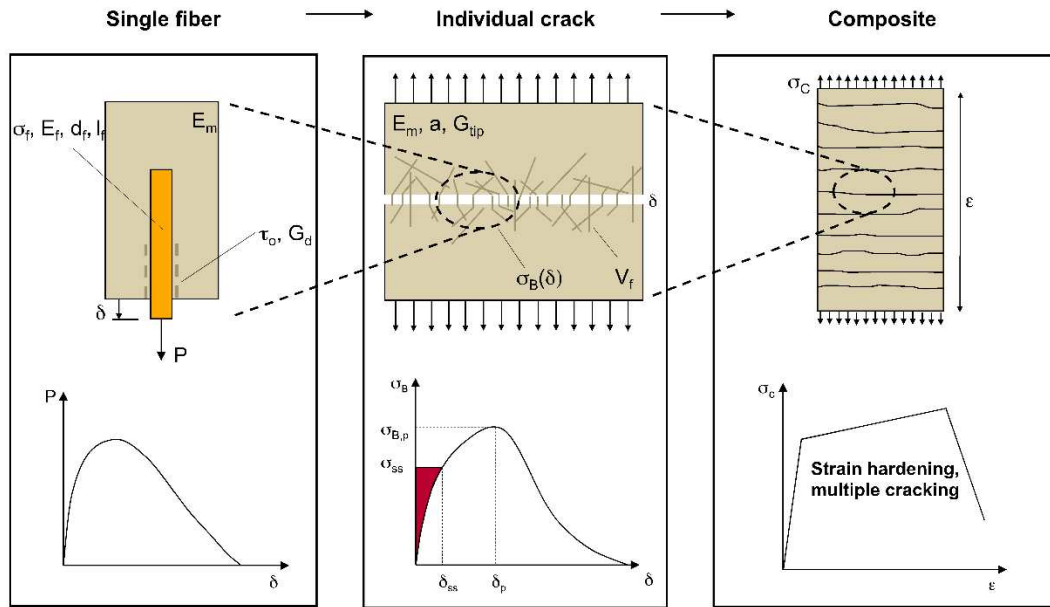


Figure 3.6: Schematic presentation of correlation between responses in three distinct scale levels of SHCC (pullout of single fiber: microscale; single crack opening: mesoscale; multiple cracking: macroscale) [20]

Thus, tailoring the response of single fiber pullout is the fundamental step towards developing a strain hardening behavior in mesoscale and multiple cracking at macroscale. As shown in Figure 3.7a, for a fiber with an embedment length of $l_e$ in a matrix to start sliding out under a pulling process, its chemical bond with the surrounding matrix should be initially overcome. The deterioration of chemical bond along the embedded length of the

fiber occurs due to matrix tunnel cracking. The required energy for a full debonding progress is known as chemical debonding energy $G_d$.



(a)



(b)
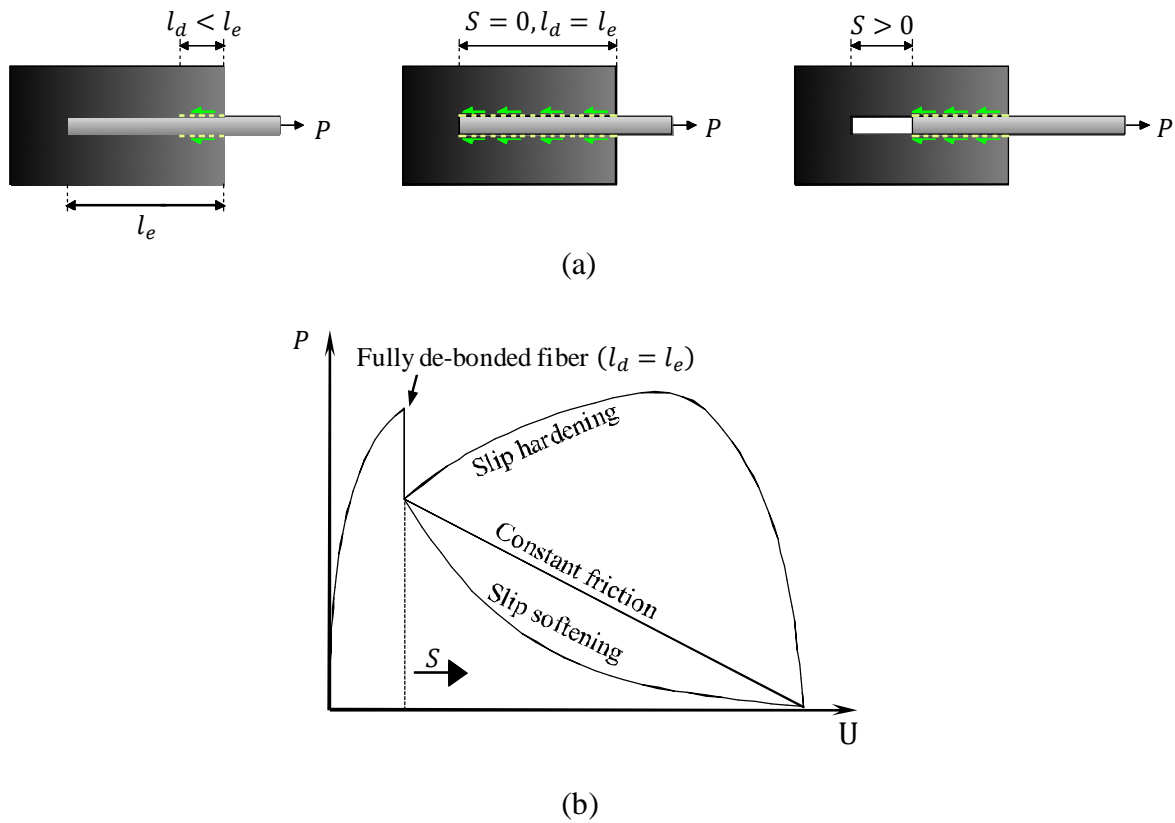
Figure 3.7: General profile of a single fiber pullout (a) stages of fiber debonding and sliding during pulling out process, (b) possible pullout load *versus* fiber displacement responses for a full fiber pullout process that depend to the type of and fiber/materix interface properites [7].

Once the debonded length, $l_d$, reached the fiber embedded length, $l_e$, the whole fiber sliding process will start. Fiber sliding can dissipate a notable amount of energy, especially when sliding accompanies a slip-hardening process (see Figure 3.7b). The slip-hardening occurs specially in the case of polymeric fibers whose surface roughness is lower than their surrounding matrix. Thus, during the sliding of these fibers out of the matrix tunnel, abrasion causes a progressive peeling at fiber surface that enhances fiber's sliding resistance. Fiber sliding is essential to assure "steady-state" micro-crack propagation, which is a governing condition for a tensile strain hardening response to occur. This concept will be further

introduced and discussed in the present section. Therefore, a precisely tailored chemical bond is crucial to prevent fiber rupture before it starts sliding, especially in the case of fibers with high water affinity (e.g. hydrophilic fibers). Moreover, slip hardening effect should be carefully tailored to achieve sufficient energy absorption and pull load resistance at full fiber pullout.

According to Li et al. [21], for a composite with a volume fraction $V_f$ of short randomly dispersed discrete fibers, the fibers-bridging stress *versus* crack opening, $\sigma_B(w)$, can be predicted by integrating over the contribution of those fibers that cross the matrix crack plane:

$$\sigma_B(w) = \frac{4V_f}{\pi d_f^2} \int_{\emptyset=0}^{\pi/2} \int_{z=0}^{(l_f/2)cos\emptyset} P(w)\, p(\emptyset)p(z)\, dz d\emptyset \tag{3-5}$$

where $l_f$ is the fiber length, $d_f$ is the fiber diameter, $p(\emptyset)$ and $p(z)$ are probability density functions of fibers' orientation angle and centroidal distance from the crack plan, respectively.

Assuming that all the fibers are aligned to the tensile loading direction and they all will fully pullout under a constant frictional bond between fiber and matrix ($\tau_0$), Equation (3-5) could be simplified as [22]:

$$\sigma_B(w) \begin{cases} 2V_f \sqrt{(2G_d + \tau_0 w)\dfrac{E_f}{d_f} - \dfrac{V_f E_f w}{L_f}} & w \leq w_c \\[4mm] \dfrac{4V_f \tau_0}{L_f d_f}\left(\dfrac{L_f}{2} - w\right)^2 & w < w_c < \dfrac{L_f}{2} \end{cases} \tag{3-6}$$

where, $w_c$ is the crack opening corresponding to the complete debonding of fibers, $E_f$ is the fiber's modulus of elasticity and $G_d$ as introduced before is the energy required for fibers being fully debonded along the embedded length (chemical debond energy), which can be derived from the sudden drop in the load at the onset of fiber sliding, when the fiber is fully deboned along its length, according to a single fiber pullout test, as described in [23].

Integrating equation (3-6) based on the definition of the complementary energy, as analytically indicated in equation (3-3), $J_b$ could be written as:

$$J_b = \frac{V_f l_f}{d_f}\left(\frac{{\tau_0}^2 {l_f}^2}{6d_f E_f} - 2G_d\right) \tag{3-7}$$

Neglecting the chemical bond, $G_d$, which is valid for the case of hydrophobic fibers, and replacing equation (3-7) in (3-3), the critical fibers volume fraction, $\left(V_f^{crit}\right)_{tension}$, to achieve a strain hardening response in tension for a given fiber, matrix and fiber-matrix interface properties could be theoretically obtained as:

$$\left(V_f^{crit}\right)_{tension} = \frac{6d_f^2 E_f}{\tau_0^2 l_f^3} J_{tip} \tag{3-8}$$

Using the knowledge derived from this micromechanical model, Li and co-workers [3, 4] tailored and introduced practically the synthetic fibers as the discrete reinforcement to a cementitious matrix. To the resulting material the designation Engineered Cementitious Composite (ECC) was attributed. Only 2% in volume of Polyethylene Spectra-900 (PE), a polymeric fiber with high modulus of elasticity (120 GPa) and tensile strength (2600 MPa), has provided a strain hardening capacity of 3.5% to its original brittle cement based matrix. Further, the Plasma treatment of these PE fibers increased the frictional bond strength almost two times, upgrading the composite strain ductility to 7%, while a tensile strength of 6 MPa was assured [24, 25].

The initial efforts to develop a SHCC utilizing Polyvinyl Alcohol (PVA) fibers have resulted in a composite with a maximum strain capacity of around 0.5% [26-28]. By using this micromechanical approach, and considering the effect of the chemical bond, Li et al. [6] have successfully developed a very ductile PVA-ECC by modifying both the matrix and the fiber-matrix interface. In fact, they realized that the presence of the hydroxyl group in the molecular chains of the hydrophilic PVA fibers develops a strong chemical bond with surrounding hydrated cement particles. This strong chemical bond proportionates a further increase in the frictional fiber pullout resistance due to the bonded matrix particles to the fiber surface and increased fiber surface abrasion.

As Equation (3-7) indicates, the complementary energy, $J_b$, decreases by increasing the chemical bond, $G_d$. Moreover, a very high chemical bond, $G_d$, can also lead to premature fiber rupture during debonding or pulling out. Redon et al. [23] and Li et al. [8] tailored a suitable sizing for PVA fibers utilizing different quantities of an oiling agent as a fiber coating to reduce chemical bond at fiber-matrix interface. The results of both single fiber pullout tests and tensile tests on composites showed coating PVA fibers surface with 1.2% of an oiling agent (based on fiber's weight ratio) can optimize the interface of PVA/cement-matrix for developing fine enough saturated multiple cracking.

## 3.3 Durability and Elevated Temperature Performance of SHCC

Porosity and cracking are major causes for the concrete permeability, which in turn facilitates the ingress of harmful liquids and gases. A controlled crack width development up to the tensile strength of SHCC is a unique characteristic that contributes for the enhancement of the durability performance of the composite and its underlining substructure, as compared to the ordinary concretes or even FRCs.

Figure 3.8a demonstrates the development of crack width along with the evolution of tensile stress-strain curve in a typical PVA-ECC with 2% of fibers. According to this figure, after an early strain, the crack width opening is stabilized far below 100 µm. This limit is often proposed to control permeability of concretes in aggressive environments. Contrary to concrete or even FRCs, whose crack opening width depends on the percentage of the longitudinal reinforcement, SHCC is an inherently self-controlled crack width material (see Figure 3.8b).

Therefore, in the cracked stage, comparing to other cementitious composites, lower permeability and multiple cracking of SHCC result in a superior performance under freeze and thaw loading [29-31], restrained shrinkage induced cracking [32, 33], water and chloride penetration and steel corrosion resistance [34-38], and fatigue cracking [39].
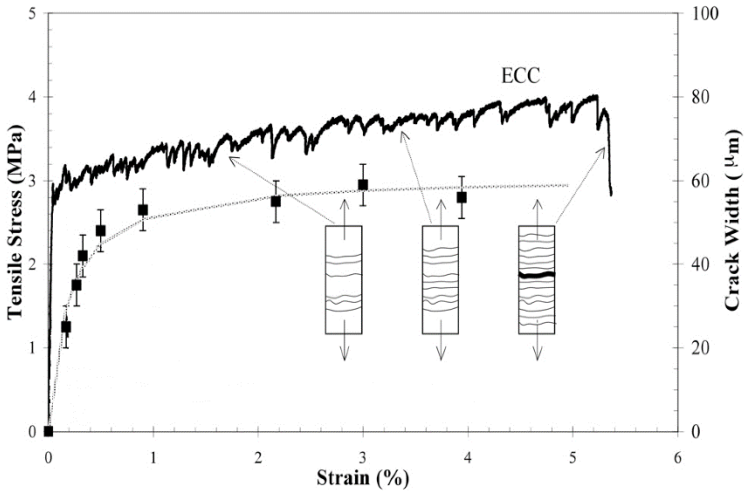
(a)
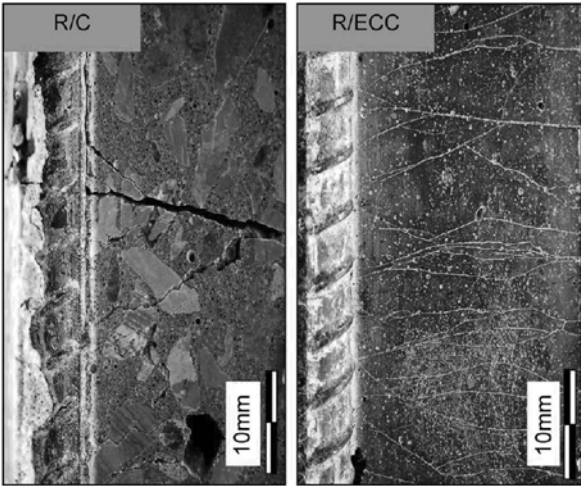


(b)

Figure 3.8: Crack width control in a PVA-ECC, (a) tensile stress-strain behavior of a typical PVA-ECC and crack width development [40], and (b) comparison of crack width and crack development in steel reinforced concrete (R/C) with steel reinforced ECC (R/ECC) subjected to tensile loading [41]

Regarding the performance of PVA-ECC under elevated temperatures, different conclusions, from reduction in tensile strain capacity and increase in tensile strength to its contrary can be found in the literature. This may point out that the fiber-matrix interface is influenced by high temperatures, however, its degradation or strengthen depends strongly on the matrix constituents. According to the observation of Wu et al [29], for temperatures

higher than 50 °C, increase in composite tensile strength, reduction in tensile strain capacity and increase in the maximum crack width were identified (see Figure 3.9). According to these authors, the changes in composite mechanical properties can be mainly associated with the aggregates thermal coefficient, PVA fibers thermal stability and cement hydration progress rate at higher temperatures. However, it was realized that a proper modification of matrix composition can minimize the adverse effects of high temperatures (studied up to 200 °C) on composite mechanical properties. For example, adding silica fume and using quartz sand instead of river sand noticeably decrease the sensitivity of material tensile properties regarding the increase in temperature. Contrary to this conclusion, but in agreement with the results reported by Mechtcherine et al. [42], Oliveira et al. [43] investigation showed a noticeable increase in strain capacity of PVA-SHCC containing quartz sand in its matrix, for an in-situ temperature increase from 20 °C to 100 °C, together with reduction in both first tensile cracking strength and ultimate tensile strength of this composite. The higher strain ductility was mainly attributed to the larger crack width caused by changes in interface properties of PVA fiber and the surrounding matrix at an elevated temperature.



(a)                                         (b)
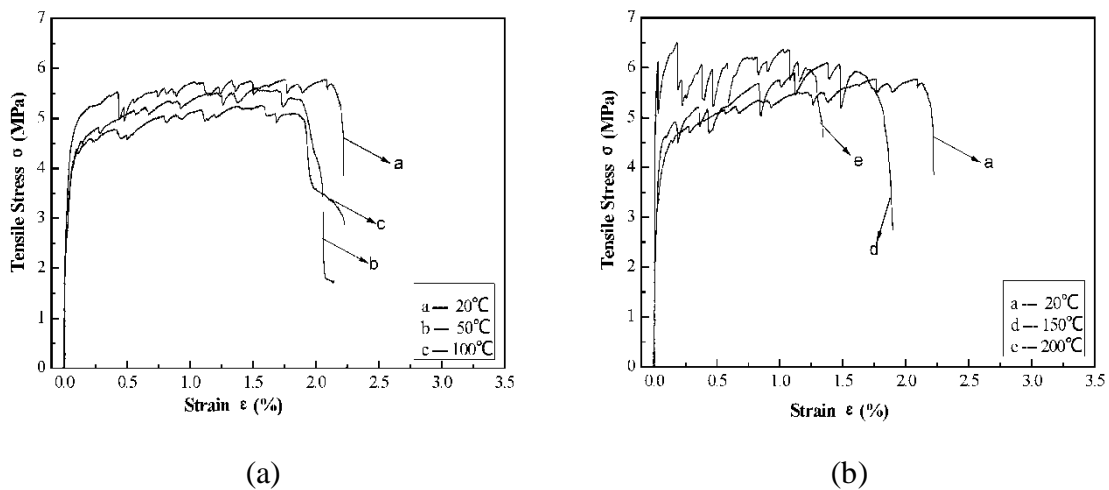
Figure 3.9: Effect of elevated temperature on tensile stress-strain response of PVA-ECC following observations of Wu et al [29]
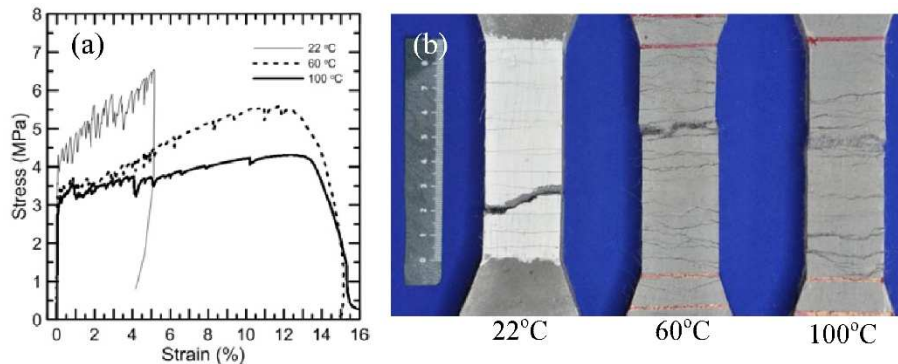
Figure 3.10: Effect of elevated temperature on tensile stress-strain response of PVA-ECC following observations of Oliveira et al. [43]

## 3.4 Structural Applications of SHCC

Comparing to regular constructional materials such as concrete or even conventional FRCs, the higher cost of SHCCs is restricting their applications to the cases where their distinct characteristics can be exploited. Hence, elements of a structure demanding a high durability, high ductility, high energy dissipation capacity, high toughness, enhanced bursting or spalling resistance, or a reliable corrosion protection are the most appropriate ones for SHCCs applications.

In this regard, investigation of Maalej and Li [38] demonstrated potential application of SHCCs as a durable cover for the steel reinforcements of an RC beam. According to their investigation, a maximum crack width of 1.6 mm observed at a peak load of a regular RC beam tested under four point bending was altered to an impermeable cracking of 0.2 mm in width, at the same load level, when the beam's cover was built of PE-ECC. This result suggests the potential use of SHCCs in enhancing structural durability.

Promising results obtained from cyclic testing of short-span steel reinforced PVA-ECC beams (R/ECC beams) [44] suggested potential application of SHCCs in construction of seismic resistant members with the demand for a high energy dissipation capacity, such as coupling beams or shear walls. A reflection of this study was the adoption of precast R/ECC coupling beams in the construction of two high-rise RC residential buildings in Japan, 27-story Glorio Roppongi in Tokyo and 41-story Nabeaure Tower in Yokohama. These

coupling beams connected the core walls on each floor to provide high vibration damping and energy absorption during an earthquake (Figure 3.11).
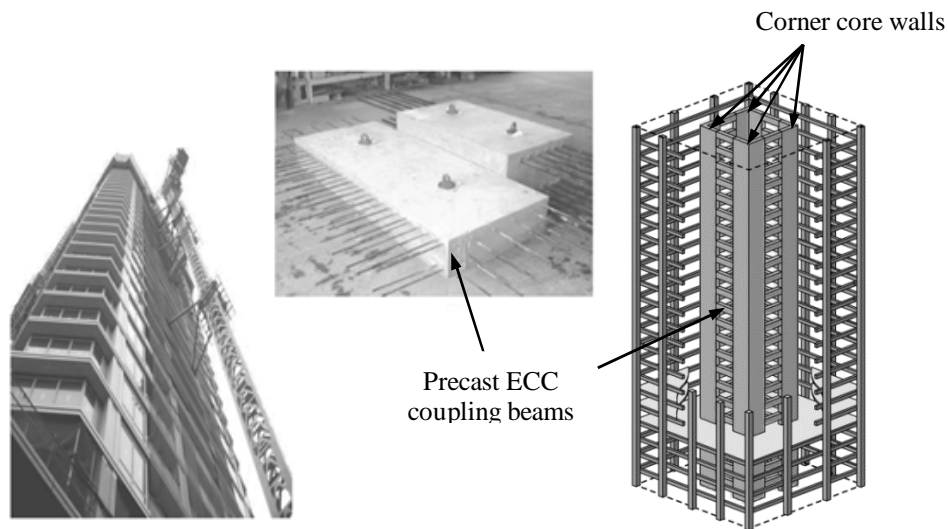


Figure 3.11: Nabeaure Yokohama Tower with ECC coupling beams (Designed by Mitsubishi Jisho Sekkei Inc. & Kajima Corp.; Constructed by Kajima Corp.; Completed in 2007)

High damage tolerance is another distinct characteristic of SHCCs. Figure 3.12 represents the results of indentation tests performed on PVA-ECC panel (Figure 3.12a) and on a counterpart mortar panel (Figure 3.12b) [44]. The relative surface area of the punched indenter to the surface area of the panel (1%, 5% and 10%) was the parameter of the study. The pictures on the left side of Figure 3.12a and Figure 3.12b compare failure modes observed in the PVA-ECC and mortar panels, respectively. While radially distributed multiple fine cracks, observed after removing the indenter, evidenced the high damage tolerance of SHCC, the fracture of the mortar panel into few pieces indicated a brittle failure initiated at inevitably existing defects. The diagrams on the right side of Figure 3.12a and Figure 3.12b illustrate the load-displacement response obtained from indentation tests on the PVA-ECC panel and the mortar one, respectively. Comparison of these results clearly reveals that the bearing displacement capacity of PVA-ECC is almost one order larger than the mortar panel one. Moreover, the indentation load capacity of a PVA-ECC panel for a

relative surface area of 1% is almost twice the one of the mortar panel. However, this difference decreases with the increase of the relative surface area of the indenter.

A further development of this study was the investigation on the possibility of connecting ECC sandwich panels to each other by using a dry joint configuration [44]. As depicted in Figure 3.13, this joint is composed of two sandwich panels connected by means of bolted steel plates. Results of joint shear tests performed on a specimen made of ECC sandwich panels *versus* its counterpart composed of lightweight concrete panels (both reinforced with 0.75% longitudinal and transverse steel reinforcement) are presented in Figure 3.13. In spite of brittle failure of the specimen built of a lightweight concrete with major splitting cracks running along the holes up to the failure of ECC specimen, there was almost no visible damage in its joint region. Indeed, even though the failure of the ECC specimen was caused by crushing at its supported portions, still this specimen attained a shear load carrying capacity almost double of that attained with the lightweight concrete specimen.
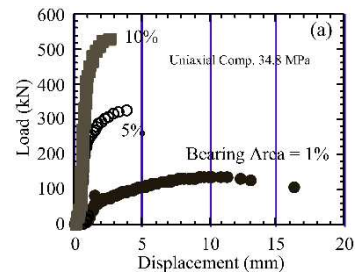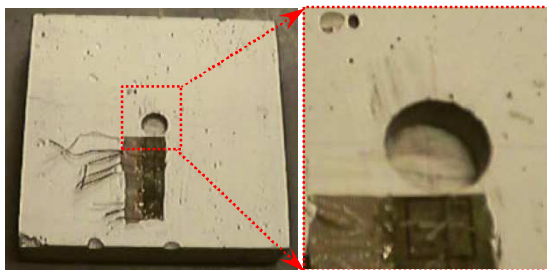


(a)
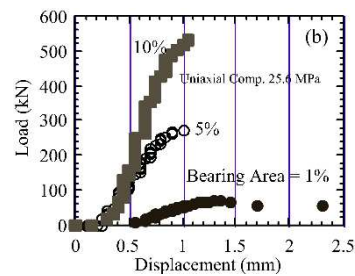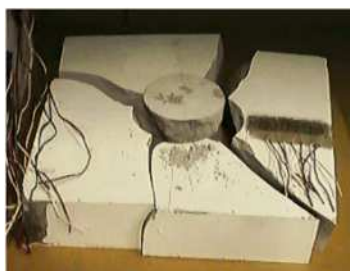


(b)

Figure 3.12: Results of bearing indention test on (a) ECC, and (b) mortar panels [44]

<center>(a)                          (b)                          (c)</center>
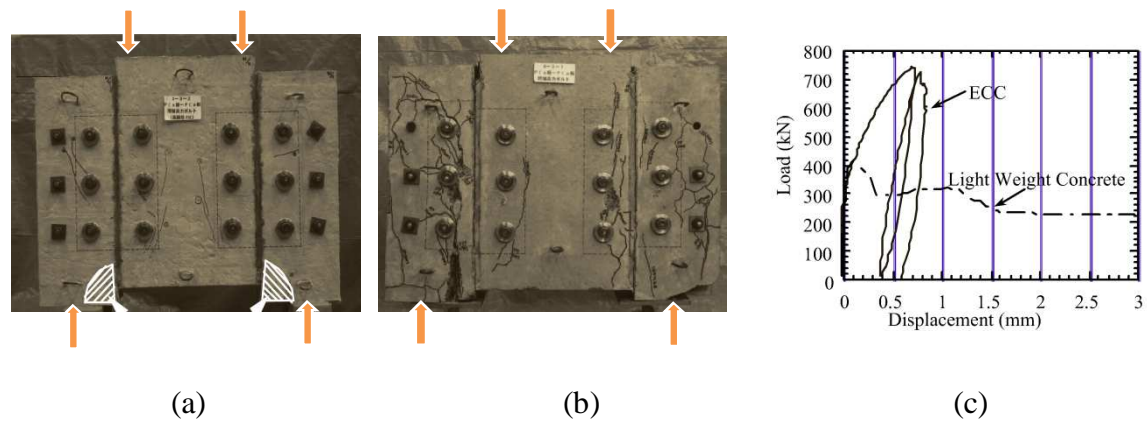
Figure 3.13: Dry joint test configuration and results [44], (a) specimen made of ECC panels failed by crushing at supporting regions while almost no damage was observed at the joint region, (b) specimens made of light weight concrete failed with splitting cracks along the holes, (c) load-displacement response of shear test on ECC and lightweight dry joint specimens.

The effectiveness of a similar concept was recently examined in the retrofitting of a two-thirds-scale model of a steel moment resisting frame (MRF) as a prototype of a two-story steel building, designed in California in the 1980's [45]. The proposed seismic retrofitting system was composed of series of two vertically connected prefabricated infill panels fixed at their superior and inferior boundaries to the horizontal elements of the MRF (see Figure 3.14a and Figure 3.14b).

Two seismic events, each in an individual phase, were simulated to evaluate the performance of the proposed retrofitting technique. In the second phase of testing (simulation of the second earthquake) all the panels were replaced with similar intact ones. Test results revealed that micro-cracks propagated in HPFRC infill panels, dissipated significant amount of the service level earthquake energy. For both earthquakes loading types (Design Level or a Maximum Considered Earthquake) the seismic demands in terms of story and residual drift ratios for the retrofitted MRF presented a 40% reduction as compared to the bare frame. Figure 3.14c illustrates the crack propagation and failure localization at HPFRC infilled panels corresponding to the final state of the testing at phase I and II.

(a)                                                    (b)

Phase I                                        Phase II

(c)
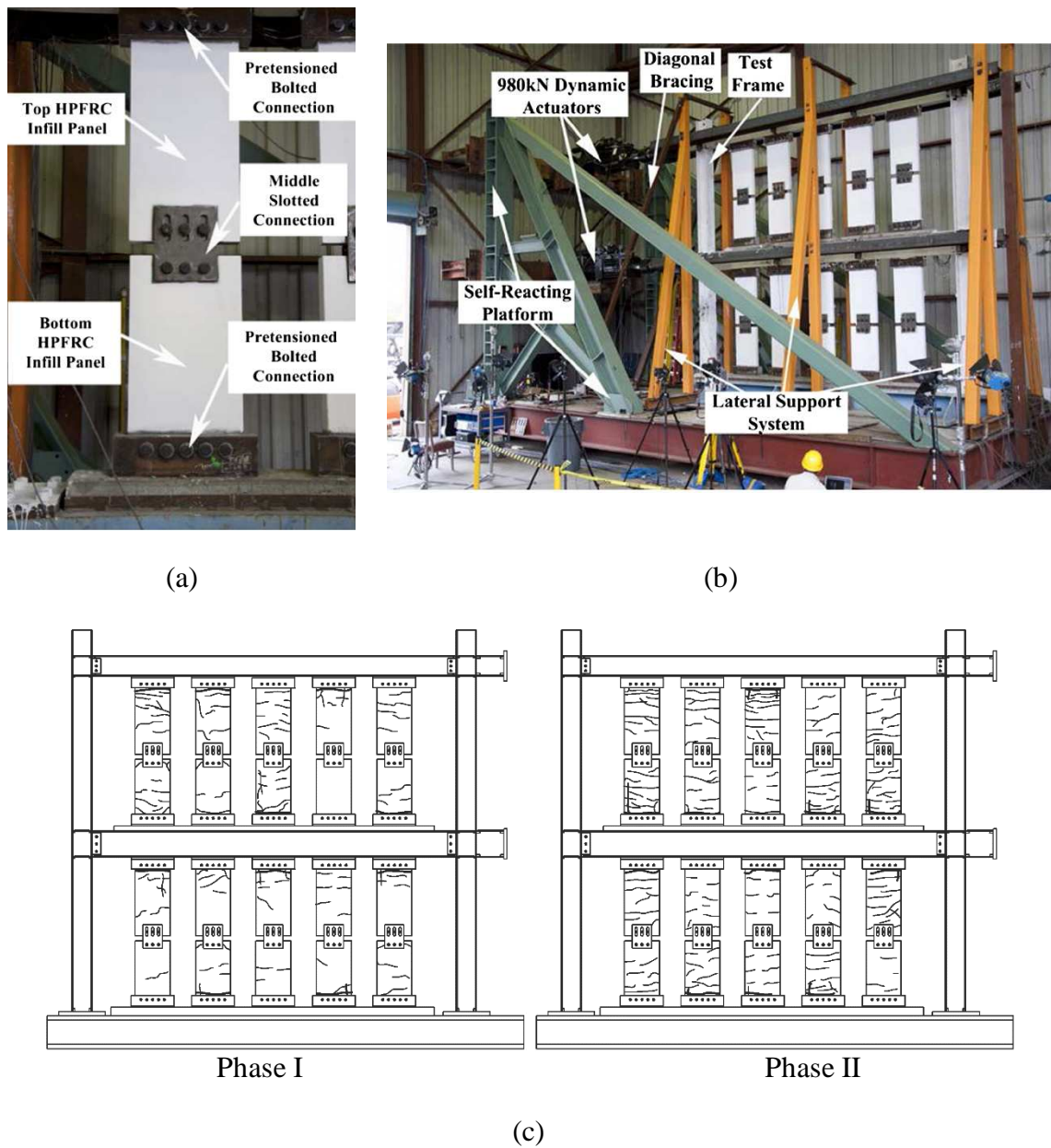
Figure 3.14: Application of precast HPFRC panels in retrofitting of a steel moment resisting frame (MRF), (a) details of prefabricated retrofitting system, composed of two vertically placed panels connected to each other using a steel joint and fixed to the horizontal elements of the steel MRF at their extremities, (b) arrangement of several prefabricated panel in a prototype steel frame of a two-story steel building, designed in California in the 1980's, (c) crack propagation at the end of each of two testing phases

Figure 3.15 depicts a bridge deck located at southeast Michigan, USA, whose conventional expansion joint was replaced with an ECC "link slab" [46]. The proposed system benefits from the high ductility of ECC to accommodate the tensile deformation caused by thermal expansion and contraction of the adjacent girders, while the maximum crack width in the deformed link is fine enough to prevent penetration of aggressive liquids causing deteriorative effects to the bridge's underlying constituents (e.g., penetration of saturated water with de-icing agents which causes corrosion of steel girders). The high durability of the proposed system results in lower maintenance and repair costs, assuring a sustainable repair/construction solution for bridge applications.



(a)
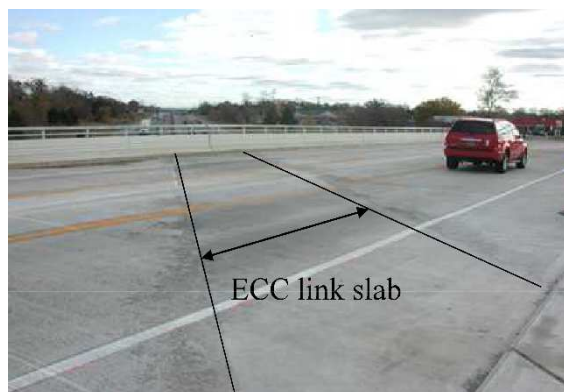


ECC link slab

(b)

Figure 3.15: The conventional expansion joint of a bridge deck located at southeast Michigan, USA, replaced with ECC "link slab" as a deformable and durable solution [46]

Another interesting application of SHCC was demonstrated with the repair of one-third-scale interior RC beam-column joints [47]. These specimens had inadequate seismic detailing and were damaged in the joint region due to an earthquake simulated loading. An HPFRC mixture with steel fiber volume fraction of 2% (brass-coated fibers with a length of 6 mm and diameter of 0.15 mm), possessing a tensile and a compressive strength of 8.5 and 75 MPa, respectively, was used to repair these joints. A 15 mm thick jacket of this HPFRC cast all around the joint and the column region of the damaged beam-column joints resulted in a notable increase in the lateral load carrying capacity, in both displacement ductility and energy dissipation capacity, and also a much lower specimens' stiffness degradation rate. The HPFRC jacket successfully transformed the joint shear failure, observed in the virgin specimens, into a ductile flexural failure localized in the beams. For a quantitative interpretation of these results, the scale effect should, however, be taken into account.

Attaching SIFCON precast composite blocks to the joint region of exterior RC beam-column joint is another successful example of exploiting potential energy dissipation capacity and toughness of SHCCs in retrofitting of RC members [48]. Figure 3.16 illustrates the configuration of such a two-thirds-scale RC beam-column joint retrofitted with SIFCON blocks of 50 and 100 mm in thickness attached to the joint's critical regions by means of chemical anchors. Results of testing under lateral cyclic loading revealed a significant enhancement in lateral load resistance and initial stiffness of the retrofitted specimens, along with a more ductile failure when compared to the results obtained from testing the un-retrofitted control specimen. The proposed retrofitting configuration contributed to a very high energy dissipation for the RC beam-column joint. However, the relatively high thickness of the precast elements may cause architectural disturbance, which could be considered as a shortcoming of this system. Moreover, the increased stiffness of the retrofitted regions and the decreased length of the column and beam elements may consequently increase shear demands of this elements. A relatively high weight of these precast elements, due to their large geometry, may also adversely affect their practical feasibility.

Retrofitting of damaged/undamaged RC beams (lacking shear or flexural capacity) by adhesively bonded prefabricated CARDIFRC strips to the beams tension face and lateral

faces is another investigated application of SHCCs [49, 50]. Comparison between the results of flexural tests performed on the small-scale retrofitted beams and the results of control beams confirmed the effectiveness of the proposed technique in increasing the stiffness, ductility and energy absorption. A superior performance of retrofitting with CARDIFRC strips of 16 mm thickness in comparison with 20 mm ones was observed, which may lead to the conclusion that the retrofitting effectiveness of this system beyond an optimum thickness (lower than 20 mm) decreases.

In another study an ECC layer was added to the beams flexural strengthened with FRP system [51]. The results showed that ECC, covering the FRP system, can indeed be used to delay debonding of the FRP, contributing for a more effective use of the FRP material.
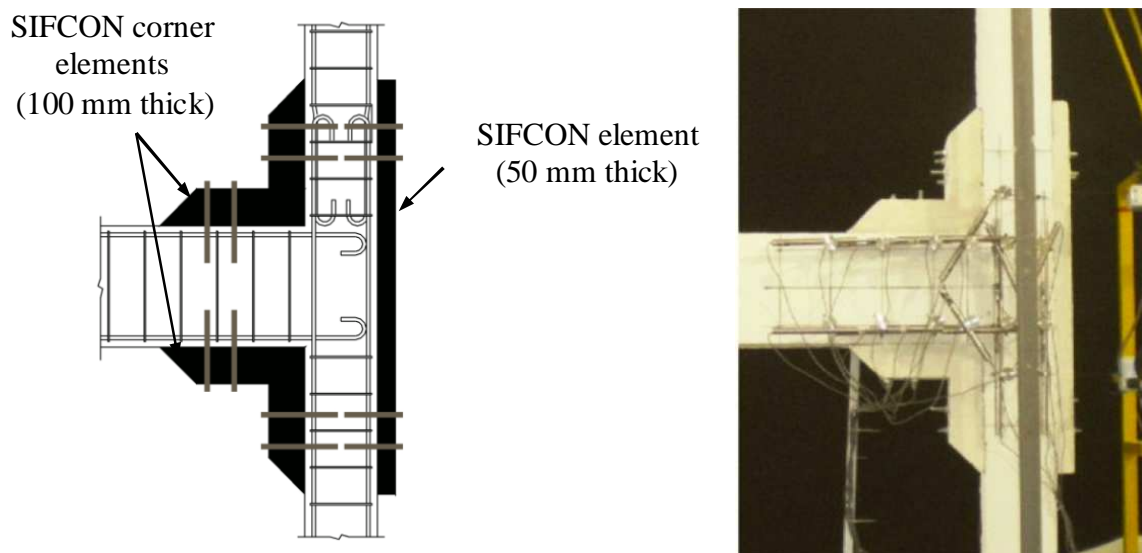


Figure 3.16: SIFCON precast composite blocks attached by chemical anchors to critical regions of exterior RC beam-column joint as a high toughness retrofitting solution [48]

The high ductility of SHCC was also employed to increase flexural strength and deflection ductility of masonry beams. By testing in bending masonry elements strengthened with a thin layer of SHCC (15 mm or 20 mm) applied to their tension face, Esmaeeli et al. [52] demonstrated that higher load carrying capacity and ductility is achievable when compared to flexural strengthening methodologies based on the use of thicker layers (30 mm) of ordinary steel FRC (see Figure 3.17).
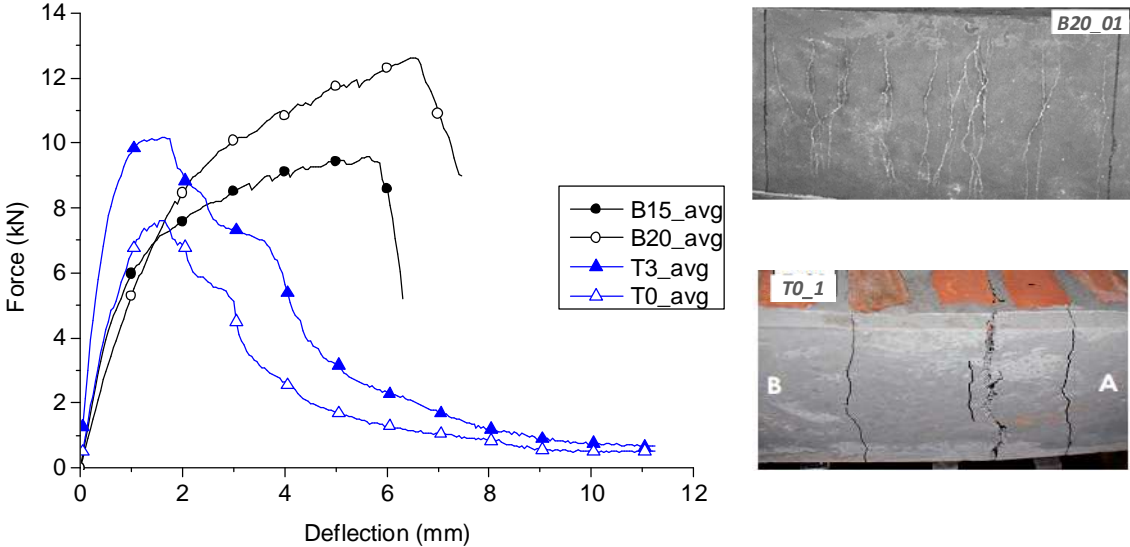
Figure 3.17: Comparison of the average force versus mid-span deflection curves and crack propagation of the masonry beams flexurally strengthened with SHCC (B15_avg and B20_avg) and steel FRC layer (T3_avg and T0_avg) [52]

# Bibliography

[1] Naaman AE, Reinhardt HW. Proposed classification of HPFRC composites based on their tensile response. Materials and Structures. 2006;39(5):547-55.

[2] Homrich JR, Naaman AE. Stress-strain properties of SIFCON in uniaxial compression and tension. DTIC Document; 1988.

[3] Li VC, Mishra DK, Wu HC. Matrix Design for Pseudo Strain-Hardening Fiber Reinforced Cementitious Composites. RILEM Journal Materials and Structures. 1995;28(183):586 - 95.

[4] Wu HC, Li VC. Trade-off between strength and ductility of random discontinuous fiber reinforced cementitious composites. Cement and Concrete Composties. 1994;16:23-9.

[5] VC Li CW, S Wang, A Ogawa, T Saito. Interface Tailoring for Strain-Hardening Polyvinyl Alcohol-Engineered Cementitious Composite (PVA-ECC). ACI Materials Journal. 2002;99(5).

[6] Li VC, Shuxin W, Wu C. Tensile Strain-hardening Behavior of Polyvinyl Alcohol Engineered Cementitious Composite (PVA-ECC). ACI Materials Journal. 2001;98(6):483-92.

[7] Redon C, Li VC, Wu C, Hoshiro H, Saito T, Ogawa A. Measuring and Modifying Interface Properties of PVA Fibers in ECC Matrix. ASCE Journal of Materials in Civil Engineering. 2001;13(6):399-406.

[8] Li VC, Wu C, Ogawa A, Saito T. Interface Tailoring for Strain-hardening PVA-ECC. ACI Materials Journal. 2002;99(5):463-72.

[9] Chanvillard G, Rigaud S. Compelete Characterisation of Tensile Properties of DUCTAL® UHPFRC According to the French Recommendations. In: 4th International

RILEM Workshop on High Performance Fiber - Reinforced Cement Composites (HPFRCC4). 2003:65-79.

[10] Karihaloo BL, Alaee FJ, Benson SDP. A new technique for retrofitting damaged concrete structures. In: Proceedings of the ICE - Structures and Buildings. 2002;152:309 – 18.

[11] Benson SDP, Karihaloo BL. CARDIFRC - Manufacture and Constitutive Behaviour. In: 4th International RILEM Workshop on High Performance Fiber - Reinforced Cement Composites (HPFRCC4). 2003:65-79.

[12] Benson S, Karihaloo B. CARDIFRC®–Development and mechanical properties. Part I: Development and workability. Magazine of Concrete Research. 2005;57(6):347-52.

[13] Benson S, Nicolaides D, Karihaloo B. CARDIFRC®–Development and mechanical properties. Part II: Fibre distribution. Magazine of Concrete Research. 2005;57(7):421-32.

[14] Benson S, Karihaloo B. CARDIFRC®–Development and mechanical properties. Part III: Uniaxial tensile response and other mechanical properties. Magazine of Concrete Research. 2005;57(8):433-43.

[15] Wille K, Naaman A, El-Tawil S, Parra-Montesinos G. Ultra-high performance concrete and fiber reinforced concrete: achieving strength and ductility without heat curing. Materials and Structures. 2012;45(3):309-24.

[16] Ranade R, Stults MD, Li VC, Rushing TS, Ronth J, Heard WF. Development of high strength high ductility concrete. In: R.D. Toledo Filho FAS, E.A.B. Koenders and E.M.R. Fairbairn, editor. 2nd international RILEM conference on strain hardening cementitious composites (SHCC2-Rio). Rio do Janeiro, Brazil: RILEM Publications SARL; 2011. p. 1 - 8.

[17] Marshall DB, Cox BN. A J-integral Method For Calculating Steady-State Matrix Cracking Stress in Cmposites. Mechanics of Materials. 1988;7(8):127-33.

[18] Rice JR. A path independent integral and the approximate analysis of strain concentration by notches and cracks. Journal of applied mechanics. 1968;35(2):379-86.

[19] Marshall DB, Cox BN. A J-integral method for calculating steady-state matrix cracking stresses in composites. Mechanics of Materials. 1988;7(2):127-33.

[20] Fischer G, Popovici V, Sorger K. Protective Steel Pipe Coating with Ductile Engineered Cementitious Composites (ECC). 2010, http://www.brederoshaw.com/non_html/techpapers/BrederoShaw_TP_ECC_Feb2010.pdf.

[21] Li VC, Wang Y, Backer S. A micromechanical model of tension softening and bridging toughening of short random fiber reinforced brittle matrix composites. Journal of the Mechanics and Physics of Solids. 1991;39(5):607-25.

[22] Wang S. Micromechanics Based Matrix Design for Engineered Cementitious Composites. Ann Arbor, USA: University of Michigan; 2005.

[23] Redon C, Li V, Wu C, Hoshiro H, Saito T, Ogawa A. Measuring and Modifying Interface Properties of PVA Fibers in ECC Matrix. Journal of Materials in Civil Engineering. 2001;13(6):399-406.

[24] Li VC, Wu HC, Chan YW. Effect of plasma treatment of polyethylene fibers on interface and cementitious composite properties. Journal of American Ceramic Society. 1996;79(3):700-4.

[25] Li VC, Wu HC, Chan YW. Interface Property Tailoring for Pseudo Strain-Hardening Cementitious Composites. In: Sih GC, Carpinteri A, Surace G, editors. Advanced Technology for Design and Fabrication of Composite Materials and Structures. Netherland: Kluwer Academic Publishers; 1995. p. 261-8.

[26] Shao Y, Shah SP. Mechanical Properties of PVA Fiber Reinforced Cement Composites Fabricated by Extrusion Processing. ACI Materials Journal. 1997;94(6):555-64.

[27] Betterman LR, Ouyang C, Shah SP. Fiber-Matrix Interaction in Microfiber-Reinforced Mortar. Advanced Cement Based Materials. 1995;2(2):53-61.

[28] Shah SP, Peled A, Aldea CM, Akkaya Y. Scope of high performance fiber reinforced cement composites. In: Third International RILEM Workshop on High Performance Fiber Reinforced Cement Composites. 1999:113 -29.

[29] Wu R, Wittmann FH, Wang P, Zhao T. Influence of Elevated and Low Temperature on Properties of SHCC.  3rd International RILEM Conference on Strain Hardening Cementitious Composites (SHCC3-Delft). Dordrecht, Netherlands: RILEM Publications SARL; 2014. p. 3 - 8.

[30] Paul SC, Ebell G, Zijl GPAGv, Schmidt W. Cracked and Uncracked SHCC Specimens under Different Exposure Conditions.  3rd International RILEM Conference on Strain Hardening Cementitious Composites (SHCC3-Delft). Dordrecht, Netherlands: RILEM Publications SARL; 2014. p. 25 - 32.

[31] Lepech M, Li VC, Fischer G, Li V. Durability and Long Term Performance of Engineered Cementitious Composites (ECC).  International RILEM Workshop on High Performance Fiber Reinforced Cementitious Composites in Structural Applications: RILEM Publications SARL; 2006. p. 165-74.

[32] Wittmann FH, Furtwängler K, Mao X, Fischer G, Li V. Optimizing material properties by means of the instrumented ring test.  International RILEM Workshop on High Performance Fiber Reinforced Cementitious Composites in Structural Applications: RILEM Publications SARL; 2006. p. 115-24.

[33] Ahmed SaM, Hirozo and Suzuki, Seisuke and Nishiwaki, Tomoya. Experimental study on restrained shrinkage-induced cracking of mortars with different toughness. In: 5th

International Concrete under Severe Conditions : Environment and Loading CONSEC '07. Tours, France: Laboratoire Central des Ponts et Chausses (LCPC); 2007:1061-8.

[34] Lepech M, Li VC. Water permeability of cracked cementitious composites. Proceedings of Eleventh International Conference on Fracture2005. p. 20-5.

[35] Martinola G, Bauml M, Wittmann FH. Modified ECC applied as an effective chloride barrier. Proc of the JCI Int Workshop on Ductile Fibre Reinforced Cementitious Composites (DFRCC)–Application and Evaluation (DRFCC-2002), Takayama, Japan2002. p. 171-80.

[36] Maalej M, Ahmed SF, Paramasivam P. Corrosion durability and structural response of functionally-graded concrete beams. Journal of advanced concrete technology. 2003;1(3):307-16.

[37] Sahmaran M, Li M, Li VC. Transport properties of engineered cementitious composites under chloride exposure. ACI Materials Journal. 2007;104(6).

[38] Maalej M, Li VC. Introduction of strain-hardening engineered cementitious composites in design of reinforced concrete flexural members for improved durability. ACI Structural Journal. 1995;92(2).

[39] Leung CKY, Cheung YN, Zhang J. Fatigue enhancement of concrete beam with ECC layer. Cement and Concrete Research. 2007;37(5):743-50.

[40] Weimann M, Li VC. Hygral behavior of engineered cementitious composites (ECC). International Journal for Restoration of Buildings and Monuments. 2003;9(5):513-34.

[41] Fischer G, Li VC. Effect of fiber reinforcement on the response of structural members. Engineering Fracture Mechanics. 2007;74(1–2):258-72.

[42] Mechtcherine V, Silva FdA, Müller S, Jun P, Filho RDT. Coupled strain rate and temperature effects on the tensile behavior of strain-hardening cement-based composites (SHCC) with PVA fibers. Cement and Concrete Research. 2012;42(11):1417-27.

[43] Oliveira AM, Silva FA, Fairbairn EM, Filho RDT. Temperature and Internal Moisture Effects on the Tensile Behavior of Strain-Hardening Cement-Based Composites (SHCC) Reinforced with PVA Fibers. 3rd International RILEM Conference on Strain Hardening Cementitious Composites (SHCC3-Delft). Dordrecht, Netherlands: RILEM Publications SARL; 2014. p. 51 - 60.

[44] Kanda T, Watanabe S, Li VC. Application of pseudo strain hardening cementitious composites to shear resistant structural elements. AEDIFICATIO Publishers, Fracture Mechanics of Concrete Structures. 1998;3:1477-90.

[45] Lignos D, Moreno D, Billington S. Seismic Retrofit of Steel Moment-Resisting Frames with High-Performance Fiber-Reinforced Concrete Infill Panels: Large-Scale Hybrid Simulation Experiments. Journal of structural engineering. 2014;140(3).

[46] Lepech M, Li V. Application of ECC for bridge deck link slabs. Materials and Structures. 2009;42(9):1185-95.

[47] Shannag MJ, Barakat S, Abdul-Kareem M. Cyclic behavior of HPFRC-repaired reinforced concrete interior beam-column joints. Materials and Structures. 2002;35(6):348-56.

[48] Misir I, Kahraman S. Strengthening of non-seismically detailed reinforced concrete beam–column joints using SIFCON blocks. Sadhana. 2013;38(1):69-88.

[49] Alaee F, Karihaloo B. Retrofitting of Reinforced Concrete Beams with CARDIFRC. Journal of Composites for Construction. 2003;7(3):174-86.

[50] Maheri MR, Karihaloo BL, Alaee FJ. Seismic performance parameters of RC beams retrofitted by CARDIFRC®. Engineering Structures. 2004;26(14):2069-79.

[51] Maalej M, Leong KS. Engineered cementitious composites for effective FRP-strengthening of RC beams. Composites Science and Technology. 2005;65(7–8):1120-8.

[52] Esmaeeli E, Manning E, Barros JAO. Strain Hardening Fibre Reinforced Cement Composites for the Flexural Strengthening of Masonry Elements of Ancient Structures. Construction and Building Materials. 2013;38(special issue):1010-21.

## Chapter 4: Development of Hybrid Composite Plate (HCP)

### 4.1 Introduction

This chapter is dedicated to the development of a thin prefabricated plate nominated Hybrid Composite Plate (HCP), to be used as an innovative element in strengthening and repairing of RC structures. In development of HCP, its features are tailored to achieve a robust alternative for the traditionally known techniques in retrofitting jobs based on using FRPs. Hence, HCP is developed mainly to be used for retrofitting of RC structures located in severe environmental conditions or those require the development of high level of tensile stresses in their retrofitting element (delayed/prevented CFRP debonding).

Within this chapter, initially an introduction to the structural concept of HCP and its expected performance in retrofitting of RC elements are presented. Furthermore, the methodology adopted in processing of PVA-SHCC, as one of two constituents of HCP, is presented and discussed.

Finally, the construction technique of HCP and its effectiveness for the retrofitting of RC structures are assessed through a preliminarily experimental program. Series of shear-deficient short-span RC beams are prepared and then retrofitted with different schemes, including attaching HCP to their lateral faces. These beams along with two other beams acting as reference specimens, one as-built beam and the other one retrofitted with conventionally bonded CFRP sheets, were subjected to three point flexural tests.

A discussion based on the results of testing these retrofitted beams in comparison with results of the reference beams is adopted to evaluate the HCP potential as a retrofitting element to be applied to RC structures.

### 4.2 HCP Material-Structural Concept

HCP combines the potential structural effectiveness of prefabricated SHCC reinforced with CFRP in retrofitting of RC structures. As illustrated in Figure 4.1, CFRP is attached on the face of the SHCC plate either in the form of externally bonded sheets, designated as HCP[S], or in the form of laminates placed into the pre-swan grooves on this face, designated

as HCP$^{(L)}$. The orientation of the bonded CFRPs is set based on the retrofitting demand. For example, if flexural strengthening is under consideration, carbon fibers are oriented along the length of the HCP, while for the shear strengthening they can be arranged inclined or parallel to the HCP's width.



SHCC plate

Bonded carbon fabric

SHCC plate

CFRP laminate bonded inside the grooves

(a)                                          (b)
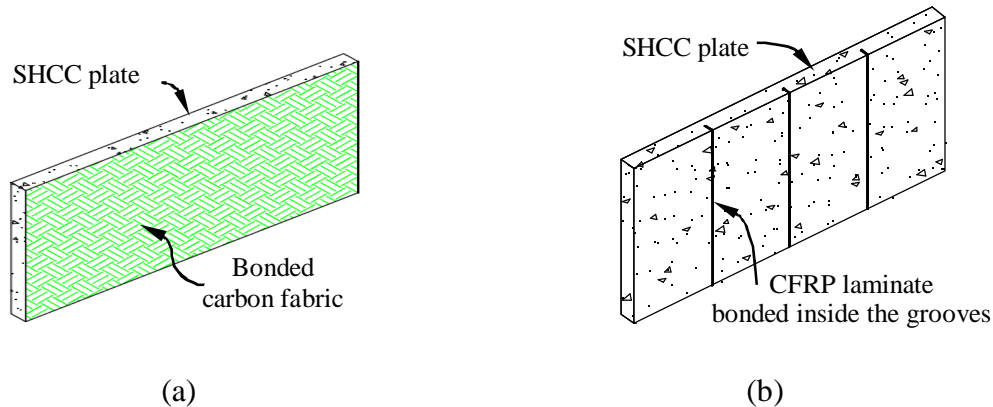
Figure 4.1: Configuration of HCPs (a) HCP$^{(S)}$: bonded carbon fabric to a face of a prefabricated SHCC plate, and (b) HCP$^{(L)}$: bonded CFRP laminates into the pre-sawn grooves on a face of a prefabricated SHCC plate, (note that the orientation of FRP bonded to the SHCC plate should be adjusted according to the strengthening demand)

As it was discussed in previous chapter, SHCC is a cementitious matrix reinforced with short discrete fibers, capable of developing higher tensile capacity than the strength corresponding to its first cracking, if stretched beyond this point. An appreciable amount of ductility under tensile loading is one of the most desired characteristics of SHCC which originates from the formation of multiple diffused fine cracks before SHCC reaches its ultimate tensile capacity. However, the ultimate tensile strength of SHCC is generally limited to two or three times of its matrix tensile strength. On the other hand, CFRP has a high tensile strength with an almost linear-elastic response up to its tensile rupture, hence providing only a very low ductility.

Therefore, as depicted schematically in Figure 4.2, HCP integrates the synergetic advantages of CFRP and SHCC, namely strength and ductility, in retrofitting of RC structures. Thanks to the high ductility of SHCC, to transfer forces between HCP and RC substrate, this thin prefabricated plate can be attached to the substrate not only by means of

adhesive but also using only anchors, or a combination thereof. Potential applications of this technique, as schematically presented in Figure 4.3, are for: flexural or shear strengthening, confining columns with rectangular cross-section, and improving seismic performance (more specifically energy dissipation capacity) of beam-column joints.
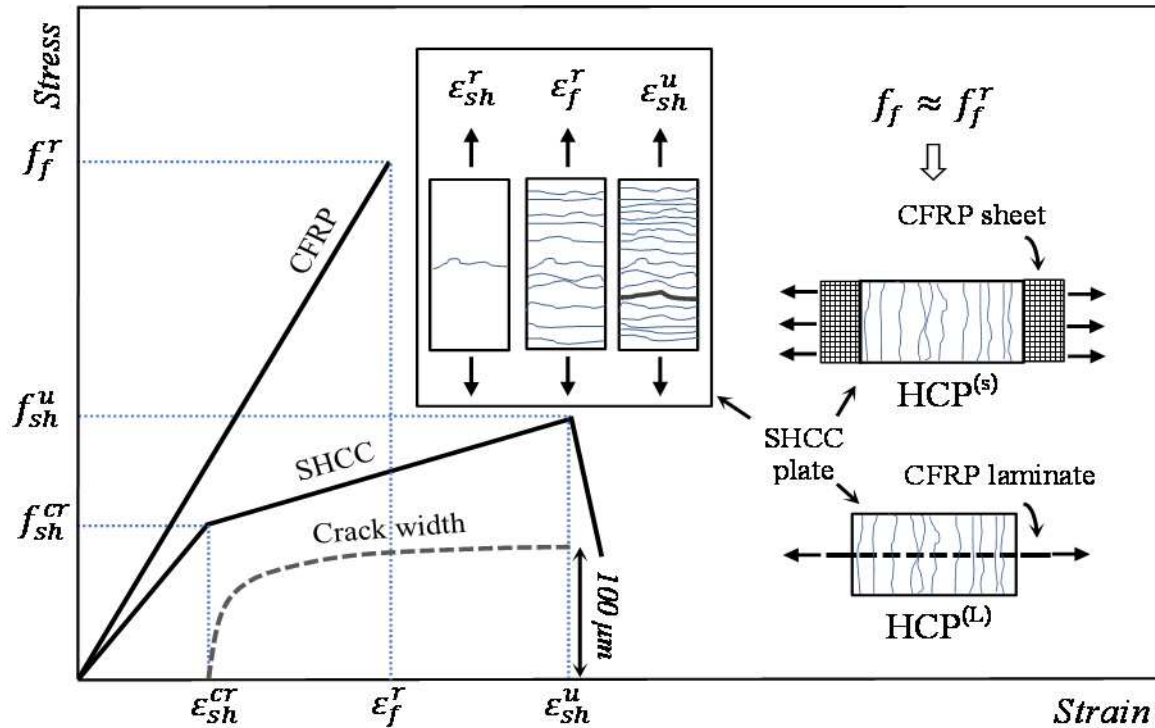


Figure 4.2: Schematic presentation of tensile behavior of CFRP and SHCC, crack propagation and crack width in SHCC at different loading stages, and crack propagation close to the rupture of CFRP at HCP (in this figure $\varepsilon_{ch}^{cr}$ and $\varepsilon_{sh}^{u}$ are tensile strain in SHCC corresponding to the stress at the first cracking ($f_{sh}^{cr}$) and to the ultimate tensile strength ($f_{sh}^{u}$), respectively. $f_{f}^{r}$ is the stress corresponding to the rupture of CFRP and $\varepsilon_{f}^{r}$ is its corresponding strain).

**Lateral View**



**Section A-A**　　　　**Section B-B**　　　　**Section C-C**
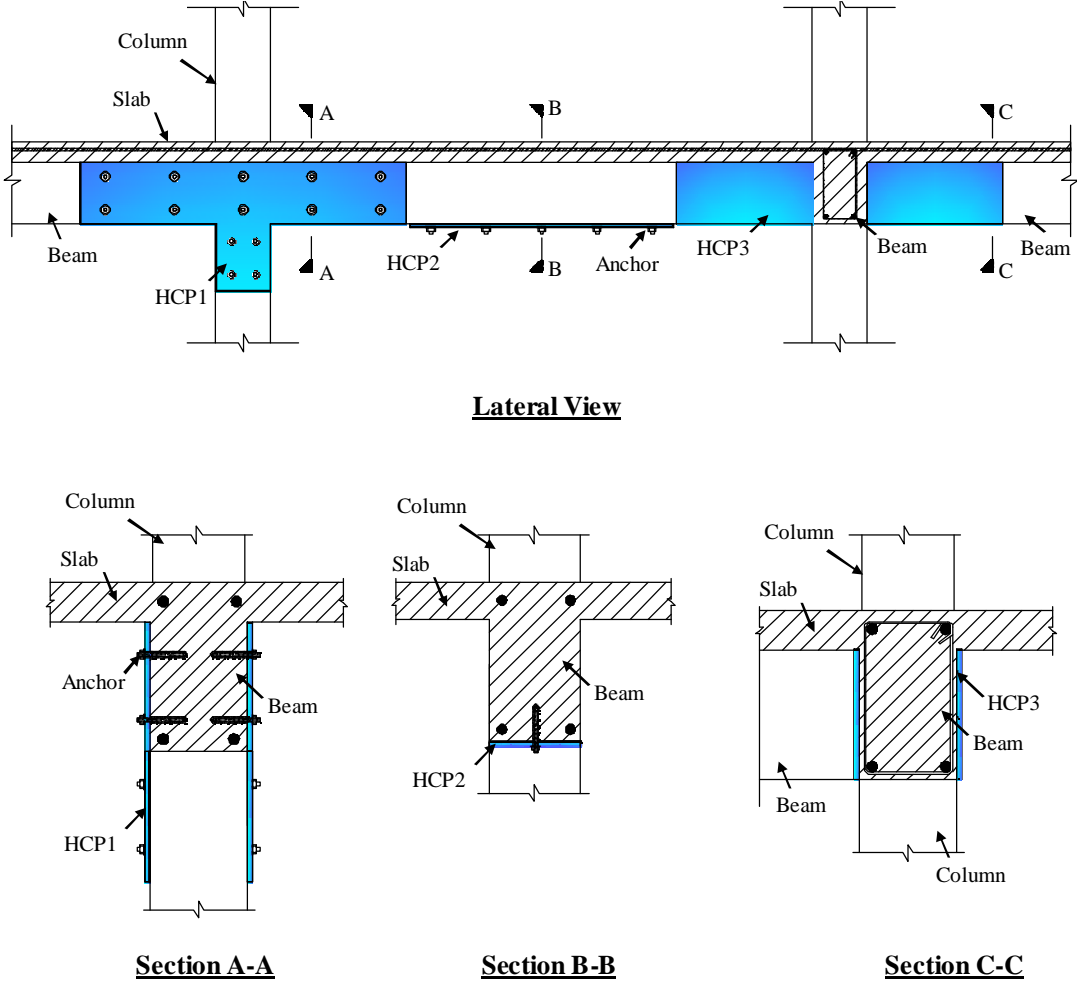
Figure 4.3: HCPs attached to the critical regions of a deficient RC structure for the strengthening purpose (HCP1 is attached to the beam-column joint region to improve seismic performance, HCP2 is attached to the bottom of the beam to increase flexural strength and HCP3 is bonded to the lateral faces of the beams to enhance shear capacity. Note that for the connection of HCP to concrete a combination of anchors and adhesive in the case of HCP1, only anchors in the case of HCP2, and only adhesive in the case of HCP3 are considered only to exemplify different connections)

If anchors are the only connection system, the stress transfer between the HCP and the RC element occurs mainly at the fastened locations and through the bearing capacity of the SHCC plate. According to this configuration, any increase in the deformation of the

retrofitted element is accompanied by a sliding between the strengthening layer and the concrete substrate, thus desirable for ductility enhancement applications.

When anchors are used in combination with HCP-RC interface bonding adhesive, they are primarily aimed at providing a vertical pressure to the HCP in order to delay/prevent a possible detachment, but they also have another beneficial effect. In fact, the anchors contribute, through the SHCC bearing capacity, in transferring the shear stresses released at the detached regions of the HCP and those resulting from a further increase in deformation demand of the retrofitted element.

As compared to the anchored HCP, a connection based on combination of anchors and adhesive is suitable to mobilize tensile capacity of a high stiffness HCP, where is needed. Such connection is also expected to improve the serviceability performance of the retrofitted element more notably than a discrete connection made of only anchors, since restricts cracks width and the deflection of the retrofitted element.

Moreover, HCP is developed to suppress, even if partially, the shortcomings of FRP systems (discussed in chapter 2) in structural strengthening. In fact, since the FRP bonded face of HCP is the one placed in contact with the retrofitted RC member, SHCC acts as a protective cover for CFRP constituents, which provides insulation for both FRP and bonding material used in the structure of an HCP. Therefore, this system is expected to endure higher levels of temperature in comparison to conventional applications of FRP system. Furthermore, up to the rupture strain of CFRP materials, which is often below 2%, normally, impermeable fine diffused cracks form in the SHCC, with a maximum crack width limited to 0.1 mm, which potentially assures a long-time performance for the constituents of the HCP system, and enhances the durability of the elements to be strengthened (see Figure 4.2).

Hence, compared to the FRP strengthening techniques, HCP is more suitable for the strengthening applications where RC members are subjected to an aggressive environment, to a relatively high temperature or considerable temperature variations, and to the risk of vandalism.

Moreover, as the detachment of HCP connected to RC elements by means of both adhesive and anchors is expected to be prevented or at least significantly delayed, this system

offers an enhanced reliability and effectiveness specially in strengthening RC elements demanding a remarkable upgrade in their structural performance.

This technique is also potentially appropriate where the concrete cover has a poor quality and/or strength, since anchors are expected to transfer the interlayer shear stresses to the element's core concrete, beyond the level of the main steel reinforcements.

Furthermore, the proposed technique is independent of the thickness of the concrete cover, which is important if compared to the strengthening method based on bonding FRP bars/laminates into the pre-sawn grooves on concrete cover (NSM-FRP).

If increasing the shear capacity of the RC member is the strengthening objective, the notable contribution of SHCC plate in resisting shear stresses is combined with tensile contribution of FRP elements to significantly upgrade the RC member's shear strength.

Finally, in contrast to FRP systems that are susceptible to premature buckling under compressive stresses, an HCP retrofitted element is expected to present a notably higher compressive capacity due to the contribution of SHCC in the mechanism of resisting compressive stresses and the enhanced compressive strength of the confined concrete (e.g., in the case of an HCP strengthened rectangular column with an HCP-RC connection based on adhesive and post-tensioned chemical anchors).

Moreover, as compared to TRM systems, a much superior bond strength at the interface of HCP constituents (CFRP and SHCC), and at the interface between HCP and concrete is attainable.

## 4.3 SHCC Mix Processing

According to the material-structural requisites of an HCP, its ductile cementitious plate should possess a tensile strain capacity in the range of rupture strain of CFRP sheet/laminate (generally between 1.4% and 1.7%). In terms of tensile strength, a moderate capacity, e.g., between 3 and 5 MPa, is set as another mechanical constraint in developing SHCC. Moreover, such a composite should comply with the durability requirements of an HCP. Hence, the maximum crack width at the peak load should be limited enough to provide a satisfactory long-term performance under service loading conditions. The literature review

on mechanical characteristics and durability performances of the existing strain hardening cementitious composites, presented in chapter 3, suggests the PVA-SHCC (originally designated PVA-ECC [1]) as an appropriate composite to be used in production of HCP.

This SHCC exhibits ultra-ductile behavior under tensile loading for a moderate content of short discrete PVA fibers (2% in composite volume) [2]. The mechanism of self-crack width control in PVA-SHCC limits its maximum crack opening at the peak of tension load to an impermeable width [3]. Besides its lower cost among the other SHCCs with comparable characteristics, resulted from its engineering tailor on the basis of micromechanical models, the technology of processing and using PVA-SHCC is rapidly broadening in both laboratory and constructional scales around the world [4-8]. Moreover, there are an appreciable amount of studies available on long-time durability and thermal stability of PVA-SHCC as compared to the other SHCCs. This is why the ongoing report of "RILEM Technical Committee 240-FDS" with designation of "A framework for durability design of fiber-reinforced strain-hardening cement-based composites (SHCC)", is mainly on the basis of the results obtained from testing PVA-SHCCs.

To tailor an ultra-high ductile composite, the synergistic interaction between the cementitious matrix, PVA-fiber, and fiber-matrix interface should be exploited. Hence, for a specific fiber with a given geometry, mechanical properties and surface treatment (e.g., PVA fibers), characteristics of cementitious matrix should be constrained to the requirements of micromechanical models explained in section 3.2.1. Therefore, for the oil coated short PVA fibers dispersed in a cementitious matrix, lowering the matrix fracture toughness and crack initiation strength along with densifying the fibers-matrix interface transition zone (ITZ) are the main principles in SHCC processing.

In the current research work, the ingredients used for matrix processing are selected in compliance with both the availability of local materials in north Portugal and the constraints of PVA-SHCC micromechanical models. Processing this composite in the framework of present study is also relied on the previous experiences and studies of the author in developing PVA-SHCC [8]. In the next sections a description of the used constituents is presented.

### *4.3.1 Constituents of Composite Mixture*

### *4.3.1.1 PVA Fibers*

The short PVA fibers used in this study are produced by Kuraray Company with the designation RECs15×8. Geometrical and mechanical properties along with a figure of these fibers are presented in Table 1. Due to the presence of hydroxyl groups on the surface of PVA fibers, they exhibit a high affinity to water, known as hydrophilicity. Consequently, the formation of hydrogen bonding at the interface of fibers and the surrounding cementitious particles results in developing a strong chemical bond. Excessive chemical bonding, as discussed in section 3.2.1, causes premature rupture of fibers for only a limited sliding, consequently reduces fibers-bridging complementary energy $(J_b)$. This problem was partially treated by coating external surface of fibers using 1.2% by their mass of a hydrophobic oiling agent that optimizes the chemical bonding [2, 9]. Pervious investigations, adopting micromechanical ECC design models, revealed that a fiber content of 2% of composite's volume is required to practically assure the development of an ultra-ductile PVA-SHCC, provided that cementitious matrix possess appropriate characteristics [1]. Therefore, in the current study the same content of fibers is used.

Table 4.1: Properties of PVA fiber PVA RECs15×8

| Diameter | Length | Nominal tensile strength | Modulus of elasticity | Density | Elongation | |
|---|---|---|---|---|---|---|
| μm | mm | MPa | GPa | gr/cm$^3$ | % | |
| 40 | 8 | 1600 | 40 | 1.3 | 7 |  |

### *4.3.1.2 Sand (SA)*

In development of PVA-SHCC, minimizing matrix crack tip toughness, $J_{tip}$, (or equivalently matrix fracture energy) is fundamental to assure the chance of a higher tensile ductility due to an increased $J_b/J_{tip}$ [10]. Therefore, to control matrix fracture toughness and reduce its first cracking strength, mixing large aggregates or high contents of fine aggregates should be avoided.

Mixing a moderate amount of fine sand is appropriate to main both matrix fracture toughness and crack initiation strength sufficiently low, since both aggregates' interlock and tortuosity of crack path are reduced. Moreover, if compared to a matrix made of only cementitious paste, introducing fine sand not only contributes to the cost efficiency of material, but also reduces the risk of shrinkage and creep, associated with a cement high content [11], and enhances material's modulus of elasticity. From rheological point of view, fine sands help in uniform dispersion of PVA fibers inside the cementitious matrix.

Depending on the type of the sand, its particle size distribution and maximum particle size, and also the composition of the binder (B), the ratio of SA/B in a PVA-SHCC may vary between 0.36 and 0.69, to accomplish both micromechanical and rheological requirements of composite [12-15]. Taking into account this range of SA/B and the past experiences of the author in developing PVA-SHCC [8], in this research work, silica sand with a maximum grain size below 500 $\mu$m and a specific gravity of 2630 kg/m$^3$ is used.

### 4.3.1.3 Cement (C)

Portland cement type I 42.5-R with the physical properties reported in Table 4.2, was selected as one of the constituents of the two-parts binder (cement and fly ash) used in the matrix mix.

Table 4.2: Summarized physical specification of cement type I 42.5-R

| Parameter | Value |
|---|---|
| Specific gravity | 3150 kg/m$^3$ |
| Blaine fineness | 387.3 m$^2$/kg |
| Initial setting time | 116 min |
| Final setting time | 147 min |

### *4.3.1.4 Fly Ash (FA)*

The early versions of PVA-SHCCs incorporated high cement content as the only binder, in the range of 830 to 1200 kg/m$^3$ , mainly reduce the matrix fracture toughness.

However, high cement dosage is not only responsible for a high hydration heat and drying shrinkage but increases the material cost and adversely affects its sustainability in terms of its impact on environment. Partially substituting cement with fly ash, which is a coal combustion residue with pozzolanic characteristics, is an alternative that positively addresses both material sustainability and cost efficiency.

Moreover, fly ash can dilute the concentrated cement at the fiber-matrix interface, hence, reducing chemical bonding. Finally, fly ash with its spherical shape particles finer than cement, is suitable to increase densification of *ITZ*, thus, enhancing fiber-matrix frictional bond.

Beneficial effects of partial cement substituting with fly ash in traditional concretes is limited to a replacement that ranges between 10% and 25% of total cement mass [16, 17]. In the case of PVA-SHCC, however, using a high volume of fly ash (HVFA) was found to be useful in reducing both matrix fracture toughness and strength at crack initiation, also assuring nearly constant long-term composite characteristics, namely tensile strain ductility and crack width, since the changes in the *ITZ* is minimized [12, 13]. Furthermore, a high content of fly ash improves the rheological properties of the composite and helps in better fibers dispersion.

On the other hand, increasing the amount of fly ash adversely affects composite compressive strength, for example, increasing FA/C from 1.2 to 5.6 was reported to be responsible for an average drop of 59% in the 90 days compressive strength of PVA-SHCC, while at the same age, composites with FA/C of 5.6 exhibited a much better performance in terms of tensile strain ductility and residual crack width [13].

Fly ash used in present study, with specific gravity of 2420 kg/m$^3$, complies with the minimum requirements indicated in EN-450 [18] to be used as a partial replacement of cement in concrete. Based on the specifications of this standard the adopted fly ash is categorized in class B and group N considering the loss of ignition and fineness, respectively.

Chemical composition and other properties of the fly ash used in this research work are indicated in Table 4.3.

Table 4.3: Fly ash properties and chemical composition according supplier

| | | | |
|---|---|---|---|
| $Cl^-$ | 0 % | MgO | 1.9 % |
| $SO_3$ | 0.12 % | $P_2O_5$ | 1.92 % |
| CaO free | 0.1 % | Total alkalis | 0.25 % |
| CaO reactive | 2.7 % | Retained on No. 325 sieve | 15 % |
| $SiO_2$ reactive | 40.8 % | I.A.$_{28D}$* | 79 % |
| $SiO_2 + Al2O_3 + Fe_2O_3$ | 89.9 % | I.A.$_{90D}$** | 99 % |

\* Strength activity index with Portland cement at 28 days
\*\* Strength activity index with Portland cement at 90 days

### 4.3.1.5 Chemical Admixtures (SP & VMA)

To achieve uniform fiber dispersion during composite flow, self-consolidating is a key requirement for a fiber reinforced cementitious composite. It also contributes in increasing composite workability and minimizing the required energy to place composite inside the moulds. Such a high deformability initially needs that the self-weight of composite overcomes its yield-strength, which is proportional to the interparticle forces. Furthermore, an adequate viscosity should be available to achieve a homogenous flow of the fresh mixture.

Electrostatic forces between cement particles are one of the strongest interparticle attractions that may result in cement particles flocculation, resisting composite yielding and flow. Such a phenomenon also causes a notable segregation between composite constituents, even if sufficient external energy causes in composite yielding.

High range water reducer admixtures (HRWRAs), also known as superplasticizers (SP), are generally used to disperse cement particles and reduce water demand, while an enhanced workability for the obtained self-consolidating mixture is assured [19]. Despite the beneficial effects of SPs in improving matrix deformability, these chemical admixtures may adversely affect the viscosity requirements for uniform fiber dispersion during mixing and placing composite. Moreover, the repulsive effect of SPs on cement particles decreases over time,

resulting in early loss of workability. Employing viscosity modifying agents (VMAs) with electrosteric stabilization characteristic is an alternative to supress these shortcomings, since adding VMAs into cementitious mixtures enhances mixture viscosity and reduces van der Waals attraction between adjacent particles [20]. VMAs are traditionally used in developing self-consolidating high performance concretes to avoid or minimize the washout, segregation or settlement of ingredients, and water bleeding [19, 21].

Although a higher viscosity is appropriate for a better dispersion of fibers in the matrix and assures a homogenous flow of composite in its fresh state (preventing the fibers settlement), and consequently improves composite ductility in the hardened state [22], a too high plastic viscosity reduces composite fluidity. In the other word, while a high viscosity favors a homogenous mixing of fibers into the matrix, more than a moderate viscosity adversely affects composite fluidity. Therefore, a careful selection and adjustment of concentration of each of these chemical admixtures is essential to process a self-consolidating composite that maintains good consistency and workability characteristics with uniformly dispersed PVA fibers.

In this research work, an aqueous solution of modified polycarboxylates with a density of $1.06 \pm 0.02$ kg/dm$^3$ and a solid content of $26.5 \pm 1.3\%$ supplied with Sika® Company under designation of "Sika® ViscoCrete® 3002 HE" is used as the superplasticizer (SP).

The adopted viscosity modifying agent (VMA) was a hydroxypropyl methyl cellulose (HPMC)-based light solid powder supplied with Dow® Chemical Company.

### 4.3.1.6 Water (W)

Water to binder content (W/B) plays a significant role in adjusting chemical and frictional bonds at the interface between PVA fibers and their surrounding matrix. A high W/B helps in lowering the fiber-matrix chemical bonding, since the concentration of cement particles at the *ITZ* is reduced. From a micromechanical point of view, lower chemical bonding promotes the chance of fibers sliding which is basically essential to achieve sufficient fibers-bridging complementary energy, $J_b$. However, a too high W/B result in a low fiber-matrix frictional bond and consequently inadequate fibers crack bridging strength,

which is not in favor of satisfying the strength criterion according to SHCC micromechanical design concept (see Equation (3-4)).

Furthermore, for a given solid concentration, W/B has an inverse relation with both matrix toughness and crack initiation strength. According to the SHCC micromechanical model, to achieve a strain hardening response, lowering both these characteristics should be aimed at (see Equations (3-3) and (3-4)).

A literature review reveals that depending on binder composition, the W/B varies between 0.21 and 0.40 to satisfy the above-mentioned conditions for matrix and matrix-fiber interface properties [12-15]. In the selection of water content achieving sufficient compressive strength and modulus of elasticity for the composite is another constraint.

### 4.3.2 Composite Mix Processing Methodology

From the previous discussions, it can be found that developing a PVA-SHCC involves calibration of several coupled variables and only their careful adjustment results in a composite satisfying both fresh-state and hardened-state requisites, namely rheological properties for good fiber dispersion, adequate workability, and sufficient multiple-cracking and strength under tensile loading.

The composite mix processing methodology adopted in current research work is based on minimizing the number of these variables. This aim is fulfilled, considering the results of the statistical analysis conducted by Yang et al. [22] on sensitivity of PVA-SHCC to the proportions of its constituents. Following the outcome of their experimental study, these researchers reported that W/B, SP/B and VMA/B have the highest influence in altering the mixture rheological properties, while W/B is the most important factor affecting composite mechanical properties (the binder was composed of cement and fly ash). Taking these findings into account, in this research work, the concentrations of cement, sand and fly ash are treated as constant parameters, while the content of water and admixtures are taken as variables.

Following the discussion presented in section 4.3.1.4, a high content of fly ash although increases SHCC ductility, adversely affects its compressive strength. Therefore, the bearing capacity of SHCC will be reduced, and a premature crushing of SHCC at the interface

regions with anchors restricts exploiting the full retrofitting potential of HCP. Furthermore, only moderate tensile strain ductility is sufficient to fulfill CFRP-SHCC strain compatibility and to achieve local stress redistribution at the HCP anchored regions. Considering this discussion to process PVA-SHCC in this research work, FA/C of 1.2 was chosen as one of the constraints among others.

Furthermore, the SA/B of 0.5 was selected as an approximately average value of those reported in the literature by the other researchers (see discussion in section 4.3.1.2).

The contents of variable parameters (W, SP and VMA) were carefully adjusted to process a PVA-SHCC with optimal fresh state workability and adequate mechanical properties, both constrained with the requirements of HCP construction. Considering the range of W/B found in literature (discussed in section 4.3.1.6), ratios of 0.25, 0.30 and 0.35 were the selected trial for this parameter.

The general framework for processing of PVA-SHCC is then set based on optimizing the fresh state properties of composite at each given W/B contents, and then characterizing the hardened state properties of each of these rheologically optimized composites. The mixture is accepted if its mechanical properties accomplish the requirements of a composite to be used in construction of HCP (see section 4.2).

Optimizing composite fresh state properties was consisted of two sequential phases: matrix and composite phases. In the matrix phase, mortar mixtures containing similar solids (binder and sand) concentrations were prepared to study the optimized concentration of SP at each given W/B. The optimized concentration of SP, also known as saturation dosage, is defined as an SP concentration that beyond it no further benefit is achieved.

Although traditionally, in development of self-consolidating concrete (SCC), the saturation dosage of SP is investigated using a cement paste [23], it is also known that in the mortar phase other factors such as concentration of solid aggregates may influence the optimized SP dosage obtained from the paste examinations [24]. Hence, in this research work, the SP optimum dosage at each given W/B, and with constant solid concentrations, is investigated directly in mortar phase. Mini-slump cone device is used to measure the diameter of self-weight spread of the mortars ass the indicator for mortar's deformability.

The optimum concentration is then defined as the content of SP that any further increase beyond this dosage introduces only a marginal or zero changes in the mortar flow spread.

The first trial in preparing the mortar mixtures, with the lowest water content (W/B = 0.25) and no SP, revealed a notable water bleeding and segregation at the boundary of the flow spread. To prevent this segregation and achieve mortars with sufficient consistency, a constant VMA/B of 0.1 was added to all the mortar mixtures trials.

Optimizing VMA concentration was investigated at the composite phase. Adopting the calibrated concentration of the SP for each given W/B contents, found in mortar phase, composites with variable amount of VMA/B and a fixed content of PVA-fibers (2% of composite volume) were prepared. Consistency of each of these composites in terms of fibers dispersion and workability was examined to select the optimum concentration of VMA.

The deformability and fluidity of composites were measured by means of the tests executed using mini slump cone and V-funnel devices, respectively, with the geometrical specifications depicted in Figures 4.4a and 4.4b, correspondingly. In the absence of a feasible quantitative technique, fibers dispersion was evaluated only by means of visual and touching inspection to assure a composite mixture almost free of clumped fibers and with well dispersed fibers (if fibers are transported by the flow of the paste up to the spread's border).

Finally, for each given W/B the optimized concentrations of SP and VMA were used to prepare PVA-SHCC mixtures of larger volumes, and to prepare thin plates for composites tensile characterizations in the hardened state.

The abovementioned adopted strategy for processing PVA-SHCC is schematically illustrated in a flowchart showed in Figure 4.5. Details on mixing procedure, casting and curing the PVA-SHCC plates, geometry and preparing method of the tensile specimens, and the tensile tests are discussed in the following sections.
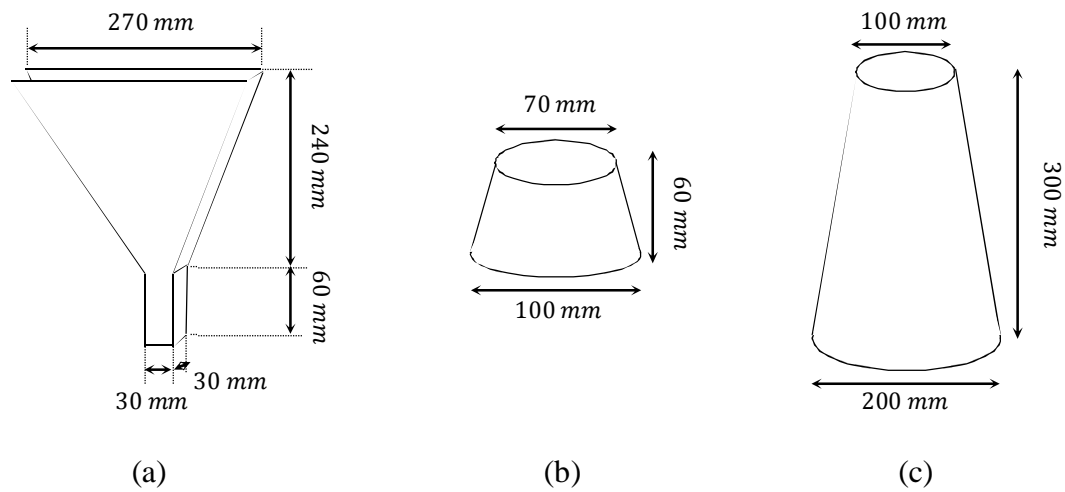
Figure 4.4: Geometrical specifications of the apparatuses used to characterize fresh state rheological properties of the mixtures, (a) V-funnel to measure fluidity of the composites, (b) mini-slump cone to measure deformability of mortar matrix and composite, and (c) the conventional slump-cone to verify self-consolidating of the processed SHCC

### *4.3.3 Mixing Procedure*

An automatic planetary rotating mixer with a bowl of apparent capacity of 10 liters was used to prepare mortars and composite mixtures. The adopted mixing procedures, sequences of adding mixture ingredients into the mixer and the mixing duration, for matrix and composite mixtures can be found in Tables 4.4 and 4.5, respectively.

For both the matrix and the composite mixtures initially dry solid ingredients, including cement, fly ash and sand, were introduced into the bowl of mixer and mixed for 30 seconds. In the matrix phase, where the optimization of SP is investigated, half of the water combined with all SP was mixed for 150 seconds. Finally, the remaining part of water combined with all VMA was introduced and the mortar mixing followed for more 150 seconds.

In the case of composite mixture, SP was first mixed with half of the total water and then this mixture was introduced into the mixer bowl. After 30 seconds of mixing, the remaining part of water in combination with the VMA was introduced and the mixing procedure using a high speed was continued for 150 seconds. Finally, fibers were gradually added and mixed for around 300 seconds with high speed. It is worth noting that adopting a higher mixing speed is beneficial in achieving a homogenous PVA-SHCC mixture. In fact,

due to shear thickening characteristics of VMA, a higher shear rate enhances the viscosity of the matrix, which favors better a fibers dispersion.
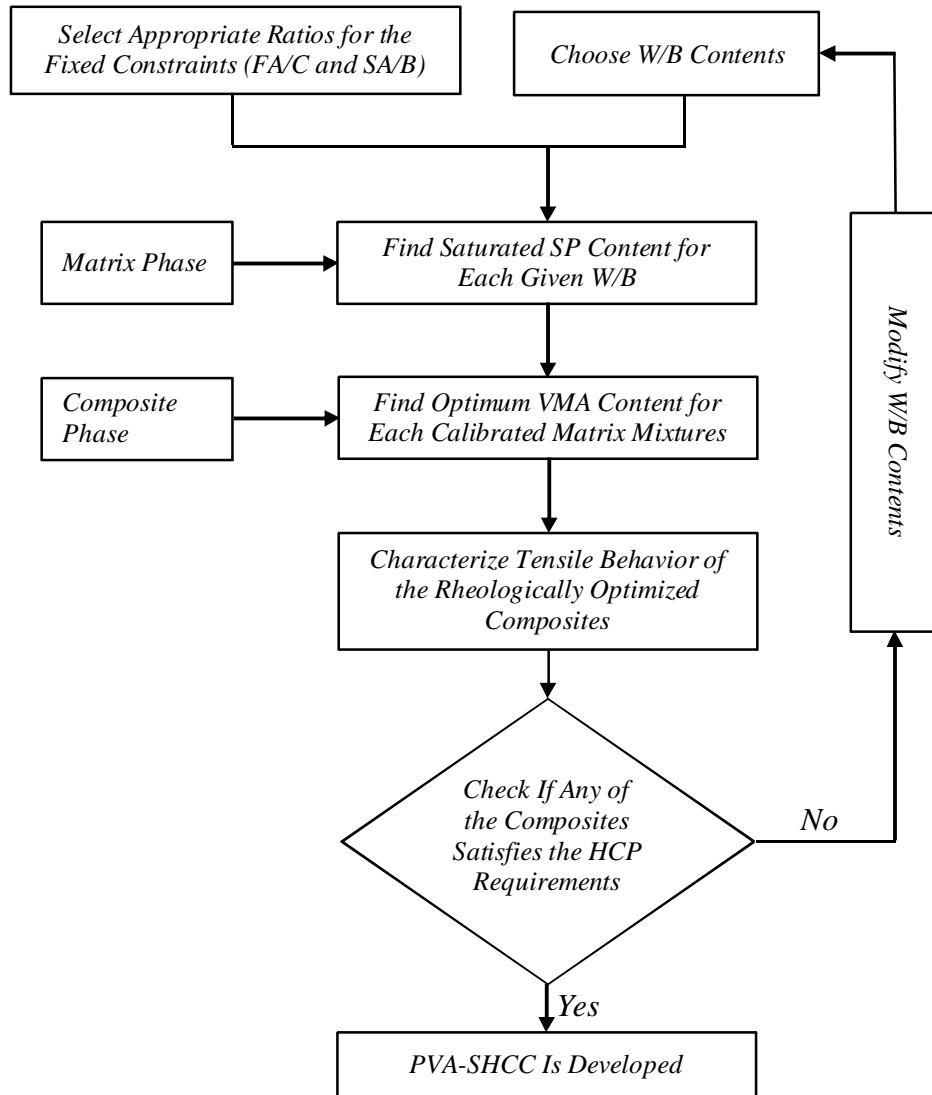


Figure 4.5: Adopted strategy for processing PVA-SHCC

Table 4.4: Matrix mix procedure

| Steps | Ingredients mixed at each step | Duration (s) | Speed |
|-------|-------------------------------|--------------|-------|
| Step 1 | Binder (C & FA) + SA | 30 | Low |
| Step 2 | 0.5W + SP | 150 | Low |
| Step 3 | 0.5W + VMA | 150 | Low |

Table 4.5: Composite mix procedure

| Steps | Ingredients mixed at each Step | Duration (sec) | Speed |
|-------|-------------------------------|----------------|-------|
| Step 1 | Binder (C & FA) + SA | 30 | Low |
| Step 2 | 0.5W + SP | 150 | Low |
| Step 3 | 0.5Water + VMA | 150 | High |
| Step 4 | PVA-Fibers | 300 | High |

### 4.3.4 Optimizing SP Content (Matrix Phase)

Details of mortar mix compositions used to investigate saturation dosage of SP for each given W/B contents with constant amount of solid ingredients are shown in Table 4.6. After preparing each mixture (mortar matrix), the mini-slump cone, placed on a smooth leveled plate, was filled and then lifted slowly upwards to have mortar flowing under its self-weight (see Figure 4.6). When the mortar stopped further flowing, its largest spread diameter and the one perpendicular to this diameter were measured. The average of these two diameters, $D_m^{avg}$, was calculated and reported in the last column of Table 4.6. These data are used in Figure 4.7 to graphically demonstrate the relation between spread diameter and SP/B concentration for each given W/B contents. In this table, the content of the row corresponding to the saturated SP dosage is presented in bold.



<div align="center">(a)            (b)</div>
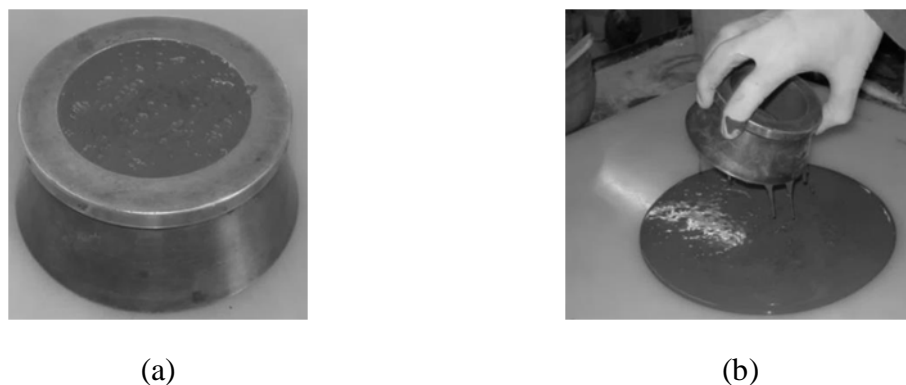
Figure 4.6: Mini-slump cone used to measure deformability of mixtures: (a) the cone was placed on a smooth plate and filled with the mixture, and (b) the cone was slowly lifted upward to let mixture flow under its self-weight

Table 4.6: Mass proportions of mortar mixtures and the corresponding average spread diameter of mini-slump test

| Mix label | W/B (%) | FA/C (%) | SA/B (%) | VMA/B (%) | SP/B (%) | $D_m^{avg}$ (mm) |
|---|---|---|---|---|---|---|
| M1W25 | | | | | 3.00 | 291 |
| M2W25 | | | | | 2.75 | 290 |
| M3W25 | | | | | 2.50 | 293 |
| **M4W25** | 25 | 120 | 50 | 0.10 | **2.25*** | **290** |
| M5W25 | | | | | 2.00 | 277 |
| M6W25 | | | | | 1.50 | 245 |
| M1W30 | | | | | 2.50 | 336 |
| M2W30 | | | | | 2.25 | 336 |
| **M3W30** | 30 | 120 | 50 | 0.10 | **2.00*** | **332** |
| M4W30 | | | | | 1.75 | 318 |
| M5W30 | | | | | 1.25 | 280 |
| M1W35 | | | | | 2.25 | 381 |
| M2W35 | | | | | 2.00 | 384 |
| **M3W35** | 35 | 120 | 50 | 0.10 | **1.85*** | **382** |
| M4W35 | | | | | 1.65 | 372 |
| M5W35 | | | | | 1.50 | 354 |
| M6W35 | | | | | 2.25 | 381 |

* The optimum content of SP at each given W/B
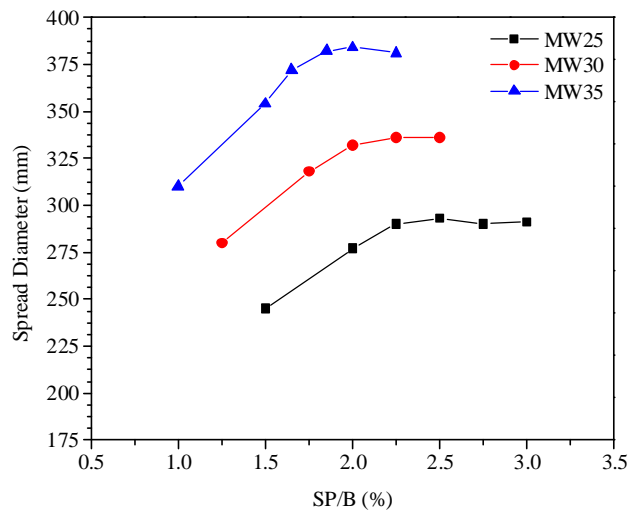
Figure 4.7: Mini-slump test spread diameter *vs* superplasticizer concentration for different water contents (see Table 4.6)
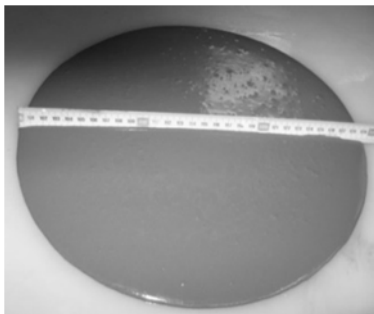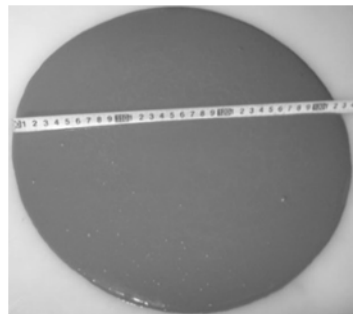


M4W25 (W/B: 25% & SP/B: 2.25%)          M3W30 (W/B: 30% & SP/B: 2.0%)
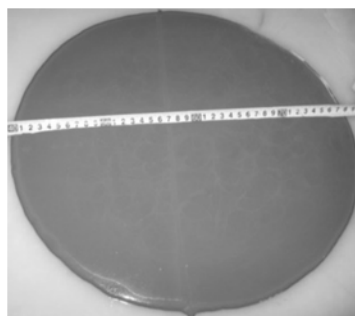


M3W35 (W/B: 35% & SP/B: 1.85%)

Figure 4.8: Mini-slump flow deformation of mixtures with optimized SP content at the given W/B (see also Table 4.6)

### 4.3.5 Optimizing VMA Content (Composite Phase)

As mentioned before, uniform fiber dispersion during composite mixing and flow is essential to develop a PVA-SHCC with adequate fresh and hardened state properties. Although a higher mixture's viscosity promotes better fiber dispersion during mixing stage, too high viscosity reduces significantly composite fluidity and deformability, causing low composite workability.

Taking into account these requirements, obviously the concentration of shear thickening VMA should be carefully adjusted to exploit its proper functioning under both high and moderate shear agitation (the stages of mixing fibers into the matrix and the composite placing, respectively).

Therefore, optimizing VMA content in this research work was followed by introducing variable amounts of VMA into SP optimized mortar mixtures at each given W/B and then mixing 2% PVA fibers (in percentage of composite mix volume) in each of these mixtures.

Deformability and consistency of each composite mixture were initially evaluated by executing a mini-slump test. V-Funnel flow rate was measured only for those composites with well-dispersed fibers.

For each W/B contents, the mixture with the highest deformability and fluidity was selected to characterize its hardened-state tensile properties. Based on the results of these tests, the composite with adequate mechanical properties is selected to be used for construction of HCP. Further, another mixture of this selected composite is prepared and its large-scale fresh-state deformability examined by means of a conventional slump testing device. The geometrical specifications of this slump cone are illustrated in Figure 4.4c. Moreover, cylindrical specimens were cast using the remaining part of this mixture to characterize the compressive strength and modulus of elasticity of the developed SHCC.

A similar approach to that described in the mortar phase was adopted to perform deformability test using mini-slump cone device in the composite phase as well. To evaluate composite flow rate, the V-funnel was fully filled with the composite and after a minute of resting, the stopper at the bottom of the funnel was removed and composite started to   flow

(see Figure 4.9). The time elapsed between removing the stopper and the first observed light at the bottom of funnel was registered as flow rate time.



Figure 4.9: Composite flowing out of V-funnel

The composite mix proportions along with the results obtained from their rheological characterization and the author's observations are indicated in Table 4.7. In this table, the row with its contents presented in bold corresponds to the VMA/B resulted in the highest fluidity (lowest funnel-flow time) at the given W/B. Photos of flow spread of rheologically optimized composites are depicted in Figure 4.10.

From Table 4.7, it can be concluded that the optimum VMA concentration increases with the increase in W/B, however, no linear relationship can be established between them. Moreover, while for VMA contents lower than the optimum dosage clumping of fibers with or without segregation has occurred, higher VMA concentrations than this optimum dosage reduces both composite deformability and fluidity.

126

Table 4.7 Proportions of composite mixtures and their corresponding rheological properties in consequence of changing VMA/B at each given W/B

| Mix label | W/B (%) | FA/C (%) | SA/B (%) | SP/B (%) | VMA/B (%) | $D_{cm}^{avg}$ (mm) | T (sec) | observations |
|---|---|---|---|---|---|---|---|---|
| C1W25 | | | | | 0.10 | 178 | N/A | slightly clumped fibers with boundary water segregation |
| **C2W25** | 25 | 120 | 50 | 2.25 | **0.13*** | **185** | **21** | good fibers dispersion and no segregation |
| C3W25 | | | | | 0.15 | 169 | 32 | good fibers dispersion and no segregation |
| C1W30 | | | | | 0.13 | N/A | N/A | clumped fibers |
| C2W30 | | | | | 0.15 | N/A | N/A | clumped fibers |
| C3W30 | 30 | 120 | 50 | 2.00 | 0.17 | 224 | 28 | good fibers dispersion but some surface water bleeding |
| **C4W30** | | | | | **0.20*** | **245** | **13** | good fibers dispersion and no segregation |
| C5W30 | | | | | 0.23 | 198 | 44 | good fibers dispersion and no segregation |
| C1W35 | | | | | 0.20 | N/A | N/A | clumped fibers and significant boundary water segregation |
| **C2W35** | 35 | 120 | 50 | 1.85 | **0.23*** | **255** | **11** | good fibers dispersion and no segregation |
| C3W35 | | | | | 0.25 | 225 | 27 | good fibers dispersion and no segregation |

* The optimum dosage of VMA
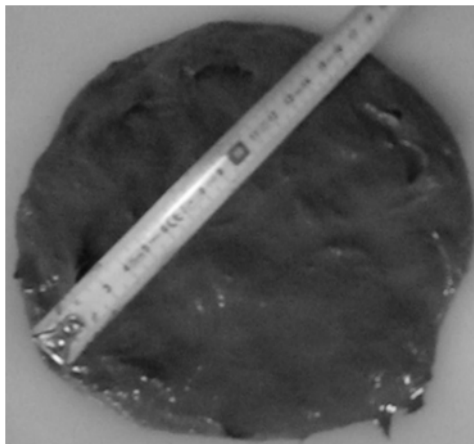
C2W25 (VMA/B: 0.13%)          C4W30 (VMA/B: 0.20%)



C2W35 (VMA/B: 0.23%)

Figure 4.10: Flow spread of composites with optimized VMA content at different W/B (see also Table 4.7)

As it is discussed in section 4.3.6.4, according to the results of tensile characterization, C4W30 (see Table 4.7) exhibits adequate mechanical properties and it is selected as the composite to be used in HCP fabrication. In order to verify the large-scale flow deformability of the developed PVA-SHCC and to compare with the requirements of a self-consolidating concrete, another mixture of C4W30 was prepared. Part of this mixture was used to measure composite deformability by executing a conventional slump cone test, with the dimensions showed in Figure 4.4c. The slump cone was placed on a smooth levelled plate and after being fully filled with the fresh composite, was slowly lifted up to have mixture flowing and

spreading under its self-weight. Once the spreading of composite was stopped, its two orthogonal diameters, one of them was the largest spread diameter, were measured.

A photo of the large-scale flow spread of the developed SHCC is depicted in Figure 4.11. The average of the measured diameters for this spread was 670 mm. Considering that the slump flow diameter of the processed SHCC is in the range of 600 mm to 720 mm, proposed by Okamura et al. [25] to categorize a concrete as self-consolidating, the developed SHCC satisfies the deformability requirements of a self-consolidating composite.

As mentioned before, the remaining part of this fresh PVA-SHCC was used to prepare specimens for characterizing the composite compressive strength and modulus of elasticity. Five cylindrical specimens, 72 mm in diameter and 150 mm in height were cast, without any external vibration, and then cured with the same procedure and condition adopted for the curing of tensile specimens.
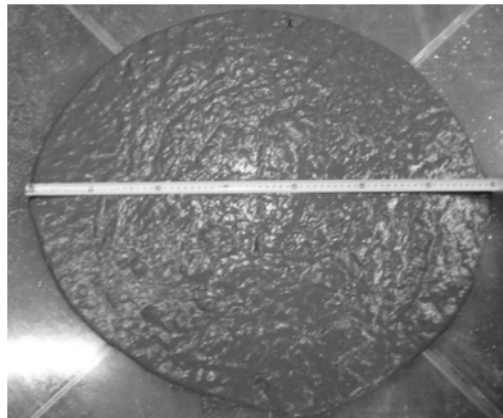


Figure 4.11: Conventional slump flow spread of the developed PVA-SHCC with average spread diameter of 670 mm (C4W30 with VMA/B of 0.2%, see also Table 4.7)

### 4.3.6 Characterizing Composites Tensile Properties

A direct tensile test is the only appropriate testing method, known till now, in order to capture properties of fiber reinforced composites with the tensile strain hardening potential [26].

The results of direct tensile tests executed on the un-notched specimens provide information regarding the SHCC first cracking strength, post cracking ultimate tensile

strength, ultimate tensile strain capacity, and if necessary cracks sizes and distribution along the length of the specimen corresponding to different strain stages.

However, the results of tensile tests on the un-notched specimens may not characterize accurately the post-peak response of an SHCC. In fact, when one of the cracked sections reaches its maximum fibers-bridging strength, it is the opening of this localized crack which has the major contribution in the further elongation of the specimen. Due to load decay, this branch of force-elongation of SHCC is recognized as the softening regime of the tensile response. However, in the case of un-notched specimens, not only the boundary conditions of this crack is affected by the neighboring cracks, also the elongation measured by the Linear Voltage Differential Transformer (LVDT) gauges includes other sources of the specimen's deformation (such as elastic deformation of the intact composite in between the adjacent cracks) which reduces the accuracy of the evaluated material post-peak response.

Therefore, comprehensive characterization of the SHCC tensile response also requires the evaluation of a single crack opening behavior, which can be obtained by executing direct tensile test on notched specimens [27]. In such specimens, once the crack is fully developed along at the weakened section, the tensile response of a notched-specimen can be interpreted in terms of fibers-bridging stress ($\sigma_B$) *versus* crack opening displacement (COD). Such information also reveals the potential of multiple cracking of the developed composite, since both composite cracking strength and fibers-bridging strength are approximately obtained and compared to each other. Due to the stress concentration at the edges of the notched section, however, the crack initiation expected to occur at a lower average tensile stress.

If ultimate crack bridging strength is sufficiently larger than the stress at the crack initiation, it can be concluded that both matrix and fiber-matrix *ITZ* properties are well-tailored, and a strain hardening PVA reinforced cementitious composite is potentially achieved. Therefore, only rheological properties of composite in fresh-state remains responsible for SHCC tensile strain ductility (the capacity of multiple cracking), since it controls the size of flaws, and the distribution of flaws and fibers in the specimen.

Dumbbell-shaped specimens, also known as doge-bone specimens, are the most common shape of the specimens used in characterizing SHCCs tensile behavior [28-30]. The geometrical specifications of these specimens may vary depending on the size of the largest

ingredient of the composite mixture and the adopted test setup. The configuration of these types of specimens is designed to promote the multiple cracking in the region with the lowest width, where the specimen elongation is also measured. Moreover, this configuration avoids premature failure of the specimen at the vicinity of the gripped-ends, where a high stress concentration is expected. Hence, a dumbbell-shaped specimen assures a safe stress transition from the specimen's gripped-ends, the region with the wider sections, to the part of the specimen that multiple cracking is expected to occur (the portion of the specimen with the lowest width).

Characterizing the tensile behavior of SHCCs using dumbbell-shaped specimens is particularly of interest since a minimum effort for specimens' preparation before their testing is needed. Nevertheless, it is reasonable to assume that the fibers orientation and distribution in such a configuration may not represent those expected in the casting of the plates with larger dimensions, e.g. the SHCC plates being used in fabrication of HCP. Consequently, the evaluation of material tensile response can be affected by the shape of the specimen and the casting process.

To minimize this effect, in this research work, tensile specimens are extracted from a larger plate that the influence of composite flow on fibers dispersion and orientation is much closer to that of the SHCC plates to be used in development of HCP. Details on geometry of the casted plates, casting process and the extracted tensile specimens are presented in the following section.

### *4.3.6.1 Preparation of Tensile Specimens*

Three plates of 490 mm × 500 mm × 20 mm were cast inside the acrylic molds, using around five liters of the optimized composites prepared with each given W/B contents. For the casting purpose, a conventional slump cone placed in the center of the mold was filled with the composite and slowly lifted up, see Figure 4.12. This strategy was adopted to maintain the similarity in composite pouring for the casting of all three composite mixtures. All composites flowed homogenously under their self-weight and, except for C2W25, were filled the mold up to its corners without the need of any external vibration. In the case of CW25, however, imposing external vibration to the lateral faces of the mold was inevitable for its further flow up to filling the corners of the mold.

Just after these plates have been cast, they were sealed with a plastic sheet and kept in a room temperature for 24 hours before de-molding, in order to prevent loss of moisture in the early age. After de-molding, all the specimens were cured in a constant temperature and humidity of 20°C and 57%, respectively. It should be noted that, to cut the tensile specimens from the plates, all of them were taken out at the age of 14 days for few hours and, after cutting, they were cured again in their previous controlled conditions.

Each of the three plates was cut, by using a diamond saw machine, according to the arrangement represented in Figure 4.13a. From each plate, 10 specimens of two different sizes were extracted. All specimens have a width of 70 mm, but the specimens 1 to 6, and 7 to 10 had a length of 350 mm and 244 mm, respectively.



(a) (b)
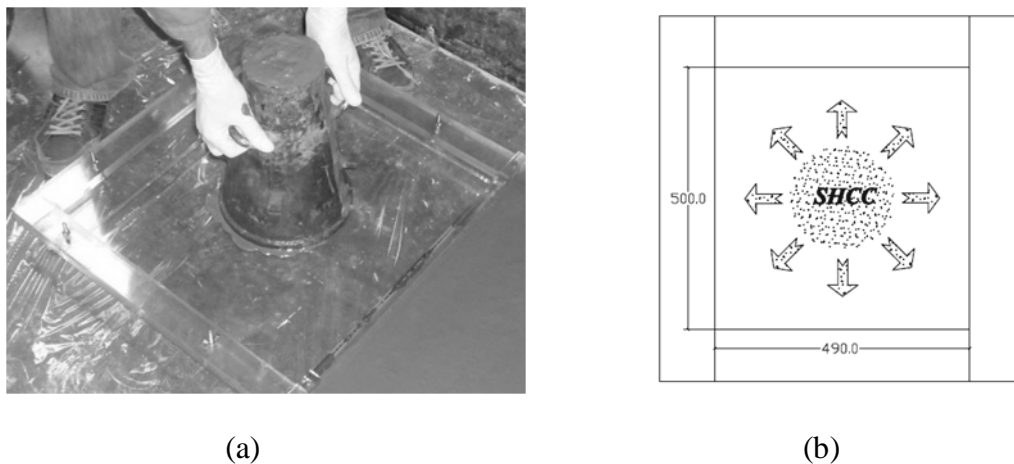
Figure 4.12: Casting composite plates: (a) using slump cone for casting (b) the self-compacting composite was spread diagonally maintaining high homogeneity for the casted plates (dimensions in mm and the depth of the mold is 20 mm).

To study the single crack opening behavior a notch was executed in each lateral faces at half of the length of specimens 7 to 10. The geometry of this notch is depicted in Figure 4.13b. The specimens 1 to 6, without executing any notch, were considered for characterization of multiple cracking under direct tensile loading. These un-notched specimens were only prepared and tested if their multiple cracking potential was approved

following the results of single crack opening tests executed on their corresponding notched specimens.

The preparation of un-notched specimens includes grinding their irregular surface to achieve an almost uniform thickness in the range of 18 ± 0.02 mm along the specimens' length. Metallic plates (end tabs) of 100 mm × 70 mm × 1.25 mm were then glued to the both ends of the specimens to ease their clamping and minimize the risk of specimen sliding inside the jaws of the wedge grips, while the stress concentrations inside and at the vicinity of gripped-ends are also avoided.



(a)                                                    (b)
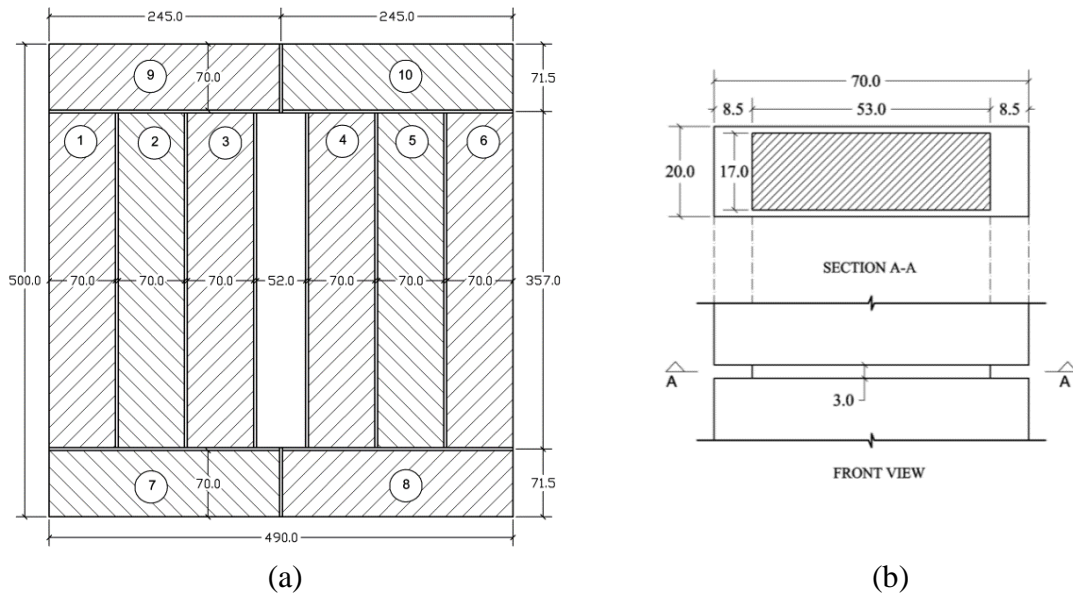
Figure 4.13: Details of tensile specimens: (a) cutting pattern of the tensile rectangular specimens from the plates, and (b) notch geometry (dimensions in mm).

As shown in Figure 4.14, two rectified steel plates were mounted on an existing press machine and then the end tabs were aligned and secured at appropriate positions on top face of the bottom plate using stainless steel bars. Enough quantity of an adhesive with a moderate viscosity was poured at the central region of the end tabs and finally the SHCC specimens were placed on these tabs and fixed at their positions. The pressure of the press machine caused a uniform thickness of the adhesive at the interface between metallic plates and

SHCC. The same process was repeated to glue the end tabs to the opposite face of the specimens.



(a)                                                                (b)
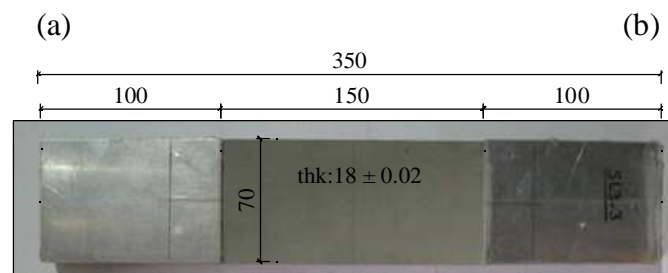


(c)

Figure 4.14: Preparation of un-notched tensile specimens, (a) metallic plates (end tabs) aligned and fixed at appropriate positions on the press machine's bottom-plate and then adhesive poured at their central region, (b) tensile specimens placed over the end tabs, and (c) a sample of un-notched SHCC specimen prepared for the tensile test and its geometrical configuration (dimensions in mm).

### 4.3.6.2 Adopted Strategy for Tensile Characterization of Composites

As mentioned before, single crack opening response of a fiber-reinforced cementitious composite provides straight forward information regarding the tensile strain hardening potential of a composite.

Despite the un-notched specimens, whose gripping ends should be treated (e.g., bonding the end tabs) before testing, there is no need to such time-consuming preparation in the case of notched specimens as the highest stress is localized at the notched section.

This preparation feasibility suggests that testing notched specimens prior to the un-notched ones is an appropriate alternative to avoid time-consuming preparation of those un-notched specimens without tensile strain hardening potential. Thus, un-notched specimens were only prepared and tested if their strain hardening potential was approved based on the results of tensile test executed on their corresponding notched specimens

### 4.3.6.3 Tensile Test Setup

The tests were performed in a servo-controlled machine equipped with a load-cell of 200 kN. As shown in Figure 4.15, two manual wedge grips secured the ends portions of the specimens providing conditions of fixed-ends rotation.

The crack opening displacements (COD) and specimens elongation, in the case of the notched and untouched specimens, respectively, were measured using four LVDTs mounted in a device that was conceived and built in order to measure possible in-plane and out-of-plane rotations of the specimens (Figure 4.15).

The initial gauge length, measuring the elongation of the untouched specimens, was 150 mm. Another external LVDT was used to control the test by imposing a displacement rate of 5 μm/s to the upper grip. Such a low displacement rate is selected to avoid possible effects of undesirable high strain rate on the tensile response of the specimens [31-33].

While in the case of un-notched specimens the test was terminated just after entering the load decay branch, in the case of notched specimens the tensile loading was continued up to a COD of 2.5 mm.

(a)           (b)
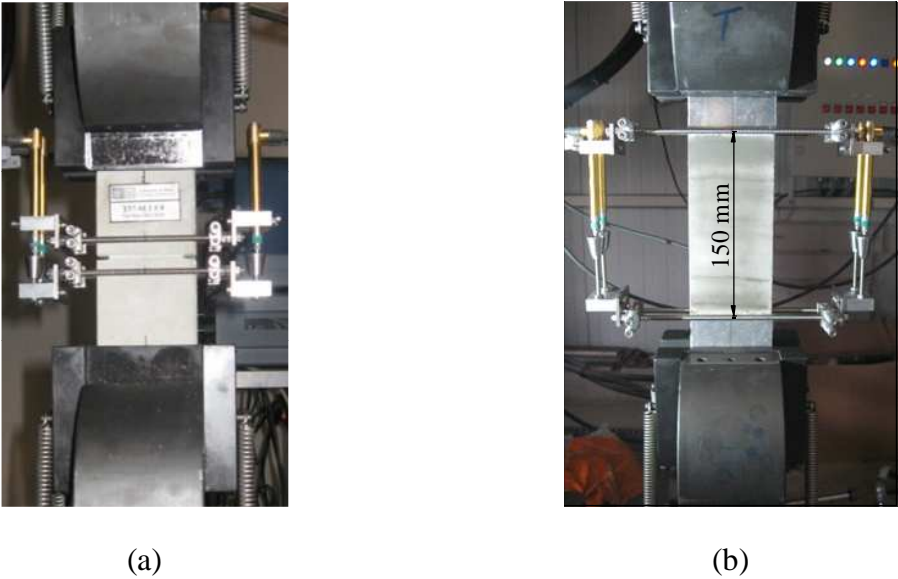
Figure 4.15: Test setup adopted for the tensile characterization of composite specimens, (a) notched specimen, and (b) un-notched specimen; (note: the external LVDT used to control the test is not shown in these figures; and the LVDTs in the case of un-notched specimens are measuring the elongation of specimens within an initial gauge length of 150 mm).

### 4.3.6.4 Tensile Test Results

*Notched Specimens:* As it was intended, and as an example showed in Figure 4.16, the fracture surface in all notched specimens, made of different composite mixtures, was localized at their reduced section, resulting in a single crack opening.





(a)           (b)
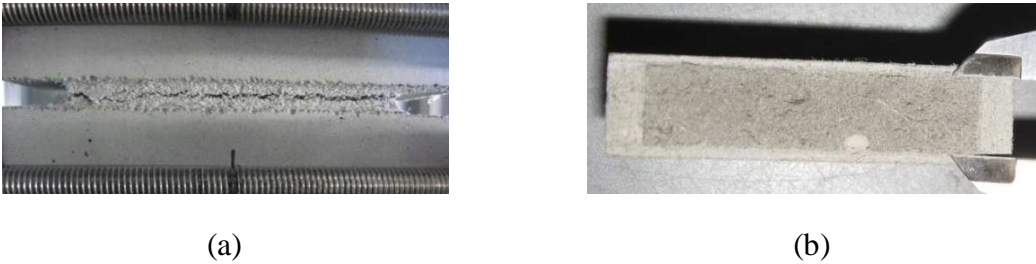
Figure 4.16: Fracture surface localized inside the notched portion of the specimens used to characterize single crack opening response of the composites (a) front view, and (b) sectional view of the fractured surface

The results of tensile tests performed on these specimens are presented in Figure 4.17, in terms of average fibers-bridging stress *versus* COD along with the upper and lower envelopes. Stress at each COD is calculated by dividing the tensile load to the sectional-area measured at the notched portion.



(a)

(b)



(c)
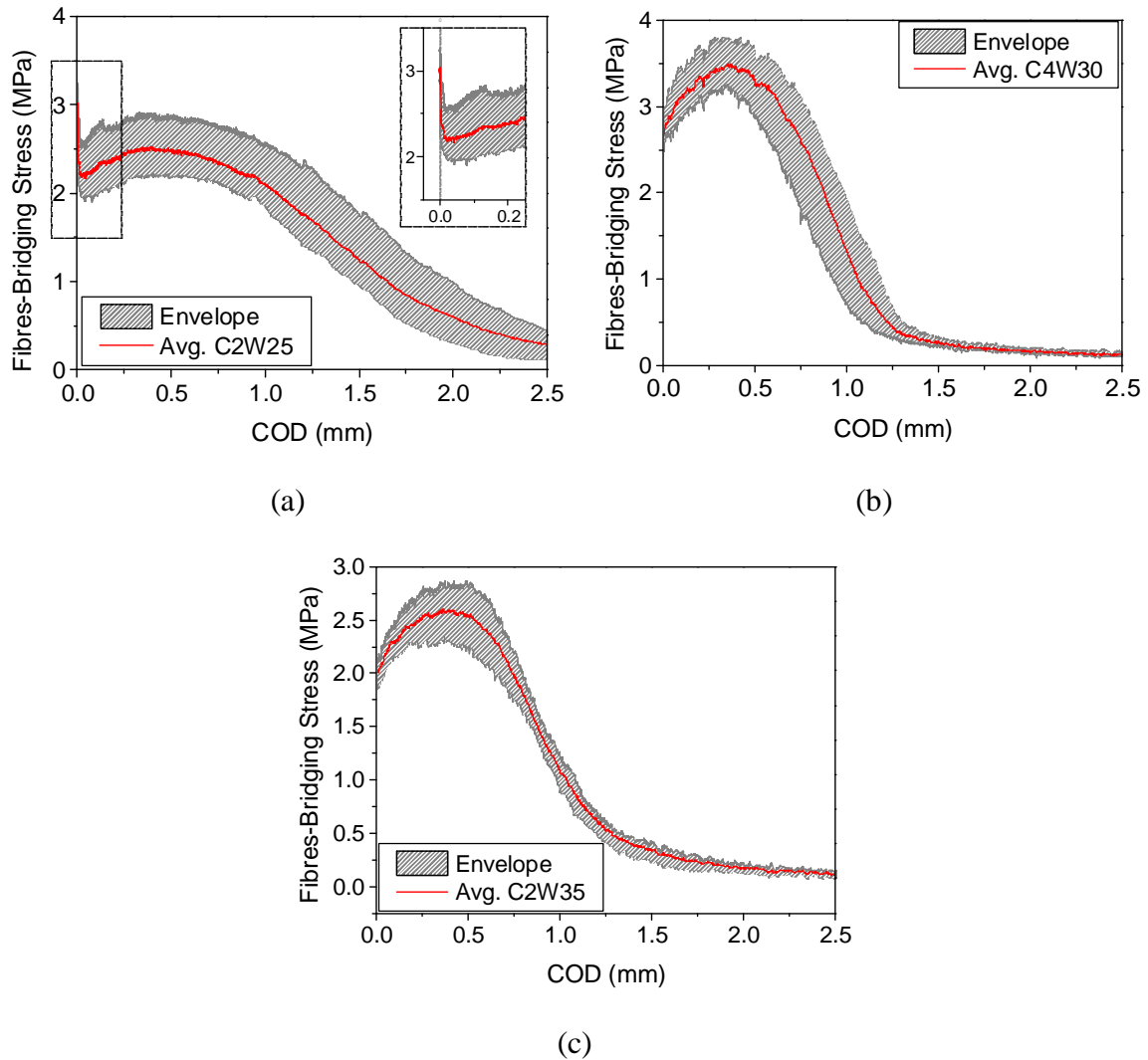
Figure 4.17: The envelopes and the average curves of single crack opening responses of notched specimens with W/B of (a) 0.25, (b) 0.3, and (c) 0.35

The average values corresponding to the stress at crack initiation $(f_{cm}^{cr})$, post cracking strength $(f_{cm}^{pc})$, and its crack opening displacement $(COD_{cm}^{pc})$ of each tested composite are indicated in Table 4.8. Moreover, as an indicator for the tensile strain hardening capacity,

the ratio of post cracking strength to the stress at crack initiation $\left(f_{cm}^{pc}/f_{cm}^{cr}\right)$ for each series of the specimens are calculated and reported in the last column of this table.

Table 4.8: The average results of tensile tests on notched specimens extracted from the plates made of different composites

| Label | W/B | $f_{cm}^{cr}$ | $f_{cm}^{pc}$ | $COD_{cm}^{pc}$ | $f_{cm}^{pc}/f_{cm}^{cr}$ |
|-------|-----|---------------|---------------|------------------|---------------------------|
|       | (%) | (MPa) | (MPa) | (mm) | - |
| C2W25 | 25 | 3.03 | 2.53 | 0.391 | 0.83 |
| C4W30 | 30 | 2.64 | 3.55 | 0.376 | 1.34 |
| C2W35 | 35 | 2.06 | 2.60 | 0.364 | 1.26 |

As it can be concluded from Figure 4.17 and also the tensile strain hardening indicators $\left(f_{cm}^{pc}/f_{cm}^{cr}\right)$, reported in Table 4.8, with the exception of the composite containing W/B of 25%, the other two mixtures exhibited a post-cracking tensile hardening behavior. In the case of C2W25, a large increase in $f_{cm}^{cr}$, as the consequence of too low water content, can be mentioned as a possible cause of its post-cracking tensile softening response. Moreover, this low water content has possibly increased the matrix crack tip toughness $\left(J_{tip}\right)$ and decreased the fibers-bridging complementary energy $\left(J_b\right)$ to such an extent that $J_b/J_{tip}$ falls below the unity, hence the strain hardening potential of this composite mixture is lost.

Comparison of single crack opening responses of C4W30 and C2W35 with W/B of 30% and 35%, respectively, reveals that C4W30 not only has a larger $f_{cm}^{pc}/f_{cm}^{cr}$, but also possess a higher $f_{cm}^{cr}$ and $f_{cm}^{pc}$. In the case of C2W35, as compared to C4W30, lower fibers-bridging strength is most likely associated with a reduced densification at *ITZ*, due to increased W/B, which lowered the fibers pull-out frictional bond.

***Un-notched Specimens:*** from analyzing the results of single crack opening behavior of each of three developed composite mixtures, C4W30 was identified as a composite with post-cracking tensile hardening with the highest multiple cracking potential. Therefore, to evaluate its tensile strain capacity, three un-notched specimens extracted from the plate cast with the same mixture were prepared for tensile testing following the instruction described

in section 4.3.6.1. Only specimens numbered 1 to 3, according to numerations presented in Figure 4.13, were prepared for the tensile characterization.

The results of tensile tests, in terms of stress *versus* strain for all three specimens, extracted from the plate cast with C4W30, are depicted in Figure 4.18. The strain, which is the average value, is calculated by dividing the mean elongation measured by the four LVDTs to the initial gauge length, 150 mm. All three specimens exhibited a tensile strain hardening behavior, with a clear diffused multiple cracking beyond the initiation of their first crack, as depicted in Figure 4.19.
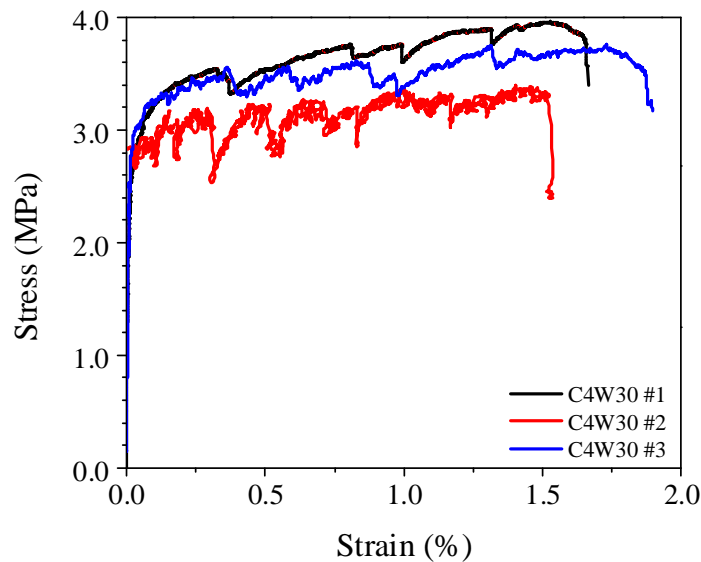


Figure 4.18: Tensile response of the un-notched specimens extracted from the plate cast with composite mixture C4W30

Tensile properties of the developed PVA-SHCC including the first cracking strength ($f_{sh}^{cr}$)the ultimate tensile strength ($f_{sh}^{u}$), and the tensile strain capacity ($\varepsilon_{sh}^{u}$) are calculated based on the average values obtained of testing three specimens and reported in Table 4.9. The coefficient of variation (CoV) of each quantity is also indicated in the same table. A relatively high CoV for both $\varepsilon_{sh}^{u}$ and $f_{sh}^{u}$ is generally expected mainly due to the randomness in distribution of flaws and fibers, and fibers' orientation in the SHCCs. Analyzing the data in Table 4.9 confirms that the developed PVA-SHCC marginally assures properties required for the development of HCP (see section 4.2).

|     |     |     |
|:---:|:---:|:---:|
| #1  | #2  | #3  |

Figure 4.19: Diffused multiple cracking in the gauge length of the un-notched specimens prepared with composite mixture C4W30 and subjected to the tensile loading

Table 4.9: Tensile properties of the developed PVA-SHCC (average of three specimens)

|      | $f_{sh}^{cr}$ | $f_{sh}^{u}$ | $\varepsilon_{sh}^{u}$ |
|------|:-------------:|:------------:|:----------------------:|
|      | (MPa)         | (MPa)        | (mm)                   |
|      | 2.75          | 3.71         | 1.54                   |
| CoV. | (2.6%)        | (7.8%)       | (10.5%)                |

### *4.3.7 Compressive Strength and Modulus of Elasticity*

Modulus of elasticity and the compressive strength of developed PVA-SHCC were determined following the specifications of LNEC E397-1993 [34] and EN 12390-3 2009 [35], respectively. The cylindrical specimens, cast with mixture C4W30 as reported in section 4.3.5, were used for this purpose. Before testing the top surface of these specimens were grounded to achieve a flat surface. According to the results of these tests, the average values of SHCC's compressive strength and modulus of elasticity were 35.2 MPa (CoV: 4.7%) and 18420 MPa (CoV: 3.2%), respectively.

## 4.4 Effects of Curing Conditions on Crack Bridging Response

It is speculated that different curing conditions could affect both fiber-matrix interface properties and matrix toughness. To contribute for the knowledge in this topic, an experimental research program was conducted to study PVA-SHCCs tensile behavior when this composite is cured under different conditions. The results derived from the fibers-bridging stress *versus* crack opening, along with microscopic photos, are used to investigate this effect.

### 4.4.1 Specimen Configuration and Preparation

Using the composite mixture C4W30, three plates, designated SL2 to SL4, were cast similar to what explained in section 4.3.6.1. Following the procedure adopted for curing the plates used for the tensile characterization of composite mixtures, after casting, SL2 to SL4 plates were also sealed with a plastic sheet and kept in a room temperature for 24 hours before de-molding. Hereafter, for the ease of discussion, the composite plate made with the aim of tensile characterization of mixture C4W30, as explained in section 4.3.6.1, is designated SL1.

Although after de-molding similar to SL1 all the specimens were cured in a constant temperature of 20° C, different humidity conditions were adopted for their rest of curing process. While SL1 is cured in a climate room with a constant relative humidity of 57% up to the age of 28 days, to verify the effect of humidity change at early age, the SL2 was cured only up to an age of 8 days at a constant humidity of 57% and then moved to another climate room of 85% humidity and cured for 28 days. To verify the effect of water curing SL3 was cured in water up to 28 days. Finally, SL4 was cured in constant relative humidity of 85% for 28 days to verify the effect of curing in higher humidity condition than that adopted for SL1. Curing conditions of these plates together with SL1 are summarized in Table 4.10.

Similarly to SL1, four tensile specimens, characterized with number 7 to 10 in Figure 4.13a, were cut from SL2 to SL4. To study the effects of different curing conditions on single crack opening response of these specimens, a notch similar to that executed in SL1 series was performed in the mid-length of each tensile specimen (see Figure 4.13b for the geometrical details of the notched section).

Table 4.10: Curing details for the PVA-SHCC plates

| Plates | First 24 hours | Up to the Age of 8 days | Up to the age of 28 days |
|--------|----------------|-------------------------|--------------------------|
| SL1* | Sealed in room temp. | 20° C, 57% humidity | 20° C, 57% humidity |
| SL2 | Sealed in room temp. | 20° C, 57% humidity | 20° C, 85% humidity |
| SL3 | Sealed in room temp. | Immersed in water at 20° C | Immersed in water at 20° C |
| SL4 | Sealed in room temp. | 20° C, 85% humidity | 20° C, 85% humidity |

* The plate used for single crack opening characterization in section 4.3.6.1.

### 4.4.2 Results of PVA-SHCC Curing Tests

Tests results are discussed in terms of the influence of the curing conditions on:

- average values for $f_{cm}^{cr}$, $f_{cm}^{pc}$ and $COD_{cm}^{pc}$,

- average absorbed energy up to $COD = 2.5$ mm $\left(G_f^{2.5}\right)$,

- average absorbed energy up to $COD_{cm}^{pc}$ $\left(G_f^p\right)$,

- average absorbed energy in the post peak regime up to $COD = 2.5$ mm $\left(G_f^{pp}\right)$, and

- the fibers-bridging stiffness (the slope of the phase between crack initiation and $COD_{cm}^{pc}$);

As illustrated in Figure 4.20, absorbed energies are calculated by integrating the area under the curves of fibers-bridging stress *versus* crack opening displacement ($COD$) up to pre-specified $COD$s.

The average and envelope of the fibers-bridging stress *versus* crack opening responses of the four specimens, except SL4, are presented in Figure 4.21. The results related to SL4 include only three specimens.

For the comparison purpose, the results derived from fibers-bridging stress *versus* crack opening responses are indicated in Table 4.11 and represented graphically in Figure 4.22. Moreover, the average response of fibers-bridging stress *versus COD* and also the evolution of the energy absorption during crack opening for different specimens are depicted in Figures 4.23a and 4.23b, respectively.
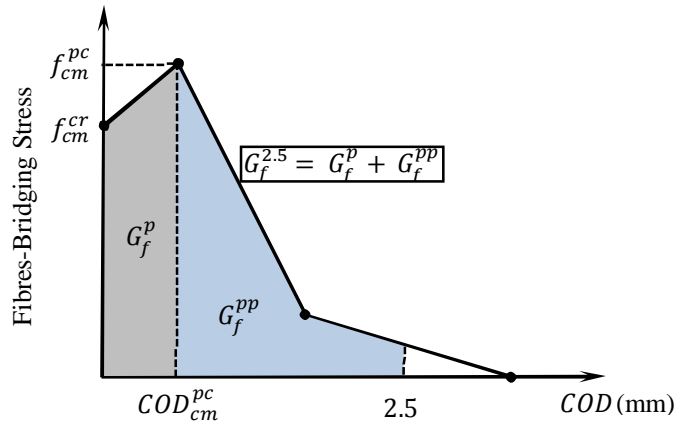
Figure 4.20: Idealized fibers-bridging stress *versus* crack opening response, and meaning of the determined parameters
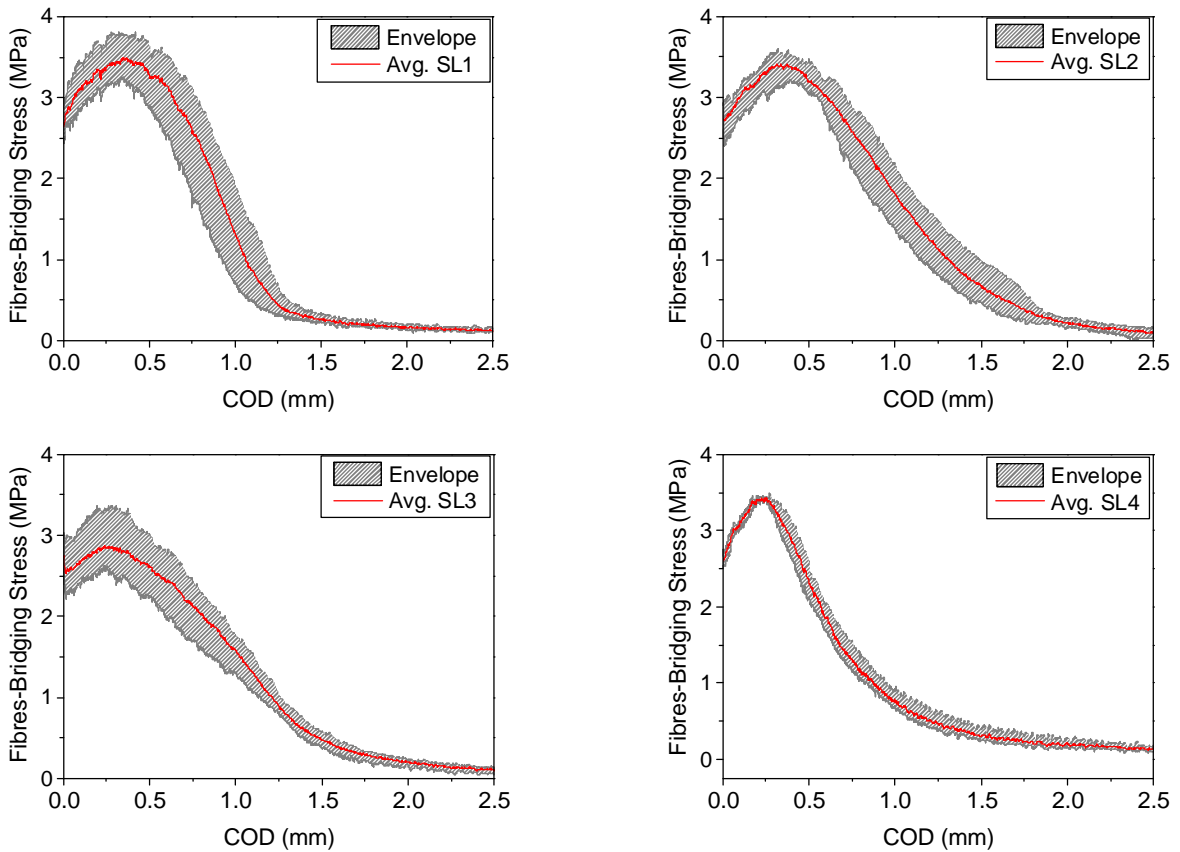


Figure 4.21: The average and the envelope results of fibers-bridging stress *versus* crack opening displacement (COD) for specimens SL1 to SL4
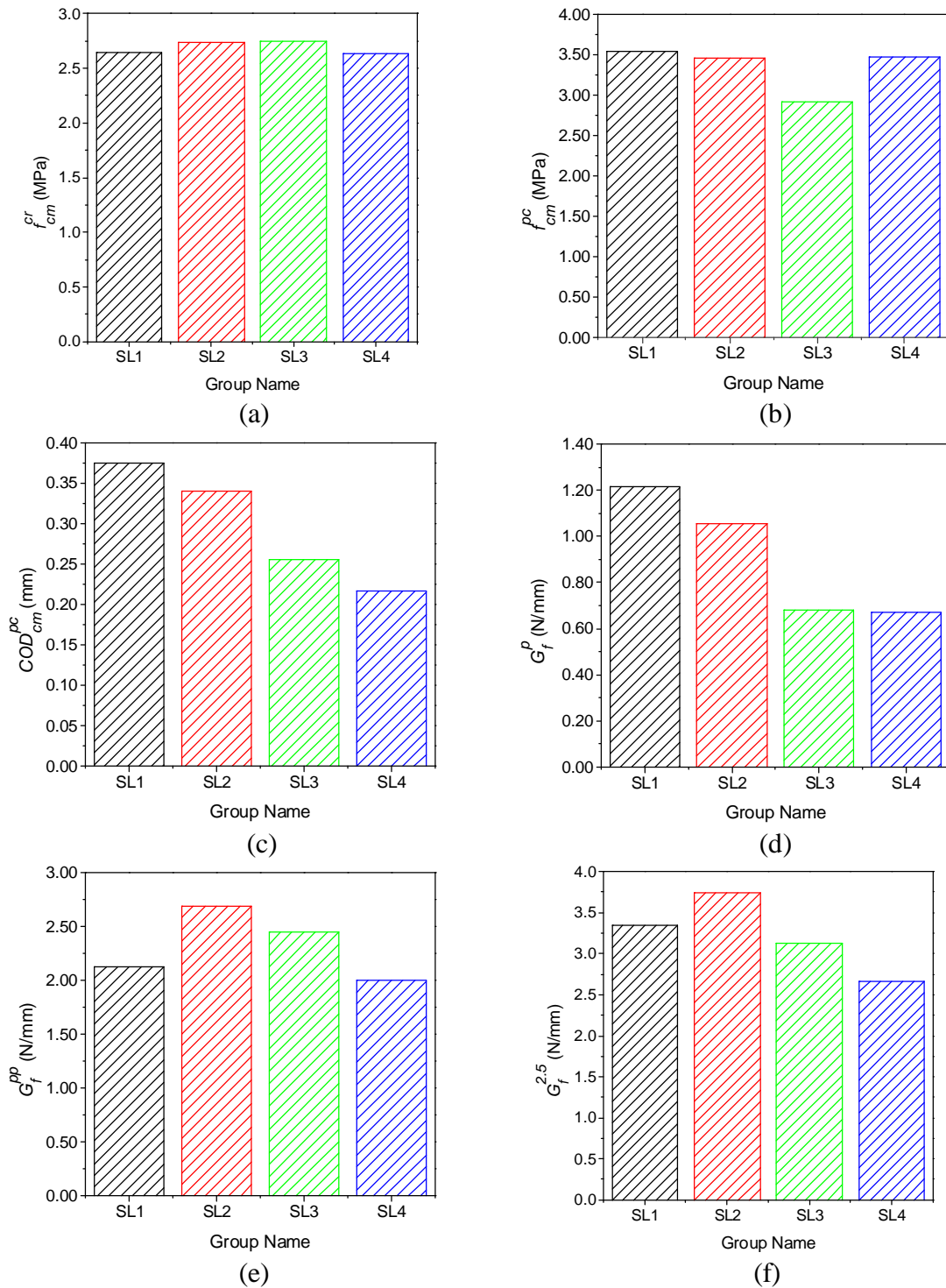
Figure 4.22: Graphical comparison of the results derived from fibers-bridging stress *versus* crack opening displacement: (a) $f_{cm}^{cr}$, (b) $f_{cm}^{pc}$, (c) $COD_{cm}^{pc}$, (d) $G_f^p$, (e) $G_f^{pp}$, (e) $G_f^{2.5}$

Table 4.11: Data obtained from average of fibers-bridging stress *versus* COD for specimens SL1 to SL4.

| Specimen | $f_{cm}^{cr}$ | $COD_{cm}^{pc}$ | $f_{cm}^{pc}$ | $G_f^{2.5}$ | $G_f^{p}$ | $G_f^{pp}$ |
|----------|---------------|-----------------|---------------|-------------|-----------|------------|
| - | (MPa) | (mm) | (MPa) | (N/mm) | (N/mm) | (N/mm) |
| SL1 | 2.64 | 0.376 | 3.55 | 3.343 | 1.213 | 2.130 |
| SL2 | 2.73 | 0.341 | 3.46 | 3.741 | 1.053 | 2.688 |
| SL3 | 2.74 | 0.247 | 2.92 | 3.127 | 0.682 | 2.445 |
| SL4 | 2.63 | 0.250 | 3.47 | 2.666 | 0.670 | 1.996 |

According to the data in Table 4.11 and Figure 4.22, the stress at cracking initiation, $f_{cm}^{cr}$, for all the specimens has almost the same values, ranging from 2.63 MPa to 2.74 MPa corresponding to SL4 and SL3, respectively. The maximum bridging stress, $f_{cm}^{pc}$, for SL1, SL2 and SL4 is almost close to 3.5 MPa, while a reduction about 20% was registered in the SL3 that was cured in water. However, the crack opening at $f_{cm}^{pc}$ ($COD_{cm}^{pc}$) increases in the following sequence: SL4, SL3, SL2 and SL1.

As shown in Figure 4.23a, the smaller $COD_{cm}^{pc}$ along with high $f_{cm}^{pc}$, presented by SL4, provided the highest bridging stiffness in the hardening branch when compared to the other specimens. Despite relatively small $COD_{cm}^{pc}$, the SL3 has presented the lowest bridging stiffness due to its smaller $f_{cm}^{pc}$. Figure 4.23a indicates that SL1 and SL2 have also a bridging stiffness similar to that of SL4. Furthermore, according to this figure, the SL4 has presented the highest tensile stress decay during the post-peak softening phase, while the opposite was observed in the SL2.

Photos of the fibers in fracture surface with a zoom magnitude of 400X, Figure 4.24, suggest that, although a significant number of fibers of SL1, SL2 and SL4 have ruptured in a pencil head shape, the majority of the fibers of SL3 seems to have been pulled out. Also the shorter pulled out length for a number of the fibers in the fracture section of SL4, when compared to the other specimens, is in full agreement with its smaller $COD_{cm}^{pc}$ and with the higher bridging stiffness in the hardening regime (see Figure 4.25). This can be justified by the stronger fiber-matrix interface bond. The more abrupt softening branch in the SL4 is

perhaps due to the rupture of the most of the fibers in hardening branch. However, these conclusions have to be further substantiated with additional study.
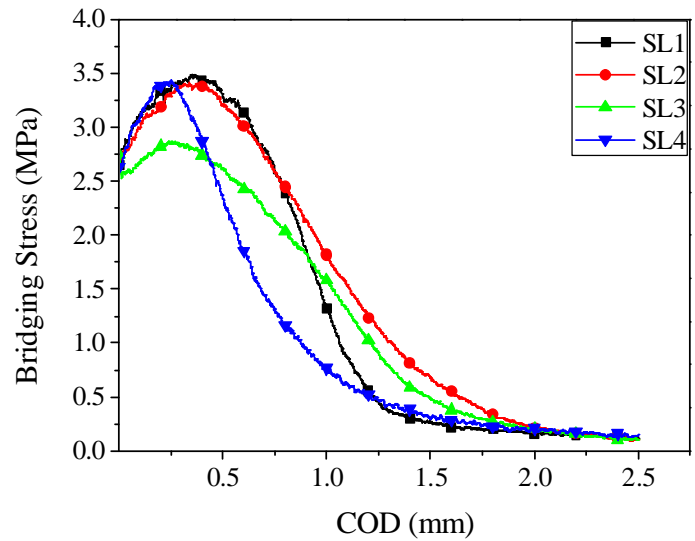


(a)
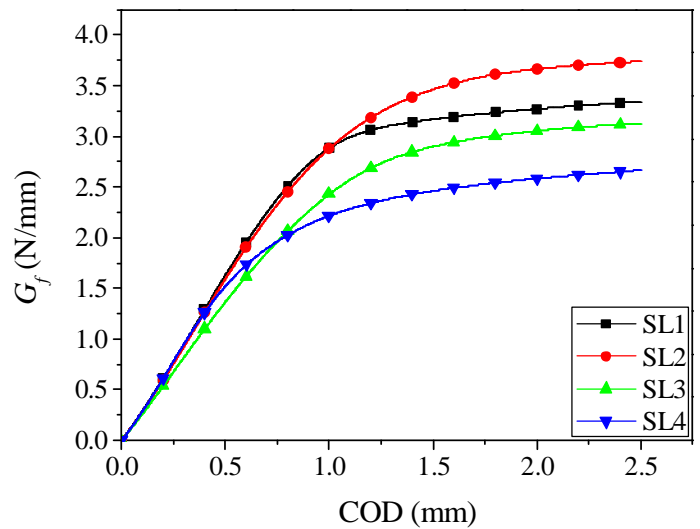


(b)

Figure 4.23: Results of the specimens tested under different curing conditions in terms of crack opening displacement *versus* (a) fibers-bridging stress, and (b) absorbed energy
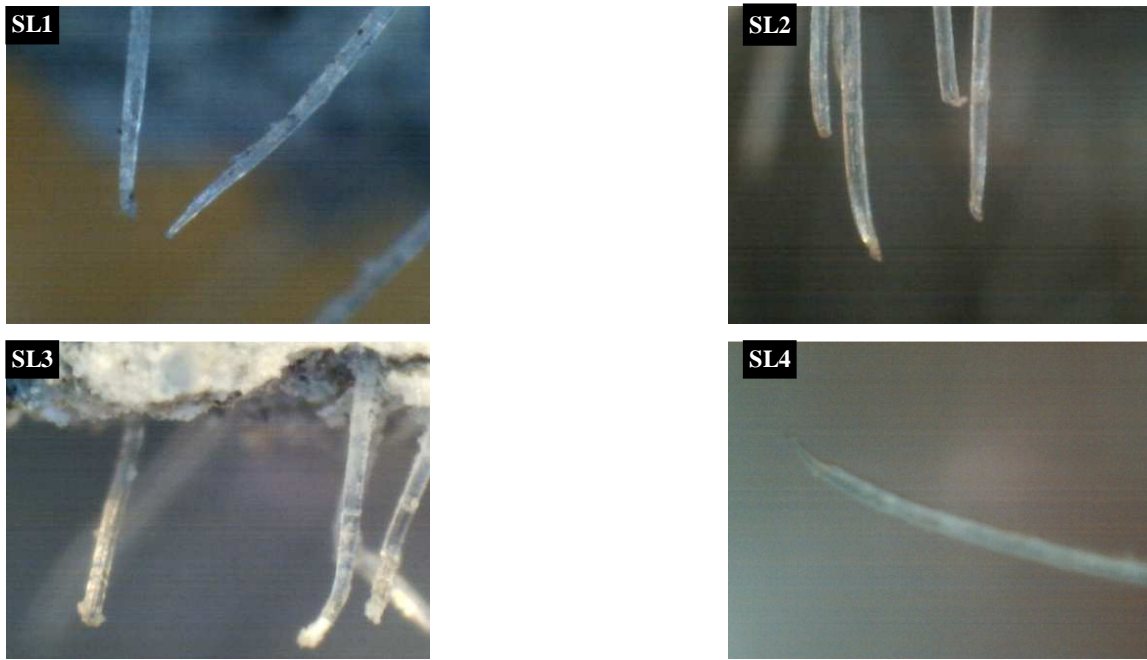
Figure 4.24: Fiber failure modes at the fractured section of the specimens (zoom magnitude: 400X).
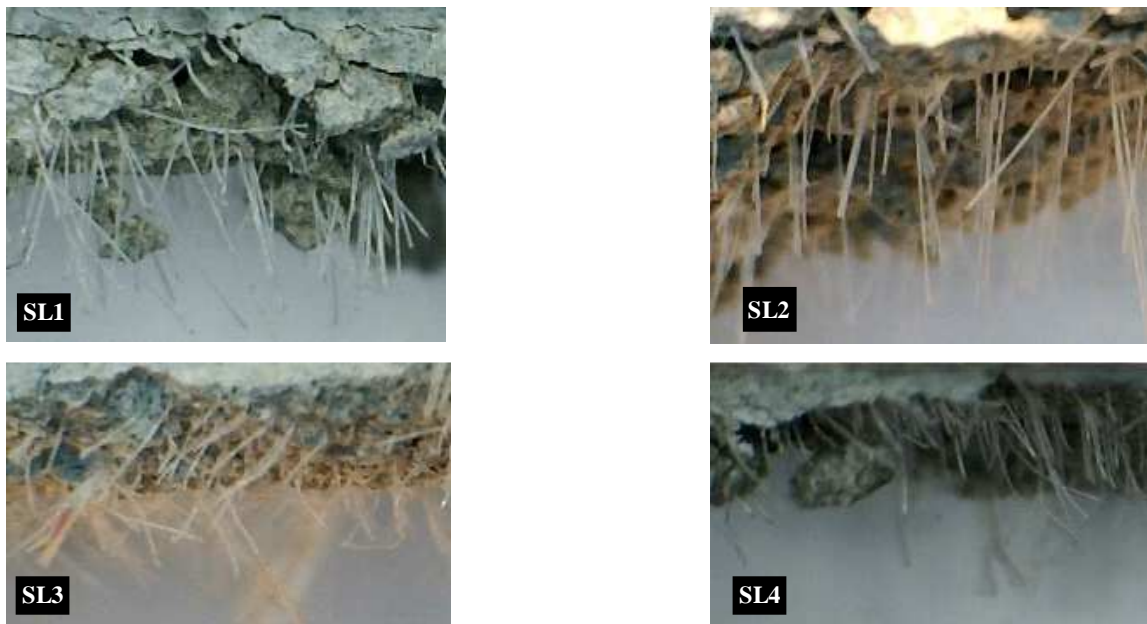


Figure 4.25: Photos of the fibers bridging the fractured surfaces of typical specimens of the tested plates (zoom magnitude: 200X).

In terms of $G_f^{2.5}$, SL2 and SL4 have presented the highest and the lowest value, 3.74 N/mm and 2.67 N/mm, respectively, see Table 4.11 and Figure 4.22. Moreover, it can be seen that SL1 and SL2 have absorbed the highest amount of energy corresponding to $G_f^p$ and $G_f^{pp}$, respectively.

Referring to the Figure 4.23b, SL1, SL2 and SL4 have the same evolution for the energy absorption up to a crack opening around 400 µm (a little above the $COD_{cm}^{pc}$). Although the potential of energy absorption for SL3 is lower than SL4 for tighter cracks, after a COD = 750 µm the SL3 has much higher rate for energy absorption.

### 4.4.3 Discussion on the Effect of Different Curing Conditions

Following the above mentioned results, it can be concluded that the stress at crack initiation apparently is not affected by curing conditions. Up to a crack width of around 300 µm, which is the maximum allowed by design standards for reinforced concrete structures, all the specimens have, in general, presented a tensile strain hardening phase. However, the water cured specimens demonstrate the lowest peak tensile strength, and, therefore, the lowest stiffness in this hardening phase.

The specimens cured at higher humidity show the smallest crack width at the peak tensile strength and the lowest energy absorbed in the fracture process up to a crack width of 2.5 mm. Therefore, the high humidity curing conditions seem to enhance the durability since cracks of smaller width can be obtained during the strain hardening phase. However, the high humidity curing conditions seem to have a detrimental effect in terms of energy absorption capacity that might have been caused by the rupture of a large number of fibers in consequence of the highest stiffness in the strain hardening phase of this composite. Curing in lower humidity at the early ages (8 days) and then under the higher humidity up to 28 days, resulted in higher energy absorption up to a crack opening of 2.5 mm.

It is speculated that the fibers-matrix chemical bond and the use of relatively high volume fraction of fly ash are the main reasons for this high level of sensitivity of PVA-SHCCs tensile response to the curing conditions. Fly ash not only affects the fibers-matrix chemical bond due to its reaction with cement by-products, it changes the densification of *ITZ*. This may also lead to a change in the slip-hardening response of the pulled out fibers.

## 4.5 Assessment of HCP Effectiveness for the Strengthening of Shear-Critical Short-Span RC Beams

According to the specifications of ACI318-14 [36], beams with any of the following conditions are categorized as short (or deep) beams:

(i) with a clear span ($L_s$) not exceeding four times the overall section depth ($h_b$) , ($L_s/h_b \leq 4$),

(ii) with a shear span ($a$) to the overall section depth ($h_b$) less than two, ($a/h_b \leq 2$);

Transfer girders, shear walls in high-rise buildings and offshore structures, and wall footings are examples of deep beams designed to transfer the loads of a column or series of them to the supporting elements. Contrary to slender beams that the assumption of a linear strain distribution along the depth of the beam at each cross section is validated by the hypothesis of "plane section remains plane after bending", in the case of deep beams the strain distribution is rather more nonlinear and complex.

As shown in Figure 4.26, in deep beams, the compressive struts formed between the loading and supporting regions, tension ties (beam bottom longitudinal reinforcement), and nodal zones (the intersections of the struts with each other and with ties), constitute a truss mechanism, also known as strut and tie mechanism, that resist the external load. In such a mechanism, volume dilation of the compressive struts causes orthogonal tensile stresses, which may result in cracking of these struts. According to literature, "shear-compression" and "shear-tension" are the most common failure modes observed in experimental testing executed on deep beams.

"Shear-compression" failure is characterized with a major diagonal crack formed along the compressive strut in the shear spans. Penetration of this diagonal crack into the compressive block of the loaded region causes concrete spalling, thus the failure of the beam (see Figure 4.27a). This mode of failure typically occurs in beams with a very low shear span to depth ratio (typically below 1.5).

"Shear-tension" failure is associated with the loss in the bond/anchorage of longitudinal tension rebars due to horizontal propagation of a secondary crack along these

reinforcements. This secondary crack descends from the closest shear-flexural crack to the supported ends of the beam. Sliding of the tension rebars promotes widening of the major inclined crack with its progress towards the loaded region. Penetration of this crack into the compressive block may result in concrete spalling below the loaded region (see Figure 4.27b).

Crushing of web concrete is another failure mode observed in deep beams with a very low shear span to depth ratio (typically below 1.0). However, for deep beams with sufficient shear capacity, a flexural failure is expected to occur.
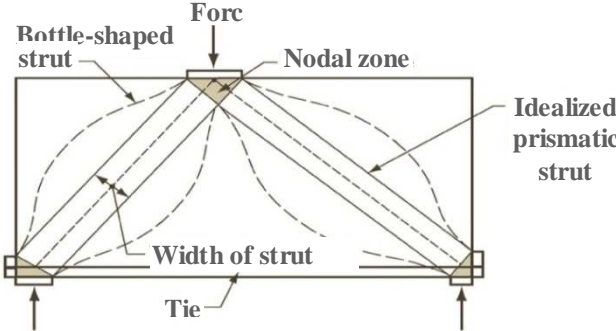


Figure 4.26: Strut and tie mechanism of load transfer in a deep beam (recreated from ACI318-14 [36])
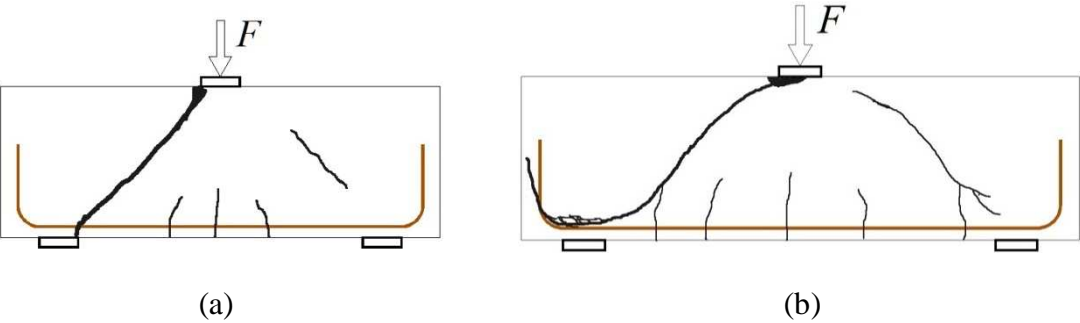


Figure 4.27: The most common failure modes observed in deep beams, (a) shear-compression, and (b) shear-tension

It is then essential to provide the deep beams with web reinforcements, horizontal and transvers bars, to sustain further tensile stresses developed orthogonal to the direction of the cracked strut; to enhance the beam's shear capacity and to improve its ductility. This is the

restraining effect of web reinforcements that delays the advances of crack tips and results in a more ductile failure mode rather than the explosive failure observed in deep beams without web reinforcement.

With the aim of preliminary assessment of the proposed HCPs, effectiveness of retrofitting deeps beams without web reinforcement is studied. Shear deficient deep beams are selected since HCPs attached to their lateral faces are not only expected to delay the initiation of diagonal cracks but also to act as the web reinforcement for sustaining the tensile stresses in orthogonal plane of diagonal cracks. Moreover, lateral confinement provided by the HCPs attached by a combination of chemical anchors and adhesive, mainly since the anchors are post-tensioned, can possibly undermine the adverse effect of triaxial stress state in compressive resistance of the diagonal struts. This confinement is also expected to delay/prevent possible sliding of longitudinal tension steel bars.

Finally, the SHCC, as one of the constituents of HCP, has sufficient compressive strength to contribute in shear transfer mechanism between the supported and loaded point of the short-beam through the diagonal compressive struts.

### 4.5.1 Details of Beams and Retrofitting Elements

Eight similar reinforced concrete (RC) beams with dimensions of 600 mm × 150 mm × 150 mm were fabricated. As depicted in Figure 4.28, the longitudinal steel reinforcements placed at the bottom and top of the beams consisted of $3\Phi10$ mm and $2\Phi6$ mm, respectively. These beams had only two steel stirrups in the alignment of the beam's supports, which were used to maintain the longitudinal steel rebars in their target positions.

One of these beams was considered as un-retrofitted reference specimen, hence tested in its as-built condition (beam "CB"). The remaining beams were retrofitted by attaching either CFRP sheet, SHCC plate, HCP$^{(S)}$ or HCP$^{(L)}$, to each of their lateral faces. The beam strengthened with CFRP sheet (beam "BFU_A") was also considered as a reference specimen, but retrofitted one.

In the case of retrofitting with either SHCC plate, HCP$^{(S)}$ or HCP$^{(L)}$, the influence of attaching system, a combination of adhesive and chemical anchors *versus* adhesive only, on the beams global behavior was investigated. To this end, taking into account the method

used to connect the retrofitting plates to the beams, these retrofitted beams were categorized in two groups:

- group I consisted of those beams with their retrofitting plates attached only by means of adhesive, and

- group II composed of beams with the their retrofitting plates attached by means of a combination of adhesive and chemical anchors;

Details of the retrofitted beams studied in this experimental program, including their designation, strengthening element and the connection adopted to attach it, are presented in Table 4.12 and Figure 4.29.
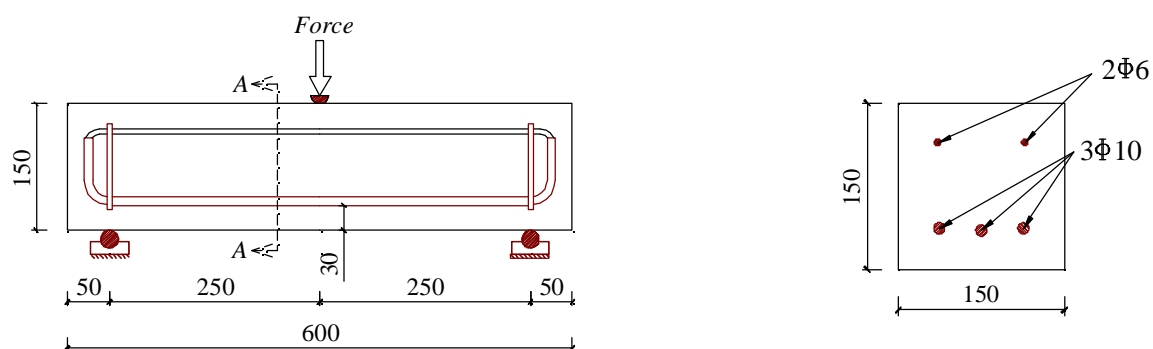


Figure 4.28: Geometry and reinforcement arrangements of concrete beams (dimensions in mm)

Table 4.12: Details of beams and the strengthening techniques

| Beam category | Designation | Strengthening technique | Attaching system |
|---|---|---|---|
| Reference beams | CB | N/A | N/A |
| | BFU_A | 1 layer of U-shape CFRP | Adhesive |
| Group I of the retrofitted beams | BS_A | SHCC plate | Adhesive |
| | BHS_A | HCP(S) | |
| | BHL_A | HCP(L) | |
| Group II of the retrofitted beams | BS_AB | SHCC plate | Adhesive & Chemical anchors |
| | BHS_AB | HCP(S) | |
| | BHL_AB | HCP(L) | |

Section B-B: BFU_A

Section B-B: BS_A & BHS_A & BHL_A

(a)

Section C-C: BS_AB & BHS_AB & BHL_AB

Details of Hilti Chemical Anchor System

(b)
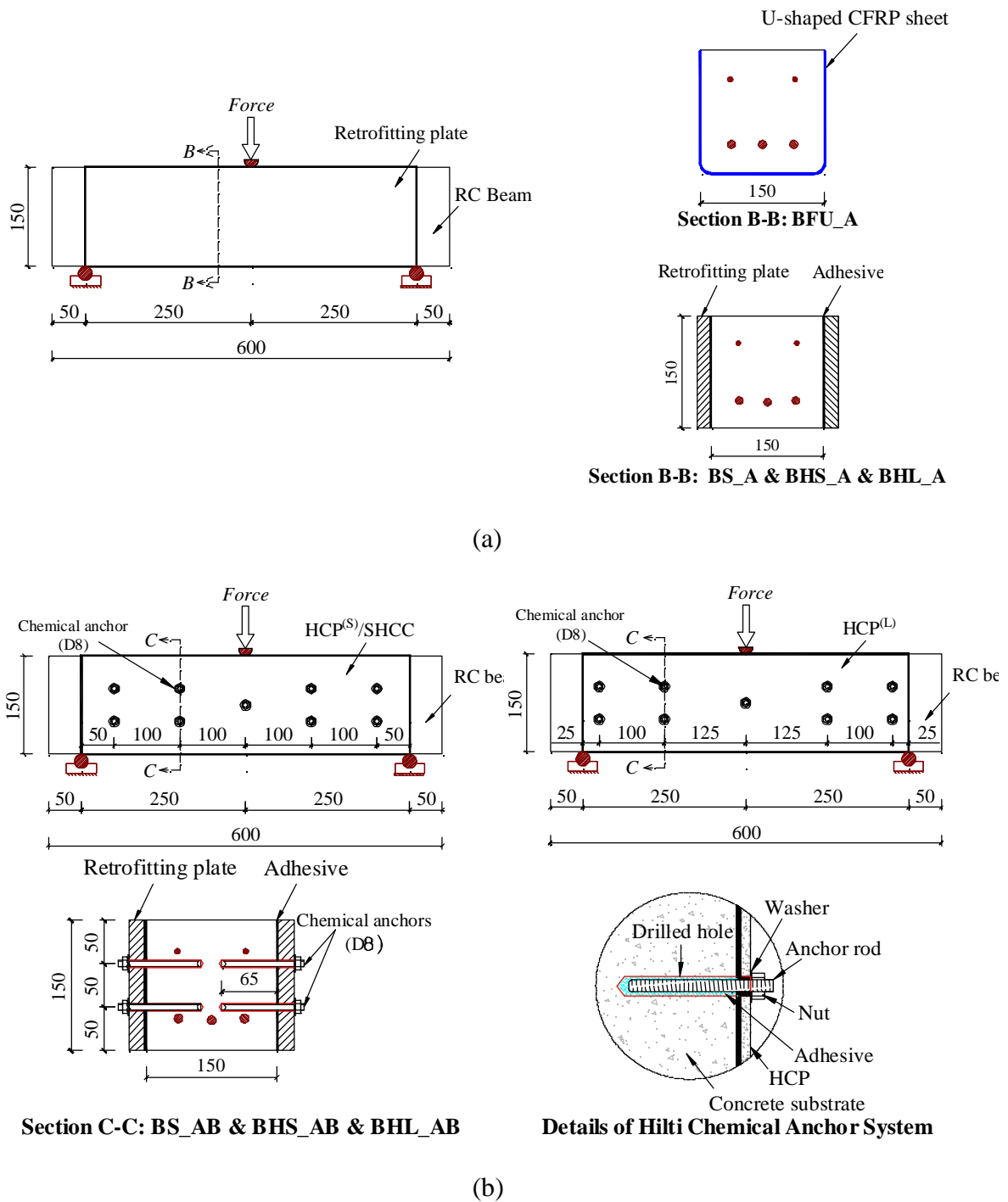
Figure 4.29: Details of the retrofitted beams, (a) the reference beam BFU_A and the beams in group I, and (b) the beams in group II

Details of the strengthening plates used in this study are illustrated in Figure 4.30. The SHCC plates were cut from larger plates cast with the mix composition C4W30 inside the molds with the dimensions showed in Figure 4.12, and adopting the same SHCC mix preparation, casting and curing procedure detailed in section 4.3.6.1.

These cut plates were then grounded to achieve a uniform thickness of about $18 \pm 0.02$ mm. Therefore, taking into account the retrofitting schemes of the beams presented in Figure 4.29, all SHCC plates, utilized either individually (see Figure 4.30a) or as a constituent of HCPs (see Figures 4.3b and 4.3c) had dimensions of 500 mm $\times$ 150 mm $\times$ 18 mm.

As depicted in Figure 4.30b, HCP$^{(S)}$ plates were prepared by bonding a single-ply unidirectional carbon fabric to the grounded face of the SHCC plates. The fabrics were bonded using epoxy adhesive with their main orientation along the width of the SHCC plate. Due to the width limitation of the carbon fabric, two side-by-side layers of 250 mm wide carbon fabrics were bonded to cover the entire length of the SHCC plate. Fabrication process of HCP$^{(S)}$ followed adopting a wet layup [37] bonding process:

i. carbon fabric and grounded face of the SHCC were saturated using a low viscosity adhesive (S&P Resin Epoxy 55),

ii. saturated carbon fabric was placed on the SHCC surface and a roller was passed to force the air bubbles out,

iii. a curing process of seven days in the laboratory environment was adopted, and

iv. finally, the glassy surface of the hardened epoxy resin was slightly roughened aiming to improve its bonding quality to the interface adhesive used to attach HCP$^{(S)}$ to the concrete substrate;

According to the details showed in Figure 4.30c, HCP$^{(L)}$ was composed of eight CFRP laminates bonded into the pre-sawn grooves of the SHCC plate following NSM technique [37] procedure:

i. grooves with a width and depth of 3 mm and 11 mm, respectively, were cut on the grounded face of the SHCC,

ii. compressed air was applied to the SHCC grooves in order to clean them from debris and dust,

iii. grooves were filled by a viscose adhesive (S&P Resin Epoxy 220). Thin layers of the same type of adhesive were also applied to the cleaned surfaces of the CFRP laminates,

iv. CFRP laminates were placed inside the grooves and a spatula was passed and pressed to removed trapped air bubbles and to finish the adhesive surface, and

v. finally, seven days of curing procedure in the laboratory environment was adopted;



(a)

(b)

(c)
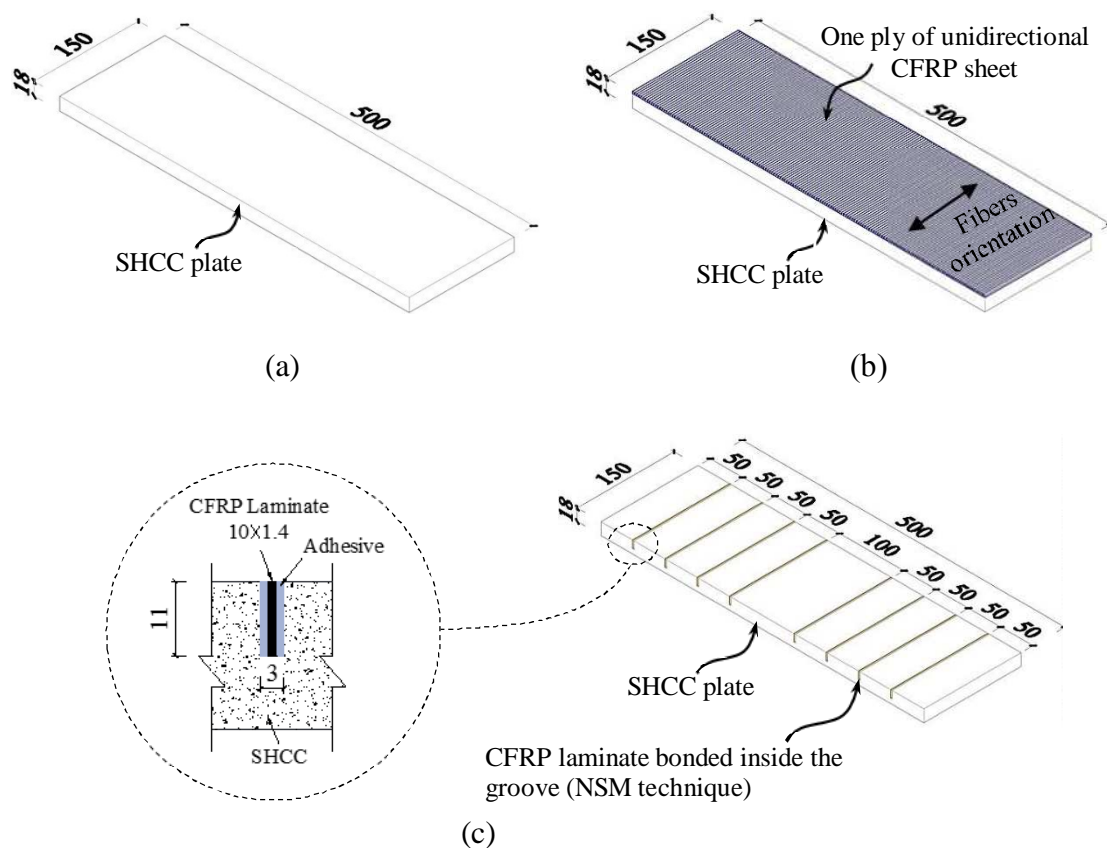
Figure 4.30: Details of the strengthening plates: (a) SHCC plate, (b) HCP[(S)], and (c) HCP[(L)] (dimensions in mm)

For those plates whose their connection system to the RC beam composed of a combination of adhesive and chemical anchors (8 mm in diameter), positions of the holes were marked and then perforation was executed using a drill bit of 10 mm in diameter (see for example Figure 4.31).



|            (a)            |            (b)            |

Figure 4.31: Perforated HCP[(S)], (a) the face with bonded CFRP sheet, and (b) exposed face

### 4.5.2 Procedure of Attaching Retrofitting Elements

To enhance the bond quality at the interface of the epoxy adhesive and concrete substrate, the lateral faces of the RC beams to be retrofitted were sand-blasted to remove 1 mm to 2 mm of cement paste and to partially expose the aggregates. This procedure was applied also to the bottom face of the RC beams selected for the strengthening of U-shaped CFRP (beam BFU_A).

In the case of BFU_A, see Table 4.12 and Figure 4.29, two side-by-side layers of a ply of 250 mm width carbon fabric was bonded to the lateral and bottom faces of the RC beam adopting a wet layup procedure and using a low viscosity adhesive (S&P 220 Resin Epoxy). Following specifications of ACI 440.2R-08 [37], bottom longitudinal corners of the beam should be rounded to a radius of at least 13 mm and then smoothed to avoid stress concentrations in the CFRP system and accumulation of air voids. Hence, during casting the beam considered for the strengthening with the U-shaped CFRP sheet, wooden bars with filleted cross-sections were placed at the interior corners of the mold along its length in order to ease the need of further grounding. Carbon fabrics were bonded with their filaments orthogonal to the longitudinal axis of the beam.

As mentioned before, the retrofitting plates of beams BS_A, BHS_A and BHL_A (group I retrofitted beams in Table 4.12) were bonded to the lateral faces of their corresponding

beams using a viscose adhesive (S&P Resin Epoxy 220). Before bonding these plates, epoxy adhesive was spread on the lateral faces of the beams and contact-face of the strengthening plates (the CFRP reinforced face in the case of HCP and the grounded face in the case of plain SHCC plate). Once the plates were placed at their positions, C-clamps were installed and tightened slowly to force flowing of adhesive between the contact surfaces. The retrofitting plates were maintained in their target positions with the pressure of these clamps up to a partial curing of adhesive, when the clamps were removed.

In the case of beams where a combination of adhesive and chemical anchors was used to attach their retrofitting plates, BS_AB, BHS_AB and BHL_AB (group II retrofitted beams in Table 4.12), initially each perforated plate was placed on the lateral face of its corresponding beam and then the positions of the holes were mapped on this concrete surface.

According to the instruction of Hilti® for the installation of chemical anchors, perforations were executed using a drill bit of 10 mm in diameter and with a depth of 65 mm. After cleaning the holes, using compressed air, they were injected with a fast curing chemical adhesive to approximately fill two-thirds of their depth. Once the 8 mm diameter anchors were placed inside the holes, the excessive adhesive was cleaned and anchors were left untouched until the initial curing time of their adhesive was reached (a few minutes depending on environmental conditions). Afterward, the viscose adhesive (S&P Resin Epoxy 220) was spread on the contact-faces of the retrofitting plates and the beam. After placing the retrofitting plates at their positions on the beam and inserting washers, the nuts were smoothly fastened to force the epoxy adhesive flowing and filling uniformly the entire contact surfaces of the retrofitting plates and the beam. Post-tensioning forces using a torque of 20 N·m was applied to the anchor rods only after the curing period of epoxy adhesive was passed. To assure that the bonding adhesive attained its maximum mechanical properties, a curing period of at least seven days was considered before testing any of the retrofitted beams.

### *4.5.3 Material Properties*

### *4.5.3.1 Concrete*

Ready-mix concrete was used to cast RC beams. In order to obtain the mean values of modulus of elasticity ($E_c$) and the compressive strength ($f_{cc}^m$) of the concrete used for casting the beams, five cylinders of 150 mm in diameter and 300 mm in depth were tested at the age of 90 days (prior testing the beams), following the specifications of LNEC E397-1993 [34] and EN 12390-3-2009 [35], respectively. According to the results of these tests, $E_c$ and $f_{cc}^m$ were 28.3 GPa and 38.2 MPa, respectively.

### *4.5.3.2 Steel Rebars*

Properties of the longitudinal rebars were determined by means of tensile tests according to the procedure recommended in ISO 15630-1-2010 [38].

From the results of the tests executed on four specimens of 10 mm diameter steel rebars, the average values of 532 MPa, 660 MPa and 195 GPa were determined as the yield strength, ultimate strength, and modulus of elasticity of tensile reinforcements, respectively.

Following the results of tensile tests on four 8 mm diameter steel rebars, the beams compressive reinforcements, average values of 427 MPa, 620 MPa and 193 GPa for the yield strength, ultimate strength, and modulus of elasticity of these compressive rebars were obtained, respectively.

### *4.5.3.3 PVA-SHCC*

Composite mixture C4W30, with the fresh state properties presented in Table 4.7, was used to cast casting the SHCC plates. Tensile and compressive properties of this PVA-SHCC can be found in Table 4.9 and sections 4.3.6 and 4.3.7, respectively.

### *4.5.3.4 Epoxy Adhesives*

From uniaxial tensile tests carried out according to the recommendations of ISO 527-2:2012 [39] on six dumbbell-shaped S&P 220 epoxy resin cured for seven days, an average tensile strength of 18 MPa and average modulus of elasticity of 6.8 GPa were obtained.

According to the supplier, S&P 50 epoxy resin develops a tensile strength of 35.8 MPa and a modulus of elasticity around 2.6 GPa at the age of 14 days.

### 4.5.3.5 CFRP

Figure 4.32 shows photos of CFRP materials used in this research work. Tensile properties of CFRP laminate (S&P laminate CFK 150/2000) with a cross section of 1.4 mm × 10 mm were characterized following the procedures proposed in ISO 527-5:2009 [40]. From the tests executed on six coupons, average values of 2647 MPa, 1.6% and 165.7 GPa were obtained for the tensile strength, strain at CFRP rupture and modulus of elasticity, respectively.

The commercial name of the utilized carbon fabric is S&P C-Sheet 240. According to the supplier, this fabric possesses a tensile young's modulus of 240 GPa, a nominal tensile strength of 3800 MPa, a design thickness (fiber weight divided by density) of 0.176 mm, and an elongation at rupture of 1.55%.



(a)                                                                (b)

Figure 4.32: Photos of CFRP materials used in this research work, (a) S&P laminates CFK 150/2000 (cut from a roll of 150 m), and (b) carbon fabric S&P C-Sheet 240

### 4.5.3.6 Chemical Anchors

As depicted in Figure 4.33, the Hilti® chemical anchor system was composed of a fast curing resin HIT-HY 200A and steel anchor rods of 8 mm in diameter with specification of HIT-V-5.8 M8X110. According to the classification of the ASTM steel grades, a notation of 5.8 indicates steel with characteristic tensile yield strength of 400 MPa and a characteristic ultimate tensile strength of 500 MPa. The total length of 8 mm diameter anchor rod is 110 mm. Based on the technical datasheets provided by the manufacturer, an average ultimate tensile load and shear load of 18.9 kN and 9.5 kN is expected for these anchor rods.

Figure 4.33: Typical image of Hilti® chemical anchor system

### 4.5.4 Bending Test Setup and Instrumentations

All beams were subjected to three point bending test and the results of these tests were used to discuss the efficiency of the adopted shear strengthening provided by the strengthening systems. Figure 4.34 shows the setup of the three point beam flexural test.

The supports were placed 50 mm far from the extremities of the beams. The load was applied using an actuator with a 150 kN load cell located at the mid span of the beam, therefore $a/h_b$ was 1.67.
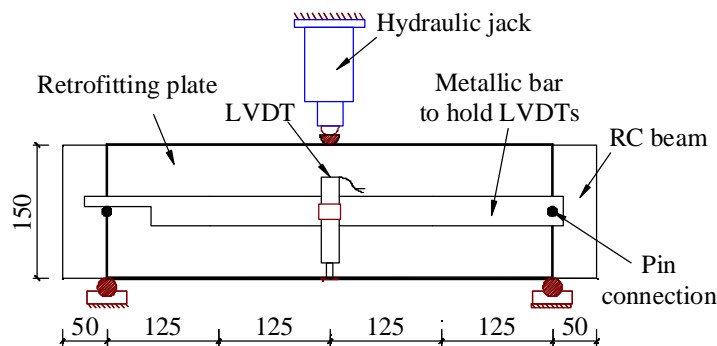


Figure 4.34: Details of the three point beam bending test setup (dimensions in mm)

Before installing the measuring instruments on the beam, the exposed surfaces of the SHCCs was painted using a concrete varnish to facilitate visualization of the micro-cracks after spraying this surface by a penetrating liquid.

An LVDT was used to measure the deflection of the beam. This LVDT was attached to a metal bar fixed at mid-height of the beam in the alignment of its supports, in order to assure

that the LVDT only measures the deflection of the beam. Another external LVDT was fixed to the body of hydraulic jack and was used to control the test loading conditions by imposing a displacement rate of 5 μm/s to the piston of the jack.

As illustrated in Figure 4.35, two LVDTs (D1 and D2), each installed in one of the shear spans, were used to measure the diagonal elongation caused by shearing and cracking in these regions. Moreover, a strain gauge "SG" was attached to the mid-length of the middle rebar in each beam to measure strain in tension rebars at the mid-span.
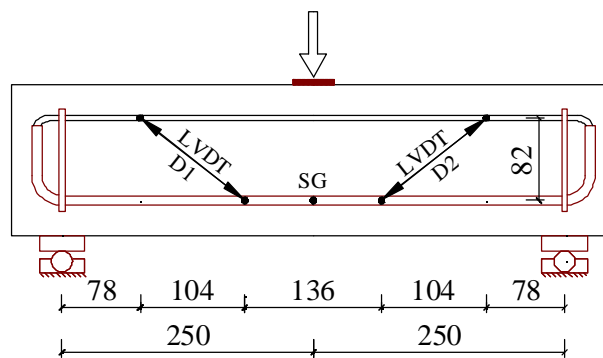


Figure 4.35: Instrumentations installed on the beams to measure diagonal elongations in each shear span (LVDTs "D1" and "D2") and strain in longitudinal rebars (strain gauge "SG")

### 4.5.5 Test Results and Discussions

#### 4.5.5.1 Crack Pattern and Failure Modes

Crack pattern and damages of the beams at the end of the testing are depicted in Figures 4.36 to 4.38. It should be noted that during and after testing groups I and II retrofitted beams, a penetrating liquid was sprayed on the exposed surface of the strengthening plates. According to this technique, since the un-cracked regions of the strengthening plate are protected by painted varnish, the sprayed liquid penetrates only into the mirco-cracks and highlights them. With the exception of beam BFU_A that its cracking was not visible due to its lateral faces being covered by CFRP sheet, the first observed crack in all the other beams was a flexural crack formed at the beam's mid-span. Following the failure modes of the specimens are discussed.

Figure 4.36: Crack pattern of beam CB at the end of the test
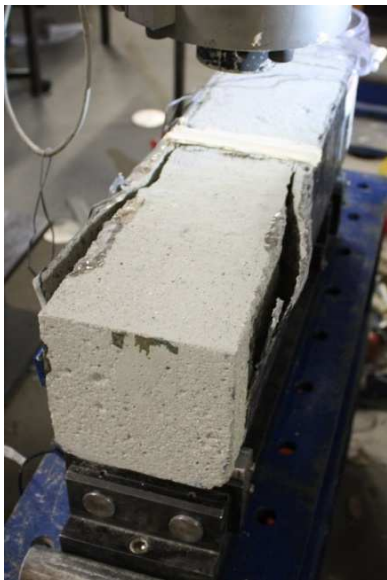


(Front view)

(Back view)

Figure 4.37: Views of failure in beam BFU_A at the end of the test (left figure shows debonding of U-shaped CFRP sheet and the right photos are presenting the front and back views of beams where major diagonal crack is developed)

*Beams CB, BS_A and BS_AB:* "shear-tension" failure occurred in all these beams. This failure mode caused with an inclined crack localized at one of the beam's shear span. In the case of beam CB, the diagonal crack emerged at the mid-depth of the beam and rapidly propagated towards the loading point and the closest supported region (see Figure 4.36). This crack, after intersecting the longitudinal rebars at the vicinity of the beam's supporting

region, propagated horizontally at the level of these rebars and caused cracking of concrete at their hooked anchored end. Following the sliding of tension steel rebars, the upper tip of this crack penetrated into the top compressive block at the loaded region, which caused the beam failure. As shown in Figure 4.38, the major diagonal crack in the case of BS_A and BS_AB, however, was composed of the inclined part of a flexural-shear crack and an inclined secondary crack descended from the lower part of this flexural-shear crack. The tips of this major diagonal crack progressed towards the loading and supporting regions. Once tension rebars were intersected with diagonal crack, similar to CB, sliding of these rebars caused increasing in crack width and penetrating of crack's upper tip into the compressive block at the loaded region. In the case of both of these beams, advancing at the tips of the major diagonal crack was much slower than that observed in beam CB. Moreover, as indicated in the close-up view of critical shear span of these beams in Figure 4.39, in the case of beam BS_AB, a band of cracks around the major diagonal crack was observed, which didn't occur in BS_A.

*Beam BFU_A:* a premature debonding of CFRP sheet, originated at the left top parts of the beam, see Figure 4.37, resulted in an unstable and rapid propagation of the shear-tension crack, formed in the left shear span of this beam, causing its failure.

*Beams BHL_A, BHL_AB, BHS_A and BHS_AB:* these beams failed similarly with a wide flexural crack formed at their mid-span. Widening of this crack was together with the initiation and propagating of longitudinal splitting cracks observed at the bottom face of the beams (see Figure 4.38), resulting in sliding of longitudinal tension rebars and cracking of concrete at the anchored region of these rebars. Finally, further progress of this flexural crack towards the beam's compressive block promoted crushing of concrete and SHCC at the top of each of these beams. It is worth mentioning that despite the emerging of inclined cracks in these beams, the HCPs were capable of restraining their unstable propagation; hence altering shear-tension failure mode observed in the other beams to the flexural failure. Visual inspection of the specimens at the end of their testing revealed that the debonding of HCP from the concrete substrate occurred only in the case of BHS_A (see the magnified bottom view of this beam in Figure 4.40).

**Front view**    **Bottom view**
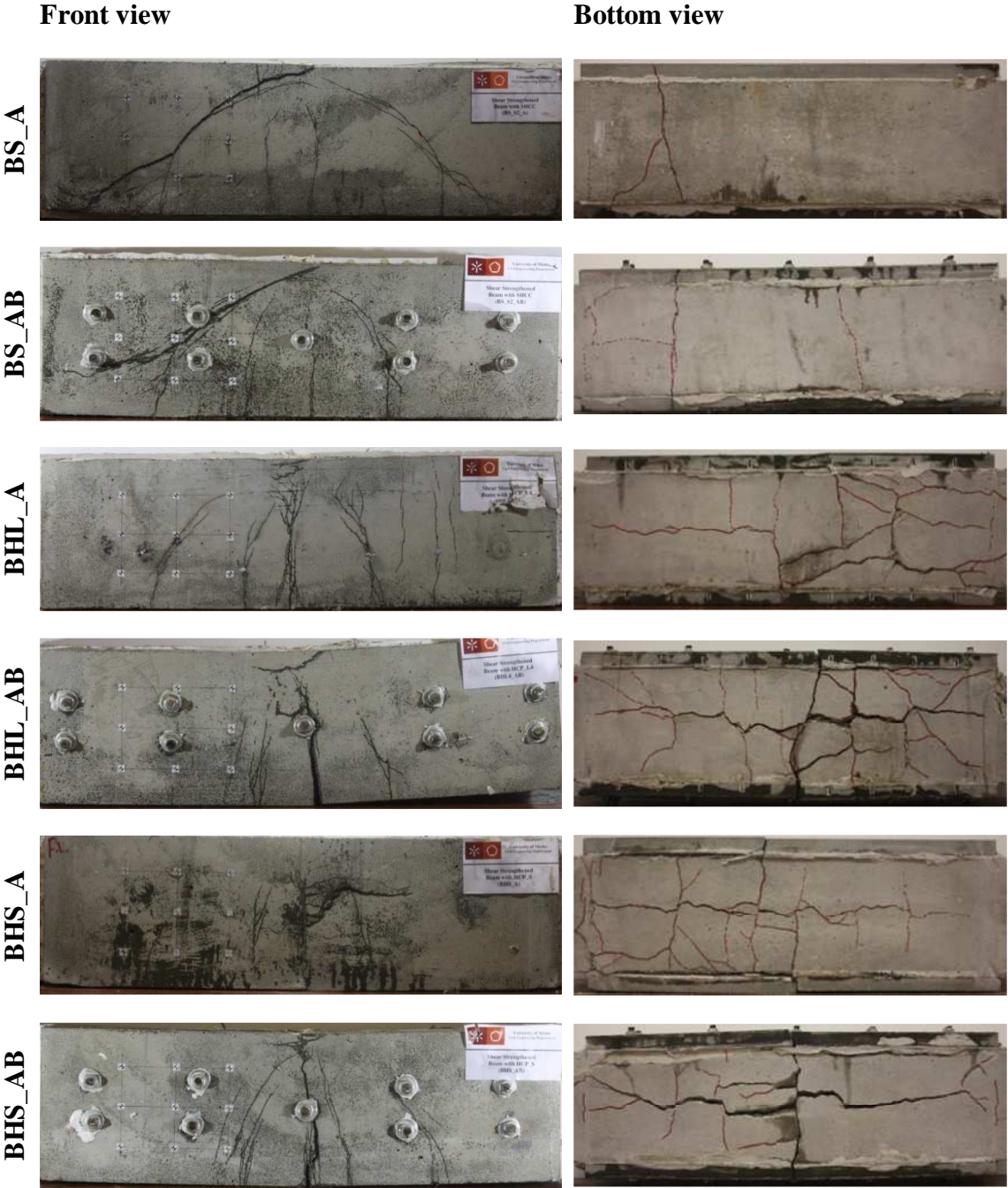


Figure 4.38: Front and bottom views of the failure of groups I and II retrofitted beams (see Table 4.12 and Figure 4.29 for the details of these beams) - The varnished surface of the strengthening plate were sprayed with a penetrating liquid to highlight the cracks

(a)                                      (b)

Figure 4.39: Close-up views of the major diagonal crack caused the failure of the beam (a) BS_A, and (b) BS_AB (arrows are indicating the band of cracks)
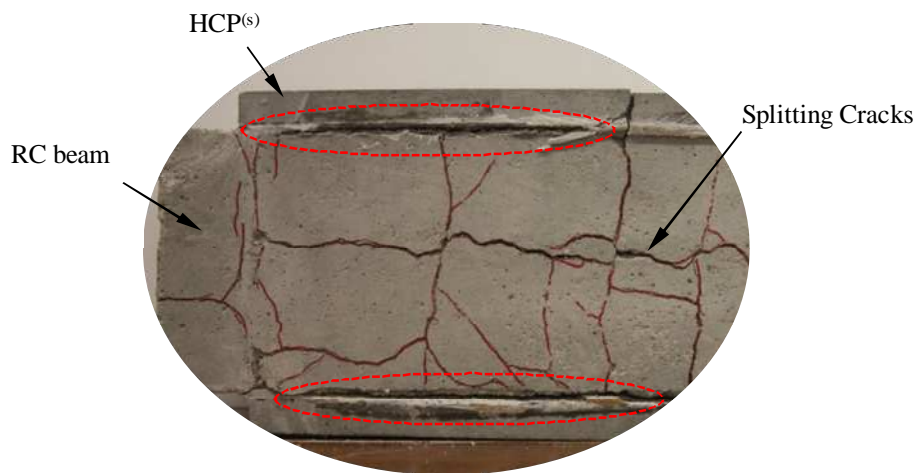


Figure 4.40: Close-up view of the bottom of the left shear span of beam BHS_A, where debonding of HCP$^{(S)}$ was observed (see the region inside the elliptical shapes)

### 4.5.5.2 Force versus Deflection Response

Figure 4.41a depicts the force *versus* mid-span deflection of the reference beams (CB and BFU_A) and the retrofitted beams in group I (BS_A, BHL_A and BHS_A). The corresponding results of retrofitted beams in group II (BS_AB, BHL_AB and BHS_AB) are presented in Figure 4.41b. The results of beams in group I are repeated again in this figure to facilitate discussion on comparison of these groups and verify the influence of chemical

anchors on the force-deflection response of the retrofitted beams. Moreover, force *versus* strain in tension rebars, measured by the strain gauge attached to the mid-length of the middle tension rebar, for all beams are depicted in Figure 4.42. The vertical dashed line in this figure refers to the average yield strain $\left(\varepsilon_{st}^{y} = 0.0027\right)$ of longitudinal tension reinforcements obtained in tensile characterization of 10 mm diameter rebars (see 4.5.3.2).

A summary of the results extracted from the abovementioned figures along with the failure modes of each beam is indicated in Table 4.13. These data composed of the force and mid-span deflection at the yield of tension steel bars ($F_y$ and $\delta_y$), if applicable, and at the peak force of the beams ($F_m$ and $\delta_m$), also the strain at tension rebars corresponding to peak force $\left(\varepsilon_{st}^{p}\right)$. Furthermore, with the exception of beam BFU_A, the force corresponding to the onset of the first crack ($F_{cr}$), observed during testing of each beam, is also reported in this table. The deflection ductility ($\mu_\delta$) of the beams, those with their longitudinal rebars yielded, are calculated and mentioned in this table as well. Finally, in Table 4.13, the percentage change in $F_{cr}$, $F_y$, $F_m$ and $\mu_\delta$ respecting to corresponding value of the reference beam (CB or BFU_A) are calculated and indicated between parentheses within the same cell of the parameter.

Following, the data of this table and the above-mentioned figures are used to discuss the effectiveness of retrofitting shear-critical short RC beams using the adopted techniques.

***Force at the Initiation of the first flexural crack*** $(\boldsymbol{F_{cr}})$**:** according to the data in Table 4.13, adhesively bonded plates (SHCCs or HCPs) to the lateral faces of the beams (retrofitted beams in group I) resulted in an increase in $F_{cr}$ ranging from 67% (BHL_A) to 85% (BS_A). Adding chemical anchors to the attaching system, however, adversely affected the gain in $F_{cr}$. In the case of these beams (group II retrofitted beams), the increase in $F_{cr}$ was between 11% (BHL_AB) and 18% (BHS_AB) lower than that obtained in their counterpart beam in group I (the beam with its plates attached only by means of adhesive). The reduction in cross-sectional area of beams at the mid-span, due to the presence of the perforated hole, and presence of some pre-existing micro-cracks are perhaps rational explanations for this adverse effect.
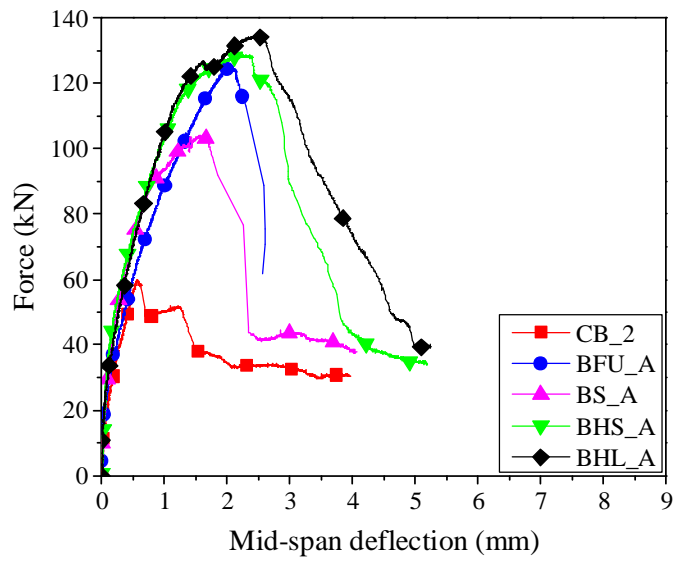
(a)
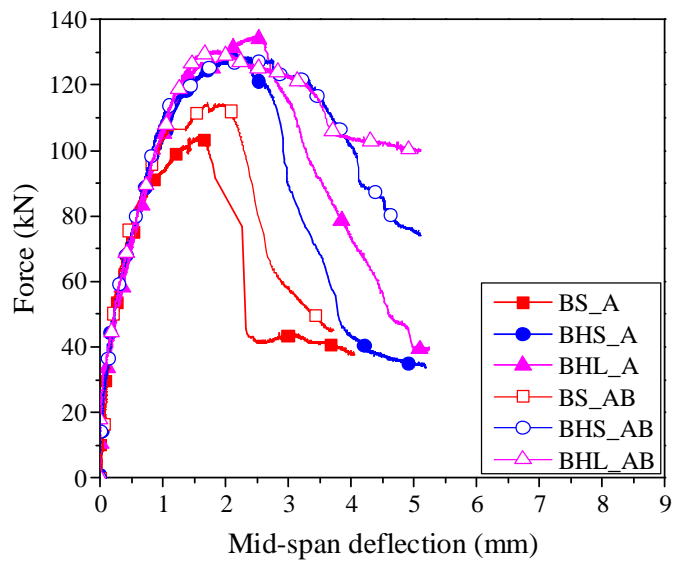


(b)

Figure 4.41: Force *vs* mid-span deflection curves of (a) reference beams and retrofitted beams in group I, and (b) retrofitted beams in groups I and II
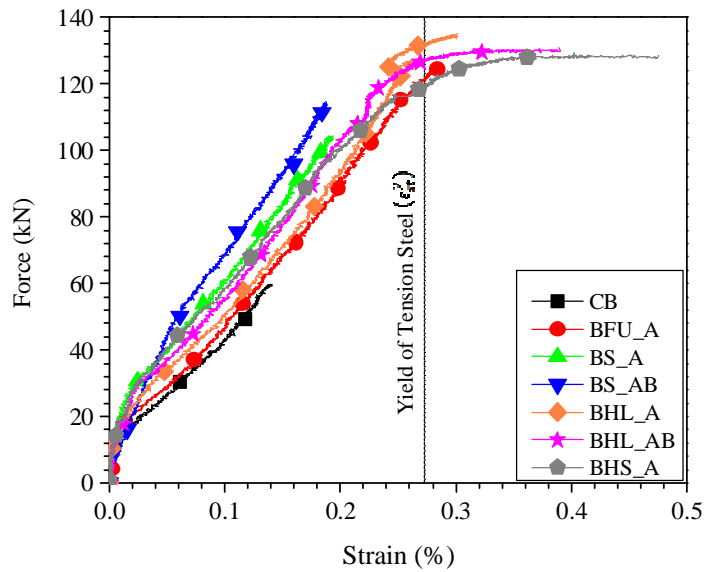
Figure 4.42: Force *vs.* strain in tension steel bars at the mid-span of beams

Table 4.13: Results obtained from the analysis of the tested beams

| Category | Beam | $F_{cr}$ (kN) | $\delta_y$ (mm) | $F_y$ (kN) | $\delta_m$ (mm) | $F_m$ (kN) | $\varepsilon_{st}^p$ (%) | $\mu_\delta$ | Failure mode |
|---|---|---|---|---|---|---|---|---|---|
| Reference beams | CB | 21 (Ref.)[a] | N/A | N/A | 0.57 | 59.8 (Ref.) | 0.14 | N/A - | shear-tension |
| | BFU_A | N/A - | 1.87 | 121.3 (Ref.) | 2.06 | 125.5 (110%) | 0.29[c] | 1.10 (Ref.) | FRP debonding |
| Group I retrofitted beams | BS_A | 39 (86%)[a] | N/A | N/A | 1.61 | 104.3 (74%) | 0.20 | N/A | shear-tension |
| | BHL_A | 35 (67%) | 2.16 | 131.6 (8.5%) | 2.49 | 134.9 (126%) | 0.30[c] | 1.15 (4.7%) | flexural |
| | BHS_A | 38 (81%) | 1.43 | 119.8 (-1.2%) | 2.24 | 129.5 (117%) | 0.48[c] | 1.57 (42.2%) | flexural |
| Group II retrofitted beams | BS_AB | 33 (57%) | N/A | N/A | 1.54 | 114.7 (92%) | 0.19[c] | N/A | shear-tension |
| | BHL_AB | 31 (48%) | 1.47 | 127.0 (4.5%) | 1.88 | 130.7 (119%) | 0.39[c] | 1.28 (16.1%) | flexural |
| | BHS_AB | 31 (48%) | 1.43[b] | 119.8[c] (-1.2%) | 2.72 | 127.9 (114%) | N/A[b] | 1.90 (73.2%) | flexural |

a) Values in parentheses are the change of each measure respecting to the corresponding value of the reference specimen. The reference specimen for this calculation is specified with "(**Ref.)**" in each column.

b) Taken equal to the yield deflection of BHL_A, see the explanation presented about $F_y$ and $\delta_y$ of this beam in current section.

c) Tension bars yielded $\left(\varepsilon_{st}^y \geq \varepsilon_{st}^y\right)$.

***Force and deflection at the yield of longitudinal tension rebars*** $(F_y$ *and* $\delta_y)$**:** according to Figure 4.42, only tension rebars of the beams retrofitted with U-shaped CFRP sheet, HCP[(L)] or HCP[(S)] have yielded. Reading the deflection corresponding to the yield of tension rebars $(\delta_y)$ from Figure 4.42, corresponding yield load $(F_y)$ for each beam was found and together with $\delta_y$ reported in Table 4.13.

In the case of beam BHS_AB, due to a technical problem, data corresponding to the yield of this beam is not available. However, very similar load-deflection responses of BHS_A and BHS_AB in Figure 4.41b, at least up to the maximum load carrying capacity of BHS_A, suggests that the yield deflection of BHS_A can be assumed as an upper limit for $\delta_y$ of BHS_AB. Thus, in Table 4.13 value of $F_y$ and $\delta_y$ for beam BHS_AB are assumed similar to that of BHS_A.

In Table 4.13, values between parentheses mentioned within the same column of $F_y$ are the percentage change in the yield load of each HCP strengthened beam, with BFU_A as the reference beam. Comparison of $F_y$ of HCP retrofitted beams with the corresponding value of beam BFU_A reveals a negligible influence of HCPs versus U-shaped CFRP sheet on the beam's yield load (between -1.2% to 8.5%).

The displacement corresponding to the yield load of each beam, $\delta_y$, is used to evaluate its deflection ductility index, which is discussed further in this section.

***Peak force and its corresponding deflection*** $(F_m$ *and* $\delta_m)$**:** all the strengthened beams presented a load carrying capacity much higher than the control beam CB. This increase in the case of bonding plain SHCC plates to the lateral faces of the beam (beam BS_A) was 74%. A further increase of 18% was obtained when chemical anchors were added to the connection system of SHCC plates (beam BS_AB).

While none of the strengthening alternatives based on attaching plain SHCC plates could sufficiently enhance $F_m$ to a comparable level of the load carrying capacity obtained by bonding one layer of U-shaped CFRP sheet (beam BFU_A), all beams strengthened with HCP resulted in a peak load higher than BFU_A. However, flexural failure of HCP strengthened beams prevented developing the full shear strengthening potential of the HCPs. Consequently, in comparison with $F_m$ of BFU_A, the largest increase in the load carrying

capacity of the HCP strengthened beams was limited to 7.5%, which was the case of BHL_A. This beam reached to an $F_m$ of 127.9 kN which is 119% larger than that of beam CB.

Adding chemical anchors to the connection system of the HCP bonded beams resulted only in a negligible change in $F_m$. This low contribution of chemical anchors in $F_m$ is associated with the flexural failure of HCP strengthened beams. This failure mode limited the developed shear forces below the one that could initiate debonding and sliding of HCPs; a phenomenon which activates anchors for shear stress transfer mechanism between the strengthening plates and the beam.

The displacements corresponding to the peak loads, $\delta_m$, reported in Table 4.13 are used to calculate the deflection ductility index of the beams, which is discussed below.

***Deflection ductility*** **($\mu_\delta$):** the capacity of beams to undergo plastic deformation beyond yield of their tension rebars, and up to a deflection corresponding to $\delta_m$ or slight decrease in $F_m$ (less than 15%) is generally defined as deflection ductility ($\mu_\delta$). In the case of current beams, $\mu_\delta$ is calculated as $\delta_m/\delta_y$ and reported in Table 4.13. Following the definition of $\mu_\delta$, it is obviously calculated only for those beams with their tension rebars yielded (beams BFU_A, BHL_A, BHL_AB, BHS_A and BHS_AB).

For the sake of comparison, the percentage change in deflection ductility of each HCP strengthened beams is calculated taking the beam BFU_A as the reference specimen. These values are reported between parentheses within the same column of $\mu_\delta$ in Table 4.13. According to these data, as compared to retrofitting based on bonding U-shaped CFRP sheet (beam BFU_A), the shear strengthening of beams by means of attaching HCPs improved the beams deflection ductility, but with different scales. The lowest enhancement in $\mu_\delta$ (4.7%) belongs to BHL_A, which is a consequence of premature sliding of tension longitudinal rebars (see discussions regarding the effectiveness of chemical anchors in section 4.5.5.3). Adding post-tensioned chemical anchors (beam BHL_AB), however, led to a larger increase in $\mu_d$, being 16% higher than corresponding value of BFU_A.

Both HCP$^{(S)}$ strengthened beams have presented higher $\mu_\delta$ than beams strengthened with HCP$^{(L)}$. The beam BHS_AB showed the largest deflection ductility with an increase of 73%, as compared to that of BFU_A. If $\mu_\delta$ of beam BHS_AB is compared to that of BHS_A, it

can be found that adding chemical anchors resulted in an increase of 21% in the deflection ductility.

### 4.5.5.3 Contribution of Chemical Anchors

From the constructional point of view, presence of anchors not only facilitates the installation process of the strengthening plates, but also their fastening pressure contributes in improving the flow of viscose epoxy adhesive at the interface of the strengthening plate and beam. Hence, adding chemical anchors to the connection system of the strengthening plates and beams is recommended in order to achieve a more homogenous interface at the connection of the plates and beams.

Contribution of post-tensioned chemical anchors in the performance of retrofitted beams is discussed through comparing the test results of the groups I specimens with their counterpart specimens in group II, and also considering the beams failure modes. For this purpose, the evolution of force $(F)$, strain in tension rebars ($\varepsilon_{st}$) and elongation of diagonal LVDT ($\Delta_d$), respecting the mid-span deflection ($\delta$) of each beam in group I and its counterpart specimen in group II, up to slightly beyond $\delta_m$, are integrated in a single multi-axis graph. These graphs are designated $(F, \varepsilon_{st}, \Delta_d - vs - \delta)$ and shown in Figures 4.43a and 4.43b for BS and BHL specimens, respectively. In these graphs $\Delta_d$ corresponds to the measurement of the LVDT registered the largest deformation, also vertical and horizontal dashed-lines indicate $\delta_m$ and $\varepsilon_{st}^y$, respectively.

Following, these figures are used to discuss the influence of anchors on the performance of the retrofitted beams (note that due to an improper functioning of equipment registering the measurements of the strain gauge and diagonal LVDTs in beam BHS_AB, such graphs to compare beam BHS_A and BHS_AB are not available).

***Strengthened beams failed in shear-tension mode:*** Figure 4.43a demonstrates $(F, \varepsilon_{st}, \Delta_d - vs - \delta)$ of beams BS_A and BS_AB, both failed in shear-tension. If the $F - \delta$ of these beams is considered, with the exception of initial loading stages, a stiffer response for BS_AB than BS_A can be recognized. However, the major difference in $F - \delta$ response is associated with the post-peak behavior.
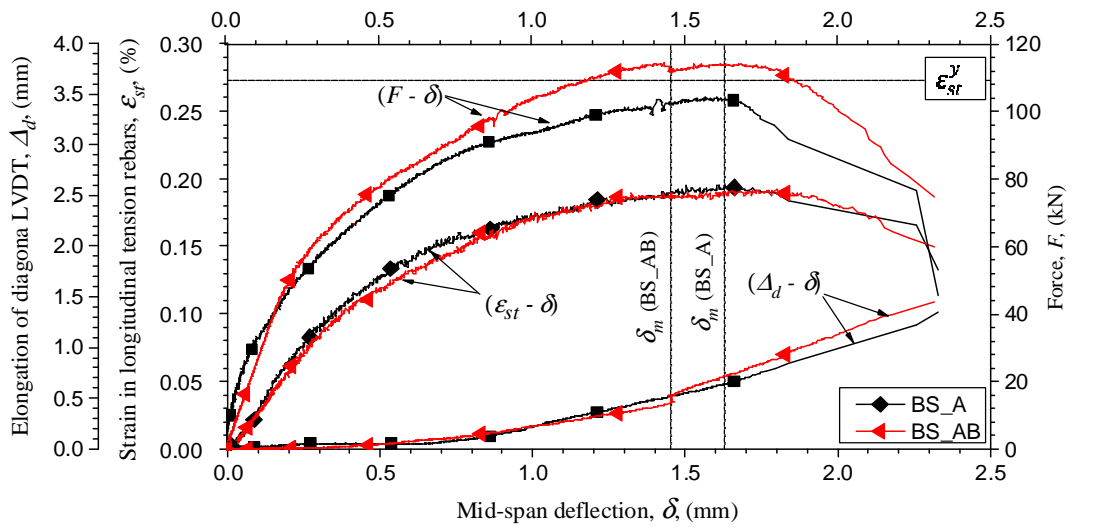
(a)
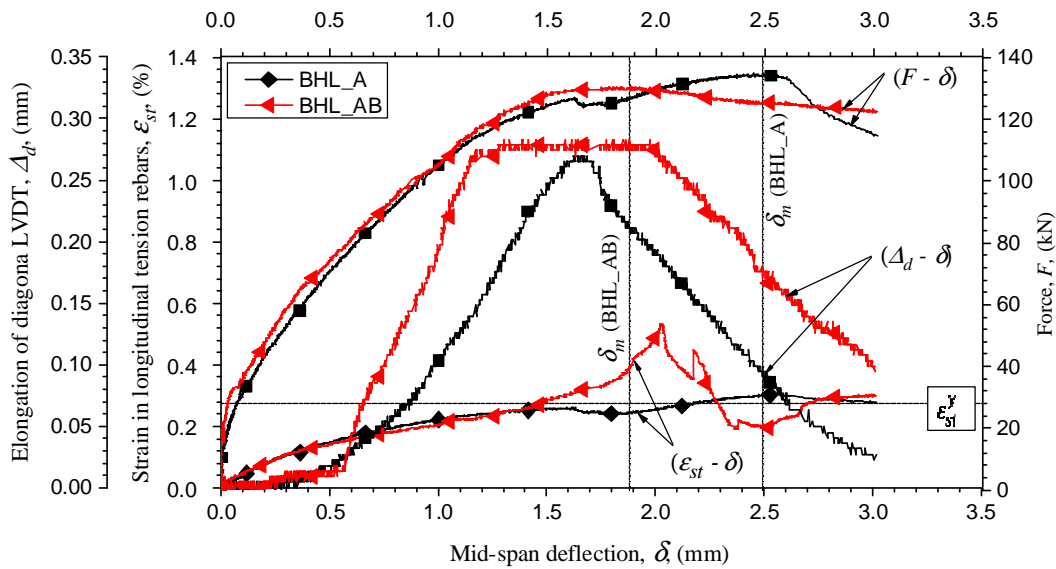


(b)

Figure 4.43: Mutli-axis diagrams representing the relation between force, strain in the longitudinal tension rebars and elongation of diagonal LVDT with the mid-span deflections of beams (a) BS_A and BS_AB, and (b) BHL_A and BHL_AB.

In the case of the beam without chemical anchors (BS_A) the load-deflection response enters a softening regime slightly beyond the deflection corresponding to its peak load $(\delta_m)$, together with a decreasing trend in $\varepsilon_{st}$ and increasing width of the inclined shear crack $(\Delta_d)$.

On the other hand, the $F - \delta$ of BS_AB shows almost a plateau region between deflections corresponding to the $\delta_m$ and the initiation of the load decay ($1.54 \leq \delta \leq 1.75$), while in this region both $\varepsilon_{st}$ and $\Delta_d$ are increasing.

If this analysis is interpreted taking into account the shear-tension failure mode of these beams, it can be concluded that beyond the peak load sliding of tension rebars at the distance between the intersection of the diagonal crack and tension rebars and the hooked end of rebars was more severe in BS_A than that in BS_AB.

This conclusion suggests that the confining pressure exerted to the concrete enclosed between SHCC plates, due to post-tensioning of chemical anchors, has delayed the debonding rate at the concrete-rebars interface; therefore, in the case of BS_AB a load decay at the close vicinity beyond its $\delta_m$ was prevented.

***Strengthened beams failed in flexure:*** according to the ($F,\ \varepsilon_{st},\ \Delta_d - vs - \delta$) of beams BHL_A and BHL_B, showed in Figure 4.43b, both of these beams exhibited very similar load-deflection responses up to $\delta$=1.62 mm. In the case of BHL_A, for the ascending branch of load-deflection beyond this deflection and up to $\delta_m$, while the increasing trend of $\Delta_d$ turned into a decreasing one, there is almost always a smooth increase in $\varepsilon_{st}$. This scenario is associated with the sliding of longitudinal tension rebars with their hooked end pressure on the concrete causing reduction in the width of shear cracks.

On the other hand, in the case of beam BHL_AB, when $\delta$ reached to 1.62 mm the ascending trend of $\Delta_d$ shifted into a constant plateau and this behavior was continued until $\delta = 2.0$ mm, where both the load and the $\Delta_d$ are decreasing. During 1.6 mm $\leq \delta \leq 2.0$ mm, however, $\varepsilon_{st}$ is always increasing and only decreases beyond $\delta$= 2.0 mm, which is also slightly larger than $\delta_m$ ( = 1.88 mm). This behavior corresponds to a delayed sliding of the longitudinal tension rebars of this beam, as compared to that of BHL_A. In fact, this is the confining pressure of the post-tensioned chemical anchors that restricted the sliding of rebars. Consequently, the location of the splitting cracks observed along the tension rebars in BHL_A has shifted to the mid-width, beyond the chemical anchors, in the case of BHL_AB (see bottom views of corresponding beams in Figure 4.38).

The advantage of this reduced rate in sliding of tension rebars is reflected in the smoother load decay in the post-peak regime of the beams whose retrofitting plates attached using a combination of adhesive and post-tensioned chemical anchors (see and compare softening regimes of the force-deflection responses of beams BHL_A and BHL_AB in Figure 4.41b).

As mentioned before, due to an improper functioning of the data logger which was registering the measurements of the strain gauge and diagonal LVDTs in beam BHS_AB, performing the abovementioned analysis for HCP[(S)] strengthened specimens is not possible. However, smoother softening regime of the force-deflection of beam BHS_AB compared to BHS_A (see Figure 4.41b), and the similarity of their splitting crack pattern to that of beams BHL_A and BHL_AB (see bottom views of corresponding beams in Figure 4.38), respectively, can be interpreted as the contribution of post-tensioned chemical anchors in restricting the sliding of tension rebars in the case of BHS_AB. Moreover, chemical anchors of beam BHS_AB prevented the debonding of strengthening plates, which was observed in the case of beam BHS_A at the end of its testing (see Figure 4.40).

## 4.6 Summary and Conclusions

Within this chapter the material-structural concept of the proposed strengthening technique, designated as Hybrid Composite Plate (HCP), was introduced and the advantages and potential applications of this novel retrofitting element were discussed. Two different types of HCP, differing in the technique used to reinforce their SHCC plate were developed, namely HCP[(S)] and HCP[(L)]. The SHCC plate of HCP[(S)] is reinforced with EB-CFRP sheet, while in the case of HCP[(L)] the NSM-CFRPs are used to reinforce the SHCC plate. The CFRP reinforced face of the HCP is considered to be in contact with concrete substrate, hence in this system SHCC potentially protects CFRP constituents against severe environmental conditions, temperatures higher than $T_g$, impact loads and vandalism.

Within the framework of developing HCP, a methodology to process PVA-SHCC based on calibrating minimum number of variables (W/B, SP/B and VMA/B) was proposed and experimentally validated. According to this approach, initially the rheological properties of composite mixtures containing different W/B were optimized within a two-phase study (matrix and composite phase). Furthermore, based on the results of tensile tests the

mechanical properties of rheologically optimized composites at each given W/B were determined and the composite with adequate mechanical properties was used for construction of HCP. If none of the developed composites possesses the required mechanical properties the above-mentioned strategy should be repeated for different W/B contents. However, in this study the first trials of W/B was sufficient to process a PVA-SHCC possessing fresh- and hardened-sate properties in compliance with HCP development requisites.

Afterwards, the structural efficiency of HCP was assessed through retrofitting short-span shear-critical RC beams. The results of three-point flexural tests executed on the beams, retrofitted with either SHCC-plates, HCP(L) or HCP(S) attached to their lateral faces, were compared to those of the as-built beam and the beam strengthened with adhesively bonded U-shaped CFRP sheet. Moreover, for beams strengthened with SHCC-plates or HCPs, two different types of connections between the strengthening plate and concrete substrate were investigated; one with only epoxy adhesive and the other one with a combination of epoxy adhesive and chemical anchors.

- According to the tests results, plain SHCC-plates bonded to the lateral faces of the beam increased the load carrying capacity up to 74%, as compared to that of the as-built beam, with only 24% enlargement in the beam's width. The premature detachment of the retrofitting scheme, occurred in the case of the beam with externally bonded U-shaped CFRP sheet, was not observed in the other beams, except for the one strengthened by means of adhesively bonded HCP(S).

- HCPs were capable of altering the shear-tension failure mode, occurred in the as-built beam and the ones strengthened with SHCC plates, to a flexural failure mode, independent of their connection system to the RC beams. Moreover, an increase of up to 126% in the load carrying capacity of the HCP retrofitted beams, as compared to that of the as-built beam, was attained.

- The improvement in the deflection ductility in the case of HCP strengthened short-span shear-critical beams was more notable than that of the beam strengthened with U-shaped CFRP sheet. However, the extent of this

enhancement was a function of the type of the HCP and its connection with the concrete substrate.

- The main advantage of introducing chemical anchors to the adhesive-based connection of strengthening plates to the concrete substrate, within the context of the study performed on the retrofitting of short-span beams, was restricting the sliding of the beams' longitudinal tension rebars. The structural advantage of this enhancement was reflected in reducing the rate of the post-peak load-decay in the case of retrofitted beams failed in flexure (HCP retrofitted ones), and higher shear capacity in the case of the retrofitted beam failed in shear (the beam retrofitted with SHCC plates).

- These above-mentioned results highlight the promising HCPs' potential for retrofitting shear-critical deep or slender RC beams.

## Bibliography

[1] Li VC, Wang S, Wu C. Tensile strain-hardening behavior of polyvinyl alcohol engineered cementitious composite (PVA-ECC). ACI Materials Journal. 2001;98(6).

[2] Li VC, Wu C, Wang S, Ogawa A, Saito T. Interface tailoring for strain-hardening polyvinyl alcohol-engineered cementitious composite (PVA-ECC). ACI Materials Journal. 2002;99(5).

[3] Weimann M, Li VC. Hygral behavior of engineered cementitious composites (ECC). International Journal for Restoration of Buildings and Monuments. 2003;9(5):513-34.

[4] Li VC, Lepech MD, Li M. Field demonstration of durable link slabs for jointless bridge decks based on strain-hardening cementitious composites. 2005.

[5] Maalej M, Leong KS. Engineered cementitious composites for effective FRP-strengthening of RC beams. Composites Science and Technology. 2005;65(7–8):1120-8.

[6] Rokugo K, Kunieda M, Lim S. Patching repair with ECC on cracked concrete surface. Proc of ConMat05, Vancouver, Canada [CD-ROM]. 2005.

[7] Li VC, Li M, Lepech MD. High performance material for rapid durable repair of bridges and structures. 2006.

[8] Esmaeeli E, Manning E, Barros JAO. Strain Hardening Fibre Reinforced Cement Composites for the Flexural Strengthening of Masonry Elements of Ancient Structures. Construction and Building Materials. 2013;38(special issue):1010-21.

[9] Redon C, Li V, Wu C, Hoshiro H, Saito T, Ogawa A. Measuring and Modifying Interface Properties of PVA Fibers in ECC Matrix. Journal of Materials in Civil Engineering. 2001;13(6):399-406.

[10] Kanda T, Li VC. New micromechanics design theory for pseudostrain hardening cementitious composite. Journal of engineering mechanics. 1999;125(4):373-81.

[11] Kesner K, Billington SL. Tension, Compression and Cyclic Testing of Engineered Cementitious Composite Materials. Cornell University, School of Civil and Environmental Engineering, Ithaca, New York 14853; 2004.

[12] Wang S, Li VC. Engineered cementitious composites with high-volume fly ash. ACI Materials Journal. 2007;104(3).

[13] Yang E-H, Yang Y, Li VC. Use of high volumes of fly ash to improve ECC mechanical properties and material greenness. ACI Materials Journal. 2007;104(6).

[14] Li VC, Mishra DK, Wu H-C. Matrix design for pseudo-strain-hardening fibre reinforced cementitious composites. Materials and Structures. 1995;28(10):586-95.

[15] Fischer G, Li VC. Design of Engineered Cementitious Composites (ECC) for Processing and Workability Requirement. In: BMC 7. Poland; 2003:29-36.

[16] Zhang MH, Canmet. Microstructure, crack propagation, and mechanical properties of cement pastes containing high volumes of fly ashes. Cement and Concrete Research. 1995;25(6):1165-78.

[17] Reiner M, Rens K. High-Volume Fly Ash Concrete: Analysis and Application. Practice Periodical on Structural Design and Construction. 2006;11(1):58-64.

[18] BS EN 450-1:2012. Fly ash for concrete - Part 1: Definition, specifications and conformity criteria: European Committee for Standardization.

[19] Domone PL. Self-compacting concrete: An analysis of 11 years of case studies. Cement and Concrete Composites. 2006;28(2):197-208.

[20] Kong H-J, Bike SG, Li VC. Constitutive rheological control to develop a self-consolidating engineered cementitious composite reinforced with hydrophilic poly(vinyl alcohol) fibers. Cement and Concrete Composites. 2003;25(3):333-41.

[21] Malm R. Shear cracks in concrete structures subjected to in-plane stresses. KTH, School of Architecture and the Built Environment (ABE), Civil and Architectural Engineering, Structural Design and Bridges; 2006.

[22] Yang E-H, Sahmaran M, Yang Y, Li VC. Rheological control in production of engineered cementitious composites. ACI Materials Journal. 2009;106(4).

[23] Gomes P, Gettu R, Agullo L, Bernad C. Experimental optimization of high strength self compacting concrete. In: Proceedings of Second International Symposium on SCC. Kochi; 2001:377–86.

[24] Madhuvan S, Kumar KMC, Dattatreya JK. Effect of Superplasticizers Compatibility on the Workability, Early Age Strength and Stiffening Characteristics of OPC, PPC, and PSC Pastes and Mortar. International Journal of Research in Engineering and Technology [IJRET]. 2014;3(15):419-25.

[25] Okamura H, Ozawa K. Mix-design for self-compacting concrete. Concrete library of JSCE. 1995;25:107-20.

[26] Wille K, El-Tawil S, Naaman AE. Properties of strain hardening ultra high performance fiber reinforced concrete (UHP-FRC) under direct tensile loading. Cement and Concrete Composites. 2014;48(0):53-66.

[27] Pereira EB, Fischer G, Barros JAO. Direct assessment of tensile stress-crack opening behavior of Strain Hardening Cementitious Composites (SHCC). Cement and Concrete Research. 2012;42(6):834-46.

[28] Jun P, Mechtcherine V. Behaviour of Strain-hardening Cement-based Composites (SHCC) under monotonic and cyclic tensile loading Part 1 – Experimental investigations. Cement and Concrete Composites. 2010;32(10):801-9.

[29] Kamal A, Kunieda M, Ueda N, Nakamura H. Evaluation of crack opening performance of a repair material with strain hardening behavior. Cement and Concrete Composites. 2008;30(10):863-71.

[30] Benson S, Karihaloo B. CARDIFRC®–Development and mechanical properties. Part III: Uniaxial tensile response and other mechanical properties. Magazine of Concrete Research. 2005;57(8):433-43.

[31] Yu JH, Dai L. Strain rate and interfacial property effects of random fibre cementitious composites. The Journal of Strain Analysis for Engineering Design. 2009;44(6):417-25.

[32] Douglas KS, Billington SL. Rate dependence in high-performance fiber reinforced cementbased composites for seismic applications. In: Int RILEM Workshop on HPFRCC in Structural Applications. 2006;49:17-26.

[33] Yang E, Li VC. Rate dependence in engineered cementitious composites. International RILEM Workshop on High Performance Fiber Reinforced Cementitious Composites in Structural Applications: RILEM Publications SARL; 2006. p. 83-92.

[34] Shrestha J, Ueda T, Zhang D. Durability of FRP Concrete Bonds and Its Constituent Properties under the Influence of Moisture Conditions. Journal of Materials in Civil Engineering. 2014 (Special Issue):A4014009.

[35] Teng J, Chen J, Smith ST, Lam L. Behaviour and strength of FRP-strengthened RC structures: a state-of-the-art review. Proceedings of the ICE-Structures and Buildings. 2003;156(1):51-62.

[36] ACI Committee: 2014. Building code requirements for structural concrete (ACI 318-14) and commentary (ACI 318R-14). American Concrete Institute.

[37] ACI 440.2R-08:2008. Guide for the Design and Construction of Externally Bonded FRP Systems for Strengthening Concrete Structures: American Concrete Institute.

[38] BS EN ISO 15630-1:2010. Steel for the reinforcement and prestressing of concrete. Test methods. Reinforcing bars, wire rod and wire.

[39] ISO 527-2:2012. Plastics – Determination of tensile properties – Part 2: Test conditions for moulding and extrusion plastics.

[40] Arora D. Rapid Strengthening of Reinforced Concrete Bridge with Mechanically Fastened - Fiber Reinforced Polymer Strips [MSc Thesis]: University of Wisconsin – Madison; 2003.

# Chapter 5: Assessment of HCP Efficiency for Seismic Retrofitting Applications [1, 2]

## 5.1 Introduction

This chapter describes and discusses the procedure and the results of an experimental program aimed at assessing the effectiveness of HCP for seismic retrofitting applications. For this purpose, full-scale damaged gravity load designed (GLD) interior RC beam-column joints were repaired by means of attaching HCPs. In this experimental program, for each of the HCP retrofitted specimen there was also a counterpart beam-column joint retrofitted based on cast-in-place SHCC reinforced with NSM-CFRP laminates. Results of these two different retrofitting strategies are also compared and discussed to verify the influence of the interface bond between the retrofitting scheme and the concrete substrate on seismic performance of these repaired beam-column joints.

## 5.2 Experimental Program

The experimental program comprised the retrofitting of four full-scale damaged interior beam-column joints, which were categorized in two main groups. In the first group (group I), two of these specimens were retrofitted by attaching prefabricated HCPs to the exterior faces of their elements, while a technique based on cast-in-place SHCC reinforced with NSM-CFRP laminates was adopted to retrofit the other two beam-column joints, specimens in the second group (group II). In fact, each specimen in the second group was the counterpart of one of the specimens in the first group, but adopting a different retrofitting strategy.

Retrofitting schemes adopted for each of the specimens in a group varied considering the number of the faces of the framed element's that was retrofitted. While, for the beam-column joints in the first group retrofitting scheme was only applied to the front and rear faces of the elements, for the beam-column joints of the second group, all the external faces of the specimens' elements were covered employing the adopted retrofitting strategy.

After retrofitting, these specimens were subjected to the same loading history as previously imposed to their virgin state. To assess the effectiveness of each of the proposed retrofitting solutions, the results determined based on cyclic testing of the retrofitted specimens are compared to those obtained in their virgin state. Furthermore, performance of the retrofitting strategies applied to the specimens in each group is compared with each other. Finally, a comparison between the results obtained from testing each HCP retrofitted specimen with those obtained from the cast-in-place retrofitted counterpart is presented. This latter comparison aims at discussing the influence of two different interfacial bond properties, the interface bond between SHCC and concrete, on the performance of the retrofitted specimens.

### 5.2.1 Damaged Specimens

Four damaged interior RC beam-column joints were selected among a series of tested specimens. These specimens were the subject of an experimental research in the scope of another PhD thesis [3]. Following, a review on the configuration of these specimens, their material properties, the adopted test setup and loading pattern, and a summary of their test results and the observed damages is presented.

### 5.2.1.1 Design Configuration of the Damaged Specimens

Configurations of pre-1970th RC buildings were adopted for the design process of these beam-column joints. Therefore, plain steel bars were used as the reinforcement of beams and columns of these specimens. No transverse reinforcement in the joint region was applied, and 90° hook arrangement was adopted for the stirrups and hoops in beams and columns, respectively. The beams and the columns of these full-scale specimens had a length of the half-span and the half-story, respectively, of common RC buildings. The geometries and steel configurations of the selected specimens for the retrofit, JPA0 and JPC in group I and JPA3 and JPB in group II, are shown in Figure 5.1. It should be noted that the shorter length adopted for the inferior column of the specimens, associated to a steel element with equivalent stiffness, allows to represent the behavior of the assemblage and to accommodate the load cells and pin connection at the bottom of the column, as it is evident in the test setup presented in section 5.2.1.3.
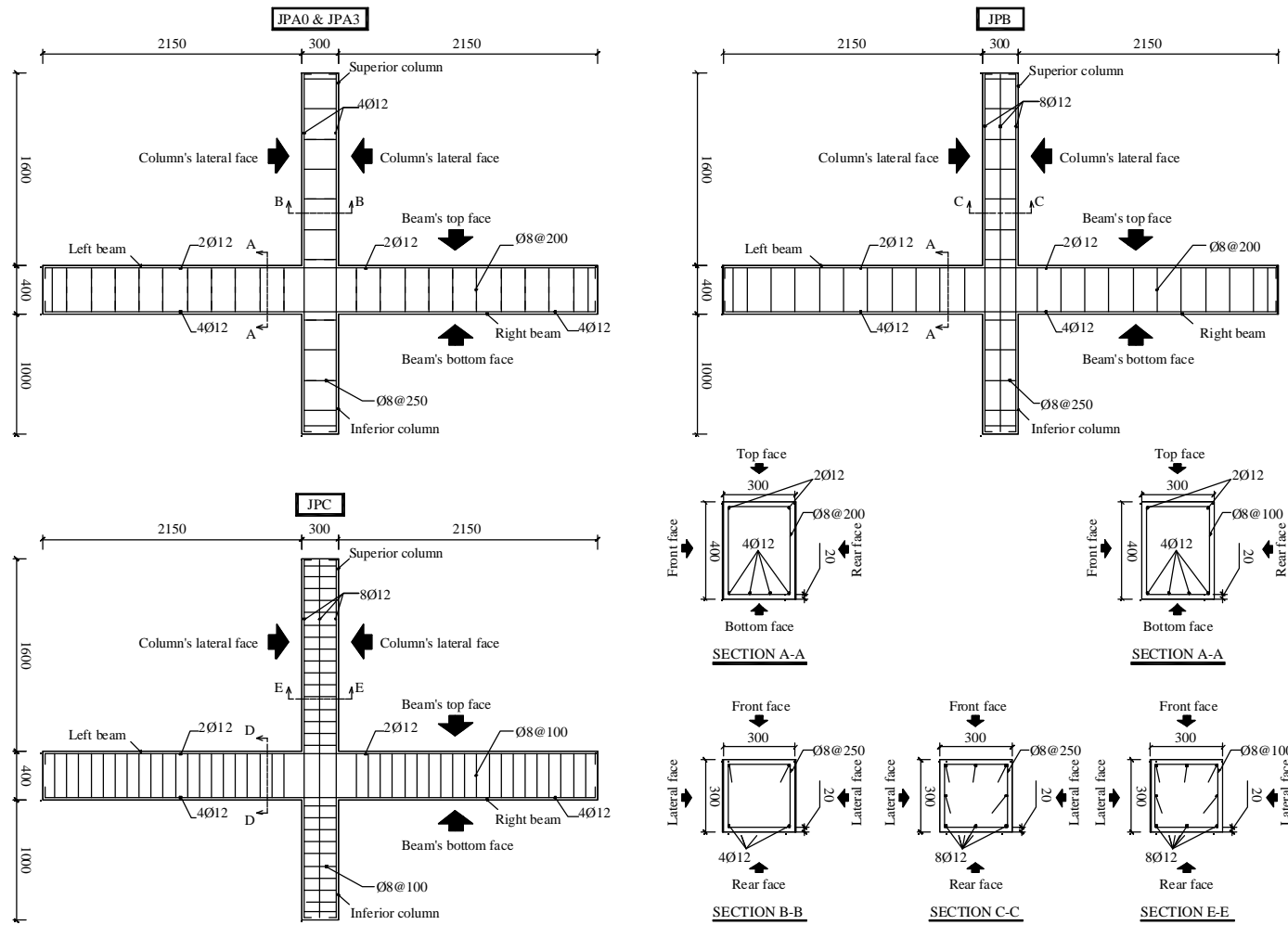
Figure 5.1: Details of the adopted configurations for the interior beam-column joints.

### *5.2.1.2 Material Properties of the Beam-Column Joints*

According to [3], the average concrete compressive strength, measured in cubes of 150 mm edge, was equal to 23.8 MPa with an estimated characteristic compressive strength of 19.8 MPa, corresponding to the C16/C20 concrete strength class according to the grading of EC2 [4]. Longitudinal steel bars were characterized with average values of 590 MPa and 640 MPa, for the yield and the ultimate tensile strength, respectively, and an elasticity modulus of 198 GPa.

### *5.2.1.3 Test Setup and Loading Pattern*

The cyclic tests were conducted at the Civil Engineering Department of the University of Aveiro. A lateral reversal displacement history was imposed to the top of the superior column combined with a constant axial load of 450 kN. This axial force ($N$) represents the gravity load corresponding to an axial compressive stress of 21.3% of the average concrete compressive strength. The lateral load was constituted of a series of displacement-controlled cycles, in push (positive displacement) and pull (negative displacement) direction, with an incremental magnitude up to 4% interstory drift. The concept of the interstory drift is defined as the percentage ratio of the lateral displacement at the loaded end of the column to the total length of column, measured from supported section to the loaded one. After three cycles of loading that introduced a drift level of 0.13%, each level of displacement was repeated three times, as it is shown in Figure 5.2.

The specimens were tested horizontally according to the test setup illustrated in Figure 5.3. The idealized test setup, representing the support and loading conditions, are also depicted in this figure. Since the test specimens were positioned horizontally, four devices of reduced-friction with high-load carrying capacity were arranged to support the specimen's self-weight (see Figures 5.3 and 5.4).

As shown in Figure 5.5 (also see Figure 5.3), the left and right beams were secured, close to their free extremities, by the mechanical rolling devices fixed to the reaction frames. This supporting condition allowed only sliding along the beam's longitudinal axis and in-plane rotations at the supported ends of the beams.

At the lower end of the inferior column, a pinned connection was used to release only the in-plane rotation at this end. The inferior column's vertical and axial reactions were

measured using two load-cells secured to each one of two reaction steel frames at this region (see Figures 5.3 and 5.6).

The lateral displacement was introduced using a hydraulic actuator constrained at one end to the steel reaction frame and at its stroke end to the top of the superior column, using two in-plane rotational pinned connections. To measure the imposed lateral force, this actuator was also equipped to a load-cell (see Figures 5.3 and 5.7).



| Cycle Numbers | $d_c^p$ (mm) | Max drift (%) |
|---|---|---|
| 1 | ±1 | 0.033 |
| 2 | ±2 | 0.067 |
| 3 | ±4 | 0.133 |
| 4 to 6 | ±6 | 0.20 |
| 7 to 9 | ±10 | 0.33 |
| 10 to 12 | ±15 | 0.50 |
| 13 to 15 | ±20 | 0.67 |
| 16 to 18 | ±25 | 0.83 |
| 19 to 21 | ±30 | 1.00 |
| 22 to 24 | ±40 | 1.33 |
| 25 to 27 | ±50 | 1.67 |
| 28 to 30 | ±60 | 2.00 |
| 31 to 33 | ±70 | 2.33 |
| 34 to 36 | ±80 | 2.67 |
| 37 to 39 | ±90 | 3.00 |
| 40 to 42 | ±100 | 3.33 |
| 43 to 45 | ±110 | 3.67 |
| 46 to 48 | ±120 | 4.00 |
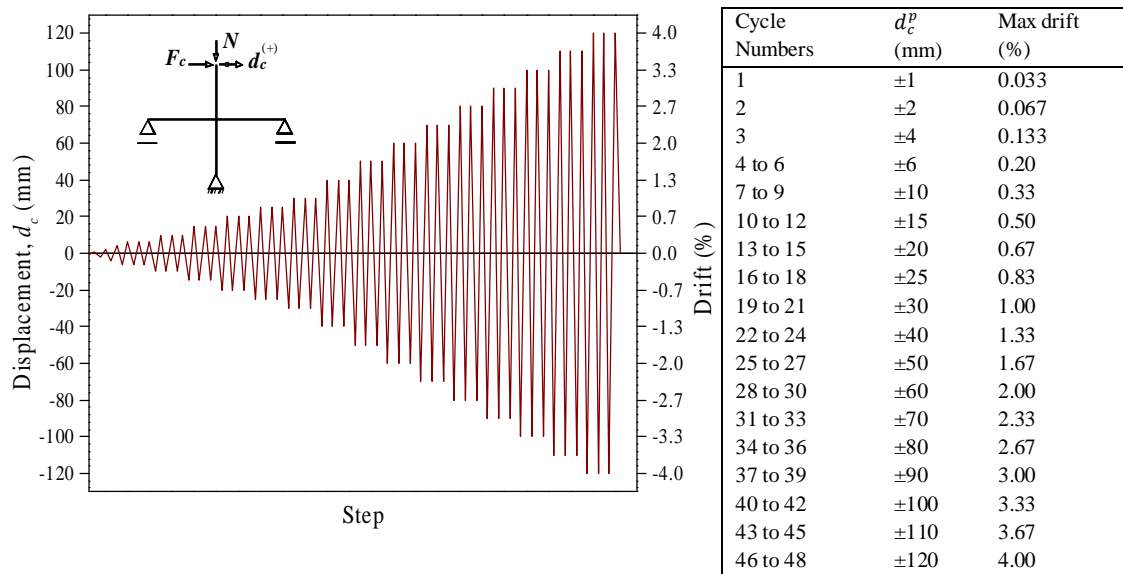
Figure 5.2: Loading history adopted for the lateral displacement cycles ( $d_c^p$ : peak displacement for the corresponding cycle or set of cycles).

According to Figure 5.8 (see also Figure 5.3), to impose axial compressive load to the columns, a pair of pre-stressed threaded steel bars, one at the top and the other below the columns, were used. At the top end of the superior column, a hydraulic-actuator equipped to a load-cell, was embedded. Threaded steel bars were constrained to this actuator which was itself fixed to the top of the superior column. The other end of these threaded bars was constrained to the bottom of the inferior column. Thus, the compressive force of the column was imposed by tensioning these longitudinal steel bars. All the steel reaction frames were fixed to the strong floor employing pre-stressed threaded steel bars.
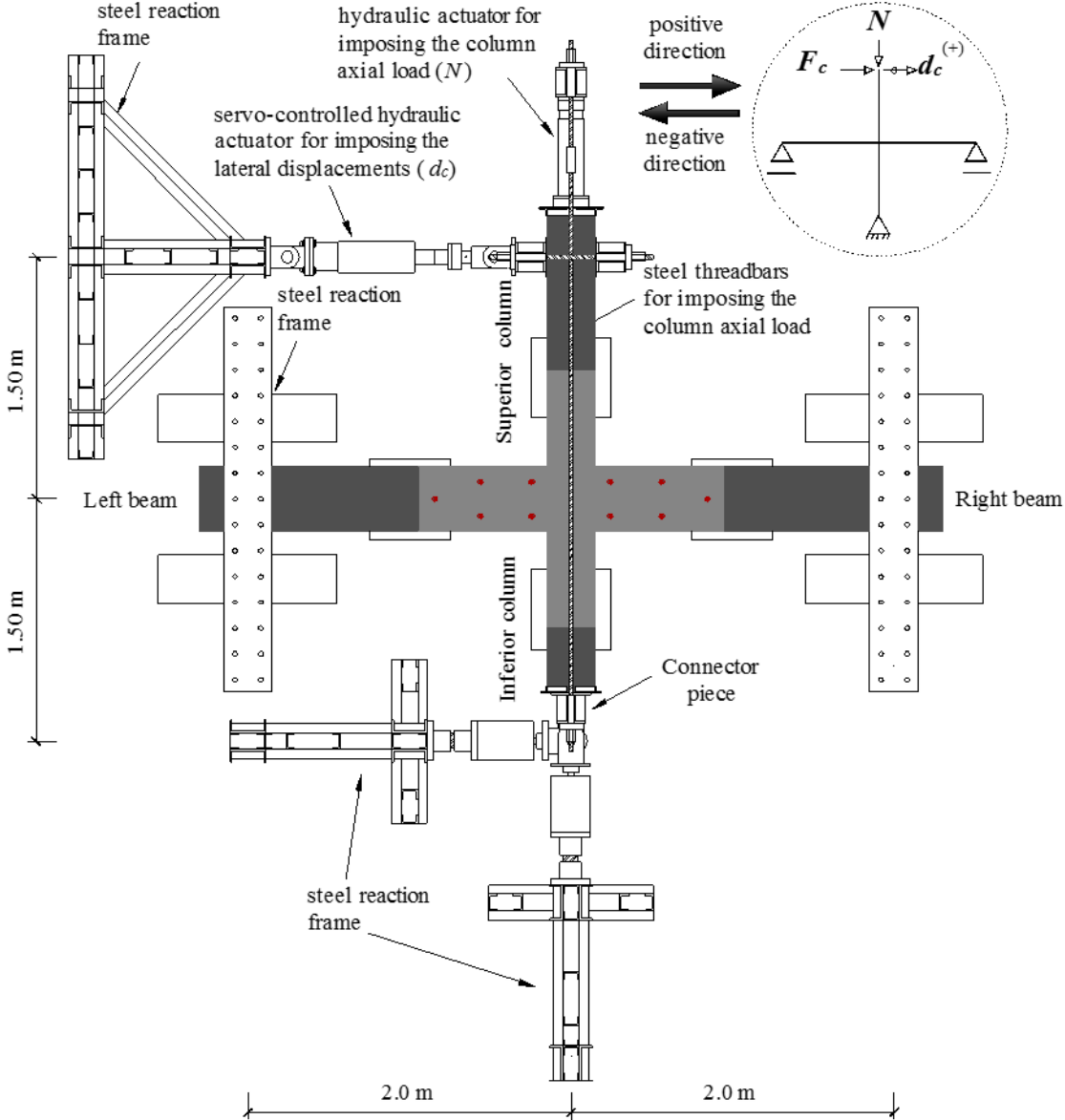
Figure 5.3: Test setup for the horizontally placed specimens [3]
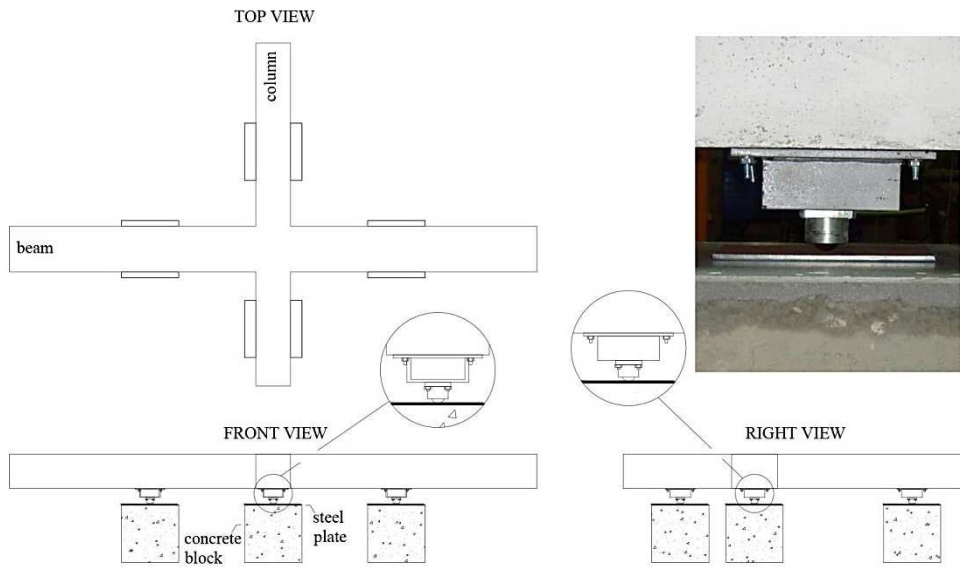
Figure 5.4: Arrangement of the devices used to carry the self-weight of the specimens [3]
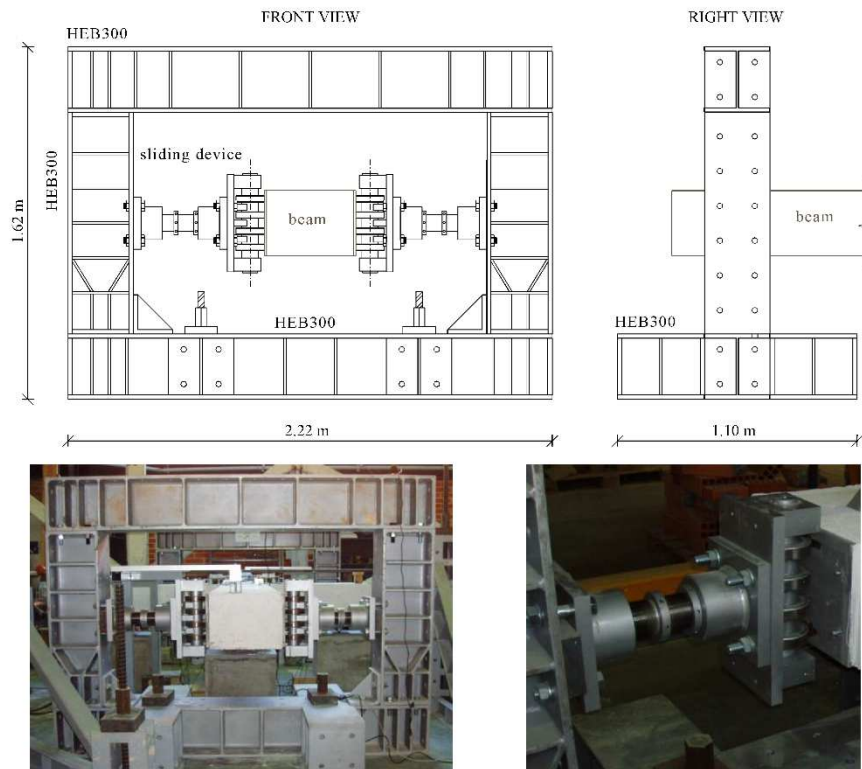


Figure 5.5: Details of reaction steel frames and sliding devices to simulate the boundary conditions at the end of the beams of the specimens [3]
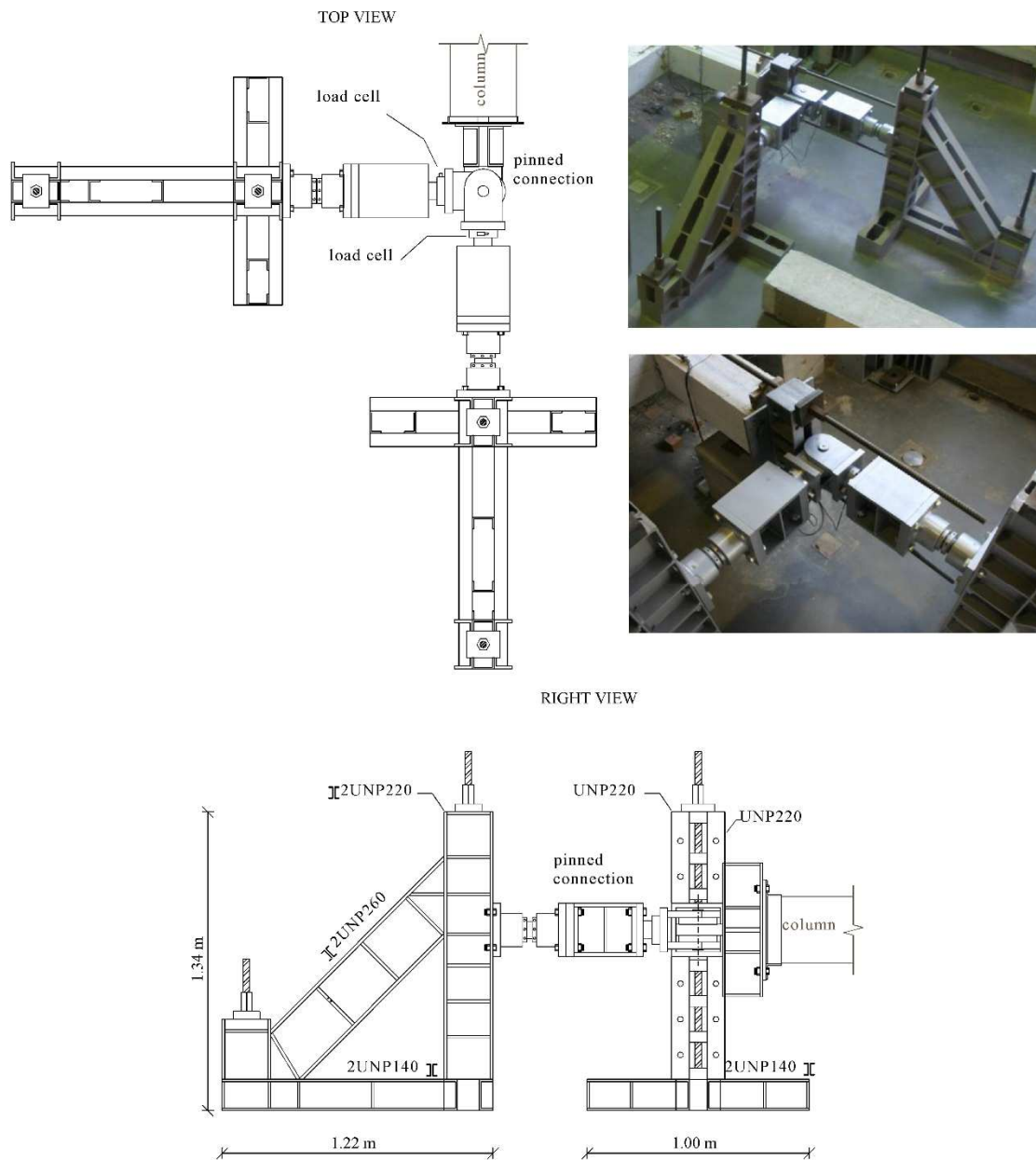
Figure 5.6: Details of steel reaction frames along with load-cells and pinned-connections at the extremity of the inferior column [3]
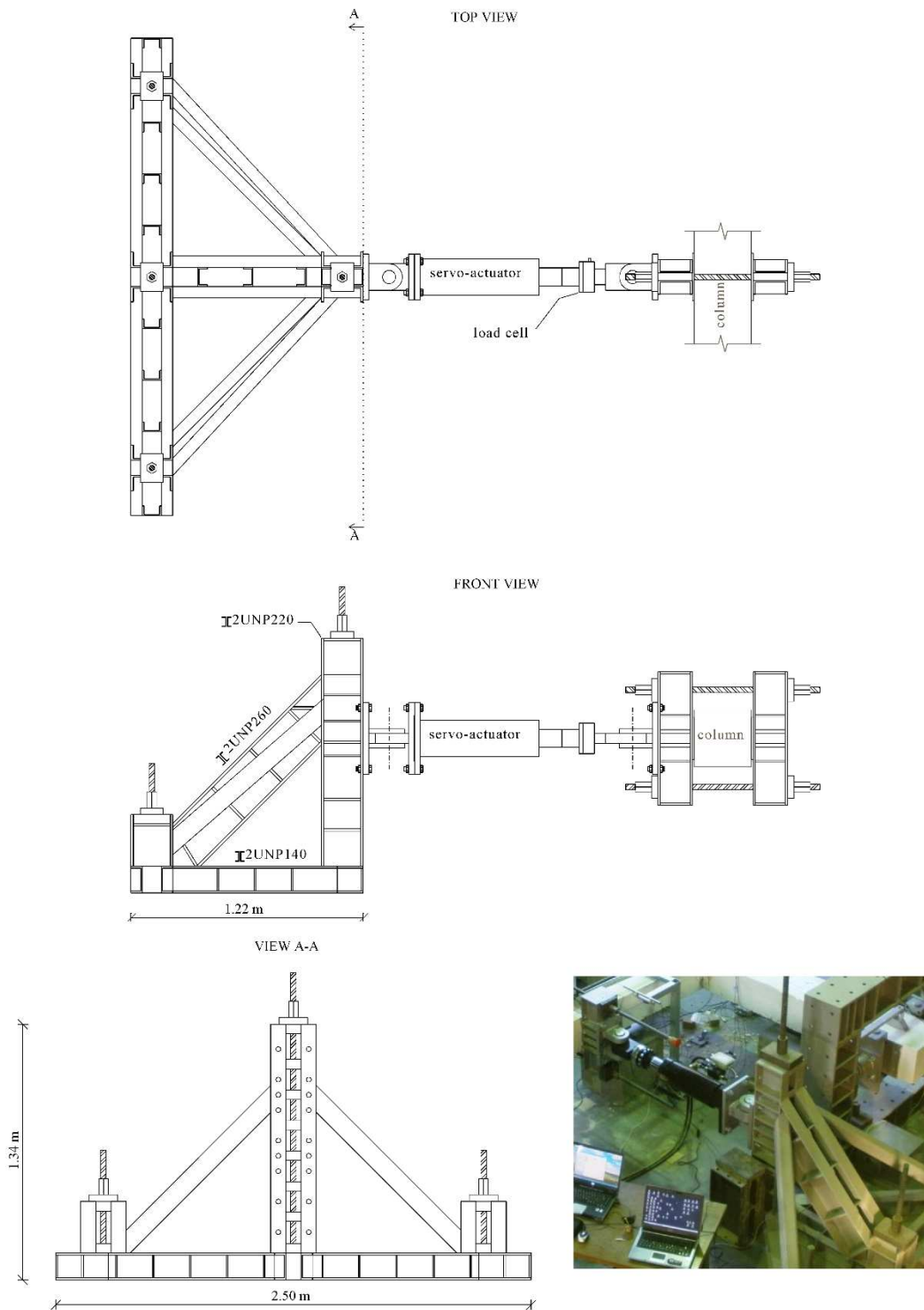
Figure 5.7: Details of steel reaction frames, load-cell and hydraulic servo-actuator at the top extremity of the superior column to apply the lateral displacements [3]
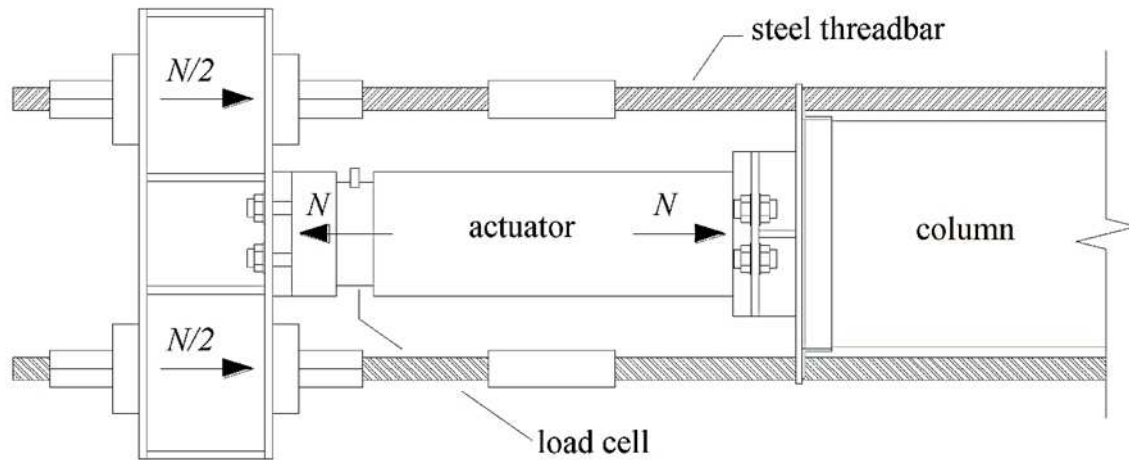
Figure 5.8: Imposing axial force to the column using a pair of pre-stressed threaded steel bars, position of the load-cell and actuator at top of the superior column [3]

### 5.2.1.4 Summary of the Results and Observed Damages

The maximum load carrying capacity of 43.2, 38.3 and 39.5 kN was registered for JPA0, JPC and JPB, respectively, at the drift levels of 2.7%, 3.3% and 2.3%. In the case of JPA3, having identical geometry and steel configuration to specimen JPA0, the test was prematurely terminated because of technical problems. Thus, the behavior of this specimen reasonably assumed to be identical to JPA0.

As consequence of deficient bond between smooth longitudinal bars and the surrounding concrete, the damages at the end of the test were mainly localized in the vicinity of the joint region into the beams and columns.

As shown in Figure 5.9, the extent of the damages includes concrete crushing and spalling off at the intersections of the beams and the columns, severe sliding of longitudinal reinforcement due to significant bond deterioration and, eventually, flexural cracks localized at the beam-joint interfaces or its vicinity on the beam. Despite JPA0 that had localized damages at column-joint interfaces, in the other specimens there were only minor flexural cracks at this regions. Specimen JPA3 had also experienced damages concentrated in its joint region.

JPA0

JPA3

JPB

JPC
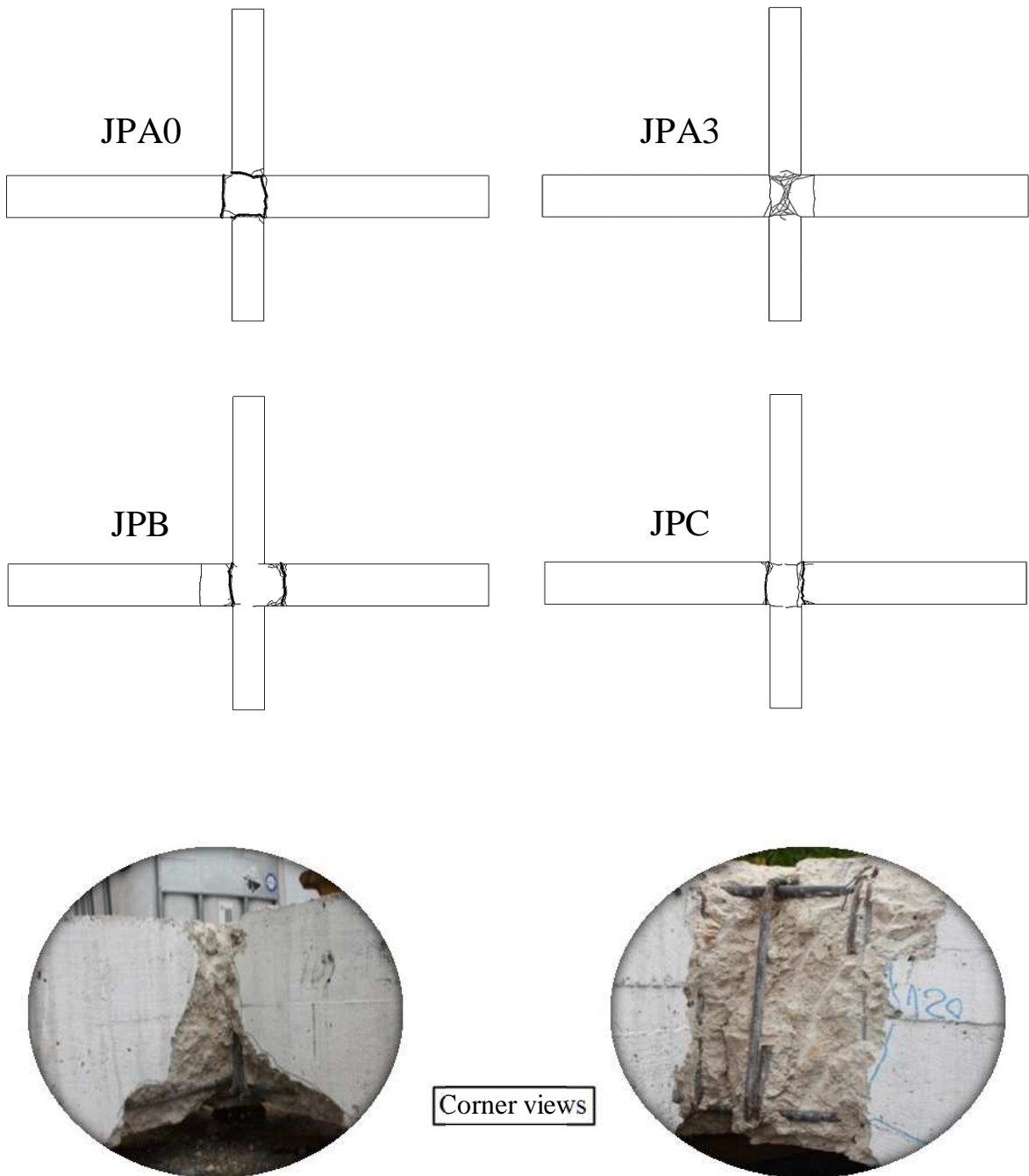
Corner views

Figure 5.9: Plan view of schematic presentation of damages in the selected beam-column joints along with typical damages observed in corner views of the specimens

### 5.2.2 Retrofitting Strategies

#### 5.2.2.1 Prefabricated Solutions

The retrofitting schemes for the both damaged specimens in group I, JPA0 and JPC, were based on attaching cross shape HCP$^{(L)}$s to the front and rear faces of the beam-column joint. However, in the case of JPC, additional "L" shaped HCP$^{(S)}$s were also attached to the lateral faces of the beam-column joint at each corner.

The retrofitting length for both beams and columns was assumed twice of the section depth of the corresponding element. Thus, HCPs have partially covered the overall length of the specimens (Figure 5.10).

In the case of cross shape HCP$^{(L)}$s, the depth of the sections covering the beams was 390 mm, while for the columns was 290 mm. The HCP$^{(L)}$ had an overall thickness of 25 mm, which was sufficient to accommodate two layers of CFRP laminates of cross section of 10 mm×1.4 mm, in two different levels (in orthogonal directions). This configuration provided a 5 mm protecting cover against the environmental actions for the epoxy used to fix CFRP laminates inside the grooves of the HCP$^{(L)}$. The grooves were cut with 5 mm of width, and 10 or 20 mm of depth, depending on the level that CFRP laminates were supposed to be placed (Figure 5.10c).

The longitudinal reinforcement of the HCPs included pairs of continuous laminates in the direction of beam's and column's axis (Figures 5.1a to 5.1c). Consequently, the laminates located in the beams were placed in a different level than the ones of the columns. In the HCP$^{(L)}$s used to retrofit JPA0, the spacing of the transverse CFRP laminates was 100 mm (Figure 5.10a). This distance was maintained in the portions of the HCP$^{(L)}$s that were covering the columns of the JPC-R specimen, while in those parts of HCP$^{(L)}$s covering the beams of this specimen the spacing of the transverse CFRP laminates was increased to 200 mm in order to take into account the smaller spacing of steel stirrups in the beams (Figure 5.10b). At the joint region of both series of the HCP$^{(L)}$s, pair of CFRP laminates forming an "X" shape configuration was mounted in an attempt of increasing the shear resistance of the joint.

194

A combination of the S&P 220 epoxy resin and chemical anchors (Hilti HIT-V 8.8 with 10 mm diameter) was used as the attaching system for the "Cross shape" HCP[(L)]s to the concrete substrate.

As it was already mentioned, for the case of JPC, HCP[(S)]s with an "L" shape configuration were attached to the lateral faces of the columns and the top and bottom faces of the beams at each corner (Figure 5.10d). In the HCP[(S)]s, also epoxy resin and chemical anchors (Hilti HIT-V 8.8 with 10 mm diameter) were used to fix these panels to the lateral faces of beams and columns. To the retrofitted JPC and JPA0 specimens, the nomination of the JPC-R and JPA0-R was attributed, respectively.

All the retrofitting process was performed with the specimens in horizontal position. For both specimens the remaining crushed and spalled off concrete at the corners of the joints was removed and then replaced with Sika Grout-213.

To seal the cracks, boreholes were drilled through the cracked sections. After cleaning the holes using compressed air, small diameter pipes were placed inside them, then the exposed crack development at the concrete substrate was sealed and then epoxy resin SikaDur-52 was injected through these pipes. After turning the specimens, the sealing process was repeated to assure that the cracked section was sealed as much as possible.

The concrete substrate was also slightly roughened using hand-held concrete scabbler to partially expose the aggregates. This surface roughening aims at improving the HCP-concrete interface bond properties.

Prior to the installation of the HCPs, chemical anchors were mounted inside the holes perforated on the beams, columns and joint regions, at the positions represented in Figure 5.10. Before mounting the anchors, the holes were partially filled with Hilti Hit-HY 200-A as a fast curing injectable bonding agent.

Before testing the specimens, a torque of 30 N·m was applied to fasten the nuts and partially confine the concrete substrate. The embedded length of the anchors inside the concrete was 115 mm. Figure 5.11 shows a view of the specimens after the HCPs have been applied.
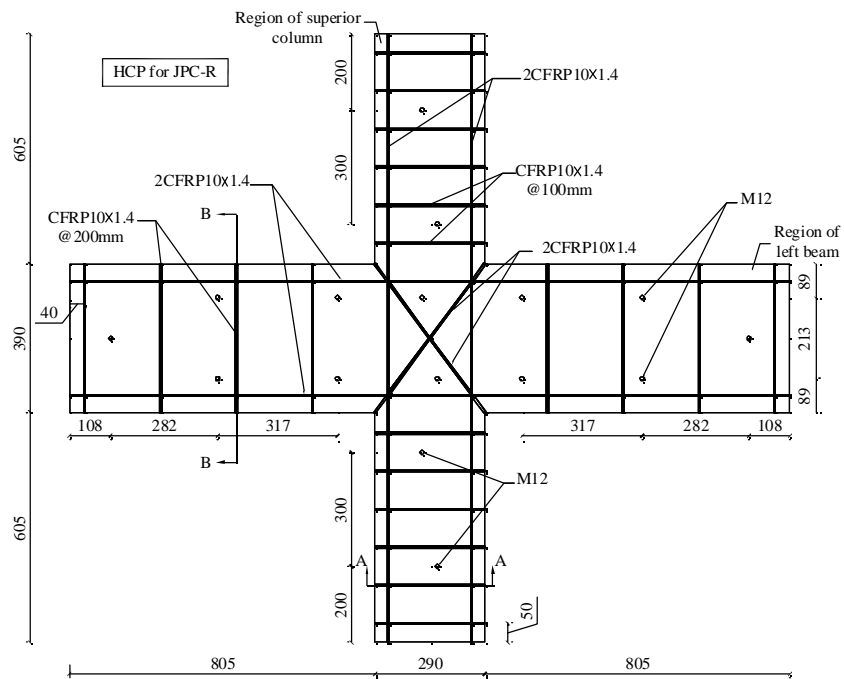
(a)
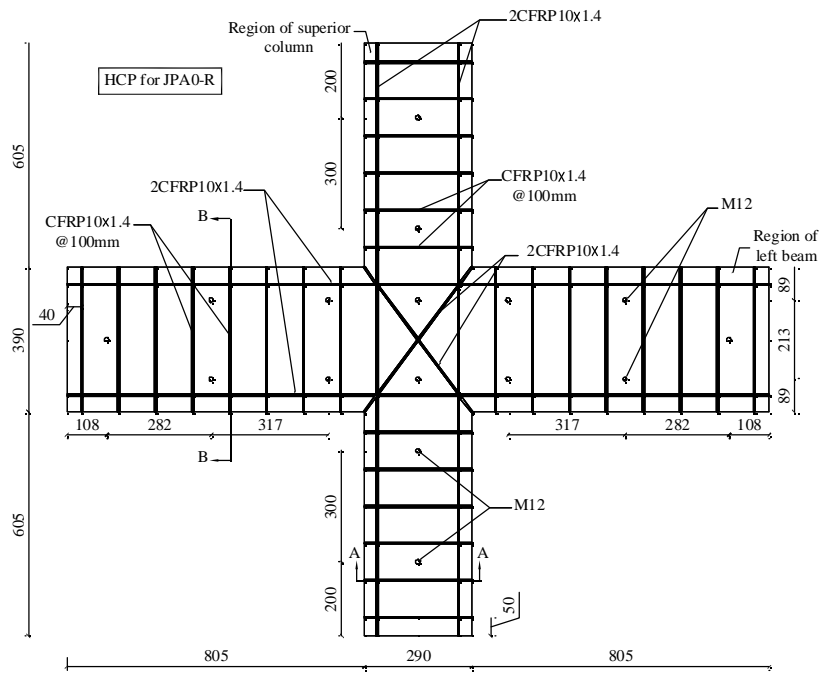
(b)

Figure 5.10: Details of the HCPs used for the repair of the damaged specimens (a) cross shape HCP[(L)] for JPA0-R, (continued in the next page)

CFRP Laminate (Longitudinal)
Epoxy Resin
SHCC Plate
CFRP Laminate (Transverse)

10
5
35  110
15

SECTION A-A

(Transverse) CFRP Laminate
150  45
10
15
SHCC Plate  CFRP Laminate (Longitudinal)  Epoxy Resin
5

SECTION B-B

(c)

Unidirectional Carbon Fabric Bonded to the Backside of the Plates

SHCC Plate (Column Part)

SHCC Plate (Beam Part)

108  140  300  150  200  200  200  190
75
108  M12
555  755
35  35

Expanded Top View of the "L" Shape HCP

25
One layer of bonded CFRP sheet
555
SHCC plate for the column
SHCC plate for the beam
755
25
790

Lateral View of the "L" Shape HCP

(d)

(Cont'd from Figure 5.10), (b) cross shape HCP$^{(L)}$ for JPC-R, (c) section views of the cross shape HCP$^{(L)}$s, and (d) "L" shape HCP$^{(S)}$ for JPC-R

.
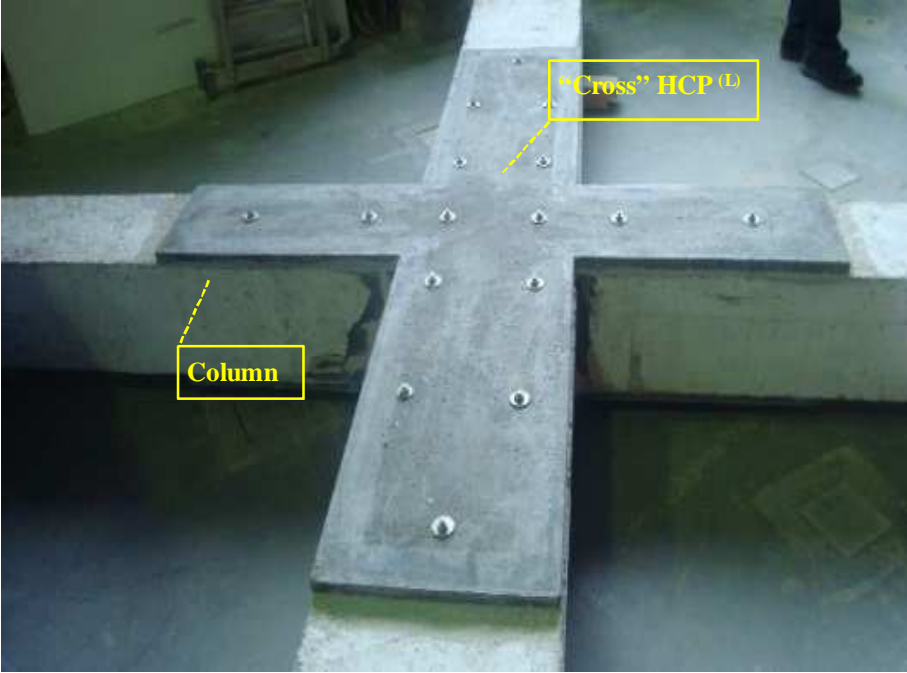


(a)
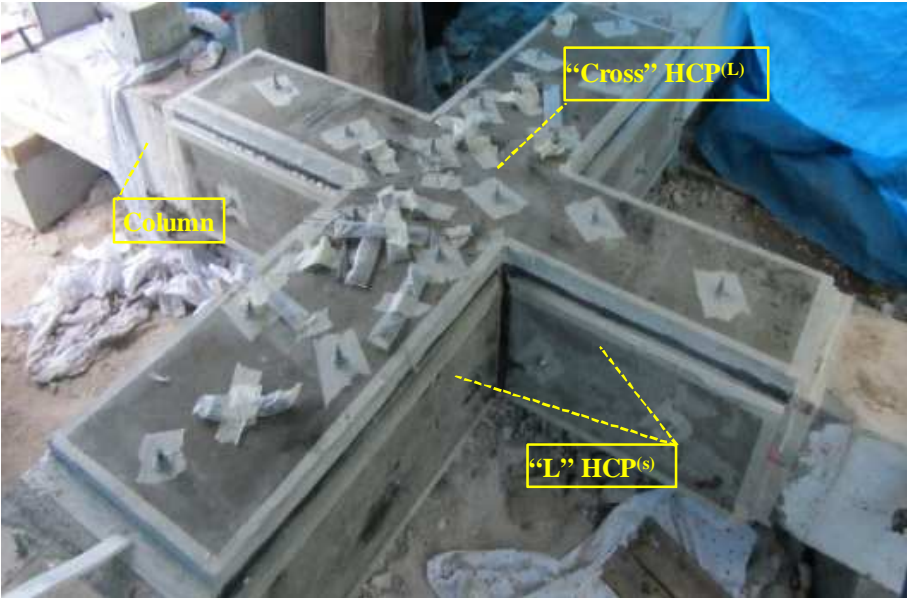


(b)

Figure 5.11: View of the retrofitted specimens of group I, (a) JPA0-R and (b) JPC-R.

### 5.2.2.2 Cast-in-Place Solution

According to the adopted retrofitting strategy for the specimens in group II, JPA3 and JPB, the concrete cover at critical regions of the damaged beam-column joints is replaced with a thin layer of a casted-in-place SHCC. Afterward, this layer of the SHCC was reinforced with CFRP laminates bonded to the saw cut grooves on that according to the NSM technique. Chemical anchors were used to improve inter-laminar shear stress transference between the SHCC and the concrete substrate.

To the retrofitted JPA3 and JPB specimens, the nomination of the JPA3-R and JPB-R was attributed, respectively. As mentioned before, the adopted retrofitting schemes for the specimens differed according to the number of faces of their elements which was retrofitted. While in JPA3-R only the front and rear faces of beams, columns and joint were retrofitted, in JPB-R all the external faces of the mentioned elements were jacketed.

Following this strategy, JPA3-R and JPA0-R were assumed to be the cast-in-place counterpart solutions for JPA0-R and JPB-R, respectively.

Similar to prefabricated solutions, the retrofitting process of the specimens in the second group was also applied with the specimens positioned horizontally and in two steps: (i) before and (ii) after turning the specimens. Following the details of each step of the cast-in-place retrofitting strategies are described.

### 5.2.2.2.1 Concrete Cover Removal and Replacement

Details of the retrofitting schemes are presented in Figure 5.12. The retrofitting length for both beams and columns was taken as twice of the section depth of the corresponding element, similar to the prefabricated solutions. Hence, using a jackhammer concrete cover was removed in the joint region and also in all lateral faces of the beams and columns of both specimens for a length of 800 and 600 mm, respectively. The concrete cover was initially removed up to a depth to expose the longitudinal reinforcements. Afterward, in an effort to increase the interface area between casted-in-place materials and existing steel bars, the removal of the concrete cover continued up to attain approximately half of the diameter of the longitudinal bars. Similar to the procedure explained for the retrofitting of the specimens in group I, the existing cracks were sealed by injecting epoxy resin SikaDur-52 before and after turning the specimens.

Wooden formworks with interior varnished faces were installed to cast the cement based materials. The lateral faces of columns and the top and bottom faces of the beams of JPA3 were casted using a mortar that was then cured for 7 days (see Figure 5.1 for the nomination of the faces of the elements of the beam-column joints). After this period of curing, the top edges of the hardened mortar were roughened and fresh SHCC was placed.

For the case of JPB, a continuous placing of SHCC starting from lateral faces of the columns and the top and bottom faces of the beams, and then moving to the front face of the specimen was followed.

Considering the variation in the thickness of the existing concrete cover, between 16 and 20 mm, and a minimum of 20 mm thickness required to accommodate two layers of CFRP laminates in the SHCC layer, a 5 mm higher finishing level for the SHCC was adopted, as measured from the level of the existing concrete cover at the extremities of the retrofitted regions.

The self-compacting characteristic of the SHCC and its high fluidity eliminated the need to any external vibration. Only the exterior face of the fresh SHCC was levelled using a thin long metal bar, with a rectangular cross section, for the finishing purpose. It should be noted that before casting the cement based materials, the concrete substrate was saturated with water in order to assure a better interface bond and a lower risk of developing shrinkage cracks.

One day after casting the SHCC the formworks were removed. A wet curing procedure was followed for at least 7 days. After at least 17 days of casting the SHCC, grooves were executed on the SHCC according to the configurations showed in Figure 5.12. Finally, following the strategy discussed in section 4.5.1, the CFRP laminates were bonded into the cut grooves.

After turning the specimens the same retrofitting process was applied to the rear face; namely: removal of the concrete cover, sealing of the cracks, roughening the top edges of newly casted materials, placing the fresh SHCC, curing of SHCC, cutting the grooves and inserting CFRP laminates.

For the case of JPB the grooves were also cut on the SHCC casted on the lateral faces of columns and the top and bottom faces of the beams, and pair of CFRP laminates was bonded into these grooves according to Figure 5.12. Therefore, for the case of JPA3-R, the longitudinal reinforcement comprised pairs of continuous laminates on each of the front and rear faces of the beams and columns (see Figure 5.12), while JPB had a similar CFRP retrofitting but also with extra pairs of CFRP laminates bonded to the each of the lateral faces of its columns, and the top and bottom faces of its beams. CFRP laminates bonded to the lateral faces of the beams and columns were continued beyond the interface of these elements with the joint region, where the occurrence of the largest bending moments is expected (moment critical sections). For this purpose, an inclined drilling was used to execute the holes. After placing the CFRP laminates, the epoxy resin was injected. The bond length of 100 mm was adopted for these CFRP laminates after moment critical section (anchorage length), since a minimum of 90 mm is characterized as the required bonding length to fully mobilize potential tensile strength of this type of CFRP laminates [5].

The adopted spacing for transverse CFRP laminates in both JPA3-R and JPB-R was 100 mm (Figure 5.12). Similar to the case of the specimens with prefabricated solutions, in an attempt to increase the shear resistance of the joint region, a pair of CFRP laminates with an X shape configuration was applied on each front and rear face of the joint region of both specimens.

### 5.2.2.2.2 Installing Chemical Anchors

Chemical anchors were installed before and after turning the specimens, when the SHCC was cured at least 20 days. 10 mm diameter anchors (HIT-V-8.8 M10X190) were mounted inside the holes perforated on the beams, columns and on the joint region, using the same strategy adopted for the specimens in group I, at the positions represented in Figure 5.12. An embedded length of 145 mm was assured for the anchors, measured from the finished surface of SHCC. Finally, a torque of 30 N·m was applied to fasten the nuts and partially confine the concrete substrate. Figure 5.13 shows a view of these specimens after have been repaired.
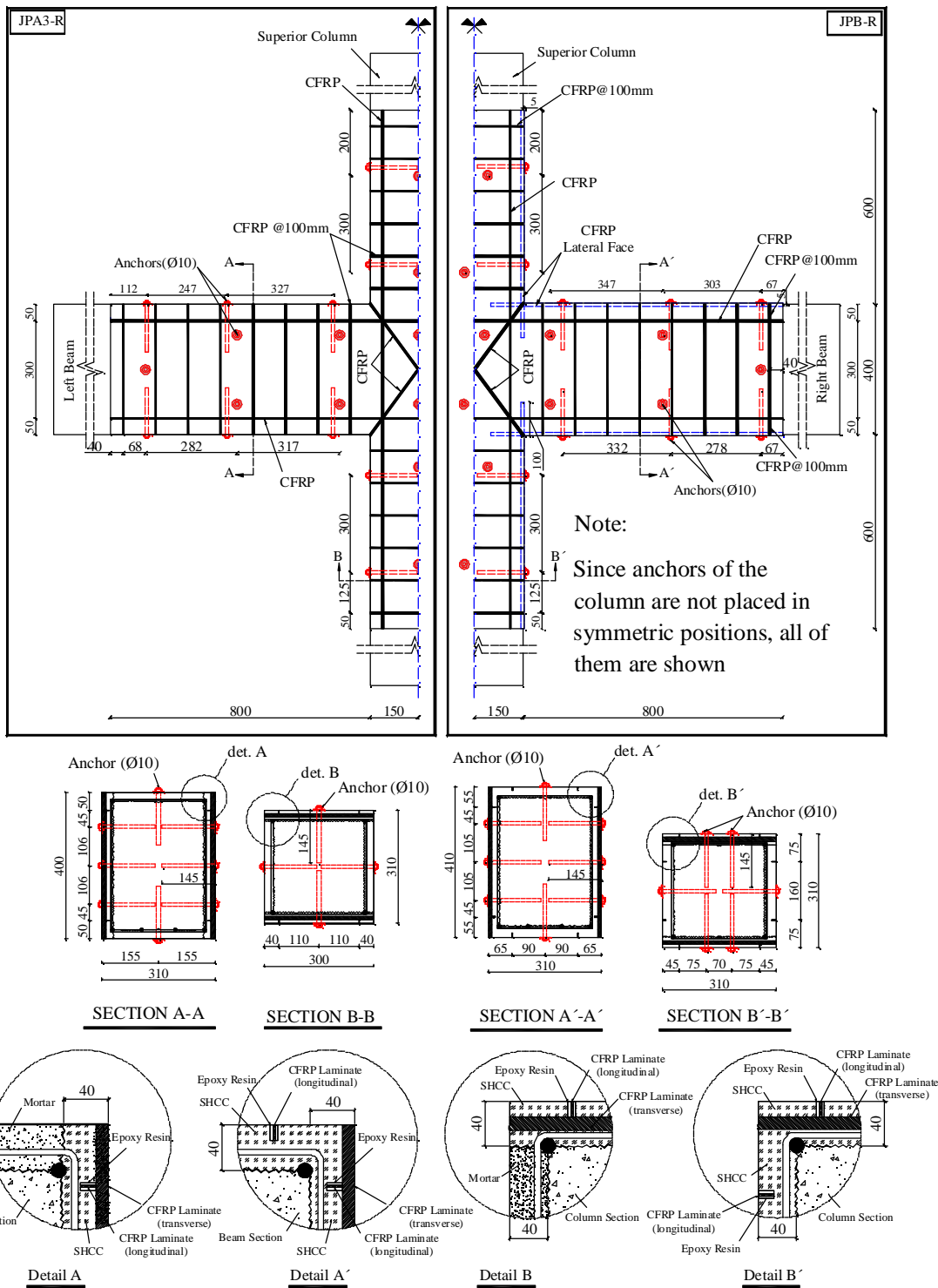
Figure 5.12: Details of the schemes used for the retrofitting of the damaged specimens (dimensions in mm)
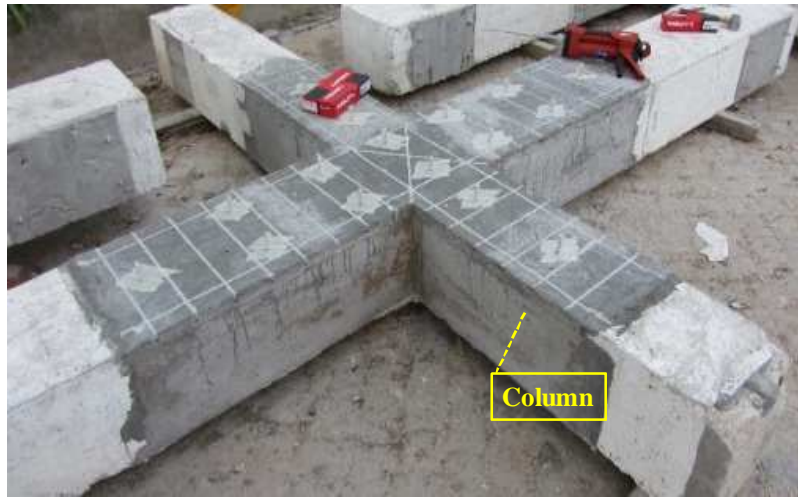
(a)



(b)

Figure 5.13: View of the retrofitted specimens of group II, (a) JPA3-R, and (b) JPB-R

### 5.2.3 Material Properties of Retrofitting System

### 5.2.3.1 SHCC

Details on fresh and hardened state properties of the self-compacting PVA-SHCC (mixture C4W30) used in casting the SHCC plates can be found in section 4.3.

### 5.2.3.2 CFRP

Tensile properties of the used CFRP laminate (S&P laminate CFK 150/2000) with a cross section of 1.4 mm ×10 mm were characterized following the procedures proposed in ISO 527-5:2009 [6]. From the tests executed in six coupons, average values of 2689 MPa, 1.6% and 165 GPa were obtained for the tensile strength, strain at CFRP rupture and modulus of elasticity, respectively.

Carbon fabrics (S&P C-Sheet 240) were cut from the same roll used to prepare HCP$^{(S)}$ for the strengthening of the short-span shear-critical beams in section 4.5. Tensile characteristics of this fabric are reported in section 4.5.3.5.

### 5.2.3.3 Epoxy Adhesives

The mechanical characteristics of the S&P Resin 220 epoxy adhesive$^®$, used to bond CFRP laminates into the grooves of the SHCC and also to bond the strengthening plates to the soffit of the beams, are reported in section 4.5.3.4.

### 5.2.3.4 Cementitious Grout

The average compressive strength of 38.4 MPa for SikaGrout-213 was obtained by means of compression tests on four cubes of 100 mm edge.

### 5.2.3.5 Chemical Anchors

Hilti$^®$ chemical anchors are composed of a fast curing resin HIT-HY 200A and the steel anchor rods. According to the classification of the steel grade 8.8 of the ASTM, the anchor rods, HIT-V-8.8 M10X190, has characteristic tensile yield strength of 640 MPa and characteristic tensile ultimate strength of 800 MPa. Based on the technical datasheets provided by the manufacturer, an average ultimate tensile load and ultimate shear load of 46.6 kN and 23.2 kN is expected for this type of anchor rods.

### 5.2.4 Test Setup and Loading Pattern

The same test setup, cyclic lateral load history and axial load in the columns used for testing the virgin specimens were adopted for testing the retrofitted ones. Figure 5.14 shows the schematic configuration of the displacement transducers (DTs) mounted on the top face of the specimens to measure the local deformations. Four slices along each beam and each

column were considered for this purpose. The axial deformation of each region, along the longitudinal CFRP laminates, was registered using a parallel pair of DTs installed in each slice. By combining diagonal, vertical and horizontal DTs in the joint region, the distortion of the panel of the joint was also evaluated.
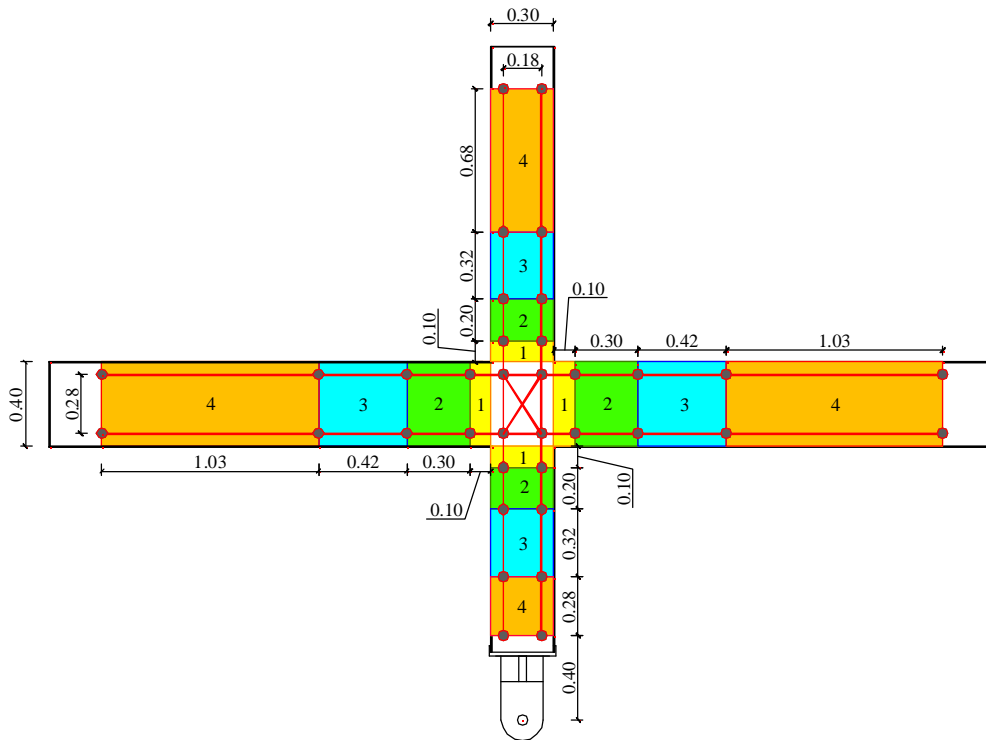


Figure 5.14: Geometry of the slices assumed on each specimen to assess local deformations (the nodes are representing the regions where the displacement transducers were supported; dimensions in mm).

## 5.3 Results and Discussion

### 5.3.1 Hysteretic Response

The hysteretic response in terms of lateral load *versus* lateral displacement (and drift), registered at the top of the superior column of each retrofitted specimen in groups I and II, are depicted in Figures 5.15 and 5.16, respectively. For the comparison purpose, the hysteretic response corresponding to the virgin state of each retrofitted specimen is also included in its corresponding graph. Moreover, the values registered for the maximum lateral

load ($F_m$) and the corresponding drifts ($d_m$) for specimens in the retrofitted and virgin states, together with the percentage of the enhancement in the lateral peak load obtained after retrofitting, are reported in Table 5.1.

Following, discussions on hysteretic responses of the retrofitted specimens *versus* the virgin ones and the responses of the specimens retrofitted with the HCP *versus* the cast-in-place solution, based on the abovementioned results, are presented.

Table 5.1: Maximum lateral load capacity and the corresponding drifts of the specimens in the retrofitted and virgin states

| Group | Specimen | Negative direction $F_m^-$ (kN) | $d_m^-$ (%) | Positive direction $F_m^+$ (kN) | $d_m^+$ (%) | Negative direction Increase in peak load (%) | Positive direction | $\alpha_{4\%}^*$ (%) |
|---|---|---|---|---|---|---|---|---|
| Group I | JPA0-R | -52.6 | -2.65 | +51.2 | +2.31 | +25.5 | +18.2 | 15.7 |
| | JPA0 | -41.9 | -2.31 | +43.3 | +2.60 | | | 24.4 |
| | JPC-R | -57.2 | -1.65 | +56.8 | +2.64 | +54.5 | +48.3 | 39.8 |
| | JPC | -36.7 | -2.94 | +38.3 | +3.25 | | | 10.5 |
| Group II | JPA3-R | -38.0 | -1.65 | +40.9 | +1.65 | -9.3 | -5.5 | 19.6 |
| | JPA3 | -41.9 | -2.31 | +43.3 | +2.60 | | | 24.4 |
| | JPB-R | -52.7 | -1.62 | +57.14 | +2.33 | +48.9 | +44.5 | 25.6 |
| | JPB | -35.4 | -1.99 | +39.55 | +2.24 | | | 10.5 |

$\alpha_{4\%}$ is the average degradation in peak load at 4% drift (the average of positive and negative loading directions). This degradation in each loading direction is equal to $[1 - (F_{4\%}/F_m)]\%$, where $F_{4\%}$ is the residual lateral load carrying capacity at 4% drift of the considered loading direction.
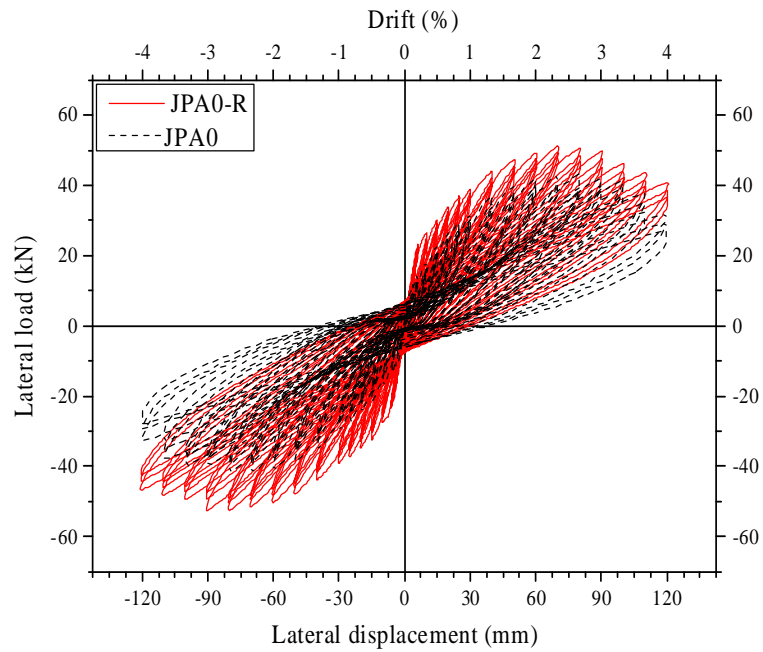
(a)
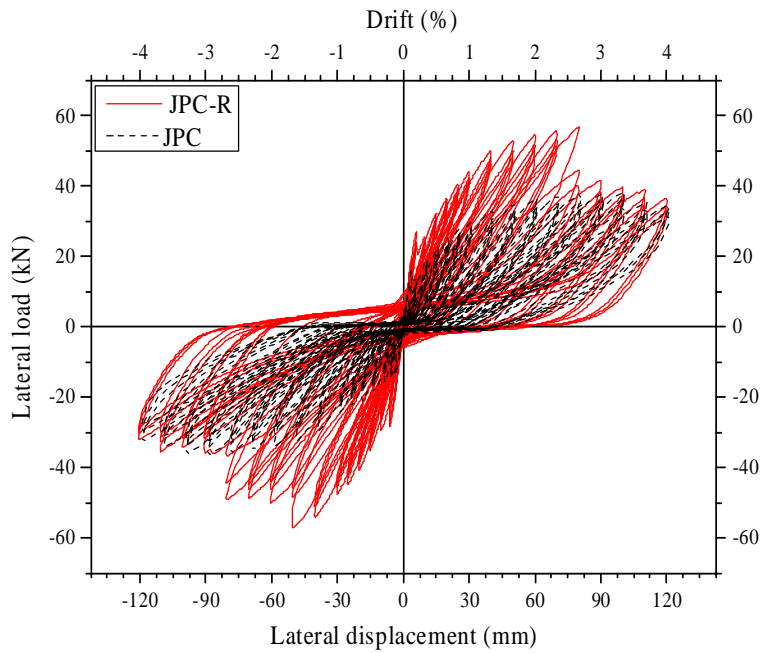


(b)

Figure 5.15: Hysteretic responses of the specimens (a) JPA0-R and (b) JPC-R in the retrofitted and virgin states
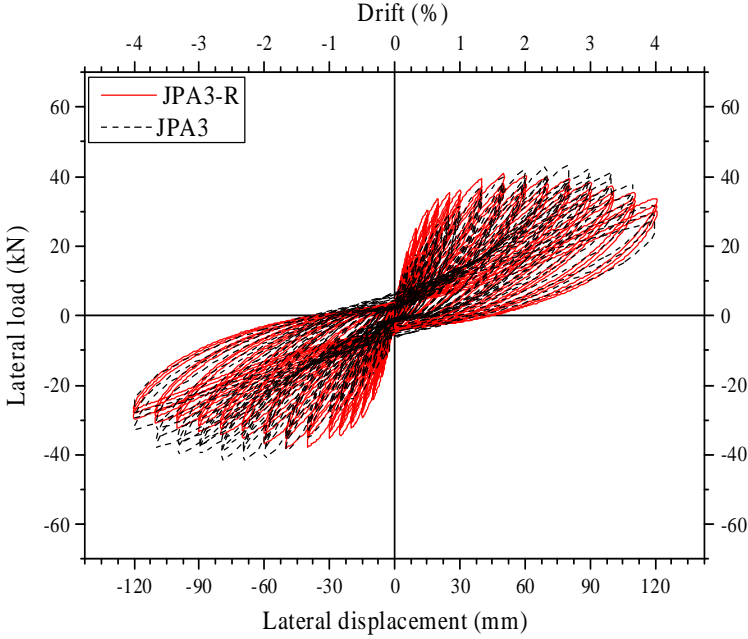
(a)
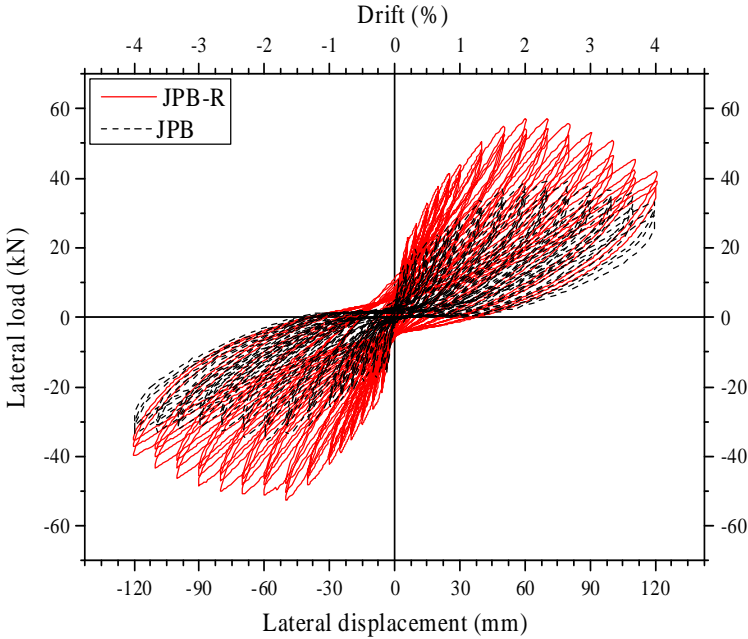


(b)

Figure 5.16: Hysteretic responses of the specimens (a) JPA3-R, and (b) JPB-R in the retrofitted and virgin states

Prefabricated solutions: as shown in Figure 5.15, the hysteretic responses of both JPA0-R and JPC-R indicate successful retrofitting solutions, since in comparison with the results obtained with the corresponding specimen in the virgin state, higher load carrying capacities were obtained. By using the proposed retrofitting technique, the pinching effect observed in the reversal loops of JPC was also slightly improved.

According to the results presented in Table 5.1, the prefabricated retrofitting technique provided an increase of 25.5% and 18.2% in terms of maximum lateral load carrying capacity of JPA0 for the negative and positive displacement, respectively. The corresponding values for JPC-R are even larger, so that an increase of 54.5% and 48.3% was obtained for the negative and positive direction, respectively. A relatively different hysteretic response for the positive and negative loading directions of JPC-R is correlated to an unsymmetrical damage distribution, which is further discussed in the next sections.

Cast-in-place solutions: as shown in Figure 5.16, the retrofitting techniques adopted for JPA3-R and JPB-R, resulted in stable loops with smooth decay of load carrying capacity in the post-peak stage of the structural response.

According to the results indicated in Table 5.1, the cast-in-place retrofitting technique adopted for JPA3-R recovered up to 93% of the maximum lateral load carried out by this specimen in its virgin state, calculated as the average load in the positive and negative directions. Applying the cast-in-place retrofitting technique to all lateral faces of the framed elements, as was done in JPB-R, resulted in a significant increase in terms of lateral load carrying capacity. This increase was +48.9% and +44.5% for negative and positive directions, respectively, when compared to the corresponding values recorded in the virgin state of this specimen (JPB).

For both the cast-in-place retrofitting techniques average value of the drift corresponding to the maximum lateral load, in negative and positive direction, has decreased. This can be attributed to a lower shear deformation at the joint region due to the contribution of the retrofitting scheme in confining the concrete of the joint core, and also in increasing the shear stiffness of the joint panel, up to the peak load.

### 5.3.2 Damage Evolution and Failure Modes

<u>Prefabricated solutions</u>: Figures 5.17 and 5.18 shows the damages registered at the end of the test on the front face of specimens JPA0-R and JPC-R. The damage evolution and failure modes of these specimens are described in the following paragraphs.

JPA0-R: initiation of the first series of cracks was at the cycles corresponding to a drift of 0.33%. These cracks were formed at the bottom face of the left beam and also at the bottom and top face of the right beam at the vicinity of the first series of the anchors, almost inside slice 2 (see Figure 5.17 and also Figure 5.14).

Further increase in the displacement demand led to the formation of a crack crossing the section of the right beam, while in the left beam the relevant damage seems to have become restricted to the increase of the crack's width on the beam's bottom face.

Although a single crack was formed on the lateral faces of the beams, during their widening up to a drift of 1.3%, multiple hairline cracks were formed on the surface of HCP$^{(L)}$ at the vicinity of the locations of these cracks. At cycles corresponding to 1% drift, diagonal cracks started to appear at the beam-column intersections. By further increase in the amplitude of the drift cycles, these inclined cracks started propagating toward the opposite corners forming an "X" shape crack pattern coinciding with the inclined CFRP laminates positioned in the joint of the HCP (Figure 5.17).

When the drift cycles reached the value of 1.3%, horizontal and vertical cracks started to appear inside the joint region, between the intersections of longitudinal CFRP laminates of the beams and columns. At the drift of 2.0%, the retrofitted corners at the intersection of beams and columns started to spall off. The widening and propagation of the cracks inside the joint region may have governed the failure mode of the JPA0-R specimen.

The visual inspection of the joint panel after the test revealed the bulged faces of the HCP$^{(L)}$s in the joint region with "X" shape cracks along with crushing of the old concrete, which was confined inside the HCP$^{(L)}$s. Thus, joint shear failure was identified as the failure mode of the JPA0-R.
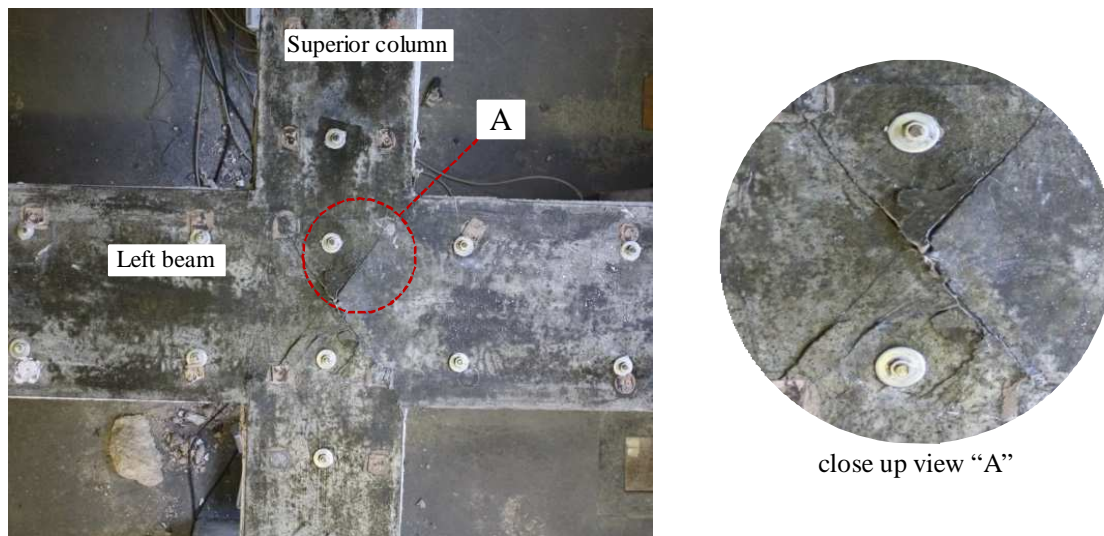
Figure 5.17: Inclined cracks and bulging of the joint region of JPA0-R at the end of the test.

JPC-R: the onset of the first crack was at the $2^{nd}$ cycle of the set of cycles corresponding to 0.2% of drift in negative direction. This crack was formed at the top face of the right beam, on its un-retrofitted portion, in a distance of 80 mm far from the extremity of the retrofitted region. During the positive displacement of this drift level, a second crack was also observed out of the retrofitted region, at a distance of 40 mm far from the extreme edge of the HCPs on the top face of the left beam. At 0.33% of negative drift, the first crack has progressed in terms of length and width. At the same level of drift but in the positive direction, a third crack was formed at the bottom face of the right beam in a distance approximately equal to the crack which was already formed at the top face of this beam.

During the following cycles, the propagation of the existing crack on the left beam seems to have been restricted by the presence of the HCP, while the existing cracks on the right beam have propagated up to become connected. It should be noted that, since the sliding of the longitudinal bars of both beams was restricted by the adoption of 90° bend extremities for these bars, further increase in displacement demand, up to 1.67% drift, was followed by higher load carrying capacity. This higher load is a consequence of the moment redistribution towards other regions of the beam-column assembly not so damaged.

During both the positive and the negative displacements of the cycles corresponding to 1% drift, further cracks on both the left and right beams adjacent to the beam-column

interfaces were formed (Figure 5.18). The sequence of the cracks occurrence was at: i) bottom face of the left beam; ii) bottom face of the right beam; iii) top face of the right beam; iv) top face of the left beam. By increasing the drift up to 1.3%, these cracks on the left beam intersected each other. The crack on the bottom face of the right beam has widened and propagated, while the crack at the top face in this region has only experienced a small increase in its width. This was due to the action of the previously cracked region of the right beam out of the retrofitted zone, which acted as the governing damage region on the right beam. By repeating the cycles with the same level of the drift, the cracks at the vicinity of the beam-column interfaces progressed into the bonded region of the CFRP sheet on the left side of the superior and inferior column, as well as towards the right side of the inferior column. When the drift cycles corresponding to 1.67% were imposed, this detachment progress met the first level of anchors positioned in the superior and inferior columns. Further detachment of the CFRP sheet in normal and tangential directions was resisted by the flexural resistance of the SHCC plate and bearing capacity of the anchors, respectively. At a drift cycle of 2.67% the SHCC plate reached its flexural-tensile capacity and failed. At the higher levels of drift, only the width of these cracks has increased without any further crack formation. Thus, flexural capacity of the beams was the governing failure mode of JPC-R

By the end of the test, to visualize the developed micro-cracks, the surface of the HCPs that was varnished before testing, was sprayed with a penetrating liquid. As a result of this technique, it was visible multiple diffuse micro-cracks inside the joint panel zone with diagonal orientation, fish spinal shape micro-cracks along the longitudinal CFRP laminates on the HCP[L], and diffuse micro-cracks in the vicinity of macro-cracks around the anchors in the joint region and in the first slice of both beams (see Figure 5.18 and also Figure 5.14).
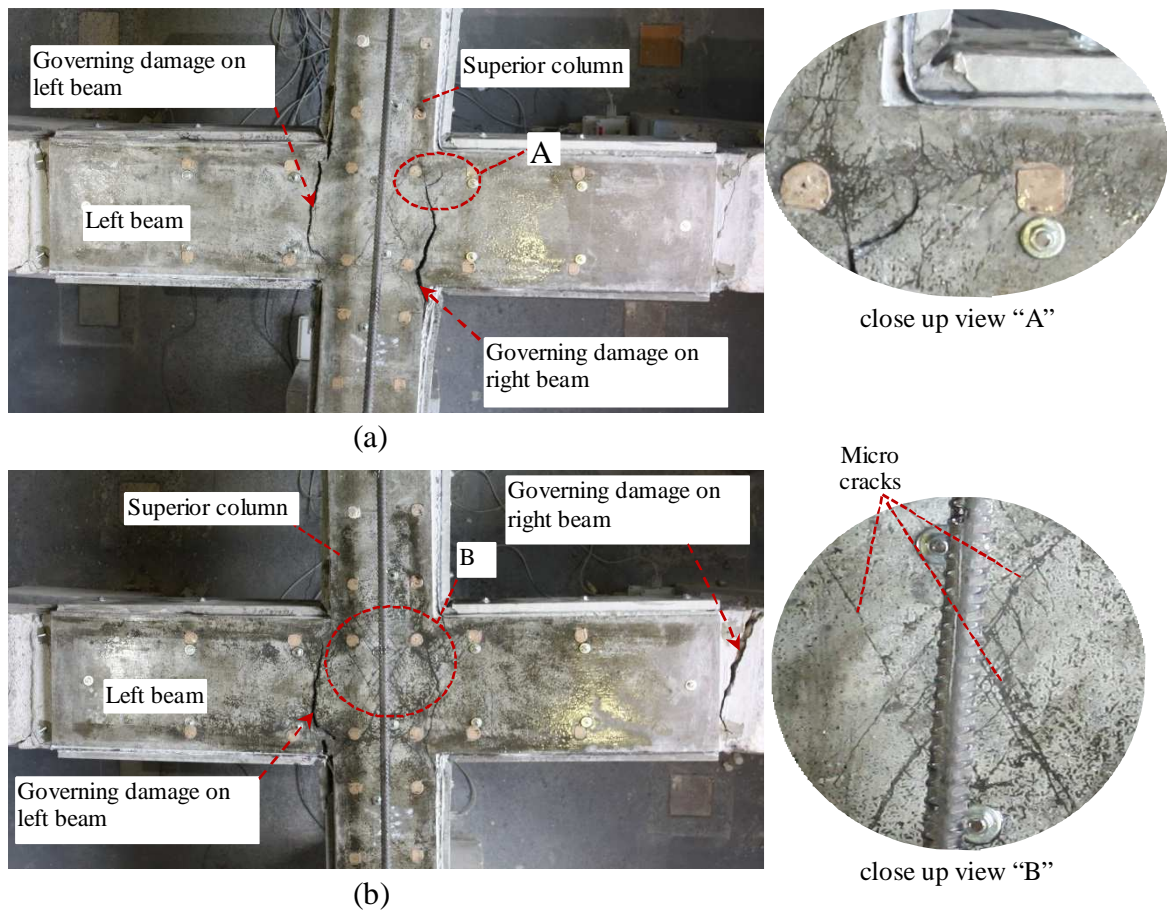
Figure 5.18: Damage distribution along the beam-column joint elements with close up views of micro-cracks at the end of testing of the JPC-R corresponding to (a) positive loading direction, and (b) negative loading direction

when failure mode of JPC-R (beam' flexural failure) is compared to that observed in JPA0-R (joint shear failure), the performance of the "L" shape HCP(S)'s in reducing the shear stresses of the joint panel of JPC-R is revealed. In fact, in the case of JPC-R, due to the continuity of the retrofitting system at the junction of the beams and columns, where they are subjected to the largest bending moments, the "L" shape panel was submitted to high tensile stresses, mainly due to the contribution of the CFRP sheet. The effectiveness of the bond adhesive and anchors, as well as the flexural capacity of the SHCC plate, have assured a proper medium for the transference of these tensile stresses to the interior of the beam and column (therefore lower shear stress were transferred to the joint region) by preventing the

progressive detachment of the CFRP sheet. In fact the detachment of the CFRP sheet has only propagated up to the position of the first anchor in the column.

Cast-in-place solutions: Figure 5.19 shows the pattern of the developed micro cracks, and major damages registered at the end of the test on the front faces of specimens JPA3-R and JPB-R. The schematic representation of these damages is showed at the left side of the corresponding photo for the purpose of better assessment of the developed damage. The damage evolution is described in the following paragraphs.



(a)



(b)
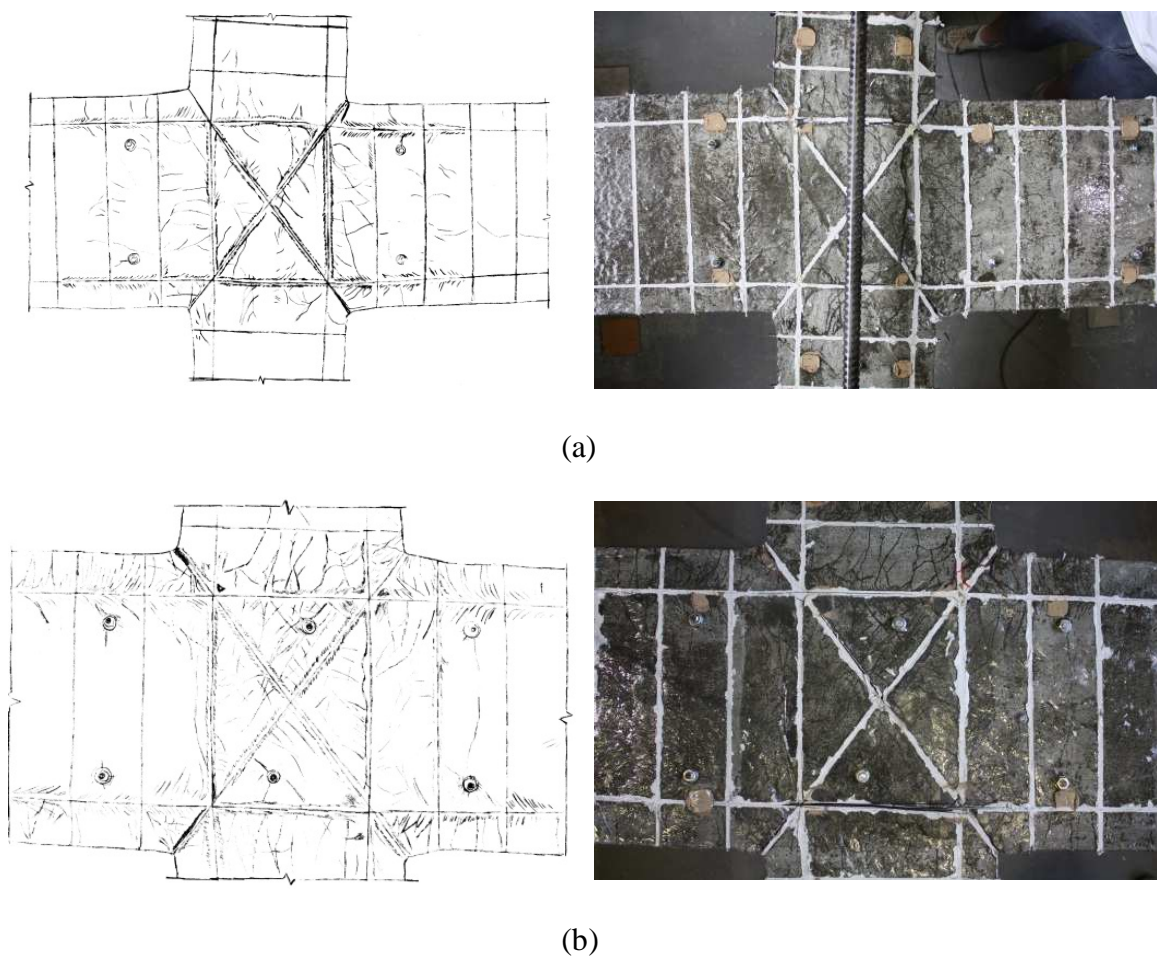
Figure 5.19: Damage propagation at the failure of (a) JPA3-R and (b) JPB-R

JPA3-R: the first series of cracks has initiated at the cycles corresponding to 0.33% of drift. These cracks were formed at the top face of the left and the right beams at a distance of 100 mm from the lateral faces of the column (interface of slice 1 and 2). At cycles

corresponding to 0.5% of drift, cracks at the bottom faces of both left and right beams, symmetric to the cracks on top face, were observed. Some relative sliding between retrofitting layer and concrete substrate was observed when cycles of 0.83% drift were reached.

The first series of the inclined cracks at the junction of the beams and columns was observed in all four corners at the cycles corresponding to 1% of drift. Further increase in the lateral displacement at the top of the superior column resulted in the progress of these cracks into the interface of the epoxy adhesive/SHCC of the bonded "X" shape CFRP system at the joint region. Thus, for any larger displacement demand, damages were localized at the joint region in the form of progressive separation between the epoxy adhesive and the SHCC. Finally, at drift cycles of 1.67%, due to the load reversal effects, the debonding was almost progressed along the entire length of the elements of the "X" shape CFRP configuration. As a consequence of this debonding, a total loss in contribution of these inclined CFRP laminates as a part of shear resisting mechanism of the joint region was occurred. Thus, shear failure of the joint region was the governing failure mode of JPA3-R.

JPB-R: The onset of the first series of cracks was at the set of cycles corresponding to 0.5% of drift. These cracks were formed at the top and bottom faces of the left and right beams in a distance of approximately 90 mm far from lateral faces of the column (inside slice 1, see Figures 5.19 and 5.14). The inclined cracks at the junction of the beams and columns were initially formed at cycles corresponding to a drift level of 0.83%. Similar to the case of JPA3-R, these set of cracks resulted in a progressive debonding along the interface of epoxy adhesive/SHCC of the "X"-shaped CFRP system at the joint region. At drift cycles of 1.67% this debonding was already progressed along the entire length of the inclined CFRP laminates. At the same cycles, the longitudinal steel bars at the top face of the right beam started to have significant sliding, so that the concrete cover perpendicular to the bended end of these bars was cracked. As it will be discussed in section 5.3.3, sliding of these rebars resulted in degradation of flexural capacity of the beams when the top face of them was in tension. The non-symmetrical response of JPB-R, in negative and positive loading directions, can be caused by this phenomenon. At the next sets of the cycles, corresponding to 2% of drift, the already cracked concrete cover over the bended portion of

these bars was spalled off. Afterward, any further increase in drift demand just followed by widening of the existing "X"-shaped cracks at the joint region. Therefore, the shear failure at the panel of the joint resulted in degradation of lateral load resistance of JPB-R in both negative and positive loading directions.

### 5.3.3 Flexural Capacity of Beams

When the flexural capacity of the columns and the shear capacity of the beams and columns are adequate, the failure mechanism of the interior beam-column joints depends either on the flexural capacity of the beams subjected to reversal loadings (the case of JPC-R) or the shear capacity of the joint panel (the case of JPA0-R, JPA3-R and JPB-R). Equation (5-1) presents the state of the static equilibrium between the maximum developed moments at the left and the right beams with respect to the lateral force at the top of the column.

$$Vc = \frac{M^R + M^L}{L_c} \qquad (5\text{-}1)$$

where $Vc$ is the shear force in the column, $M^R$ and $M^L$ are the values of the internal bending moment developed at the beam-column interfaces of the right and the left beam, respectively. The sign of the bending moment is assumed positive when the bottom face of the beam is in tension and negative when this face is in compression. In this equation, $L_C$ is the total length of the column between its lateral supports. According to Equation (5-1), any reduction in the flexural capacity of the left or right beams may result in the loss of lateral capacity of the beam-column assembly, unless this reduction could be compensated through the moment redistribution to other parts of the structure.

The maximum moments (at the mid-section of slice 1 on the left and the right beams) *versus* the drift demands were calculated by considering the force values registered in the load cells and equilibrium conditions, and the obtained results are illustrated in Figure 5.20 and Figure 5.21. Note that in these figures, for the convenience of understanding, the multiplied value of $M^L$ by -1 is presented. Thus, the beams´ bending moments corresponding to the negative and the positive loading directions are presented in the first and the third quadrants of Cartesian system, respectively (see the schematic representation in Figure 5.20 and Figure 5.21).

The registered maximum bending moments for these specimens during both the positive and the negative loading displacements are indicated in Table 5.2. Corresponding values for their virgin state and the percentage of the increase in their flexural capacities achieved after the retrofitting are also reported in this table. In Table 5.2, $M^{L^+}$, $M^{L^-}$, $M^{R^+}$ and $M^{R^-}$ indicate the positive and negative bending moments in the left or right beams. According to the adopted convention, a positive moment corresponds to the case that the bottom face of the beam is in tension whilst the moment is negative if this face is in compression.

Table 5.2: Maximum bending moments developed in the beams of the retrofitted and the virgin specimens.

| Group | Specimen | Negative direction | Positive direction | | | Negative direction | Positive direction | | |
|---|---|---|---|---|---|---|---|---|---|
| | | Absolute values | | | | Variation | | | |
| | | $M^{L^+}$ (kN.m) | $M^{R^-}$ (kN.m) | $M^{L^-}$ (kN.m) | $M^{R^+}$ (kN.m) | $\Delta M^{L^+}$ (%) | $\Delta M^{R^-}$ (%) | $\Delta M^{L^-}$ (%) | $\Delta M^{R^+}$ (%) |
| Group I | JPA0-R | +92.95 (-3.00)* | -54.03 (-2.65) | -52.11 (+2.31) | +90.69 (+2.99) | +22.5 | +34.5 | +30.8 | +13.4 |
| | JPA0 | +75.85 (-2.32) | -40.16 (-2.32) | -39.84 (+2.59) | +79.95 (+2.59) | | | | |
| | JPC-R | +114.13 (-2.66) | -55.58 (-1.65) | -51.09 (+2.64) | +106.4 (+2.64) | +61.3 | +74.8 | +47.5 | +45.1 |
| | JPC | +70.75 (-3.28) | -31.79 (-2.94) | -34.64 (+1.94) | +73.34 (+3.25) | | | | |
| Group II | JPA3-R | +65.94 (-1.64)* | -39.6 (-1.64) | -43.04 (+1.65) | +71.17 (+2.65) | -13.1 | -1.4 | +8.0 | -11.0 |
| | JPA3 | +75.85 (-2.32) | -40.16 (-2.32) | -39.84 (+2.59) | +79.95 (+2.59) | | | | |
| | JPB-R | +108.81 (-2.62) | -57.16 (-1.62) | -55.64 (+1.66) | +107.46 (+2.33) | +56.2 | +79.4 | +62.2 | +41.8 |
| | JPB | +69.68 (-4.0) | -31.87 (-1.99) | -34.30 (+2.58) | +75.78 (+2.44) | | | | |

* Values in parentheses indicate the corresponding drift in percentage at maximum bending moment.

(a)

(b)
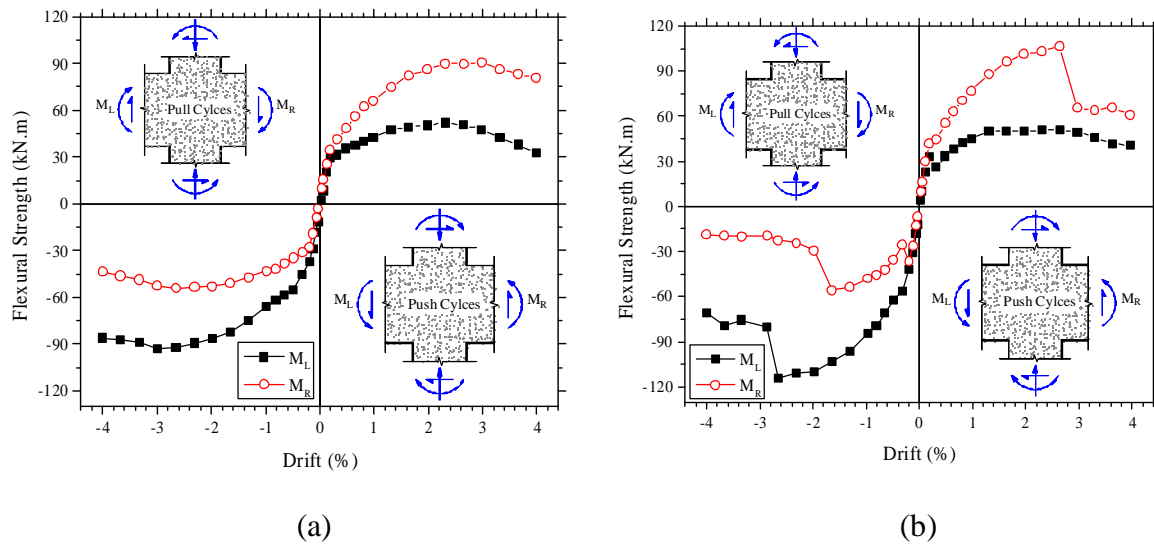
Figure 5.20: Development of the resisting bending moment at the interfaces of the beams with columns for specimen (a) JPA0-R and (b) JPC-R



(a)

(b)
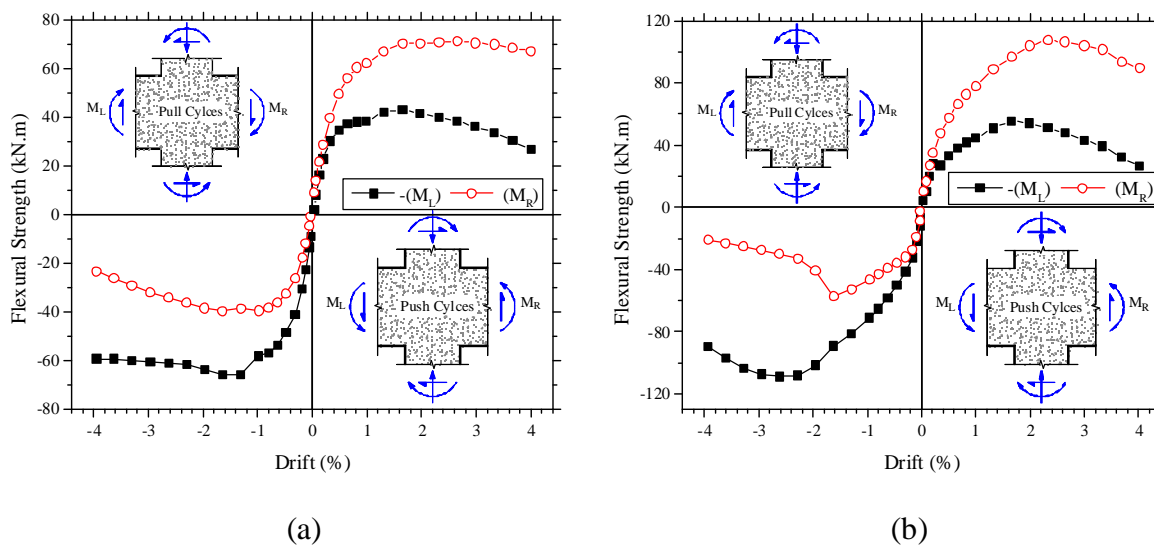
Figure 5.21: Development of the resisting bending moment at the interfaces of the beams with columns (a) JPA3-R, and (b) JPB-R

Considering the abovementioned results, following discussions on flexural performance of the beams of each retrofitted beam-column joints of groups I and II are presented.

Prefabricated solutions: according to Figure 5.20a, the maximum bending moments developed in the left ($M^L$) and the right ($M^R$) beams of JPA0-R, during the negative

displacement, were -92.95 kN·m at a drift of -3.00% and -54.03 kN·m at a -2.65% drift, respectively. During the positive displacement, the left and the right beams reached their maximum bending moment, +52.11 kN·m and +90.69 kN·m, at drift levels of +2.31% and +2.99%, respectively.

As depicted in Figure 5.20b, the values of maximum bending moments for JPC-R in the left and the right beams, during the negative displacement were -114.13 kN·m at a drift level of -2.66 % and -55.58 kN·m at -1.65 % of drift, respectively. The developed maximum bending moment for the positive displacement, in the left and the right beams were +51.09N·m and +106.4 kN·m at drift level of +2.64%, respectively. A sudden reduction observed in bending moment capacity of the right beam during negative loading, at drift cycle of 1.67% (Figure 5.20b), is associated to a noticeable sliding of longitudinal steel bars at the superior face of that beam. Sliding of these bars has initiated out of the retrofitted region where damage was already extensive, and then progressed along the beam toward its supporting extremity. Due to this process a sudden drop in lateral load carrying capacity of JPC-R was registered at this level of drift (Figure 5.15b), after which the specimen presented a structural softening behavior for any further loading in the negative direction.

As mentioned in previous section, where the damage evolution of JPC-R was discussed, at a drift cycle of 2.67% the SHCC plate installed on the lateral face of the column reached its flexural-tensile capacity, and failed. Failure of this plate resulted in the loss of the contribution of the CFRP sheet for the flexural retrofitting of the beam. As a direct consequence, the tensile stresses in the longitudinal CFRP laminates of the HCP[L], at the bottom face of the right beam, increased significantly and one of these CFRP laminates ruptured. Therefore, the maximum bending capacity of the right beam during positive displacement (+106.4 kN·m at 2.67% drift) was reached by the rupture of this longitudinal CFRP laminate. In consequence of significant bond deterioration between this laminate and surrounding SHCC in the joint region, the flexural capacity of the left beam was also limited due to the sliding of this laminate during the lateral load reversal. This justifies the sudden drop in both positive and negative displacements at a drift level of 2.67%, as shown in Figure 5.15b.

According to the data presented in Table 5.2, the flexural capacity of the JPA0 after the retrofit increased up to 34.54% and 30.80%, for the negative and positive loading directions, respectively. The retrofitting system adopted in the JPC provided a larger increase in the resisting bending moments, since values of 74.8% and 47.5% are obtained for the negative and the positive loading, respectively. It should be noted that the values registered for the JPA0-R do not necessarily represent the flexural capacity of the beams, since the beam-column joint shear failure was the governing mode.

Cast-in-place solutions: according to Figure 5.21a, the maximum bending moments developed in the left ($M^L$) and the right ($M^R$) beams of JPA3-R, during the negative displacement, were +65.94 kN·m and -39·6 kN·m both at a drift level of -1.64%. During the positive displacement, the left and the right beams reached their maximum bending moment, -43.04 kN·m and +71.17 kN·m, at drift levels of +1.65% and +2.65%, respectively.

As depicted in Figure 5.21b, the values of maximum bending moments for JPB-R in the left and the right beams, during the negative displacement were +108.81 kN·m at a drift level of -2.62% and -57.16 kN·m at -1.62% of drift, respectively. The developed maximum bending moment for the positive displacement, in the left and the right beams were -55.64 kN·m and +107.46 kN·m at drift levels of +1.66% and +2.33%, respectively. A sudden reduction observed in bending moment capacity of the right beam during negative loading at drift cycle of 1.67% (Figure 5.21b) was caused by a significant sliding of longitudinal bars at the top face of the right beam, as discussed in previous section.

According to the data reported in Table 5.2, after retrofitting, in average and for the positive bending moments, up to 88% of flexural capacity of the beams of JPA3 was recovered. For the negative bending moments, the flexural capacities of the beams in virgin state were fairly restored. The retrofitting system adopted for JPB, however, provided a much larger increase in resisting bending moments of the beams. Based on this retrofitting technique an average increase of 49% and 71% for the positive and negative moments were obtained, respectively. It should be noted that the values registered for flexural resistance of both retrofitted specimens do not necessarily represent the flexural capacity of the beams, since the degradation in beam-column joint shear capacity was the prevailing failure modes of both specimens.

### 5.3.4 Drift Components

The lateral displacement of a beam-column joint can be decomposed into the contribution of the deformation developed in each of its elements. These drift components are mainly the shear and the flexural deformations of both the columns and beams, and the the distortion of the panel of the joint region in shear. I

In general, the shear deformation of the beams and columns has low contribution to the overall drift, as it is also the case of this study, and therefore can be neglected.

It should be noted that, since the measurements of DTs for the specimens of group II were deficient, the decomposition of drift components is evaluated and presented only for beam-column joints in group I (specimens retrofitted with prefabricated HCPs),

### 5.3.4.1 Contribution of Flexural Deformations of Beams and Columns

Flexural deformation of each element (beams and columns) is calculated using the relative rotation between sections at the extremities of each slice, $\theta_i^R$ ($i$ is the number of each slice; see Figures 5.14 and 5.22). Based on the measures of the pair of DTs installed on slice $i$, the relative rotation, $\theta_i^R$, is obtained from equation (5-2),

$$\theta_i^R = \frac{\Delta_i^t - \Delta_i^b}{d_i}, \qquad i = 1, 2, 3, 4 \tag{5-2}$$

Where, $\Delta_i^t$ and $\Delta_i^b$ are the measures of each of two DTs installed on slice $i$, and $d_i$ is the distance between these DTs.

As shown in Figure 5.22 and equations (5-3), knowing the relative rotation at each slice, $\theta_i^R$, and assuming zero rotation at the interface of the element and joint ($\theta_1 = 0$), the absolute value of rotation at extremities of the others slices, $\theta_j$ ($j$: 2, 3, 4, 5; number of each section), can be determined.

$$\theta_j = \sum_{i=1}^{j-1} \theta_i^R, \qquad j = 2, 3, 4, 5 \tag{5-3}$$

Where, $\theta_j$ is the absolute rotation at section $j$.
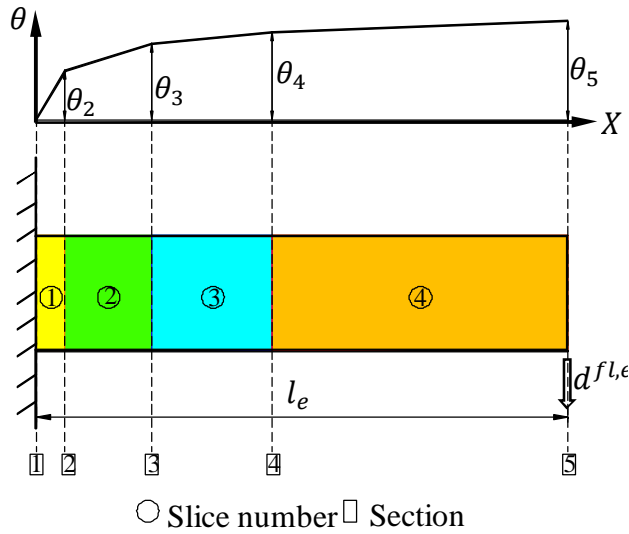
Figure 5.22: Adopted distribution of rotation along a given element (beam or column) of the beam-column joint

The distribution of rotation along the element is approximated assuming a linear change of slope along each slice (see Figure 5.22). By integrating rotations along the total length of the element, the flexural deformation at the end of the element, $d^{fl,e}$, can be estimated from following equation (5-4).

$$d^{fl,e} = \sum_{i=1}^{4} \theta_i^R (L_b - X_i) \tag{5-4}$$

where, $d^{fl,e}$ is the flexural deformation at the end of the element and $X_i$ is distance of centre of slice $i$ from the fixed end of the element and $L_b$ is the length of the beam.

Finally, the contribution of beams flexural deformations in lateral displacement at loaded section of the superior column, $d_c^{fl,b}$, can be approximated according to equation (5-5).

$$d_c^{fl,b} = (d^{fl,lb} - d^{fl,rb}) \left( \frac{2l_c + h_b}{2l_b + h_c} \right) \tag{5-5}$$

A similar approach can be employed to obtain the flexural contribution of columns at total lateral displacement of the loaded section of the superior column.

### *5.3.4.2 Contribution of Shear Distortion of the Joint Panel*

The contribution of the joint panel to the interstory drift, $d_c^{js}$, is calculated using the joint shear distortion $\gamma_j$. Measured values by the diagonally placed DTs are used to obtain the joint distortion at each level of interstory drift according to Figure 5.23 and equations (5-6) to (5-7) .

$$\gamma_j = \gamma_1 + \gamma_2 \tag{5-6}$$

$$\gamma_j = \frac{\Delta_2 - \Delta_1}{2l_d}\left(tan\varphi + \frac{1}{tan\varphi}\right) \tag{5-7}$$

where, $\Delta_1$ and $\Delta_2$ are the shortening and elongation measured by pair of diagonal DTs installed in the joint region, and $l_d$ is the initial distance between supporting points of DT.

Taking into account the boundary conditions at the end of each element and establishing the kinematic relations between the elements of the beam-column joints, see Figure 5.24 and equations (5-8) and (5-9), the contribution of joint panel in lateral displacement at the loaded section of the superior column, $d_c^{js}$, can be approximated from equation (5-10).

$$d_c^{js} = 2 \times l_c\gamma_1 - h_b\gamma_2 \tag{5-8}$$

$$\gamma_2 = \frac{h_c}{2l_b}\gamma_1 \tag{5-9}$$

$$d_c^{js} = \left(2l_c\gamma_1 - \frac{h_c h_b}{2l_b}\right)\gamma_1 \tag{5-10}$$
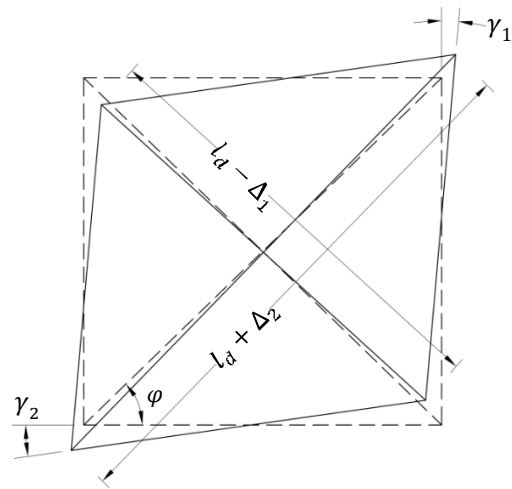
Figure 5.23: Calculation of the joint distortion based on measurements of diagonal DTs
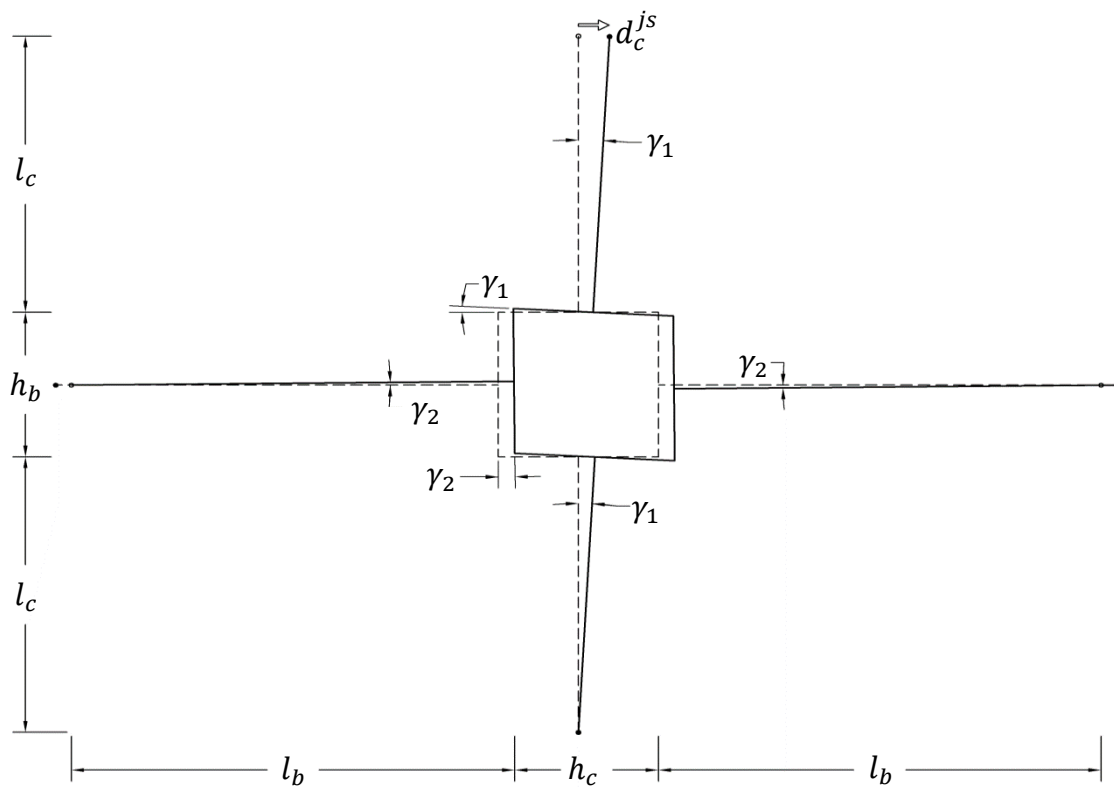


Figure 5.24: Contribution of joint distortion in lateral displacement at top of the superior column, $d_c^{js}$.

### 5.3.4.3 Discussion on the Results of Drift Components Decomposition

Figure 5.25 illustrates the contribution of each of the abovementioned components as the percentage of each level of the interstory drift during the steps of the positive displacements. The remaining portion of the graphs includes the shear deformation of the beams and columns, rigid body motion of the specimens due to the flexibility of supporting frames and finally local deformations at the supporting regions of the specimens.

According to the Figure 5.25a, the contribution of the beams flexural deformation in lateral displacement of JPA0-R increased up to 59% at the level of 1% drift. After this level of the drift the beams flexural contribution started decreasing, and reached to its minimum contribution of 19% at 4% drift. The joint distortion contribution started increasing after the drift level above 1.3% and at 3% drift has reached 35%, which was larger than the contribution of the other components. The maximum contribution of the joint distortion, 37%, has occurred at 3.33% of drift. The flexural contribution of the columns varied between 22% and 40%. Considering the observed damages and Figure 5.25a, it can be concluded that at 4% of drift the fixed end rotation of the column, due to the excessive sliding of the unbounded longitudinal reinforcements inside the joint region, and the joint shear distortion have dominated the interstory drift.

Figure 5.25b shows the contribution of the drift components in the interstory drift of JPC-R. It can be seen that the beams flexural contribution up to 1% of drift has increased up to 59%, similar to what was observed for JPA0-R. Between this drift level and 2.64% drift, the contribution of the beams flexural deformation was almost constant, but above 2.64% drifts the beams flexural contribution has increased and reached its maximum contribution of 86% at 4% of drift. Except at the drift level of 0.2%, where the contribution of the joint distortion was more than 20%, up to a drift level of 1% the joint distortion had almost a constant contribution with an average value of 12%. By increasing the imposed drift the contribution of the joint distortion has also increased and reached its maximum value of 23.8% at a drift level of 2.33%. Above this level of drift, the joint distortion had a reduction tendency so that at 4% of drift its contribution was only 5.2%. The column flexural contribution had a general tendency to decrease with the increase of the drift, with a 39% of contribution at a drift level of 0.2%, and 5.5% at the end of the test. This hierarchy of the contribution of each drift

components for lateral displacement of JPC-R explains how the retrofitting system was efficient to decrease the joint shear distortion and, therefore, to maintain the columns undamaged.
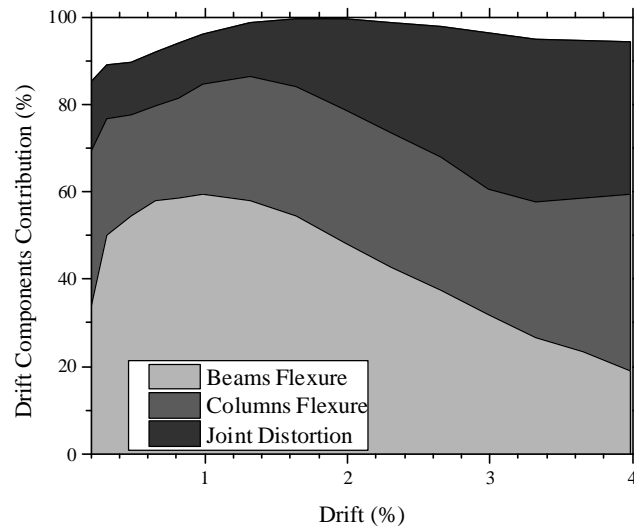


(a)
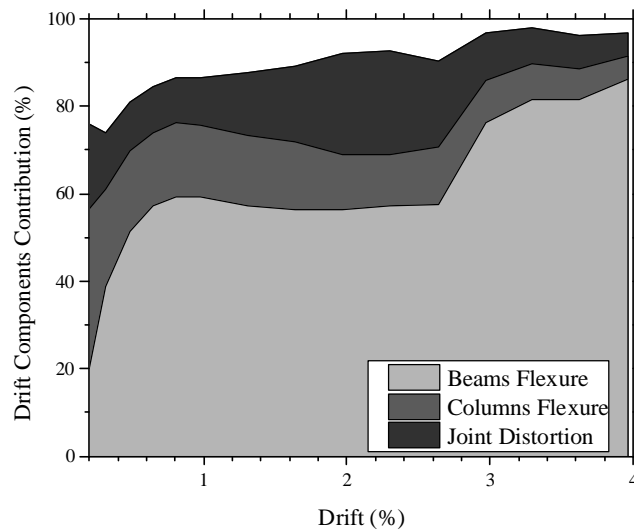


(b)

Figure 5.25: Contribution of the beams flexure, the columns flexure, and the joint shear distortion to the overall drift of (a) JPA0-R, and (b) JPC-R

### 5.3.5 Cumulative Dissipated Energy

Energy dissipation capacity of a RC element is the consequence of inelastic deformation and damage propagation. Opening and closing of cracks contribute significantly to the energy dissipation capacity, as well. Therefore, for SHCC material with the potential of formation multiple diffused micro cracks, a high level of energy dissipation under cyclic loadings is expected.

As shown in Figure 5.26, the amount of dissipated energy per cycle, $E_i$ (with $i$ being the number of the cycle), can be calculated from the enclosed area in each loading cycle, as presented by the hysteresis response of lateral load *versus* lateral displacement. Summation of the dissipated energy with respect to the increment in lateral drift results in cumulative dissipated energy up to each given level of interstory drift.
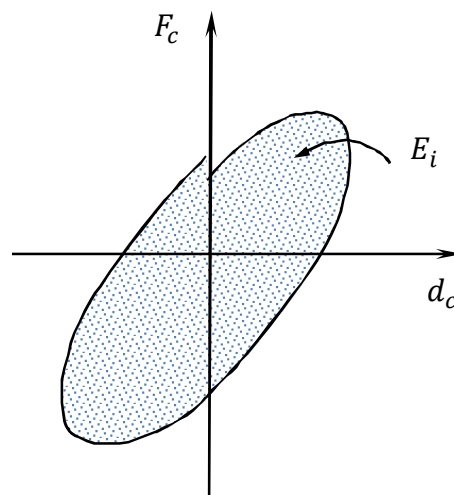


Figure 5.26: Schematic presentation of the concept of dissipated energy at each cycle, $E_i$

The evolution of the dissipated energy at the retrofitted and virgin state of the specimens in groups I and II are presented in Figures 5.27 and 5.28, respectively. Moreover, the amount of cumulative dissipated energy at 4% drift, $E_{4\%}$, for both retrofitted and virgin states of the specimens, is reported in Table 5.3. The increase in the amount this cumulative dissipated energy, $\Delta E_{4\%}$, after retrofitting is indicated in the last column of this table. Following, discussions on the evolution of the dissipated energy of the specimens in each group can be found.

Prefabricated solutions: considering the results presented in Figure 5.27, both adopted retrofitting solutions for the specimens in the first group, JPA0-R and JPC-R, have provided an energy dissipation capacity higher than the one registered in the corresponding specimen in virgin state during all loading steps. In this respect, the retrofitting solution applied in JPC specimen was more effective. In fact, at 4% drift, the dissipated energy of JPA0-R was 52.3 kN·m, which is 23% larger than the energy dissipated in JPA0, while the JPC-R reached 54.03 kN·m corresponding to an increase of 84% comparing to dissipated energy of JPC.

Cast-in-place solutions: following the results depicted in Figure 5.28, during all loading steps, both retrofitting solutions of the specimens in the second group, JPA3-R and JPB-R, have provided a cumulative dissipated energy higher than the one registered in their corresponding virgin state. In this respect, the retrofitting solution applied in JPB specimen was more effective. In fact, at 4% of drift the cumulative dissipated energy of JPA3-R was 44.4 kN·m, which was only 5% larger than the corresponding value in JPA3, while the JPB-R reached 53.4 kN·m indicating an increase of 95% comparing to value calculated for JPB.



(a)    (b)
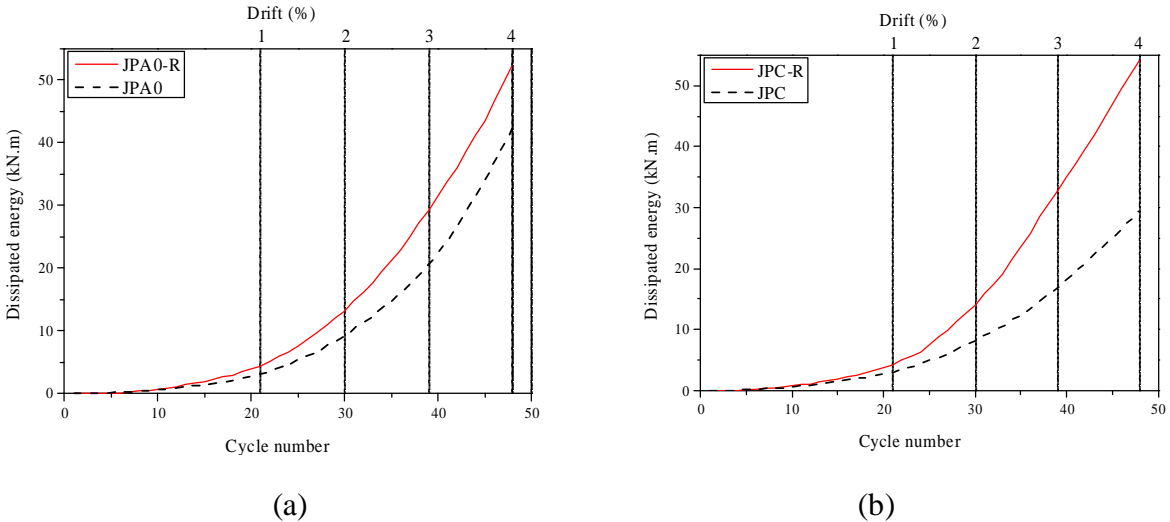
Figure 5.27: Evolution of the dissipated energy during the cyclic loading of (a) JPA0-R and JPA0, and (b) JPC-R and JPC

(a)　　　　　　　　　　　　　　(b)
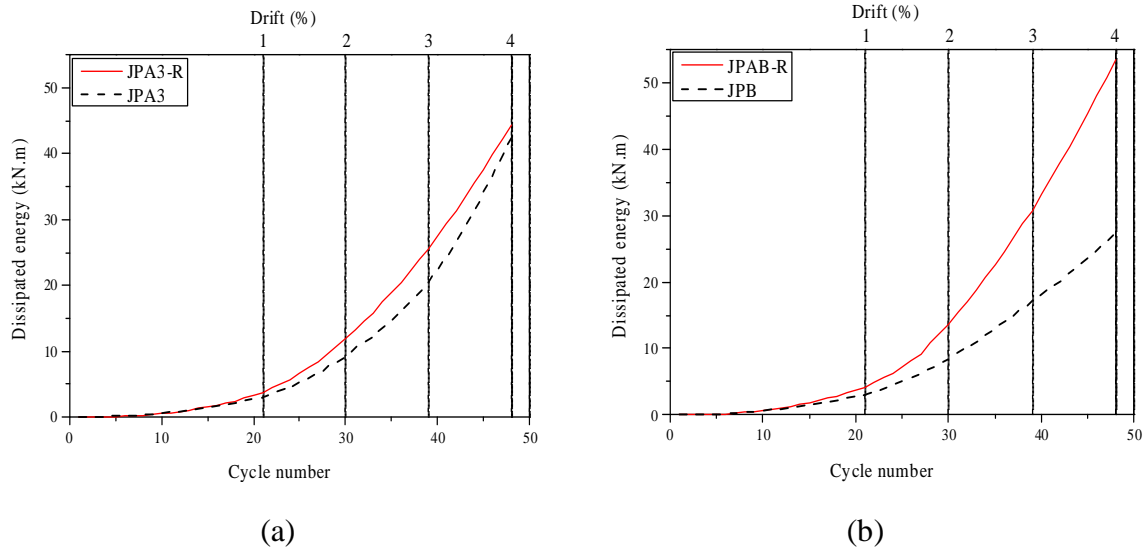
Figure 5.28: Evolution of the dissipated energy during the cyclic loading a) JPA3-R and JPA3, and b) JPB-R and JPB

Table 5.3: Cumulative dissipated energy at 4% of drift

| Group | Specimen | $E_{4\%}$ kN·m | $\Delta E_{4\%}$ (%) |
|---|---|---|---|
| Group I | JPA0-R | 52.3 | +23 |
| | JPA0 | 42.4 | |
| | JPC-R | 54.0 | +84 |
| | JPC | 29.4 | |
| Group II | JPA3-R | 44.4 | +5 |
| | JPA3 | 42.4 | |
| | JPB-R | 53.4 | +95 |
| | JPB | 27.4 | |

$E_{4\%}$ is the cumulative dissipated energy at 4% of drift;
$\Delta E_{4\%} = \left[1 - E_{4\%}^{R}/E_{4\%}^{V}\right]$, where superscripts "$R$" and "$V$" denote retrofitted and virgin states, respectively.

### 5.3.6 Secant Stiffness

As a consequence of reversal and repeated actions of cyclic loading, the stiffness of a beam-column joint can be deteriorated. To assess the stiffness degradation, the secant stiffness, $K_s$, is estimated during the drift evolution, and its relationship is represented in

Figures 5.30 and 5.31, for the specimens in groups I and II, respectively, in their both retrofitted and virgin states. The secant stiffness is taken as the slope of the straight line which connects the peak loads at the positive and the negative displacements of the load *versus* displacement envelop at each level of the drift (see Figure 5.29).

Moreover, the amount of initial secant stiffness at, $K_s^i$, for both retrofitted and virgin states of the specimens, is reported in Table 5.4. The changes in the initial secant stiffness, $\Delta K_s^i$, after retrofitting is indicated in the last column of this table.
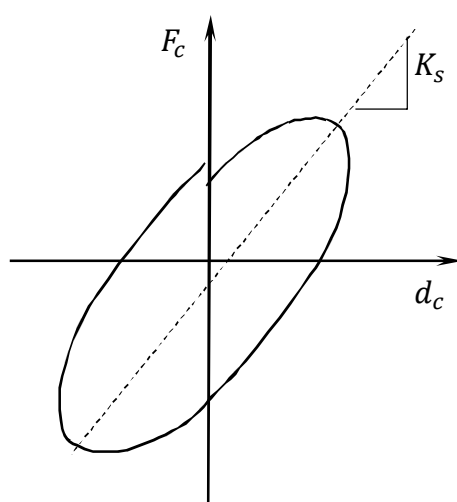


Figure 5.29: Schematic representation of the adopted definition for secant stiffness, $K_s$, at each cycle

Table 5.4: Initial secant stiffness of the specimens

| Group | Specimen | $K_s^i$ kN/m | $\Delta K_s^i$ (%) |
|---|---|---|---|
| Group I | JPA0-R | 5058 | +1.6 |
| | JPA0 | 4979 | |
| | JPC-R | 6807 | +22.5 |
| | JPC | 5557 | |
| Group II | JPA3-R | 4087 | -18.0 |
| | JPA3 | 4979 | |
| | JPB-R | 5275 | -2.5 |
| | JPB | 5411 | |

$K_s^i$ is the initial secant stiffness;

$\Delta K_s^i = \left[1 - \left(K_s^i\right)^R / \left(K_s^i\right)^v\right]$, where superscripts "*R*" and "*V*" denote retrofitted and virgin states, respectively.



(a)            (b)
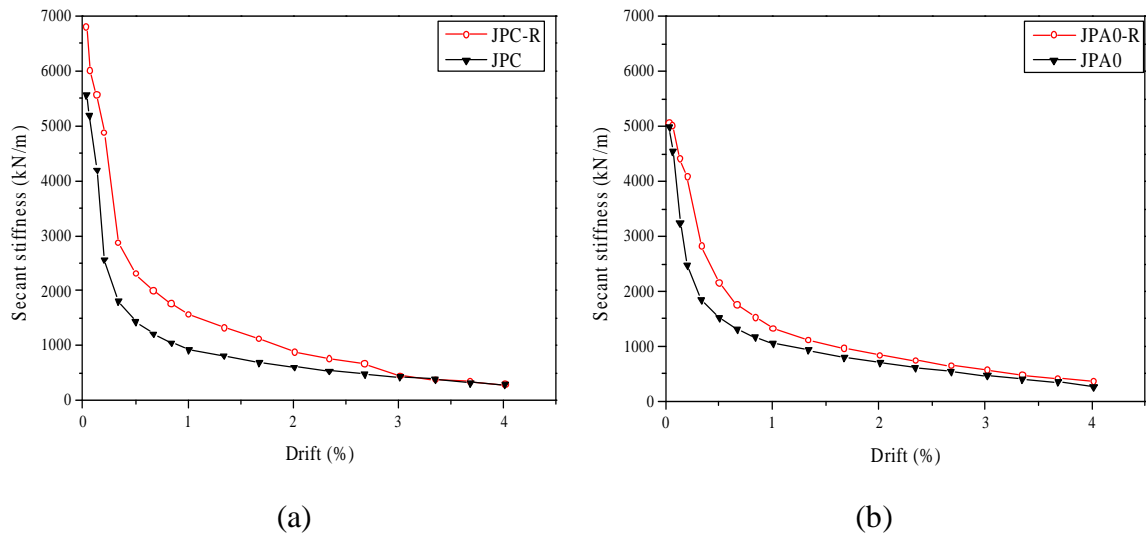
Figure 5.30: Secant stiffness of (a) JPA0-R and JPA0, and (b) JPC-R and JPC



(a)            (b)
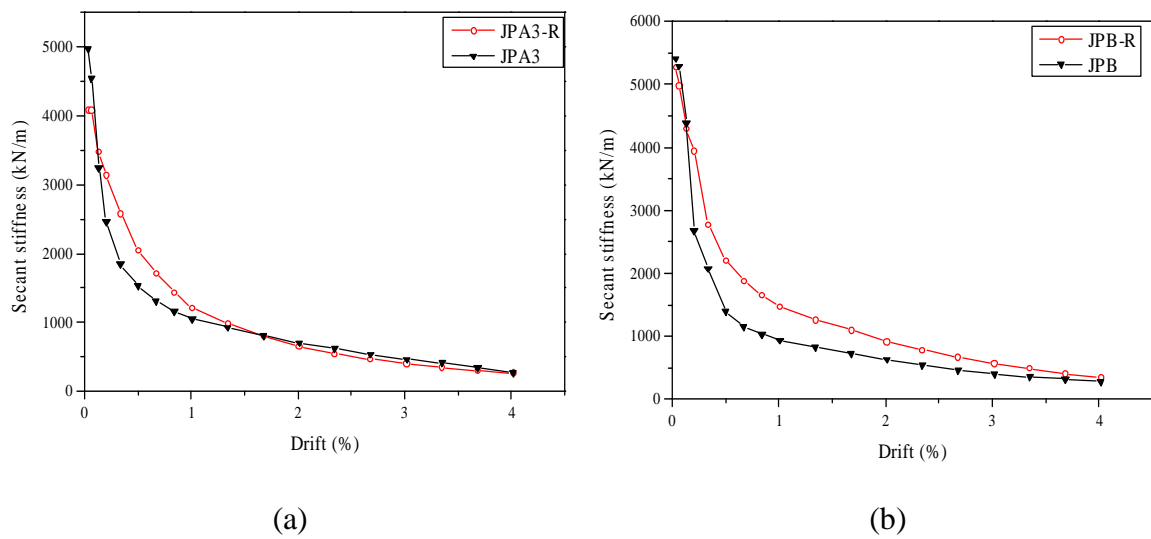
Figure 5.31: Secant stiffness evolution in (a) JPA3-R and JPA3, and (b) JPB-R and JPB

Prefabricated solutions: according to Figure 5.30 both specimens in the first group, JPA0-R and JPC-R, presented higher secant stiffness in their retrofitted state than in their virgin state, at least up to 3% drift. In terms of initial secant stiffness, JPA0-R presented almost the same stiffness as in its virgin state, while the initial secant stiffness of JPC-R was 22.5% higher than the value registered in its virgin state (see Table 5.4). This increase is attributed

to the larger cross section after the retrofit, and higher level of concrete confinement introduced by the post-tension effect of the chemical anchors in all lateral faces of the framed elements. In addition, it should be mentioned that both retrofitting systems were able to restore (at least) the initial stiffness.

For the case of JPA0-R, when the first crack was formed, at 0.33% drift, the initial secant stiffness reduced more than 44%. Due to the concentration of damage at the top face of the right beam of JPC-R, out of the retrofitted region, and initiation of the sliding of the longitudinal plain steel bars in this region, a significant drop in its secant stiffness at a drift level of 0.33% was registered. This stiffness reduction was about 58% of the initial secant stiffness.

Cast-in-place solutions: according to the Figure 5.31 and Table 5.4, the retrofitting technique adopted for JPA3-R has just restored 82% of the initial secant stiffness of this specimen in its virgin state, while the technique applied on the JPB-R has almost restored the initial secant stiffness registered in JPB (its virgin state). This can be explained by a less effective bond between the casted mortar and the old concrete of JPA3-R.

Considering the degradation of the secant stiffness at the end of each sets of loading cycles, JPA3-R had greater secant stiffness than JPA3 between loading cycles corresponds to 0.13% and 1.67%. After 1.67% the secant stiffness of the retrofitted and virgin state was fairly similar. For the case of JPB-R, after 0.13% of drift, the adopted retrofitting scheme resulted in a slower degradation in secant stiffness than its virgin state.

### 5.3.7 Displacement Ductility

Ductility is the potential of a lateral load resisting system to undergo large inelastic deformations during its post-peak regime with only slight reduction in its ultimate lateral load carrying capacity. The ductility is generally quantified as a normalized displacement or a rotation index depending if the ductility is aimed to be assessed in terms of local or global behavior, respectively. For the case of the present study, the displacement ductility index $(\mu_d)$ is calculated as the ratio of the ultimate lateral displacement $(d_u)$ and the displacement at the yield point $(d_y)$. The ultimate point can be defined as the displacement corresponding to a load level in the post-peak response of the specimen that is a fraction of the peak

load ($F_m$). According to the available literature, this ratio can be taken between 10% and 20% [7-9]. The yield displacement can be obtained from a bi-linear curve assuming equivalent elastic-perfectly plastic response. To estimate this bi-linear curve, two conditions should be fulfilled: (i) the area under this curve should be equal to that for the envelope of load *versus* lateral displacement, and (ii) the deviation between these two curves, measured based on the absolute sum of the areas enclosed between these curves, should be the minimum (see Figure 5.32).

The displacement ductility index is then calculated as the ratio between the ultimate displacement and the yield displacement. In this context it was assumed for the ultimate displacement the one corresponding to 10% loss of the peak load ($0.9F_m$).
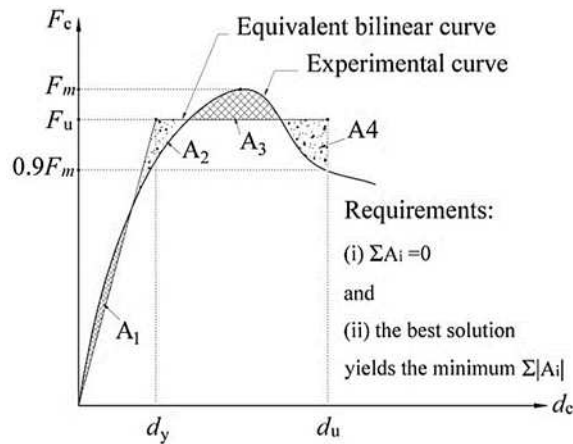


Figure 5.32: Schematic representation of the definition of the equivalent bilinear curve for the evaluation of the displacement ductility index

The envelope of the load *versus* drift and also the equivalent elastic-perfectly plastic curves estimated for both retrofitted and virgin specimens are presented in Figures 5.33 and 5.34 corresponding to specimens in group I and II, respectively.

Table 5.5 also indicates the yield and the ultimate displacement obtained for the calculation of the displacement ductility index for the positive and negative loading, where $\mu_\delta^V$ and $\mu_\delta^R$ are the ductility for the specimen in the virgin and retrofitted state, respectively. The reported ductility index is calculated as the average ductility using the corresponding values of displacement ductility in both positive and negative displacements.

(a)

(b)
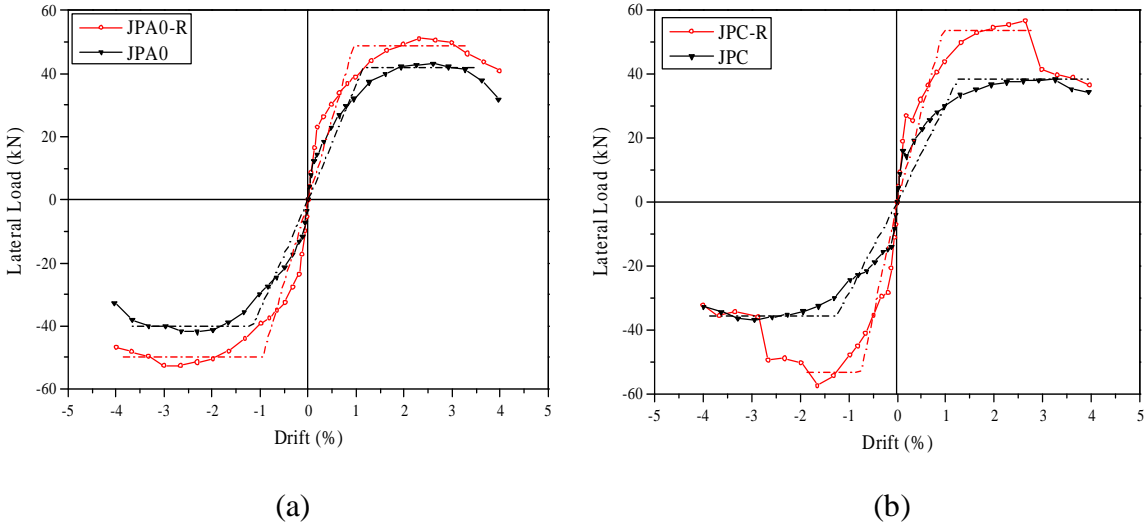
Figure 5.33: Envelope of the load *versus* drift for both retrofitted and virgin specimens along with the equivalent elastic-perfectly plastic curves of (a) JPA0-R and JPA0, and (b) JPC-R and JPC



(a)

(b)
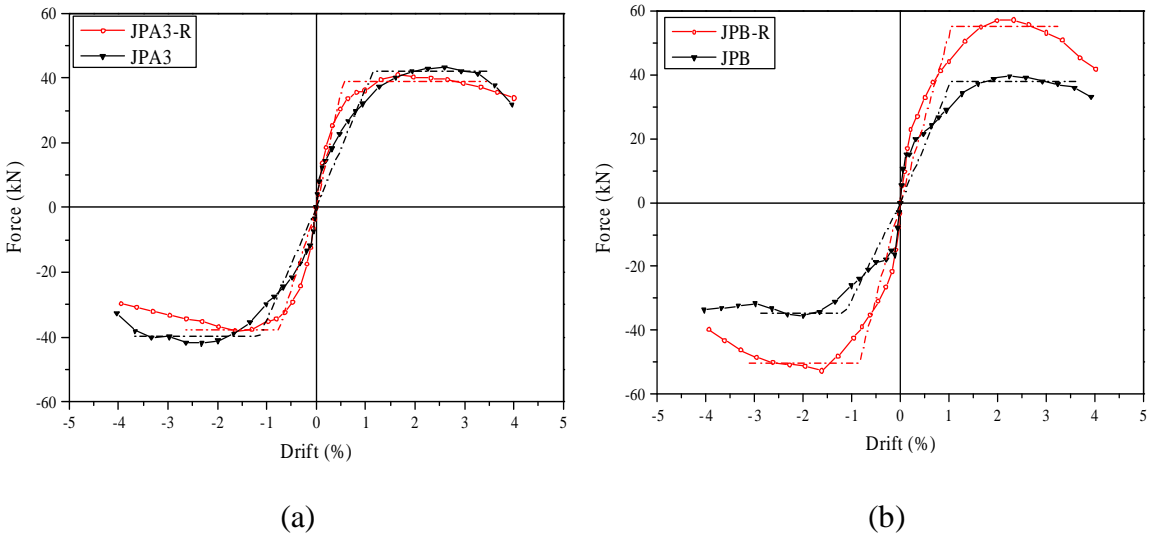
Figure 5.34: Envelope of the load versus drift for both retrofitted and virgin specimens along with the equivalent elastic-perfectly plastic curves of (a) JPA3-R and JPA3, and (b) JPB-R, and JPB

Table 5.5: Details of components for the evaluation of displacement ductility factor

| Group | Specimen | Negative direction | | Positive direction | | $\mu_\delta$ | $\dfrac{\mu_\delta^R - \mu_\delta^V}{\mu_\delta^V}$ |
|-------|----------|---------------------|---|---------------------|---|------|------|
| | | $d_y^-$ (mm) | $d_u^-$ (mm) | $d_y^+$ (mm) | $d_u^+$ (mm) | | |
| Group I | JPA0-R | -28.5 (-0.95)* | -116 (-3.86) | +28.6 (+0.95) | +100.5 (+3.35) | 3.8 | +22.6% |
| | JPA0 | -34.5 (-1.15) | -110.5 (-3. 68) | +34.5 (+1.15) | +105.2 (+3.51) | 3.1 | |
| | JPC-R | -22.5 (-0.75) | -57.6 (-1.92) | +28.5 (+0.95) | +82.9 (+2.76) | 2.7 | -18.2% |
| | JPC | -37.5 (-1.25) | -117.3 (-3.91) | +37.5 (+1.25) | +117.7 (+3.92) | 3.3 | |
| Group II | JPA3-R | -22.5 (-0.75) | -79.2 (-2.64) | +16.5 (+0.55) | +102.9 (+3.43) | 4.88 | +56% |
| | JPA3 | -34.5 (-1.15) | -110.5 (-3. 68) | +34.5 (+1.15) | +105.2 (+3.51) | 3.13 | |
| | JPB-R | -25.5 (-0.85) | -93.3 (-3.11) | +31.5 (+1.05) | +97.2 (+3.24) | 3.37 | +12 % |
| | JPB | - 34.5 (-1.15) | -87.6 (-2.92) | +31.5 (+1.05) | +108.9 (+3.63) | 3.00 | |

* Values in parentheses indicate the corresponding drift in percentage at maximum bending moment

Prefabricated solutions: according to the results included in Table 5.5, it is verified that for both retrofitted specimens in group I, JPA0-R and JPC-R, the yield displacement has decreased when compared to the value registered in corresponding specimen in the virgin state. The reduction of the yield displacement is a consequence of the stiffness increase provided by the retrofitting system, with the main impact during the initial cycles. In terms of displacement ductility, the retrofitting strategy has assured an increase of 22.66% for the JPA0 specimen, while JPC-R presented a reduction of 18.2% in comparison to the displacement ductility registered in its virgin state. This reduction in ductility of JPC-R can be attributed to the loss of the right beam´s rotational ductility at the concentrated damage zone localized out of the retrofitted region, where the sliding of longitudinal steel bars at the superior face of the beam was initiated. Furthermore, due to the failure of HCP[(S)]s at the

lateral face of the column, the CFRP sheet bonded to the critical section of the right beam lost its anchorage mechanism, which has promoted a gradient of tensile stress leading to the rupture of CFRP laminate at the bottom face of the HCP$^{(L)}$ on the right beam.

Moreover, in comparison with JPA0-R, a lower damage in the joint region of JPC-R restricted the occurrence of any excessive joint shear distortion. Therefore, a reduction in displacement ductility of JPC-R is also defined by a lower contribution of the shear deformation at the joint region to the lateral displacement at the top of the column.

<u>Cast-in-place solutions</u>:    for both retrofitted specimens in group II, JPA3-R and JPB-R, the average of the yield displacements, in negative and positive directions, has decreased when compared to the average value registered for their corresponding specimens in the virgin state. The reduction of the yield displacement is a consequence of lower stiffness degradation assured by the retrofitting system, mainly during the cycles up to 1.15% of drift. According to the results included in Table 5.5, and comparing to the displacement ductility registered in the specimens' virgin state, the retrofitting strategy has assured an increase of 56% and 12% in displacement ductility of JPA3-R and JPB-R, respectively. The higher increase in displacement ductility of JPA3-R can be attributed to the larger sliding between the retrofitting scheme and the concrete substrate, and also due to the existence of larger damages before retrofitting of this specimen.

### 5.3.8 HCP versus Cast-in-Place Solution

The HCP retrofitted beam-column joints (JPA0-R and JPC-R) are compared to their cast-in-place retrofitted counterpart (JPA3-R and JPB-R). This comparison includes the percentage difference in the achieved displacement ductility, $\Delta\mu_\delta$, the dissipated energy at 4% drift, $\Delta E_{4\%}$, the peak of lateral load at top of the superior column, $\Delta F_P$, and the beams' maximum positive and negative moments, $\Delta M^+$ and $\Delta M^-$, respectively. To calculate each of these criterions, the average value obtained in the positive and negative loading directions for the HCP retrofitted beam-column joint and for its cast-in-place retrofitted counterpart is compared according to equation (5-11). The results of these calculations are indicated in Table 5.6.

$$\Delta I = \left( \frac{I_{AVG}^H - I_{AVG}^C}{I_{AVG}^C} \right) \times 100 \tag{5-11}$$

where,

$\Delta I$ is the percentage of increase (or decrease) in criterion $I$ ($I$: $\mu_\delta$, $E_{4\%}$, $F_P$, $M^+$ and $M^-$);

$I_{AVG}^H$ and $I_{AVG}^C$ are the average of the positive and negative loading directions of criterion $I$ for the HCP retrofitted beam-column joint and its cast-in-place retrofitted counterpart, respectively.

Table 5.6: Comparison of the results obtained from HCP retrofitted beam-column joints with their counterpart retrofitted adopting a cast-in-place solution.

| Specimen | $\Delta\mu_\delta$ (%) | $\Delta E_{4\%}$ (%) | $\Delta F_P$ (%) | $\Delta M^+$ (%) | $\Delta M^-$ (%) |
|---|---|---|---|---|---|
| JPA0-R JPA3-R | -22.1 | +17.8 | +31.8 | +34.2 | +28.8 |
| JPC-R JPB-R | -19.9 | +1.1 | +4.0 | +2.0 | -5.5 |

According to the results presented in Table 5.6, both two-sided and four-sided HCP retrofitted beam-column joints showed lower displacement ductility, as compared to their cast-in-place retrofitted counterparts. This can be mainly attributed to the different interface bond properties between the retrofitting scheme and the concrete at each of these techniques. In fact, in contrary to a cast-in-place solution, an adhesively bonded scheme (HCP) adversely affected the process of multiple crack propagation in SHCC, due to excessive constraints at the interface level between SHCC and concrete. Hence, as a consequence of this restricted crack propagation, displacement ductility is reduced.

Both four-sided retrofitted specimens, JPC-R and JPB-R, resulted in almost similar quantities for the dissipated energy in 4% of drift, the peak of the lateral load and the moment capacities of beams (both positive and negative moments). However, considering the same criterions, a two-sided HCP solution resulted in superior performance, as compared to its cats-in-place retrofitted counterpart. This indicates an enhanced composite action between

the cast-in-place retrofitting scheme and the concrete by covering all faces of the elements of beam-column joints. This improvement can be explained by the effect of the restrained shrinkage at the edges of the SHCC at each corner of the elements. In fact, in the case of four-sided cast-in-place retrofitting solution, JPB-R, three faces of the elements were casted simultaneously and the remained face was casted after turning the specimen. Even, development of a high quality bond at the intersections of the fresh SHCC and the hardened one is expected, since the hydration process in the old SHCC is still under progress, due to a high content of fly ash in the SHCC mixture. Hence, the restraining shrinkage at all corners of the SHCC have resulted a confining pressure that enhanced the pure bond between SHCC and concrete substrate, as compare to the two-sided cast in place solution.

## 5.4 Summary and Conclusions

In this chapter, the effectiveness of HCPs for retrofitting of damaged RC beam-column joints was experimentally assessed. RC interior beam-column joints used in this study were full-scale prototypes representative of pre-1970's gravity load designed RC frame-type buildings. These specimens were already damaged, since they have been tested in their virgin states under a simultaneous action of a constant column axial load and a lateral cyclic displacement.

HCPs with two different configurations were used to repair each of two specimens categorized in the first group. In the second group, there were two other damaged beam-column joints and each of them repaired with NSM-CFRP laminate reinforced cast-in-place SHCC, to be the counterpart of one of the specimens in first group.

The main difference between adopted retrofitting techniques for the specimens, either in the first or second group, was the number of the faces of the elements of the beam-column joints which the retrofitting scheme was applied. Thus, one specimen in each group was retrofitted employing the retrofitting scheme to its front and rear faces (two-sided retrofitting scheme) and for the other specimen, the retrofitting scheme was applied to all faces of its elements (four-sided retrofitting scheme).

After retrofitting, these specimens were tested using the same test setup and loading configuration applied to their virgin state.

Test results from different retrofitting strategies (two-sided *versus* four-sided scheme) were compared to each other and discussed, to verify the effectiveness of HCPs based on the adopted configuration for retrofitting of the damaged beam-column joints.

Moreover, to assess the influence of the interface bond between the retrofitting scheme and the concrete substrate on the seismic performance of the retrofitted beam-column joint, the results obtained from HCP retrofitted ones were compared to their counterpart retrofitted with a cast-in-place solution.

According to the obtained results and observations and presented discussions, following conclusions can be pointed out of this study:

- Both two-sided and four-sided HCP retrofitting, and also the four-sided cast-in-place technique showed a superior performance in terms of hysteretic response, lateral load carrying capacity, energy dissipation capacity, beams flexural resistance and degradation of the secant stiffness as compared to the test results in their virgin state.

- A two-sided cast-in-place retrofitting technique was fairly capable of restoring hysteretic response, the lateral load carrying capacity and energy dissipation performance, and increase the ductility registered in the virgin state of this specimen.

- While a two-sided HCP retrofitting technique was capable of restoring the initial secant stiffness of the specimen's virgin state, the initial secant stiffness of its cast-in-place retrofitted counterpart was 18% lower than the virgin state.

- A stronger interfacial bond between SHCC and concrete substrate (adhesively bonded *versus* pure bond) adversely affected the displacement ductility of the retrofitted specimen, while, no adverse effect of the energy dissipation capacity was observed.

- Adding "L" shape HCPs to the retrofitting configuration resulted in lower shear stress development inside the joint region and, therefore, higher stability and in lower damage in the panel of the joint. Thus, beams flexural failure was the failure mode in the case of four-sided HCP retrofitted beam-column joint, while its counterpart cast-in-place retrofitted one failed by joint shear failure. In fact, in this latter specimen, since the CFRP laminates of the lateral faces of the columns and the top and bottom faces of the beams

were anchored into the beam-column joint interfaces, higher shear stresses was transferred to the joint panel zone.

- A high capacity of stress redistribution in SHCC resulted in multiple crack formation around anchored regions, but no bearing failure was observed. Moreover, due to the presence of chemical anchors, the progress in detachment of the CFRP sheets at the higher displacement demands was effectively restricted.

- Considering that the progress of the inclined cracks in the joint region resulted in debonding failure between the adhesive of the "X" shaped CFRP laminates and the SHCC, effectiveness of this configuration of CFRP laminates in the joint region is under question. Hence, bonding a horizontal or vertical arrangement of transverse CFRP laminates at this region is recommended.

- The final geometry of the retrofitted specimens was only slightly affected by the proposed retrofitting interventions, but the seismic performance of these specimens was significantly improved.

- In the cast-in-place retrofitting, the developed SHCC was able to easily flow and fill the relatively small gaps between formworks and the concrete substrate without the need of any vibration, which is an important requisite for a cast-in-place retrofitting intervention.

## Bibliography

[1] Esmaeeli E, Barros JAO, Sena-Cruz J, Varum H, Melo J. Assessment of the efficiency of prefabricated hybrid composite plates (HCPs) for retrofitting of damaged interior RC beam–column joints. Composite Structures. 2015;119:24-37.

[2] Esmaeeli E, Barros JAO, Sena-Cruz J, Fasan L, Li Prizzi FR, Melo J, et al. Retrofitting of interior RC beam–column joints using CFRP strengthened SHCC: Cast-in-place solution. Composite Structures. 2015;122:456-67.

[3] Fernandes CAL. Cyclic Behaviour of RC Elements with Plain Reinforcing Bars [PhD Thesis]. Aveiro, Portugal: Univeristy of Aveiro; 2012.

[4] EN 1992-1-1:2004. Eurocode 2: Design of Concrete Structures, Part 1-1: General Rules and Rules for Buildings2004.

[5] Costa IG, Barros JAO. Evaluation of the influence of adhesive properties and geometry of carbon fiber laminates using pull-out tests. Department of Civil Engineering, University of Minho; 2012. p. 16.

[6] ISO 527-5:2009. Plastics – Determination of tensile properties – Part 5: Test conditions for unidirectional fibre-reinforced plastic composites. Genève, Switzerland.

[7] Paulay T. Equilibrium criteria for reinforced concrete beam–column joints. ACI Structural Journal. 1989;86:8.

[8] EN 1998-3:2005. Eurocode 8: Design of structures for earthquake resistance — Part 3: Assessment and retrofitting of buildings.

[9] Fardis M, Biskinis D. Deformation capacity of R.C. members, as controlled by flexure or shear. in: Performance based engineering for earthquake resistant reinforced concrete structures: A Volume Honoring Shunsuke Otani: University of Tokyo; 2003.

# Chapter 6: Assessment of HCP$^{(L)}$ Efficiency for Flexural Strengthening

## 6.1 Introduction

This chapter reports details of an experimental program and its relevant obtained results on the assessment of the effectiveness of HCP$^{(L)}$ for flexural strengthening of under-reinforced RC beams.

Moreover, an analytical formulation to predict ultimate moment capacity of such strengthened beams is presented. Finally, by employing a section-layer analysis technique, the moment-curvature of each of the retrofitted beams was obtained and then was introduced into a numerical model to estimate the load-deflection response of these RC beams. To evaluate the accuracy of the adopted numerical approach, the estimated results were then compared to the results of the experimental tests.

## 6.2 Experimental Program

To experimentally assess the efficacy of HCP$^{(L)}$ for the flexural strengthening, seven under-reinforced RC beams with identical geometry, and flexural and shear steel reinforcing were cast using a batch of concrete.

### 6.2.1 Details of the Tested Beams

These beams with a total length of 2500 mm had a cross section of 150 mm in width and 300 mm in depth. Two 10 mm diameter deformed steel rebars were placed as the longitudinal reinforcement at both the top and the bottom portions of the beams. Thus, the beams were under-reinforced with a tensile reinforcement ratio of 0.35%.

To ensure sufficient shear capacity for beams at the highest flexural retrofitting demand, stirrups made of 8 mm diameter steel rebars were placed with a center-to-center spacing of 100 mm.

One of the beams was considered as the as-built reference specimen (FB_R) and its flexural behavior was characterized by performing a four-point bending test in its as-built condition (Figure 6.1). The other six beams were then strengthened by attaching either a

SHCC plate or a HCP$^{(L)}$, with the same width of the beam section, to their tension face (the face of the beams subjected to tension strain under bending deformation).

FB0_G was the only beam that was strengthened by a SHCC plate adhesively bonded to its tension face. According to the details in Figure 6.2, the SHCC plate used for the strengthening of this beam had a thickness of 20 mm and a length of 2000 mm. This beam was considered also as a reference beam.

The remaining beams were strengthened by attaching a HCP$^{(L)}$ to their soffit. The HCP$^{(L)}$ of all of these beams had identical length and thickness as the SHCC plate of FB0_G, however, these strengthened beams were categorized in two main groups. The HCP$^{(L)}$ used to strengthen the beams of the first group had only two CFRP laminates, while the specimens of the second group were strengthened using the HCP$^{(L)}$s containing four CFRP laminates.

As Figure 6.3 demonstrates, the first group of strengthened beams was composed of three specimens, whose differences are limited to the technique adopted to attach the HCP$^{(L)}$ to their soffit. The HCP$^{(L)}$ of these beams was attached by means of: (i) only chemical anchors (beam FB2_B), (ii) only epoxy adhesive (beam FB2_G), and (iii) a combination of epoxy adhesive and chemical anchors (beam FB2_BG).

In the two beams forming the second group a combination of chemical anchors and epoxy adhesive was used to attach the HCP$^{(L)}$. The HCP$^{(L)}$ of these specimens were composed of four CFRP laminates. However, the attaching systems of these beams were different considering the size and the configuration of the anchors.

As it is shown in Figure 6.4a, in the case of the beam designated FB4_BG_Phi10, one row of chemical anchors with 10 mm in diameter was used, while for the other beam, FB4_BG_Phi8, a staggered configuration of 8 mm diameter of chemical anchors was adopted (Figure 6.4b).

The arrangement of CFRP laminates in the structure of HCP$^{(L)}$ was another difference for the beams of this group. In the case of FB4_BG_Phi10, a double-CFRP laminate was bonded into each of the two pre-sawn grooves on the SHCC plate.

To accommodate a double-configuration of CFRP laminate, these grooves were cut with a width of 7 mm and a depth of 11 mm. In the case of FB4_BG_Phi8, a staggered

configuration of the chemical anchors was adopted. For this HCP$^{(L)}$ there were three grooves with equal depth of 11 mm but different width. The central groove had a width of 7 mm to provide enough space to accommodate a double-CFRP laminate, and the two lateral grooves had a width of 5 mm to bond only one CFRP laminate inside each of them. Details of the configuration of the grooves with single-laminate or double-laminate are depicted in Figure 6.5. A summary of the configurations of these beams is reported in Table 6.1.

Table 6.1: Details of beams and configuration of the strengthening plate

| Group | Label | Tension steel ratio ($\rho$) | Detail of HCP$^{(L)}$ or SHCC plate | | | | Connection system |
| | | | Thickness (mm) | Width (mm) | Length (mm) | N | |
|---|---|---|---|---|---|---|---|
| Reference | FB_R | 0.35% | - | - | - | - | - |
| | FB0_G | | 20 | 150 | 2000 | 0 | Epoxy |
| Group I | FB2_B | 0.35% | 20 | 150 | 2000 | 2 | Phi10 |
| | FB2_G | | | | | 2 | Epoxy |
| | FB2_BG | | | | | 2 | Phi10 + Epoxy |
| Group II | FB4_BG_Phi10 | 0.35% | 20 | 150 | 2000 | 4 | Phi10 + Epoxy |
| | FB4_BG_Phi8 | | | | | 4 | Phi8 + Epoxy |

$\rho = A_{st}/bd$ where, $A_{st}$ is the total area of tension steel bars, $b$ is the width and $d$ is the effective depth of the beam's cross section.
Phi10: one row of chemical anchors of 10 mm diameter.
Phi8: two rows of chemical anchors of 8 mm diameter with a staggered configuration.
N is the number of CFRP laminates adopted in the structure of the HCP$^{(L)}$.
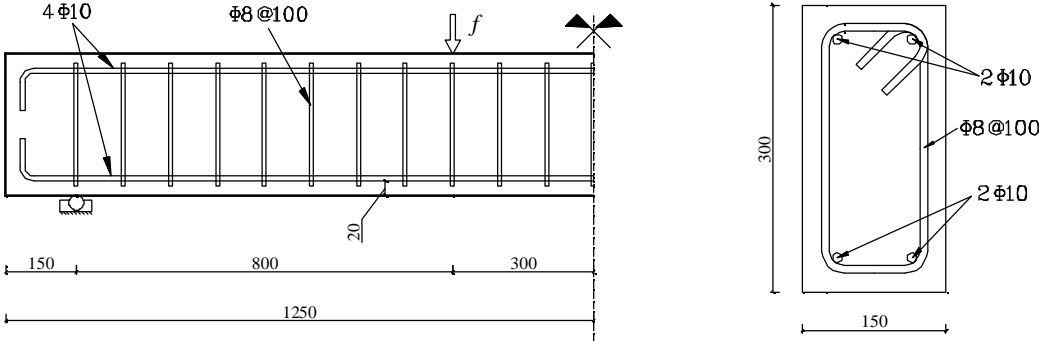
Figure 6.1: Geometry and steel arrangements of the as-built beam (dimensions in mm)
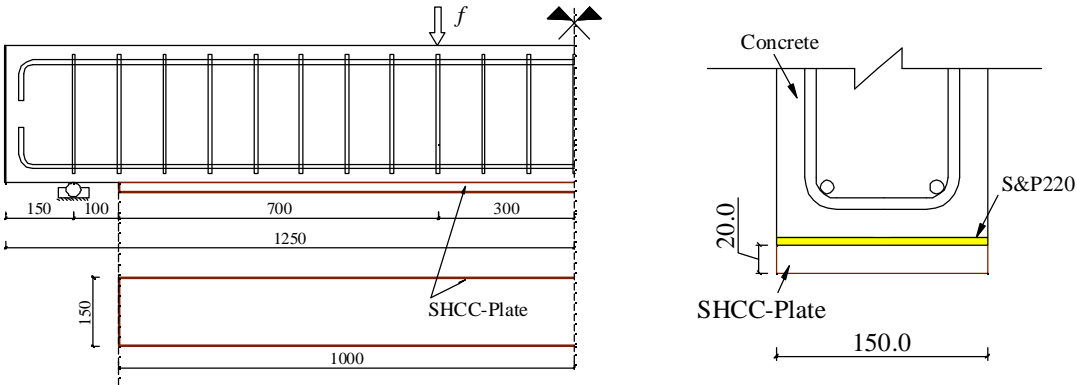


Figure 6.2: Configuration of the beam strengthened with SHCC plate (FB0_G) (dimensions in mm)

(a)



(b)



(c)
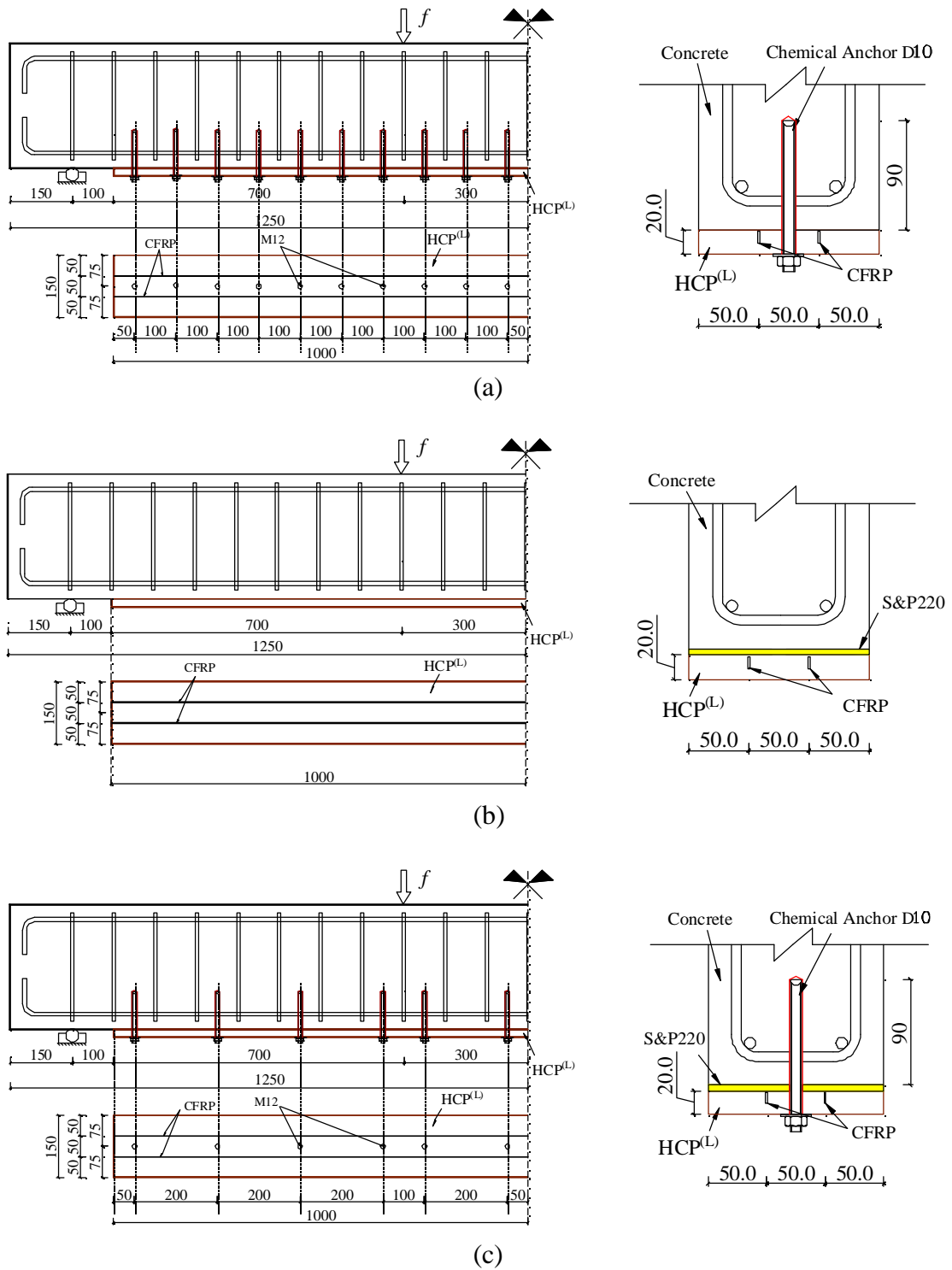
Figure 6.3: Configuration of the beam strengthened with HCP$^{(L)}$ in group I, (a) FB2_B, (b) FB2_G, and (c) FB2_BG (dimensions in mm)

(a)



(b)
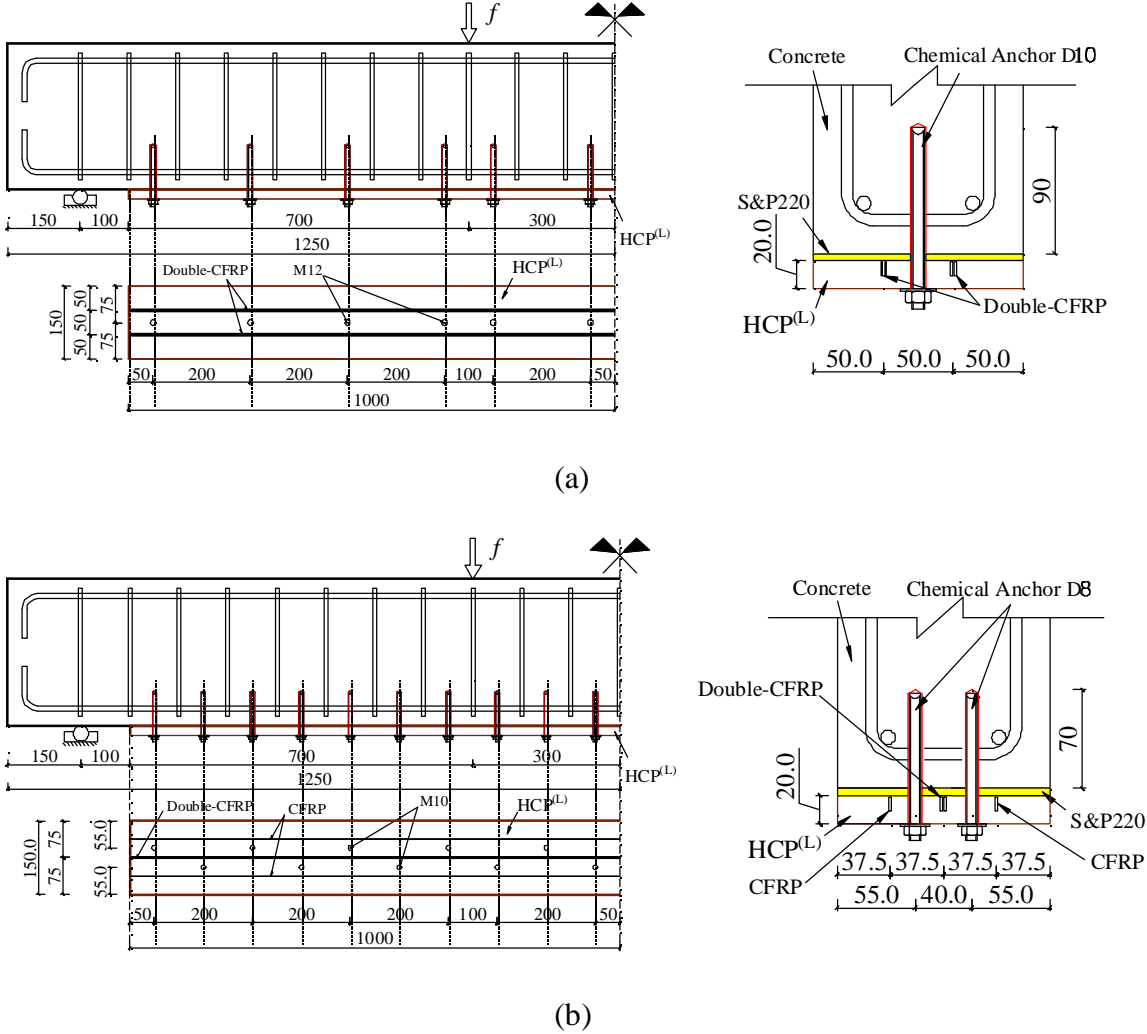
Figure 6.4: Configuration of the beam strengthened with HCP$^{(L)}$ in group II, (a) FB4_BG_Phi10, and (b) FB4_BG_phi8 (dimensions in mm)

Figure 6.5: Configuration of bonded CFRP laminates into the grooves of HCP$^{(L)}$ (a) single-CFRP laminate and (b) double-CFRP laminate (dimensions in mm)

### 6.2.2 Strengthening Strategy

SHCC plates were cast in acrylic molds with dimensions of 2000 mm $\times$ 150 mm $\times$ 20 mm. PVA-SHCC mix procedure and mix composition was same as that described in Section 4.3 for composite C4W30, however, these mixtures were prepared in a planetary rotatable mixer with a potential of mixing 25 liters. In order to cast six SHCC plates, three batches of mixtures of 13 liters were prepared to fill two molds in each casting.

The SHCC mixture was initially poured slowly into the center of the mold (Figure 6.6). Thanks to the self-compacting character of the tailored SHCC, it flowed and filled more than half of the molds spaces at each sides of the pouring location, without introducing any external vibration. Afterwards, casting was continued by pouring the SHCC from the center of each of the remaining regions at the end portions of the molds. After leveling the top surface of the fresh SHCC, the casted specimens were covered and sealed with plastic sheets.

These SHCC plates were cured following the procedure adopted for the specimen SL1 in section 4.4. Thus, the plates were de-molded only after 24 hours of curing the sealed SHCCs at room temperature. Afterwards, these SHCC plates were supported on a wooden bar and moved to the climate room with a constant temperature and a relative humidity of 20° C and 57%, respectively. These plates were kept in the climate room up to their attaching to the beams, this time period has exceeded 28 days.

Figure 6.6: Casting of the SHCC plates from the mid-length of the acrylic molds

As the next step, except for one SHCC plate, grooves with a geometry presented in Figure 6.5 and according to the details of HCP(L)s depicted in Figure 6.3 and Figure 6.4 were cut on the top face (respecting to casting direction) of the SHCC plates. The remaining plate, the one without grooves, was used to strengthen the beam FB0_G.

All the grooves were then cleaned using compressed air and filled by epoxy adhesive. CFRP laminates, already cleaned by acetone, were placed at the mid-width of each groove.

To construct the double-CFRP laminate, small spacers, with a width of 10 mm and a thickness of 1.5 mm, were placed between adjacent faces of two CFRP laminates. This strategy assured the flow of the epoxy adhesive into this gap, covering both lateral faces of each laminate. When the gap between adjacent laminates and also between the laminates and the groove's wall were fully filled with epoxy resin, spacers were removed and epoxy resin was introduced in place of them.

For both types of configurations of CFRP laminates (single and double), after placing CFRPs inside the grooves, the remaining gaps were filled by an extra epoxy adhesive using a spatula. Finally, the excessive epoxy adhesive was removed by a leveling procedure and the strengthened plates were cured in the room environment for at least two days before attaching them to the beams.

To enhance the bond quality at the interface of the epoxy adhesive and the beam, the tension face of the beams needs to be roughened. For this purpose, tension face of the beams was sand-blasted to remove 1 to 2 mm of cement paste and to partially expose the aggregates (Figure 6.7).
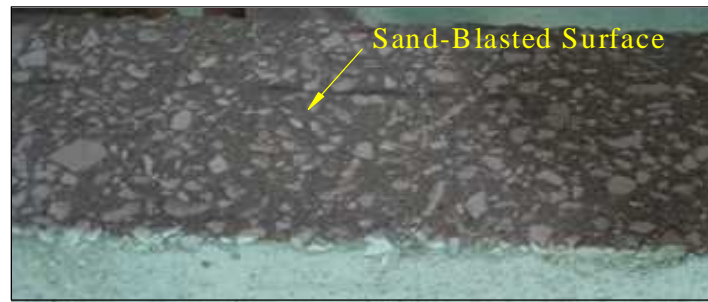
Figure 6.7: Tension faces of the beams roughened by means of sand-blasting

The beams were positioned upside-down to facilitate attaching the strengthening plates to their tension face in laboratory condition. Therefore, at this position, the strengthening plates were attached to the top face of the beams. In the cases where chemical anchors were used in the attaching system, their positions were marked and then drilled on the HCP$^{(L)}$s. Afterwards, each perforated plate was placed on its corresponding beam and the positions of the holes were mapped on the top face of the beams.

Except for FB4_BG_Phi8, a 12 mm diameter drill bit was used for perforating the beams. In compliance with the effective depth indicated in the technical datasheet of the chemical anchors, a perforation depth of 90 mm was adopted for these beams (see details of beams FB_B, FB2_BG and FB4_BG_Phi10 in Figure 6.3a, Figure 6.3c and Figure 6.4a). For the case of FB4_BG_Phi8, a drill bit of 10 mm in diameter was used to perforate holes of 70 mm in depth inside the beams (see Figure 6.4b).

Prior placing anchors, the holes were injected with a fast curing chemical adhesive to approximately fill a two-third of their depth. After inserting anchors the excessive chemical adhesive was removed.

Before placing the HCP$^{(L)}$ on the beam, the epoxy adhesive was spread on the contact surfaces of both HCP$^{(L)}$ and beam's concrete substrate. It should be noted that the contact face of the HCP$^{(L)}$ was the one in which CFRP laminates were installed. After placing the HCP$^{(L)}$ on the tension face of the beam, by fastening the nuts the epoxy adhesive was forced to flow and fill uniformly the entire contact surfaces of the HCP$^{(L)}$ and the beam. A view of some of the beams after applying the strengthening scheme can be found in Figure 6.8.

Figure 6.8: Images of some of the beams after fixing the strengthening plates (note that beams are positioned upside-down)

For the beams in which epoxy adhesive was the only component used for attaching the strengthening scheme, the plate was pressed against the beam in order to force adhesive to flow between the contact faces. Finally, some weights were put on top of the plate aiming to hold it in its position. For in-situ application, a few number of anchors is recommended to facilitate the installation process of the strengthening plate.

Thanks to the high ductile characteristic of these plates, the HCP$^{(L)}$ can locally deform while only diffused fine cracks may form. In fact, fastening of the nuts during attaching the plate can press it against the surface of the beam. This results in a better adjustment at the level of the contact surfaces, especially when some irregularities at the surface of the substrate exist. To assure that bonding adhesive attains its maximum mechanical properties, a curing period of adhesive at least seven days was considered before testing the corresponding beam [1]. Prior to testing the beams, a torque of 30 and 20 N·m was applied to post-tension the anchor rods of 10 and 8 mm, respectively.

Finally, surface of the strengthening plates was painted using a varnish to facilitate visualization of the micro-cracks after spraying this surface by the penetrating liquid.

### 6.2.3 Test Setup and Monitoring Instruments

As schematically represented in Figure 6.9, a four-point bending test setup, with a clear supporting span ($l_s$) of 2200 mm and a shear loading span ($a_s$) of 800 mm, was prepared to experimentally evaluate the flexural response of the beams. A constant displacement rate of 0.01 mm/s, measured by the internal LVDT of the jack, was adopted to experimentally evaluate the flexural response of the beams.
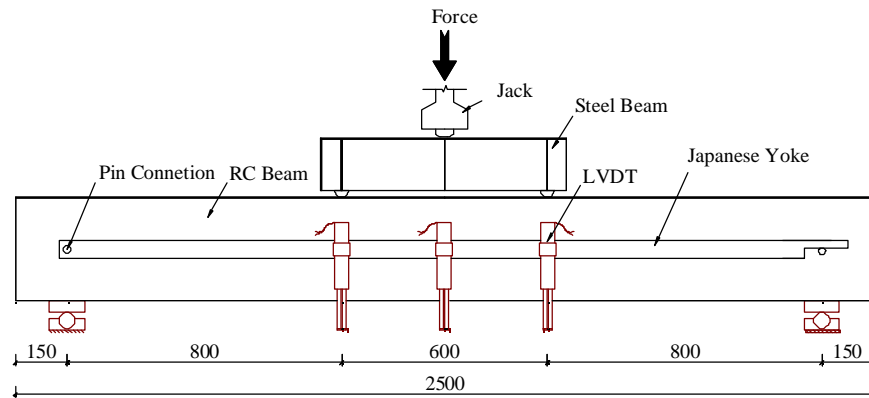
Figure 6.9: Four point bending test setup (dimensions in mm)

The deflection at the mid-span and the loaded sections of the tested beams were measured using three LVDTs supported on a Japanese yoke (a steel bar fixed to the mid-height of the beam at the locations of the beam's supports, using a pin connection at one end and a rolling connection at the other end). The displacement at the loaded section was measured aiming to calibrate a finite element model which is out of the scope of current study.

Strain gauges were used to measure the local deformation for a limited number of locations along the longitudinal reinforcement. For all specimens, including reference beam, a strain gauge (SM) was bonded to the mid-length of one of the longitudinal tension steel bars. For the specimens strengthened with HCP$^{(L)}$, strain gauges were used to measure the tensile strain in CFRP laminates at mid-span (PM), under the loaded section at the right span of the beam (PL), and at the theoretical curtailment (PTC). The calculations of theoretical curtailment section and the details of positioning of the strain gauges are presented in section 6.2.5.3.

Only a few numbers of strain gauges was used to minimize the disturbance of the bond between CFRP laminates and surrounding SHCC along the strengthened length of the beam. However, some of these strain gauges did not function properly, possibly due to the damages introduced by the fastening pressure of the anchors. A proper functioning of all of the strain gauges installed on FB2_G justifies this explanation. Regarding the strain gauges bonded to the steel bars, only for the case of FB_R the results were reliable!

### 6.2.4 Material Properties

### 6.2.4.1 Concrete

Modulus of elasticity and the compressive strength of the ready-mix concrete used for casting the beams were determined following the specifications of LNEC E397-1993 [2] and EN 12390-3:2009 [3], respectively. Thus, four cylinders of 150 mm in diameter and 300 mm in depth at the age of 90 days were tested. According to the results of these tests, an average modulus of elasticity of 32.52 GPa and an average compressive strength of 31.26 MPa was obtained.

### 6.2.4.2 SHCC

Details on fresh and hardened state properties of the self-compacting PVA-SHCC (mixture C4W30) used for casting the SHCC plates can be found in section 4.3.

### 6.2.4.3 Epoxy Adhesive

The mechanical characteristics of the S&P Resin 220 epoxy adhesive, used to bond CFRP laminates into the grooves of the SHCC and also to bond the strengthening plates to the soffit of the beams, were reported in section 4.5.3.4.

### 6.2.4.4 CFRP Laminates

CFRP laminates (S&P laminate CFK 150/2000) were cut from the same roll used to prepare HCP$^{(L)}$s for the repair of damaged RC beam-column joints in chapter 5. Thus, tensile characteristics of these laminates can be found in section 5.2.3.2.

### 6.2.4.5 Steel Rebars

Properties of the longitudinal steel rebars and the steel stirrups were determined by means of tensile tests according to ISO 15630-1-2010 [4].

From the results of these tensile tests on four specimens of 10 mm diameter steel rebars (longitudinal reinforcements), average values of 536 MPa, 629 MPa and 215.8 GPa were determined as the yield stress, ultimate strength, and modulus of elasticity, respectively. For the yield stress, ultimate strength, and modulus of elasticity of 8 mm diameter steel rebars (stirrups), average values of 555 MPa, 643 MPa, and 216.6 GPa , respectively, were obtained on the basis of tensile testing on four specimens.

### 6.2.4.6 Chemical Anchors

In the cases where the connection system of HCP$^{(L)}$ to the RC beam included chemical anchors, a Hilti$^{®}$ system with a fast curing resin (HIT-HY 200A) was employed. In this system either 8 mm or 10 mm diameter anchor rods with specification of HIT-V-5.8 M8X110 and HIT-V-8.8 M10X190, respectively, were used. Characteristics of these anchors rods can be found in sections 4.5.3.6 and 5.2.3.5.

### 6.2.5 Design Procedure of the Retrofitting Systems

The number of CFRP laminates used in HCP$^{(L)}$ for the strengthening of the first and second groups of beams was determined considering the required section area to attain a balance failure of the strengthened beam. The balance failure mode is defined as a simultaneous CFRP rupture $\left(\varepsilon_f = \varepsilon_f^r\right)$ and crushing of concrete in compressive block $\left(\varepsilon_{cc}^t = \varepsilon_{cc}^u\right)$. It can be assumed that for this mode of failure, tension steel bars are already yielded $\left(\varepsilon_{st} \geq \varepsilon_{st}^y\right)$.

### 6.2.5.1 Calculation of the Balance Section Area of the CFRP Laminates

Figure 6.10 shows the schematic stress-strain distribution along the depth of the cross-section of a HCP$^{(L)}$ strengthened beam. For the case of a balance failure mode, based on the assumption that plane sections remain plane after bending, and assuming a perfect bond between constituent materials, a linear strain distribution along the depth of the cross-section is adopted (see Figure 6.10b). By employing the equivalent rectangular stress distribution according to the Figure 6.10c, the section area of the balance CFRP laminates $\left(A_f^b\right)$ can be calculated.

By employing the equivalent rectangular compressive stress distribution recommended by EC2 [5] and considering the force components indicated in Figure 6.10b and Figure 6.10c, the state of equilibrium of the section $\left(\sum F = 0\right)$ can be formulated based on strain compatibility and stress distribution along the depth of the section, resulting equations (6-1) to (6-7).

The position of the neutral axis, $n$, can be also calculated by using equation (6-8). After replacing $n$ in the equation (6-7) and solving it, the balance section area of CFRP laminates $\left(A_f^b\right)$ can be obtained from equation (6-9).

According to EC2 [5], the equivalent rectangular compressive block is composed of a uniform compressive stress of $f_{cd} = \alpha_{cc}f_{ck}/\gamma_c$ distributed in a height of $\lambda n$ (see Figure 6.10c). Assuming unit value for partial safety factor $(\gamma_c)$ and strength reduction factor $(\alpha_{cc})$ also using an average compressive strength $(f_{cc}^m)$ instead the characteristic value $(f_{ck})$ then $f_{cd} = f_{cc}^m$. For a concrete with a characteristic strength equal or lower than 50 MPa, the recommended value for $\lambda = 0.8$ and for $\varepsilon_{cu} = -0.0035$.

To simplify, the analysis, the contribution of the part of concrete in tension is neglected in static equilibrium of the section. Moreover, as it is shown in Figure 6.11, tensile behavior of the SHCC and the steel bars are assumed to be elastic-perfectly plastic with their maximum strength equal to the stress at the first cracking of the SHCC $(f_{sh}^{cr})$ and the yielding of tension steel bars $\left(f_{st}^y\right)$ (the behavior of steel under uniaxial compression was considered identical to its tensile response). According to this strategy, $A_f^b = 64.4$ mm$^2$ was obtained (note that in these equations for the stresses, strains or forces in compression a negative sign is adopted) and four CFRP laminates providing $A_f = 56$ mm$^2$ were adopted for the HCP$^{(L)}$ of the beams in the second group and half of this reinforcement, $A_f = 28$ mm$^2$, was assigned to the HCP$^{(L)}$ of the beams in the first group.

$$\varepsilon_{sc} = \varepsilon_{cc}^u \frac{(n - d')}{n} \tag{6-1}$$

$$F_{cc} = \lambda n b f_{cc}^m \quad \text{with} \quad \lambda = 0.8 \quad \text{EC2 [5]} \tag{6-2}$$

$$F_{sc} = \begin{cases} E_{sc}A_{sc}\varepsilon_{cc}^u \dfrac{(n - d')}{n} & \varepsilon_{sc} \leq \varepsilon_{sc}^y \\ f_{sc}^y A_{sc} & \varepsilon_{sc} > \varepsilon_{sc}^y \end{cases} \tag{6-3}$$

$$F_{st} = A_{st}f_{st}^y \tag{6-4}$$

$$F_f = A_f^b f_f^r \tag{6-5}$$

$$F_{sh} = A_{sh} f_{sh}^{cr} \tag{6-6}$$

$$F_{cc} + F_{sc} + F_f + F_{st} + F_{sh} = 0 \tag{6-7}$$

$$n = \frac{\varepsilon_{cc}^u d_f}{(\varepsilon_{cc}^u - \varepsilon_f^r)} \tag{6-8}$$

$$A_f^b = \begin{cases} -\left(0.8nbf_{cc}^m + E_{sc}A_{sc}\varepsilon_{cc}^u \dfrac{(n-d')}{n} + A_{st}f_{st}^y + A_{sh}f_{sh}^{cr}\right)/\left(E_f\varepsilon_f^r\right), & \varepsilon_{sc} \leq \varepsilon_{sc}^y \\[2ex] -\left(0.8nbf_{cc}^m + f_{sc}^y A_{sc} + A_{st}f_{st}^y + A_{sh}f_{sh}^{cr}\right)/\left(E_f\varepsilon_f^r\right), & \varepsilon_{sc} > \varepsilon_{sc}^y \end{cases} \tag{6-9}$$

where in the above equations,

$b$ and $h$ represent the width and depth of beam, respectively,

$d'$, $d_f$, $d_{sh}$ and $d_{st}$ are the distance of the centroids of compression steel, CFRP laminates, SHCC, and tension steel, respectively, from the extreme compressive fiber,

$f_{cc}^t$ and $f_{cc}^m$ are the stress in the extreme compressive fiber of the concrete and the mean compressive strength of concrete cylinder, respectively,

$F_{cc}$, $F_{sc}$, $F_{st}$, $F_{sh}$, and $F_f$ indicate the resultant forces in compression concrete, compression steel bars, tension steel bars, in SHCC, and CFRP laminates, respectively,

$n$, $x$, and $a$ represent the depth of natural axis, the distance of a fiber from natural axis, and the distance of resultant compressive force from neutral axis,

$\varepsilon_{cc}^t$, $\varepsilon_f$, $\varepsilon_{sc}$, $\varepsilon_{st}$, and $\varepsilon_{sh}$ are the strains in the extreme compressive fiber of concrete, CFRP laminates, compression steel reinforcement, tension steel reinforcement, and the centroid of the SHCC, respectively,

$\varepsilon_{cc}^u$, $\varepsilon_f^r$, and $\varepsilon_{sc}^y$ are the strains at the ultimate concrete compressive strength, rupture of CFRP laminates and corresponding to the yield of compression steel reinforcement, respectively,

$f_{sc}^y$, $f_{st}^y$, $f_f^r$, and $f_{sh}^{cr}$ are the yield strength of compression steel bars, yield strength of tension steel bars, rupture stress of CFRP, and cracking strength of SHCC (tensile stress at the onset of first crack), respectively,

$A_f$, $A_{sc}$, $A_{st}$, and $A_{sh}$ are the section areas of CFRP laminates, compression steel reinforcement, the tension steel reinforcement, and SHCC, respectively,

$A_f^b$ represents the balanced section area of CFRP laminates,

$E_{sc}$ and $E_{st}$ are modulus of elasticity of compression and tension steel reinforcements, respectively.
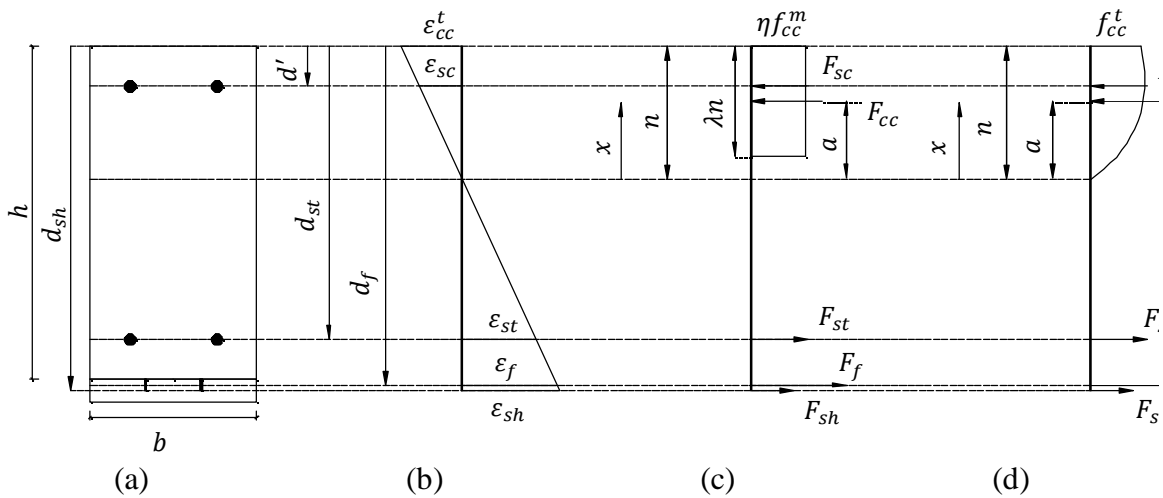


Figure 6.10: Schematic presentation of internal strain and stress distribution for a HCP$^{(L)}$ strengthened RC section at ultimate state, (a) section configuration, (b) strain distribution, (c) simplified stress profile using equivalent concrete compressive rectangular block, (d) stress profile based on concrete parabolic compressive stress-strain curve.
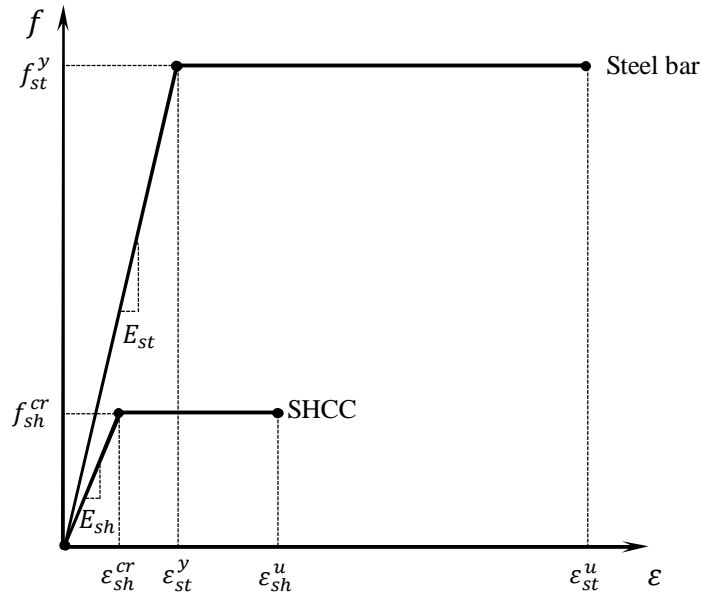
Figure 6.11: Schematic presentation of the idealized elastic-perfectly plastic response assumed for the tensile stress-strain relationship of the SHCC and the steel bars

### 6.2.5.2 Flexural Capacity of the HCP(L) Strengthened Beams

Since for both groups of strengthened beams, the total section areas of CFRP laminates utilized in the structure of the HCP(L)s were less than $A_f^b$, the rupture of the CFRP laminates is the expected failure mode, provided that detachment of the HCP(L) is not the prevailing failure.

Considering that at the failure of these beams, the maximum concrete compressive strain is lower than $\varepsilon_{cc}^u$, the moment capacity ($M_R$) is calculated adopting two different stress distribution for concrete in compression: (i) constant stress distribution (Whitney block), and (ii) nonlinear stress distribution. Further, the flexural capacities obtained from these approaches are compared in order to verify the accuracy of prediction based on using an equivalent compression block as a simplified method.

In both of these strategies, the flexural capacity at CFRP rupture is calculated assuming that tension steel bars are already yielded and the compression steel bars are still in their linear-elastic regime. The assumptions used for the tensile contribution of the concrete, the idealized stress-strain relationships for SHCC and steel bars in the calculation of balance amount of CFRP laminates (see section 6.2.5.1) are applied herein as well.

*Rectangular compressive stress distribution:* considering Figure 6.10a to Figure 6.10c and simplifying the equations of static equilibrium of the section ($\sum F = 0$), developed based on strain compatibility and stress distribution as indicated in equations (6-10) to (6-19), the depth of neutral axis, $n$, can be found by solving the quadratic equation (6-20). Constants of this latter equation are introduced in equations (6-21) to (6-23). Thus, the depth of neutral axis, $n$, can be calculated from equation (6-24). Finally, the flexural capacity ($M_R$) of the beams of groups I and II can be calculated from equation (6-25).

$$\varepsilon_f = \varepsilon_f^r \tag{6-10}$$

$$\varepsilon_{cc} = \varepsilon_f^r \frac{n}{\left(n - d_f\right)} \tag{6-11}$$

$$\varepsilon_{sc} = \varepsilon_f^r \frac{(d' - n)}{\left(d_f - n\right)} \tag{6-12}$$

$$F_{cc} = \lambda n b f_{cc}^m \quad \text{with} \quad \lambda = 0.8 \quad \text{EC2 [5]} \tag{6-13}$$

$$F_{sc} = E_{sc} A_{sc} \left[\varepsilon_f^r \frac{(d' - n)}{\left(d_f - n\right)}\right] \qquad \varepsilon_{sc} < \varepsilon_{sc}^y \tag{6-14}$$

$$F_{st} = A_{st} f_{st}^y \qquad \varepsilon_{st} \geq \varepsilon_{st}^y \tag{6-15}$$

$$F_f = A_f f_f^r \tag{6-16}$$

$$F_{sh} = A_{sh} f_{sh}^{cr} \tag{6-17}$$

$$F_{cc} + F_{sc} + F_f + F_{st} + F_{sh} = 0 \tag{6-18}$$

$$-\lambda b f_{cc}^m n^2 - \left(A_{st} f_{st}^y + A_f f_f^r + A_{sh} f_{sh}^u + E_{sc} A_{sc} \varepsilon_f^r - \lambda b f_{cc}^m d_f\right) n + \left(A_{st} f_{st}^y + A_f f_f^r + A_{sh} f_{sh}^{cr}\right) d_f + E_{sc} A_{sc} \varepsilon_f^r d' = 0 \tag{6-19}$$

$$\boldsymbol{A n^2 + B n + C = 0} \tag{6-20}$$

$$\boldsymbol{A = -\lambda b f_{cc}^m} \tag{6-21}$$

$$B = -\left(A_{st}f_{st}^{y} + A_{f}f_{f}^{r} + A_{sh}f_{sh}^{cr} + E_{sc}A_{sc}\varepsilon_{f}^{r} - \lambda b f_{cc}^{m}d_{f}\right) \tag{6-22}$$

$$C = \left(A_{st}f_{st}^{y} + A_{f}f_{f}^{r} + A_{sh}f_{sh}^{cr}\right)d_{f} + E_{sc}A_{sc}\varepsilon_{f}^{r}d' \tag{6-23}$$

$$n = \frac{-B \pm \sqrt{B^2 - 4AC}}{2A} \tag{6-24}$$

$$M_R = A_{st}f_{st}^{y}d_{st} + A_{f}f_{f}^{r}d_{f} + A_{sh}f_{sh}^{cr}d_{sh} + E_{sc}A_{sc}\left[\varepsilon_{f}^{r}\frac{(d'-n)}{(d_f-n)}\right]d' + 0.5\lambda^2 n^2 b f_{cc}^{m} \tag{6-25}$$

where, in the above equations, $\varepsilon_{cc}$ corresponds to the compressive strain in concrete and $f_{sh}^{u}$ represents the ultimate tensile strength of SHCC

*Nonlinear compressive stress distribution:* as it is presented schematically in Figure 6.10d and mathematically in equation (6-26), a parabolic stress distribution for concrete in compression block, recommended by EC2 [5], is also employed.

By simplifying the equations of equilibrium of the section, equations (6-27) to (6-36), the depth of neutral axis, $n$, can be found by solving the cubic equation (6-37) with its constants presented in equations (6-38) to (6-43). The flexural capacity $(M_R)$ of the beams of groups I and II can be calculated from equation (6-44). In this equation $a$ is the distance of the location of the concrete compressive resultant force, $F_{cc}$, from neutral axis (see Figure 6.10d) and can be obtained from simplified version of equation (6-45), as presented in equation (6-46).

$$f_{cc} = f_{cc}^{m}\left\{2\left(\frac{\varepsilon_{cc}}{\varepsilon_{cc}^{m}}\right) - \left(\frac{\varepsilon_{cc}}{\varepsilon_{cc}^{m}}\right)^2\right\} \qquad 0 \le \varepsilon_{cc} \le \varepsilon_{cc}^{u} \text{ (with } \varepsilon_{cc}^{m} \text{ being strain at } f_{cc}^{m}) \tag{6-26}$$

$$F_{cc} = b\int_{0}^{n}\left(f_{cc}^{m}\left\{2\left(\frac{\varepsilon_{cc}}{\varepsilon_{cc}^{m}}\right) - \left(\frac{\varepsilon_{cc}}{\varepsilon_{cc}^{m}}\right)^2\right\}\right)d_x \tag{6-27}$$

$$\varepsilon_{cc} = \varepsilon_{f}^{r}\frac{x}{(n-d_f)} \tag{6-28}$$

$$F_{cc} = -b \frac{f_{cc}^m}{(n - d_f)^2} \frac{\varepsilon_f^r}{\varepsilon_{cc}^m} \left[ d_f n^2 - \left( 1 - \frac{\varepsilon_f^r}{3\varepsilon_{cc}^m} \right) n^3 \right] \tag{6-29}$$

$$F_{sc} = E_{sc} A_{sc} \left[ \varepsilon_f^r \frac{(d' - n)}{(d_f - n)} \right] \qquad \varepsilon_{sc} < \varepsilon_{sc}^y \tag{6-30}$$

$$F_{st} = A_{st} f_{st}^y \qquad \varepsilon_{st} \geq \varepsilon_{st}^y \tag{6-31}$$

$$F_f = E_f A_f \varepsilon_f^r \tag{6-32}$$

$$F_{sh} = A_{sh} f_{sh}^{cr} \tag{6-33}$$

$$F_f + F_{st} + F_{sh} + F_{cc} + F_{sc} = 0 \tag{6-34}$$

$$T = F_f + F_{st} + F_{sh} \tag{6-35}$$

$$-b f_{cc}^m \frac{\varepsilon_f^r}{\varepsilon_{cc}^m} \left[ d_f n^2 - \left( 1 - \frac{\varepsilon_f^r}{3\varepsilon_{cc}^m} \right) n^3 \right] - E_{sc} A_{sc} \varepsilon_f^r \left( n d_f - n^2 - d' d_f + d' n \right) +$$
$$T d_f{}^2 + T n^2 - 2 T d_f n = 0 \tag{6-36}$$

$$\boldsymbol{A} n^3 + \boldsymbol{B} n^2 + \boldsymbol{C} n + \boldsymbol{D} = 0 \tag{6-37}$$

$$\gamma = b f_{cc}^m \frac{\varepsilon_f^r}{\varepsilon_{cc}^m} \tag{6-38}$$

$$\mu = E_{sc} A_{sc} \varepsilon_f^r \tag{6-39}$$

$$\boldsymbol{A} = \gamma \left( 1 - \frac{\varepsilon_f^r}{3\varepsilon_{cc}^m} \right) \tag{6-40}$$

$$\boldsymbol{B} = \mu + T - \gamma d_f \tag{6-41}$$

$$\boldsymbol{C} = -\mu \left( d_f + d' \right) - 2 T d_f \tag{6-42}$$

$$\boldsymbol{D} = \mu d' d_f + T d_f{}^2 \tag{6-43}$$

therefore,

$$M_R = F_f d_f + F_{st} d_{st} + F_{sh} d_{sh} + F_{sc} d' + F_{cc}(n - a) \tag{6-44}$$

where, $a$ is the distance of the location of the resultant force $F_{cc}$ from neutral axis (see Figure 6.10) and can be obtained according to equation (6-45) with its simplified form in equation (6-46):

$$a = \frac{\int_0^n x f_{cc} \, d_x}{\int_0^n f_{cc} \, d_x} \qquad \text{(with } f_{cc} \text{ being the compressive stress in concrete)} \tag{6-45}$$

$$a = \frac{n \left[ \dfrac{2}{3} - \dfrac{n}{4(n - d_f)} \dfrac{\varepsilon_f^r}{\varepsilon_{cc}^m} \right]}{\left[ 1 - \dfrac{n}{3(n - d_f)} \dfrac{\varepsilon_f^r}{\varepsilon_{cc}^m} \right]} \tag{6-46}$$

*Comparison of the adopted approaches:* The predicted $M_R$ of the beams of groups I and II based on the abovementioned strategies are indicated and compared in Table 6.2. According to these results, the formulation based on equivalent compressive stress block (simplified method) estimates a flexural capacity similar to the one obtained using a nonlinear distribution of compressive stresses (a difference less than 0.5%).

Table 6.2: Predicted flexural capacity ($M_R$) of beams of groups I and II based on either an equivalent compressive stress block ($M_{R1}$) or nonlinear distribution of compressive stresses ($M_{R2}$) and comparison of these two approaches.

| $M_{R1}$ (kN·m) | | $M_{R2}$ (kN·m) | | $\frac{M_{R1} - M_{R2}}{M_{R2}}$ (%) | |
|---|---|---|---|---|---|
| Group I | Group II | Group I | Group II | Group I | Group II |
| 45.9 | 66.5 | 45.7 | 66.2 | 0.44 | 0.45 |

### 6.2.5.3 Sections of Theoretical Curtailment and Positions of the Strain Gauges

The theoretical curtailment is defined as a location where, for a specified bending load demand of the strengthened beam, extending the strengthening plate beyond that is not required anymore. In the other word, the moment demand is the same as the capacity of the

as-built beam. This location was found according to the expected maximum moment capacities for the strengthened beams when FRP rupture is the failure mode, as discussed in previous section. Figure 6.12 shows the profile of the bending moment of the strengthened beams along their half span when the maximum moment at the pure bending zone reaches the flexural capacity (the bending moment corresponding to the rupture of CFRP laminates). The moment capacity of the un-strengthened beam is also plotted in this Figure. The section where beyond that the flexural demand is less than the moment capacity of the un-strengthened beam is then determined as the position of the theoretical curtailment. Considering the position of the theoretical curtailment, the arrangement of the strain gauges on the CFRP laminates of the HCP(L)'s are also depicted in Figure 6.12.



(a)                                          (b)
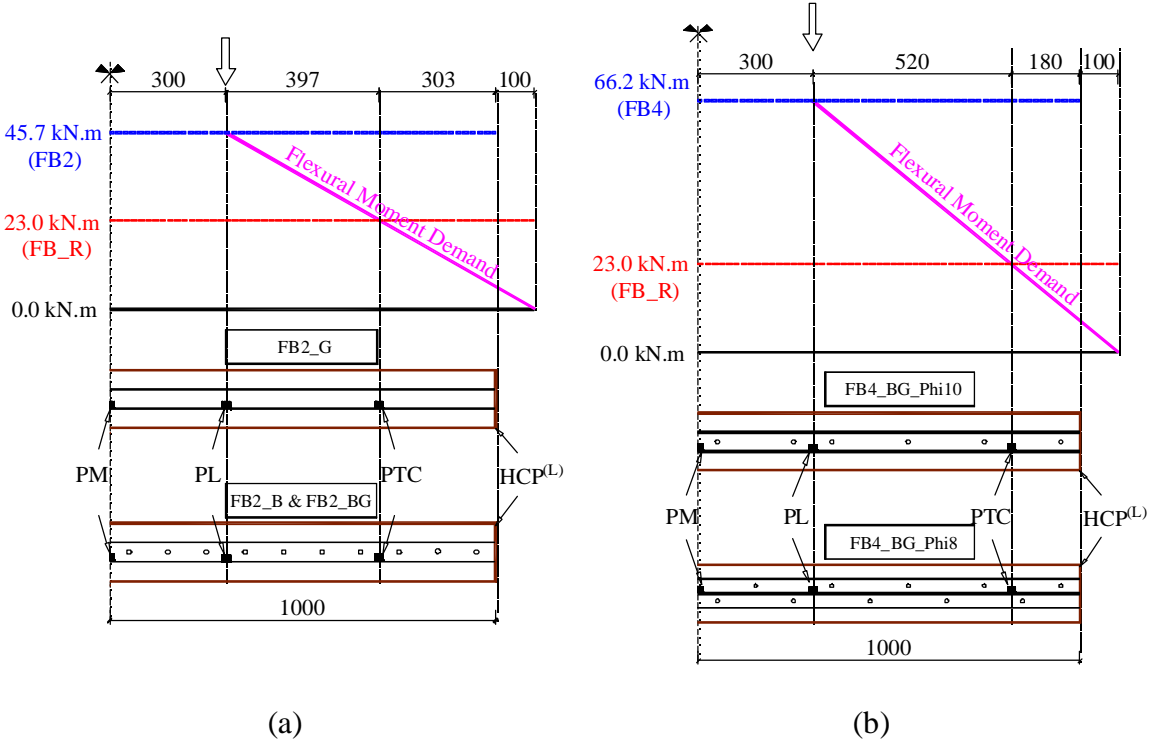
Figure 6.12: Position of the theoretical curtailment sections and the arrangement of the strain gauges (PM, PL and PTC) for (a) Beams with two CFRP laminates (group I), and (b) beams with four CFRP laminates (group II).

The moment capacity of the reference beam (FB_R) was calculated assuming that concrete crushing $(\varepsilon_{cc}^t = \varepsilon_{cc}^u)$ occurs following the yield of the tension steel bars $(\varepsilon_{st} \geq \varepsilon_{st}^y)$ while the compression steel bars are yet functioning in the linear-elastic range $(\varepsilon_{sc} < \varepsilon_{sc}^y)$. Considering Figure 6.10c, but with $F_f = F_{sh} = 0$, and the same assumptions of the section 6.2.5.1, the moment capacity $(M_R)$ can be calculated based on a static equilibrium at the beam's section. Therefore, by replacing equations (6-1) to (6-4) into (6-7), the depth of natural axis $(n)$ can be found from equation (6-47):

$$A_{st}f_{st}^y = 0.8nbf_{cc}^m + E_{sc}A_{sc}\varepsilon_{cc}^u \frac{(n - d')}{n} \tag{6-47}$$

Finally, the moment resistance of the reference beam is calculated as 22.4 kN·m by using the following equation:

$$M_R = A_{st}f_{st}^y(d_{st} - d') - 0.8nbf_{cc}^m(0.4n - d') \tag{6-48}$$

## 6.3 Experimental Tests Results and Discussions

The load-deflection curves registered for all the tested beams are presented in Figure 6.13. A summary including the values for the loads and their corresponding mid-span deflections at the onset of cracking ($F_{cr}$ and $\delta_{cr}$), at the yield of tension steel bars ($F_y$ and $\delta_y$) and at the ultimate state of the beams ($F_u$ and $\delta_u$), is reported in Table 6.3. The service load, $F_{400}$, at deflection equal to the beam's span divided by 400 $\left(\delta_{400} = \frac{l_s}{400}\right)$, the deflection ductility ($\mu_\delta = \delta_u/\delta_y$), and the maximum strain measured by the strain gauge "PM" and the failure mode of each beam are indicated in the same table.

In the following sections, these results are used to discuss the failure mode and the overall behavior of each beam, and also to compare the flexural behavior of the strengthened beams.
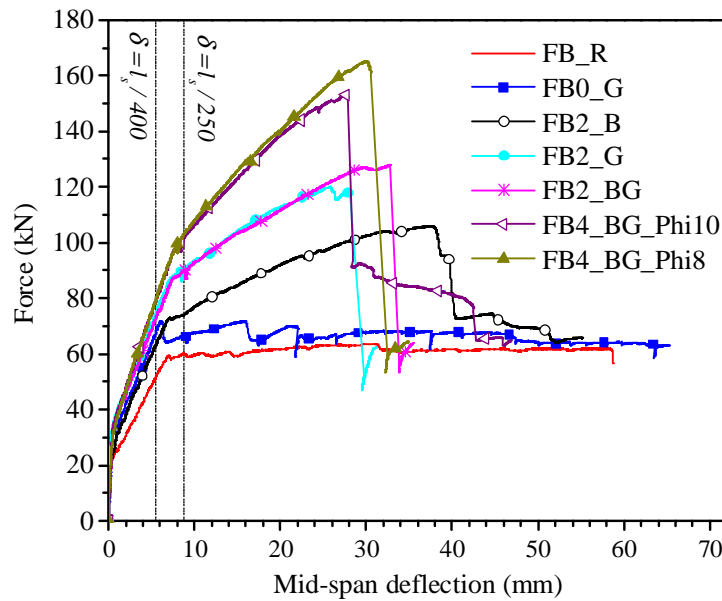
Figure 6.13: Load-deflection curves of the beams obtained from four point bending tests

Table 6.3- Results obtained from the analysis of the tested beams

| beam | first crack | | steel yield | | ultimate | | service | deflection ductility | strain gauge "PM" | failure mode[c] |
|---|---|---|---|---|---|---|---|---|---|---|
| | $\delta_{cr}$ (mm) | $F_{cr}$ (kN) | $\delta_y$ (mm) | $F_y$ (kN) | $\delta_u$ (mm) | $F_u$ (kN) | $F_{400}$ (kN) | $\mu_\delta$ | % | - |
| FB_R | 0.31 | 21.5 | 7.1 | 59.3 | 58.4 | 61.8 | 51.8 | 8.2 | | |
| | - | - | - | - | - | - | - | - | - | SY-CC |
| FB0_G | 0.53 | 33.3 | 6.1 | 71.8 | 65.3 | 61.03 | 67.9 | 10.7 | - | |
| | (71%)[a] | (55%) | (-14%) | (21%) | (12%) | (-1.2%) | (31%) | (30%) | - | |
| FB2_B | 0.44 | 23.5 | 7.1 | 72.9 | 37.5 | 106.0 | 63.1 | 5.3 | 1.19 | SH |
| | (42%) | (9%) | (0%) | (23%) | (-36%) | (72%) | (22%) | (-36%) | [74%][b] | |
| FB2_G | 0.54 | 33.2 | 7.2 | 87 | 25.9 | 120.0 | 74.9 | 3.6 | 1.33 | DH |
| | (74%) | (54%) | (1%) | (47%) | (-56%) | (94%) | (45%) | (-56%) | [83%] | |
| FB2_BG | 0.57 | 34.5 | 7.5 | 87.3 | 32.8 | 128.1 | 73.1 | 4.4 | 1.58 | RL |
| | (84%) | (60%) | (6%) | (47%) | (-44%) | (107%) | (41%) | (-47%) | [99%] | |
| FB4_BG_Phi10 | 0.60 | 32.2 | 7.6 | 96.8 | 27.7 | 153.2 | 79.1 | 3.6 | 1.25 | |
| | (94%) | (50%) | (7%) | (63%) | (-53%) | (148%) | (53%) | (-56%) | [78%] | DH |
| FB4_BG_Phi8 | 0.62 | 34.7 | 7.7 | 97.6 | 30.0 | 165.2 | 79.8 | 3.9 | 1.33 | |
| | (100%) | (61%) | (8%) | (65%) | (-49%) | (167%) | (54%) | (-53%) | [83%] | |

a) Values in brackets () are the change of each measure regarding its corresponding value in FB_R beam,

b) Values in brackets [ ] are the percentage ratio of the strain measured in CFRP laminate at the mid-span of the beam to the average strain obtained at the rupture of CFRP laminates in tensile tests, and

c) Failure modes: tension steel yield followed by concrete crushing (SY-CC), splitting of HCP[(L)] (SH), detachment of HCP[(L)] (DH), rupture of CFRP laminates of HCP[(L)] (RL);

### 6.3.1.1 Failure Modes and Overall Behavior

Following, discussions on the failure mode and overall behavior of each of the tested beams are presented. Moreover, in present section, figures indicating the failure mode and the extent of damages in each beam, at the end of the testing, are depicted. For each of the strengthened beams, both the front view and the bottom view of the beam are showed to illustrate the developed damages on both the RC beam and the strengthening plate. To visualize the micro-cracks formed at the exposed face of the strengthening plate, at the end of the test of each beam, a penetrating liquid was sprayed on the surface of the plate.

### 6.3.1.1.1 Reference Beams

Figure 6.14 shows the damages propagated along the length of the reference specimen (FB_R) at the end of the test. Following the yield of the tension steel bars, this beam was failed by crushing of compressive concrete at the mid-span.



Figure 6.14: Propagated damages at the end of the test of FB_R

In the case of FB0_G, the maximum load ($F_m$) was reached at the onset of the yield of the tension steel bars. A sudden drop immediately after the yield of the steel bars in the load-deflection curve of FB0_G can be observed, followed by a gradual increase up to the yield load again, at a deflection of 16 mm (see Figure 6.13). As the consequence of a further increase in the beam's deflection, the sequences of load drop and recovering continued, but with a decreasing trend in the recovered level of the maximum load. When the width of cracks in SHCC was wide enough for losing the strain hardening contribution, this process of stress redistribution along the beam stopped. At this stage, load was stabilized at an almost comparable level to the failure load of FB_R, and finally this beam failed by concrete crushing, at the left loaded section at the left span the beam. The state of damage of this beam at the end of the test is presented in Figure 6.15.
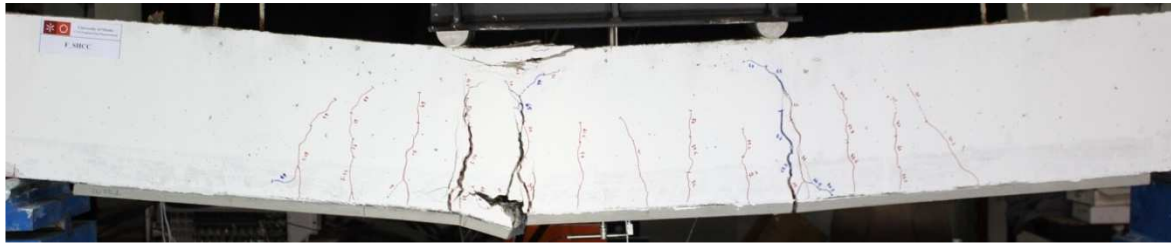
(a)



(b)

Figure 6.15: Propagated damages at the end of the test of FB0_G, (a) front view, and (b) bottom view

### 6.3.1.1.2 Group I Beams

Beam FB2_B failed with a splitting crack in HCP$^{(L)}$, which progressed along the alignment of the chemical anchors. The onset of this failure mode was at the shear-out rupture of SHCC behind the closest anchor to the right support of the beam (see Figure 6.16). Further, a splitting crack at the bearing zone of the second anchor initiated and progressed towards the first anchor. These sequences of splitting crack initiation and propagation between the adjacent anchors continued by increasing the beam's deflection, and with a step-by-step load decay in the post-peak regime (see Figure 6.13).

Beam FB2_G failed by detachment of HCP$^{(L)}$ with part of concrete cover bonded to it (Figure 6.17b). As demonstrated in this figure, the detachment of concrete cover originated from the location of a high stress concentration of a flexural-shear crack formed at the right shear-span of the beam close to the loaded section. This detachment then progressed towards the end of the HCP$^{(L)}$, to the nearest beam's support. By further deflection of this beam, the detachment of the HCP$^{(L)}$ continued from its origin towards the beam's mid-span. This failure mode in an RC beam flexurally strengthened with a bonded plate/FRP to its tension face is often recognized as an intermediate flexural-shear crack-induced detachment [6].
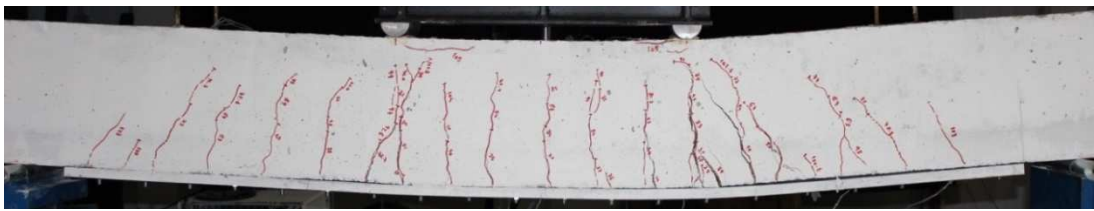
(a)



(b)

Figure 6.16: Propagated damages at the end of the test of FB2_B, (a) front view, and (b) bottom view



(a)



(b)

Figure 6.17: Propagated damages at the end of the test of FB2_G, (a) front view, and (b) bottom view

In the case of FB2_BG, the full tensile potential of the HCP$^{(L)}$ attached by means of epoxy adhesive and chemical anchors to the tension face of this beam was mobilized. Thus, at a location close to the loaded section at the right side of the beam, rupture of the CFRP laminates occurred. The full exploitation of HCP$^{(L)}$ was obtained despite of the onset of an IC detachment at the location of a flexural-shear crack (see Figure 6.18), which indicates a suitable contribution of chemical anchors in delaying the progress of this detachment.



(a)
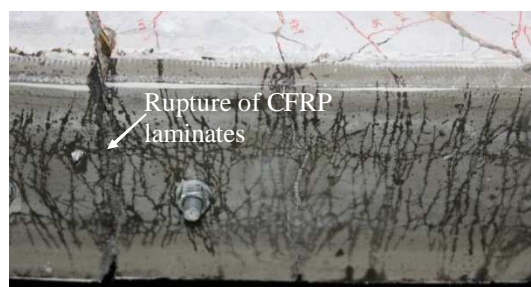


(b)

Figure 6.18: Propagated damages at the end of the test of FB2_BG, (a) front view, and (b) bottom view

### 6.3.1.1.3 Group II Beams

As it is shown in Figure 6.19 and Figure 6.20, both beams in group II, FB4_BG_Phi10 and FB4_BG_Phi8, failed by the detachment of HCP$^{(L)}$ with part of concrete cover bonded to it. The progress of the detachment was similar to that observed in FB2_G, since an intermediate flexural-shear crack-induced detachment was recognized for these beams as well, but at a load level much higher than the corresponding one registered in FB2_G. For both beams in this group the contribution of concrete cover for transferring the interfacial shear stresses developed between the strengthening layer and the tension face of the beam

has decreased with the detachment progress. Consequently, a high tensile stress in the HCP[(L)] needed to be transferred to the beam's soffit by means of only shear resistance of chemical anchors. Due to the stress concentration at bearing zone of the last anchor, close to the termination of the HCP[(L)], a piece of SHCC behind the closest anchor to the right support of the beam was detached by a shear-out rupture (see Figure 6.19b and Figure 6.20b). A high shear stress in the anchors caused their permanent deformation (observed by visual inspection at the failure), meaning that the anchors were already yielded. As a consequence of the yielding of the anchors, and therefore their excessive rotation, separation of HCP[(L)] was followed with a shear-punch mechanism at some of the anchored regions (see Figure 6.19b and Figure 6.20b). This secondary phenomenon, shear-punching, is expected to be delayed (or prevented) if washers with a larger clamping surface area are used.



(a)



(b)

Figure 6.19: Propagated damages at the end of the test of FB4_BG_Phi10, (a) front view, and (b) bottom view

(a)
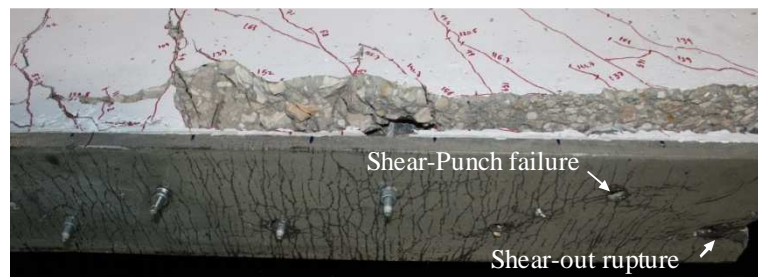


(b)

Figure 6.20: Propagated damages at the end of the test of FB4_BG_Phi8, (a) front view, and (b) bottom view

### 6.3.1.2 Comparative Behavior

### 6.3.1.2.1 Load and Deflection at the First Crack

The load at the onset of the first crack, $F_{cr}$, was registered during testing of each beam and is reported in Table 6.3, together with its corresponding deflection, $\delta_{cr}$. In comparison with the reference beam (FB_R), an increase between 50% and 61% in $F_{cr}$ for beams with a plate connected to their tension face by means of either epoxy adhesive or a combination of epoxy adhesive and chemical anchors (beams FB0_G, FB2_G, FB2_BG, FB4_BG_Phi10 and FB4_BG_Phi8) was obtained. The increase in corresponding deflection of these beams, $\delta_{cr}$, was between 71% and 100% as registered for FB0_G and FB4_BG_Phi8, respectively. An increase of 42% in $\delta_{cr}$ of FB2_B for only 9% increase in

the corresponding load, as compared to the results of the reference beam, was obtained. In fact, when HCP[(L)] is attached using only chemical anchors, in addition to stress concentration at the fastened locations, a substantial sliding between the strengthening plate and the beam

is expected, resulting a smaller contribution of the plate for the initial flexural stiffness of the beam when compared to the strengthening solutions where adhesive was used. The amount of this sliding depends on the roughness of the surfaces in contact, inter-laminar pressure caused by post-tensioning of the anchors, distance between adjacent anchors, and also on the existing gaps between the anchors and the holes of the HCP[(L)].

### *6.3.1.2.2 Load and Deflection at the Yield of Tension Steel Bars*

Since most of the strain gauges bonded to the tension steel bars did not functioned correctly, an apparent yield point was identified from the beams load-deflection curves. This apparent yield corresponded to the load at the onset of a substantial decrease in the slope of the post-cracking regime.

According to this criterion, all of the strengthening techniques assured in a higher yield load, $F_y$, compared to the corresponding value for FB_R. The maximum increase in $F_y$ was 65%, registered in the beam FB4_BG_Phi8, and the minimum increase was 21%, which was attained by FB0_G. Both FB2_G and FB2_BG showed an identical increase of $F_y$ (47%), indicating that adding the post-tensioned anchors did not affect the load corresponding to the yield initiation of the tension steel bars. This result is consistent for FB4_BG_Phi10 and FB4_BG_Phi8, since despite having different layouts and sectional area of the anchors, both presented almost identical yield loads.

Comparison of FB0_G and FB2_G shows an increase of 21% in $F_y$ as a result of bonding two single-CFRP laminates to the SHCC plate. The average increase for HCP[(L)] with four CFRP laminates was 35%. Despite this increase in $F_y$, there was only a marginal increase in the corresponding deflection, $\delta_y$, of the HCP[(L)] strengthened beams when compared to FB_R.

### *6.3.1.2.3 Ultimate Load and Corresponding Deflection*

The ultimate load ($F_u$) for beams with a smooth degradation in their post-peak phase (beams FB_R and FB0_G), is defined as the point where the decrease in maximum registered load reaches 15%, unless the concrete crushing is predominant. In the other hand, for the beams with a sudden drop just beyond the peak load, the ultimate and maximum loads ($F_m$) coincide.

According to the above mentioned criteria, the ultimate load ($F_u$) of FB0_G (61.03 kN) was almost the same as FB_R (61.8 kN), but occurred in a 12% higher ultimate deflection($\delta_u$).

Attaching HCP[(L)] to the tension face of the beam by means of only anchors (beam FB2_B) resulted in an increase of 72% in $F_u$ when compared to the one registered for the reference beam (FB_R). At this ultimate load, the strain gauge "PM" registered a strain level of 1.19% in the CFRP laminates. In the other words, 74% of the potential tensile strength of the HCP[(L)] was mobilized by this attaching layout. The mid-span deflection at the ultimate load, $\delta_u$, of FB2_B was 37.5 mm, which is 36% lower than the corresponding deflection of the beam FB_R.

When epoxy adhesive was used instead of chemical anchors to attach the HCP[(L)] (beam FB2_G), $F_u$ was further increased in13%. A higher tensile stress of CFRP laminates was therefore mobilized to the extent that the strain at "PM" was 12% higher than the corresponding value in beam FB2_B. The beam FB2_G reached a $\delta_u$ of 25.9 mm, which was 56% and 31% lower than the corresponding deflection of FB_R and FB2_B, respectively. The reduction in deflection at the ultimate load of FB2_G regarding to FB2_B is attributed to a restricted sliding at the interface of HCP[(L)] and beam.

Finally, the combination of chemical anchors and epoxy adhesive, for fixing HCP[(L)] to the FB2_BG beam, assured the full strengthening potential of HCP[(L)], providing to this beam an ultimate load and deflection of 128 kN and 32.8 mm, respectively. This ultimate load was 107% larger than the corresponding load obtained by FB_R. The HCP[(L)] reached its strengthening capacity, since CFRP laminates have ruptured in the pure bending zone, close to the loaded section at the right side of the beam (see Figure 6.18).

It is worth to mention that the first series of horizontal cracks in concrete cover corresponding to the detachment progress was observed at a load level of 122 kN, which is very close to the ultimate load of FB2_G (120 kN). However, due to an effective functioning of the anchors, despite initiation of detachment through the concrete cover and its propagation towards the end of the HCP[(L)] (see Figure 6.18), the tensile resistance of CFRP laminates was fully exploited. Considering the maximum load obtained for FB2_BG, a flexural capacity of 51.2 kN·m was achieved, which is 12% higher than the predicted values

based on the analytical solutions (see section 6.2.5.2). The $\delta_u$ of FB2_BG was 32.8 mm, being 26.7% higher than the corresponding value of FB2_G, but 44% lower than the deflection registered at the ultimate load of FB_R.

The onset of detachment of HCP$^{(L)}$ of FB4_BG_Phi10 was at a load level of 134 kN, when a horizontal crack, originated from an existing flexural-shear crack at the vicinity of the loaded section at the right shear span of the beam, has progressed. However, due to a the resisting contribution of the anchors, the detachment progress was delayed and an ultimate load of 153.2 kN was attained. For this load level a strain of 1.25% at the mid-length of the CFRP laminates which was measured by "PM", which is 78% of ultimate tensile strain of the CFRP laminates. The mid-span deflection of FB4_BG_Phi10 at the occurrence of maximum load was 27.7 mm, 53% lower than the corresponding value for FB_R.

Initiation of detachment of HCP$^{(L)}$ of FB4_BG_Phi8 has occurred at load level of 137 kN, which is slightly higher than the corresponding load in FB4_BG_Phi10. This indicated that a staggered configuration of the anchors resulted in a greater distribution of the tensile stress along the width of the strengthening plate [7] and reduced the shear-lag mechanism associated with using a single row of anchors [8]. As a result, a more uniform interfacial stress distribution along the concrete cover was expected. Consequently, an $F_u$ of 165 kN was attained, being 167% and 8% higher than the corresponding values for FB_R and FB4_BG_Phi10, respectively. For this load level a strain value of 1.33% was measured by the strain gauge "PM", corresponding to mobilization of 83% of CFRP laminates' tensile strain capacity.

The flexural capacity of the FB4_BG_Phi8 beam was 66.1 kN·m, almost the same as the one predicted by the analytical approach at the rupture of CFRP laminate, an assuming simplified elastic-perfectly plastic responses for SHCC and steel bars. The mid-span deflection of FB4_BG_Phi8 at the occurrence of the ultimate load was 49% lower than the one of the FB_R, but slightly higher than the registered value in the FB4_BG_Phi10.

### 6.3.1.2.4 Ductility

As a general trend, in comparison with FB_R, attaching HCP$^{(L)}$ to the beam's soffit reduced the deflection corresponding to the ultimate load ($\delta_u$) while a marginal change in

the mid-span deflection corresponding to the yield of tension steel bars $\left(\delta_y\right)$ can be observed.

As it was discussed in the previous section, in comparison with the results registered in the FB_R beam, the minimum and the maximum reduction in $\delta_u$ was 36% and 56% , and have occurred in theFB2_B and FB2_BGbeams, respectively. In consequence of this reduction, the deflection ductility, $\left(\mu_\delta = \delta_\mathrm{u}/\delta_\mathrm{y}\right)$, in the strengthened beams was lower than that obtained for the reference beam (FB_R). However, still a lower bound of 3.6 for displacement ductility (beam FB4_BG_Phi10) was achieved.

Moreover, all the strengthened beams presented an adequate ductility considering the specifications of ACI 440.2R-08 [9]. According to this specification, an RC beam flexural strengthened with a FRP bonded system has enough ductility if the strain in steel reinforcement at the failure of beam is greater than 0.005 mm/mm. Considering the strain levels recorded in the CFRP laminates of all of the strengthened beams, it can be concluded that the strain in tension steel bars were higher than 0.5% (section 6.4.2). Finally, comparing the ductility values obtained in FB2_BG and FB4_BG_Phi8 beams, and taking into account that detachment of HCP$^{(L)}$ was the governing failure mode in the FB4_BG_Phi8, it can be concluded that a double amount of CFRP laminates in the structure of the HCP$^{(L)}$ had a relatively low adverse effect in $\mu_\delta$, a reduction of about 11.5%.

### 6.3.1.2.5 Service Limit States

To verify the cracking status on both the strengthening layer and the lateral faces of the beams, there was a pause in the loading procedure at a 10 mm displacement measured by the internal LVDT of the jack. This measured deflection by the internal LVDT of the beam corresponds to a beam's mid-span deflection between 8.1 mm and 8.9 mm registered by the middle LVDT supported on the Japanese Yoke. This deflection was selected in compliance with a deflection equal to a clear-span divided by 250 $\left(\delta_{250} = \frac{l_s}{250}\right)$ which is recommended as a service limit deflection by EC2 [5].

Except in the case of FB0_G, there was no crack visible to the naked eye on the surface of the strengthening layer, while several cracks along the loading span at lateral faces of the beams already existed. In the case of FB0_G, at this deflection level, a crack was already

localized in the SHCC plate and was wide enough to be visible at one of the loaded sections. According to the recommendations of ACI 440.2R-08 [9], for externally FRP-bonded flexurally strengthened RC beams, to avoid inelastic deformations, the yielding of existing steel bars under service load should be prevented. Therefore, the stress in the existing steel bars under service load should be limited to 80% of the yield stress. This stress reduction limit takes into account the stress increase in the steel bars due to effects of long-term loadings such as creep, shrinkage and cyclic fatigue. It also includes the statistical uncertainty level on the yield stress of the steel bars. Obviously at this service load, the deflections of all the strengthened beams are far below $\delta_{250}$.

If the specifications of Portuguese design code between 60's and 80's are considered, deflection of the beams at service load, $F_{400}$, should be limited to the beam's span divided by $400$ $\left(\delta_{400} = \frac{l_s}{400}\right)$. According to this criterion, the service load, $F_{400}$, of the beams of group II has more than 53% increase comparing to that of the reference beam.

This increase for beams of group I with a continuous bond between HCP[(L)] and RC was higher than 41%. When a discrete connection of HCP[(L)] to RC beam was used, the case of FB2_B, this increase was much lower (22%). It should be noted that bonding only a SHCC plate of 20 mm thickness (beam FB0_G) resulted in 31% increase in $F_{400}$, however, only a marginal safety to the yield load $\left(F_y\right)$ exists (5.7%). This safety margin in the case of the beams of group II was higher than 22%.

### 6.3.1.2.6 Strain Profile along the CFRP Laminates of the HCP[(L)]

Figure 6.21 represents the strain profile in CFRP laminates along the HCP[(L)] at different load levels for FB2_G and FB4_BG_Phi10. Positions of the strain gauges are measured from beam's right support, where the failure occurred.
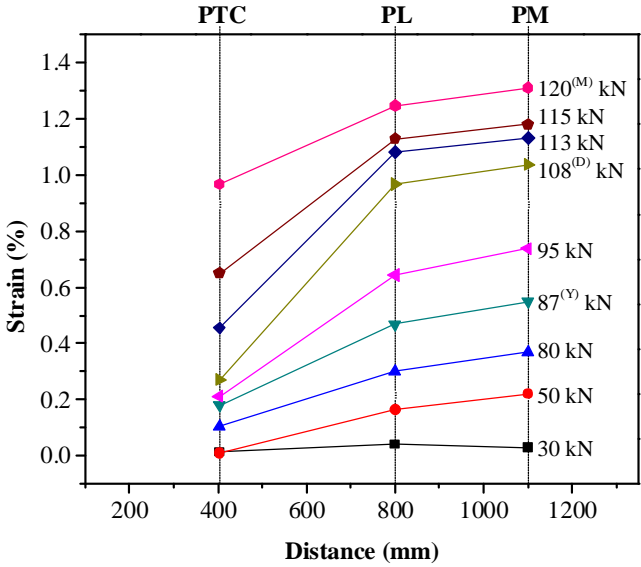
(a)
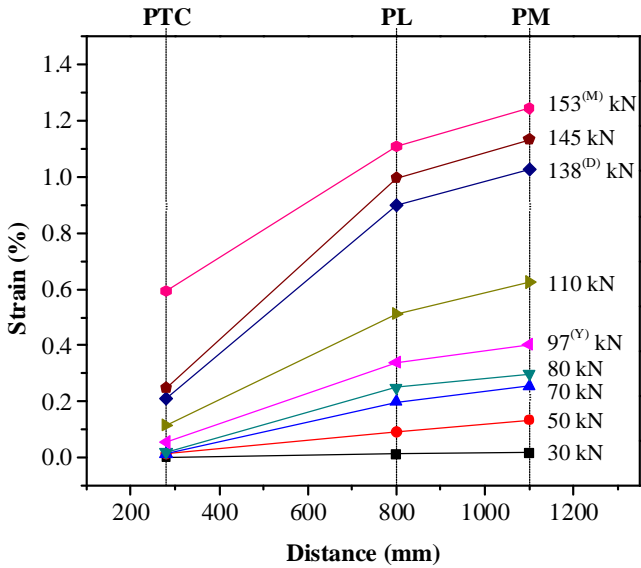


(b)

Figure 6.21: Strain profile in CFRP laminate along the length of the beam at different load levels, with the distance measured from the right support, for (a) FB2_G, and (b) FB4_BG_Phi10, (in these figures superscripts "Y", "D" and "M" denote the load at the yield of the tension steel bars, at the initiation of detachment, and at the maximum load, respectively).

In these figures, strain profiles at the load corresponding to the yield of tension steel bars, the onset of detachment of HCP[(L)] and the maximum load are denoted by "Y", "D" and "M", respectively. For both of these beams, at the onset of detachment of concrete cover, a sudden increase in the strain measured under the loaded section, and similarly in the strain measured at the mid-span, can be recognized.

The strain values corresponding to the onset of detachment, as measured by the strain gauge "PL", were 0.9% and 0.97% for FB2_G and FB4_BG_Phi10, respectively. A larger strain value measured for FB4_BG_Phi10 can be attributed to the effect of post-tensioning force in chemical anchors, which in turn resulted in confining of the concrete cover.

Therefore, it can be concluded that the strain corresponding to detachment of HCP[(L)] is independent of the number of CFRP laminates in its structure. The role of chemical anchors in delaying the detachment progress is obvious when strain values measured at "PTC" for these two beams are compared.

In fact, in FB2_G further loading beyond the onset of detachment of HCP[(L)] resulted in a high increase in the strain measured by "PTC", while the corresponding strain value in FB4_BG_Phi10 had a gradual increase up to a load level very close to the failure of this beam.

## 6.4 Numerical Simulation

Several studies showed that a layered-section model can be used to predict moment-curvature $(M - \chi)$ of composite sections, which can be employed in a numerical strategy to estimate the load-deflection of the elements failing in bending, with enough accuracy compared to the experimental results [10, 11]. According to this strategy, a cross-section is discretized into several thin layers (see Figure 6.22).

Based on the assumption that plane sections remain plane after bending, for a gradual increase in curvature of the cross-section the state of the strain at the middle of each layer is determined. Then, for each state of the strain, the stress values can be obtained using the constitutive law of the corresponding material of each layer. Since the distribution of the stress along the depth of the cross-section is already determined, the state of the static

equilibrium can be checked and then established, if needed, through an iterative solution by adjusting the depth of the neutral axis. When the stress distribution accomplishes the state of equilibrium of the section, the bending moment ($M$) for that corresponding curvature ($\chi$) is calculated. The algorithm of this approach is depicted in Figure 6.23. According to this this algorithm, a VBA code was implemented into an excel file to calculate the moment-curvature of a flexurally strengthened cross-section (see Annex A)
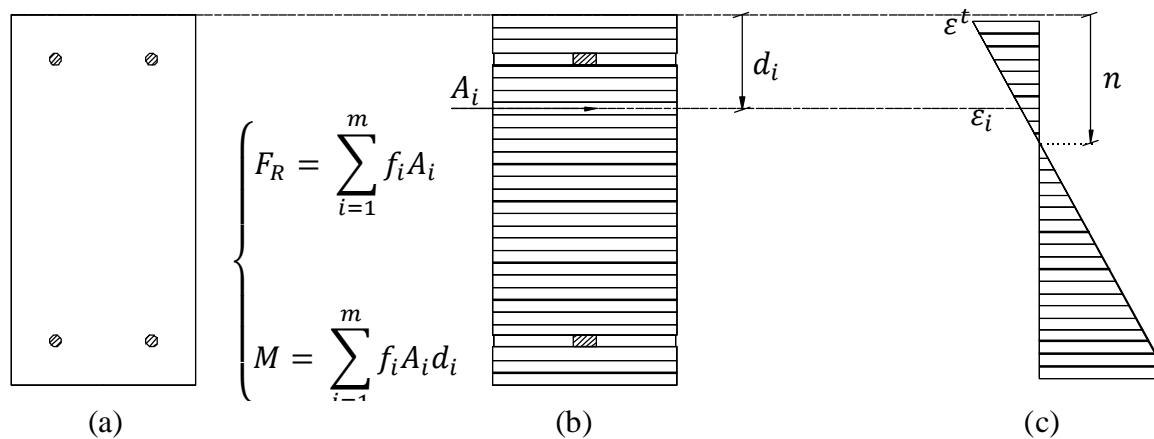


Figure 6.22: Concept of layer-Section for the calculation of the moment-curvature of a composite section, (a) RC section, (b) RC section discretized into layer, and (c) strain distribution at the middle-height of each layer ($f_i$, $A_i$ and $d_i$ are the stress, layer area and depth at the middle of the layer, respectively. $F_R$ is the residual force, unbalanced force, at the end of each iteration and $M$ is the calculated moment for each given curvature of $\chi$ ).

```
┌─────────────────────────────┐
│ Input section geometry and  │
│ materials constitutive laws │
└─────────────────────────────┘
               │
               ▼
┌─────────────────────────────┐
│ Introduce the strain increment │
└─────────────────────────────┘
               │
               ▼
┌─────────────────────────────┐
│ Assume the depth of natural │
│            axis             │
└─────────────────────────────┘
               │
               ▼
┌─────────────────────────────┐
│ Evaluate the strain at the center │
│       of each fiber         │
└─────────────────────────────┘
               │
               ▼
┌─────────────────────────────┐
│ Calculate the corresponding │
│ stress at the center of each fiber │
└─────────────────────────────┘
               │
               ▼
┌─────────────────────────────┐
│ Check the state of static   │
│ equilibrium of the section  │
└─────────────────────────────┘
               │
               ▼
           ◇ Check the state
             of static
    No ◄──── equilibrium at
             the section ◇
               │ Yes
               ▼
┌─────────────────────────────┐
│ Calculate the curvature and the │
│      bending moment         │
└─────────────────────────────┘
               │
               ▼
    No ◄──── ◇ Verify the stop
             condition ◇
               │ Yes
               ▼
┌─────────────────────────────┐
│     Stop calculation        │
└─────────────────────────────┘
```

Figure 6.23: Algorithm of numerical strategy to calculate moment-curvature of a section

The evolution of the moment-curvature $(M - \chi)$ can be used in a numerical model to estimate the load-deflection of a simply supported beam which is discretized into Euler-Bernoulli elements. According to the algorithm presented in Figure 6.24, in this method for each load increment, $\Delta F^q$, the bending moment at the centroid of each element, $M_e^q$, is calculated. Afterwards, tangential flexural rigidity of each element, $(EI)_{Te}^q$, is evaluated from the element's $(M - \chi)$. The tangential stiffness matrix of each element, $\underline{K}_{Te}^q$, is then calculated using $(EI)_{Te}^q$. By assembling tangential stiffness of each element, the tangential stiffness of the structure, $\underline{K}_{TE}^q$, is obtained. Finally, by solving the system of linear equations, $\underline{K}_{TE}^q \Delta \underline{u}^q = \Delta \underline{F}^q$, the increment in nodal displacements, $\Delta \underline{u}^q$, is obtained and the matrix of nodal displacements, $\underline{u}^q = \underline{u}^{q-1} + \Delta \underline{u}^q$, will be updated.
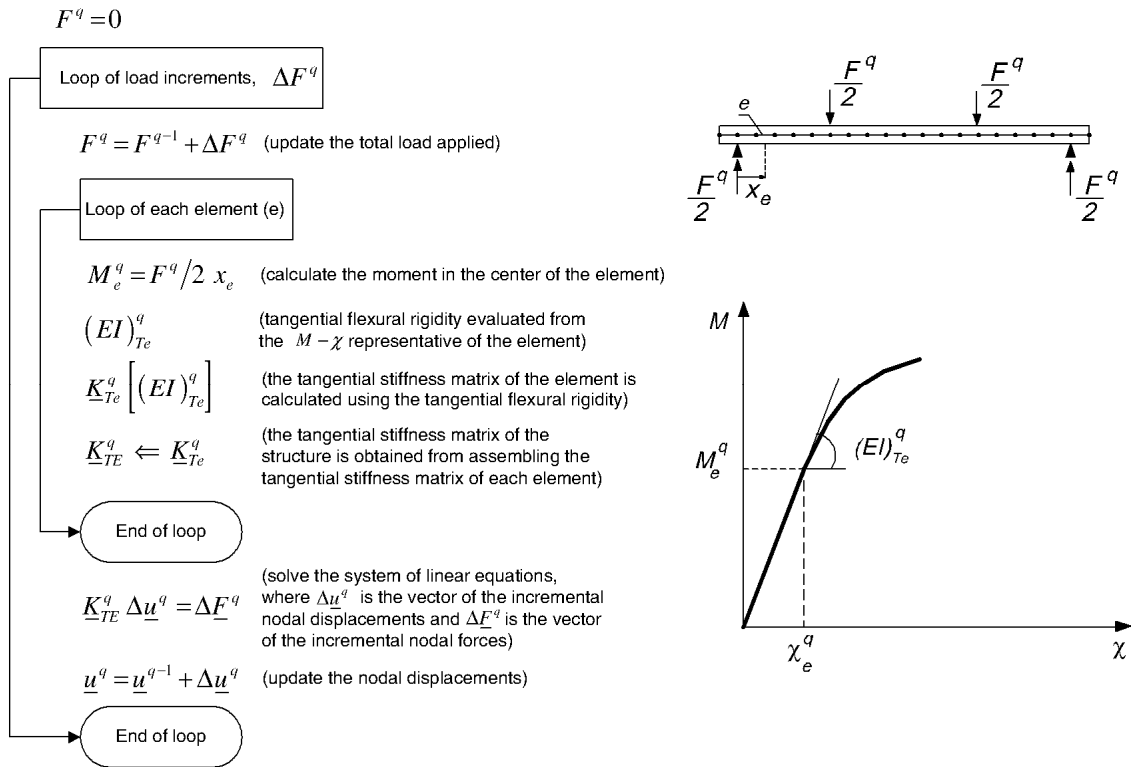


Figure 6.24: Numerical algorithm to simulate the load-deflection response of RC elements failing in bending [11].

The beams of this study were simulated using the abovementioned numerical strategy. Incorporating the materials constitutive laws described in the next section, a code was

embedded in an Excel datasheet by the author to calculate the moment-curvature of the beam's sections, while DefDocros [11] was used to predict the load-deflection response based on the obtained $M - \chi$.

The corresponding $M - \chi$ for each configuration of the beams' cross-section was calculated using fibers of 1 mm thick along the depth of the section. To estimate the load-deflection response, the beams were discretized into two-dimensional elements of 10 mm in length.

### 6.4.1 Constitutive Laws of the Materials

### 6.4.1.1 SHCC in Tension

As the CFRP tensile stress-strain relationship $(f_{sh} - \varepsilon_{sh})$ in Figure 6.25 indicates, the tensile behavior of SHCC is modelled assuming an elastic-linear stress-strain response up to the formation of the first crack according to equation (6-49a). The post-cracking response of SHCC is simulated using a linear ascending branch corresponding to the tensile strain hardening phase as presented in equation (6-49b). Following this hardening branch, the reduction in stress is taken into account adopting a bi-linear regime (6-49c to (6-49e) up to a zero stress state. The elastic modulus $(E_{sh})$, the stress at the first crack $(f_{sh}^{cr})$, the tensile strength $(f_{sh}^u)$ and the tensile strain hardening capacity $(\varepsilon_{sh}^u)$ are introduced based on the average results of direct tensile tests (see section 4.3.6.4) and parameters for the softening regime are adopted from [12]. Values of the parameters used to define the tensile stress-strain relationship of the SHCC are reported in Table 6.4.

$$f_{sh} = E_{sh}\varepsilon_{sh} \qquad\qquad\qquad \varepsilon_{sh} \leq \varepsilon_{sh}^{cr} \qquad\qquad (6\text{-}49a)$$

$$f_{sh} = f_{sh}^{cr} + \left(\frac{f_{sh}^u - f_{sh}^{cr}}{\varepsilon_{sh}^u - \varepsilon_{sh}^{cr}}\right)(\varepsilon_{sh} - \varepsilon_{sh}^{cr}) \qquad\qquad \varepsilon_{sh}^{cr} < \varepsilon_{sh} \leq \varepsilon_{sh}^u \qquad\qquad (6\text{-}49b)$$

$$f_{sh} = f_{sh}^u + \left(\frac{\mu f_{sh}^{cr} - f_{sh}^u}{\gamma_1 \varepsilon_{sh}^u - \varepsilon_{sh}^u}\right)(\varepsilon_{sh} - \varepsilon_{sh}^u) \qquad\qquad \varepsilon_{sh}^u < \varepsilon_{sh} \leq \gamma_1 \varepsilon_{sh}^u \qquad\qquad (6\text{-}49c)$$

$$f_{sh} = \mu f_{sh}^{cr} - \left[\frac{\mu f_{sh}^{cr}}{(\gamma_2 - \gamma_1)\varepsilon_{sh}^u}\right](\varepsilon_{sh} - \gamma_1 \varepsilon_{sh}^u) \qquad \gamma_1 \varepsilon_{sh}^u < \varepsilon_{sh} \leq \gamma_2 \varepsilon_{sh}^u \qquad (6\text{-}49\text{d})$$

$$f_{sh} = 0 \qquad \gamma_2 \varepsilon_{sh}^u < \varepsilon_{sh} \qquad (6\text{-}49\text{e})$$
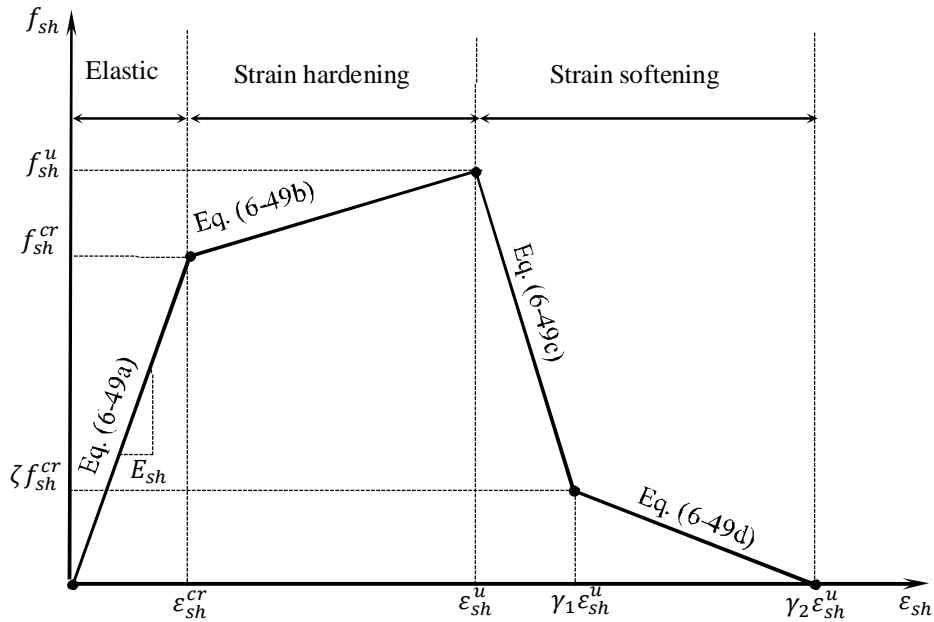


Figure 6.25: Constitutive law to simulate tensile behavior of SHCC

Table 6.4: Values adopted for the parameters defining tensile constitutive law of SHCC (see Figure 6.25)

| $E_{sh}$ (MPa) | $f_{sh}^{cr}$ (MPa) | $f_{sh}^u$ (MPa) | $\varepsilon_{sh}^u$ (%) | $\zeta$ | $\gamma_1$ | $\gamma_2$ |
|---|---|---|---|---|---|---|
| 18420 | 2.5 | 3.75 | 1.54 | 0.11 | 5 | 9 |

### *6.4.1.2 CFRP Laminates*

In compliance with the results of tensile tests, the stress-strain response of CFRP laminates is considered linear-elastic with a maximum tensile strain corresponding to the average strain obtained at the rupture of laminates (see Figure 6.26).
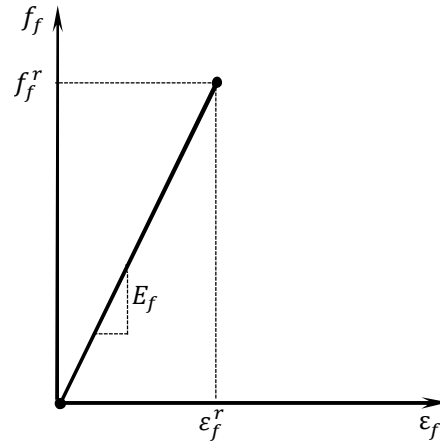
Figure 6.26: Constitutive law for CFRP laminates uniaxial tension.

### 6.4.1.3 Reinforcing Steel Bars

The uniaxial stress-strain relationship for the steel bars $(f_{st} - \varepsilon_{st})$ is based on the proposed model by Park and Paulay [13], represented schematically in Figure 6.27 and mathematically in equations (6-50a) to (6-50c). Steel bars are assumed to behave similarly under monotonic compression and tension loadings. Values defining parameters of the stress-strain relationship of the steel bars (Figure 6.27) are the same obtained from the experimental results of the tensile tests of longitudinal bars (see section 6.2.4.5) and they are listed in Table 6.5.

$$f_{st} = E_{st}\varepsilon_{st} \qquad\qquad \varepsilon_{st} \leq \varepsilon_{st}^{y} \tag{6-50a}$$

$$f_{st} = f_{st}^{y} \qquad\qquad \varepsilon_{st}^{y} < \varepsilon_{st} \leq \varepsilon_{st}^{sh} \tag{6-50b}$$

$$f_{st} = f_{st}^{y}\left[\frac{m(\varepsilon_{st} - \varepsilon_{st}^{sh}) + 2}{60(\varepsilon_{st} - \varepsilon_{st}^{sh}) + 2} + \frac{(\varepsilon_{st} - \varepsilon_{st}^{sh})(60 - m)}{2(30r + 1)^2}\right] \qquad \varepsilon_{st}^{sh} < \varepsilon_{st} \tag{6-50c}$$

where,

$$r = \varepsilon_{st}^{u} - \varepsilon_{st}^{sh} \tag{6-50d}$$

$$m = \frac{(f_{st}^{u}/f_{st}^{y})(30r + 1)^2 - 60r - 1}{15r^2} \tag{6-50e}$$
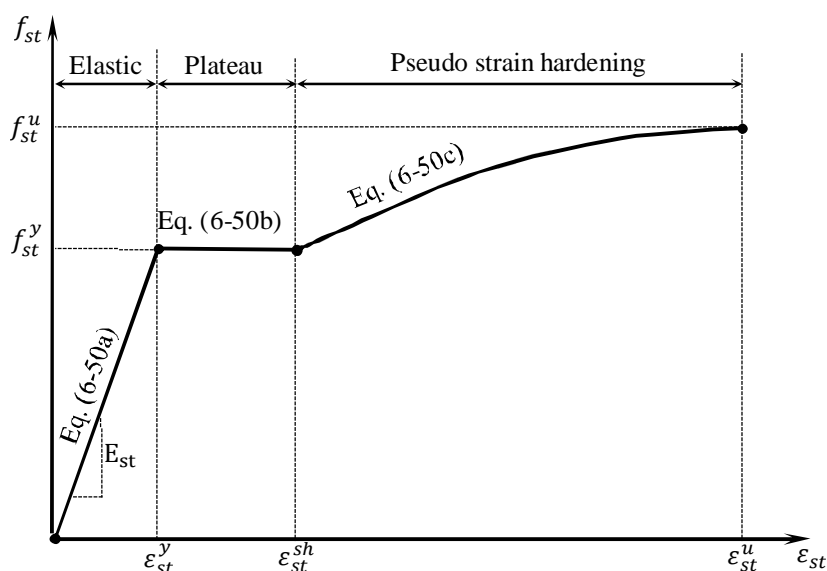
Figure 6.27: Constitutive law for steel reinforcement under both uniaxial compression and uniaxial tension [13].

Table 6.5: Values of the parameters defining constitutive law of the longitudinal steel bars (Figure 6.27)

| $E_{st}$ (GPa) | $\varepsilon_{st}^{y}$ (%) | $f_{st}^{y}$ (MPa) | $\varepsilon_{st}^{sh}$ (%) | $f_{st}^{sh}$ (MPa) | $\varepsilon_{st}^{u}$ (%) | $f_{st}^{u}$ (MPa) |
|---|---|---|---|---|---|---|
| 215.8 | 0.25 | 536 | 2.5 | 536 | 12 | 629 |

### 6.4.1.4 Concrete

Concrete in compression is formulated using the Mander model [14], see Figure 6.28 and mathematically in equations (6-51a) to (6-51d). With the exception of the strain corresponding to the maximum compressive strength ($\varepsilon_{cc}^{m}$), which is calculated using the recommendations of EC2 [5] and indicated in equation (6-51e), other parameters of this model are taken from the results of uniaxial compression tests.

Table 6.6 reports values of the parameters adopted to define the constitutive law of concrete under compression.

$$f_{cc} = \frac{\kappa \alpha f_{cc}^m}{\alpha - 1 + \kappa^\alpha} \qquad\qquad \varepsilon_{cc} \leq 2\varepsilon_{cc}^m \qquad\qquad (6\text{-}51\text{a})$$

$$f_{cc} = \left(\frac{2\alpha f_{cc}^m}{\alpha - 1 + 2^\alpha}\right)\left(\frac{\varepsilon_{cc}^f - \varepsilon_{cc}}{\varepsilon_{cc}^f - 2\varepsilon_{cc}^m}\right) \qquad\qquad 2\varepsilon_{cc}^m < \varepsilon_{cc} \leq \varepsilon_{cc}^f \qquad\qquad (6\text{-}51\text{b})$$

Where, $\varepsilon_{cc}$ represents the concrete compressive strain, and κ, α:

$$\kappa = \varepsilon_{cc}/\varepsilon_{cc}^m \qquad\qquad (6\text{-}51\text{c})$$

$$\alpha = \frac{E_c}{E_c - (f_{cc}^m/\varepsilon_{cc}^m)} \qquad\qquad (6\text{-}51\text{d})$$

$$\varepsilon_{cc}^m = 0.07\,(f_{cc}^m)^{0.31} \ \leq 2.8\,(\%) \quad [5] \qquad\qquad (6\text{-}51\text{e})$$
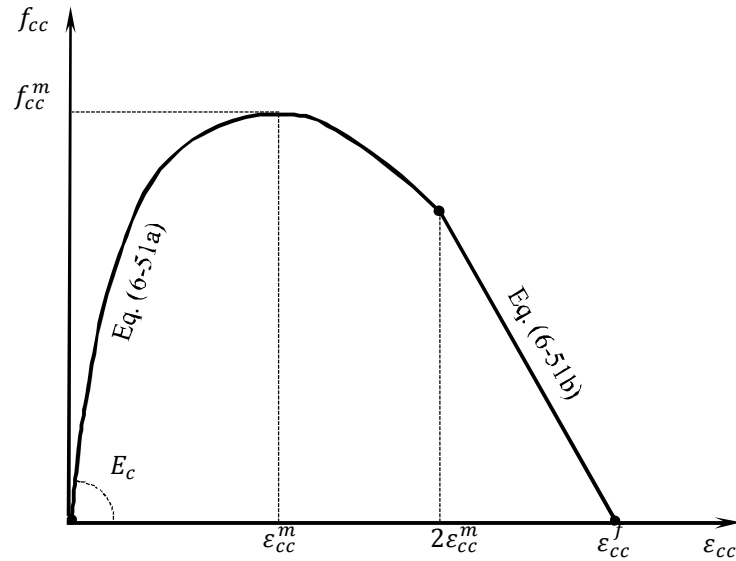


Figure 6.28: Adopted constitutive laws for concrete under monotonic uniaxial compression [14] .

Table 6.6: Parameters defining constitutive law for concrete under compression (see Figure 6.28)

| $E_c$ (GPa) | $f_c^m$ (MPa) | $\varepsilon_c^m$ (%) | $f_c^t$ (MPa) |
|---|---|---|---|
| 32.52 | 31.26 | 0.2 | 2.45 |

Tensile behavior of concrete is simulated by a linear-elastic phase, followed by a post-cracking regime. Concrete tensile strength $(f_{ct}^{cr})$ is calculated using the specifications of EC2 [5], indicated in equation (6-52).

Tensile post-cracking response of a reinforced concrete $(f_{ct} - \varepsilon_{ct}^{cr})$ highly depends on interaction between concrete and the reinforcement at their interface level. This phenomenon results in a higher stiffness for a reinforced concrete subjected to tensile loading in comparison to the stiffness expected for a bare reinforcement. To address this interaction in numerical simulation, a tension-stiffening response can be used to define the post-cracking behavior of RC concrete subjected to tensile loading. According to the literature this tension-stiffening can be modeled using a multi-linear descending curve for concrete reinforced with steel bars, FRP or a combination of them [11, 15].

For the purpose of present study, a multi-linear tension-stiffening model that takes into account the contribution of concrete up to the ultimate strength of reinforcement [16], according to Figure 6.29a and equations (6-53a) to (6-53d), is adopted. The effective concrete embedment-zone (part of concrete that contributes in the stiffness of the reinforcing bars) is defined as an area of concrete around the center of the bar with a width and depth equal to 15 times of the steel bar diameter [17], (see Figure 6.30). For the other parts of concrete a tension-softening model [17], defined by equations (6-54a) to (6-54d) and represented in Figure 6.29b, is adopted.

$$f_{ct}^{cr} = 0.3 \, (f_{cc}^m - 8)^{2/3} \tag{6-52}$$

Tensile model for steel/FRP reinforced concrete (tension-stiffening in post-cracking), see Figure 6.29a:

$$f_{ct} = E_c \varepsilon_{ct} \qquad\qquad \varepsilon_{ct} \le \varepsilon_{ct}^{cr} \qquad\qquad (6\text{-}53a)$$

$$f_{ct} = f_{ct}^{cr} + E_c \left(\frac{\beta_1 - 1}{\psi_1 - 1}\right)(\varepsilon_{ct} - \varepsilon_{ct}^{cr}) \qquad\qquad \varepsilon_{ct}^{cr} < \varepsilon_{ct} \le \psi_1 \varepsilon_{ct}^{cr} \qquad\qquad (6\text{-}53b)$$

$$f_{ct} = \beta_1 f_{ct}^{cr} \qquad\qquad \psi_1 \varepsilon_{ct}^{cr} < \varepsilon_{ct} \le \psi_2 \varepsilon_s^{y} \qquad\qquad (6\text{-}53c)$$

$$f_{ct} = \beta_1 f_{ct}^{cr} + f_{ct}^{cr}\left(\frac{\beta_2 - \beta_1}{\psi_3 \varepsilon_s^{u} - \psi_2 \varepsilon_s^{y}}\right)\left(\varepsilon_{ct} - \psi_2 \varepsilon_s^{y}\right) \qquad \psi_2 \varepsilon_s^{y} < \varepsilon_{ct} \le \psi_3 \varepsilon_s^{u} \qquad\qquad (6\text{-}53d)$$

Tensile model plain concrete (tension-softening in post-cracking), see Figure 6.29b:

$$f_{ct} = E_c \varepsilon_{ct} \qquad\qquad \varepsilon_{ct} \le \varepsilon_{ct}^{cr} \qquad\qquad (6\text{-}54a)$$

$$f_{ct} = f_{ct}^{cr} + E_c \left(\frac{\varphi - 1}{\xi_1 - 1}\right)(\varepsilon_{ct} - \varepsilon_{ct}^{cr}) \qquad\qquad \varepsilon_{ct}^{cr} < \varepsilon_{ct} \le \xi_1 \varepsilon_{ct}^{cr} \qquad\qquad (6\text{-}54b)$$

$$f_{ct} = \varphi f_{ct}^{cr} + E_c \left(\frac{-\varphi}{\xi_2 - \xi_1}\right)(\varepsilon_{ct} - \xi_1 \varepsilon_{ct}^{cr}) \qquad\qquad \xi_1 \varepsilon_{ct}^{cr} < \varepsilon_{ct} \le \xi_2 \varepsilon_{ct}^{cr} \qquad\qquad (6\text{-}54c)$$

$$f_{ct} = 0 \qquad\qquad \xi_2 \varepsilon_{ct}^{cr} < \varepsilon_{ct} \qquad\qquad (6\text{-}54d)$$

To calibrate parameters of the tension-stiffening model, the evolution of tensile strain in longitudinal steel bar of FB_R and in longitudinal CFRP laminate of FB2_BG, versus bending moment obtained from fiber-section analysis are compared to those obtained in experimental tests. Hence, employing an inverse analysis, the parameters of the tension-stiffening model were adjusted to obtain the best match between the aforementioned results (strain *versus* moment from numerical and experimental studies).
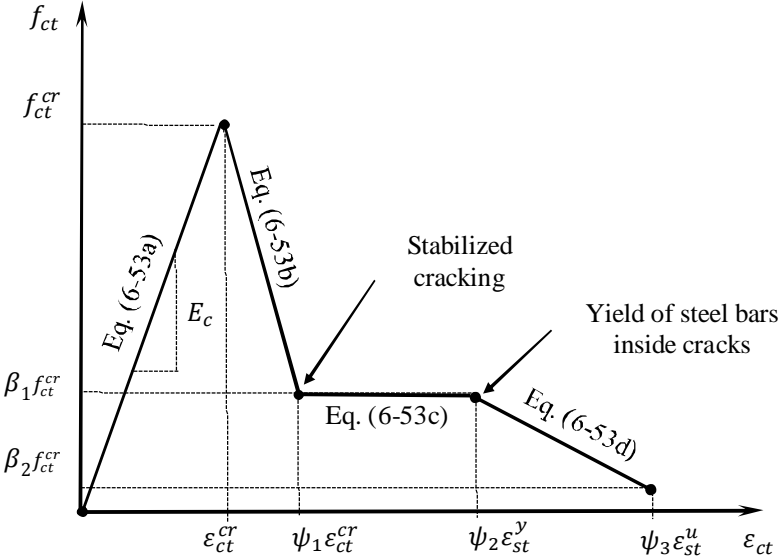
(a)
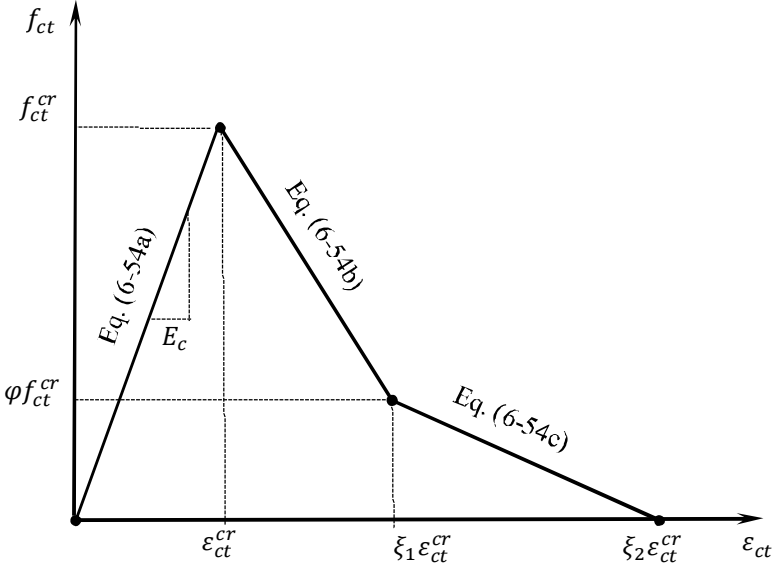


(b)

Figure 6.29: Proposed tensile models for (a) steel/FRP reinforced concrete, and (b) plain concrete [17].
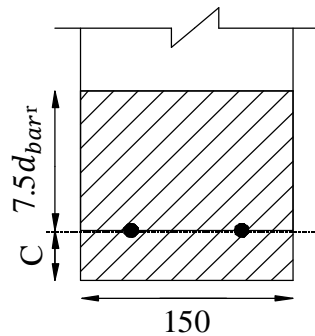
Figure 6.30: The effective concrete embedment-zone ("C" represents the depth of concrete cover and $d_{bar}$ is the diameter of longitudinal steel bars).

### 6.4.2 Numerical versus Experimental Strain Evolution in Longitudinal Reinforcement

Figure 6.31a and Figure 6.31b compare strain *versus* moment obtained from layer-section model analysis with the corresponding one from experimental test (strain values registered at the mid-length of the specified longitudinal reinforcement of FB_R and FB2_BG).

The strain *versus* moment obtained for FB4_BG_Phi8 is also presented in Figure 6.31c, that confirms the accuracy of the tension-stiffening model for the beams flexurally strengthened by HCP[(L)]. Values for the parameters of the tension-stiffening law, which resulted in the most fitted strain *versus* moment curve of the numerical model to the experimental tests, are indicated in Table 6.7. Values for the parameters of the tension-softening model were adopted from [17] and are also reported in the same table.

Figure 6.31b and Figure 6.31c also indicate the strain evolution in the steel bars of beams FB2 and FB4, respectively, obtained from the numerical strategy. According to these data, the strain values in longitudinal steel bars FB2 and FB4 are 1.42% and 1.16%, respectively. As discussed in section 5.2.5.2.4, these values are much higher than 0.005 mm/mm, which is one of the requisites in an FRP-bonded flexurally strengthened RC beam in order to be recognized as a ductile section [9].

Table 6.7: Parameters defining tensile post-cracking response of concrete (Figure 6.29)

| | $\varphi$ | $\xi_1$ | $\xi_2$ | $\beta_1$ | $\beta_2$ | $\psi_1$ | $\psi_2$ | $\psi_3$ |
|---|---|---|---|---|---|---|---|---|
| Plain concrete | 0.33 | 5 | 16 | - | - | - | - | - |
| Steel reinforced concrete | | | | 0.45 | 0.20 | 5.0 | 0.85 | 0.95 |
| CFRP reinforced concrete | | | | 0.60 | 0.45 | 5.0 | 0.85 | 0.95 |
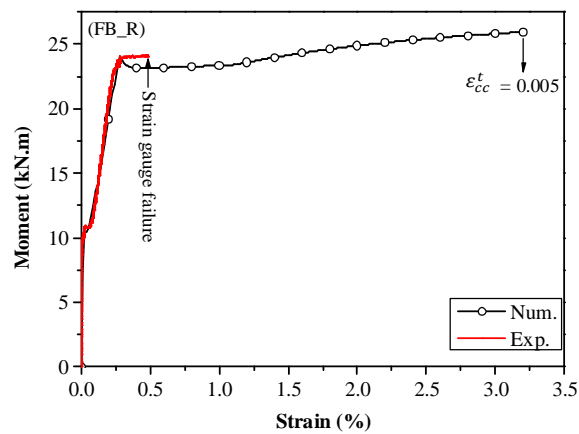


(a)
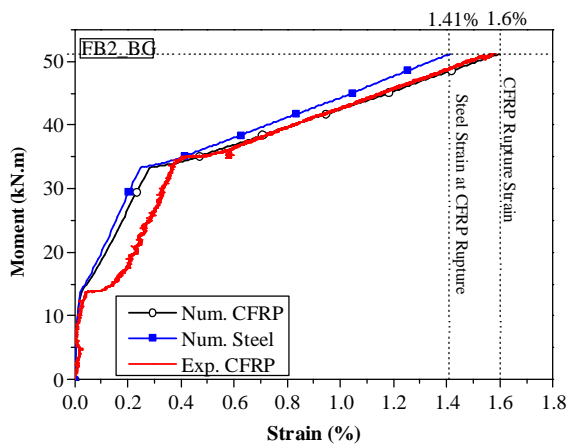


(b)
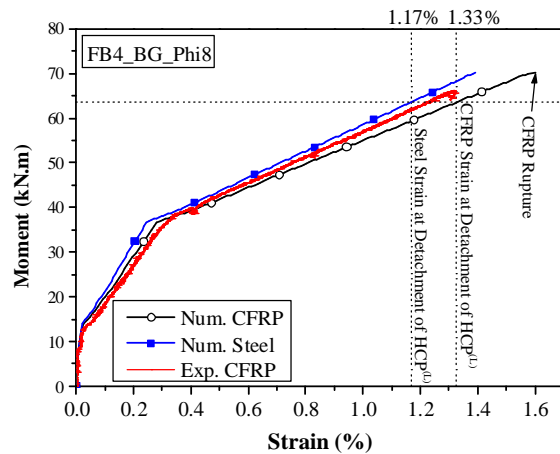
(c)

Figure 6.31: Comparison of the evolution of the mid-span strain in steel/CFRP reinforcement *versus* moment obtained from numerical and experimental studies in beam, (a) FB_R, (b) FB2_BG, and (c) FB4_BG_Phi8

### 6.4.3 Numerical versus Experimental Load-Deflection Responses

Load-deflection responses obtained from experimental test and numerical model of each beam are represented in Figure 6.32. In general, a good agreement between numerical and experimental results can be observed. The model was capable of predicting with enough accuracy the load and deflection at the formation of the first crack, and also the corresponding values at the onset of yield of tension steel bars.



(a)  (b)

(c)  (d)
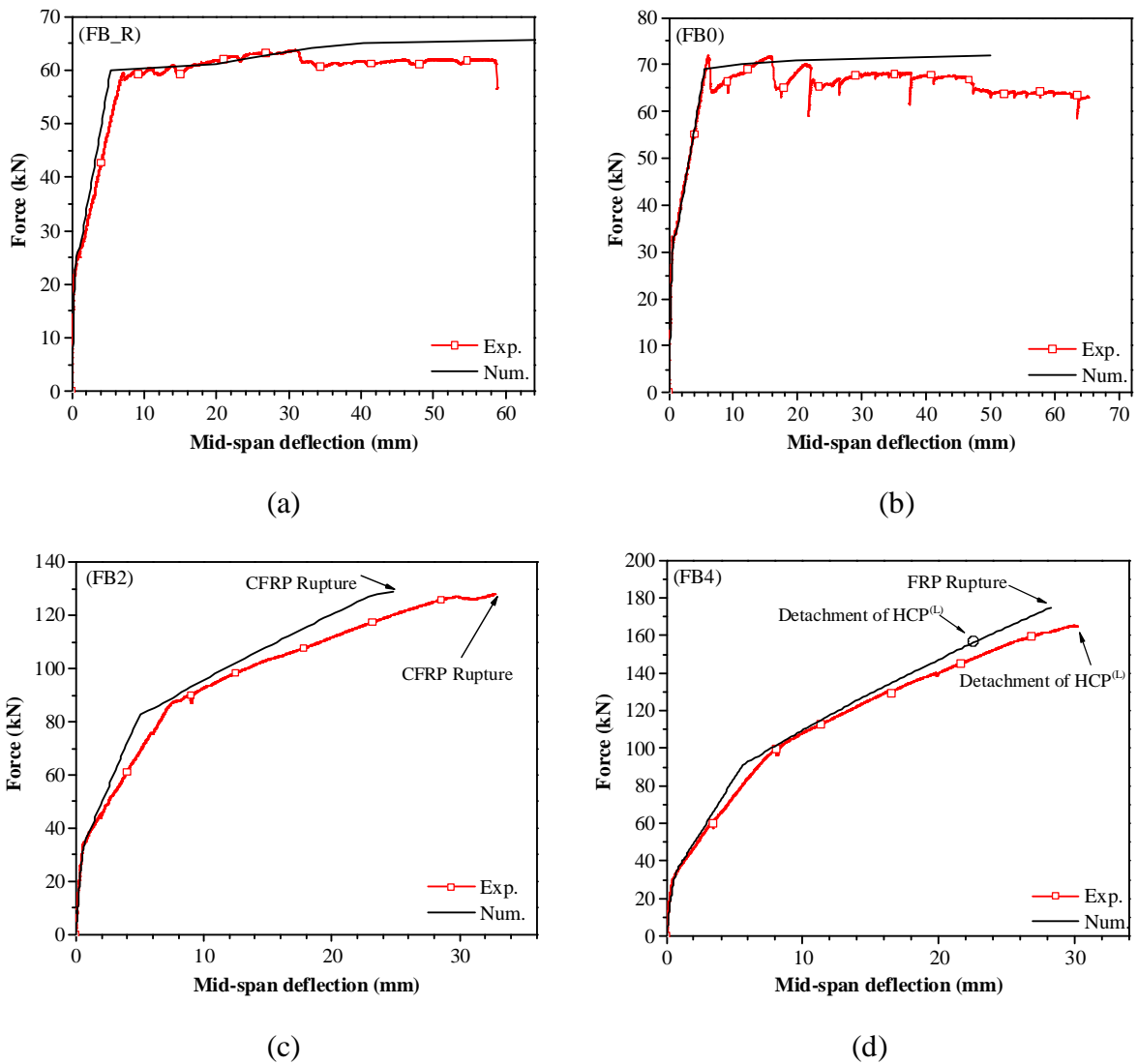
Figure 6.32: Comparison of the force-deflection curves of the numerical simulations with the experimental tests of specimens (a) FB_R, (b) FB0, (c) FB2, and (d) FB4

A slightly higher post-cracking and post-yielding stiffness presented by numerical simulation is attributed to the fact that the numerical strategy follows the Euler-Bernoulli theory to calculate the deflection in each element of the beam, which in turn eliminates the stiffness reduction due to the flexural-shear cracking or shear cracking along the beam's span. Moreover, following a perfect bond assumption, the sliding at the interface of the CFRP-laminates and the surrounding SHCC, and also between the HCP[(L)] and the beam's soffit, is not taken into account, while the detachment progress was observed in all HCP[(L)] strengthened beams. Thus, a higher post-yield stiffness and a lower ultimate deflection predicted by the adopted numerical strategy were expected.

## 6.5 Summary and Conclusions

This chapter described the investigation was executed on the experimental assessment of the efficiency of HCP[(L)] for the flexural strengthening of under-reinforced RC beams and discussed its relevant results.

Moreover, an analytical approach to predict the ultimate moment-capacity of an RC cross-section strengthened with HCP[(L)] was presented.

Finally, a numerical strategy was employed to predict the load-deflection behavior of these beams, failing in bending. According to this numerical strategy, a layer-section model was developed and used to estimate evolution of the moment *versus* curvature of a composite section; with the assumptions of a perfect-bond between the intervening materials and that a plane section remains plane after bending. The obtained moment-curvature curve was then introduced to a numerical algorithm to predict the load-deflection response of the beam.

In the experimental phase, seven beams with identical geometry and steel configuration were casted by the same batch of concrete. These beams, including one as-built beam and six strengthened ones, were tested adopting a four-point bending configuration.

The as-built beam and the one strengthened with an adhesively bonded SHCC plate were tested as the reference beams for comparing the flexural behavior of the HCP[L] strengthened beams. The HCP[L] strengthened beams were categorized in two main groups depending on the number of CFRP laminates of their HCP[L].

Group I was composed of three beams each of them strengthened with an HCP[L] containing two CFRP laminates. Beams in group I differed by the technique used to attach HCP[L] to the beam's soffit. The connection of the HCP[L] of these beams was made either by means of a combination of chemical anchors and epoxy adhesive or an individual application of each of these two techniques.

In the case of beams of group II, each HCP[L] had four CFRP laminates. For these beams, a combination of epoxy adhesive and chemical anchors was adopted to attach HCP[L]. Moreover, the strengthening layouts of the beams of this group were also different based on the configuration of the CFRP laminates in the HCP[L] cross section, and the diameter and arrangement of the chemical anchors (one row anchors *versus* staggered arrangement of them).

Based on the abovementioned experimental, analytical and numerical studies, the following relevant conclusions can be pointed out:

- In comparison with the results of the reference beam, all of the adopted strengthening schemes resulted in a superior response in terms of the load and deflection at the onset of cracking, yield load of the tension steel bars, and ultimate load.

- The deflection ductility of all the HCP[L] strengthened beams, compared to the reference beam, was decreased. However, a satisfactory lower bound of 3.6 for deflection ductility at a 153% increase in the ultimate load was preserved. The largest deflection ductility of the HCP[L] strengthened beams was 5.3, corresponding to strengthening solution based on HCP[L] fixed to the RC beam by means of only chemical anchors.

- When a combination of epoxy adhesive and chemical anchors was used to attach HCP[L] to the beam's soffit, the full strengthening potential of HCP[L] containing two CFRP laminates at a satisfactory deflection ductility of 4.4 was mobilized.

- A staggered configuration of the anchors delayed the progress of detachment in concrete cover, as compared to the configuration that incorporates a layout of one row of anchors. Hence, comparing to the latter connection configuration, both higher flexural capacity and deflection ductility with the staggered layout of anchors can be achieved. Using this configuration of anchors in combination with epoxy adhesive, a significant increase in load carrying capacity (167%, compared to the reference beam) with a satisfactory deflection ductility of about 4.0 was attained. For this strengthening configuration up to 83% of the potential strengthening of HCP[L] was mobilized.

- The detachment in NSM-CFRP strengthened RC beams often involves fracture and disintegration of the concrete surrounding the bonded strips. However, none of the HCP[L] strengthened beams had any sign of such failure at the SHCC around the CFRP laminates. This indicates how the fibers reinforcement mechanisms of arresting micro-cracks in a strain hardening composite prevents the formation of the macro-cracks and contribute for the maintenance of the integrity of the HCP[L] up to the development of high tensile strain in CFRP laminates.

- Based on a simplified concrete compressive block and assuming a full composite action, the analytical formulation predicted the ultimate moment capacity of the beam, failed by CFRP rupture, with a 12% tolerance.

- The adopted numerical strategy, based on a section-layer model, has predicted with satisfactory agreement, the general load-deflection response of both the as-built one beam and the strengthened ones (FB_R, FB0_G, FB2_BG) tested experimentally. However, in the cases where concrete cover detachment is a prevailing failure mode (FB4_BG), to predict the load-deflection response with

a higher precision, further investigations are required to identify several parameters incorporating the contribution of the anchors in a modified numerical approach (e.g. criteria for the detachment initiation, the detachment progress, and the occurrence of different failure modes in the HCP$^{(L)}$).

## Bibliography

[1] Costa IG, Barros JAO. Assessment of the long term behaviour of structural adhesives in the context of NSM flexural strengthening technique with prestressed CFRP laminates In: 11th International Symposium on Fiber Reinforced Polymers for Reinforced Concrete Structures (FRPRCS11). Guimaraes; 2013.

[2] Shrestha J, Ueda T, Zhang D. Durability of FRP Concrete Bonds and Its Constituent Properties under the Influence of Moisture Conditions. Journal of Materials in Civil Engineering. 2014 (Special Issue):A4014009.

[3] Teng J, Chen J, Smith ST, Lam L. Behaviour and strength of FRP-strengthened RC structures: a state-of-the-art review. Proceedings of the ICE-Structures and Buildings. 2003;156(1):51-62.

[4] BS EN ISO 15630-1:2010. Steel for the reinforcement and prestressing of concrete. Test methods. Reinforcing bars, wire rod and wire.

[5] EN 1992-1-1:2004. Eurocode 2: Design of Concrete Structures, Part 1-1: General Rules and Rules for Buildings2004.

[6] Teng JG, Smith ST, Yao J, Chen JF. Intermediate crack-induced debonding in RC beams and slabs. Construction and Building Materials. 2003;17(6–7):447-62.

[7] Martin J, Lamanna A. Performance of Mechanically Fastened FRP Strengthened Concrete Beams in Flexure. Journal of Composites for Construction. 2008;12(3):257-65.

[8] Rizzo A, Galati N, Nanni A. Strengthening of off-system bridges with mechanically fastened pre-cured FRP laminates. ACI Special Publication. 2005;230.

[9] ACI 440.2R-08:2008. Guide for the Design and Construction of Externally Bonded FRP Systems for Strengthening Concrete Structures: American Concrete Institute.

[10] El-Tawil S, Ogunc C, Okeil A, Shahawy M. Static and Fatigue Analyses of RC Beams Strengthened with CFRP Laminates. Journal of Composites for Construction. 2001;5(4):258-67.

[11] Barros JAO, Fortes AS. Flexural strengthening of concrete beams with CFRP laminates bonded into slits. Cement and Concrete Composites. 2005;27(4):471-80.

[12] Esmaeeli E, Manning E, Barros JAO. Strain Hardening Fibre Reinforced Cement Composites for the Flexural Strengthening of Masonry Elements of Ancient Structures. Construction and Building Materials. 2013;38(special issue):1010-21.

[13] Park R. Reinforced concrete structures: John Wiley & Sons; 1975.

[14] Mander J, Priestley M, Park R. Theoretical Stress-Strain Model for Confined Concrete. Journal of structural engineering. 1988;114(8):1804-26.

[15] Nayal R, Rasheed HA. Tension stiffening model for concrete beams reinforced with steel and FRP bars. Journal of Materials in Civil Engineering. 2006;18(6):831-41.

[16] Wanser J, Sigrist V. Accounting for Tension Stiffening in Finite Element Modelling. In: 8th fib International PhD Symposium in Civil Engineering. Department of Civil Engineering, Technical University of Denmark; 2010.

[17] Massicotte B, Elwi AE, MacGregor JG. Tension-stiffening model for planar reinforced concrete members. Journal of Structural Engineering. 1990;116(11):3039-58.

# Chapter 7: Characterization and Optimization of HCP$^{(L)}$-Concrete Connection

## 7.1 Introduction

This chapter describes the methodology and the results of the study on characterization and optimization of the connection between HCP$^{(L)}$ and RC elements. This study was performed in two phases. The main objective of the first phase (Phase I) was to characterize

(i) The local bond stress-slip law at the interface of the CFRP laminate and the SHCC in the structure of the HCP$^{(L)}$;

(ii) The local bond stress-slip law at the interface of the adhesively bonded HCP$^{(L)}$ and reinforced concrete; and

(iii) The pull response of the HCP$^{(L)}$ attached to the RC block by means of only chemical anchors.

Since experimental tests are time consuming, labor intensive and costly, a combination of them and Finite Element (FE) models were employed in this phase to achieve the abovementioned objectives with a minimum number of experimental tests. The experimental program was composed of pull tests executed on three different groups of HCP$^{(L)}$-Concrete connection specimens. The outcomes of testing each group were then used to calibrate the unknown parameters in FE modelling through performing series of inverse analyses. At the second phase (Phase II) of this study, the calibrated FE model in previous phase was extended to execute a comprehensive parametric study. In this phase of study initially effective CFRP-SHCC bond length $L_b^{ef}$ was estimated. Further FE models were prepared based on this $L_b^{ef}$ and according to a parametric study the optimized parameters for an HCP$^{(L)}$ and its connection to an RC block are proposed. HCP$^{(L)}$ in these models had two rows of CFRP laminates each bonded to a groove. Following the results of this FE study, the most effective configuration for adding chemical anchors to an adhesive based HCP$^{(L)}$-to-Concrete connection, was proposed. Moreover, the optimum width of HCP$^{(L)}$ with two rows of CFRP laminates based on the grooves distance from the plate-edge was predicted.

## 7.2 Phase I: Experimental Program

The experimental program was composed of three groups of specimens (groups "A" to "C"); each to achieve the necessary information to calibrate the parameters of an HCP[(L)]-Concrete connection through performing inverse analyses using FE models.

Since the results of group "A" specimens are used to extract the local bond stress-slip law at the interface of the adhesively bonded HCP[(L)] to the RC block, localizing the failure of these specimens at this interface zone was the main design consideration.

Specimens in group "B" were designed aiming to localize the failure at the interface of CFRP laminate and the surrounding SHCC (in the structure of the HCP[(L)], since their results were used to estimate the local bond stress-slip law at the interface of CFRP and SHCC.

Finally, group "C" specimens were tested to obtain information on bearing response of the HCP[(L)] attached to the RC block by means of only chemical anchors. Considering the expected failure mode of the specimens in this group, these test results were used to calibrate shear response (fracture Mode II) of the SHCC.

### 7.2.1 Details of the specimens

RC blocks had dimensions of 400 mm × 200 mm × 150 mm and they were cast by the same batch of concrete used to prepare the short-span shear-critical beams in section 4.5. These blocks were cast in wooden molds with four threaded steel rods placed inside each of them. The steel rods, made of ASTM steel grade 8.8 with a diameter of 20 mm, were considered as the longitudinal reinforcement of the concrete blocks. Moreover, they provided the possibility of constraining these blocks to the supporting system of the pull test setup.

Configurations of groups "A" and "B" specimens are depicted in Figure 7.1, and in the case of group "C" specimens in Figure 7.2. Additional details of these specimens and the values of the parameters shown in these figures are mentioned in Table 7.1.
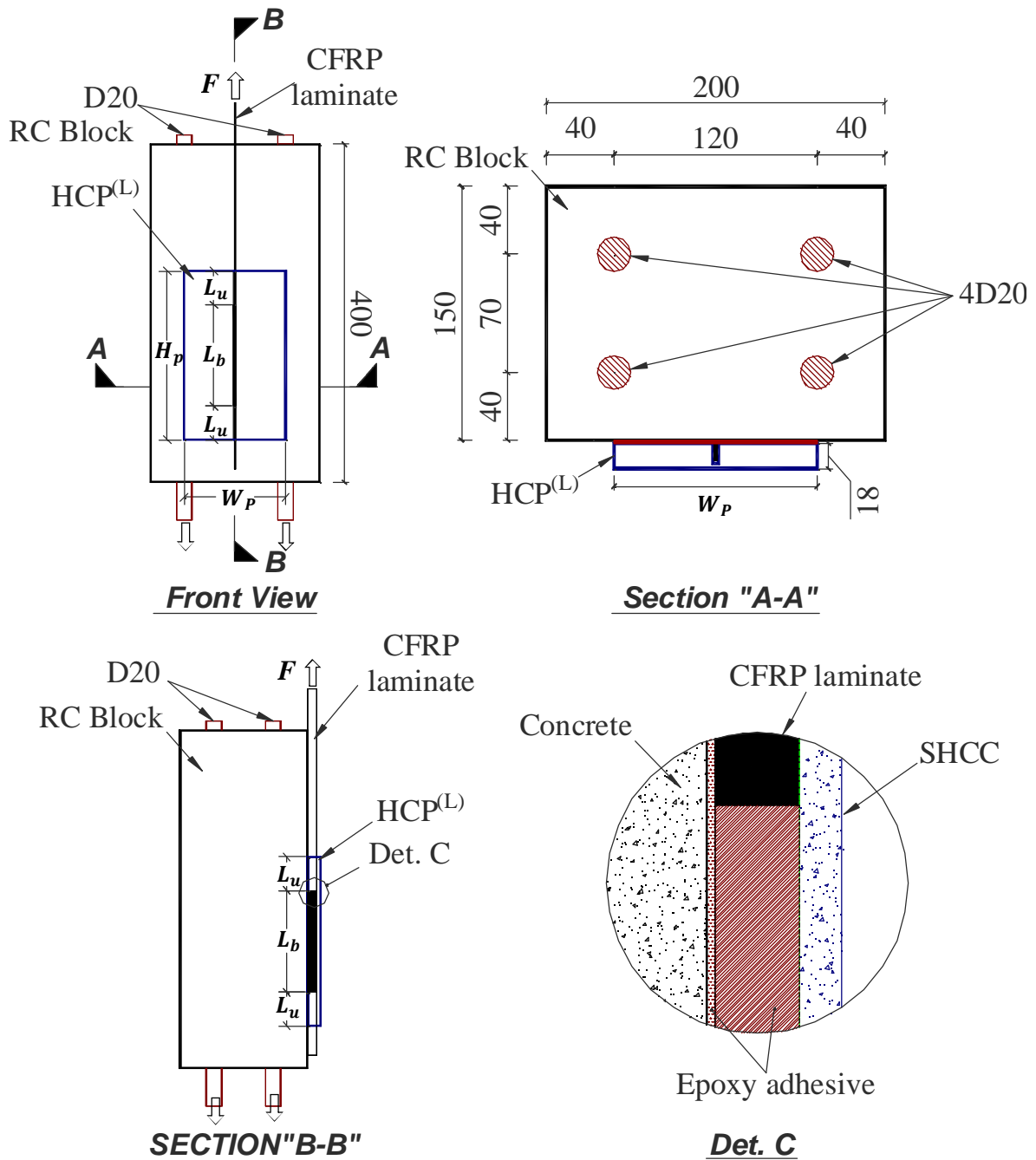
Figure 7.1: Configurations of the specimens in groups "A" and "B" (note that dimensions are in mm; $L_u = 0$ and 30 mm for specimens in group "A" and "B", respectively, and the details of the parameters can be found in Table 7.1).
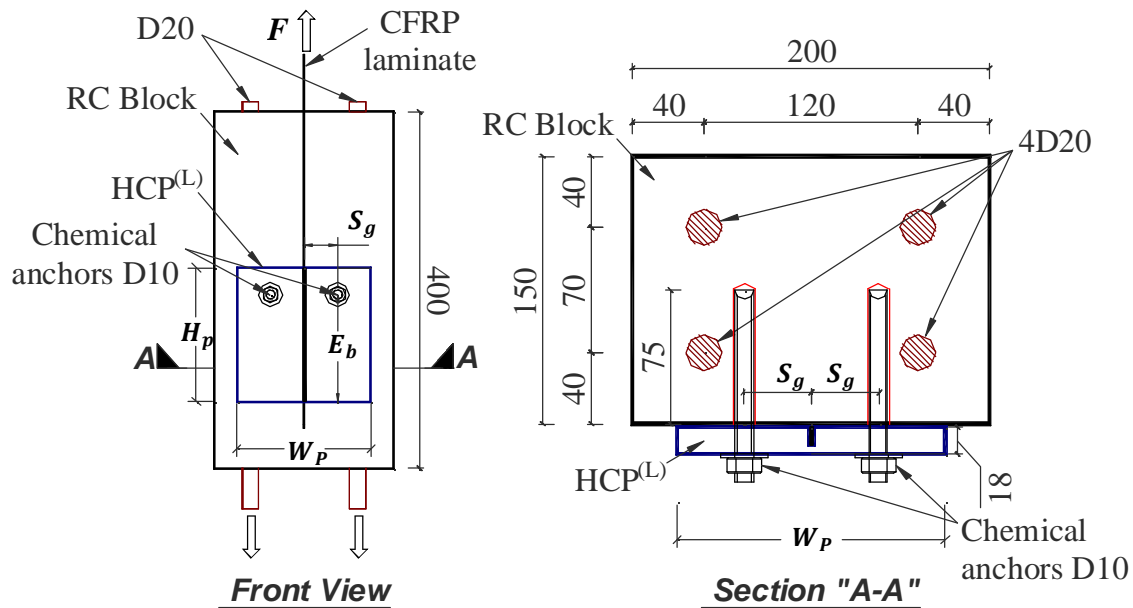
Figure 7.2: Configuration of the specimens in group "C" (note that dimensions are in mm; $L_b = H_p$; and the values of the other parameters are defined in Table 7.1).

Table 7.1: Details of the configuration of the connection specimens according Figures 7.1 and 7.2.

| Category | Labels | $N_R$ | $L_b$ (mm) | $H_p$ (mm) | $W_p$ (mm) | $N_b$ (mm) | $D_b$ (mm) | $S_g$ (mm) | $E_b$ (mm) |
|---|---|---|---|---|---|---|---|---|---|
| | A_W50 | 2 | 150 | 150 | 50 | 0 | | | |
| A | A_W75 | 2 | 150 | 150 | 75 | 0 | | | |
| | A_W100 | 2 | 150 | 150 | 100 | 0 | | | |
| | B_Lb30 | 2 | 30 | 90 | 150 | 0 | | | |
| B | B_Lb45 | 2 | 45 | 105 | 150 | 0 | | | |
| | B_Lb60 | 2 | 60 | 120 | 150 | 0 | | | |
| | B_Lb90 | 2 | 90 | 150 | 150 | 0 | | | |
| C | C_Sevb90 | 1 | 150 | 150 | 150 | 2 | 10 | 37.5 | 90 |
| | C_Sevb120 | 2 | 150 | 150 | 150 | 2 | | | 120 |

$N_R$: number of repeated tests, $L_b$: CFRP-SHCC bond length, $H_p$: height of the HCP(L), $W_p$: width of the HCP(L), $N_b$: number of chemical anchors, $D_b$: diameter of the anchor rods, $S_g$: distance between anchors and groove, $E_b$: distance of the anchors from bottom edge of the HCP(L).

### 7.2.1.1 Specimens in group "A"

All HCP$^{(L)}$'s used to prepare the specimens in this category had an identical thickness $(t_p)$ of 18 mm ± 0.02 mm. As shown in in Figure 7.1, for all specimens in group "A", the bond length between CFRP laminate and the SHCC plate $(L_b)$ was equal to the height of the HCP$^{(L)}$ $(H_p)$.

The parameter of the study of group "A" specimens was the width of the HCP$^{(L)}$ $(W_p)$, since the main test objective was characterizing the effective width of the plate $(W_p^{ef})$. This width is defined as the measure beyond which only a marginal increase in pull force capacity can be achieved. Thus, all the HCP$^{(L)}$'s used to build the specimens in this subcategory had equal $H_p$ of 150 mm.

For each $W_p$, the test was repeated using two similar specimens in subcategory "A1". In one of these two repeated specimens, the relative sliding between HCP$^{(L)}$ and the RC block, at the top edge (HT) and mid-height (HM) of the HCP$^{(L)}$, was measured. This information was collected to be used in calibration of the constitutive law of the interface of HCP$^{(L)}$-Concrete. To measure the relative sliding, a pair of LVDTs was installed at the right and left edges of the HCP$^{(L)}$ at each of the specified levels according to the configurations in Figure 7.7a. The relative sliding between HCP$^{(L)}$ and the substrate concrete at each of these specified levels was then evaluated from the average of the measures of each pair of these LVDTs (see section 7.2.3 for additional details).

### 7.2.1.2 Specimens in group "B"

Since the aim of testing specimens in group "B" was to characterize the response of CFRP-SHCC interface, at the design of these specimens special attention was given to avoid premature failure at the HCP$^{(L)}$-Concrete interface. Hence, 30 mm of the CFRP laminates' length at both top and bottom parts of the HCP$^{(L)}$ were left un-bonded (Figure 7.1 with $L_u$= 30 mm) .

This consideration assures that the failure occurs at the interface of CFRP-SHCC, so that the information associated with the bond stress-slip response at this interface zone can be obtained. As it is discussed in section 7.2.3, this information was obtained through measuring

the relative sliding between CFRP and SHCC at two specified levels, in one of the two repeated tests of the specimens B_Lb45, B_Lb60 and B_Lb90.

### 7.2.1.3 Specimens in group "C"

Specimens in group "C" were designed to investigate the response of the HCP$^{(L)}$ attached to the RC block by means of only chemical anchors. According to the details showed in Figure 7.2, the HCP$^{(L)}$ of each specimen had a single CFRP laminate with two holes symmetrically positioned at each of its sides.

The HCP$^{(L)}$ was supported with two anchors of 10 mm in diameter adhesively anchored into the RC block. The parameter of the study was the vertical position of the anchors, measured from the bottom edge of the HCP$^{(L)}$ $(E_b)$, taken as 90 and 120 mm. The distance between anchors and groove $(S_g)$ in these specimens was equal to 37.5 mm. Moreover, $L_b$ of all specimens in this group was the same as $H_p$, identical to 150 mm.

Considering the expected failure mode of the specimens in this group, the experimental results were used to calibrate the shear response of the SHCC (fracture Mode II), incorporating inverse analyses in the FE simulations.

### 7.2.2 Preparation of the Specimens

SHCC plates used to prepare HCP$^{(L)}$s were cut from larger plates with a dimension of 2000 mm × 150 mm × 20 mm. The molds, pouring technique and also curing process were the same as the ones adopted in casting the plates for strengthening the RC beams in section 6.2.2.

These plates were then cut into smaller pieces to extract the required plates to prepare HCP$^{(L)}$s according to the dimensions specified in the Figure 7.1, Figure 7.2 and Table 7.1. Afterwards, the irregular face of these SHCC plates (the top face considering the SHCC casting), was rectified to achieve a uniform thickness of 18 mm ± 0.02 mm. Finally, the grooves were executed with the same configuration showed in Figure 4.30.

As illustrated in Figure 7.3, two metallic plates, each of 50 mm × 15 mm × 1.5 mm, were bonded to one end of the CFRP laminates. These end tabs were used to facilitate the CFRP

clamping at its gripped-end and also to prevent the stress concentrations at this region, hence, avoiding premature rupture of the CFRP during pull test.
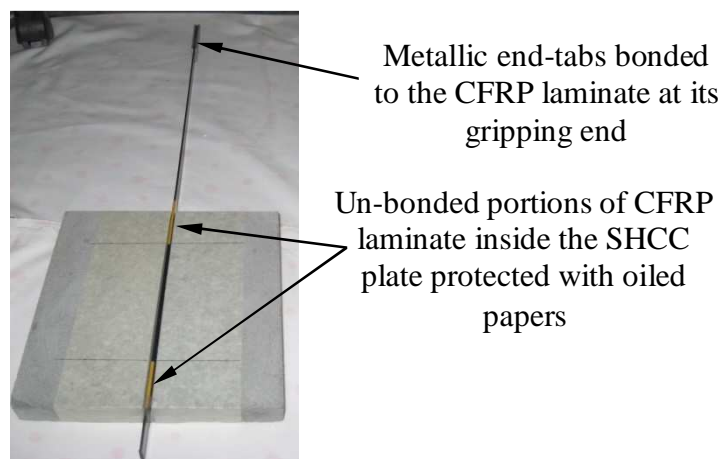


Figure 7.3: Oiled papers wrapped around portions of the CFRP laminates right beyond the top and the bottom regions of the designed bond length for the HCP[(L)]s prepared to make specimens in group B.

For the HCP[(L)]s of the specimens in group "B", as shown in see Figure 7.3, before placing CFRP laminates inside the grooves, which were already filled by adhesive, oiled papers (low adhesive interacting papers) were wrapped around portions of the CFRP laminates just beyond the top and bottom regions of the designed bond length of CFRP-SHCC, the portions characterized with $L_u$ in Figure 7.1.

To bond CFRP laminates into the grooves and also to bond the HCP[(L)] to the RC blocks, the procedures described in sections 6.2.2 and 4.5.2 were followed.

In order to enhance bonding quality between the HCP[(L)] and the substrate, in the case of groups "A" and "B" specimens, one face of the RC block with a dimension of 400 mm × 200 mm was roughened using a sandblasting procedure (see Figure 7.4).

For the specimens in group "C", 10 mm diameter anchors, with the installation procedure explained for Hilti[®] chemical anchors in section 4.5.2, were adopted (see also details in Figure 7.2).
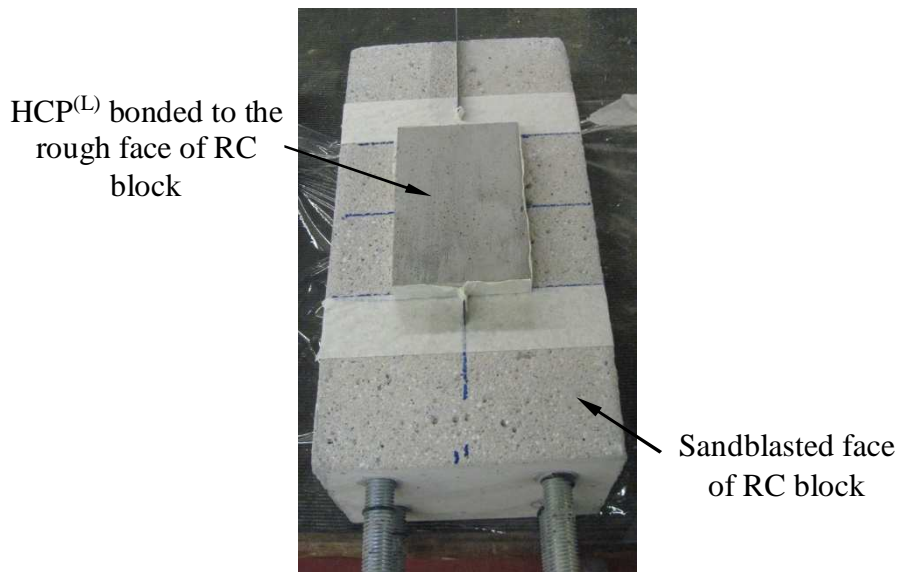
Figure 7.4: HCP$^{(L)}$ attached to the sandblasted face of the RC block (the face with dimensions of 400 mm $\times$ 200 mm)

### 7.2.3 Test Setup and Monitoring Instruments

As shown in Figure 7.5, setup of the pull tests was composed of a base and a top support, securing the specimen and the hydraulic jack, respectively. Both of these supports were bolt connected to a column, which was welded at its top and bottom portions to an existing reaction steel frame. The test setup was designed with enough rigidity to minimize its deformational effect on the results of the pull tests.

The base support had four slotted holes, designed to secure the RC block through constraining its longitudinal threaded rods. The constraining system was composed of the nuts and small perforated metallic plates acting as the washers (see detail "b" in Figure 7.5). Therefore, the imposed pull force to the specimens was transferred to the base-support by the reaction of the longitudinal steel rods of RC blocks.

To fasten the nuts, an identical torque of 40 N.m was employed in all specimens. To transmit tensile force of the actuator to the specimens, a manual wedge grip, connected to the load-cell of the actuator as showed in detail "a" of Figure 7.5, was adopted. The CFRP laminate at its end tabs was clamped inside the jaws of this grip.

The pull force was imposed at a constant displacement rate of 5 $\mu m/s$, which was controlled by an LVDT supported on the body of the actuator, with its tip measuring the displacement of the body of the grip (see detail "a" in Figure 7.5).

As represented in Figure 7.4, the relative sliding between HCP[(L)] and the RC block, in specified specimens of group "A", was measured using a pair of LVDTs which were fixed to the lateral faces of the HCP[(L)] at its top (HT) and the mid-height (HM) levels. The tip of each of these LVDTs was placed on an L-shaped narrow plate fixed to the RC block.

To assure that LVDTs are measuring the relative sliding at the desired levels, L-shaped plates were adhesively fixed to the RC block only in a bond length of 5 mm at both upper and lower parts of the central horizontal-axis of the support of their corresponding LVDT.

In the case of the specified specimens in group "B", the sliding of CFRP laminate respecting to the SHCC plate at the loaded-end and free-end was measured using two LVDTs, each measuring one of these displacements. As shown in Figure 7.7, the definition of the loaded-end of CFRP laminate refers to the extremity of the CFRP-SHCC bond length closer to the CFRP gripped end (where the force is applied). The other extremity of this bond length is then called as the free-end of CFRP laminate. According to Figure 7.7, an LVDT was fixed to the CFRP laminate just beyond the top and bottom edges of HCP[(L)]. The tip of each of these LVDTs was placed on narrow straight plate supported with L-shaped plates at each of its ends. Both of these L-shaped plates were adhesively fixed to the SHCC with bond lengths of 5 mm at both upper and lower parts of the loaded-end or freed-end levels of CFRP laminate.

As illustrated in the detail "1" of Figure 7.7, the measurement of the top LVDT doesn't not purely represent the relative sliding at the loaded-end, since it also includes the deformation of the un-bonded portion of CFRP laminate between the LVDT support and the CFRP loaded-end ($L_u$+15 mm = 45 mm). Since these results are used to extract CFRP-SHCC local bond stress-slip law, by means of inverse analysis approach and based on comparison of the results of FE modellings and experimental tests, instead of subtracting this FRP deformation, the relative displacement between CFRP at the supported zone of the LVDT and SHCC at the loaded-end level of CFRP are compared with each other.
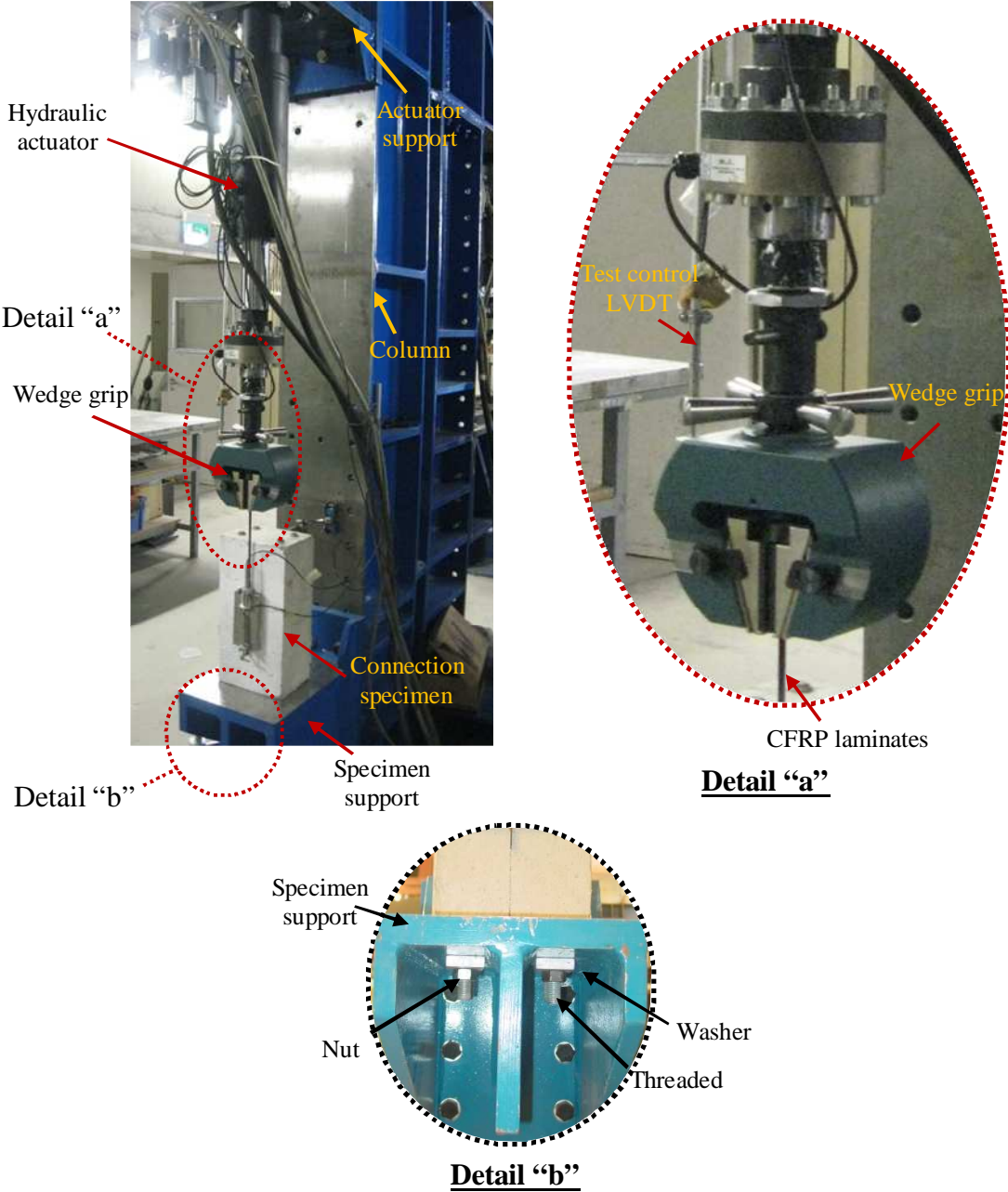
Figure 7.5: Details of the adopted test setup for pull tests
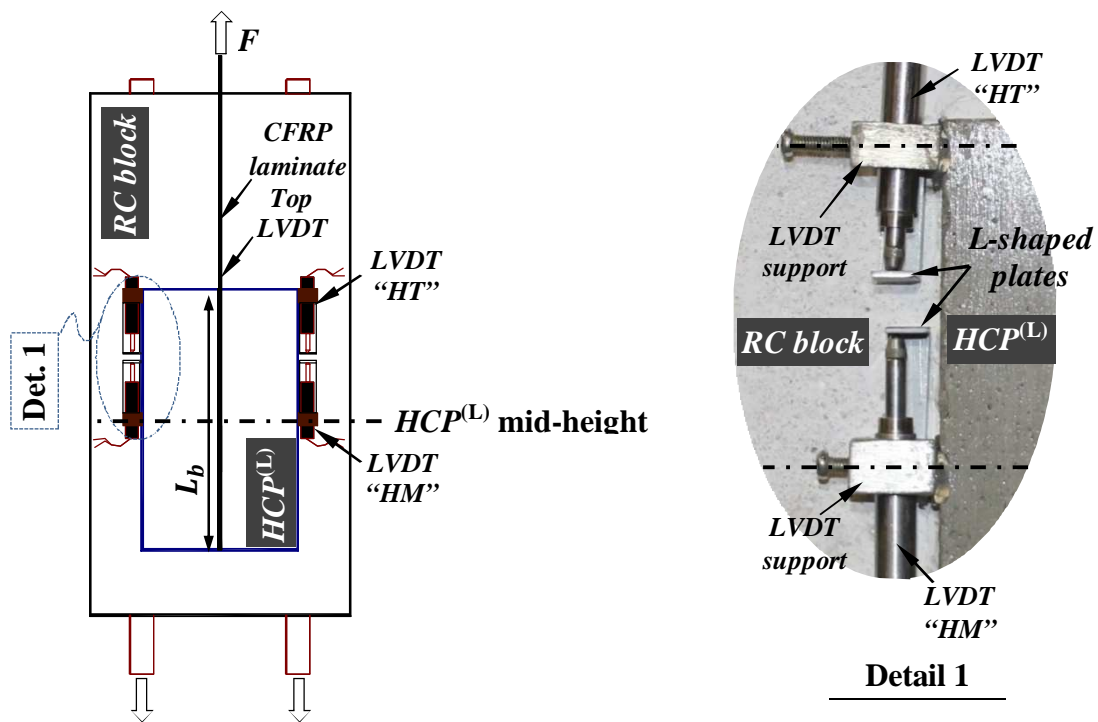
Figure 7.6: Arrangement of the LVDTs in specimens of group "A" to measure the relative sliding between HCP[(L)] and RC block at the top (HT) and the mid-height (HM) levels of the HCP[(L)] (note that the supports of LVDTs and the L-shaped plates are fixed to the lateral faces of HCP[(L)] and concrete, respectively. These elements are adhesively bonded in a length of 5 mm at both upper and lower parts respecting the central horizontal-axis of the supporting devices for their corresponding LVDT, see detail 1)
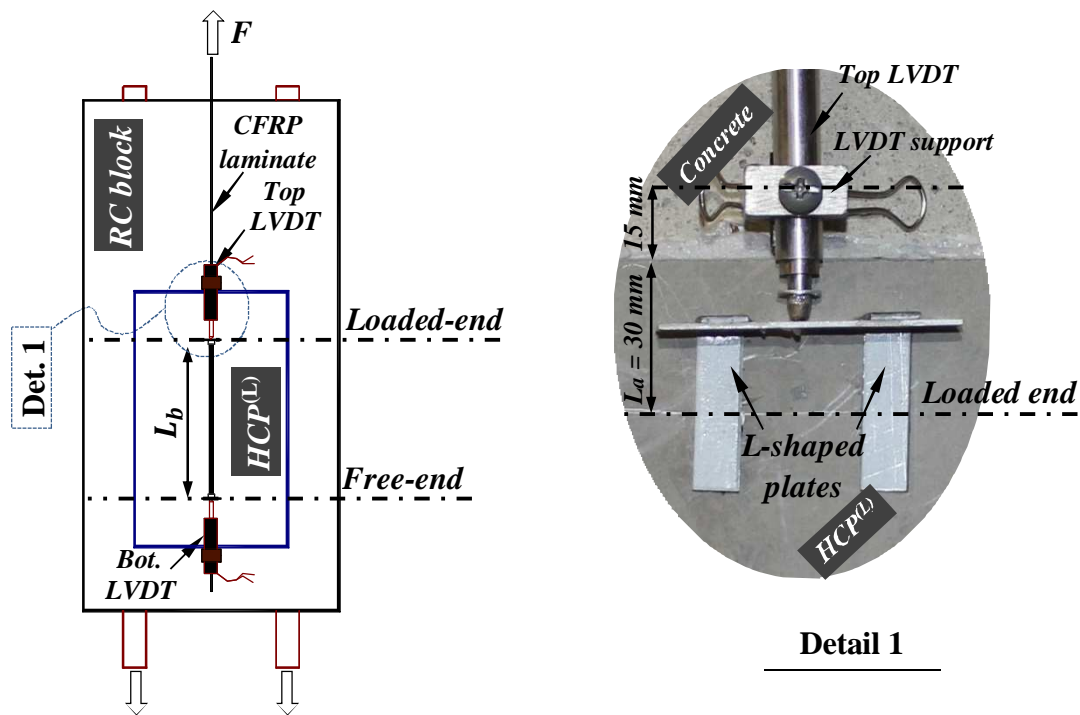
Figure 7.7: Arrangement of the LVDTs to measure the relative sliding between CFRP and SHCC at the loaded-end and at the free-end for the specimens in group "B" (note that the LVDTs support and the L-shaped plates are fixed to CFRP laminate and HCP[(L)], respectively. These elements are adhesively bonded in a height of 5 mm at the upper and lower parts of their corresponding dot-dash lines indicated in details 2. Moreover, a similar detail applies to the free-end of CFRP laminate)

### *7.2.4 Material Properties*

### *7.2.4.1 Concrete*

RC blocks were cast with the same batch of the ready-mix concrete used to prepare the short-span shear-critical beams in section 4.5. The mechanical properties of this concrete, at the age of 90 days, can be found in section 4.5.3.1.

### *7.2.4.2 SHCC*

Details on fresh and hardened state properties of the self-compacting PVA-SHCC (mixture C4W30) used in casting the SHCC plates can be found in section 4.3.

### *7.2.4.3 Epoxy Adhesive*

Mechanical characteristics of the S&P Resin 220 epoxy adhesive®, used to bond CFRP laminates into the grooves of the SHCC and also to bond the strengthening plates to the soffit of the beams, are reported in section 4.5.3.4.

### *7.2.4.4 CFRP Laminates*

CFRP laminates (S&P laminate CFK 150/2000) were cut from the same roll used to prepare HCP(L)s for the strengthening of the short-span shear-critical beams in chapter 4. Tensile characteristics of these laminates are reported in section 4.5.3.5.

### *7.2.4.5 Threaded Steel Rods*

Threaded rods with 20 mm of diameter were made of ASTM steel grade 8.8. Therefore, they are characterized with characteristic tensile yield and ultimate strengths of 640 MPa and 800 MPa, respectively.

### *7.2.4.6 Chemical Anchors*

In the case of the specimens with their HCP(L) mechanically connected to the RC block, a Hilti® system of chemical anchors was employed. In this system, anchor rods of 10 mm in diameter with specification of HIT-V-8.8 M10X190, and mechanical properties mentioned in section 5.2.3.5, were used.

### 7.2.5 Results of the Experimental Tests

The maximum pull force $(F_p)$ and the failure modes of each specimen are reported in Table 7.2. In the case of repeated tests, also average peak force $(F_p^{avg})$ is reported in this table. Following, there is a discussion on the test results of the experimental program based on the pull force capacity and the observed failure modes of the tested specimens.

The graphs showing the pull force *versus* relative sliding measured by the LVDTs at the specified locations of the specimens in groups "A" and "B", and also those corresponding to the pull force *versus* gripped-end displacement of the specimens in group "C" can be found in section 7.3.4, where the FE results are compared to the experimental ones.

Table 7.2: Results of the pull tests on connection specimens

| Category | Labels | $F_p$ (kN) | $F_p^{avg}$ (kN) | Prevailing failure |
|---|---|---|---|---|
| A | A_W50(1) | 17.95 | 17.92 | Cohesive failure in SHCC |
|  | A_W50(2) | 17.89 |  |  |
|  | A_W75(1) | 25.01 | 24.00 |  |
|  | A_W75(2) | 22.98 |  |  |
|  | A_W100(1) | 24.26 | 25.18 |  |
|  | A_W100(2) | 26.09 |  |  |
| B | B_Lb30(1) | 14.08 | 14.53 | CFRP/adhesive adhesion failure |
|  | B_Lb30(2) | 14.98 |  |  |
|  | B_Lb45(1) | 20.83 | 21.45 |  |
|  | B_Lb45(2) | 22.07 |  |  |
|  | B_Lb60(1) | 24.42 | 25.35 |  |
|  | B_Lb60(2) | 26.28 |  |  |
|  | B_Lb90(1) | 30.57 | 31.29 | Rupture of CFRP laminate |
|  | B_Lb90(2) | 32.00 |  |  |
| C | C_Sevb90(1) | 15.09 | N.A. | Inclined cracking |
|  | C_Sevb120(1) | 23.92 | 23.67 |  |
|  | C_Sevb120(2) | 23.41 |  |  |

### 7.2.5.1 Specimens in group "A"

Figure 7.8 presents the typical failure and crack pattern of the specimens in group "A". According to this figure, these specimens failed by detachment of the HCP[(L)] while a thin layer of SHCC remained bonded to the concrete block. This cohesive fracture indicates that SHCC is the weakest link at the shear transference path between HCP[(L)] and RC block.



**A_W50**

Inter-laminar shear failure of SHCC (cohesive fracture)

**A_W100**

**A_W50**
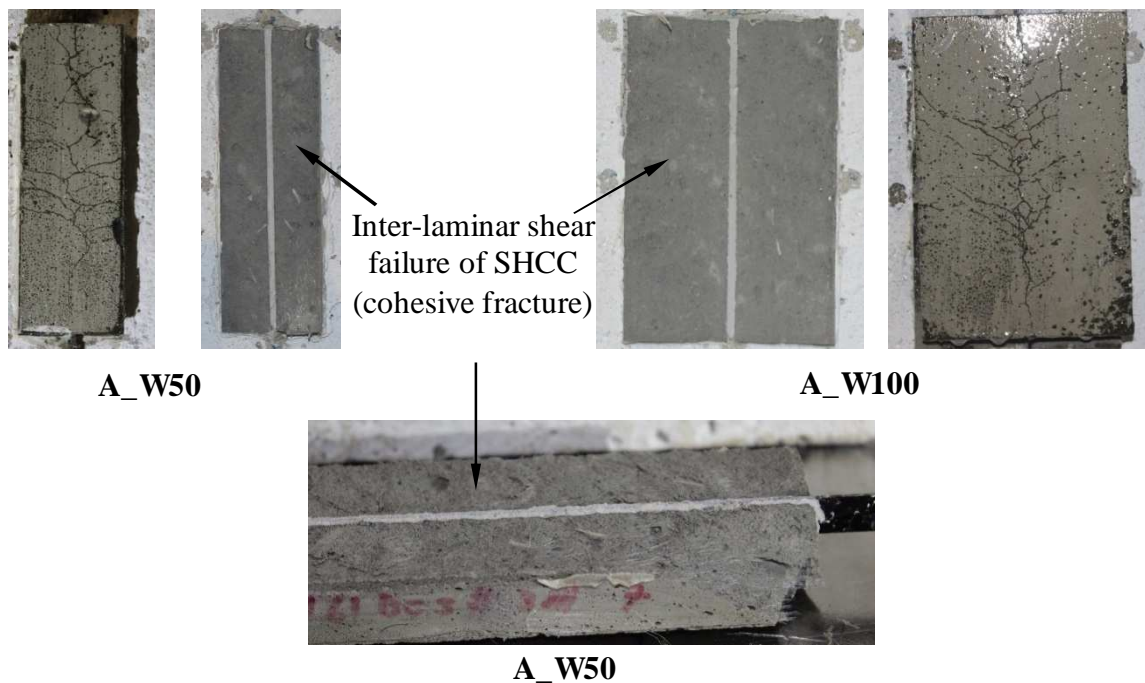
Figure 7.8: Typical SHCC cohesive failure and crack propagation at the end of the test for the specimens in group "A"

The low inter-laminar shear resistance of SHCC is mainly attributed to the absence of coarse aggregates in its micro-structure [1]. It is well known that in granular composites, coarse aggregates offer a relatively high interlocking mechanism to resist sliding and progress of the shear cracks. Moreover, considering the casting of the SHCC plates, the content of the fibers oriented out of the casting plane (along the plate through thickness) is considerably low, which in turn fibers can only marginally contribute in inter-laminar shear resistance of the cracked-SHCC.

At the end of the testing of the specimens and after spraying the surface of the HCP[(L)] with a penetrating liquid, only a fish-spine micro-crack pattern was visible as presented in Figure 7.8.

The obtained results in terms of average peak-load (indicated in Table 7.2) indicate that in consequence of increasing $W_p$ from 75 mm to 100 mm, $F_p^{avg}$ changes less than 5%. Therefore, for an adhesively bonded HCP[(L)], $W_p^{ef}$ is taken as 75 mm, which corresponds to mobilization of $F_p^{avg}$ equal to 24 kN back to the concrete.

### 7.2.5.2 Specimens in group "B"

Results of the pull tests, executed on the specimens in group "B", showed an increase in $F_p^{avg}$ from 14.5 kN to 25.4 kN for the changes in $L_b$ from 30 mm to 60 mm, with an adhesion debonding failure occurred at the interface of CFRP/adhesive in all these specimens. CFRP laminate reached its full tensile capacity, hence ruptured, at $L_b$= 90 mm (Figure 7.9).
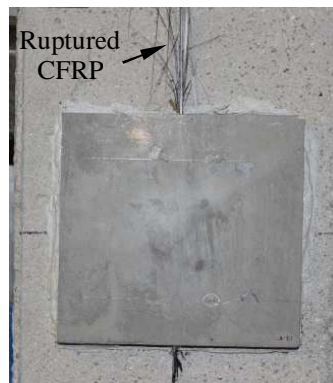


Figure 7.9: Rupture of CFRP laminates for specimens B_Lb90

It should be noted that this rupture force (31.29 kN) is almost 16% lower than the one obtained based on tensile characterization of CFRP laminates (37.1 kN), reported in section 7.2.4.4. This lower rupture load in pull connection tests is attributed to both the lack of lateral confinement for the CFRP laminate (e.g, gripped-end pressure) and a non-uniform stress distribution at the upper extremity of the bond length of CFRP laminate, as compared to the characterization based on tensile tests. These both effects promote the rupture

initiation in some filaments of CFRP at a load lower than the CFRP rupture obtained in tensile tests.

### 7.2.5.3 Specimens in group "C"

In the case of these specimens, the load transfer mechanism between HCP[(L)] and the supporting chemical anchors was a series of inclined compressive struts formed between the bonded length of the CFRP laminate and each of the chemical anchors.

Figure 7.10 shows the distribution of the maximum principle strain (major strain) obtained using a digital image processing technique on figures registered during the pulling test of specimen C_Sevb90_N10(1). It should be noted that Figure 7.10 is only presented to explain the load transfer mechanism and the failure mode of HCP[(L)] connected with anchors, hence, a detailed analysis of this mechanism is out of the scope of the current research work.
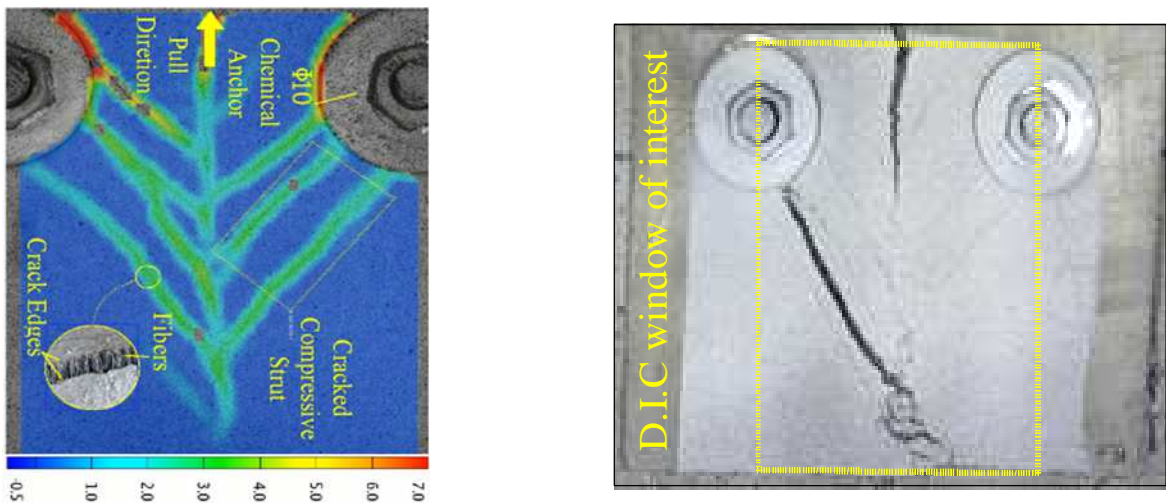


Figure 7.10: Major strain distribution analyzed using digital image correlation technique in a window of interest showed in the right image and the role of fibers in bridging cracks formed in compressive struts (specimen C_Sevb90_N10(1) at the load level of 95% of HCP[(L)] peak pull force).

As it can be seen in this Figure 7.10, inclined compressive struts transfer the tensile force from the bonded CFRP laminate to the anchors. This load transference process is followed by the formation of diagonal cracks, whose opening is restricted by crack bridging

mechanisms of the PVA fibers. The ultimate pull load capacity of the HCP[(L)] is reached when a major crack forms in one of these compressive struts.

According to the obtained results with the anchor rods located at $E_b$ of 90 mm and 120 mm, average $F_p^{avg}$ of 14.2 kN and 23.7 kN, respectively, can be mobilized back to the concrete. Thus, an increase of 30 mm (33%) in the height of the plate, below the level of the anchors, resulted in a 67% larger pull force capacity.

## 7.3 Phase I: Finite Element Models Calibration

Finite element (FE) models were developed and then calibrated based on the obtained results of the experimental tests. The main objective of these simulations, as mentioned before, was to perform inverse analysis and to estimate the local bond stress-slip law at the interface of the CFRP laminate and the SHCC in the structure of the HCP[(L)], the local bond stress-slip law at the interface of the adhesively bonded HCP[(L)] and RC block, and the pull behavior of the HCP[(L)] attached by means of only chemical anchors.

The FEM study in this phase was to calibrate HCP[(L)]-RC connection models, which further, in the second phase of the study, is used to carry out a comprehensive parametric study and optimize the HCP[(L)] features and its connection.

### 7.3.1 Model Calibration Strategy

The results obtained from each group of specimens in the experimental study were used to calibrate those unknown constitutive laws involved in the simulation process of the specimens. The parameters of these constitutive laws were obtained based on inverse analyses using FE models, whose results were compared with those obtained in experimental tests. The calibrated constitutive laws are the bond stress-slip response at the interface of CFRP-SHCC and at the interface of HCP[(L)]-Concrete, also in-plane shear model (Mode II) of the SHCC.

#### 7.3.1.1 Calibration of the constitutive laws of the interface regions

Considering the cohesive SHCC failure of the specimen in group "A", the results of these specimens were used to calibrate the constitutive law for the interface of HCP[(L)]-Concrete.

In the first series of simulations in this step, using an inverse analyzing technique, a primary HCP$^{(L)}$-Concrete law was calibrated under assumption of a perfect bond between CFRP laminate and SHCC. This constitutive law was used in simulation of specimens in group "B" to calibrate a primary interface law at CFRP-SHCC connection zone.

Further, an iterative modelling between the models of group "A" and group "B" specimens was adopted to account for the effect of constitutive laws of these both interface regions (interface of CFRP-SHCC and interface of SHCC-Concrete). This approach led to recalibrate these constitutive law taking into account the possible damage progress in any of these interface zones, as expected from the experimental tests.

### 7.3.1.2 Calibration of in-plane shear behavior of SHCC

The failure mode of the specimens in group "C" was inclined shear cracking without any visible crushing at the bearing regions. Therefore, knowing the uniaxial tensile response of the SHCC (mode I, characterized by tensile tests), the in-plane shear model (mode II) was calibrated employing an inverse analysis in the corresponding FE models.

### 7.3.2 Boundary Conditions and Mesh Size of Finite Element Models

Abaqus-Explicit package, FE modelling software, was used to simulate the connection specimens. Taking the advantage of symmetry, only half of the geometry of the specimens was modelled. The supporting system of the specimens was simplified to an analytically rigid surface.

Boundary conditions that were applied to the symmetry plane, to the top edge of CFRP laminate, to the supporting rigid surface and to the bottom of the longitudinal rods, along with the details of the FE mesh are presented in Figure 7.11. Based on a mesh objectivity analysis, a detailed mesh of approximately 3.5 mm for each edge of the 3D elements was adopted. The loading was applied using a quasi-static analysing technique with a monotonic increasing displacement that was imposed to the top of the CFRP laminate.

(a)

(b)



(c)

(d)
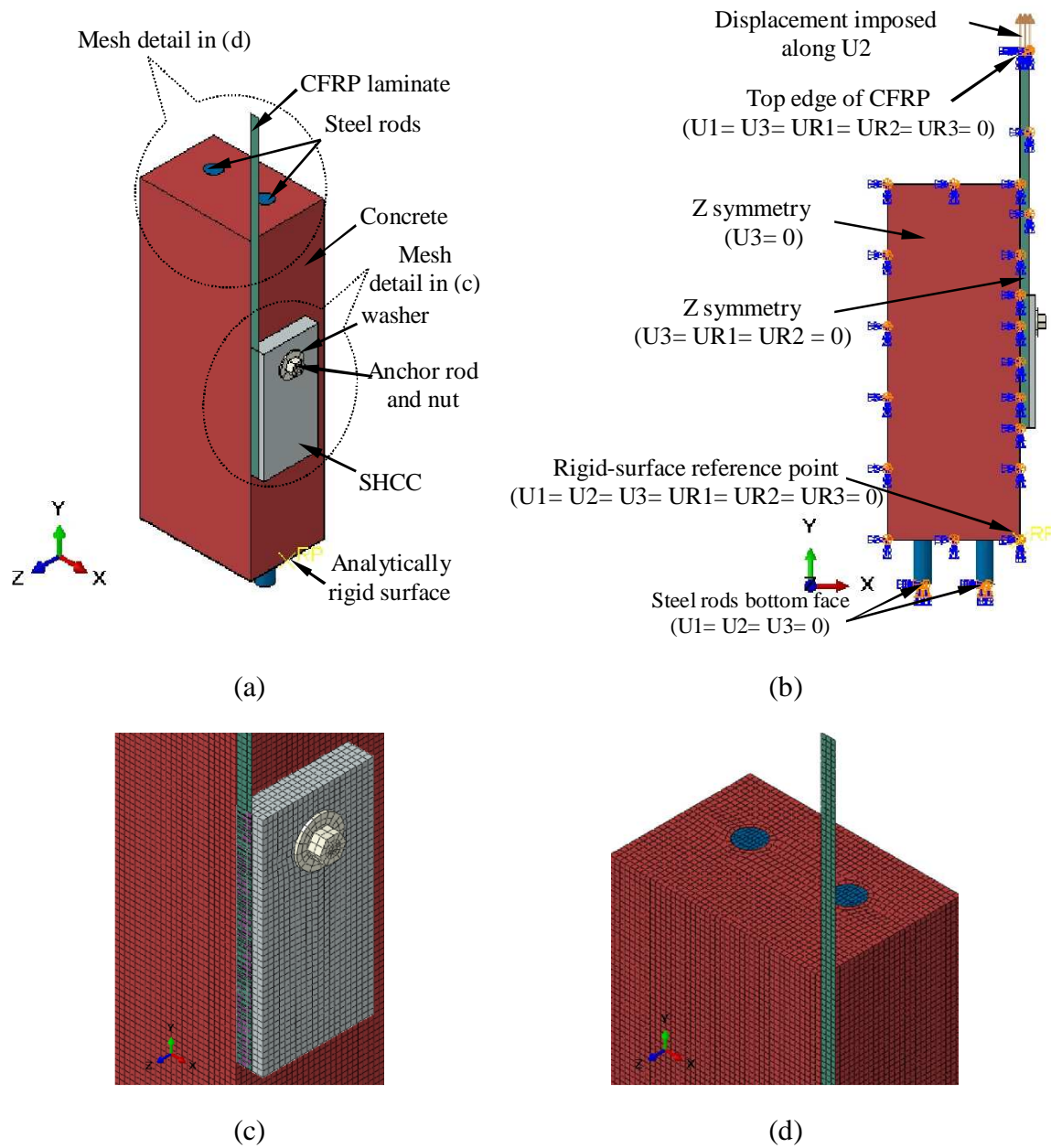
Figure 7.11- Details of the FEM modellings (a) half of the geometry, (b) loading and boundary conditions, (c and d) details of mesh configuration (note that: for the specimens in groups "A" and "B" no anchorage system was modelled and an interface elements embedded between HCP[(L)] and RC block; "U" and "UR" are the translation and the rotational degrees of freedom, respectively; and local orientations 1, 2 and 3 are parallel to the X, Y and Z in global coordinate system, respectively).

### 7.3.3 Material Models and Element Types

### 7.3.3.1 SHCC

SHCC was modelled using 8-node first-order (linear) interpolation 3D solid elements. "Cracking Model" of Abaqus-Explicit in conjunction with the option of removing the degraded element is used to simulate the SHCC.

The "Cracking model" is formulated based on the decomposition of total strain rate $(d\varepsilon)$ into elastic strain rate $(d\varepsilon^{el})$ and cracking strain rate $(d\varepsilon^{cr})$, as demonstrated in the following equation:

$$d\varepsilon = d\varepsilon^{el} + d\varepsilon^{cr} \tag{7-1}$$

Abaqus "Cracking model" assumes that the material behaves linear-elastically in compression. This assumption has enough accuracy in the current study since crushing of concrete was not observed in any of the experimental tests discussed in section 7.2.5. However, depending on the magnitude of the compressive strains, developed at the bearing region of the anchor-based-connections, the model may eliminate some nonlinearity caused by response of concrete in compression beyond its linear-elastic limit.

The model assumes an isotropic linear-elastic tensile response up to the material cracking strength $(\sigma_n^{cr})$. Afterwards, according to the Figure 7.12, the post-cracking response of the material can be defined either by direct introduction of the Mode I fracture energy $\left(G_f^I\right)$ or a multi-linear definition of tensile stress ($\sigma_n$) *versus* crack opening displacement $(w^{cr})$, or cracking strain $(\varepsilon^{cr})$. In the case that $G_f^I$ is the only introduced parameter, a simple linear decay of cracking stress up to a crack opening displacement corresponding to crack stress-free state will be followed, see Figure 7.12a.

Abaqus "Cracking Model" follows a smeared crack approach to simulate cracking. According to this approach, the un-cracked material between the cracks is modelled using an isotropic linear-elastic response, while the cracks are simulated following a continuum approach, meaning that the discrete cracks are distributed along a characteristic length known as crack band width $(l_{cr})$ of the element. In other words, instead of simulating the cracks individually, e.g. introducing discontinuity in mesh, the stress and material stiffness

associated to the material integration point are modified to take into account the effect of the presence of the cracking. Following the Hillerborg's approach [2], $l_{cr}$ is a mesh dependent character which is used to assure the dissipation of identical fracture energy $(G_f)$ for any mesh refinement. Abaqus assumes the cubic root of the volume of a three dimensional element as this characteristic length.

Cracking Model of the Abaqus uses the concept of fixed orthogonal-cracks. Thus, at the onset of cracking at any given material point, the direction normal to the first crack is aligned to the direction of the maximum principal tensile stress. Any subsequent crack at this material point, therefore, can be only formed in the orthogonal directions to this first crack.

As illustrated in Figure 7.13, the tensile response of SHCC can be decomposed into three main phases. The first phase follows a linear-elastic relation with a slope identical to the modulus of elasticity of SHCC $(E_{sh})$ up to the stress corresponding to the onset of the first crack $(f_{sh}^{cr})$.



(a)                                                            (b)
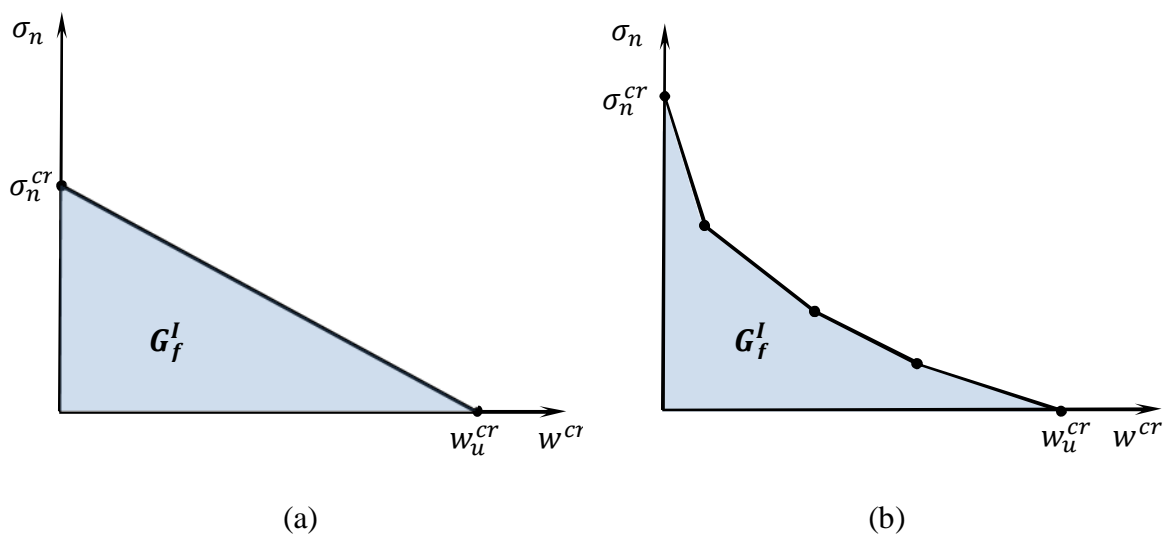
Figure 7.12: Definitions of post-cracking response in Abaqus cracking model: (a) Mode I fracture energy concept, (b) multi-linear stress *vs.* cracking opening displacement

The second phase of the tensile behavior, beyond the occurrence of the first crack, is associated with the formation of multiple cracking that is known as the strain hardening

regime. As discussed in section 4.3.6.2, the tensile response of SHCC at the first and second phases can be characterized by executing direct tensile tests on un-notched specimens. In this case, tensile behavior of the SHCC is reported in terms of tensile stress *versus* average tensile strain. The response of this second phase can be also simplified as a straight line that connecting the points $(f_{sh}^{cr}, \varepsilon_{sh}^{cr})$ and $(f_{sh}^u, \varepsilon_{sh}^u)$ to each other.

Following the discussion in section 4.3.6.2, the third phase of the tensile response of SHCC is related to the crack localization and follows a stress descending branch (stress-softening response), where the opening of a single crack dominates the tensile behavior. Response of SHCC in this phase can be precisely captured by performing tensile tests on notched specimens.

As mentioned before, the input data describing multi-linear post-cracking behavior in "Cracking model" can be either introduced in terms of stress *versus* cracking strain ($\varepsilon^{cr}$) or stress *versus* crack opening displacement ($\delta^{cr}$).

To homogenize the post-cracking response of SHCC, showed in Figure 7.13, the strain hardening phase of the tensile response of the SHCC should be converted into a displacement field. This aim was achieved through multiplying the average strain by the elements' characteristic length ($l_{cr}$). Afterwards, the average stress-crack opening displacement of the post-peak phase, obtained from tensile test on notched specimens and reported for composite mixture C4W30 in Figure 4.17 and Table 4.8, was merged to the end of this hardening phase (see Figure 7.14).

To maintain the continuity of the pre- and post-peak responses, the tensile peak strength obtained from the notched specimens, see Table 4.8, was adopted as $f_{sh}^u$. The values of the parameters defining the tensile behavior of SHCC can be found in Table 7.3.
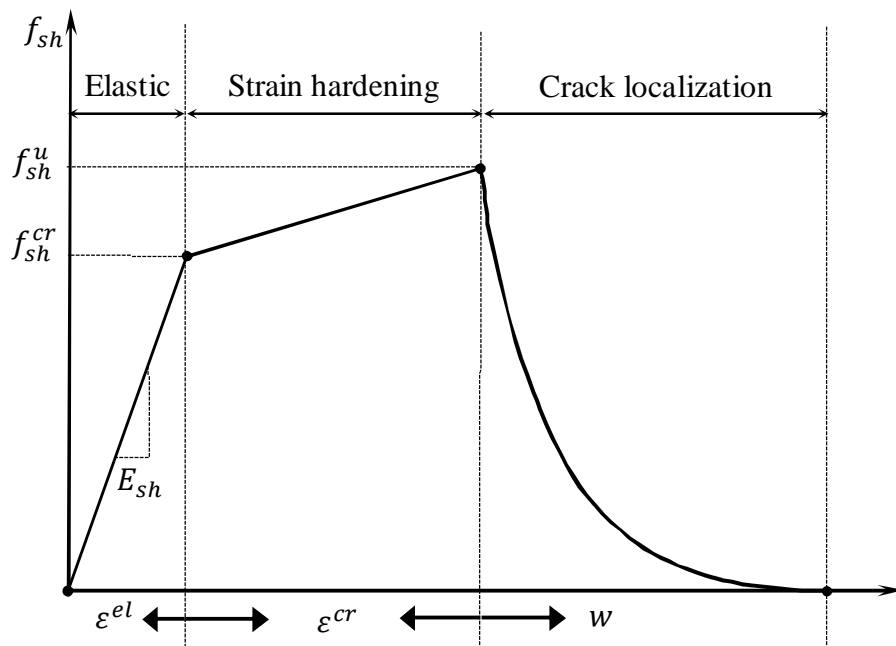
Figure 7.13: Schematic presentation of tensile behavior of SHCC
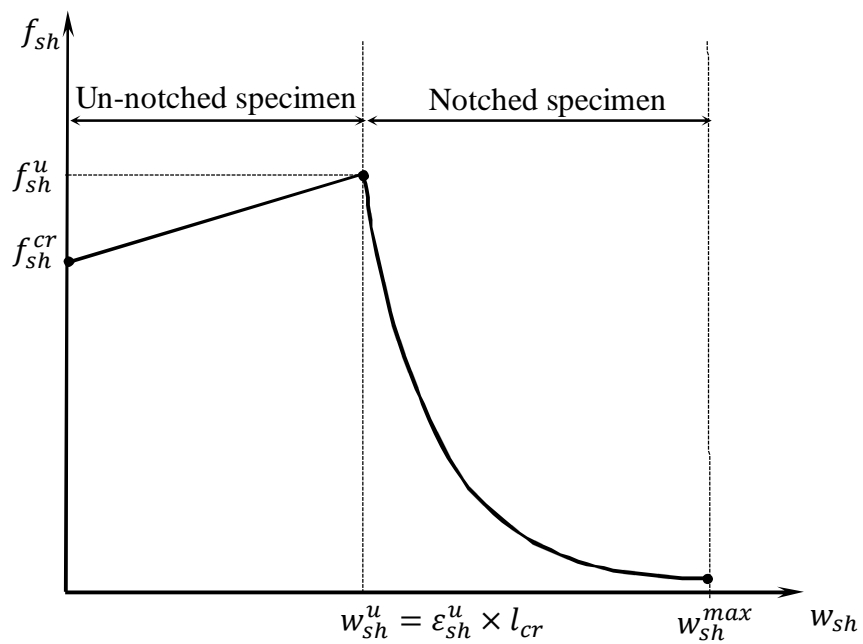


Figure 7.14: Homogenized tensile post-cracking response of SHCC based on displacement

Table 7.3: Parameters defining tensile constitutive law of SHCC (see Figure 7.13)

| $E_{sh}$ (MPa) | $f_{sh}^{cr}$ (MPa) | $f_{sh}^{u}$ (MPa) | $\varepsilon_{sh}^{u}$ (%) |
|---|---|---|---|
| 18420 | 2.75 | 3.55 | 1.54 |

The "Cracking Model" identifies the crack initiation using a Ranking yield surface. As it is shown in Figure 7.15 in deviatoric plane, Ranking criterion assumes that the condition for the onset of a crack is met when the maximum principal stress exceeds the tensile strength of the material.

Although the crack initiation condition is based on Mode I fracture only, both Mode I and Mode II are included in the crack evolution, post-cracking behavior, through the definition of the tension-softening (or tension-hardening) and the shear-retention models, respectively.
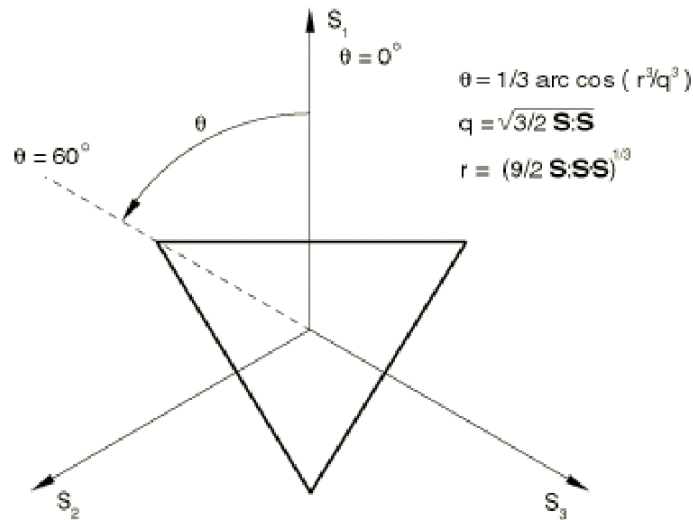


Figure 7.15: Rankine yield surface in deviatoric plane (S1, S2 and S3 are the first, the second and the third stress invariants, respectively) [3].

The post-cracking shear response, Mode II, is associated with the amount of crack opening normal to the fracture surface. The Mode II response is then coupled to Mode I by

using a shear-retention model that correlates shear stiffness to the amount of crack opening in the crack normal direction.

As an example, the dependency of the total shear stress ($\tau_{nt}$) to the total shear strain ($\gamma_{nt}^{cr}$) through a stiffness $D_{nt}^{II}(\varepsilon_n^{cr}, \varepsilon_t^{cr})$ for direction $t$ of a cracked surface, as depicted in Figure 7.16, is presented herein (the same approach is applied to $s$ direction):

$$\tau_{nt} = D_{nt}^{II}(\varepsilon_n^{cr}, \varepsilon_t^{cr})\gamma_{nt}^{cr} \tag{7-2}$$

where,

the value of $D_t^{II}(\varepsilon_n^{cr}, \varepsilon_t^{cr})$ depends on crack opening and can be expressed as:

$$D_{nt}^{II}(\varepsilon_n^{cr}, \varepsilon_t^{cr}) = \mu(\varepsilon_n^{cr}, \varepsilon_t^{cr})G \tag{7-3}$$

where, $G$ is the shear modulus of intact concrete and $\mu(\varepsilon_n^{cr}, \varepsilon_t^{cr})$ is a user-defined shear-retention factor.
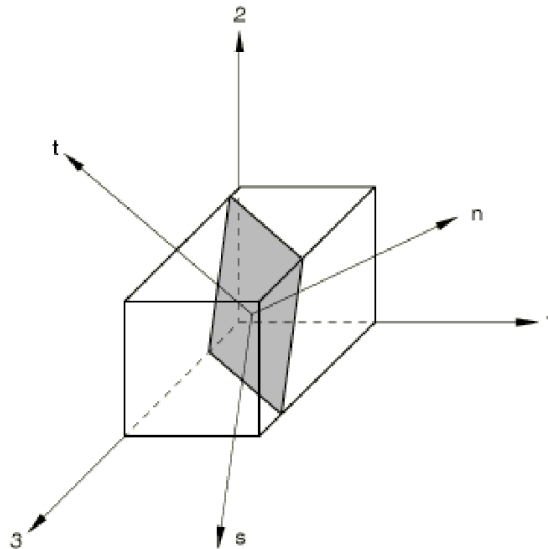


Figure 7.16: Representation of a cracked surface and definitions of crack local coordinates $n$, $s$ and $t$ [3]

When only one crack exists, the most common mathematical form of shear retention model for the concrete is the one proposed by Rots and Blaauwendraad [4]. This model is

formulated based on the strain corresponding to a fully open crack $(\varepsilon^{cr}_{n,max})$ and a power low $(p)$, which are both introduced as material parameters. This formulation is represented in equation (7-4) and schematically illustrated in Figure 7.17. According to this shear retention model, when a crack opening strain tends to a zero value, the shear-retention tends to infinity that represents the crack initiation threshold. At $\varepsilon^{cr}_{n,max}$ the shear-retention factor is zero, which indicates a complete loss of interlock of the aggregates of a granular material.

$$\mu(\varepsilon^{cr}_n) = \frac{\left(1 - \dfrac{\varepsilon^{cr}_n}{\varepsilon^{cr}_{n,max}}\right)^p}{1 - \left(1 - \dfrac{\varepsilon^{cr}_n}{\varepsilon^{cr}_{n,max}}\right)^p} \tag{7-4}$$
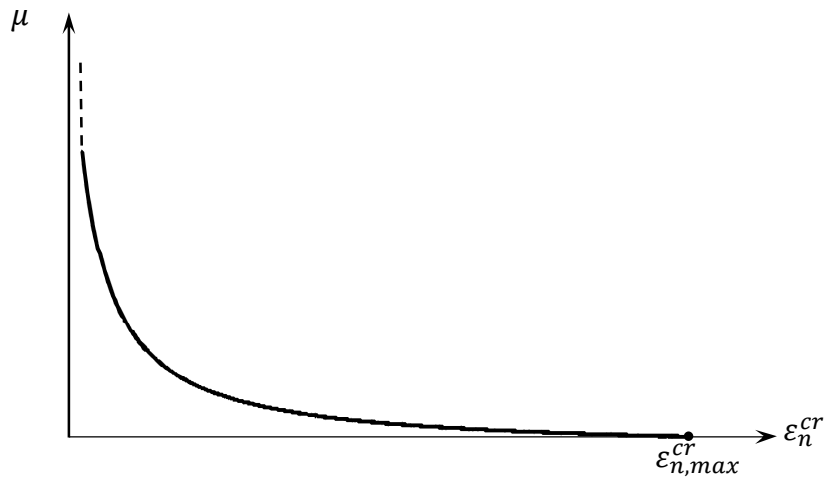


Figure 7.17: Relation between shear retention factor and crack opening in normal direction for concrete [4]

For the sake of the user's convenience, Abaqus receives parameters of the shear-retention in traditional form, $\rho(\varepsilon^{cr}_n)$, that changes between one and zero for a closed crack and a fully open one, respectively. Further, using equation (7-6), Abaqus converts this $\rho(\varepsilon^{cr}_n)$ to the $\mu(\varepsilon^{cr}_n)$ for the purpose of internal calculations:

$$\rho(\varepsilon_n^{cr}) = \left(1 - \frac{\varepsilon_n^{cr}}{\varepsilon_{max}^{cr}}\right)^p \tag{7-5}$$

$$\rho(\varepsilon_n^{cr}) = \frac{\mu}{1 + \mu} \tag{7-6}$$

When a crack is simultaneously opening and shearing, Abaqus uses a total stress-strain shear retention model to calculate the shear stiffness. Following is the example for simultaneous crack opening in $n$ and $t$ directions (similar approach is applied to crack opening in $n$ and $s$ directions).

$$\gamma_{nt}^{cr} = \gamma_{nt}^{cr,n} + \gamma_{nt}^{cr,t} = \frac{t_{nt}}{D_{nt}^{II,n}} + \frac{t_{nt}}{D_{nt}^{II,t}} \tag{7-7}$$

$$D_{nt}^{II}(\varepsilon_n^{cr}, \varepsilon_t^{cr}) = \frac{D_{nt}^{II,n} D_{nt}^{II,t}}{D_{nt}^{II,n} + D_{nt}^{II,t}} \tag{7-8}$$

where,

$$D_{nt}^{II,n} = \mu(\varepsilon_n^{cr}) \, G \tag{7-9}$$

$$D_{nt}^{II,t} = \mu(\varepsilon_t^{cr}) \, G \tag{7-10}$$

Abaqus provides the possibility of introducing an arbitrary definition of shear retention factor *versus* normal crack opening strain (or displacement) in a multi-linear form. Considering the lack of studies in the literature on the shear retention model of the SHCC, it was assumed that up to a normal crack opening corresponding to the cracking strength at Mode I, the shear strength of the SHCC is linearly proportional to the shear deformation through the intact shear modulus, $G$.

For the cracked status of the material, a trilinear descending relationship defines the shear-retention model, as depicted in Figure 7.18. Therefore, parameters $\rho_1$, $\rho_2$, $\varphi_1$ and $\varphi_2$ need to be calibrated through an inverse analysis technique.
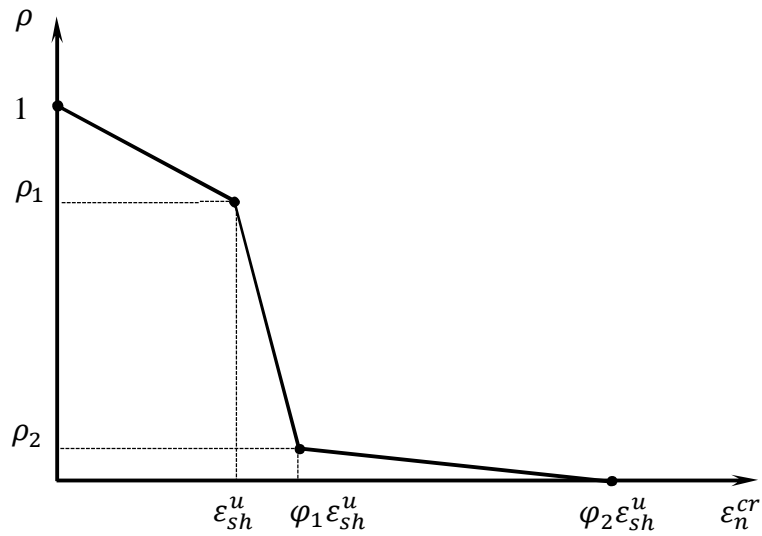
Figure 7.18: Assumed trilinear shear retention model for SHCC Interface behavior

### 7.3.3.2 Interfaces

The interface regions were modelled using three-dimensional 8-node cohesive elements with four integration points, presented in Figure 7.19. Interface elements were used to simulate the interaction between SHCC and the CFRP laminate and also between HCP[(L)] and concrete.
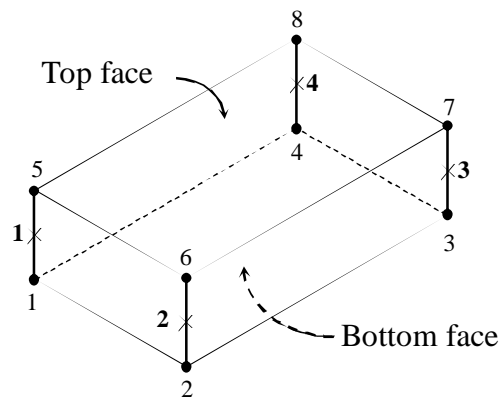


Figure 7.19: Three-dimensional 8-node cohesive element with four integration points at the middle-space of top and bottom surfaces (symbol "×" indicates the integration points)

A traction-separation model was used to define the constitutive law of the cohesive elements. This approach is specifically useful when macroscopic characteristics of the interface zone such as thickness, stiffness and strength cannot be directly measured. According to this technique the constitutive thickness of the elements are taken equal to unity, being independent of their geometry. This technique assures that the nominal strain values represent directly the relative separation/sliding between the top and bottom faces of the cohesive element at each material point.

At any given material point of the three-dimensional cohesive elements, used to model interface zones in this study, one normal and two transverse separation components exist. Each of these separation components is coupled to a stress component at that material point through a traction-separation constitutive law.

The traction-separation constitutive law is composed of a linear elastic branch that is followed by a stress degradation phase after meeting a damage initiation criterion. The shape of the degradation phase is controlled by a damage evolution law. The simplest form of a traction-separation law includes linear stress degradation for a progressing separation up to a stress free state with its enclosing area corresponding to debonding fracture energy of $G_c$, as presented in Figure 7.20.

In the first phase of the traction-separation constitutive law an elasticity matrix with its off-diagonal terms set to zero defines the relation between the stress components and their corresponding separation components assuring an uncoupled normal and shear response. Note that the separation components represent the strain components as a thickness of unity by default is assumed for cohesive elements. This relation is presented in the following equation, where the stress components are correlated to the strain components through an uncoupled elasticity matrix.

$$\begin{Bmatrix} t_n \\ t_t \\ t_s \end{Bmatrix} = \begin{bmatrix} K_n & & \\ & K_t & \\ & & K_s \end{bmatrix} \begin{Bmatrix} \varepsilon_n \\ \gamma_t \\ \gamma_s \end{Bmatrix} \tag{7-11}$$

where, $t_n$ is the normal traction to the top (or bottom) face of the interface element while $t_t$ and $t_s$ are the shear traction components, with $\varepsilon_n$, $\gamma_t$ and $\gamma_s$ being their corresponding strain components, respectively. A damage initiation criterion based on maximum nominal

stress, showed by equation (7-12), controls the onset of the degradation of the elastic response at each material point:

$$max\left\{\frac{\langle t_n \rangle}{t_n^p}, \quad \frac{t_t}{t_t^p}, \quad \frac{t_s}{t_s^p}\right\} = 1 \tag{7-12}$$

where, $t_n^p$ is the peak value of the traction component when the deformation is purely normal to the interface surface and $t_t^p$ and $t_s^p$ are the peak values of traction components where deformation is purely along $t$ or $s$ directions, respectively. The symbol $\langle \ \rangle$ is the Macaulay bracket, which indicates that a pure compressive stress state does not initiate damage.

Damage evolution is introduced by multiplying the equivalent elastic stress at any given strain by scalar damage variable $(d)$. For the separation/sliding beyond damage initiation, $d$ increases from 0 to 1 at each material point, as depicted in Figure 7.20. Following equations define the degradation of the components of elastic traction vector due to the damage progress:

$$
\begin{aligned}
t_n &= \begin{cases} (1-d)t_n^e & t_n^e \geq 0 \\ t_n^e & t_n^e < 0 \end{cases} \\
t_t &= (1-d)t_t^e \\
t_n &= (1-d)t_n^e
\end{aligned}
\tag{7-13}
$$

where $t_n^e$, $t_t^e$ and $t_n^e$ are the traction components assuming an elastic traction-separation behavior for each given strain components (undamaged state).

The behavior of the interface elements in this study was defined using the abovementioned constitutive law, along with a mode-independent damage evolution and a fully degraded element removal option. Details of assumed curves for the constitutive laws, dedicated to each interface element, are discussed below.
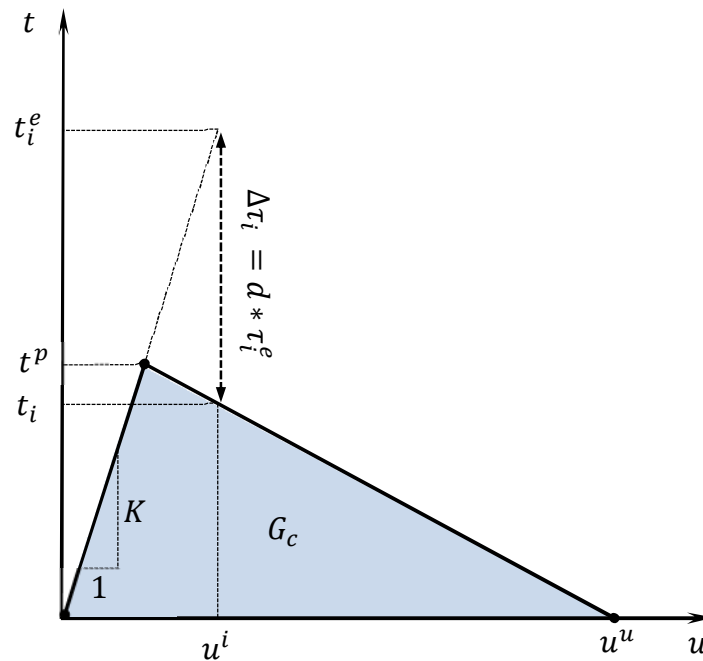
Figure 7.20: Simple form of traction-separation law

*CFRP-SHCC interface response:* according to the observation from the experimental tests of the specimens in group "B", the debonding progress passed through at the interface of CFRP laminate and the adhesive. In the FE models, for simplicity, the adhesive material is not geometrically simulated. Instead, its contribution assumed to be indirectly introduced in definition of the traction-separation constitutive law of the corresponding interface element.

Splitting failure occurred along the CFRP laminate in the specimens in group "C" was associated to a separation normal to the interface zone. Observation of the de-bonded part of the CFRP laminate revealed that the detachment progressed into the SHCC, since the detachment volume comprised of adhesive with a thin layer of SHCC material bonded to that. Following this finding, a large value for the parameters defining elastic traction-separation response normal to the interface element was introduced, meaning that the constitutive law of the SHCC governs the failure in the normal direction.

Identical parameters of stiffness and peak stress at elastic phase were adopted to define the interface response for transverse shear sliding ($K_S = K_t = K$ and $t_s^p = t_t^p = t^p$).

The local bond stress-slip relationship to model the interface response of CFRP-SHCC is defined using a trilinear law with the damage initiation at a peak bond stress $t^p$. The adopted law for progressive degradation in the bond stress follows a bilinear softening response that reaches to a stress free state at ultimate sliding of $u^u$ (see Figure 7.21).
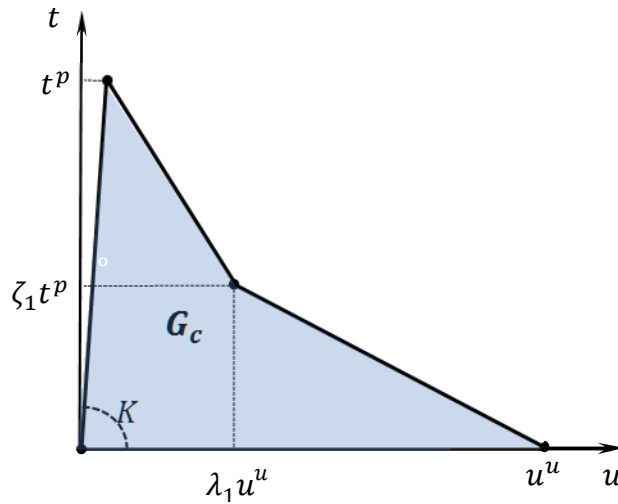


Figure 7.21: Adopted local bond stress-slip law for the interface of CFRP-SHCC

*SHCC-Concrete interface response:* the detachment progress into the SHCC plate of the specimens in group "A" suggests that the interface elements should be capable of representing anisotropy in shear response of SHCC material. Therefore, the embedded interface element should represents the combined response of the adhesive and a thin layer of the SHCC material in both transvers directions while the failure normal to the interface plane is controlled by constitutive law assigned to the SHCC. As illustrated in Figure 7.22, the shape of local bond stress-slip relationship, beyond the elastic response phase, is assumed to be a trilinear model with the onset of damage corresponding to a peak stress equal to the first cracking strength of the SHCC. Identical parameters of stiffness and peak stress at elastic phase were used to introduce the interface response for transverse shear sliding ($K_S = K_t = K$ and $t_s^p = t_t^p = t^p$). An approach to estimate stiffness parameter ($K$), for the first trial in simulation, is to use the equation (7-14), which assumes that the detached portion of SHCC and the adhesive act as a system composed of two parallel springs [5]:

$$K = \frac{1}{\frac{t_a}{G_a} + \frac{t_{sh}}{G_{sh}}} \qquad\qquad (7\text{-}14)$$

where, $t_a$ and $G_a$ are the thickness and the shear modulus of adhesive, respectively, and $t_{sh}$ and $G_{sh}$ are the effective thickness and the shear modulus of SHCC. The effective thickness can be taken almost the same as the thickness of the SHCC remained bonded to the concrete HCP$^{(L)}$ cohesive failure.
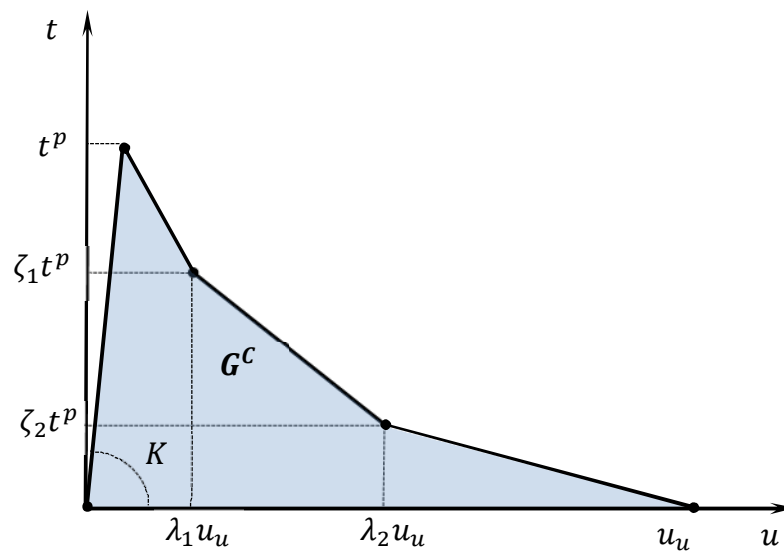
Figure 7.22: Adopted local bond stress-slip law for the interface of HCP$^{(L)}$-Concrete

### 7.3.3.3 Concrete

Concrete block was modelled by eight-node first-order (linear) interpolation solid elements. Concrete damaged plasticity model (CDP) was used to simulate the behavior of concrete. The CDP model employs concepts of isotropic damage elasticity combined with isotropic tensile and compressive plasticity to represent the inelastic behavior of concrete. Tensile cracking and compressive crushing are the main two failure mechanisms in CDP model.

### 7.3.3.3.1 Uniaxial Tensile and Compression

CDP incorporates the concept of uniaxial tensile and compression models based on damage plasticity, as showed in Figure 7.23. In these Figures, $d_t$ and $d_c$ are the tensile and

the compression damage variables, respectively. These damage variables were employed to characterize the degradation of the elastic stiffness in the unloading response at any point of the softening regimes of the tensile and the compression responses. Specifying these damage variables are mainly important in the case of reversal loadings, however, CDP turns into a classical plasticity for a zero assumption of these damage variables. In this latter case, the slope of unloading path (see Figure 7.23) remains the same as material initial stiffness $(E_0)$. Therefore, the plastic strains in tension $(\tilde{\varepsilon}_{ct}^{pl})$ and compression $(\tilde{\varepsilon}_{cc}^{pl})$ will be equal to the tensile cracking strain $(\tilde{\varepsilon}_{ct}^{cr})$ and inelastic compression strain $(\tilde{\varepsilon}_{cc}^{in})$, respectively. In current study, zero values were adopted for these damage variables.

*Tensile Behavior:* As depicted in Figure 7.23a, tensile behavior up to the onset of micro-cracking (concrete tensile strength, $f_{ct}^{cr}$) is governed by a linear elastic relationship. The post-cracking tensile behavior is then introduced by a softening stress-strain curve. The post-cracking response can be also introduced in terms of stress-crack opening with its enclosed area representing the mode I fracture energy $(G_f^I)$. Further, Abaqus converts this given stress-crack opening constitutive law to the stress-cracking strain adopting a characteristic length similar to the concept of the crack band-width described in section 7.3.3.1. Thus, using this technique and the elements having an aspect ratio closest to unity, the mesh sensitivity issue is relieved up to a significant extent. To define the stress-crack opening relationship, exponential function of Cornelissen et al. [6], presented mathematically in equation (7-15) and graphically in Figure 7.24, was used. By adopting this relationship for the post-cracking response of concrete, a multi-linear definition of the stress versus crack-opening displacement was introduced as the input data. Concrete tensile strength $(f_{ct}^{cr})$ was obtained according to equation (3-1).

$$f_{ct} = f_{ct}^{cr}\left[f(w) - \frac{w}{w_0}f(w_0)\right] \tag{7-15}$$

where,

$$f(w) = \left[1 + \left(\frac{c_1 w}{w_0}\right)^3\right]exp\left(-\frac{c_2 w}{w_0}\right) \tag{7-16}$$

In the abovementioned equations, $w$ is the crack width, $w_0 = 5.14\, G_f^I / f_{ct}^{cr}$ is the crack width at which the tensile stresses cannot be any further transferred, and finally, $c_1$ and $c_2$ are the material constants with their proposed values for a concrete with normal density, being 3.0 and 6.93, respectively. The value of $G_f^I$ was calculated according to the relationship recommended by CEB-FIP 1993 [7]:

$$G_f^I = G_{f0}(f_{cm}/10)^{0.7} \tag{7-17}$$

where, $G_{f0}$ is the base value of fracture energy and is proportional to the maximum aggregate size ($d_{max}$). The value of $G_{f0}$ can be obtained from table 2.1.3 of CEB-FIP 1993 [7].
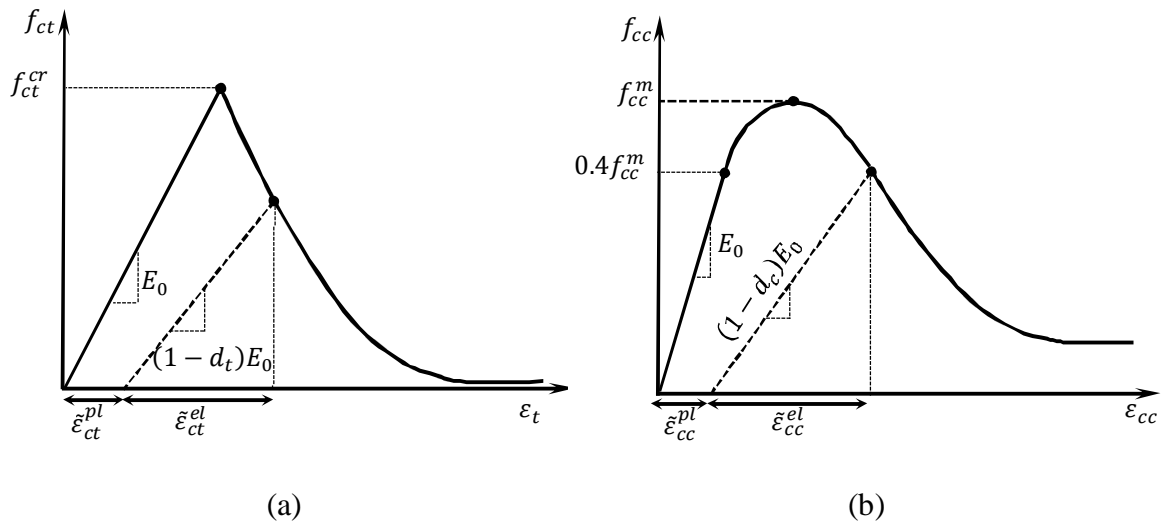


Figure 7.23: Concrete behavior in CDP under uniaxial loadings: (a) tensile and (b) compression

*Compression behavior:* as illustrated in Figure 7.23b, up to the onset of the initial yield at compression stress of $0.4 f_{cc}^m$, the compression response is assumed to be linear elastic. Afterward, a strain-hardening ascending branch that is followed by a strain-softening descending curve describes the plastic response of concrete. The strength corresponding to transition of the strain-hardening into the strain-softening is the material ultimate compressive strength ($f_{cc}^m$). The Mander model [8], introduced in detail in section 6.4.1.4,

was used to define the hardening and softening regimes of concrete subjected to the uniaxial compression loading.

Values of the essential parameters to define concrete uniaxial tensile and compression behaviors are summarized in Table 7.4.
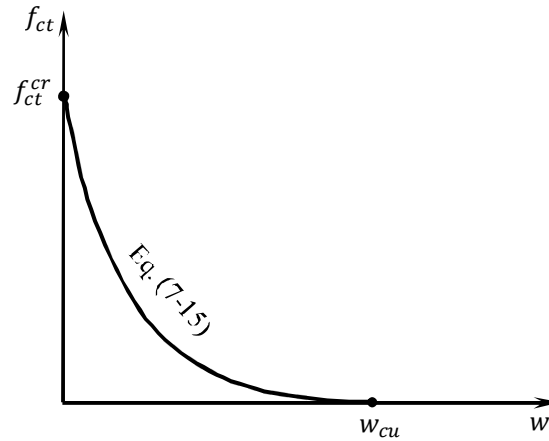


Figure 7.24: Stress-crack opening response of concrete proposed by Cornelissen et al. [6]

Table 7.4: Parameters to define uniaxial tension and uniaxial compression of concrete

| $E_c$ (GPa) | $f_{cc}^m$ (MPa) | $\varepsilon_{cc}^m$ (%) | $E_0$ (GPa) | $f_{ct}^{cr}$ (MPa) | $G_{f0}$ (N//m) | $d_{max}$ (mm) | $G_f^I$ (N/m) |
|---|---|---|---|---|---|---|---|
| 28.3 | 38.2 | 0.22 | 27.4 | 2.91 | 27.8 | 12.5 | 71.0 |

### *7.3.3.3.2 Plastic Flow and Yield Surface*

CDP is formulated based on a non-associated potential plastic flow rule with a Drucker-Prager hyperbolic function as its potential flow function. This potential flow function ($P$) is mathematically represented in equation (7-18) and graphically illustrated in Figure 7.25:

$$P = \sqrt{(\epsilon.\sigma_{t0}.tan\psi)^2 + \bar{q}^2} - \bar{p}.tan\psi \tag{7-18}$$

where, $\bar{p}$ and $\bar{q}$ are the Mises equivalent effective stress and effective hydrostatic pressure, respectively.

$\psi$ is the dilation angle that defines the ratio between plastic volume change and plastic shear strain for granular materials. The value of dilation angle is measured in $p - q$ plane at a high confining pressure. Based on the sensitivity analyses, Malm [9] reported that an appropriate value for dilation angle of concrete may range from 30 to 40 degrees. Thus, for the purpose of the present study the average dilation angle of 35° was adopted.

$\epsilon$ is the flow potential eccentricity and defines the rate at which the function of flow potential approaches to asymptote. The value of the eccentricity was taken 0.1 as suggested by the CDP model [3].

Finally, $\sigma_{t0}$ is the tensile cracking strength under uniaxial tensile loading which is taken equal to $f_{ct}^{cr}$.
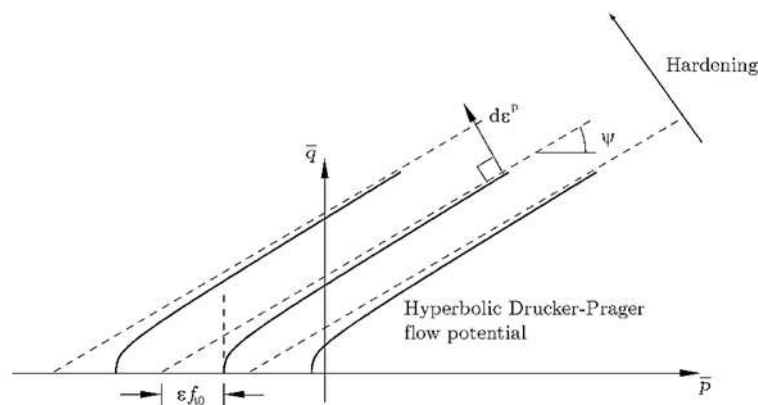


Figure 7.25: Drucker-Prager hyperbolic flow potential function in meridional plane [3]

CDP model employs the yield function developed by Lubliner et. el. (1998) and includes modifications proposed by Lee and Fenves (1998). Two hardening variables control the evolution of the failure surface. These hardening variables known as the equivalent plastic strain in tension $\left(\tilde{\varepsilon}_{ct}^{pl}\right)$ and the equivalent plastic strain in compression $\left(\tilde{\varepsilon}_{cc}^{pl}\right)$ are related to the failure mechanisms under tension and compression loading states, respectively. Figures 7.26 and 7.27 illustrate typical yield surfaces in the deviatoric plane and in the plane stress conditions, respectively.

Abaqus receives two essential parameters for the definition of yield function: $K_c$ and $\sigma_{b0}/\sigma_{c0}$. The first parameter, $K_c$, with its default value $K_c = 2/3$, is the ratio of the

second stress invariant on the tensile meridian to the second stress invariant on the compressive meridian at the first yield surface (Figure 7.26). This parameter varies in the range of $0.5 < K_c \leq 1.0$.

$\sigma_{b0}/\sigma_{c0}$ is the ratio of initial equibiaxial compressive yield stress (see $\sigma_{b0}$ in Figure 7.27) to initial uniaxial compressive yield stress (see Figure 7.23b where $\sigma_{c0} = 0.4 f_{cc}^m$). The default value for this ratio is 1.16.

Following the above-mentioned descriptions, it can be concluded that in CDP four plasticity parameters needs to defined: $\psi$, $\epsilon$, $K_c$ and $\sigma_{b0}/\sigma_{c0}$. Values adopted for these parameters are reported in Table 7.5.
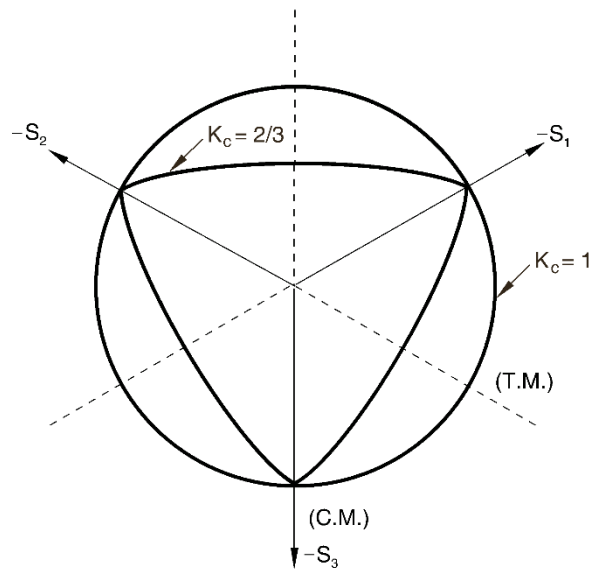


Figure 7.26: Illustration of yield surface in deviatoric plane for $K_c = 2/3$ and $K_c = 1$. In this Figure S1, S2 and S3 are the first, second and third stress invariants, respectively. T.M. and C.M. indicate the tensile meridian and compressive meridian, respectively [3].
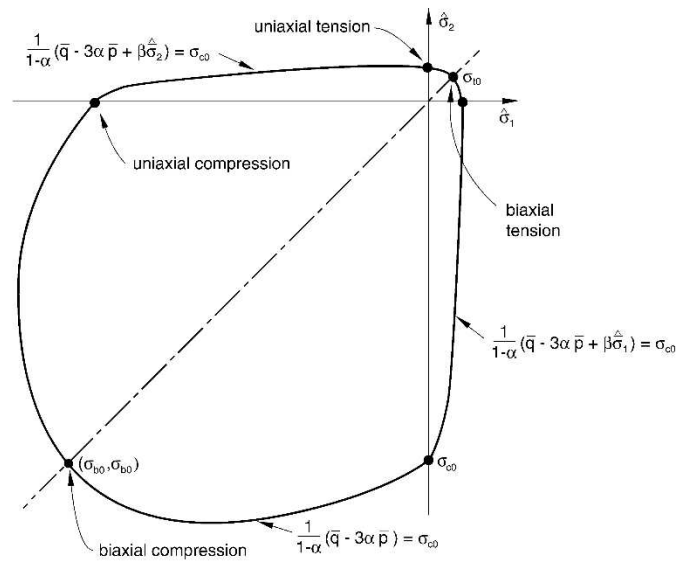
Figure 7.27: Yield surface under biaxial stress condition in effective stress plane [3]

Table 7.5: Adopted values for the plasticity parameters of concrete model

| $\psi$ | $\epsilon$ | $K_c$ | $f_{b0}/f_{c0}$ |
|---|---|---|---|
| 35° | 0.1 | 0.667 | 1.16 |

### 7.3.3.4 Steel Rods

Steel bars were simulated in both tension and compression with identical behavior using an isotropic linear elastic-perfectly plastic response as showed in Figure 6.11. In compliance with the ASTM steel grad 8.8, values of 200 GPa and 640 MPa were adopted as the material elasticity modulus and the yield strength, respectively. The steel bars were meshed using 8-node solid elements. A perfect bond between the exterior surface of the three dimensional steel bars and the surrounding concrete elements was introduced using tie constraints.

### 7.3.3.5 CFRP Laminates

4-node shell elements were used to model the CFRP laminate. A linear-elastic isotropic constitutive law up to meeting a stress based failure criterion was adopted to simulate behavior of the CFRP laminates. Although unidirectional CFRP composites are essentially

an orthotropic material, when the principal stress is oriented to the fibers direction, as is the case of the pull tests, employing an isotropic model has enough accuracy [10]. All the stress is released as soon as any material point reaches average tensile stress corresponding to the CFRP rupture characterized from direct tensile tests.

### 7.3.3.6 Modelling the Interaction between the Individual Parts

The anchor rod, the bolt and the washer were modelled as a unique piece. These part instances were meshed using 8-node three-dimensional solid elements. A perfect bond between the elements of the anchor rod and the surrounding concrete, using embedded element option, was introduced. Employing a perfect bond relied on the assumption that practically a sufficient bond length between the anchor rod and the concrete is provided. Thus, it is reasonable to expect that the possible failure mode at this region is dominated either by the fracture of a wedge of the concrete or by the plastic failure of the anchor rod, instead of debonding.

The interaction between the anchor rods and the bearing surfaces of the holes of the SHCC, between the washers and the SHCC and also between the RC block and the analytically rigid surface (the supporting plate) was simulated using a contact model. A "hard" contact "frictionless" constitutive low assigned to the contact regions.

A "hard" contact defines the interactions along the normal direction of the surfaces. It assumes that any pressure can be transmitted between the contacted surfaces while at their separation the contact pressure turns to zero. The "frictionless" behavior means that the contacted surfaces can freely slide over each other along the tangential directions without transmitting any shear stress.

### 7.3.4 Comparison of the Results of FE Modelling and Experimental Tests

Values of the parameters defining the local bond stress-slip law at the interface of the CFRP-SHCC and also interface of HCP(L)-Concrete, obtained from inverse analysis, are presented in Table 7.6. Values obtained for the parameters defining shear retention model are indicated in Table 7.7.

Table 7.6: Parameters obtained for the local bond stress-slip laws as graphically presented in Figure 7.21 and Figure 7.22.

| Interface law | $\tau^p$ (MPa) | $K$ (N/mm) | $\zeta_1$ | $\lambda_1$ | $\zeta_2$ | $\lambda_2$ | $G_c$ (N/mm) | $u^u$ (mm) |
|---|---|---|---|---|---|---|---|---|
| CFRP-SHCC | 24.50 | 6100 | 0.40 | 0.175 | - | - | 10.68 | 2.0 |
| HCP[(L)]-Concrete | 2.75 | 1650 | 0.70 | 0.054 | 0.15 | 0.54 | 1.96 | 2.5 |

Table 7.7: Parameters of the shear retention model, graphically presented in Figure 7.18.

| $\rho_1$ | $\rho_2$ | $\varphi_1$ | $\varphi_2$ |
|---|---|---|---|
| 0.82 | 0.21 | 1.22 | 4.8 |

The degradation of the interface elements and the evolution of the maximum principal tensile strain in the SHCC at the loading stages corresponding to the 80%, 90% and 100% of pull force capacity of specimens A_W75 and B_Lb60, among others, are selected and presented in Figures 7.28 and 7.29, respectively. Concept of maximum principal strain used as an indicator to represent propagation of the tensile damages in the SHCC.

As it was expected, and in compliance with the experimental observations, at the peak load of the specimens in group "A", the degradation of the interface elements of HCP[(L)]-Concrete was the governing failure mode, while, for group "B" specimens the degradation of the CFRP-SHCC interface elements was the prevailing failure.

80% $F_p^{FEM}$    90% $F_p^{FEM}$    100% $F_p^{FEM}$

SHCC plate

HCP$^{(L)}$-Concrete interface    CFRP-SHCC interface

(a)

80% $F_p^{FEM}$    90% $F_p^{FEM}$    100% $F_p^{FEM}$

SHCC plate
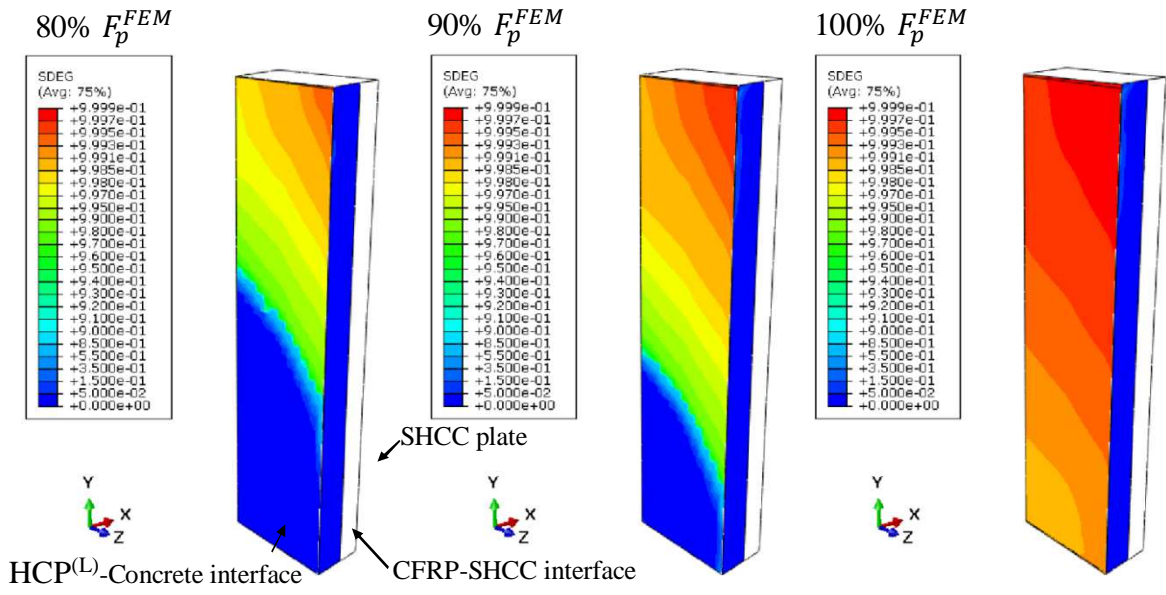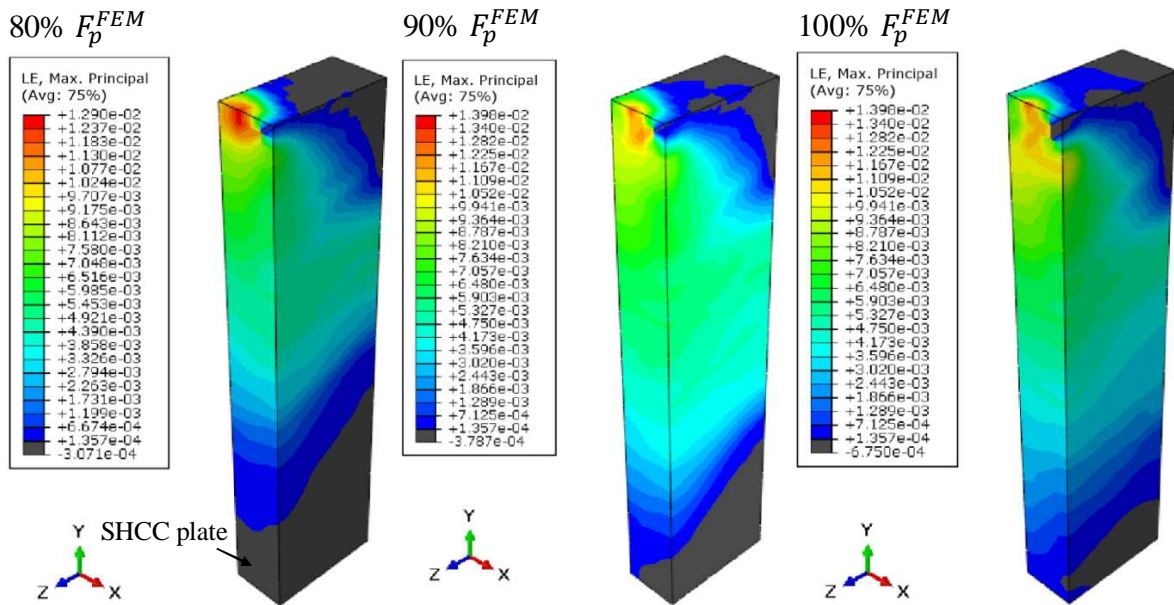
(b)

Figure 7.28: FE results of specimen A_W75, (a) degradation at interface elements (SDEG), and (b) evolution of the maximum principal tensile strains in SHCC (LE).

80% $F_p^{FEM}$       90% $F_p^{FEM}$       100% $F_p^{FEM}$

(a)

80% $F_p^{FEM}$       90% $F_p^{FEM}$       100% $F_p^{FEM}$

(b)
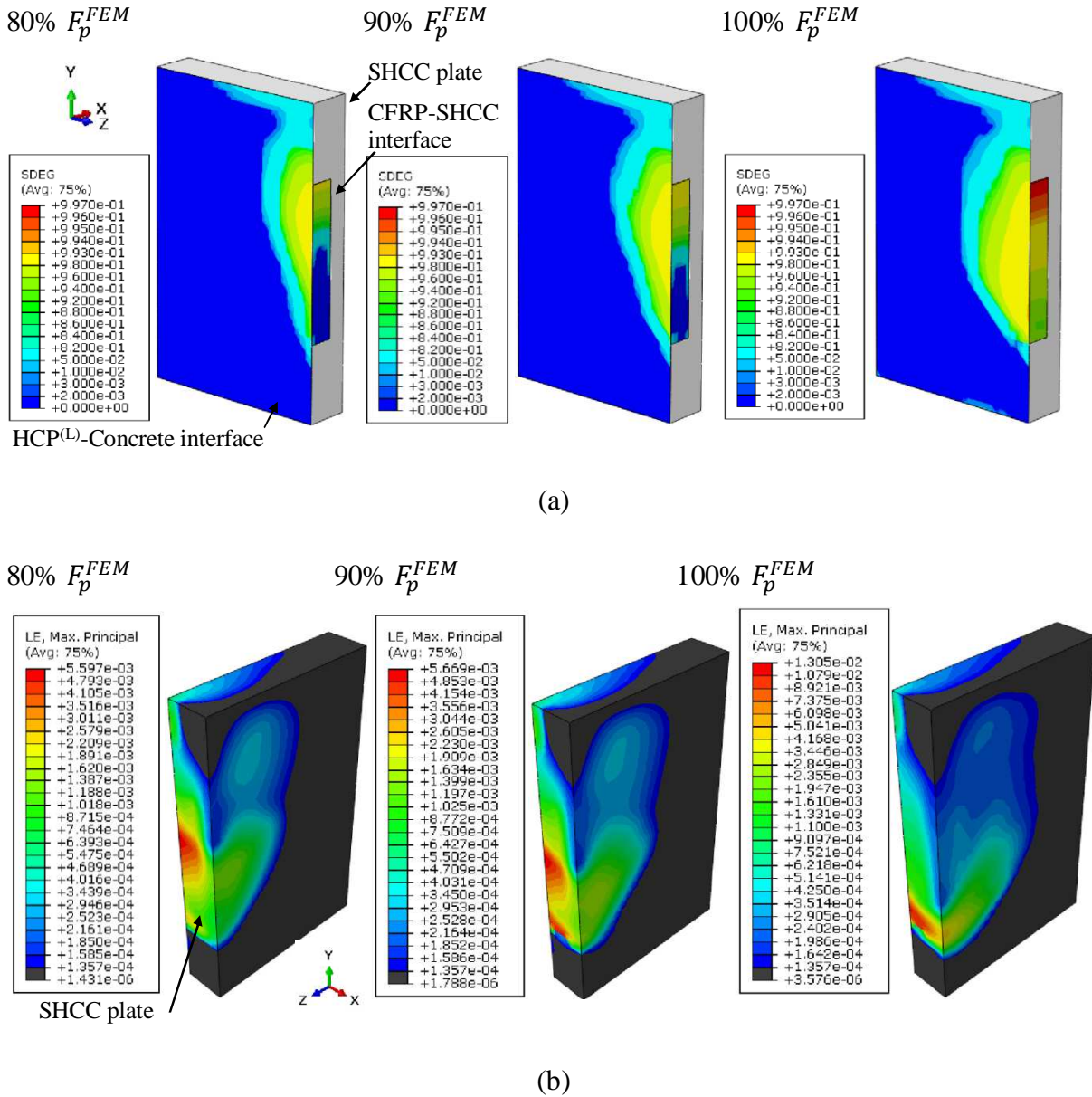
Figure 7.29: FE results of specimen B_Lb60, (a) degradation at interface elements (SDEG), and (b) evolution of the maximum principal tensile strains in SHCC (LE).

Experimental and FE curves representing the pull force *versus* relative sliding at the top (HT) and at the mid-height (HM) of the HCP(L) in group "A" specimens are depicted in Figure 7.30 and their corresponding pull force capacities are presented and compared in Table 7.8.

Considering these results, it can be concluded that despite the complex stress fields and the simplified assumptions in the FE modelling, a satisfactory predictive performance is achieved when the results of the FE simulations are compared to those obtained from experimental tests. This confirms enough accuracy of the constitutive law calibrated for the interface of HCP[(L)]-Concrete.
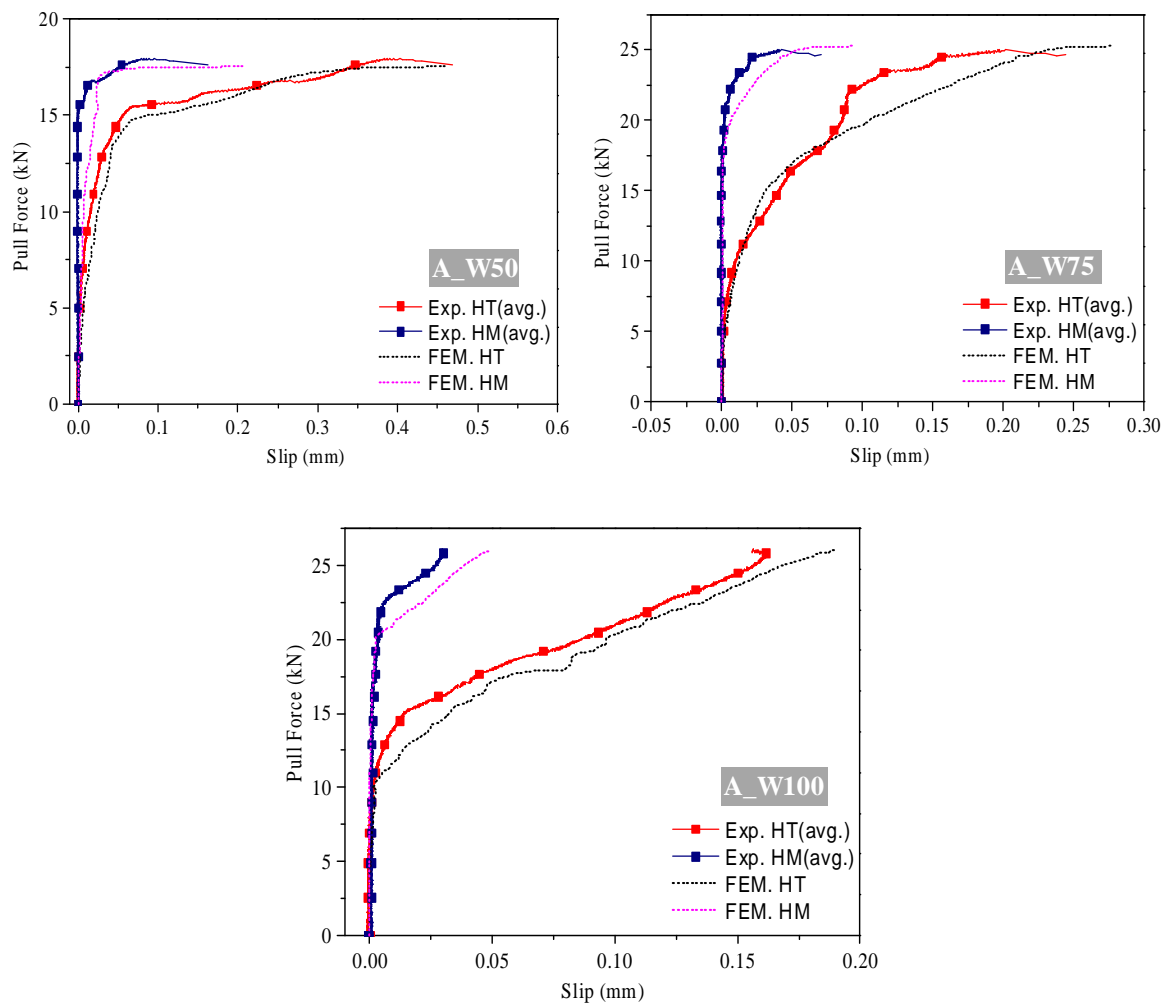


Figure 7.30: Comparison of the experimental and FE curves obtained for the evolution of the pull force *versus* relative sliding at the top (HT) and at the mid-height (HM) of the HCP[(L)] of the specimens in group "A"

Table 7.8: Comparison of the results of experimental tests and FE simulations for the specimens in group "A" in terms of pull force capacity.

| Category | Labels | $F_p^{exp}$ (kN) | $F_{p.avg}^{exp}$ (kN) | $F_p^{FEM}$ (kN) | $\Delta_F/F_{p.avg}^{exp}$ (%) |
|---|---|---|---|---|---|
| A | A_W50(1) | 17.95 | 17.92 | 17.54 | -2.1 |
| | A_W50(2) | 17.89 | | | |
| | A_W75(1) | 25.01 | 24.00 | 25.26 | 5.3 |
| | A_W75(2) | 22.98 | | | |
| | A_W100(1) | 24.26 | 25.18 | 26.12 | 3.7 |
| | A_W100(2) | 26.09 | | | |

$\Delta_F = F_{p.avg}^{exp} - F_p^{FEM}$

The pull force *versus* relative sliding at the loaded-end and also at the free-end of CFRP laminate obtained from both experimental tests and FE simulations of the specimens in group "B" are graphically compared in Figure 7.31. Note that in these figures the loaded-end measurements also include the deformation of CFRP at between the loaded-end of CFRP-SHCC bond and the region where LVDT is secured to CFRP The obtained peak pull force capacities are presented and compared in Table 7.9. A good agreement between the results of the FE models and the experimental tests confirms the accuracy of the local bond stress-slip law obtained by the inverse analysis technique.

Table 7.9: Comparison of the results of the experimental tests and the FE models of the specimens in group "B" in terms of peak pull force.

| Category | Labels | $F_p^{exp}$ (kN) | $F_{p.avg}^{exp}$ (kN) | $F_p^{FEM}$ (kN) | $\Delta_F/F_{p.avg}^{exp}$ (%) |
|---|---|---|---|---|---|
| B | B_Lb45(1) | 20.83 | 21.45 | 20.95 | -2.3 |
| | B_Lb45(2) | 22.07 | | | |
| | B_Lb60(1) | 24.42 | 25.35 | 24.07 | -5.1 |
| | B_Lb60(2) | 26.28 | | | |
| | B_Lb90(1)[a] | 30.57 | 31.29 | 31.62 | 1.1 |
| | B_Lb90(2)[a] | 32.00 | | | |

[a] CFRP rupture was the observed failure mode in the experimental specimens while the predicted failure mode of the FEM was CFRP-SHCC interface failure

$\Delta_F = F_{p.avg}^{exp} - F_p^{FEM}$
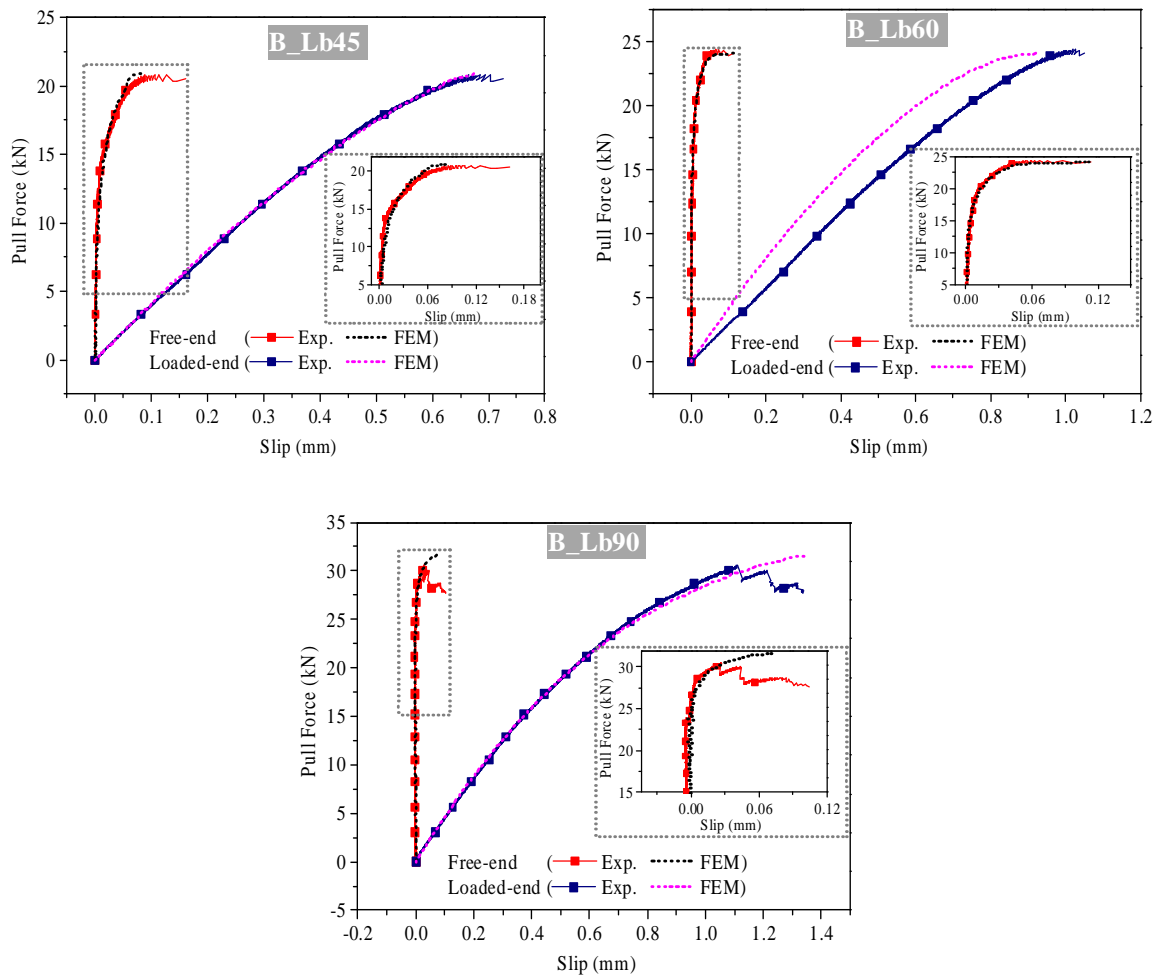
Figure 7.31: Pull force *versus* relative sliding at the loaded-end and at the free-end of CFRP laminate obtained in the experimental tests and FE simulations of the specimens in group "B" (note that the loaded-end measurements also include the deformation of CFRP at between the loaded end of CFRP and the region where LVDT was secured to CFRP).

Figure 7.32 compares the pull force *versus* CFRP gripped-end displacement obtained from the experimental tests and the FE models of the specimens in group "C". The peak pull force obtained from these studies are indicated and compared in Table 7.10. The state of the damages, at the peak load, obtained from both the experimental tests and the FE models are presented and compared in Figure 7.33. Again, the concept of maximum principal strain was used to indirectly represent damage propagation in FE model. According to these results,

both the pull force-displacement responses and the progressed damages confirm the adequacy of the simulation techniques. Hence, the obtained shear retention law for SHCC by an inverse analysis approach can be used with enough accuracy to perform a comprehensive parametric study which is discussed in the next section.
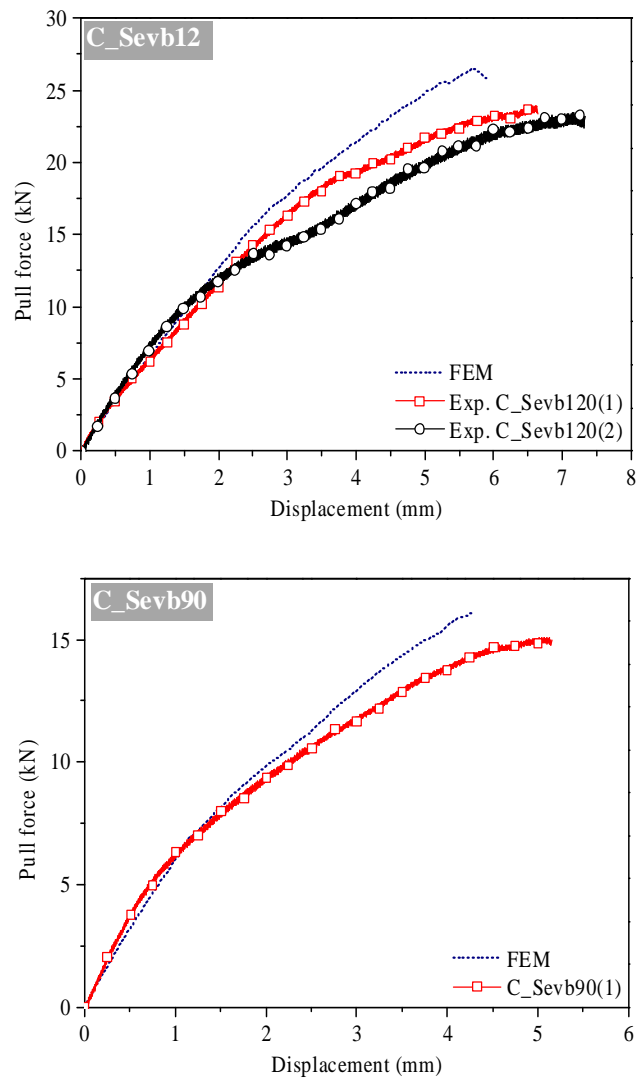


Figure 7.32: Pull force *versus* displacement at CFRP gripped-end obtained from the experimental tests and the FE models of group "C" specimens
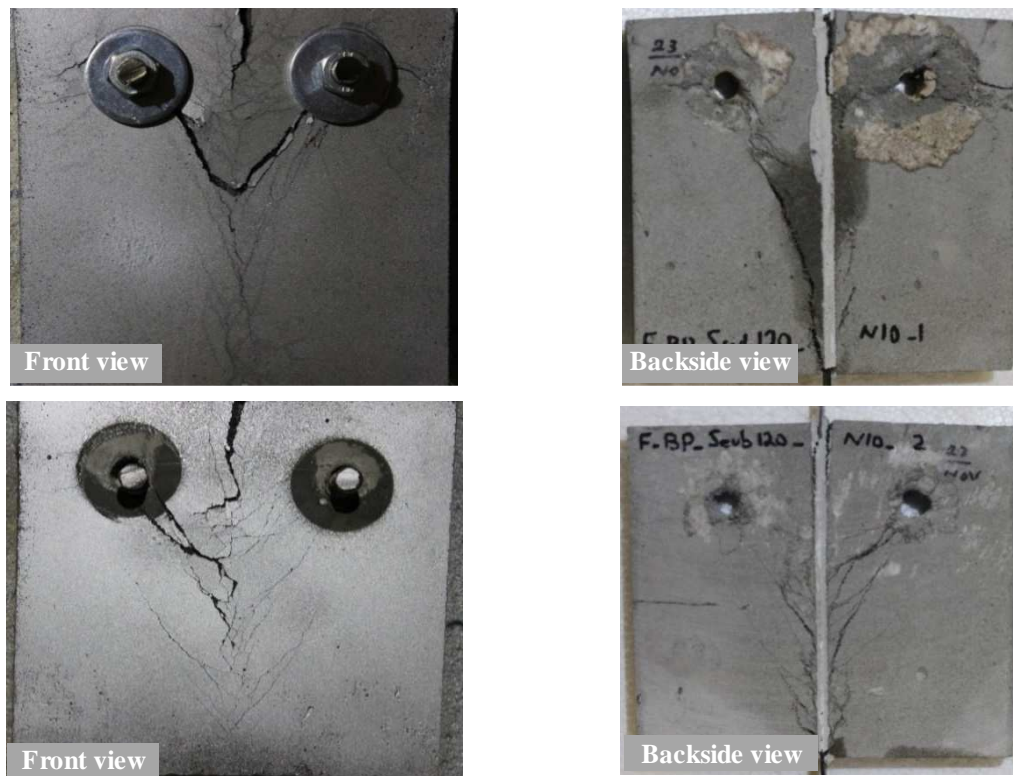
(a)
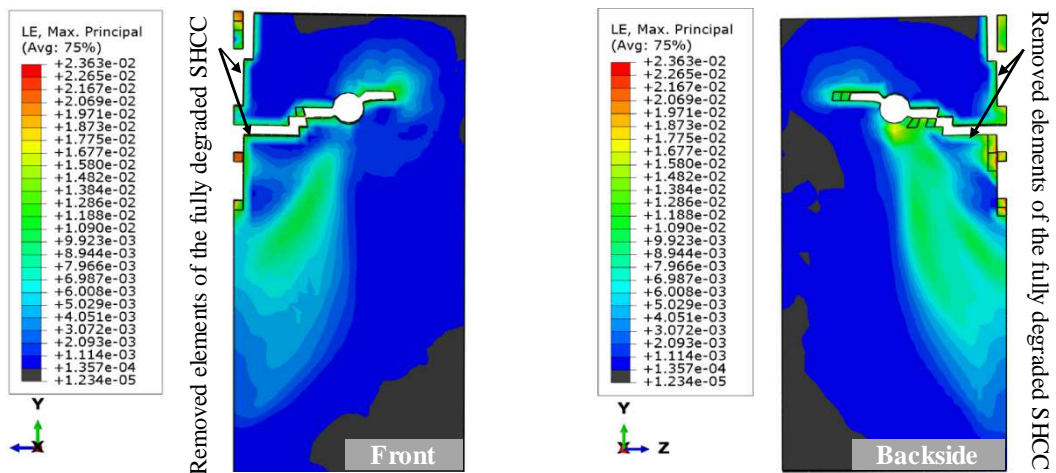


(b)

Figure 7.33: Comparison of the state of damages at the peak load of the specimen C_Sevb120 obtained from the (a) experimental tests for two repeated specimens, and (b) FE simulation (note that the maximum principal strain is presented as an indirect damage indicator in FE).

Table 7.10: Comparison of the results of the experimental tests and FE models of the specimens in group "C" in terms of peak pull force.

| Labels | $F_p^{exp}$ (kN) | $F_{p.avg}^{exp}$ (kN) | $F_p^{FEM}$ (kN) | $\Delta_F/F_{p.avg}^{exp}$ (%) |
|---|---|---|---|---|
| C_Sevb90(1) | 15.09 | 15.09 | 16.11 | 6.8 |
| C_Sevb120(1) | 23.92 | 23.67 | 26.15 | 10.5 |
| C_Sevb120(2) | 23.41 | | | |

$\Delta_F = F_{p.avg}^{exp} - F_p^{FEM}$

## 7.4 Phase II: Parametric Study

In this phase, a comprehensive parametric FE study was developed based on the parameters and the models calibrated in phase I. In this second phase of study initially the relationships between the load carrying capacity and the bond length of the CFRP-SHCC was obtained. Following this outcome the effective CFRP-SHCC bond length $\left(L_b^{ef}\right)$ was estimated.

Further, taking into account this $L_b^{ef}$, FE models were prepared and analysed aiming at optimizing the width of HCP(L) and the HCP(L)-Concrete connection system composed of both chemical anchors and adhesive. HCP(L) of these latter models were composed of two rows of CFRP laminates each bonded to a groove on SHCC plate.

These series of the analyses were limited to the specific type of CFRP laminate, concrete and SHCC used in the experimental study of current chapter. However, CFRP laminates were simulated using isotropic linear-elastic behavior without introducing any failure criterion.

This approach prevents CFRP rupture, hence the effective bond length $\left(L_b^{ef}\right)$ can be estimated, and parameters influencing the behavior of HCP(L) and its connection to the RC elements can be evaluated. $L_b^{ef}$ is defined as the CFRP-SHCC bond length beyond which only a marginal increase in pull force capacity is expected.

### 7.4.1 CFRP-SHCC Bond Length

The dependency of the pull force capacity of HCP$^{(L)}$ to the bond length of CFRP-SHCC $(L_b)$ was studied using FE modelling of specimens demonstrated in Figure 7.34a. Therefore, in these series of FE models $L_b$ was the only parameter of the study. As depicted in this figure, the un-bonded lengths $(L_u)$ of CFRP at the top and the bottom parts of the HCP$^{(L)}$ were kept constant, equal to 30 mm. The HCP$^{(L)}$ had dimension of $W_p$ and $t_p$ equal to 150 mm and 18 mm, respectively, and $H_p$ of $(L_b+60)$ mm.
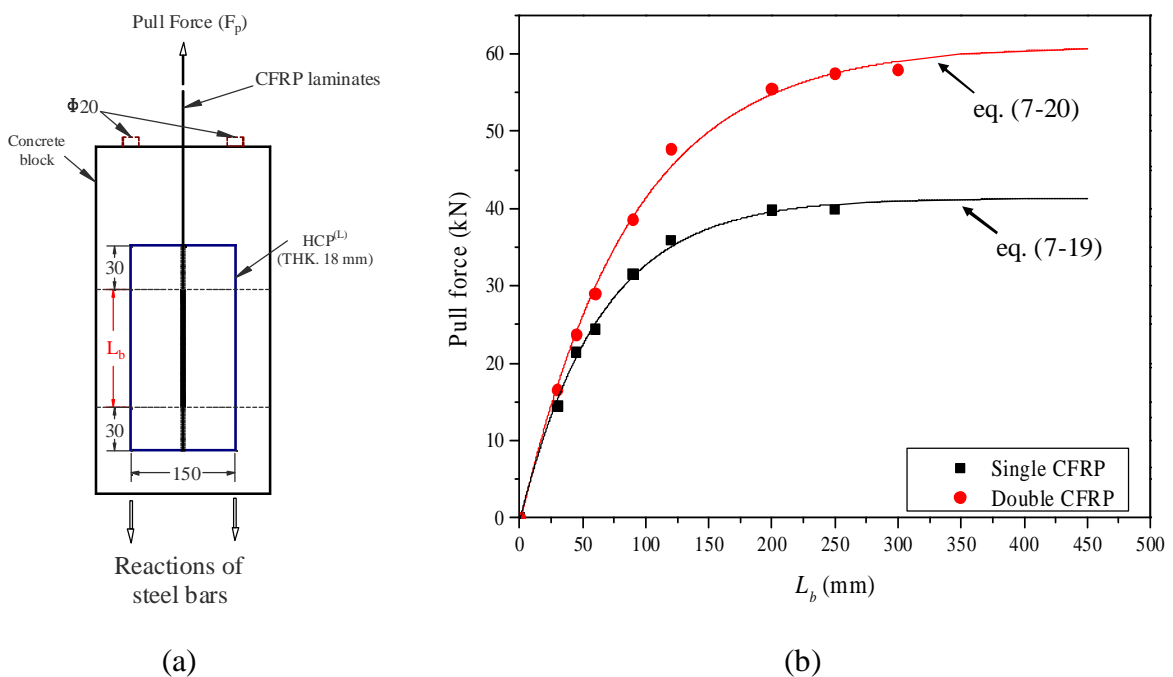


Figure 7.34: Dependency of pull force capacity $(F_p)$ to the bond length of CFRP-SHCC $(L_b)$, (a) Configurations of FE models, and (b) FE results in terms of $F_p$ *vs.* $L_b$ (dimensions are in mm)

In order to study the influence of CFRP axial stiffness, the FE models were simulating HCP$^{(L)}$s with either a single- or double-CFRP laminate configuration (see Figure 6.5). Double-CFRP laminate is introduced in FE models through assigning a cross-sectional area of 28 mm$^2$ (the sum of the cross-section area of two CFRP laminates) to the FRP corresponding shell elements. Hence, this simplification assumes a perfect bond between

two CFRP laminates. The results of this study in terms of pull force capacity *versus* bond length ($F_p - L_b$) are represented in Figure 7.34b and Table 7.11.

Table 7.11: Results of FE simulations on dependency of the pull force capacity of HCP[(L)] to the bond length of the CFRP-SHCC (see Figure 7.34)

| FE models | CFRP-SHCC bond length ($L_b$) (mm) | Pull force capacity ($F_p$) (kN) | |
|---|---|---|---|
| | | Single-CFRP | Double-CFRP |
| B_Lb30F | 30 | 14.5 | 16.5 |
| B_Lb45F | 45 | 21.5 | 23.7 |
| B_Lb60F | 60 | 24.4 | 29.0 |
| B_Lb90F | 90 | 31.5 | 38.5 |
| B_Lb120F | 120 | 35.9 | 47.7 |
| B_Lb200F | 200 | 39.8 | 55.5 |
| B_Lb250F | 250 | 39.9 | 57.5 |
| B_Lb300F | 300 | - | 57.9 |

Adopting a curve fitting approach, an exponential function defining the mathematical relationship between $F_p$ and $L_b$ for each series of the models (single- or double-CFRP laminate) was estimated. These relations for single- and double-CFRP configurations are presented in equations (7-19) and (7-20), respectively.

Effective bond length $\left(L_b^{ef}\right)$ of 200 and 250 mm with corresponding $F_p$ of 39.5 kN and 57.5 kN were determined for the HCP[(L)]s with single- and double-CFRP configurations, respectively. It should be noted that the obtained $L_b^{ef}$ for the specimens with a single CFRP laminate is not practically achievable, since CFRP laminate used in this project reaches its rupture capacity at a bond length of 90 mm (see section 7.2.5.2).

Single-CFRP laminate bonded to each groove:
$$F_p = 41.70(1 - e^{-0.0157L_b}) \quad (R^2 = 0.997)$$
(7-19)

Double-CFRP laminate bonded to each groove:
$$F_p = 61.05(1 - e^{-0.0115L_b}) \quad (R^2 = 0.996)$$
(7-20)

### *7.4.2 Position of Chemical Anchors*

FE models were prepared to study the possible enhancement could obtain in the pull load carrying capacity in consequence of adding anchors in connection of an adhesively bonded HCP$^{(L)}$ to an RC block. Moreover, these models were used to predict the most effective positions of anchors.

The first series of simulations was composed of one model without any anchor and other models containing an anchor of 10 mm in diameter. This anchor was located on the vertical axis of symmetry of the HCP$^{(L)}$ and its distance from the bottom edge of the plate $(E_b)$ was assumed as the parameter of the study, see Figure 7.35a.

The effect of adding a second anchor was studied through analyzing the second series of models with the configuration represented in Figure 7.36a. In this series of the models, the parameter of the study was the distance between the two anchors ($V_b$).



(a)                                        (b)
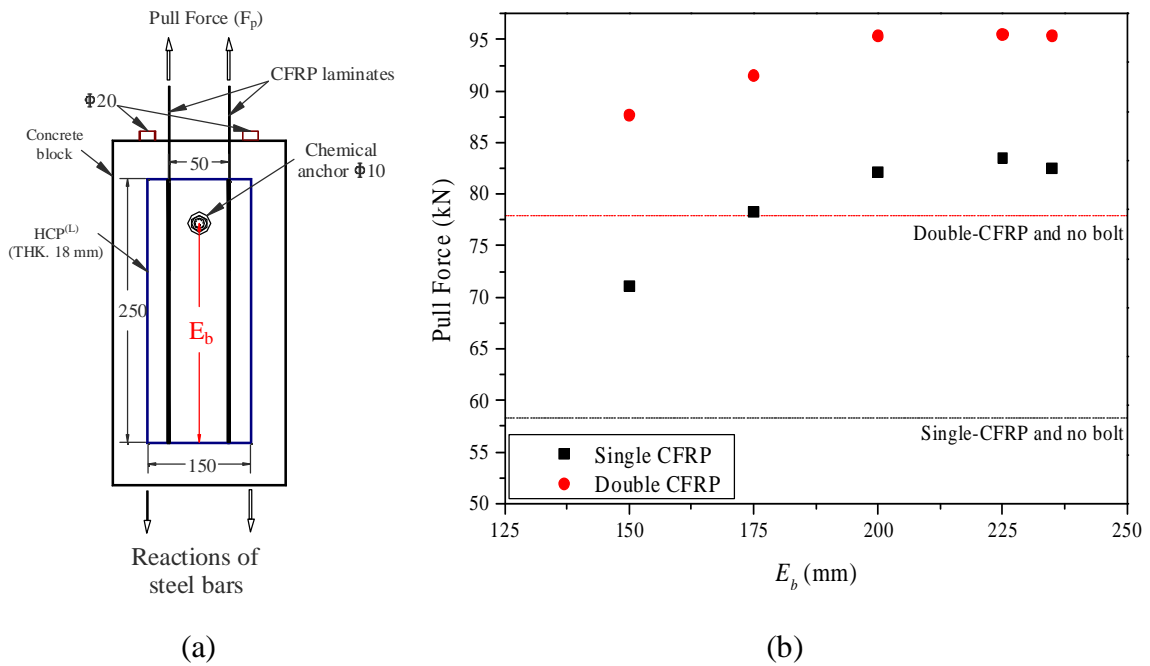
Figure 7.35: Effect of the position of a single anchor $(E_b)$ on pull force capacity of an adhesively bonded connection of HCP$^{(L)}$-Concrete, (a) configuration of FE models, and (b) FE results in terms of $F_p$ *vs.* $E_b$.

(a)                                             (b)
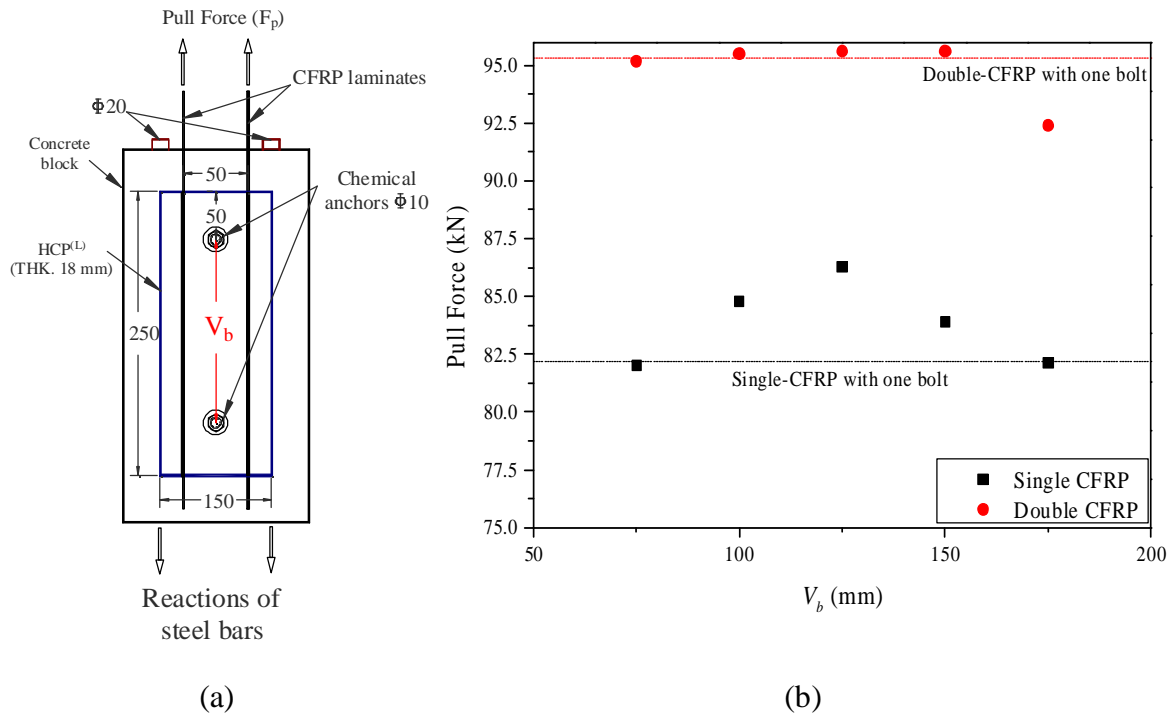
Figure 7.36: Effect of the position of second anchor ($V_b$) on pull force capacity of an adhesively bonded connection of HCP$^{(L)}$-Concrete, (a) configuration of FE models, and (b) FE results in terms of $F_p$ *vs.* $V_b$.

As depicted in Figures 7.35a and 7.36a, it was assumed that the HCP$^{(L)}$ in both series of models have two grooves, each of them located 25 mm away from the vertical axis of symmetry of the HCP$^{(L)}$, which also coincides with the vertical axis of symmetry of the anchor/anchors. In order to also take into account the influence of FRP's axial stiffness, in each series, models with HCP$^{(L)}$ composed of either single- or double-CFRP laminate, bonded into their grooves, were simulated.

HCP$^{(L)}$ in all of the models had dimensions of 150 mm, 250 mm and 18 mm for $W_p$, $H_p$ and $t_p$, respectively (the height of the HCP$^{(L)}$ was taken equal to $L_b^{ef}$ of a double-CFRP laminate configuration obtained in section 7.4.1).

Results of the analyses of the first series of the specimens, for both single- and double-CFRP configurations, are reported in Table 7.12 and represented in Figure 7.35b. According to these results, the most effective position of a single anchor ($E_b$) is between 200 mm and 235 mm.

Taking into account practical considerations for the plate edge distance, e.g. safe perforation process, $E_b$ is suggested as 200 mm, which corresponds to pull force capacities of 82 kN and 95 kN for connections composed of HCP[L] with single- and double-CFRP configurations, respectively (note that CFRP failure criterion was not introduced into the simulations)

For an HCP[L] only adhesively bonded to the RC block (model M_Ref in Table 7.12), and contains single- or double- CFRP configurations, the peak pull force is 58 kN and 78 kN, respectively. Therefore, in consequence of adding a single anchor at $E_b$= 200 mm of an adhesively bonded HCP[L] with a single-CFRP configuration, an increase of 41% in peak pull force capacity is attainable. The corresponding increase in the case of HCP[L] with double-CFRP configuration is 22%, meaning that doubling of the stiffness of CFRP laminates reduces up to 50% the efficiency obtained in consequence of adding an anchor to the connection system of HCP[L]-RC.

Table 7.12: Influence of anchor's distance from the bottom edge of the HCP[L] (see Figure 7.36)

| Label | $E_b$ (mm) | HCP[L] with single CFRP | | HCP[L] with double CFRP | |
|---|---|---|---|---|---|
| | | $F_p$ (kN) | Increase in $F_p$** (%) | $F_p$ (kN) | Increase in $F_p$** (%) |
| M_Ref * | N.A. | 58.3 | N.A. | 77.9 | N.A. |
| M_Eb235 | 235 | 82.5 | +41.5 | 95.4 | +22.5 |
| M_Eb225 | 225 | 83.5 | +43.1 | 95.5 | +22.6 |
| M_Eb200 | 200 | 82.2 | +40.9 | 95.3 | +22.4 |
| M_Eb175 | 175 | 78.3 | +34.2 | 91.5 | +17.5 |
| M_Eb150 | 150 | 71.1 | +22.0 | 87.7 | +12.6 |

\* Reference model: Connection composed of HCP[L] adhesively bonded to RC block without any anchor
\*\* Percentage increase in pull force capacity $(F_p)$ of a connection model after adding an anchor at position $E_b$, when the $F_p$ of model M_Ref is the reference value.

Results of the analyses of the second series of the models, depicted in Figure 7.36b and indicated in Table 7.13, revealed that adding a second anchor has only a marginal effect in the pull force capacity. According to the results of these analyses, the most effective position

of this anchor is at a distance of 125 mm far from the top anchor $(V_b = 125\ mm)$. However, adding this anchor is recommended specially in the case of increased risk of plate-end peeling; e.g. simply supported beams flexurally strengthened with an HCP[(L)] terminated far from the supports.

Table 7.13: Obtained results from analyses of the models with $V_b$ being the parameter of the study (see Figure 7.36)

| Label | $V_b$ (mm) | HCP[(L)] with single CFRP | | HCP[(L)] with double CFRP | |
|---|---|---|---|---|---|
| | | $F_p$ (kN) | Increase in $F_p$** (%) | $F_p$ (kN) | Increase in $F_p$** (%) |
| M_Eb200* | NA | 82.2 | | 95.3 | |
| M_Vb75 | 75 | 82.0 | -0.2 | 95.2 | -0.1 |
| M_Vb100 | 100 | 84.8 | +3.2 | 95.5 | +0.2 |
| M_Vb125 | 125 | 86.3 | +5.0 | 95.6 | +0.3 |
| M_Vb150 | 150 | 83.9 | +2.1 | 95.6 | +0.3 |
| M_Vb175 | 175 | 82.1 | -0.1 | 92.4 | -3.0 |

\* Reference model: see Figure 7.36a and Table 7.12 for details of this model.
\*\* Percentage increase in pull force capacity $(F_p)$ of a connection model after adding the second anchor at position $V_b$, when $F_p$ of the model M_Eb200 with only one anchor is the reference value.

### 7.4.3 Distance between Anchors and Grooves

The analysis of this series of the FE models aimed at characterizing the influence of the distance of grooves from the anchors $(S_g)$ on pull load capacity of the HCP[(L)]-Concrete connection. Geometrical details of these models are represented in Figure 7.37a. The HCP[(L)] had the same dimensions adopted for the models in previous section (250 mm ×150 mm ×18 mm). As it was proposed following the results of previous section, positions of the anchors in terms of $E_b$ and $V_b$ were taken 200 and 125 mm, respectively. Similar to previous FE modelling studies, two series of the connections were simulated; one with HCP[(L)]s containing single-CFRP laminate and the other one with double-CFRP laminate configuration. Results of the FE analysis in terms of pull force *vs.* grooves distance $(F_p - S_g)$ are reported in Table 7.14 and also graphically presented in Figure 7.37b. According to these results, by increasing in $S_g$, a decreasing trend in pull force capacity of the HCP[(L)] is observed. This outcome is explained by the load transfer mechanism of the

anchored HCP[(L)] to the RC blocks, discussed in section 7.2.5.3. Following this discussion, inclined SHCC compressive struts were identified as the main force transfer mechanism between CFRP laminate and the anchors. Reduction in the pull force capacity in consequence of larger values of $S_g$ is associated with the increased inclination of longitudinal axis of the compressive struts from the longitudinal axis of the CFRP laminate, which lowers the expected efficiency from contributions of these struts in shear transfer mechanism.



(a)                                                                 (b)
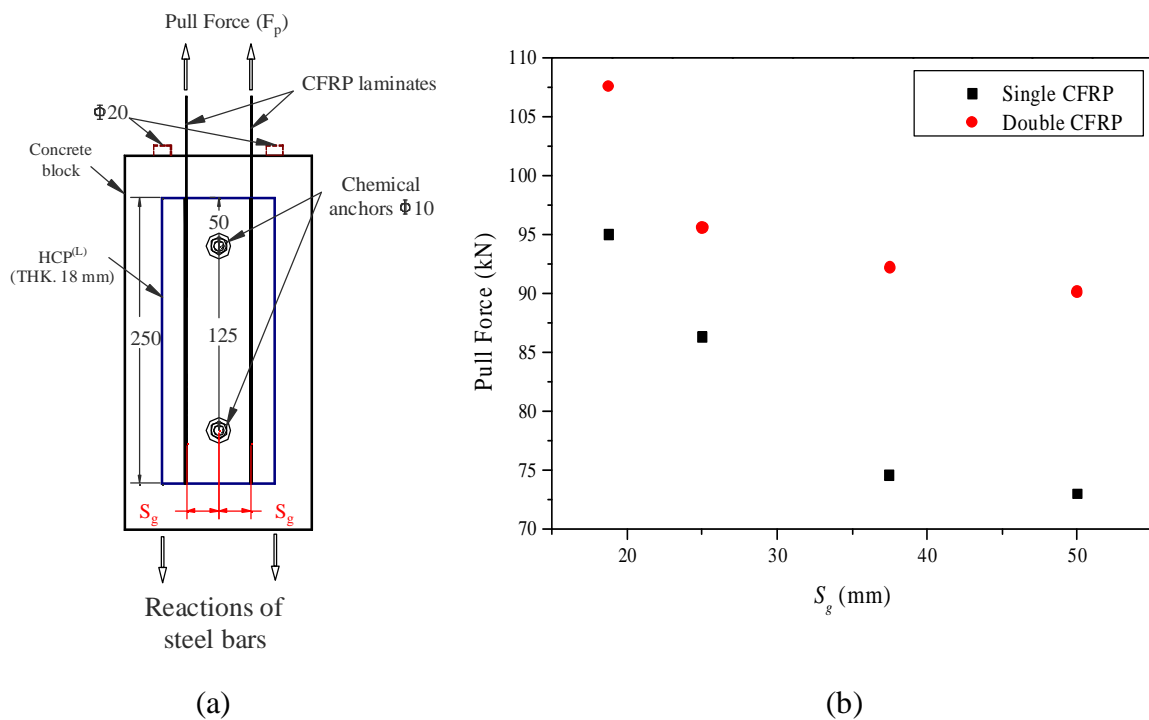
Figure 7.37: Effect of distance of the grooves from the anchors $\left(S_g\right)$ on pull force capacity of HCP[(L)]-Concrete connection, (a) configuration of FE models, and (b) FE results in terms of $F_p$ *vs.* $S_g$.

Taking into account the results presented in Figure 7.37b along with the practical considerations, an optimized $S_g$ is recommended to be taken 25 mm. HCP[(L)]'s with this groove spacing is expected to attain pull force capacities of 86 kN and 96 kN for single- and double-CFRP configurations, respectively.

Table 7.14: Obtained results from analyses of the models with $S_g$ being the parameter of the study (see Figure 7.37a)

| Label | $S_g$ (mm) | HCP$^{(L)}$ with single CFRP | | HCP$^{(L)}$ with double CFRP | |
|---|---|---|---|---|---|
| | | $F_p$ (kN) | Increase in $F_p$** (%) | $F_p$ (kN) | Increase in $F_p$** (%) |
| M_Sg18.75 | 18.75 | 95.0 | +10.1 | 107.6 | +12.6 |
| M_Vb125 * | 25.00 | 86.3 | N.A. | 95.6 | N.A. |
| M_Sg37.5 | 37.50 | 74.6 | -13.6 | 92.2 | -3.6 |
| M_Sg50 | 50.00 | 74.9 | -13.2 | 90.2 | -5.6 |

\* Reference model (see Figure 7.36a and Table 7.14 for details of this model).

\*\* Percentage increase in pull force capacity $(F_p)$ in consequence of changing $S_g$, when $F_p$ of model M_Vb125 with $S_g$ = 25 mm is the reference value)

### 7.4.4 Width of the HCP$^{(L)}$

In this series of models, the width of the HCP$^{(L)}$ $(W_p)$ was taken as the parameter of the study, which varies in the range of 100 mm and 200 mm. The other parameter of these models was the same as the FE models in section 7.4.3, but with $S_g$ = 25 mm. (see Figure 7.38a).

According to the results obtained from the FE analyses and a curve fitting approach, illustrated in Figure 7.38b and reported in Table 7.15, the rate of the increase in the peak pull force capacity in consequence of increasing $W_p$, diminishes at a plate width of 150 mm and 250 mm for HCP$^{(L)}$s composed of single- and double-CFRP laminate, respectively. These effective widths were corresponding to the mobilizing peak pull forces of 87 kN and 108 kN, to the RC block, respectively.

Following the curve fitting approach, an exponential function defining the mathematical relationship between $F_p$ and $W_p$ for each series of models was obtained. These relationships for single- and double-CFRP configurations are presented in equations (7-21) and (7-22), respectively.

Single-CFRP laminate bonded to each groove: (7-21)

$$F_p = 88.21 - 1439.88e^{-0.0412W_p} \quad (R^2 = 0.982)$$

Double-CFRP laminate bonded to each groove:

$$F_p = 109.51 - 260.92e^{-0.0194W_p} \quad (R^2 = 0.999) \tag{7-22}$$
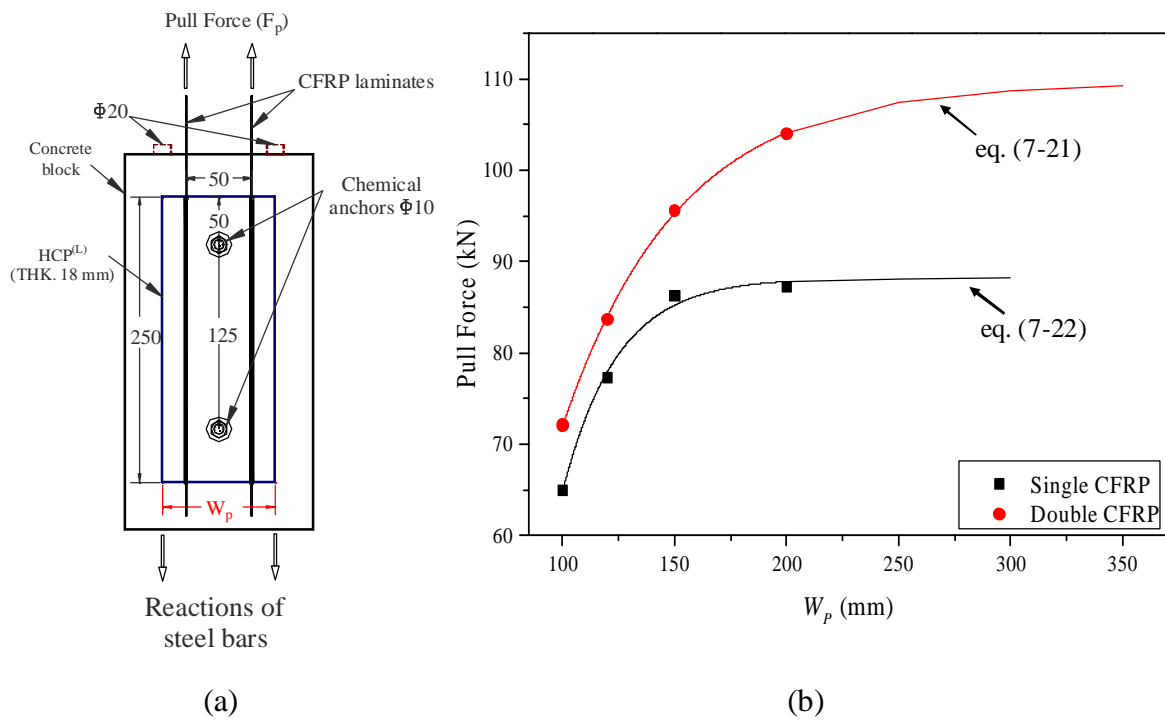


Figure 7.38: Effect of changes in the width of HCP$^{(L)}$ $(W_p)$ on pull force capacity of HCP$^{(L)}$-Concrete connection, (a) configuration of FE models, and (b) FE results in terms of $F_p$ *vs.* $W_p$.

Table 7.15: Obtained results from analyses of the models with $W_p$ being the parameter of the study (see Figure 7.38a)

| Label | $W_p$ (mm) | HCP$^{(L)}$ with single CFRP | | HCP$^{(L)}$ with double CFRP | |
|---|---|---|---|---|---|
| | | $F_p$ (kN) | Increase in $F_p$** (%) | $F_p$ (kN) | Increase in $F_p$** (%) |
| M_Wp100 | 100 | 65.0 | -24.7 | 72.1 | -24.6 |
| M_Wp120 | 120 | 77.3 | -10.5 | 83.7 | -12.4 |
| M_Vb125* | 150 | 86.3 | N.A. | 95.6 | N.A. |
| M_Wp200 | 200 | 87.3 | 1.1 | 104.0 | 8.8 |

* Reference model, see Figure 7.36a and Table 7.14 for details of this model.
** Percentage increase in pull force capacity $(F_p)$ of a connection as a results of changing $W_p$ with the $F_p$ of the model M_Vb125, with $W_p = 150$ mm, was taken as the reference value.

### 7.4.5 Failure mechanism of HCP$^{(L)}$-Concrete connection composed of epoxy adhesive and chemical anchors

The mechanism of failure for model M_Wp200 with double-CFRP laminate configuration is disused herein. Details of configuration of this model can be found in Figure 7.38a and Table 7.15.

The evolution of maximum principle strain in SHCC (indirect tensile damage indicator), von Mises equivalent stress in both top and bottom anchors, maximum principle plastic strain in concrete (indirect tensile damage indicator), scalar damage index for bond degradation in interface elements and the strain distribution along the length of CFRP laminate in different loading stages for model M_Wp200 are presented in Figure 7.39. The loading stages correspond to 50%, 76%, 78%, 87% and 100% of pull force capacity and also 78% of pull force capacity in post-peak regime.

Considering the damage state at the interface of SHCC-Concrete and the stress level in top anchor at loading stages of 50% $F_p$ and 76% $F_p$ it can be found that in consequence of severe damage in the interface of SHCC-Concrete which is progressed up to vicinity of the top anchor, the maximum stress in this anchor from 142 MPa has increased almost three times and reached 423 MPa. At the higher levels of loading, contribution of this top anchor

in shear stresses transfer mechanism between HCP[(L)] and RC block controlled the rate of damage progress at SHCC-Concrete interface zone towards the bottom edge of the plate. This top anchor was yielded at 85% $F_p$.

The contribution of the bottom anchor was only significant at a load level very close to peak pull force, when the damage was already progressed at a large portion of the interface of SHCC-Concrete and sliding of the HCP[(L)] promoted stress concentrations at this anchor.

At a load level of 78% of pull force capacity, a macro crack at the vicinity of the top anchor on the SHCC with removed elements can be observed. This macro crack developed at a maximum principle strain higher than 1.54% (the tensile strain hardening capacity of SHCC).

The failure of connection was due to a complete damage progress at the interface of CFRP-SHCC between two anchors; see figures corresponding to peak load $\left(F_p\right)$ and 78% $F_p$ in post-peak. At the peak force, a strain level of 1.32% is developed in CFRP laminates, which corresponds to exploiting 83% of its ultimate tensile strength. At this stage a relatively large amount of maximum principle plastic strain, 3.8%, was concentrated in concrete at the vicinity of the bottom edge of the plate, which indicates the formation of a macro crack at this region.
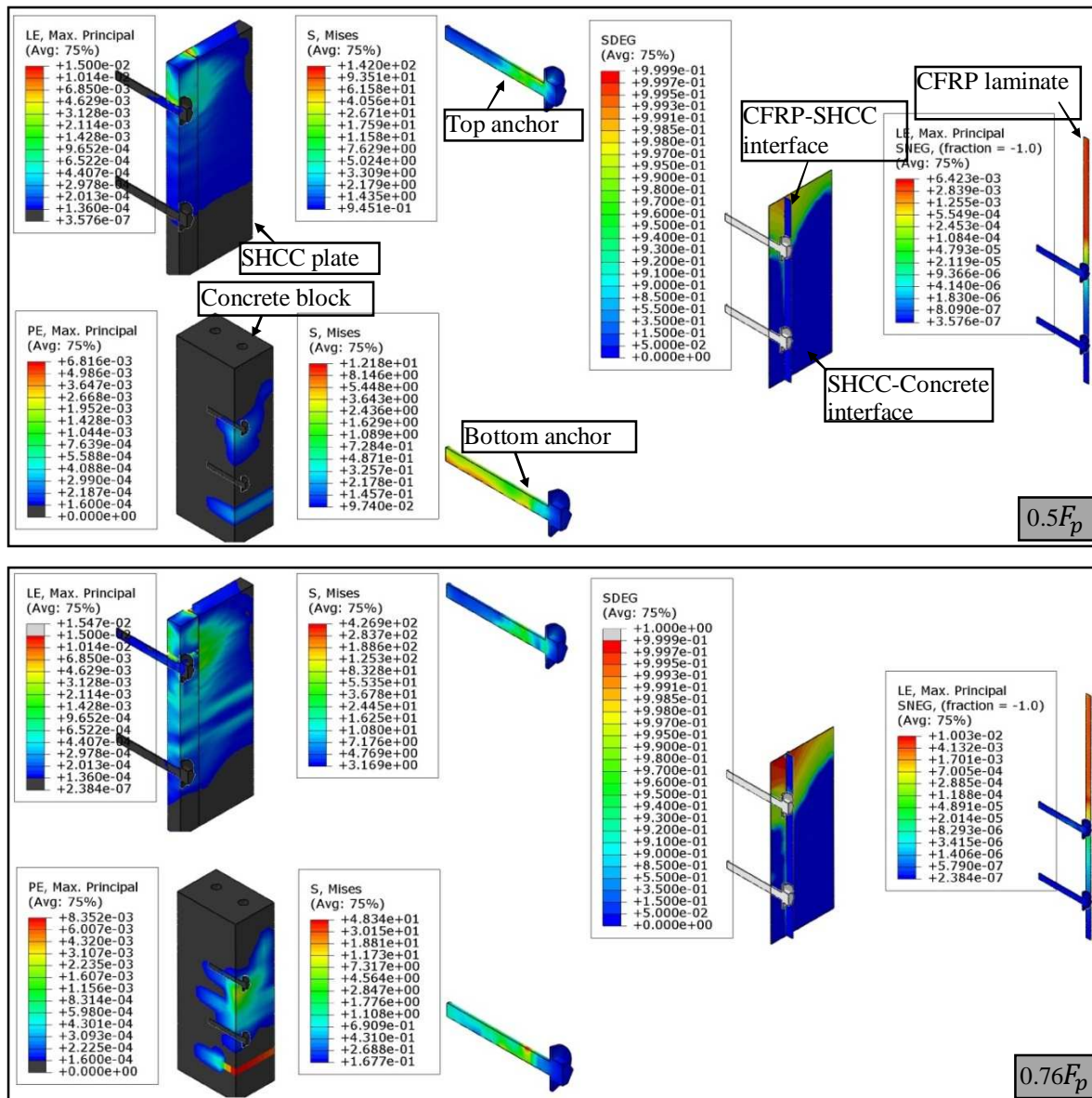
Figure 7.39: Damage evolution in M_Wp200 with double-CFRP laminate configuration in different loading stages of 50%, 76%, 78%, 87% and 100% of pull force capacity $\left(F_p\right)$ and at 78% of that but in post-peak regime, where "LE" is the state of maximum principle strain - in SHCC acts as indirect tensile damage indicator, "S" is the von Mises equivalent stress in top and bottom anchors, "PE" is the maximum principle plastic strain in concrete- indirect tensile damage indicator, and "SDEG" is the scalar damage index for bond degradation in interface elements (continued in next two pages).
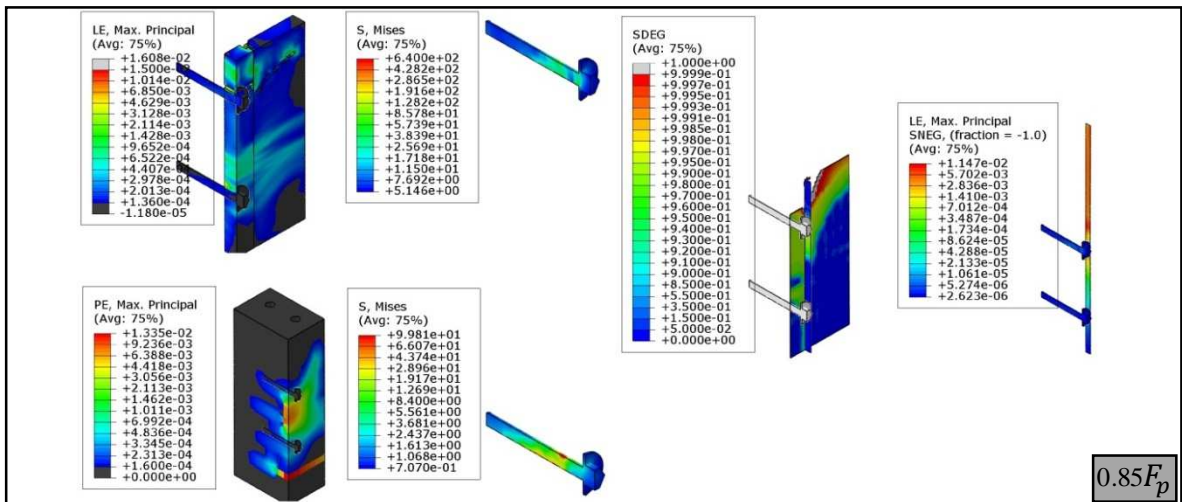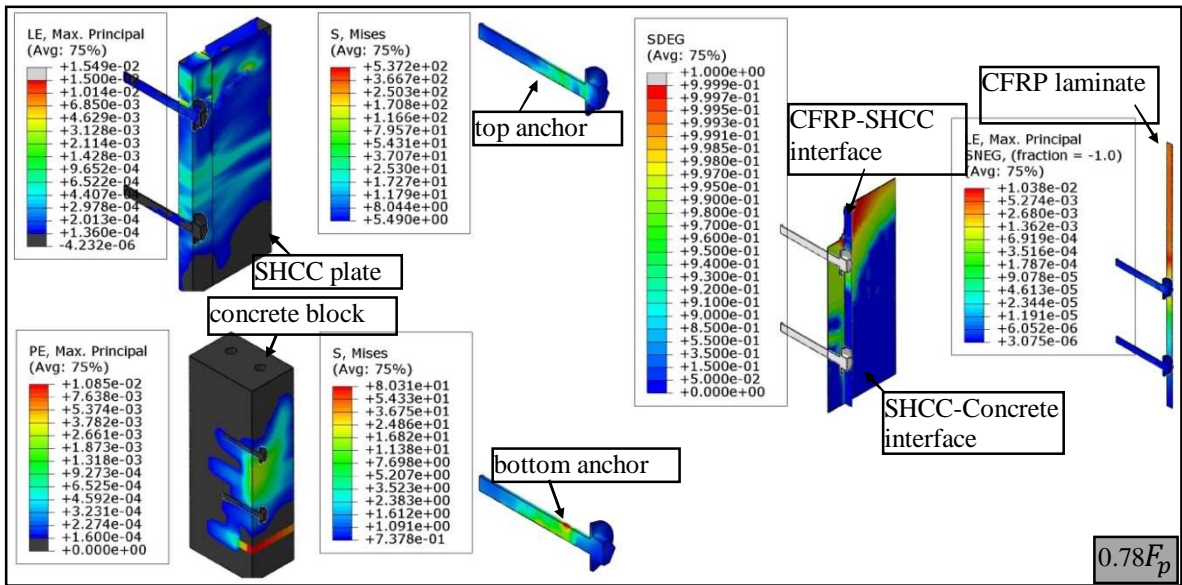
Continued from Figure 7.39
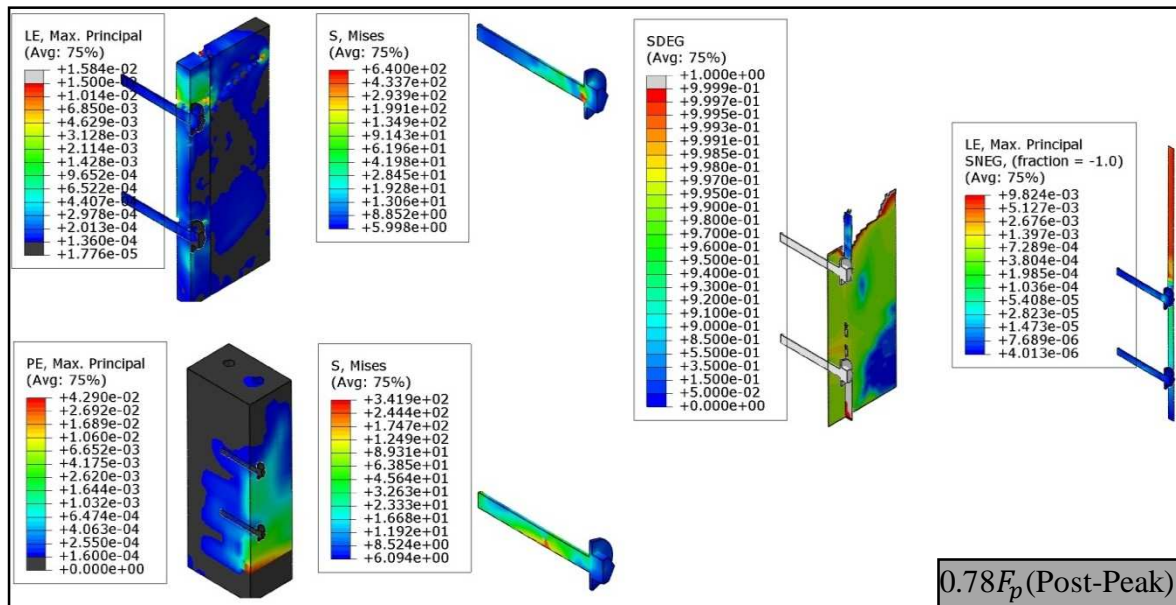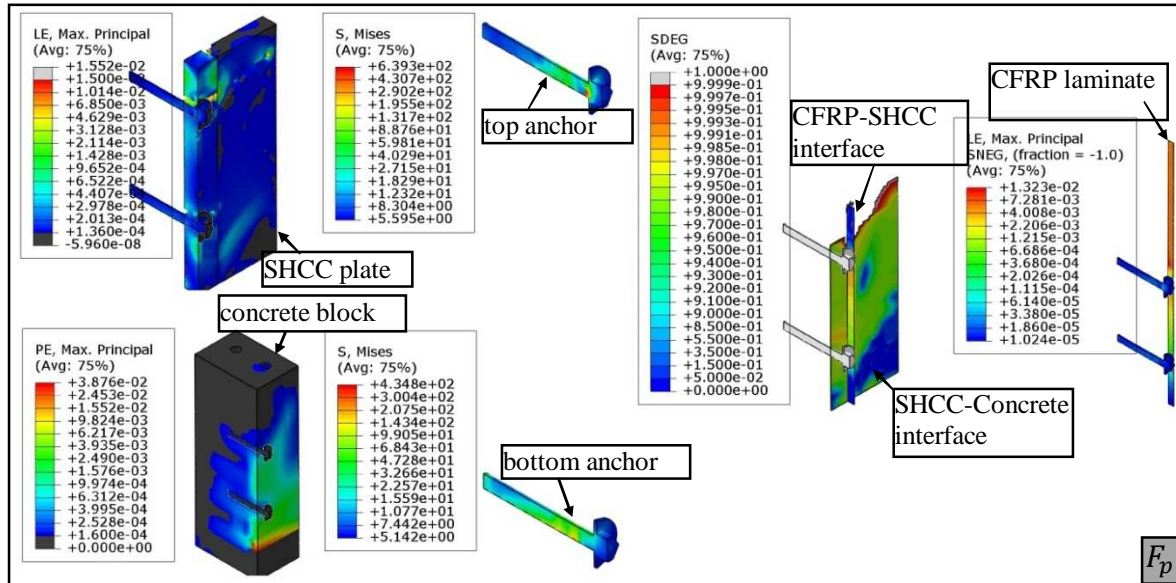
Continued from Figure 7.39

## 7.5 Summary and Conclusions

The characterization and optimization of the connection between HCP$^{(L)}$ and RC elements were studied through executing both experimental tests and FE simulations. Based on the results obtained from experimental tests and the adopted inverse analyses through FE simulations in the first phase of the study, the constitutive laws defining the local bond stress-slip models at the interface of the CFRP-SHCC and at the interface of the adhesively bonded HCP$^{(L)}$ to concrete, and also the shear-retention model for SHCC were estimated.

In the second phase of the study, based on a comprehensive FE modelling, initially, the relationships between the pull force capacity and CFRP-SHCC bond length was proposed and the CFRP-SHCC effective bond length was obtained.

Furthermore, in this second phase, the behavior of connection system between HCP$^{(L)}$ and RC block, composed of a combination of epoxy adhesive and chemical anchors, was studied. HCP$^{(L)}$ of these studies was composed of two rows of CFRP laminates. Following the results of these analyses, the effective width of this HCP$^{(L)}$, the most effective positions of the anchors and the distance of the grooves from the anchors were proposed.

It is worth noting that in all FE models two types of HCP$^{(L)}$, single-CFRP or double-CFRP laminate bonded in each of two grooves, were analyzed to also assess the influence of CFRP stiffness in the pull force capacity of the HCP$^{(L)}$.

According to the results of the above-mentioned studies, the following conclusions are notable among the others:

- For an adhesively bonded HCP$^{(L)}$ to the RC block, the SHCC is the weakest element of this connection, though, a cohesive failure of SHCC is expected to be the prevailing failure mode. The inter-laminar shear failure occurred in SHCC is associated with the absence of coarse aggregates in its structure and low content of fibers oriented out of its casting plane (along the plate through thickness).

- According to the results of the pull tests a CFRP-SHCC bond length of 90 mm is sufficient to mobilize the full tensile capacity of a single CFRP laminate with the specified mechanical and geometrical properties mentioned in this chapter.

- For connections including only chemical anchors, formation of inclined compressive struts are the main mechanism to transfer the tensile force from the CFRP laminate to the supporting anchors. This load transfer process is followed by the formation of diagonal cracks, whose opening was arrested by the fiber crack bridging mechanisms. This contribution of fibers resulted in maintenance of SHCC integrity up to a relatively high pull force.

- According to the results of the FE analyses, for an identical CFRP-SHCC bond length, larger CFRP stiffness results in a higher pull force capacity. However, the rate of this enhancement associates directly with the CFRP-SHCC bond length.

- Effective CFRP-SHCC bond lengths $\left(L_b^{ef}\right)$ of 200 and 250 mm, corresponding to pull force capacities $\left(F_p\right)$ of 39.5 kN and 57.5 kN, were determined for single- and double-CFRP configurations, respectively. However, due to the lower tensile rupture strength of the type of CFRP laminates studied in these studies, practically the bond development length of a single CFRP laminate is limited to the rupture force of the laminates.

- Increasing the distance of grooves from the alignment axis of the anchors inversely affected the pull force capacity. Taking into account, both the FE results and the practical considerations, a distance of 25 mm between groove and anchors was proposed.

- In the case of an HCP[(L)] with two rows of single-CFRP laminates which is adhesively bonded to the RC block, adding a single anchor positioned 200 mm far from the bottom edge of the plate resulted in 41% increase in the peak of pull force capacity. However, doubling the CFRP-laminates' stiffness reduced this efficiency up to 50%. Although adding a second anchor had only a marginal effect in connection pull force capacity, using this anchor is recommended specially to avoid the risk of plate-end peeling. In this case, the most effective distance between two anchors is 125 mm.

- For an HCP[(L)] composed of two rows of single-CFRP laminates bonded on an SHCC plate of 18 mm in thickness, optimized width and height of 150 mm and

250 mm, respectively, were obtained. This HCP[(L)] mobilized 87 kN pull force to the concert substrate when the HCP[(L)]-Concrete connection is composed of epoxy adhesive and two chemical anchors. For a double-CFRP laminate configuration this effective width was 250 mm, which was corresponding to a pull force capacity of 108 kN.

## Bibliography

[1] Suryanto B, Nagai K, Maekawa K. Modeling and analysis of shear-critical ECC members with anisotropic stress and strain fields. Journal of advanced concrete technology. 2010;8(2):239-58.

[2] Hillerborg A, Modéer M, Petersson PE. Analysis of crack formation and crack growth in concrete by means of fracture mechanics and finite elements. Cement and Concrete Research. 1976;6(6):773-81.

[3] ABAQUS. (2011) `ABAQUS Documentation', Dassault Systèmes, Providence, RI, USA.

[4] Rots J, Blaauwendraad J. Crack models for concrete, discrete or smeared? Fixed, multi-directional or rotating? 1989.

[5] Guo Z, Cao S, Sun W, Lin X. Experimental study on bond stress-slip behaviour between FRP sheets and concrete. FRP in construction, proceedings of the international symposium on bond behaviour of FRP in structures2005. p. 77-84.

[6] Cornelissen H, Hordijk D, Reinhardt H. Experimental determination of crack softening characteristics of normalweight and lightweight concrete. Heron. 1986;31(2):45-56.

[7] CEB-FIP MC90:1993. Design of concrete structures. CEB-FIP-Model-Code 1990.

[8] Mander J, Priestley M, Park R. Theoretical Stress-Strain Model for Confined Concrete. Journal of structural engineering. 1988;114(8):1804-26.

[9] Malm R. Shear cracks in concrete structures subjected to in-plane stresses. KTH, School of Architecture and the Built Environment (ABE), Civil and Architectural Engineering, Structural Design and Bridges; 2006.

[10] Obaidat Y. Structural retrofitting of concrete beams using FRP - debonding issues: Lund University; 2011.

## Chapter 8: Concluding Remarks

### 8.1 Summary and Conclusions

The present research work proposed a novel retrofitting element composed of a thin plate of SHCC reinforced with CFRP, and designated as "Hybrid Composite Plate (HCP)". According to the technique adopted to reinforce the SHCC plate, HCP was recognized as HCP$^{(S)}$ and HCP$^{(L)}$.

In the case of HCP$^{(S)}$ the SHCC plate is reinforced with carbon fabrics externally bonded to one of its faces, while in the structure of HCP$^{(L)}$, CFRP laminates are bonded into pre-sawn grooves on one of the faces of this plate. On the basis of the present research work HCP$^{(L)}$ has been patented in Portugal with the patent number 107111 [1].

This is the reinforced face of the HCP which is placed in contact with the concrete member to be retrofitted; hence, in this system, SHCC potentially protects the constituents of CFRP against severe environmental conditions.

The investigation reported in this thesis was mainly dedicated to the development of HCP and assessment of its structural efficiency to upgrade RC members with a variety of retrofitting demands. In this framework, the construction methodology (including SHCC material processing) to manufacture each type of HCP was introduced. The feasibility of attaching this prefabricated element to the RC members by means of either chemical anchors, adhesive or a combination thereof was investigated and validated.

Following, the main conclusions derived from the efficiency assessment of HCP for retrofitting RC elements with different structural upgrading demands, and optimizing HCP$^{(L)}$-Concrete connection are presented.

**Shear Strengthening:** The structural efficiency of HCP was preliminarily assessed through retrofitting short-span shear-critical RC beams. The results of three-point bending tests executed on the beams, retrofitted with either SHCC-plates, HCP$^{(L)}$ or HCP$^{(S)}$ attached to their lateral faces, were compared to those of the as-built beam and the beam strengthened with adhesively bonded U-shaped CFRP sheet. Moreover, for beams strengthened with SHCC-plates or HCPs, two different types of connections between the strengthening plate

and concrete substrate were investigated; one with only epoxy adhesive and the other one with a combination of epoxy adhesive and chemical anchors.

- According to the tests results, plain SHCC-plates bonded to the lateral faces of the beam increased the load carrying capacity up to 74%, as compared to that of the as-built beam, with only 24% enlargement in the beam's width. The premature detachment of the retrofitting scheme, occurred in the case of the beam with externally bonded U-shaped CFRP sheet, was not observed in the other beams, except for the one strengthened by means of adhesively bonded HCP$^{(S)}$. According to these observations, it seems that in the case of side-plates adhesively bonded to the concrete member, HCP$^{(S)}$ has a lower debonding resistance than HCP$^{(L)}$. However, an additional study is needed to comprehensively compare the retrofitting efficiency can be provided by each of these HCPs.

- HCPs were capable of altering the shear-tension failure mode, occurred in the as-built beam and the ones strengthened by SHCC plates, to a flexural failure mode, independent of their connection system to the RC beams. Moreover, an increase of up to 126% in the load carrying capacity of the HCP retrofitted beams, as compared to that of the as-built beam, was attained.

- The improvement in the deflection ductility in the case of HCP strengthened short-span shear-critical beams was more notable than that of the beam strengthened with U-shaped CFRP sheet. However, the extent of this enhancement was a function of the type of the HCP and its connection with the concrete substrate.

- The main advantage of introducing chemical anchors to the adhesive-based connection of strengthening plates to the concrete substrate, within the context of the study performed on the retrofitting of short-span beams, was restricting the sliding of the beams' longitudinal tension rebars. The structural advantage of this enhancement was reflected in reducing the rate of the post-peak load-decay in the case of retrofitted beams failed in flexure (HCP retrofitted ones), and higher shear

capacity in the case of the retrofitted beam failed in shear (the beam retrofitted with SHCC plates).

- These above-mentioned results highlight the promising HCPs' potential for retrofitting shear-critical deep or slender RC beams. Considering the limitations caused by the scale-effect and premature flexural failure of the HCP strengthened short-span shear-critical beams, a further study adopting large-scale deep and slender beams needs to be carried out in order to assess HCPs' performance for shear strengthening.

**Flexural Strengthening:** The efficiency of HCP$^{(L)}$ for flexural strengthening of large-scale RC beams was experimentally investigated. The influence of the configuration of CFRP laminates in the structure of HCP$^{(L)}$ and the connection of HCP$^{(L)}$ to the RC beam on the flexural performance of the strengthened beams were studied.

- In comparison with the results of the as-built beam, all adopted strengthening schemes presented a superior performance in terms of the load and deflection at the onset of cracking, yield load of the tension steel rebars, and ultimate load.

- HCP$^{(L)}$ strengthened beams, independent of the HCP$^{(L)}$ connection system, satisfied the ductility requirements recommended by ACI 440.2R-08 [2] for flexural strengthened beams. The largest deflection ductility, however, was obtained when only chemical anchors are used. In this case, the load carrying capacity was 72% larger than that of as-built beam, and up to 74% of tensile capacity of CFRP laminates at the peak load was mobilized. These results confirm a notable bearing capacity of HCP$^{(L)}$ provided from high ductility of the SHCC material.

- Adding anchors to an adhesively bonded HCP$^{(L)}$-RC beam connection prevented concrete cover detachment in the case of HCP$^{(L)}$ with lower CFRP stiffness $\left(E_f A_f\right)$, and delayed this detachment progress in the case of HCP$^{(L)}$ with higher CFRP stiffness. While in the former case the full tensile capacity of CFRP was exploited, in the latter one up to 83% of the tensile strength of CFRP laminates was mobilized. The increase in the flexural load carrying capacity in each of these

beams, as compared to the as-built beam, reached 107% and 167%, respectively. Moreover, it was found that the configuration of chemical anchors significantly affects their advantage in terms of preventing/delaying concrete cover detachment progress.

- All beams strengthened with HCP$^{(L)}$, fixed to the beam's soffit by means of either adhesive or a combination of adhesive and chemical anchors, presented deflections lower than $\frac{l_s}{250}$ at the service load corresponding to a stress level of $0.8 f_{st}^{y}$ in longitudinal tension steel rebars (recommendations of ACI 440.2R-08). Up to this deflection limit there were no visible cracks on the surface of the HCP$^{(L)}$s of these beams. When service limit state of Portuguese code between 60's and 80's is considered (the deflection limit of $\frac{l_s}{400}$), then compared to the results of the as-built specimen, the attainable increase in the service load, depending on HCP$^{(L)}$ stiffness and connection system, can be as high as 54%.

- It was also found that an HCP$^{(L)}$ connection based on a combination of chemical anchors and adhesive improves the serviceability performance of the retrofitted element more notably than a discrete connection made of only chemical anchors, since in the former connection the restrained sliding between the retrofitting element and the RC beam limits the beam's deflection as compared to the latter connection. Within this context, a further research is recommended to understand both the contribution of the HCP$^{(L)}$ and the influence of its connection system on the cracks size and distribution on the retrofitted beam.

- The proposed analytical approach and the developed section-layer based numerical model, were capable of predicting the flexural strength and load-deflection response of HCP$^{(L)}$ retrofitted RC beams (those including adhesive in their connection system), with a high precision, provided that the rupture of CFRP laminates is the prevailing flexural failure mode.

- In the cases where the detachment of concrete cover is expected, although the developed numerical strategy estimates the general load-deflection response with sufficient accuracy, the ultimate load needs to be restricted adopting a criterion

for the initiation of concrete cover detachment, for example, the CFRP strain at the initiation of the concrete cover detachment.

**Enhancing Seismic Performance:** HCP potential to dissipate a large amount of energy under cyclic loadings, e.g. seismic agitations, was another interesting characteristic assessed within the present research work. This HCP feature is due to the high SHCC toughness, in fact, forming several micro-cracks, their propagation, and their opening and closing in SHCC during the load reversals can dissipate a notable amount of energy in the retrofitted RC structures. This HCP potential was assessed through an experimental study carried out by repairing full-scale severely damaged beam-column joints and testing them under a combination of column axial load and lateral cyclic displacements (the same loading pattern imposed to their as-built virgin state).

- As compared to the test results of the beam-column joints in their virgin state, their responses in the repaired state showed a superior performance not only in terms of energy dissipation capacity, but also lateral load carrying capacity, beams flexural resistance and a lower degradation rate of their secant stiffness. For example, in the case of repairing based on attaching HCPs to all lateral faces of the elements of the beam-column joint, the enhancement in energy dissipation capacity was 84%.

- The comparison of NSM-CFRP reinforced cast-in-place SHCC solution with the attached HPCs revealed that a stronger interfacial bond between SHCC and concrete substrate adversely affects the displacement ductility and energy dissipation capacity of the retrofitted specimen. However, the negative influence on energy dissipation capacity was less pronounced.

- L-shape HCP$^{(S)}$ attached to each corner of the beam-column joint, using a combination of chemical anchors and adhesive, provided a continuous path of stress transfer between beams and columns, which consequently lowered shear stresses inside the joint region and prevented its shear failure.

- A high capacity of stress redistribution in SHCC resulted in multiple diffused crack formation around anchored regions, but no bearing failure was observed.

Moreover, due to the presence of chemical anchors, the progress in detachment of the CFRP sheets was efficiently restricted.

**HCP$^{(L)}$-Concrete Connection Optimization:** the following main conclusions can be drawn regarding the study performed on characterization and optimization of HCP$^{(L)}$ and its connection with the concrete substrate:

- The local bond stress-slip laws at the interfaces of CFRP-SHCC and HCP$^{(L)}$-Concrete were identified by means of a combination of experimental tests and inverse analysis based on FE modellings on series of connection specimens. Moreover, a shear-retention model for Mode II behavior of SHCC was calibrated.

- It was found that a CFRP-SHCC bond length of 90 mm is sufficient to mobilize the full tensile capacity of a single CFRP laminate with the geometrical and mechanical properties indicated in this study.

- SHCC was recognized as the weakest link in an adhesive-based connection between the HCP$^{(L)}$ and the RC block. The cohesive failure of SHCC was the prevailing failure mode due to the absence of coarse aggregates in its structure and low content of fibers oriented out of its casting plane (along the plate through thickness). Improving the shear characteristics of SHCC through modifying its matrix ingredients or mixing hybrid-fibers need to be investigated.

- Following a parametric FE study, the relationships between the HCP$^{(L)}$ pull force capacity and the CFRP-SHCC bond length, for the CFRP laminates of two different axial stiffness, were formulated. It was found that for an identical CFRP-SHCC bond length, higher CFRP stiffness results in a higher pull force capacity. The rate of this enhancement is directly related to the CFRP-SHCC bond length. Moreover, the effective CFRP-SHCC bond lengths were determined.

- According to the parametric FE study the optimized width of an HCP$^{(L)}$ composed of two rows of CFRP laminates, and details of its connection to the RC block aiming to mobilize the highest pull force to the substrate were determined and proposed. However, this study was limited to the specific types of SHCC, CFRP laminates and concrete used in the experimental program of this chapter.

Finally, it is reasonable to assume that HCP potentially offers superior long-term durability and temperature endurance than conventional FRP systems. In fact, the self-controlled fine crack width feature of SHCC assures that even up to the rupture strain of CFRP, the cracks in HCP remain impermeable against the penetration of harmful substances. Moreover, the epoxy adhesive used in the structure of HCP and in contact surface with the concrete substrate are covered with SHCC against temperatures relatively higher than $T_g$.

## 8.2 Suggestions for Future Works

- The study of the retrofitting of large-scale shear-critical beams by means of attaching HCP is interesting since in this system it is expected that the limitation in the bond length, imposed by the beam's web geometry, can be compensated through adding chemical anchors, which for example is not an appropriate solution in the case of shear-retrofitting using conventional externally bonded FRP systems.

- Further investigation is suggested to fully characterize the influence of anchors arrangement in preventing/delaying concrete cover detachment where RC beams are flexurally strengthened with HCP. The outcomes of this study can be implemented in the numerical strategy proposed in the present research work to improve its prediction of load-deflection response of such a retrofitted beam.

- It is interesting to study the influence of using bonding adhesives of different mechanical properties (e.g., of lower modulus of elasticity) on the performance of RC elements retrofitted with HCPs and subjected to cyclic loading (e.g., seismic loads).

- One of the concerns regarding the proposed cross-shape HCP as the repair scheme for the beam-column joints is perhaps associated with the relatively large length of its elements. Therefore, from the application feasibility point of view, a further investigation is recommended to verify the possibility of in-field assembling of several shorter pieces of HCPs.

- Further study employing the FE models developed in this research work can be carried out in order to assess the influence of remaining parameters on SHCC-RC connection response. Among others, perhaps the influence of mechanical properties of SHCC on the bearing capacity of HCP$^{(L)}$ and also concrete compressive strength in connection capacity and failure mode are the most important parameters to be investigated.

- Comparison of both short-term and long-term retrofitting efficiencies using HCP with those of FRP and TRM can be considered as an extension to the present research work as well.

**Bibliography**

[1] Esmaeeli E, Barros J, Sena-Cruz J. Portuguese Patent No. 107111 "Painel compósito híbrido para o reforço de estruturas de betão existentes e respetivo método de produção e de aplicação". Instituto Nacional da Propriedade Industrial. Portugal2013.

[2] ACI 440.2R-08:2008. Guide for the Design and Construction of Externally Bonded FRP Systems for Strengthening Concrete Structures: American Concrete Institute.

# Annex A

## VBA-Code to Predict Moment-Curvature of a Composite Section (Implemented in Microsoft Excel)

Outline of the "MainSheet" Excel Worksheet for the Definition of Section-Layers

| | A | B | C | D | E | F | G | H |
|---|---|---|---|---|---|---|---|---|
| 1 | Layer N | N. of Mat. Per Layer | Layer 1st Mat. | 1st Mat. Width | Layer 2nd Mat. | 2nd Mat. Width | Layer THK. | Layer Center Level (df) |
| 263 | 262 | 1 | Concrete5 | 150 | | | 1 | 261.5 |
| 264 | 263 | 1 | Concrete5 | 150 | | | 1 | 262.5 |
| 265 | 264 | 1 | Concrete5 | 150 | | | 1 | 263.5 |
| 266 | 265 | 1 | Concrete5 | 150 | | | 1 | 264.5 |
| 267 | 266 | 1 | Concrete5 | 150 | | | 1 | 265.5 |
| 268 | 267 | 1 | Concrete5 | 150 | | | 1 | 266.5 |
| 269 | 268 | 1 | Concrete5 | 150 | | | 1 | 267.5 |
| 270 | 269 | 1 | Concrete5 | 150 | | | 1 | 268.5 |
| 271 | 270 | 1 | Concrete5 | 150 | | | 1 | 269.5 |
| 272 | 271 | 2 | Steel2 | 15.7 | Concrete1 | 134.3 | 1 | 270.5 |
| 273 | 272 | 2 | Steel2 | 15.7 | Concrete1 | 134.3 | 1 | 271.5 |
| 274 | 273 | 2 | Steel2 | 15.7 | Concrete1 | 134.3 | 1 | 272.5 |
| 275 | 274 | 2 | Steel2 | 15.7 | Concrete1 | 134.3 | 1 | 273.5 |
| 276 | 275 | 2 | Steel2 | 15.7 | Concrete1 | 134.3 | 1 | 274.5 |
| 277 | 276 | 2 | Steel2 | 15.7 | Concrete1 | 134.3 | 1 | 275.5 |
| 278 | 277 | 2 | Steel2 | 15.7 | Concrete1 | 134.3 | 1 | 276.5 |
| 279 | 278 | 2 | Steel2 | 15.7 | Concrete1 | 134.3 | 1 | 277.5 |
| 280 | 279 | 2 | Steel2 | 15.7 | Concrete1 | 134.3 | 1 | 278.5 |
| 281 | 280 | 2 | Steel2 | 15.7 | Concrete1 | 134.3 | 1 | 279.5 |
| 282 | 281 | 1 | Concrete5 | 150 | | | 1 | 280.5 |
| 283 | 282 | 1 | Concrete5 | 150 | | | 1 | 281.5 |
| 284 | 283 | 1 | Concrete5 | 150 | | | 1 | 282.5 |

Outline of the "materials" Excel Worksheet for Material Properties

| | A | B | C | D | E | F | G | H | I | J | K | L |
|---|---|---|---|---|---|---|---|---|---|---|---|---|
| 1 | Steel | | CFRP | | Concrete | | Tension Softening | | Tension Stiffening | | SHCC | |
| 2 | $E_s$ | 215825 | $E_f$ | 164700 | $f_{cc}^m$ | -31.6 | $\varphi$ | 0.33 | $\beta_1$ | 0.6 | $E_{sh}$ | 18460 |
| 3 | $E_{sh}$ | 2158 | $\varepsilon_f^r$ | 0.0163 | $\varepsilon_{cc}^f$ | -0.005 | $\xi_1$ | 5 | $\beta_1$ | 0.45 | $f_{sh}^{cr}$ | 2.75 |
| 4 | $F_y$ | 536 | | | $E_c$ | 32500 | $\xi_2$ | 16 | $\psi_1$ | 5 | $\varepsilon_{sh}^u$ | 0.0154 |
| 5 | $\varepsilon_{sh}$ | 0.01 | | | | | | | $\psi_2$ | 0.85 | $f_{sh}^u$ | 3.5 |
| 6 | $\varepsilon_{su}$ | 0.1 | | | | | | | $\psi_3$ | 0.95 | $\zeta$ | 0.11 |
| 7 | $F_u$ | 629 | | | | | | | | | $\gamma_1$ | 5 |
| 8 | | | | | | | | | | | $\gamma_2$ | 9 |

## Module #1: Solver

```
Sub MomentCurvature()
'-------------------------------------------------------------------------------------------------------------------
' MomentCurvature Macro
'-------------------------------------------------------------------------------------------------------------------
Workbooks("MomentCurvature.xlsm").Activate
Sheets("MainSheet").Range("I2:Y100000").ClearContents
Sheets("MainSheet").Range("AE2:AJ100000").ClearContents

Dim material As String
Dim EP As Double
Dim fc As Double
Dim ECi As Double
Dim EPC1 As Double
Dim EPcu As Double
Dim EP200 As Double
Dim EP265 As Double
Dim EP275 As Double
Dim EP305 As Double
j = 2
EPt = 0
Inc = 0.0001 '0.00005
h = Cells(321, 8)
j = 2
F = 0
a = 0
q = 0
amin = 0
amax = 300
'--------------------------------------------- Basic Concrete Characteristics --------------------------------------
fc = Sheets("materials").Cells(2, 6)
EPcu = Sheets("materials").Cells(3, 6)
ECi = Sheets("materials").Cells(4, 6)
EPC1 = -(0.07 * (-fc) ^ 0.31) / 100
'-----------------------------------------------------Start of Solver-----------------------------------------------
If 2 * EPC1 < EPcu Then Stop
1  ' Stop
 For i = 2 To 321
   st1 = 0
   st2 = 0
   df = Cells(i, 8)
   EP = EPt / (h - a) * (df - a)
    ' EP = (EPc / a) * (a - df)
'--------------------------------------Calculate Stress in Mid-Height of Each Layer-------------------------------
   material = Cells(i, 3)
   st1 = SelectMaterial(material, EP, fc, ECi, EPC1, EPcu)
   material = Cells(i, 5)
   If material = "" Then
     st2 = 0
   Else
     st2 = SelectMaterial(material, EP, fc, ECi, EPC1, EPcu)
   End If
'-------------------------------------------------------------------------------------------------------------------
```

```
    f1 = st1 * Cells(i, 4) * Cells(i, 7)
    f2 = st2 * Cells(i, 6) * Cells(i, 7)
    F = f1 + f2 + F
    m = f1 * df + f2 * df + m

  If i = 320 Then
    f3 = F
  End If

  If i = 321 Then
    EPc = (0 - a) * EPt / (h - a)
    f4 = F
'-----------------------------------------------------Write---------------------------------------------------------
    Cells(1, 15) = a
    Cells(1, 16) = EPc
    Cells(1, 17) = F
  End If

Next i

  If Abs(F) < 0.001 Then
      q = 0
      EPc = (0 - a) * EPt / (h - a)
      x = EPt / (h - a)

      d275 = Cells(276, 8)
      EP275 = EPt / (h - a) * (d275 - a)

      material = Cells(276, 3)
      st275s = SelectMaterial(material, EP275, fc, ECi, EPC1, EPcu)

      material = Cells(276, 5)
      st275c = SelectMaterial(material, EP275, fc, ECi, EPC1, EPcu)

      d201 = Cells(201, 8)
      EP200 = EPt / (h - a) * (d201 - a)
      material = Cells(201, 3)
      st200 = SelectMaterial(material, EP200, fc, ECi, EPC1, EPcu)

      d305 = Cells(306, 8)
      EP305 = EPt / (h - a) * (d305 - a)
      material = Cells(306, 5)
      st305 = SelectMaterial(material, EP305, fc, ECi, EPC1, EPcu)

  Cells(j, 18) = x
  Cells(j, 19) = m
  Cells(j, 20) = EPt
  Cells(j, 21) = EPc
  Cells(j, 22) = a
  Cells(j, 23) = F

  Cells(j, 24) = EP305 * 100
  Cells(j, 25) = st305

  'Tension Softening
```

```
    Cells(j, 31) = EP200 * 100
    Cells(j, 32) = st200

    'Tension Stiffening
    Cells(j, 33) = EP275 * 100
    Cells(j, 34) = st275c

    'Steel Tension
    Cells(j, 35) = EP275 * 100
    Cells(j, 36) = st275s

    'df = Cells(i, 8)
    'If EP306 > 0.0159 Then GoTo 11
  '
10  'If EP306 > 0.0159 Then Stop
    j = j + 1
    EPt = EPt + Inc
    EPc = (0 - a) * EPt / (h - a)

  If EPc < EPcu Then

    GoTo 5
  Else
    GoTo 3
  End If

End If

  If F > 0 Then
    amin = a
    a = (amax + amin) / 2
    F = 0
    m = 0
  End If

  If F < 0 Then
    amax = a
    a = (amax + amin) / 2
    F = 0
    m = 0
  End If

GoTo 1

3
amin = 0
amax = 300
a = 0

GoTo 1
'------------------------------------------------------------Write--------------------------------------------------------------
11  F = 0
   m = 0
For i = 2 To 321
   st1 = 0
```

```
    st2 = 0

  df = Cells(i, 8)
  EP = EPt / (h - a) * (df - a)
  'EP = (EPc / a) * (a - df)


'----------------------------------------Calculate Stress in Mid-Height of Each Layer--------------------------------
  material = Cells(i, 3)
  st1 = SelectMaterial(material, EP, fc, ECi, EPC1, EPcu)
  material = Cells(i, 5)
  If material = "" Then
    Stop
    st2 = 0
  Else
    st2 = SelectMaterial(material, EP, fc, ECi, EPC1, EPcu)
  End If
'-------------------------------------------------------------------------------------------------------------------
  f1 = st1 * Cells(i, 4) * Cells(i, 7)
  f2 = st2 * Cells(i, 6) * Cells(i, 7)
  F = f1 + f2 + F
  m = f1 * df + f2 * df + m

  Cells(i, 9) = EP
  Cells(i, 10) = st1
  Cells(i, 11) = st2
  Cells(i, 12) = f1
  Cells(i, 13) = f2
  Cells(i, 14) = F

Next i
 GoTo 10
'--------------------------------------------------------- Write ---------------------------------------------------
4 Stop
5

End Sub
```

## Module #2: Constitutive Laws of Materials

```
Public Function SelectMaterial(material As String, EP As Double, fc As Double, ECi As Double, EPC1 As
Double, EPcu As Double) As Double
Dim st As Double
    '-------------------------------------------------------Steel------------------------------------------------------------
    Est = Sheets("materials").Cells(2, 2)
    Esh = Sheets("materials").Cells(3, 2)
    Fy = Sheets("materials").Cells(4, 2)
    EPsh = Sheets("materials").Cells(5, 2)
    EPsu = Sheets("materials").Cells(6, 2)
    Fsu = Sheets("materials").Cells(7, 2)
    EPy = Fy / Est
    '-------------------------------------------CFRP Laminate---------------------------------------------------
    Ecfrp = Sheets("materials").Cells(2, 4)
    EPrcfrp = Sheets("materials").Cells(3, 4)
    '-------------------------------------------Concrete General------------------------------------------------
    fc = Sheets("materials").Cells(2, 6)
    EPcu = Sheets("materials").Cells(3, 6)
    ECi = Sheets("materials").Cells(4, 6)
    EPC1 = -(0.07 * (-fc) ^ 0.31) / 100
    Stcr = 0.3 * (-fc - 8) ^ (2 / 3) ' MPa
    EPcr = Stcr / ECi
    '-------------------------------------------Plain Concrete---------------------------------------------------
    s0 = Sheets("materials").Cells(2, 8)
    e0 = Sheets("materials").Cells(3, 8)
    e1 = Sheets("materials").Cells(4, 8)
    m1 = ECi * (s0 - 1) / (e0 - 1)
    m2 = ECi * (0 - s0) / (e1 - e0)
    '-------------------------------------------CFRP/Steel Reinforced Concrete------------------------------------
    s2 = Sheets("materials").Cells(2, 10)
    s3 = Sheets("materials").Cells(3, 10)
    e2 = Sheets("materials").Cells(4, 10)
    e3 = Sheets("materials").Cells(5, 10)
    e4 = Sheets("materials").Cells(6, 10)
    '-------------------------------------------SHCC-------------------------------------------------------------
    Ecishcc = Sheets("materials").Cells(2, 12)
    Stcrshcc = Sheets("materials").Cells(3, 12)
    EPtushcc = Sheets("materials").Cells(4, 12)
    Stushcc = Sheets("materials").Cells(5, 12)
    EPcrshcc = Stcrshcc / Ecishcc
    A11 = Stushcc / Stcrshcc
    A22 = Sheets("materials").Cells(6, 12)
    B11 = Sheets("materials").Cells(7, 12)
    B22 = Sheets("materials").Cells(8, 12)
    '-------------------------------------------Constitutive Laws------------------------------------------------
    Select Case material

        Case "PC"
            'Compression
            L = EP / EPC1
            R = ECi / (ECi - (fc / EPC1))
            EPcc = (2 * EPC1)
            If (EPcc <= EP And EP <= 0) Then st = (fc * L * R) / (R - 1 + L ^ R)
```

If (EPcu <= EP And EP < EPcc) Then st = (2 * fc * R / (R - 1 + 2 ^ R)) * ((EPcu - EP) / (EPcu - 2 * EPC1))

If EP <= EPcu Then st = 0

'Tension

If EP >= 0 And EP < EPcr Then st = EP * ECi

If EP >= EPcr And EP <= e0 * EPcr Then st = Stcr + m1 * (EP - EPcr)

If EP > e0 * EPcr And EP < e1 * EPcr Then st = s0 * Stcr + m2 * (EP - e0 * EPcr)

If EP >= e1 * EPcr Then st = 0

Case "RC"

'Compression

L = EP / EPC1

R = ECi / (ECi - (fc / EPC1))

EPcc = (2 * EPC1)

If (EPcc <= EP And EP <= 0) Then st = (fc * L * R) / (R - 1 + L ^ R)

If (EPcu <= EP And EP < EPcc) Then st = (2 * fc * R / (R - 1 + 2 ^ R)) * ((EPcu - EP) / (EPcu - 2 * EPC1))

If EP <= EPcu Then st = 0

mmm = e2 * EPcr

'Tension

If EP >= 0 And EP < EPcr Then st = EP * ECi

If EP >= EPcr And EP <= e2 * EPcr Then st = Stcr + ECi * ((s2 - 1) / (e2 - 1)) * (EP - EPcr)

If EP > e2 * EPcr And EP < e3 * EPy Then st = s2 * Stcr

If EP > e3 * EPy And EP < e4 * EPsu Then st = s2 * Stcr + Stcr * ((s3 - s2) / (e4 * EPsu - e3 * EPy)) * (EP - e3 * EPy)

If EP >= e4 * EPsu Then st = s3 * Stcr

Case "SHCC"

If EP >= 0 And EP < EPcrshcc Then st = EP * Ecishcc

If EP >= EPcrshcc And EP < EPtushcc Then st = Stcrshcc + ((A11 * Stcrshcc - Stcrshcc) / (EPtushcc - EPcrshcc)) * (EP - EPcrshcc)

If EP >= EPtushcc And EP < B11 * EPtushcc Then st = A11 * Stcrshcc + ((A22 * Stcrshcc - A11 * Stcrshcc) / (B11 * EPtushcc - EPtushcc)) * (EP - EPtushcc)

If EP >= B11 * EPtushcc And EP < B22 * EPtushcc Then st = A22 * Stcrshcc + ((0 - A22 * Stcrshcc) / (B22 * EPtushcc - B11 * EPtushcc)) * (EP - B11 * EPtushcc)

If EP >= B22 * EPtushcc Then st = 0

Case "Steel"

Z = EPsu - EPsh

V = ((Fsu / Fy) * (30 * Z + 1) ^ 2 - 60 * Z - 1) / (15 * Z ^ 2)

'Compression

If EP < 0 Then EP1 = Abs(EP) Else EP1 = 0

If EP1 > 0 And EP1 < EPy Then st = -EP1 * Est

If EP1 >= EPy And EP1 < EPsh Then st = -Fy

If EP1 >= EPsh And EP1 < EPsu Then st = -Fy * ((V * (EP1 - EPsh) + 2) / (60 * (EP1 - EPsh) + 2) + (EP1 - EPsh) * (60 - V) / (2 * (30 * Z + 1) ^ 2))

If EP1 >= EPsu Then st = 0

'Tension

If EP >= 0 And EP < EPy Then st = EP * Est

If EP >= EPy And EP < EPsh Then st = Fy

If EP >= EPsh And EP < EPsu Then st = Fy * ((V * (EP - EPsh) + 2) / (60 * (EP - EPsh) + 2) + (EP - EPsh) * (60 - V) / (2 * (30 * Z + 1) ^ 2))

```
        If EP >= EPsu Then st = 0

    Case "CFRP"
        P = Esh * (EPsu - EPsh) / (Fsu - Fy)
        ' Tension
        If EP >= 0 And EP < EPrcfrp Then st = EP * Ecfrp
        If EP >= EPrcfrp Then st = 0
    End Select
  SelectMaterial = st

End Function
```